

eeFACT2016

58th ICFA Advanced Beam Dynamics Workshop
on High Luminosity Circular e+e-Colliders

24-27 October 2016

Cockcroft Institute at Daresbury Laboratory, UK



The goals of the eeFACT16 workshop are:

- Reviewing and documenting the state of the art in e-e+factory design.
- Preparing plans for the commissioning of SuperKEKB and advancing contributions to the FCC, CEPC & tau-charm design efforts.
- Fostering synergies and new collaborations across communities, in particular with the low-emittance light sources.
- Jointly developing novel solutions to outstanding problems.

INTERNATIONAL PROGRAMME COMMITTEE

Ralph Assmann, DESY
Marica Biagini, INFN-LNF
Alain Blondel, U. Geneva
Alex Chao, SLAC
Weiren Chou, IHEP and FNAL
Yoshihiro Funakoshi (co-Chair), KEK
Andrew Hutton, TJNAF
Eugene Levichev, BINP
Katsunobu Oide, KEK
Qing Qin (co-Chair), IHEP
Peter Ratoff, CI, Lancaster University
Jorg Wenninger, CERN
Ferdinand Willeke, BNL
Frank Zimmermann (co-Chair), CERN

LOCAL ORGANIZING COMMITTEE

Peter Ratoff, Chair, CI, Lancaster University
Peter McIntosh, CI, STFC
Andy Wolski, CI, University of Liverpool
Rob Appleby, CI, University of Manchester
Guoxing Xia, CI, University of Manchester
Sue Waller, CI, STFC

For further information
contact the meeting
administrator:
sue.waller@stfc.ac.uk



www.cockcroft.ac.uk/events/eeFACT2016



eeFACT2016

58th ICFA Advanced Beam Dynamics Workshop on High Luminosity Circular e+e-Colliders

24-27 October 2016 - Cockcroft Institute at Daresbury Laboratory, UK



Contents

Preface	i
Contents	iii
Committees	iv
Papers	1
MOOTH1 – Overview of High Energy e^+e^- Factories	1
MOOTH2 – Commissioning of SuperKEKB	4
MOOTH3 – Overview on Low Energy Collider	9
MOOTH4 – Performance and Perspective of Modern Synchrotron Light Sources	17
MOT3AH2 – Higgs Factory Concepts	25
MOT3AH3 – Implementation of Round Colliding Beams Concept at VEPP-2000	32
MOT3BH3 – Issues in CEPC Pretzel and Partial Double Ring Scheme Design	39
MOT4H6 – Simulations of Polarization Levels and Spin Tune Biases in High Energy Leptons Storage Rings	43
MOT4H7 – Ideas for Siberian Snakes and Spin Rotators in Very High Energy e^+e^- Rings	47
TUT1AH1 – Issues on IR Design at SuperKEKB	49
TUT1AH2 – Design of Interaction Region and MDI at CEPC	53
TUT1AH3 – The FCC-ee Interaction Region Magnet Design	57
TUT1BH2 – Study of Coherent Head-tail Instability Due to Beam-beam Interaction in Circular Colliders Based on Crab Waist Scheme	61
TUT2H1 – Top-up Injection for a Future Electro-positron Collider	66
TUT2H2 – Injector Linac Upgrade and New RF Gun Development for SuperKEKB	74
TUT2H3 – Design study of CEPC Booster	79
TUT2H4 – Top-up Injection Schemes for HEPS	85
TUT2H5 – Towards a Preliminary FCC-ee Injector Design	90
TUT2H6 – Electron Sources and Polarization	94
TUT3AH1 – Collective Effects Issues for FCC-ee	100
TUT3AH2 – Instability Issues in CEPC	108
TUT3AH3 – Beam-based Impedance Measurement Techniques	112
TUT3AH5 – Electron Cloud and Ion Effects and Their Mitigation in FCC-ee	120
TUT3AH6 – Electron Cloud at SuperKEKB	125
TUT3AH7 – Electron Cloud and Collective Effects in the Interaction Region of FCC-ee	130
TUT3AH9 – Feedback Systems for FCC-ee	136
TUT3BH2 – Optics Correction and Low Emittance Tuning at the Phase 1 commissioning of SuperKEKB	143
TUT3BH3 – Luminosity Tuning at KEKB	147
TUT3BH4 – Coupling and Dispersion Correction for the Tolerance Study in FCC-ee	151
WET1H1 – Beam Instrumentation Needs for a Future Electron-Positron Collider Based on PEP-II Observations	157
WET1H3 – Beam Instrumentation in SuperKEKB	164
WET1H4 – Measurement of Beam Polarization and Beam Energy in One Device	168
WET2H4 – New Cavity Techniques and Future Prospects	173
WET2H7 – LLRF Controls Including Gap Transients at KEKB and Plans for SuperKEKB	177
WET3AH2 – High Efficiency Klystron Development for Particle Accelerators	185
WET3AH3 – Extraction Line and Beam Dump for the Future Electron Positron Circular Collider	188
WET3BH1 – Improvement of Efficiency of Klystron to Apply the CPD Method	192
THS1H1 – Summary of Design Concepts	195
THS1H2 – Summary of Optics Issues	199
THS1H4 – Summary of IR and MDI Session	200
THS1H5 – Summary Beam-beam Session, eeFACT2016 Workshop	203
THS1H6 – Summary of Injector and Beam Injection	206
THS2H1 – Summary of Impedance Issues and Beam Instabilities	210
THS2H2 – Summary of Machine Tuning Session	216
THS2H3 – Summary of Beam Instrumentation and Beam Diagnostics Session	220
THS2H4 – SRF Working Group Summary	223
THS2H6 – Summary: Joint Session of Other Technologies and Energy Efficiency	231

Appendices	235
List of Authors	235
Institutes List	237

Committees

International Programme Committee:

Ralph Assmann, DESY
 Marica Biagini, INFN-LNF
 Alain Blondel, U. Geneva
 Alex Chao, SLAC
 Weiren Chou, IHEP Beijing Yoshihiro Funakoshi (co-Chair), KEK
 Andrew Hutton, TJNAF
 Eugene Levichev, BINP
 Katsunobu Oide, KEK
 Qing Qin (co-Chair), IHEP
 Peter Ratoff, CI, Lancaster University Jorg Wenninger, CERN
 Ferdinand Willeke, BNL
 Frank Zimmermann (co-Chair), CERN

Local Organising Committee:

Peter Ratoff, Chair, CI, Lancaster University
 Peter McIntosh, CI, STFC
 Andy Wolski, CI, University of Liverpool
 Rob Appleby, CI, University of Manchester
 Guoxing Xia, CI, University of Manchester
 Sue Waller, CI, STFC

OVERVIEW OF HIGH ENERGY e^+e^- FACTORIES

K. Oide*, KEK, Oho, Tsukuba, Ibaraki, Japan

Abstract

Designs of e^+e^- colliders from the Z-pole and above are introduced. Two projects, CEPC and FCC-ee, are discussed. If we compare their schemes, a partial double ring (CEPC) and a full double ring (FCC-ee), find several important differences that affect the performance. On the other hand, there are a number of similarities in both designs, such as the crab-waist scheme, crossing angle, optimization of the dynamic aperture, etc.

INTRODUCTION

At least there are two plans have been studied for high energy e^+e^- circular collider factories. One is CEPC in China, which consists of a circular Higgs factory (phase I) + super pp collider (phase II) in the same tunnel. Another is FCC-ee, which is an e^+e^- collider as potential intermediate step or a possible first step for a 100 TeV pp -collider (FCC-hh). The design of CEPC has been considering several schemes: single-ring with pretzel, partial double-ring (PDR), and full double-ring. Although CEPC has not decided the scheme yet, the main efforts have been focused on the PDR scheme in this year. Thus we pick PDR for CEPC in this article. On the other hand, FCC-ee has chosen a full double ring scheme.

DESIGN PARAMETERS

Table 1 compares important design parameters of two machines at several beam energies. The parameters are as of this workshop.

PROGRESS

As for FCC-ee, a baseline beam optics [1] has been chosen, characterized by:

- A highest-energy circular e^+e^- collider ultra-low β^* of 1 mm and more than $\pm 2\%$ dynamic momentum acceptance.
- Features a local chromatic correction for the vertical plane. The dynamic aperture was optimized by varying the strengths of about 300 independent $-I$ sextupole pairs in the arcs.
- A crab-waist scheme was implemented by reducing the strength of an existing sextupole in the chromatic correction section with proper betatron phases, instead of adding another dedicated sextupoles.
- Synchrotron radiation is accommodated by tapering the magnet strengths in the arcs, and by a novel asymmetric IR/final-focus layout.
- The RF system is concentrated in two straight sections. A common system provides maximum voltage for $t\bar{t}$ running, where operation requires only few bunches. Two separate RF systems, one for either beam, are used at lower beam energies.
- The optics was designed to match the footprint of a future hadron collider (FCC-hh) along the arcs. Due to the asymmetric interaction region (IR) layout the e^+e^- interaction point (IP) is displaced transversely by about

Table 1: Design Parameters of FCC-ee and CEPC(PDR) together with LEP2. SR: synchrotron radiation, BS: beamstrahlung. FCC-ee has two options at Z.

	FCC-ee				CEPC(PDR)		LEP2
Beam energy [GeV]	45.6		120	175	45.6	120	105
Beam current [mA]	1450		30	6.6	67.6	16.9	3
Bunches/beam	91500	30180	770	78	1100	107	4
Energy loss/turn [GeV]	0.03		1.67	7.55	0.061	2.96	3.34
SR power for two beams [MW]	100				8.2	100	22
RF voltage [GV]	0.2	0.4	3	10	0.11	3.48	3.5
Bunch length (SR) [mm]	1.6	1.2	2.0	2.1	3.78	2.7	12
Bunch length (+BS) [mm]	3.8	6.7	2.4	2.5	4.0	2.95	12
Emittance $\epsilon_{x,y}$ [nm, pm]	0.1, 1	0.2, 1	0.6, 1	1.3, 2.5	0.88, 8	2.05, 6.2	22, 250
$\beta_{x,y}^*$ [m, mm]	1, 2	0.5, 1	1, 2	1, 2	0.1, 1	0.27, 1.3	1.5, 50
Long. damping turns	1320		72	23	748	41	31
Crossing angle [mrad]	30				30		0
Beam lifetime [min]	185	94	67	57	79	20	434
Luminosity/IP [$10^{34} \text{ cm}^{-2} \text{ s}^{-1}$]	70	207	5.1	1.3	4.5	3.1	0.0012

* Katsunobu.Oide@kek.jp

9 m from the hadron IP. This allows a lepton detector to be installed in the same cavern.

- The optics, the footprint, and the dynamic aperture are compatible with a top-up injection mode of operation based on a full-energy booster ring installed in the same tunnel and, in the IR, following the path of the hadron collider ring.

Figure 1 shows the obtained dynamic aperture for FCC-ee.

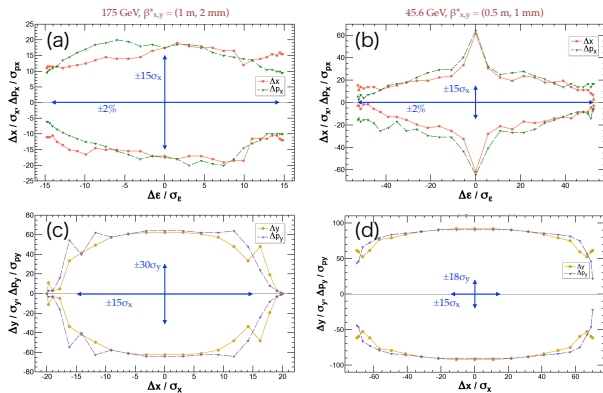


Figure 1: Dynamic apertures after an optimization of sextupoles via particle tracking. (a, c): $\beta_{x,y}^* = (1 \text{ m}, 2 \text{ mm})$, 50 turns at $t\bar{t}$, (b, d): $\beta_{x,y}^* = (0.5 \text{ m}, 1 \text{ mm})$, 2,650 turns at Z . (a, b): z - x plane with $J_y/J_x = 0.2\%$ for (a) and 0.5% for (b). (c, d): x - y plane with $\delta = \Delta E = 0$. The aperture was searched both in (a,b) x and p_x or (c,d) y and p_y directions. The number of turns is chosen to correspond to about 2 longitudinal damping times at each energy. The blue lines show the DAs required for the beamstrahlung and the top-up injection. Effects in Table 2 are taken into account except for the radiation fluctuation and the beam-beam effect.

The design of CEPC has made significant progress [2] with the partial double-ring scheme:

- Integrated optics with the arc, interaction region (IR), RF are designed with the PDR scheme.
- Difficulties of the single ring scheme such as long-range beam-beam effect, dynamic aperture due to pretzel orbit, high HOM loss due to a short bunch, etc., have been totally removed.
- The local chromaticity corrections system (LCCS) has been designed for both planes. The crab sextupoles are incorporated in the vertical LCCS sextupoles.
- $90^\circ/90^\circ$ FODO cells are employed in the arc with non-interleaved sextupole pairs.
- The dynamic aperture has been optimized by varying up to 192 sextupole families in the arc to provide nearly sufficient momentum acceptance. Almost all effects have been included except for the energy-sawtooth.

Table 2: Effects Taken into Account in the Estimation of the Dynamic Aperture for FCC-ee.

Effect	Included?	Significance at $t\bar{t}$
Synchrotron motion	Yes	Essential
Radiation loss in dipoles	Yes	Essential – improves the aperture
Radiation loss in quadrupoles	Yes	Essential – reduces the aperture
Radiation fluctuation ^a	Yes	Essential
Tapering	Yes	Essential
Crab waist	Yes	transverse aperture is reduced by $\sim 20\%$
Solenoids	Yes	minimal, if locally compensated
Maxwellian fringes	Yes	small
Kinematical terms	Yes	small
Higher order fields/errors/misalignm	No	Essential , development of correction/tuning scheme is necessary

^a not included in the optimization

- Advanced algorithms such as Multi-objective optimization have been developed and applied for the design.

Figure 2 shows the obtained dynamic aperture for CEPC PDR.

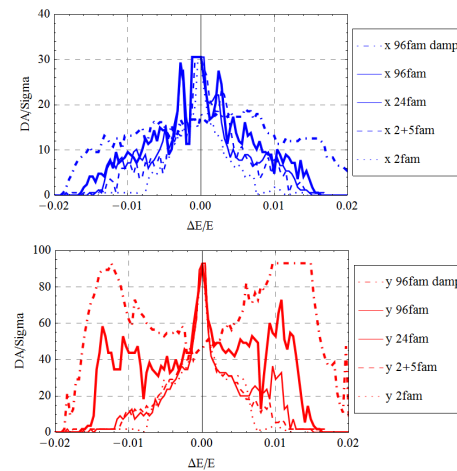


Figure 2: The dynamic apertures of CEPC PDR [2] in x - z (top) and y - z planes (bottom). The lines show the difference between the number of sextupole families. The largest ones include synchrotron radiation damping, and are approaching the goal momentum aperture $\pm 2\%$.

Table 3: Major Differences in the Design of CEPC(PDR) and FCC-ee.

	CEPC(PDR)	FCC-ee
Scheme	Partial Double Ring	Full Double Ring
Circumference [km]	61	100
\mathcal{L} at H [10^{34} cm $^{-2}$ s $^{-1}$]	3	5
\mathcal{L} at Z [10^{34} cm $^{-2}$ s $^{-1}$]	3.6	200
Energy sawtooth effect	uncorrectable, can be reduced by inserting more RF sects.	completely correctable
SR to IP	190 keV @ H	100 keV @ $t\bar{t}$
$\beta_{x,y}^*$ @ Z [m, mm]	0.1, 1	0.5, 1
Strong-strong beam-beam instability	may be weaker than FCC-ee due to smaller β_x^*	luminosity reduced by ~50% @ Z if it occurs
Local chromaticity correction	X & Y	Y
Dynamic aperture	In progress	OK without machine errors
Hadron machine	can co-exist	removes the ee machine

SIMILARITIES

Both designs for CEPC and FCC-ee are obtaining similarities, by employing the PDR scheme for CEPC:

- 2 IPs/ring, with 30 mrad crossing angle and crab waist.
- Vertical local chromaticity correction system incorporated with crab sextupoles.
- 90°/90° FODO cells in the arc.
- Non-interleaved sextupole pairs with $-I$ transformation.
- Optimization of dynamic aperture with hundreds of sextupole families.

DIFFERENCES

An apparent difference between their designs are in their circumferences: around 61 km for CEPC and 100 km for FCC-ee. The energy reach of CEPC is limited to Higgs due to the circumference, no matter which scheme is chosen. This is a choice of the project, and not an issue of the design scheme. Besides the circumference, there are important differences between two designs. Table 3 compares these differences. The major issues are:

- CEPC's luminosity is roughly 1/40 of FCC-ee's at Z . This is a main limitation by the PDR scheme, just depends on the length of the double-ring part.

- The level of synchrotron radiation toward the IP: CEPC is ~2x higher than FCC-ee.
- Tapering is not possible in PDR. Thus the effect of the energy sawtooth on the dynamic aperture must be studied.
- CEPC has smaller β_x^* , which is 1/5 of FCC-ee's. It may mitigate the strong-string beam-beam instability [3].
- CEPC has a local chromaticity correction for both planes, which enables the smaller β_x^* .

ACKNOWLEDGEMENT

The author thank Huiping Geng, Qing Qin, Dou Wang, Yiwei Wang, and Yuan Zhang for providing materials of CEPC. Also thank M. Benedikt, A. Blondel, A. Bogomyagkov, M. Koratzinos, E. Levitchev, J. Wenninger, F. Zimmermann, and all contributors for the design of FCC-ee beam optics.

REFERENCES

- [1] K. Oide, et al, arXiv:1610.07170(2016).
- [2] H.P. Geng *et al.*, presented at eeFACT2016, Daresbury, UK, September 2016, paper MOT3BH3.
- [3] K. Ohmi, presented at eeFACT2016, Daresbury, UK, September 2016, paper TUT1BH2.

COMMISSIONING OF SuperKEKB

Y. Funakoshi*, KEK, Tsukuba, Japan

Abstract

After five and half years upgrade works from KEKB to SuperKEKB, the Phase 1 commissioning of SuperKEKB was conducted from February to June in 2016. This paper describes the progress of the Phase 1 commissioning. Brief plans of the Phase 2 commissioning are also described.

INTRODUCTION

The purpose of SuperKEKB is to search a new physics beyond the standard model of the particle physics in the B meson regime. SuperKEKB consists of the injector linac, a damping ring for the positron beam and two main rings; *i.e.* the low energy ring (LER) for positrons and the high energy ring (HER) for electrons, and the physics detector named Belle II. The beam energies of LER and HER are 4GeV and 7GeV, respectively. The design beam currents of LER and HER are 3.6A and 2.6A, respectively. The design luminosity is $8 \times 10^{35} \text{cm}^{-2}\text{s}^{-1}$. Design machine parameters are shown in Table 1. More details of SuperKEKB are described elsewhere [1].

The main issues for SuperKEKB are listed below.

- IR design and dynamic aperture
- Optics corrections and low emittance tuning
- Magnet alignment strategy
- Beam-beam related issues
- Orbit control to maintain beam collision
- Beam loss and beam injection
- Effects of electron clouds
- Injector upgrade for low emittance and high intensity beams
- Detector beam background

Some of those are studied in the Phase 1 commissioning this year.

BEAM COMMISSIONING

Commissioning Strategy

The beam commissioning will proceed in three steps; *i.e.* Phase 1, 2 and 3. The Phase 1 commissioning has been already done for 5 months this year. In Phase 1, the superconducting final focus doublets and other correction coils (called QCS) and the physics detector (called Belle II) were not installed and no beam collision was performed. The

* yoshihiro.funakoshi@kek.jp

Table 1: Design machine Parameters of SuperKEKB (Values in parentheses of the emittances correspond to those at zero bunch currents).

	LER	HER	Units
Beam Energy	4.000	7.007	GeV
Beam Current	3.6	2.6	A
# of Bunches	2500		
Circumference	3016.315		m
Hor. Emittance	3.2(1.9)	4.6(4.4)	nm
Ver. Emittance	8.6(2.8)	11.5(1.5)	pm
β -function at IP(H/V)	32/0.27	25/0.30	mm
Moment. compaction	3.25	4.55	$\times 10^{-4}$
Energy spread	8.08	6.37	$\times 10^{-4}$
RF voltage	9.4	15.0	MV
Hor. tune ν_x	44.53	45.53	
Ver. tune ν_y	46.57	43.57	
Synchrotron tune ν_s	-0.0247	-0.0280	
Energy loss / turn	1.87	2.43	MeV
Damping time $\tau_{x,y}/\tau_s$	43/22	58/29	ms
Bunch length	6.0	5.0	mm
Beam-beam param. H	0.0028	0.0012	
Beam-beam param. V	0.0881	0.0807	
Luminosity	8×10^{35}		/cm ² /s

idea of Phase 1 is that we conduct sufficient vacuum scrubbing and other beam tuning such as beam injection before installing the Belle II detector. The commissioning of the damping ring, which is newly introduced for SuperKEKB, will start in November 2017. The Phase 2 commissioning of main rings will start in January 2018 and continue for about 5 months. In Phase 2, the QCS magnets and the main part of the Belle II detector will be installed. But the vertex detector will not be installed in Phase 2. This is based on an idea that the vertex detector, which is very sensitive to the beam background, should be installed after sufficient beam tuning with the QCS magnets. From the viewpoint of the accelerator tuning, we can make tuning on condition that hardware components are fully installed except for the beam background tuning to the vertex detector. The target luminosity in Phase 2 is $1 \times 10^{34} \text{cm}^{-2}\text{s}^{-1}$. The Phase 3 commissioning will start in autumn 2018. In this phase, the vertex chamber will be installed and we will continue beam tuning aiming at the design luminosity in parallel with the physics experiment.

Results of Phase 1 Commissioning

Missions in Phase 1 After five and half years of upgrade work from KEKB, the Phase 1 beam commissioning of SuperKEKB started on Feb. 1st this year and finished at the end of June this year. Missions of the commissioning in

Phase 1 are startup of each hardware component, establishment of beam operation software tools, preparation of Belle II detector, an optics study and tuning without QCS and the detector solenoid magnet and other machine studies. As for preparation for installation of the Belle II detector, vacuum scrubbing is of essential importance. The Belle II group require 1 month vacuum scrubbing with the beam current of 0.5-1 A, which corresponds to the beam dose of 360-720 Ah. In addition, the study on the beam background to the detector is also important by using a test detector named Beast. As for the optics study, Phase 1 provides us with an unique opportunity to conduct a study without the detector solenoid nor QCS. The low emittance tuning is an important item.

History of beam Commissioning Figure 1 shows the history of Phase 1 commissioning. In the figure, the red, violet and cyan dots show the beam currents, averaged vacuum pressure and the beam lifetime, respectively. The commissioning started on Feb. 1st. The first week was devoted to tuning of the beam transport lines. Tuning of the beam injection to LER (positron ring) started on Feb. 8th and the beam injection succeeded on Feb. 10th. Tuning of the beam injection to HER (electron ring) started on Feb.22nd and the beam injection succeeded on Feb. 25th. The beam currents increased gradually and the maximum beam currents of LER and HER in Phase 1 were 1010 mA and 870 mA, respectively. In the latter half of June, we had to decrease the HER beam current due to a trouble of a stripline kicker of the transverse bunch-by-bunch feedback. The beam current increase proceeded at a much faster pace than KEKB. The reasons for this short rise time of the beam currents are thought to be in the following.

- The transverse bunch-by-bunch feedback system worked validly from the very beginning of the commissioning.
- Each hardware component has been upgraded based on the experiences at KEKB and worked validly.
- Software tools for the beam operation has been established based on the experiences at KEKB and worked from the beginning.
- We had less troubles compared with the case at KEKB.

We owe the quick start of SuperKEKB largely to the experiences at KEKB. The machine parameters in Phase 1 are shown in Table 2.

Vacuum scrubbing In LER, 98 % of vacuum chambers of KEKB were replaced with new ones. In arc sections, ante-chambers with TiN coating to suppress the effects of the electron clouds and mitigate the issues of heating by the synchrotron radiation were adopted. In HER, the most of the vacuum chambers in arc sections are reused from KEKB. About 18 % of vacuum chambers in the whole ring were

Table 2: Machine Parameter in Phase 1 (Horizontal emittances are values at zero bunch currents).

	LER	HER	Units
Beam Energy	4.000	7.007	GeV
Beam Current	1010	870	mA
# of Bunches	1576	1576	
Hor. Emittance	1.8	4.6	nm
Momentum compaction	2.45	4.44	$\times 10^{-4}$
Energy spread	7.7	6.3	$\times 10^{-4}$
RF voltage	7.45	11.99	MV
Hor. tune ν_x	44.53	45.53	
Ver. tune ν_y	46.57	43.57	
Synchrotron tune ν_s	-0.0190	-0.0246	
Energy loss / turn	1.87	2.43	MeV
Damping time $\tau_{x,y}/\tau_s$	44/22	58/29	ms
Bunch length	4.8	5.4	mm

replaced with the new ones in HER. Vacuum scrubbing proceeded smoothly as is seen in Fig. 1. The averaged vacuum pressures of LER and HER were 4.7×10^{-7} Pa with the beam current of 1.01 A on June 17th and 5.7×10^{-8} Pa with the beam current of 0.87 A on June 22nd, respectively. The corresponding beam lifetime of those times of LER and HER were about 60 min. and 200 min. The main processes to determine the beam lifetime are the Touschek effect and the scattering from the residual gas particles. The cumulative doze of the beam currents in Phase 1 of LER and HER are 776 Ah and 662 Ah and we have met the requirement from the Belle II group. More details on the commissioning of the vacuum system are written elsewhere [2].

Issue related to high beam current operation One of the issues was the longitudinal coupled bunch instability observed in LER. The instability was first observed around 660mA. The mode number was ~ -40 . We needed the use of longitudinal feedback system to suppress it. At KEKB, we never needed the longitudinal feedback system. The source of the instability may be the 0 and π modes of the ARES cavities which were detuned for operational budget reduction. The ARES cavity consists of three cavities; *i.e.* an acceleration cavity, an energy storage cavity and a coupling cavity and so there are three modes near the RF frequency. The $\pi/2$ mode is used for beam acceleration. The 0 and π modes are almost symmetric with respect to the RF frequency and the contributions to the beam instability from those modes are almost canceled out. However, when the detuning frequency is large, this cancellation breaks. In HER, Sometimes, detuned cavities induced the instability due to the fundamental mode. The -1 mode damper was set up to suppress the instability.

Another problem was a nonlinear vacuum pressure rise against the beam current observed in LER. As shown in Fig. 2, the LER vacuum pressure had a nonlinear behavior and got rapidly worse with an increasing beam current. The

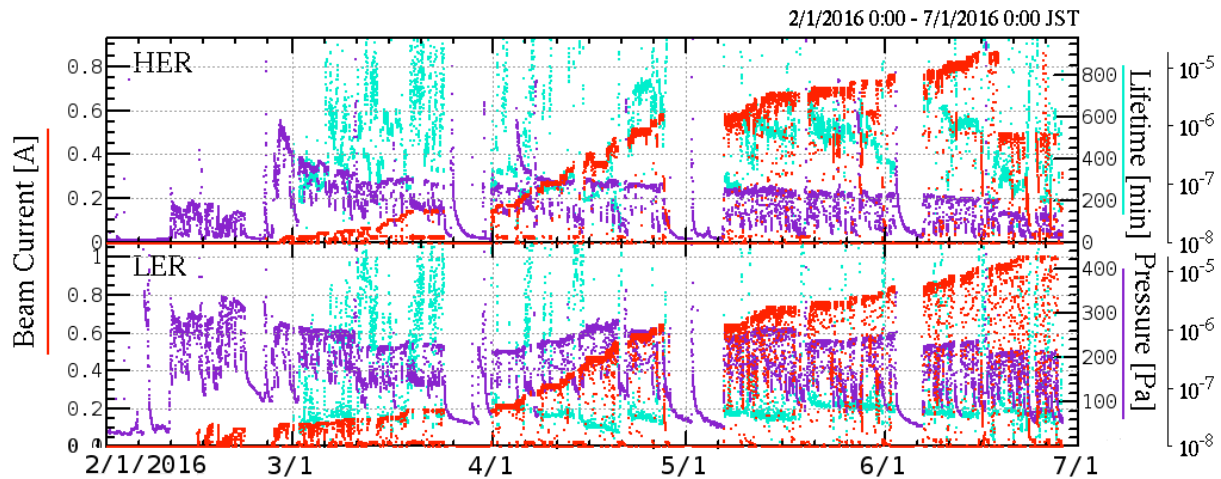


Figure 1: History of SuperKEKB operation in Phase 1.

aluminum bellows chambers were suspected of inducing this phenomenon. The other vacuum chambers in LER are applied TiN coating. But no TiN coating is applied to them. The secondary electron emission coefficient for them is high and it may induce electron multipactoring. At a test vacuum chamber without TiN coating installed in LER, the measured electron density showed a similar nonlinear behavior as function of the beam current to the vacuum pressure rise. As shown in Fig. 2, the beam current dependence of vacuum pressure at a bellows chamber became rather linear by installing a solenoid magnet or a permanent magnet which creates a solenoid-like magnetic field. The magnetic field of the solenoid magnet and the permanent magnet were ~ 50 Gauss and ~ 100 Gauss, respectively. During a short operation break in the beginning of June, permanent magnets were installed at all of ~ 800 such aluminum bellows chambers. As a result, the nonlinear vacuum pressure rise was suppressed with the filling pattern for vacuum scrubbing (1576 bunches in total, 3.06 RF bucket spacing in average) up to 1 A of the beam current.

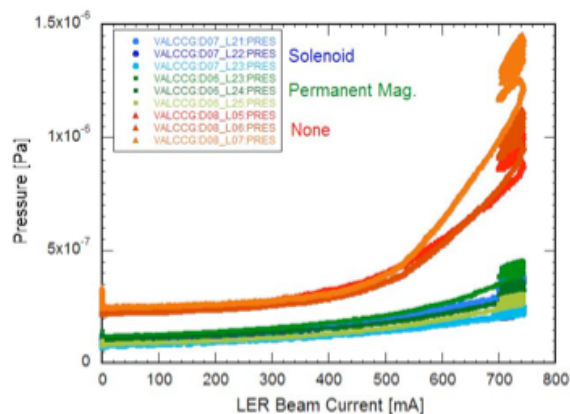


Figure 2: Nonlinear vacuum pressure against beam current in LER.

Vertical beam size blowup in LER In LER of KEKB, the electron clouds caused the vertical beam size blowup and gave a serious limit to the luminosity, although various efforts were devoted to suppress it throughout the beam operation period of KEKB. Based on the experiences at KEKB, we made more fundamental countermeasures for the problem. The vacuum chambers newly introduced are antechambers with TiN coating. In the wiggler section, the chambers have clearing electrodes. The vacuum chambers of the bending magnets have the grooved structure. In addition to those countermeasures which were already made, we plan to install solenoid magnets in the drift section which have not yet been installed in Phase 1. In Phase 1, we observed a vertical beam size blowup as shown in Fig. 3(a). In the graph, the vertical beam size with an emittance control knob is also shown. This knob can create vertical dispersions all around the ring. In the vacuum scrubbing operation, we intentionally enlarge the beam size to increase the beam lifetime mainly from the Touschek effect. In both cases, the vertical beam size started to increase at around 500 mA and showed serious blowup at higher beam currents with a filling pattern used for the vacuum scrubbing (1576 bunches in total, 3.06 RF bucket spacing in average). As is described above, permanent magnets were installed at all of ~ 800 aluminum bellows chambers in June. By installing the permanent solenoid magnets, it was also expected that the beam size blowup is suppressed. As shown in Fig. 3(b), the blowup was almost suppressed up to 800 mA with the same filling pattern except for the slow blowup which we haven't understood yet. To study the blowup in more details, we conducted a machine study with shorter bunch spacing a part of which is shown in Fig. 3(a). The details of this study are described elsewhere [3].

Optics corrections and low emittance tuning Details of the optics correction are described elsewhere [4]. In this paper, only some highlights on the low emittance tuning in Phase 1 are described. The X-Y coupling correction and dispersion correction are important to get a low vertical

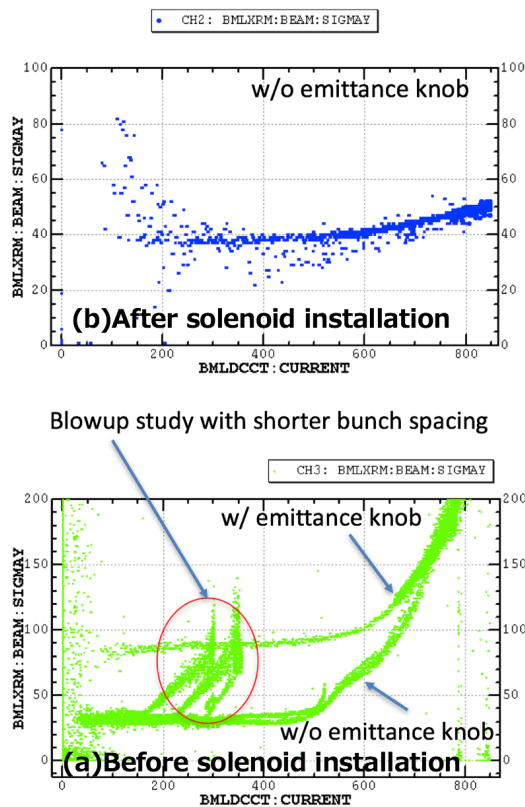


Figure 3: Vertical beam size as function of beam current in LER. (a) before solenoid installation, (b) after solenoid installation.

emittance. While the corrections in HER went well, we encountered a difficulty in the LER corrections. The obstacle of the corrections was leakage magnetic field from the Lambertson septum magnets whose main component is skew-Q. The Lambertson magnet is a part of the beam abort system. To cope with this problem, we took two measures. First, we activated skew-Q coils wound at a focusing sextupole magnet downstream of the septum magnet. Second, we installed a permanent skew-Q magnet upstream of the septum magnet. The picture and drawing of the permanent skew-Q magnet is shown in Fig. 4. With the two countermeasures, both the X-Y coupling and the vertical dispersion were improved. Figure 5 shows results of measurements of the X-Y coupling before taking the countermeasures and after them. In the measurement, vertical leakage orbits caused by 6 independent horizontal steering kicks were observed. In the graph, such 6 vertical leakage orbits are shown as function of the ring position where $s=0$ corresponds to the IP. The horizontal steering kicks were $200\mu\text{rad}$ and the horizontal orbit amplitude was about 2-3 mm in its peaks. As for correctors for X-Y coupling, we employ skew-Q windings on sextupole magnets. Around $s = -1300\text{m}$, there remains some large X-Y coupling. At the location of $s = \sim 1400\text{m}$, a Lambertson DC septum magnet is located. As a result of the two countermeasures, the residual X-Y coupling at around the Lambertson septum almost vanished. Similarly the verti-

cal dispersion was much improved by the countermeasures. Table 3 shows the reaching point of the optics corrections in Phase 1 together with typical values of KEKB LER. The dispersions and the beta-beats in the list are r.m.s values of the deviations from the design measured at the BPMs around the rings. As seen in the table, the beta-beats are already smaller than the typical values of KEKB, although the distance of the horizontal betatron tunes from the half integer is longer than KEKB. From the measured vertical dispersion and the X-Y coupling, the vertical emittances of LER and HER are estimated as $\sim 6.8\text{ pm}$ and $\sim 8.0\text{ pm}$, respectively. In LER, the vertical emittance is calculated from the beam size measurement using the X-ray monitor as $\sim 10\text{ pm}$ and is consistent with the optics measurement. On the other hand, the vertical emittance from a measurement by using the X-ray monitor in HER was $\sim 200\text{ pm}$ and there was a large discrepancy between the estimation from the optics measurement and the measurement by using the X-ray monitor. We took this issue seriously and investigated it in detail. First, we tried the calibration of the X-ray monitor by using the emittance control knob. Second, we measured the beam size with changing the vertical beta function at the source point of the X-ray monitor. As for the calibration, the calibration constant was determined to be 1.18, which means that the measured size is larger than the true beam size by a factor 1.18. From the measurement by changing the beta function at the source point, it turned out that the measured beam size of the X-ray monitor includes a large offset. The measured value is about $\sim 40\mu\text{m}$ and the offset value is more than $30\mu\text{m}$. Here, the measured size is assumed to be the square root of the square-sum of the true beam size and the offset value. This large offset was also supported by an independent analysis using a data on the beam size dependence of the Touschek beam lifetime. The origin of this large offset has not been understood. Even with this large offset and the calibration factor, an estimated vertical emittance in HER is about 40 pm and is still much larger than the estimation from the optics measurement. We will continue the investigation on this problem in Phase 2 commissioning.

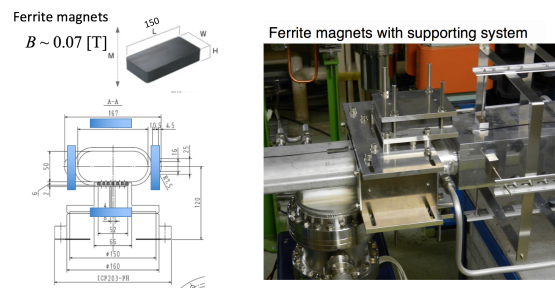


Figure 4: Picture and drawing of permanent skew-Q magnet.

Plans for Phase 2 Commissioning

In the present plan, the commissioning of the damping ring (DR) will start Nov. 20th 2017 prior to the commis-

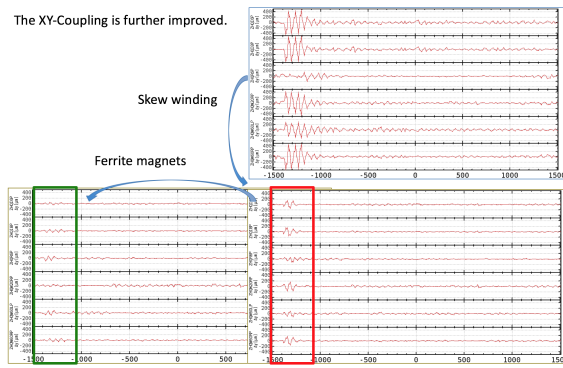


Figure 5: Improvement of X-Y coupling with two counter-measures at LER.

Table 3: Reaching point of optics corrections in Phase 1.

	LER	HER	LER KEKB	Units
X-Y coupling ^{*)}	0.9	0.6		%
$\Delta\eta_x$ r.m.s.	8	11	10	mm
$\Delta\eta_y$ r.m.s.	2	2	8	mm
$\Delta\beta_x/\beta_x$ r.m.s.	3	3	6	%
$\Delta\beta_y/\beta_y$ r.m.s.	3	3	6	%

*) Ratio of average of r.m.s values by 6 vertical leakage orbits (horizontal to vertical).

sioning of main rings. It will take about 3 months to finish the DR commissioning including vacuum scrubbing. The commissioning of HER will start in middle of January 2018 in parallel with the DR commissioning. The commissioning of LER will start in middle of February. The Phase 2 commissioning will continue for about 5 months and finish in middle of June. Important tasks in Phase 2 commissioning are in the following.

- Performance check of QCS magnets
- Squeezing IP beta functions at IP
- Belle II beam BG study and tuning
- Beam collision tuning with Nano beam scheme
- Luminosity tuning

In Phase 2, the target luminosity is $1 \times 10^{34} \text{cm}^{-2}\text{s}^{-1}$. This luminosity is achieved with the beam currents of 1.0 A (LER) and 0.8 A (HER), the horizontal beta functions at IP of 128 mm (LER) and 100 mm (HER), the vertical beta functions at IP of 2.16 mm (LER) and 2.4 mm (HER) and the vertical beam-beam parameters of 0.024 (LER) and 0.0257 (HER). With these parameters, a strong-weak beam-beam simulation shows that a luminosity of $2 \times 10^{34} \text{cm}^{-2}\text{s}^{-1}$ can be achieved. In the last 1 month, we plan to conduct the physics experiment, although there is no vertex detector. Before the physics experiment, we will operate SuperKEKB on $\Upsilon(4S)$ and we will discuss the beam energy in the physics experiment with the Belle II group.

REFERENCES

- [1] T. Abe *et al.*, Technical Design Report of SuperKEKB, in preparation and to be published as a KEK report. An preliminary version is seen in <https://kds.kek.jp/indico/event/15914/>
- [2] Y. Suetsugu *et al.*, "First Commissioning of the SuperKEKB Vacuum System", in *Proc. IPAC'16*, Busan, Korea, May 2016, paper TUOCB01.
- [3] H. Fukuma *et al.*, "Electron cloud at superKEKB", presented at eeFACT2016, Daresbury, UK, October 2016, paper TUT3AH6.
- [4] Y. Ohnishi *et al.*, "Optics Correction and Low Emittance Tuning at the Phase 1 commissioning of SuperKEKB", presented at eeFACT2016, Daresbury, UK, October 2016, paper TUT3BH2.

OVERVIEW OF THE LOW ENERGY COLLIDERS*

Q. Qin[†], Institute of High Energy Physics, Chinese Academy of Sciences, Beijing, P.R. China

Abstract

The low energy colliders cover the beam energy from 500 MeV to 2.5 GeV or more, with relatively small sizes from several ten meters to several hundred meters in circumference. The physics requirements on phi particle, charm quark, tau lepton, Ds, XYZ particles, and R value measurement. Since the beam energies are close to the low energy synchrotron radiation light sources, these machines could be used as parasitic light sources. In this paper, we will investigate some selected beam dynamics issues of the low energy colliders like DAFNE [1], VEPP-2000 [2], BEPCII [3], and CESRc [4], the ways on how to enhance the luminosity at these colliders, the operation and some upgrades during operation, and the future possible super charm tau factory.

INTRODUCTION

Colliders for high energy physics study, have been developed from the pioneer AdA, built in Frascati in 1962, to the LHC, which started its operation at CERN from 2008, within the past five decades. During this half a century, General speaking, the higher beam energy, the larger collider size. Most of the low energy collider could be run at an energy range, and some could be used as a parasitic synchrotron facility. For example, BEPCII keeps running for 10 years as a parasitic light source with the $E_b = 2.5\text{GeV}$ and $I=250\text{mA}$, and can provide photons to users with 14 beam lines. Figure 1 gives the luminosity evolution of different lepton colliders during the past 40 years.

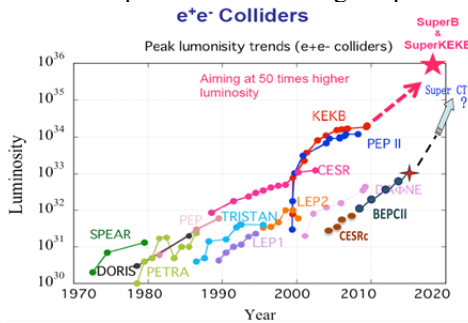


Figure 1: Lepton colliders' luminosity evolution within the past 40 years.

In this paper, low energy colliders, such as DAFNE, VEPP-2000, BEPCII and CESRc will be reviewed from their beam dynamics studies, luminosity tuning and enhancements, operation with some upgrades on the machines, to the future development to super charm-tau factory. Beam dynamics study covers such a large field that we cannot overview all of these machines and topics in this paper, so we just select several important issues. Since they are all operational machines, the topics like dynamic aperture, error effects, and interaction region design, which are all design topics, will not be included.

* Work supported by the Innovation Funding of IHEP 2015.

[†] qinq@ihep.ac.cn

DAFNE is a phi-factory collider with double-ring, running at the $E_{cm} = 1\text{ GeV}$ for phi particle with the design luminosity of $5 \times 10^{32} \text{ cm}^{-2} \text{ s}^{-1}$, locates at the LNF/INFN, Italy. The two rings of the collider are placed in parallel, with one collision point where the detector KLOE/SINDDHARTA stays. Table 1 lists the main parameters of the DAFNE ring, and Fig. 2 shows the layout and a bird-view of the collider. From 2001 to 2009, the luminosity of DAFNE was enhanced gradually, and even doubled after the crab-waist scheme was applied to the machine with the modification of the IR in 2007 to 2008. The highest luminosity was reached as high as $4.5 \times 10^{32} \text{ cm}^{-2} \text{ s}^{-1}$.

Table 1: Main Parameters of the DAFNE Ring

Energy per beam	510 MeV
Machine length	97 m
Maximum beam current (KLOE run)	2.5(e-) / 1.4(e+) A
No. of colliding bunches	100-111
RF frequency	368.67 MHz
RF voltage	100-250 kV
Harmonic number	120
Bunch spacing	2.7 ns
Max ach. Luminosity (SIDDHARTA run)	$4.5 \times 10^{32} \text{ cm}^{-2} \text{ s}^{-1}$

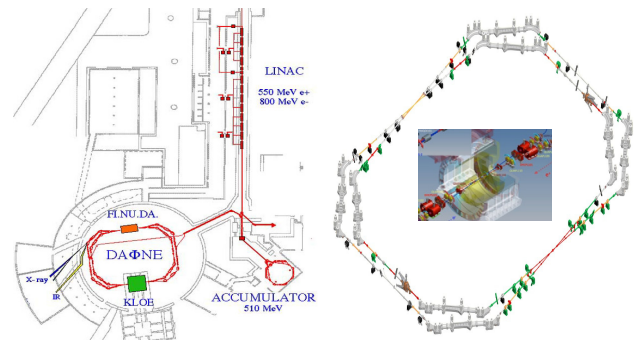


Figure 2: Schematic layout of the DAFNE machine (left) and rings with the detector (right).

The VEPP-2000 is the upgrade machine of the VEPP-2M in BINP, and started its operation from 2010, with the beam energy range from 200 MeV to 1 GeV. Figure 3 is the layout of the VEPP-2000, and its main parameters are given in the Table 2.

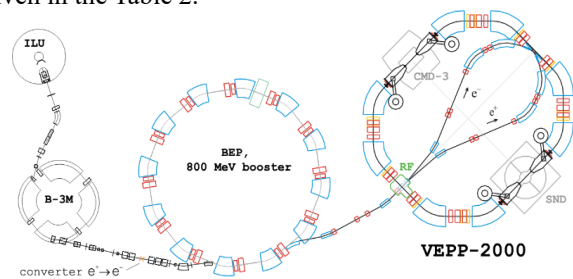


Figure 3: Layout of the VEPP-2000, and its boosters.

Table 2: Main Design Parameters of VEPP-2000@1GeV

Circumference (m)	24.388	Energy range (GeV)	0.2–1
Number of bunches	1	Number of particles	1×10^{11}
Betatron tunes	4.1/2.1	β -functions@IP (cm)	8.5
Beam-beam para.	0.1	Luminosity ($\text{cm}^{-2}\text{s}^{-1}$)	1×10^{32}

The VEPP-2000 ring has one bunch per beam to collide in the single ring. But with the round beam collision, the beam-beam parameter reached the highest value among the low energy colliders.

The BEPCII, upgrade project of the Beijing Electron Positron Collider, finished its construction by the end of 2006, and later, commissioned beams and luminosity until the national test and check in July 2009. As a double-ring collider, the BEPCII can run at the beam energy range of 1–2.1 GeV. It can be run as a factory-like machine in the energy region of tau-charm, and a synchrotron radiation (SR) light source with a bit large ring as well, which is combined by each of the outer half-ring of the two collision rings. It's a kind of machine with 3-ring configuration, shown as Fig. 4. The main parameters for both collider and SR facility are listed in the Table 3.

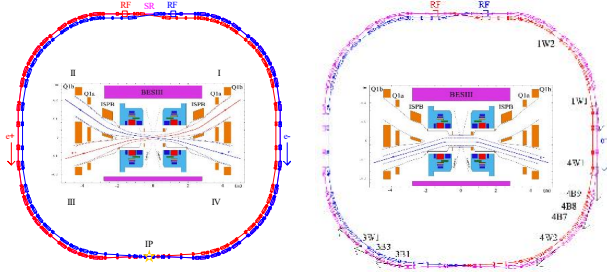


Figure 4: BEPCII collision rings (left) with the IR, and SR ring (right) with different beam trajectories at the IR.

The detector of BEPCII, BESIII, took data at different beam energy after 2009, with only running at the design energy of 1.89 GeV for one year (2010–11). During that time, the luminosity of BEPCII reached $6.5 \times 10^{32} \text{cm}^{-2}\text{s}^{-1}$. In the following years, the luminosity is enhanced gradually during machine study time, and reached the design value of $1 \times 10^{33} \text{cm}^{-2}\text{s}^{-1}$ in the April of 2016 [5].

Table 3: Main Design Parameters of the BEPCII

Parameters	Collision	SR
Beam energy (GeV)	1.89	2.5
Circumference (m)	237.53	241.13
Beam current (A)	0.91	0.25
Bunch current (mA) / No.	9.8 / 93	~1/160-300
Natural bunch length (mm)	13.6	12.0
RF frequency (MHz)	499.8	499.8
Harmonic number	396	402
Emittance (x/y)(nm·rad)	144/2.2	140
β function at IP (x/y) (m)	1.0/0.015	10.0/10.0
Luminosity ($\text{cm}^{-2}\text{s}^{-1}$)	1×10^{33}	—

With the budget of CAS, the energy of BEPCII collision mode was upgraded to 2.3 GeV as the request from high energy physics several years ago. As a result, the

possible 4-quark state particle $Z_c(3900)$ was found, which was thought as the most important physics result of the BEPCII in recent years.

The rival of the BEPCII, CESR at the Wilson lab in Cornell University, which lowered its energy from B quark region to compete with the BEPCII around 2000 as called CESRc, has an advantage of large circumference compared to the BEPCII. But after it ran at the tau energy, the peak luminosity reached only about 1/3 of its design value, as shown in the Table 4. The schematic layout of CESR/CESRc is shown in Fig. 5. It can provide synchrotron light to users as a platform of light source too. The CESRc stopped its physics running after the BEPCII started its operation for users in mid-2009.

Table 4: Design and Achieved Parameters of CESR and CESRc

Parameter	Achieved	Design	Achieved	Achieved
Circumference (m)	768	768	768	768
Beam Energy (GeV)	5.3	1.88	1.88	2.09
Luminosity ($10^{30}\text{cm}^{-2}\text{s}^{-1}$)	1250	300	65	73
I_b (mA/bunch)	8.0×45	4.0×45	1.9×40	2.6×24
I_{beam} (mA)	370	180	75	65
ξ_y	0.06	0.04	0.023	0.03
ξ_x	0.03	0.036	0.028	0.035
σ_E/E_0 (10^{-3})	0.64	0.84	0.86	0.86
$\tau_{x,y}$ (ms)	22	55	50	50
B_w (T)	-	2.1	2.1	1.9
β_y^* (cm)	1.8	1.0	1.15	1.3
ϵ_x (nm·rad)	220	220	140	125

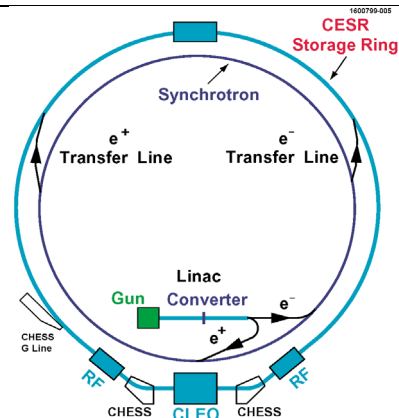


Figure 5: Schematic layout of CESR/CESRc collider.

BEAM DYNAMIC STUDY

In this section, we mainly review the studies on single beam, beam-beam and luminosity tuning, which are selected as main topics of affecting luminosity performance in the colliders, mostly the four machine mentioned in this paper, at their operation stages. Linear and non-linear lattice influence the luminosity indirectly, but by means of the working point, chromaticity tuning, optics realization, coupling control, etc.

Single Beam Dynamics

Single bunch and multi-bunch dynamics, especially the impedance caused instabilities, are the main study issues in low energy colliders. Bunch lengthening due to low frequency broadband impedance plays more important rule than other single bunch effects, since the maximized luminosity appears when the bunch length equals to the vertical beta function at IP. Multi-bunch instability is always caused by narrow band impedance in storage rings and results bunch oscillations, limiting the luminosity.

In the accumulator ring of DAFNE, the bunch lengthening was observed and measured as functions of bunch current and RF voltage, together with the corresponding analyses of wake potential and broad band impedance, as shown in Figs. 6 and 7 [6]. In the measurement at the DAFNE accumulator ring, bunch lengths were in very good agreement with the simulation results obtained at different RF voltages, confirming the validity of the calculated wake field for the bunch lengthening calculations. The low frequency broad band impedance $|Z/n|_0$ was got as 3.55Ω from the bunch lengthening measurement.

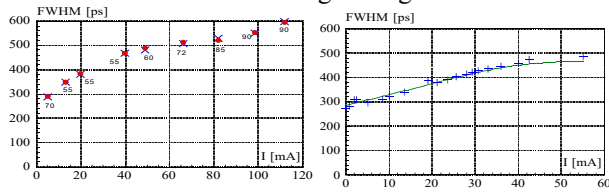


Figure 6: Bunch lengthening as functions of RF voltage (left) and bunch current (right).

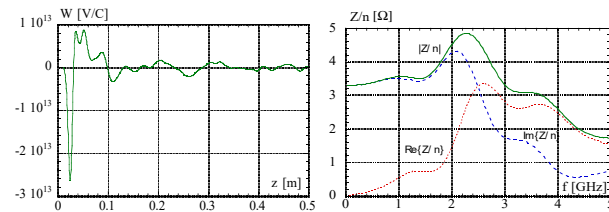


Figure 7: Analytical calculations on wake potential and impedance of the DAFNE ring.

Bunch lengthening with different momentum compaction factors in the electron ring DAFNE was also compared and fit well with the simulation from wake fields, as shown in Fig. 8. It is easy to see that the bunch lengthening is reduced due to a negative momentum compaction.

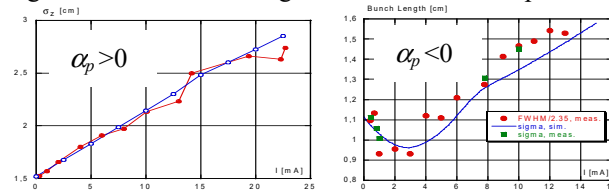


Figure 8: Bunch lengthening at different momentum compaction factors.

The vertical bunch size blow-up was observed at the DAFNE rings, shown as Fig. 9, together with the bunch lengthening. This is correlated with the longitudinal microwave instability. The measurement results show that

the threshold of microwave instability is higher for higher momentum compaction, and it is more pronounced for e-ring, which has a higher coupling impedance than e+ ring.

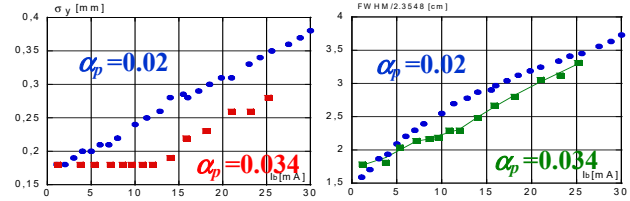


Figure 9: Vertical bunch size blow-up at different α_p (left), with bunch lengthening at same conditions (right).

The bunch lengthening was observed clearly in the two rings of BEPCII, which was considered more than 10% at the designed bunch current $I_b = 9.8\text{mA}$ [3]. The low frequency longitudinal broad band impedance got from the bunch lengthening is about 3 times larger than expected by numerical analyses. Figure 10 shows the bunch lengthening measurement in two rings of BEPCII.

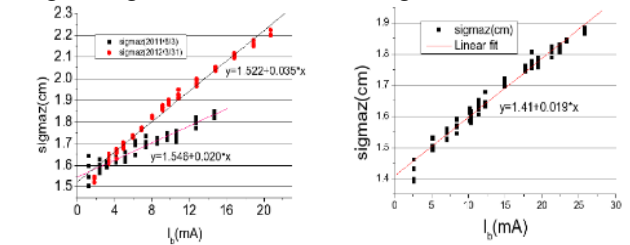


Figure 10: Bunch lengthening at two rings of BEPCII (Left: e+ ring, Right: e- ring).

In the VEPP-2000, the bunch length caused by potential well distortion and microwave instability, was measured with phi-dissector, as a function of single bunch current at different RF voltage and at the beam energy of 478 MeV. The energy spread was also measured together with the bunch lengthening, as shown in Fig. 11.

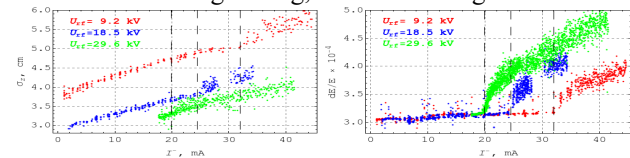


Figure 11: Bunch length measurement at VEPP-2000.

It is very clear that bunch lengthening happens due to potential well distortion at very low bunch current, and is enhanced at the threshold of microwave instability. The higher the RF voltage, the less bunch lengthening, but the lower the threshold current of microwave instability.

As an effective way, longitudinal feedback systems are adopted in DAFNE and BEPCII when longitudinal dipolar oscillation happened in the rings. This helps luminosity to be increased $\sim 20\%$. In CESRc, a multi-bunch instability due to electron cloud was observed clearly in the positron beam when 4ns bunch spacing was adopted [4].

Beam Parameters Optimization

In normal operation, the beam optics is usually not the exactly same as that of design. Deviations come from multipolar errors of magnets, ripple of power supplies,

and alignments as well. In small-size rings, magnet model is quite different from the real one, which also contributes the deviations of beam optics parameters. All these deviations widen the transverse stop-bands in tune diagram and make the horizontal tune difficult to move to half integer and thus result a luminosity reduction. Ways to compensate or correct the optics functions were developed and adopted in the re-modelling the lattice of rings.

In the BEPCII rings, all the dipoles and quadrupoles were re-modelled from the hard edge model to a soft edge model with nonlinear fringe field set at both ends of magnets. Then the linear part of the magnet model was modified with the code LOCO for on-line optics correction. The simulation shows a 10% increase of luminosity with the new magnet model, which is believed to help to enhance the luminosity at the design energy in April 2016. A typical beta function measurement result at the BEPCII is shown in Fig. 12 [5], which is a routine correction (every two weeks) during operation.

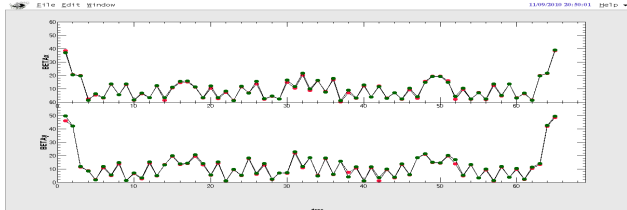


Figure 12: Difference of β functions between measured and setup along the ring of BEPCII (w/o IR).

The transverse beam coupling was diagnosed and tuned during luminosity commissioning. In CESRc, Local coupling in the interaction region was measured with beam shaker and corrected with analytical way, shown as Fig. 13 [4], while in the arc, the local coupling could be tuned with skew sextupoles.

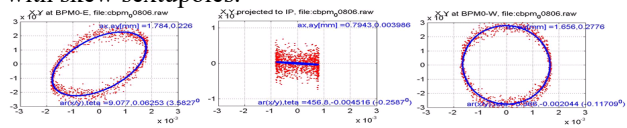


Figure 13: x-y coupling measured with two BPMs aside the IP of CESRc (hori. scale 1 mm/div, vert. 0.1mm/div).

In BEPCII, local coupling of two rings was measured and corrected via the closed orbit response and coupling coefficient tuning. Smaller coupling shows a higher luminosity in most of these small-size colliders.

Beam-beam Interaction

Interactions between two beams, which collide at IP, is the most important issue in a collider. The off-line beam-beam simulation will help us to understand the influence of beam-beam interaction, and on the other hand, results of beam-beam simulation will show the working point region of high luminosity. On-line beam-beam study for luminosity enhancement focuses on the real tunes scan and the non-linearity terms during the luminosity tuning.

Figure 14 shows the strong-strong beam-beam simulation results of single bunch collision for different horizontal tunes. The results are very much consistent to the real operation of BEPCII, in which the luminosity increased

~20% when the horizontal working point was moved close to half integer. From 2010, the storage rings of BEPCII keeps running at the half-integer region for the horizontal working point during the routine operation. The horizontal tunes could be as close to the half integer as 0.503, which requests high stability to the hardware.

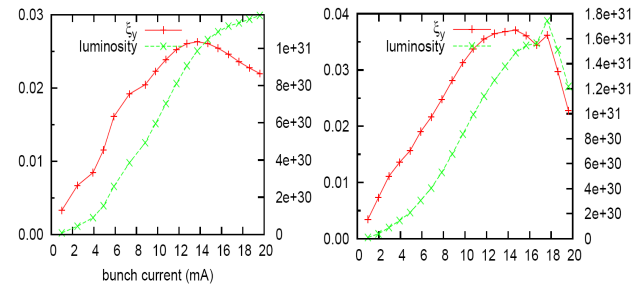


Figure 14: Beam-beam simulation with strong-strong model for single bunch collision in the BEPCII (left: $v_x \sim 0.53$, right: $v_x \sim 0.51$)

In the DAFNE rings, the peak luminosity was increased too when the horizontal working point approached to the half integer. But the lifetime of beams were increased in DAFNE, in contrast to the beam lifetime in the BEPCII. This was possible with the wigglers since dynamic aperture was satisfactory at low tunes. Figure 15 shows the luminosity of single bunch collision for different working points at the DAFNE[7].

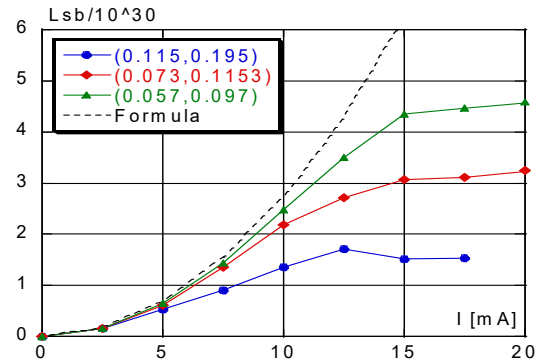


Figure 15: Luminosity of single bunch collision of DAFNE with different working point regions.

In CESRc, the horizontal tune was also chosen to be close to half integer, say ~0.526, for high luminosity. In this region, less beam-beam driving resonances were found than the high tune region, which mainly located near 0.6. Figure 16 shows clear beam-beam driving resonances but less machine resonances at different single bunch head-on collision.

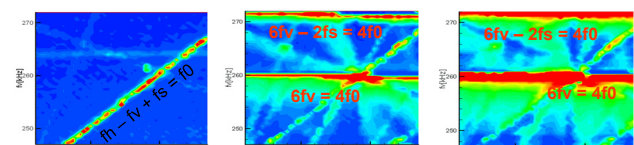


Figure 16: Tune plane exploration at high tune region of CESRc (right: single beam, middle: 0.5mA 1x1 collision, right: 1.0mA 1x1 collision).

In VEPP-2000, both “weak-strong” and “strong-strong” beam-beam simulations were done to compare with the operation data, shown in Fig. 17. It was found that the beam-beam threshold was improved with bunch lengthening, as shown in right one of Fig. 17. A “flip-flop” effect was observed in the VEPP-2000 ring, which was supposed to be the coherent beam-beam pi-mode interacted with the machine nonlinear resonances.

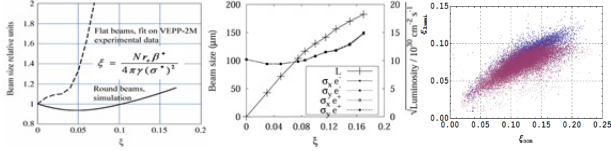


Figure 17: Vertical size dependence on beam-beam parameter with weak-strong (left), strong-strong (middle) simulations, and the bunch lengthening under different RF voltages (right, blue: $V_{rf}=17\text{kV}$; purple: $V_{rf}=35\text{kV}$).

In both long and short bunch cases, flip-flop developed for beams intensity higher than 15 mA, which meant the maximum beam-beam parameter was about 0.1 with the round beams. But the long bunch tended to mitigate the troublesome due to specific luminosity degradation for higher bunch current [2].

WAYS ON LUMINOSITY ENHANCEMENT

Higher luminosity is always the goal of colliders no matter what kind of stage they are, design or in operation. But for different machine, the way on increasing luminosity is somehow different.

Luminosity Upgrade in DAFNE

Crab-waist (CW) [8] scheme was first developed and applied in the DAFNE rings after several years’ normal commissioning on luminosity. A large Piwinski angle and a pair of crab waist sextupoles are used to make the vertical β at IP comparable with the overlap area, say $\beta_y \approx \sigma_x / \theta$. Figure 18 shows the difference of β_y at the collision area with and without crab waist scheme.

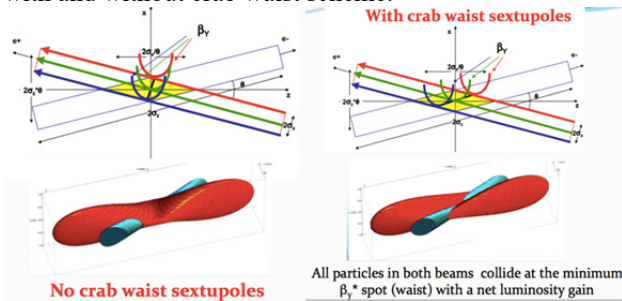


Figure 18: Collisions with/without crab-waist sextupoles.

In the CW scheme, the Piwinski angle is increased by reducing the horizontal beam size and increase the crossing angle to enhance the luminosity and decrease the horizontal tune shift. In addition, parasitic collisions become negligible due to the larger crossing angle and the smaller horizontal beam size. The luminosity gain mainly comes from the lower vertical β at IP, which can be much

smaller than the bunch length. The other benefits from CW are suppression of vertical synchrotron resonances, and the reduction of the vertical tune shift with synchrotron oscillation amplitude. Moreover, there’s no need to decrease the bunch length, which helps to solve the problems of electromagnetic high order mode heating, coherent synchrotron radiation of short bunches, and excessive power consumption. But the new beam-beam resonances are introduced by the large Piwinski angle, limiting the maximum obtainable tune shifts. A pair of sextupoles, with one placed at each side of the IP in counterphase with the IP in the horizontal plane and at $\pi/2$ in the vertical plane, provides the CW vertical β rotation. The strength of crab sextuple should satisfy the so called crab-condition as following:

$$K = \frac{1}{\theta} \frac{1}{\beta_y^* \beta_y} \sqrt{\frac{\beta_x^*}{\beta_x}}, \quad (1)$$

where is the crossing angle, and $\beta_{x,y}^*$ and $\beta_{x,y}$ the β ’s at the IP and the location of sextupoles. Thus the crab-waist transformation helps the luminosity enhancement. More details about the crab-waist scheme itself will be given by Riamondi [9] at this workshop.

The luminosity of DAFNE was increased dramatically after adopting the CW scheme in 2007. The new collision scheme based on large Piwinski angle and the CW transformation, together with an experimental detector SIDDHARTA, was commissioned. Table 5 lists the different parameters using for normal and CW optics and the corresponding luminosities and detectors [8].

Table 5: Parameters of Different Schemes at DAFNE

Parameter	Unit	KLOE	FINUDA	SIDDHARTA
I_{e-}	A	1.38	1.50	1.52
I_{e+}	A	1.18	1.10	1.00
Bunch No.		111	106	105
ϵ_x	nm-rad	340	340	250
β_x	m	1.5,	2.0	0.25
β_y	cm	1.8	1.9	0.93
Bunch length	cm	1.5-2.0	1.5-2.0	1.5-2.0
Crossing angle	mrاد	2×12.5	2×12.5	2×25
ξ_y		0.025	0.029	0.044
Luminosity (10^{32})	$\text{cm}^{-2}\text{s}^{-1}$	1.53	1.60	4.53

The peak luminosity of SIDDHARTA was got in June 2009, after two years’ upgrade and the installation of new IR and detector. Figure 19 shows the luminosity evolution of DAFNE from the very beginning of commissioning. At last, the luminosity reached 90% of the design value with the CW scheme in early 2009.

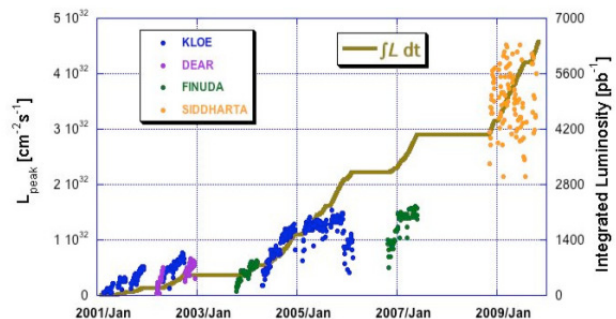


Figure 19: Luminosity evolution at DAFNE.

Luminosity Commissioning at BEPCII

The BEPCII storage rings have been running for HEP from 2009. Most of its HEP experiments are not at the design energy, 1.89 GeV/beam, but higher or less than it. This makes the luminosity enhancement during normal operation become difficult. Each year, dedicated luminosity commissioning or machine study (~3 weeks) was done during the routine operation for HEP experiments. The luminosity commissioning means the optimization of all the parameters related to ring optics, feedback systems, RF system, injection, and the stability of all the hardware systems, which was the requirement from the horizontal working point near half integer. After several years' commissioning, the main parameters are optimized from the original design values to the ones list in Table 6.

Table 6: Main Parameters of the BEPCII Rings @1.89GeV

Parameter	Original design	New design (after 2014)
Beam current	910 mA	910 mA
Bunch current	9.8 mA	7.0 mA
Bunch number	93	130
β at IP (x/y)	1/0.015 m	1/0.0135 m
Horizontal emittance	144 nm.rad	100 nm.rad
Transverse coupling	0.01	0.001-0.005
Working point (x/y)	6.53/5.58	7.505/5.58
Harmonic number	396	396
Bunch spacing	2.4 m	1.8 m
Mom. compaction	0.0235	0.0170
RF voltage	1.5 MV	1.5 MV
Natural bunch length	1.35 cm	1.15 cm
Beam-beam parameter	0.04	0.04
Luminosity ($\times 10^{33}$)	$1.0 \text{ cm}^{-2} \text{ s}^{-1}$	$1.0 \text{ cm}^{-2} \text{ s}^{-1}$

With the new lattice model, in which the magnets were considered as an ideal one plus two fringe field lenses, the optics parameters were optimized to the "New design" as listed in the above table. In the machine study dedicated to the luminosity commissioning, single bunch luminosity was tuned first, aiming at the maximum beam-beam parameter. With the help of feedback systems, multi-bunch luminosity increased linearly as the number of bunches. Smaller transverse coupling compensated the lower bunch current and also helped to increase the beam-beam parameter. Finally, the design luminosity of $1.0 \times 10^{33} \text{ cm}^{-2} \text{ s}^{-1}$ at 1.89 GeV was achieved in April 5, 2016, with the single beam current of ~850 mA and the bunch number of 119. Figure 20 shows the BEPCII luminosity evolution.

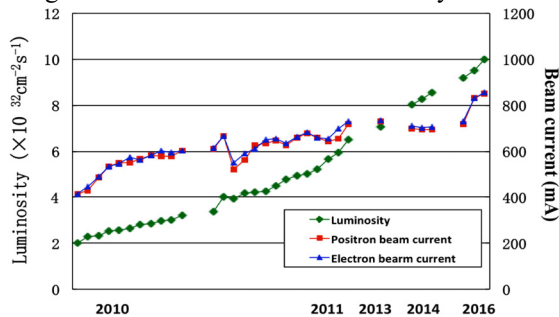


Figure 20: Luminosity evolution of the BEPCII.

Round Beam Collision at VEPP-2000 [2]

The round beam concept (RBC) [10] was studied and adopted in the VEPP-2000, to increase the beam-beam limit and then the luminosity. The longitudinal component of angular momentum as an additional integral of motion was provided by the X-Y symmetry of the transfer matrix between the two IPs and by the axial symmetry of the counter-beam force. Requirements to the ring lattice include head-on collision, low and equal β functions at IP, equal beam emittances and same fractional part of transverse tune. Two pairs of superconducting final focusing solenoid with a magnetic strength of 13 T were placed at the two IR symmetrically wrt the collision points. A "flat" combinations of solenoid polarities (++ ++ or +- -+) was found to have enough dynamic aperture. The optics, which satisfies the RBC scheme, should have the betatron tunes lie on the difference resonance $\nu_1 - \nu_2 = 2$ to provide equal emittances by eigenmodes coupling. With these setup, both lattice optics and hardware installation, VEPP-2000 started data taking from the lowest energy of collider, 160 MeV, to high energy range. Figure 21 depicts the luminosity achieved during HEP experiments at different beam energy. At the energy above 500 MeV, luminosity was limited by positron beam production rate. For the energy from 300 to 500 MeV, beam-beam effect limited the luminosity. At the lowest beam energy, the main limit factors were the small DA, IBS, and low beam lifetime.

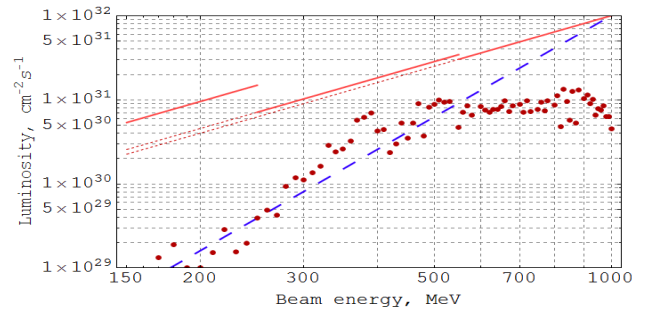


Figure 21: VEPP-2000 luminosity. (red line: peak luminosity overestimated, $L \propto \gamma^2$; blue line: fixed lattice energy scaling low, $L \propto \gamma^4$)

The achieved beam-beam parameter could be written as

$$\xi = \frac{Nr_e \beta_{nom}^*}{4\pi\gamma \sigma_{lumi}^{*2}}, \quad (2)$$

where the β function is nominal while the beam size is got from the measured luminosity. A maximum $\xi \sim 0.09$ was achieved during the regular operation. As depicted above, the beam-beam parameter could be enhanced to 0.12-0.15 with higher RF voltage. The luminosity of VEPP-2000 is about 2 to 5 times higher than that achieved by the VEPP-2M at the whole energy range of 0.16-1 GeV.

OPERATION, UPGRADE AND FUTURE

The new detector, KLOE-2 was installed at the DAFNE machine after the successful CW commissioning with SIDDHARTA. The data taking for HEP was then started with the new detector. At KLOE-2, a peak luminosity of

$2.13 \times 10^{32} \text{ cm}^{-2} \text{ s}^{-1}$ was obtained with the beam currents of 1.13A (e-) and 0.88A (e+), and the maximum integrated luminosity per day of 14.03 pb^{-1} [11]. Figure 22 shows the delivered, acquired and target integrated luminosities of KLOE-2 after its running. The comparison of old and new IR is also given in Fig. 22.

The BEPCII keeps running at different beam energy regions due to the physics requirements. Different optics parameters are adopted for different energy regions to maximization the beam-beam limit and peak luminosity. Table 7 lists the main parameters for such a kind of luminosity “levelling” at different beam energy regions.

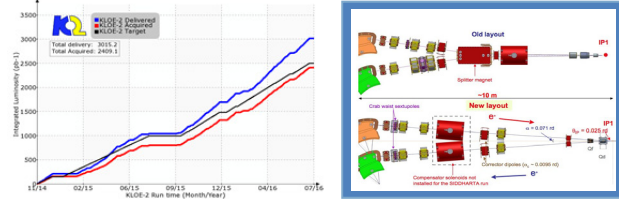


Figure 22: Integrated luminosity at KLOE-2 and the comparison of the IR before and after KLOE-2 installed.

The routine operation of BEPCII will focus on higher integrated luminosity at different beam energy. Beam energy higher than 2.4 GeV is also being considered for physics requirements. Top-up injection is the next step to increase integrated luminosity, which was already realized at the KEKB and PEP-II.

Table 7: Main Parameters of BEPCII Optics at Different Beam Energy Regions (Typical Values are Listed Here)

Beam energy (GeV)	1.0	1.89	2.3
β at IP (x/y, m)	1.0/0.012	1.0/0.0135	1.0/0.015
Hori. emittance (nm-rad)	54	122	144
Working point	6.505/5.58	7.505/5.58	7.505/5.58
Momentum compact.	0.0286	0.018	0.017
Nat. bunch length (cm)	0.6	1.15	1.5

The VEPP-2000 was run from 2010 to 2013 for HEP data taking, followed by an upgrade of its injection complex, booster, transfer channels and ring modifications from 2013 to 2016. The injection complex was improved for high intensity and higher beam energy, and thus for a high quality beam. The booster BEP was upgraded to 1 GeV and the transfer channels from BEP to VEPP should also be upgraded to 1 GeV. The modification of VEPP-2000 were new scraper, additional kicker electrodes in the ring, and new optics. The beam commissioning for K-500, BEP, and VEPP-2000 ring started in early 2016. The VEPP-2000 passed through beam scrubbing procedure and is ready to start data taking with both detectors at designed luminosity level.

Future Charm- τ Factory Design

At least 3 labs proposed to construct the super charm- τ factory at their campuses: Cabibbo lab in Italy, BINP in Russia, and USTC in China. The main requirements of the super charm- τ factory include the energy of center of mass of 1-5 GeV, with a peak luminosity of $10^{35} \text{ cm}^{-2} \text{ s}^{-1}$ at the charm/ τ threshold. Electron beam should be polarized longitudinally at IP, and the energy calibration could be as

small as $(5-10) \times 10^{-5}$ by Compton backscattering. These demands cause the consideration of the accelerator design as the following detailed conditions:

- Two rings with CW collision and single IP with the β_y^* smaller than 1 mm.
- Preservation of emittance and damping time through the energy range to optimize luminosity with SC wigglers.
- Siberian snakes to obtain longitudinally polarized e-.
- Highly efficient positron source (high rate top-up injection).
- Full energy injection (linac) with polarized e- source.

The storage ring of such a super charm- τ factory could be used as a low emittance synchrotron radiation source, accommodating tens of beam lines. As an example, BINP developed a lattice design of the super charm- τ factory. Figure 23 gives the schematic layout of this machine.

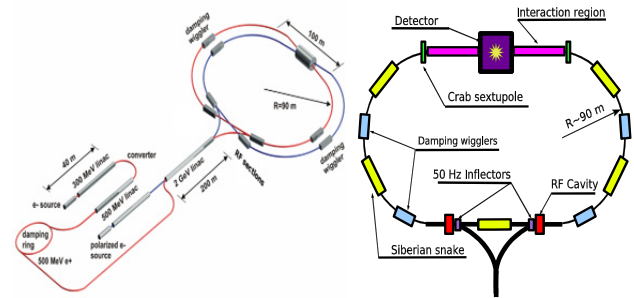


Figure 23: Schematic layout of super charm- τ factory designed in BINP (left: the whole machine; right: main accelerator parts in double-ring case with CW).

Table 8: Main Parameters of the Super Charm- τ Factory in BINP

Beam energy	1.0GeV	1.5GeV	2.0GeV	2.5GeV
Circumference	780m			
Emittance (x/y)	8nm/0.04nm @ 0.5% coupling			
Damping time (x/y/z)	30/30/15ms			
RF frequency	508MHz			
Harmonic number	1300			
Bunch current	4.4mA			
Beam current	1.7A			
Bunch length	16mm	11mm	10mm	10mm
Energy spread (10^{-4})	10.1	9.98	8.44	7.38
Momentum comp. (10^{-3})	1.0	1.06	1.06	1.06
Synchrotron tune	0.007	0.010	0.009	0.008
Beam-beam parameter	0.15	0.15	0.12	0.095
Luminosity ($10^{35} \text{ cm}^{-2} \text{ s}^{-1}$)	0.63	0.95	1.00	1.00

Table 8 compares main parameters at different beam energy from 1.0 to 2.5 GeV [12]. But due to the budget limit, the design was reduced to a circumference of 380m.

The main elements like the QD0 at IR, and the SC damping wiggler, were designed together with the lattice and IR, shown as Fig. 24. The injection facility kept the current machine at BINP, and the 2mA beam current at the damping ring was commissioned.

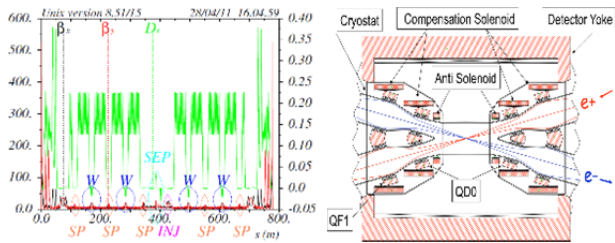


Figure 24: Optics functions along the main ring (left) and the IR design (right) for super charm- τ factory in BINP.

The design of super charm- τ factory in Cabibbo/INFN, also experienced from the relatively bigger ring to a small ring with a circumference of 330m [13]. Figure 25 shows the layout of the ring. Multi-bend achromat was adopted in the ring design to get a quite small emittance. Table 9 lists the main parameters for different beam energies.

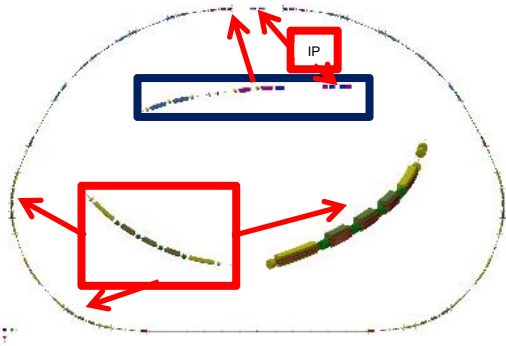


Figure 25: Layout of the super charm- τ factory designed in Cabibbo/INFN.

The design provided an option of FEL with its long linac. A lot of hardware, such as main ring dipole and gradient dipole, were designed, together with the linac and the damping ring.

Table 9: Main Parameters of the Ring for Cabibbo Super Charm- τ Factory.

Beam energy (GeV)	2.0	2.0
Circumference (m)	330.16	330.16
Crossing angle (mrad, full)	60	60
Beam-beam parameter	0.088	0.119
β_x/β_y at the IP (cm)	6/0.06	6/0.06
Emittance (nm, x/y)	5.14/0.0128	5.61/0.0140
Bunch length (mm)	6.9	7.2
Beam current (A)	1.735	2.565
Bunch current (mA)	3.38	5.00
Bunch number	513	513
RF frequency (MHz)	476	476
Harmonic number	524	524
Energy loss/turn (MeV)	0.09	0.09
Luminosity ($10^{35} \text{ cm}^{-2}\text{s}^{-1}$)	1.0	2.0

In the University of Science and Technology China, a conceptual design of super charm- τ factory was proposed in 2013, with the beam energy of 1-3.5 GeV. The luminosity aims at $5 \times 10^{34} \text{ cm}^{-2}\text{s}^{-1}$ in phase 1 and $10 \times 10^{34} \text{ cm}^{-2}\text{s}^{-1}$ in phase 2 [14]. The detailed design is still under way.

CONCLUSION

During the past decades, very fruitful beam dynamics studies were carried on at low energy colliders. Among these studies, the impedance induced instabilities are more serious than the high energy colliders. The relatively small size of rings limits the performance of low energy collider, but the parasitic synchrotron light source make it easy to be a platform for multi-disciplinary sciences.

Different ways to increase luminosity were realized in all these low energy machines as the pioneers for the family of collider. The super charm- τ factory, as the future direction for low energy collider, is very much promising to be the luminosity of $\sim 10^{35} \text{ cm}^{-2}\text{s}^{-1}$ by adopting the crab-waist scheme and could be run as a 3rd generation synchrotron light source.

ACKNOWLEDGEMENT

The author is grateful to the help of Dr. C. Malardi, M. Biagini, and M. Zobov from LNF/INFN, Dr. D. Shwartz, and E. Levichev from BINP, Dr. Y. Zhang and C.H. Yu from IHEP. Without the communication and fruitful discussion, it is difficult to get all materials well understood.

REFERENCES

- [1] C. Milardi *et al.*, "Present status of the DAΦNE and perspectives", *Int. J. Mod. Phys. A* 24, pp. 360-368 (2009).
- [2] D. Shwartz *et al.*, "Recent Beam-beam Effects and Luminosity at VEPP-2000", in *Proceedings of IPAC'14*, Dresden, Germany, June 2014, pp. 924-927.
- [3] Q. Qin, "Performance and Prospects of BEPCII", in *Proceedings of IPAC'12*, New Orleans, USA, May 2012, pp. 1030-1034.
- [4] A. Temnykh, "Overview of the Beam Dynamics Study in CESR", in *Proceedings of the 40th ICFA Workshop on Beam Dynamics in e^+e^- Factories*, Novosibirsk, April 2008.
- [5] C.H. Yu *et al.*, "BEPCII Performance and Beam Dynamics Studies on Luminosity", in *Proceedings of IPAC'16*, Busan, Korea, May 2016, pp. 1014-1018.
- [6] R. Boni *et al.*, "DAFNE Accumulator Ring Coupling Impedance Measurements", *NIM A* 418 (1998) 241-248.
- [7] B. Spataro and M. Zobov, *DAFNE Technical Note G-64*, 2005.
- [8] M. Zobov *et al.*, "Test of 'crab-waist' collisions at DAΦNE Φ-Factory", *Phys. Rev. Lett.* 104, 174801 (2010).
- [9] P. Riamondi, presented at eeFACT2016.
- [10] V.V. Danilov *et al.*, "The Concept of Round Colliding Beams," in *Proc. EPAC'96*, Sitges, p. 1149 (1996).
- [11] C. Milardi *et al.*, private communication, 2016.
- [12] E. Levichev, Baseline of Super-c-tau in Novosibirsk, *Proc. Workshop on Tau-charm at high luminosity*, 2013.
- [13] M. Biagini, tau/charm accelerator overview, in *Proc. Workshop on Tau-charm at high luminosity*, 2013.
- [14] J. Luo, private communication, 2016.

PERFORMANCE AND PERSPECTIVE OF MODERN SYNCHROTRON LIGHT SOURCES

D. Einfeld*, ESRF, European Synchrotron Light Source Facility, Grenoble Cedex, France

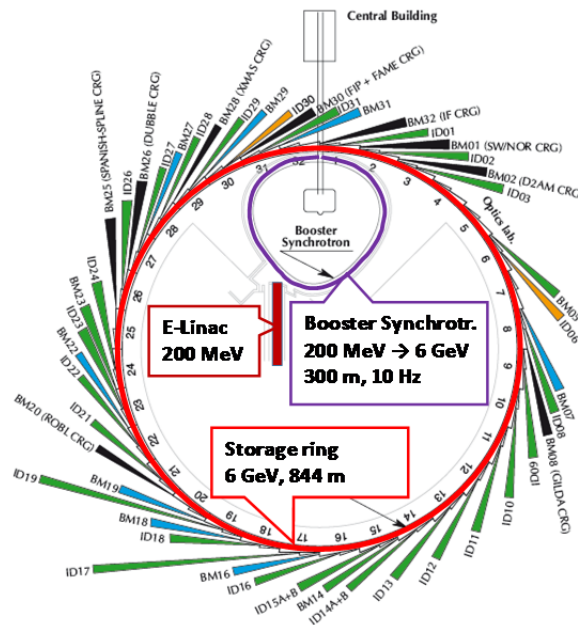
Abstract

The first synchrotron radiation was used in a so called parasitic mode from high energy machines (1st generation). At the end of the 1970s and the beginning of 1980s accelerators dedicated to the production of synchrotron radiation were built (2nd generations). With the investigation and developments of insertion devices in the middle of 1980, the 3rd generation synchrotron radiation sources were built and emittances down to some nmrad could be reached. At present around 50 Synchrotron Radiation sources are existing around the world. All of these sources reached there the specification (energy, current, emittance, beam stability, etc.) very soon after the commissioning. With the 4th generation, emittances of down to around 100 pmrad should be reached. This is still a factor of 10 away from the requirement of a diffraction limited light source. According to the expertise in designing and operating of synchrotron radiation sources this should be reachable in the future, but only with circumferences of some kilometers like Petra III or PEP-X. Overall the performances and perspective of synchrotron light source are remarkable.

INTRODUCTION

The layout of the European Synchrotron Radiation Facility (ESRF) [1] (see Fig.1) is an example of a modern Synchrotron Light Source. It starts with an electron Linac with an energy of 200 MeV, which will be injected via a transfer line into the booster synchrotron and accelerated up to 6 GeV. From the booster synchrotron the beam goes over another transfer line into the storage ring. With a repetition frequency of 10 Hz the beam will be accumulated in the storage ring until reaching its final value of 200 mA (for the ESRF).

The ESRF exist of 32 achromat's with the magnet sections and the straights for the installation of the ID's. The characteristics of the Linac, Booster and Storage-ring are changing for the different light sources. At the Swiss Light Source, ALBA and TPS [2-4] the booster is located in the storage ring tunnel in order to reduce the emittance. For these facilities the emittance of the beam is smaller as 10 nmrad. Details of all Light Sources can be found under "www.lightsources.org" within the rubric "Light sources of the world". Overall there are 47 Light Sources in the world.



32 straight section, 42 Beamlines, 12 on dipoles, 30 on ID's

Figure1: General layout of a synchrotron light source with the Linac, Booster Synchrotron, Storage-Ring and the beam lines around the storage ring.

*dieter.einfeld@esrf.fr

The brilliance (Br) of the synchrotron radiation (Eq.1) is the most important factor for the users, it is given by the emitted photon flux (Fl) per second and 0.1% resolution divided by the cross sections (Σ_x, Σ_y) and divergences (Σ'_x, Σ'_y) of the beam (see Eq.1). The emitted photon flux is proportional to the stored beam current and the characteristics of the source (bendings or insertion devices). The cross sections and the divergences of the beam are given by the emittance ϵ_x and ϵ_y as well the machine functions β_x, α_x and γ_x, η_x and η'_x are the horizontal dispersion and its derivate. The horizontal emittance of a lattice is given by the Eq. (2) [5],[6],[7]

$$B_r = \frac{Fl}{4\pi^2 \Sigma_x \Sigma'_x \Sigma_y \Sigma'_y} \quad (1)$$

$$\epsilon_x = C_q \frac{\gamma^2}{J_x} \frac{\oint \frac{H(s)}{\rho^3(s)} ds}{\oint \frac{1}{\rho^2(s)} ds} \quad (2)$$

where $C_q = 3.84 \cdot 10^{-13}$ m, the integrals are taken along the ring circumference, J_x is the horizontal partition number, ρ is the reference orbit radius, γ is the normalized energy ($\gamma = E/m_0c^2$), H is the dispersion invariant (see Eq. 3)

$$H = \gamma_x^2 \eta_x^2 + 2\alpha_x \eta_x \eta'_x + \beta_x^2 \eta_x'^2 \quad (3)$$

$$\alpha_x = -\frac{1}{2}\beta_x', \quad \gamma_x = \frac{1+\alpha_x^2}{\beta_x} \quad (4)$$

DESIGN OF LOW EMITTANCE STORAGE RINGS

Low emittance lattices were initially developed for the 3rd generation light sources on the basis of the Double Bend Achromat (DBA) [8] and Triple Bend Achromat (TBA) [9]. A general solution for a so called isomagnetic ring, a ring in which all the magnets are identical, is given by Eq. 5.

$$\epsilon_x = C_q * \frac{\gamma_0^2}{J_x} * \frac{1}{3 \cdot 4 \sqrt{15}} * F * \varphi^3 = A * \frac{F}{J_x} * \frac{E^2 * \varphi^3}{GeV^2 * rad^3} \quad (5)$$

where F is a lattice factor and φ is the deflection angle of the bending magnets, the constant $A = 31.64$ nmrad. According to Eq. 5 the emittance depends upon the deflection angle of the 3rd power or is proportional to the inverse of the number of magnets to the 3rd power ($\epsilon_x \approx 1/N_{magnets}^3$). For the DBA –the theoretical minimum emittance is given ([10], [11], [12]) with a F -value = 3 and for the TME-lattice it is $F=1$

The emittance can be decreased too, by increasing the horizontal partition number J_x , (see Eq.2) which is given by the Eq. (6):

$$J_x = 1 - D, \quad D = \frac{1}{2\pi} \int \eta(s) \left[\frac{1}{\rho^2} - 2 \frac{G}{\rho * B} \right] ds \quad (6)$$

$$\epsilon_{wi} = \epsilon_0 * \frac{U_0}{U_0 + U_{wi}} \quad (7)$$

where B is the magnetic field and G is the gradient.. The change of the emittance with damping wigglers is given by Eq. 7. Where ϵ_0 is the emittance without damping wigglers, U_0 is the emitted radiation power without wigglers and U_{wi} is the radiation power of the damping wigglers.

LATTICES OF MODERN LIGHT SOURCES

To achieve low emittance the following points should be considered:

- ▶ The number of magnets has to be large.
- ▶ For a TBA – or MBA-Lattice, the outer bending magnets must be shorter by roughly a factor 2
- ▶ The bending magnets should be combined-function with vertical focusing to increase J_x . Combined-function bending magnets have also the advantage of leading to a compact machine.
- ▶ Damping wigglers can be installed to increase the horizontal partition number J_x
- ▶ Longitudinal gradient bending magnets have the potential to decrease the emittance further.

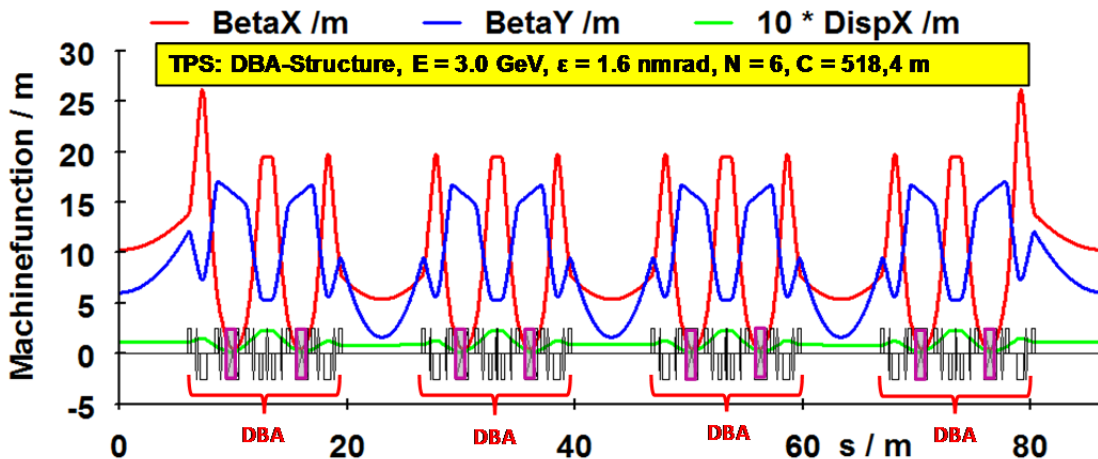


Figure 2: The lattice of the Taiwan Photon Source (TPS).

In Fig.2 is given as an example for the layout of a modern Synchrotron Light Source that one of the Taiwan Photon Source (TPS) [13]. It has a DBA structure with a TME-settings in the bendings and different lengths of the straight sections (6*12 m and 18*7m). NSLS II is reducing the emittance from 2 nmrad to 0.5 nmrad by introducing damping wigglers

A summary of the characteristics of the modern light sources is presented in Table 1. The white boxes are

sources with a DBA structure, the green boxes with a TBA and the yellow ones with a TME-lattice. A good way to compare the different light sources is to look for the available space for the installation of insertion devices as well the so called normalized emittance or K-value given by Eq. 8

$$K = 0.0316 * \frac{\epsilon_x \text{ GeV}^2 * \text{rad}^3}{E^2 * \varphi^3} \quad (8)$$

Table 1: The main parameters of modern light sources (3rd generation)

Source	Lattice	Energy (GeV)	Emitt. nmrad	Jx	Ins. Length (m)	Current (mA)	Angle (rad)	Circumf. (m)	Percent. (%)	K-Value
ALS	TBA	1.9	5.6	1.4	81	500	0.1745	196.8	41.2	9.249
BESSY II	DBA	1.9	6.4	1	89	250	0.1963	240	37.1	7.425
ELETTRA	DBA	2	7	1.32	74.78	300	0.2618	258	29.0	3.090
SLS	TBA	2.4	5	1	80.28	400	0.1745	288	27.9	5.175
SESAME	TME	2.5	25.7	1.68	54.56	200	0.3927	133.1	41.0	2.151
NSLS-xray	DBA	2.5	44.5	1	18	500	0.3927	170.08	10.6	3.725
SOLEIL	TME	2.75	3.72	1	159.6	500	0.1963	354	45.1	2.060
CLS	DBA	2.9	18.2	1.6	62.4	200	0.2618	170.4	36.6	3.821
SPEAR III	DBA	3	18.2	1.2	67	500	0.16535	234.13	28.6	14.171
ASP	TME	3	7.13	1.36	75.55	200	0.2244	216	35.0	2.221
DIAMOND	DBA	3	2.84	1	218.2	300	0.1309	561.6	38.9	4.457
ALBA	TME	3	4.29	1.3	103.44	400	0.1963	268.8	38.5	1.996
TPS	TME	3	1.6	1	210	400	0.1309	518.4	40.5	2.511
PAL-II	TME	3	5.6	1.33	118.92	400	0.2618	281.82	42.2	1.099
SSRF	TME	3	2.6	1	152	300	0.1571	432	35.2	2.360
ESRF	DBA	6	3.94	1	237.8	200	0.09817	844	28.2	3.665
APS	DBA	7	2.514	1	268.8	100	0.0785	1104	24.3	3.360
SPRING 8	TME	8	2.4	1	329	100	0.0714	1440	22.8	3.264

The K-value gives an indication of how much the emittance converges to the theoretical minimum one. The minimum K value for the TME structure is 1 and for the DBA structure is 3. These value will be reached by ELETTRA [14] and PAL II [15]. ELETTRA reaches the minimum value for the DBA-structure because the phase advance between the 2 bending magnets is π .

In order to reduce the emittance, as in the case of SESAME [16], ASP[17], ALBA[18] as well PAL II, and build a compact machine there should be a gradient in the bending magnets, leading to a partition number J_x above 1.3. According to table 1 and Eq.(6), PAL II, with a K-factor of 1.1 is the most advanced design of a synchrotron light source. Also under the aspect that 42.2 % of the circumference are dedicated to straight sections. A synchrotron light source should have a high brilliance, but

also a lot of long straight sections for the installation of the insertion devices. In table 1, there are given the length of the straight section as percentage of the circumference. SOLEIL[19] has with 45.1 the largest percentage. Most of the recent build light sources have numbers around 40 %. The ESRF and APS are coming up only with 20 to 30 %.

Completely different is the layout of PETRA III [20]. It worked as a collider and has been converted into a synchrotron light sources. The layout of PETRA III is presented in Fig.3, it is a 6 GeV machine with circumference of 2304 m and a stored current of 100 mA. In one of the octant (NE to E) a DBA structure has been introduced and in the other octants from E to NE the original FODO structure is in use. The machine functions of the FODO as well the DBA-structure are given in Fig.3.

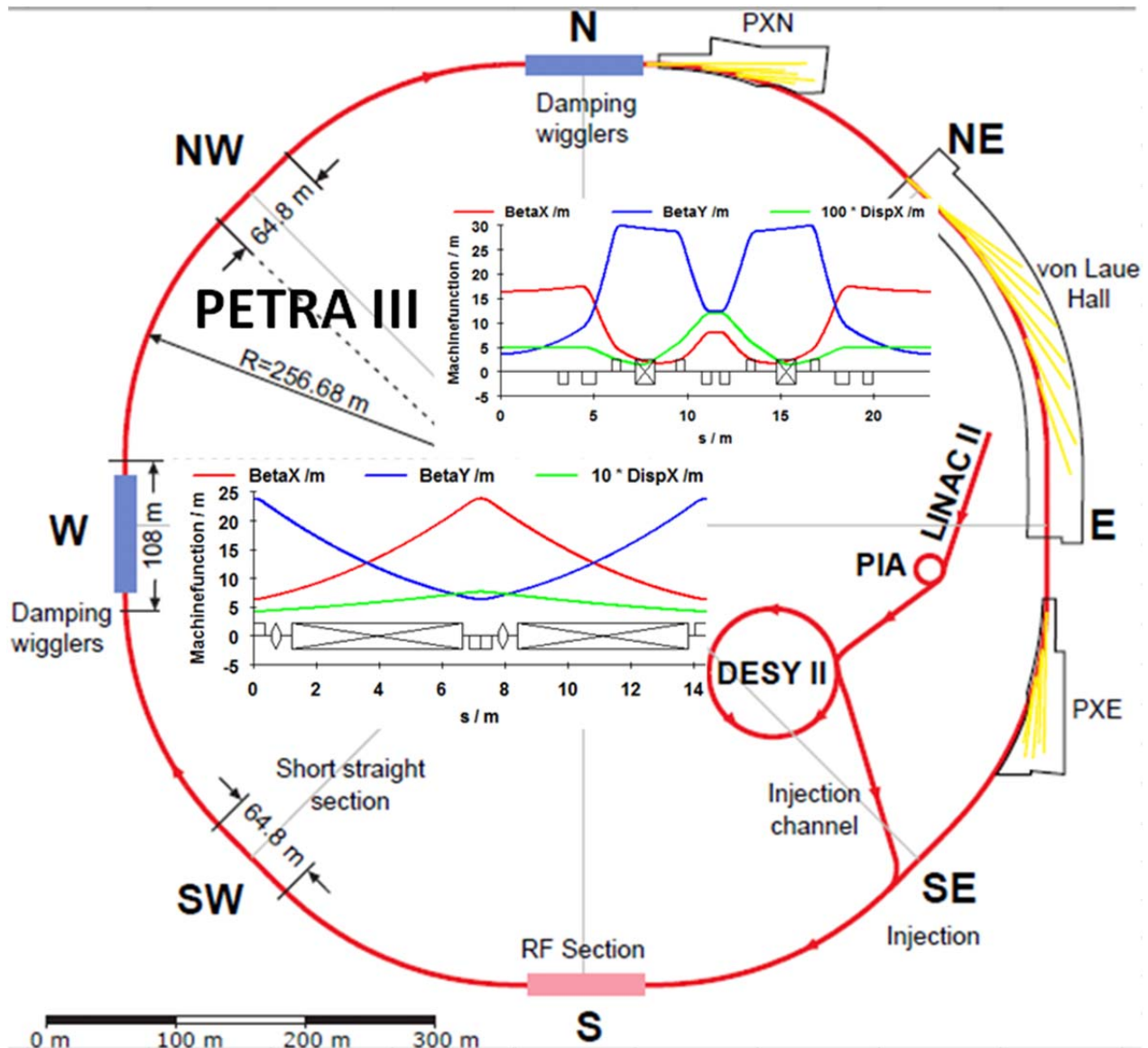


Figure 3: The layout of the Synchrotron radiation Source PETRA III.

The bare lattice of PETRA III is leading to an emittance of 8.2 nmrad (7.1 from the FODO-arcs and 1.1 from the DBA-arc) the corresponding radiation losses per turn are 521 keV from the FODO arcs and 48.7 from the DBA-arc. With the introduction of 20 damping wigglers ($B=1.52$ T and $L=4$ m) the radiation loss per turn will be increased by 4.2 MeV; this reduces the emittance by a factor 8.37 down to 1 nmrad.

For the accelerators it is of interest, in order to cross check the accuracy of the different programs, to look for the difference of the actual settings to the design ones. This can be given by the β – beating, which is the difference of the real and the designed β – values. The corresponding values for some light sources are given in [21]. According to these numbers the accuracy of the design should be better as 1 %; SOLEIL and Diamond reached 0.3 to 0.4 %. The theoretical vertical emittance should be zero, because there isn't any deflection in the vertical direction. The tolerances of the alignment

procedure gives some offset to the position of the magnets which leads to some extent to a deflection in the vertical direction. The emittance in the vertical direction gives some ideas about the correct positioning of the magnets, as well the correction procedure for the offset by correctors. Values of the vertical emittance down to 1 pmrad could be reached at the SLS and ASP [22]. A lot of rings aren't operating at the minimum vertical emittance because of the reduced lifetime which are not in favour of the users.

MODERN LIGHT SOURCES A SUMMARY

The situation of the modern light sources can be summarized as the following:

- ▶ Most of the present light sources (3rd generation) used the DBA structure.
- ▶ All the light sources reached the user requirement, that the stability of the beam should be better as 1/10 of the

beam cross section. For most of the Light Sources the beam stability is in the sub- μm region.

- ▶ In order to minimize the emittance some machines have a dispersion in the straights and use the TME-setting
- ▶ Damping wigglers have been introduced for reducing the emittance.
- ▶ Most of the light sources use the “topping up” injection mode.
- ▶ All machines have been commissioning and reached there specification in a short time.
- ▶ The vertical emittance in the range of pmrad have been reached.
- ▶ All the light sources are using closed orbit and bunch by bunch feedback systems.
- ▶ The user time goes up to over 95% of the operation time, in some case up to 99

All of this shows that the synchrotron light sources are very reliable and we can go for the next generation of synchrotron light sources, the 4th generation.

THE NEXT GENERATIONS (4TH) OF SYNCHROTRON LIGHT SOURCES

Synchrotron light sources with a factor of 10 to 20 smaller as the 3rd generation are called the 4th generation. Eq.(5) clearly favours the lattice with many bending magnets in an achromat and indeed the most challenging design make use of the so-called multiple bend achromat’s (MBA) lattices. MBA’s were first proposed by Einfeld [23] and later selected for the baseline design of MAX IV [24], based on a 7BA which delivers an emittance of 330 pmrad. The machine functions of MAX IV and the corresponding layout are shown in Fig.3. The layout of MAX IV is very well described in [25]

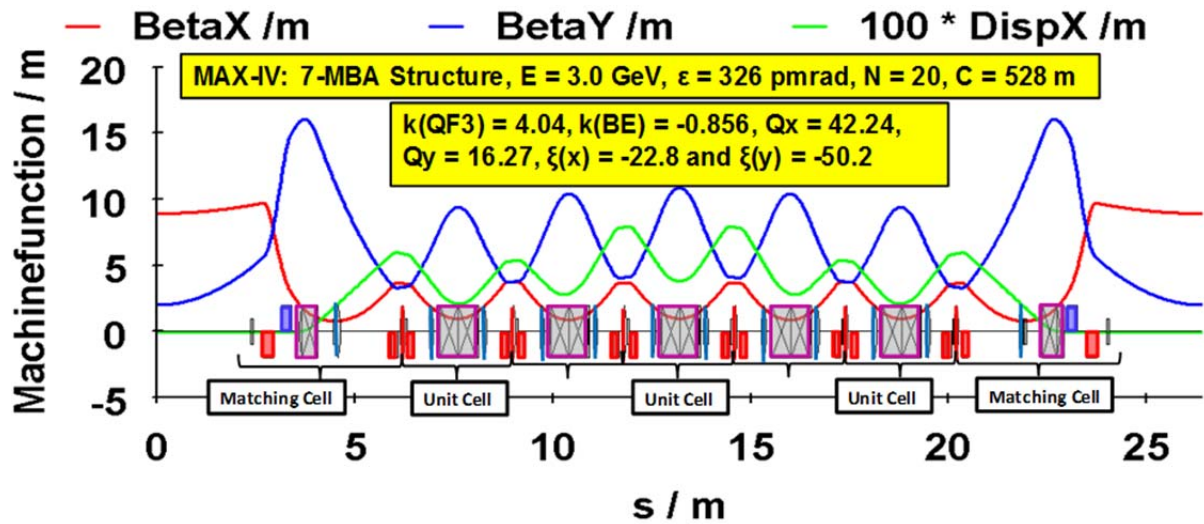


Figure 3: MBA-lattice of MAX IV with 7 bending magnets

Completely different to MAX IV is the layout of the ESRF-Upgrade project ESRF-EBS [26] with the so called “Hybrid Multi Bend Achromat” (HMBA) (see Fig.4). The project started in spring 2012.

The layout is given by 2 DBA – structures at the beginning and the end of the achromat in order to have a large dispersion function for chromaticity corrections. These 2 sections are connected with 3 combined function magnets with a gradient of 38 T/m (see Fig.4) and 4 high

gradient quadrupoles with gradients of 90 T/m (see Fig. 4). The ESRF-EBS design is very compact in order to replace the existing one in the same tunnel and leading to an emittance of 132 pmrad. For first time, the bending magnets will be build up with permanent magnets and will have a longitudinal gradient to reduce the emittance by roughly 15%. For the update of the APS [27] also a HMBA lattice will be used.

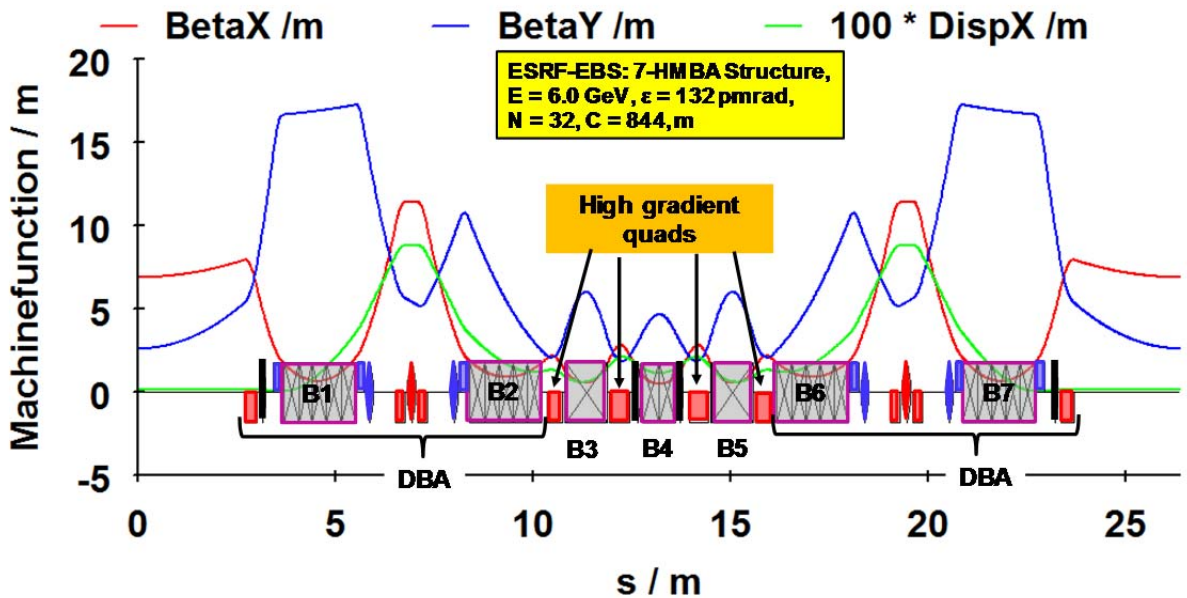


Figure 4: The lattice of the 7H MBA of the ESRF-EBS upgrade.

In parallel to the design of the ESRF-update is the design of the new 3 GeV Light source SIRIUS in Brazil with a 5 MBA [28]. In this case the 2 DBA - structure are combined with only one bending magnet. There seems to be an advantage of the HMBA against the MBA; SIRIUS with 5 bends has a smaller emittance as MAX IV with 7 bends (280 /330). Diamond is proposing an upgrade with a double DBA-structure (DDBA). This upgrade should lead to a smaller emittance as well a larger number of straight sections. This is only possible by going over from the DBA to the double DBA structure (DDBA) [29]. The introduction of one DDBA-cell has successfully already been done.

A different approach will be used for the upgrade of the Swiss Light Source (SLS). The SLS is using the idea of decreasing the emittance by introducing a longitudinal gradient in the bending magnet [30] [31]. The layout of the real unit cell is given in Fig. 5. Within the unit cell there are 5 bending magnets, in the middle one (B3) with a longitudinal gradient, followed by B2 with a horizontal gradient and B1 with a reversed field and a horizontal gradient too. The layout of the achromat with 5 unit cells and the matching section is given in Fig. 6, leading to an emittance of 134 pmrad [32]. Which means the upgrade will provide a decrease of the emittance by a factor of 37.

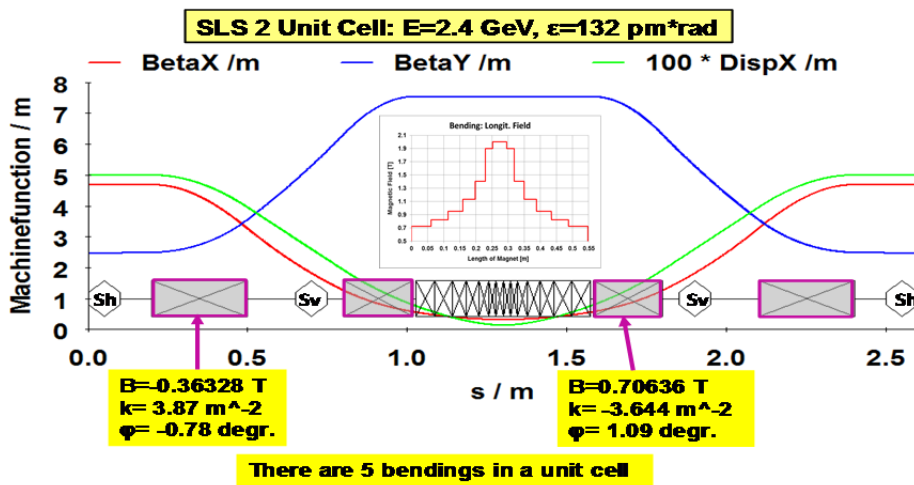


Figure 5: The unit cell for the upgrade of the SLS.

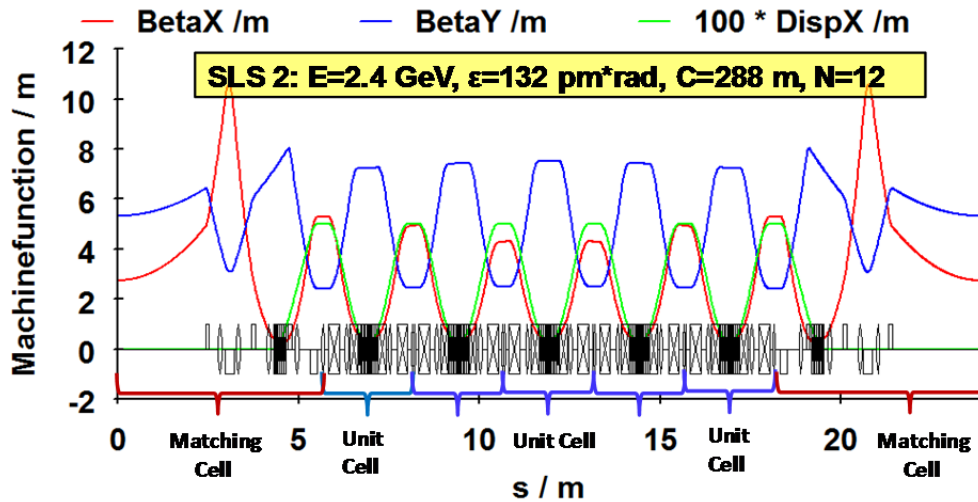


Figure 6: The layout of an achromat for the upgrade of the SLS.

DIFFRACTION LIMITED LIGHT SOURCES

The 4th Generation Light Sources with emittances around 200 pmrad are diffraction limited for photon energies up to 0.5 keV. Most of the users are interested in the range of up to 10 keV with a required emittance of 10 pmrad. The project which can meet this requirement is PEP-X. PEP-X is the idea by converting PEP II with a hexagonal tunnel into a dedicated [33].

Synchrotron Light Source (see Fig. 34) with a circular geometry. The length of the tunnel will be 2.2 km, with 6

times 243 m for arcs and 6 times 123 m for straights. Each arc with the length of 243 m includes 8 * 7 MBA achromat's with a length of 30.4 m. The layout of the 7MBA achromat's are similar to that one of MAX IV and is given in the middle of Fig.7. With overall 48*7MBA arcs, an energy of 4.5 GeV an emittance of roughly 20 pmrad can be reached. By matching the coupling factor and introducing damping wigglers an emittance of 5 pmrad can be reached. Because of the high current per bunch the emittance will be increased by the intra-beam-scattering to 10 pmrad [34].

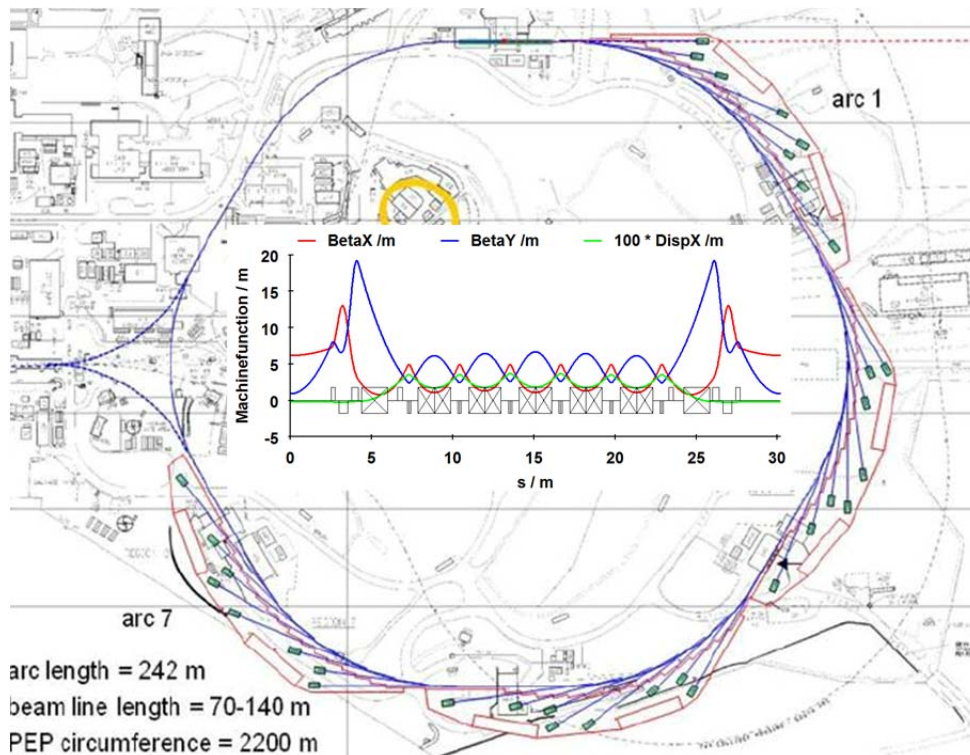


Figure 7: The layout of PEP – X with 72 7BA cells and 5m long straight.

CONCLUSION

All the synchrotron Light Sources reached their specification in a sometime and the user time goes up to 95 - 99%. All of this shows us the performance of the Light Sources is very high. There is a good agreement with the actual and the design values, which shows that the codes for the design of the different components and for the beam dynamics are very accurate. The first 4th Generation Light Source MAX IV reached already at 200 mA all the specifications and this will happen also for the upgrade of all the other projects. All of which makes us very confident to design a storage ring which meets the requirement of a “Diffraction Limited Light Source”.

REFERENCES

- [1] F. Sette, “Private communication”, ESRF, (2016)
- [2] W. Joho, M.A. Streun, Nucl. Instrum. and Methods, A 562 (2006) , pp.1-11.
- [3] G. Benedetti, D. Einfeld, Z. Marti, M.Munoz, M. Pont, in Proc. EPAC08, Genoa, Italy (2008), pp.2148-2150.
- [4] H.C. Chao et al., in Proc.PAC’09, Vancouver, Canada (2009), pp. 2258-2260.
- [5] A. Ropert, CAS CERN Accelerator School, CERN, 98-04, pp.91-126, (1998).
- [6] A. Ropert, CAS CERN Accelerator School, CERN,90-03, 158-178, (1990).
- [7] R. Maier, CAS CERN Accelerator School, CERN, 89-01, 96-130, (1989).
- [8] R. Chasman, and K. Green, IEEE Trans. Nucl. Sci. NS22, (1975) 1765
- [9] D. Einfeld and G. Muelhaupt, Nucl. Instrum. and Methods. 172, (1980).
- [10] M.Sommer, LAL/RT, 83-15, 1983.
- [11] S.Y.Lee and L.C.Teng, “Theoretical Minimum Emittance Lattice for an Electron Storage Ring”, in Proc. PAC 91, May 6-9, San Francisco, pp 2679-2681.
- [12] L.C.Teng, ANL/FNAL LS-17 (May 1985)
- [13] C.C. Kuo, H.P. Chang, G.H. Luo, H.J.Tsai, M.H. Wang, C.T. Chen, “Lattice Study for the Taiwan Photon Source”, in Proc. PAC2005, Knoxville, (2005), pp. 2989-2991.
- [14] A. Wrulich, “The Trieste Synchrotron Light Source ELETTRA”, in Proc. EPAC1988, Rome, Italy, pp 210-212.
- [15] S.H. Nam, “Major Upgrade Activity of the PLS in PAL: PLS-II”, in Proc. PAC09, Vancouver, BC, Canada, (2009), paper TH4PBC03.
- [16] G. Vignola, “Status of SESAME”, in Proc. EPAC2006, Edinburgh, Scotland, 26-30 June, paper THPLS043.
- [17] R. Dowd, M. Boland, G. LeBlanc, Y-R. E. Tan, Phys. Rev. St Accel. Beams 14, 012804 (2011).
- [18] D. Einfeld, “ALBA Synchrotron Light Source Commissioning”, in Proc. IPAC’11, San Sebastian, Spain (2011), paper MOXAA01.
- [19] J.M. Filhol et al., “Overview of the Status of the SOLEIL Project”, in Proc. EPAC 2006, Edinburgh, paper THXPA02.
- [20] K. Balewski, W. Brefeld, W.Decking, Y.L. Li, G.K. Sahoo, R.Wanzenberg, “PETRA III: A New High Brilliance Synchrotron Radiation Source at DESY”, in Proc. EPAC04, Lucarno, (2004), paper THPKF019.
- [21] R. Bartolini, ICFA, Beam Dynamics Newsletter, No. 57, April 2012, pp.13-25.
- [22] K.P. Wooton et al., Physical Review Letters 109 (19)-194801 (2012).
- [23] D. Einfeld, J. Schaper, M., Plesko, “ANKA, a Synchrotron Light Source for Microstructure Fabrication and Analysis”, in Proc. PAC’95, Dallas, TX, USA, pp 272-274.
- [24] M. Eriksson, L.-J Lindgren, M. Sjoestro, E. Wallen, L. Rivkin, A.Streun, Nucl. Instrum. Methods Phys. Res., Sect. A 587, pp.221-226, 2008.
- [25] J. Tavares. J. Synchrotron Rad. 21, 884-903.
- [26] L. Farvacque et al., “A Low-Emittance Lattice for the ESRF”, in Proc. IPAC2013, Shanghai, China pp 79-81.
- [27] M. Borland, V. Sajaev, Y.P.Sun, in Proc. NA-PAC’13, p.249, 2013.
- [28] L. Liu, N. Milas, A. H. C. Mukai, X. R. Resende, A.R.D. Rodrigues, F.H. Sa, “A New 5BA Low Emittance Lattice for Sirius”, in Proc. IPAC’13, Shanghai, China, paper TUPWO001, pp 1874-1876.
- [29] I.P.S. Martin and R. Bartolini, “Optimising the Diamond DDBA Upgrade Lattice for Low Alpha Operation”, in Proc. IPAC’15, Richmond, USA, paper MOPMA002, pp 525-528.
- [30] J. Guo and T. Raubenheimer, “Low Emittance e-/e+ Storage Ring using Bending Magnets with Longitudinal Gradient”, in Proc. EPAC’02, Paris, paper WEPLE001, pp. 1136-1138.
- [31] R. Nagaoka & A. F. Wrulich, Nucl. Instrum. Methods Phys. Res.,Sect. A 575, 292, 2007.
- [32] A. Streun, 2nd low emittance ring design workshop, Lund, 2016. <https://indico.maxiv.lu.se/event/193>
- [33] Y.Cai, K. Bane, R. Hettel, Y. Nosochkov, M-H. Wang, in Phys. Rev. STAB 15, 05002, 2012.
- [34] K. Bane, SLAC-PUB-14892, March, 2012.

HIGGS FACTORY CONCEPTS*

F. Zimmermann[†], CERN, Geneva, Switzerland

Abstract

Designs for future high-energy circular electron-positron colliders are based on both established and novel concepts. An appropriate design will enable these facilities to serve not only as “Higgs factories”, but also as Z, W and top factories, and, in addition, to become a possible first step to a higher-energy hadron collider.

PAST AND FUTURE

Figure 1 illustrates the successful history of circular e^+e^- colliders. Since 1970 the luminosity has constantly increased, on average by more than an order of magnitude per decade. SuperKEKB, presently being commissioned, will mark the next major step in the vertical direction. Future contenders are the e^+e^- collider of the CERN-hosted Future Circular Collider (FCC) study [1, 2], called FCC-ee, and the Circular Electron Positron Collider [3, 4], known as CEPC, studied by a collaboration based at IHEP Beijing.

allow searches for extremely rare decays (also enabling the hunt for sterile right-handed neutrinos); (3) running at the H pole (63 GeV/beam) for H production in the s channel, with mono-chromatization, e.g. to map the width of the Higgs and measure the electron Yukawa coupling; (4) operation at the W pair production threshold (~ 80 GeV/beam) for high precision M_W measurements; (5) operation in the ZH production mode (maximum rate of H 's) at 120 GeV; (6) operation at and above the $t\bar{t}$ threshold (~ 175 GeV/beam); and (7) operation at energies above 175 GeV per beam, should a physics case for the latter be made. Scaling from LEP, at FCC-ee some beam polarization is expected for beam energies up to about 80 GeV [6], permitting an extremely precise energy calibration for the Z and W modes of operation.

The Higgs factories FCC-ee and CEPC would also each be a possible first step towards a future highest energy hadron collider, called FCC-hh and SPPC, respectively.

LESSONS LEARNT

A key design approach consists in exploiting the lessons and recipes from past and present colliders. The demonstrated successful ingredients can be combined so as to optimize the performance and to achieve extremely high luminosity at high energy. This approach is sketched schematically in Fig. 2.

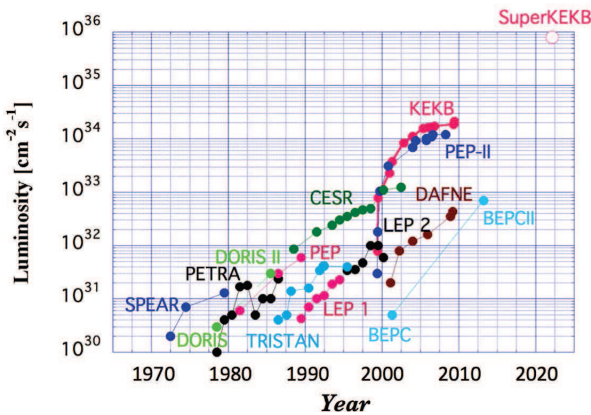


Figure 1: Luminosity trends of circular e^+e^- colliders (Courtesy Y. Funakoshi).

HIGGS FACTORY PHYSICS

In order to support extremely high precision tests of the standard model along with unique searches for rare decays, the proposed “Higgs factories” should operate over a wide range of high beam energies, from about 35 GeV to above ~ 175 GeV. For comparison, the maximum beam energy reached at LEP2 was 104.5 GeV. The FCC-ee physics programme [5] may include: (1) α_{QED} studies (with energies as low as 35 GeV) to measure the running coupling constant close to the Z pole; (2) operation on the Z pole (45.5 GeV/beam), where FCC-ee would serve as a “Tera-Z” factory for high precision M_Z and Γ_Z measurements and

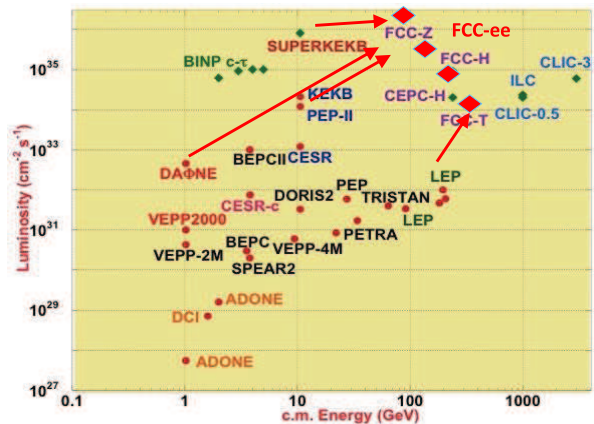


Figure 2: Luminosity as a function of c.m. energy for past, present and future e^+e^- colliders. The proposed FCC-ee and CEPC exploit lessons and recipes from precedent colliders.

At LEP and LEP-2 the operation at high beam energy (up to 104.5 GeV/beam) was demonstrated as well as the handling of synchrotron radiation with critical photon energies at the 1 MeV level. The two B-factories at SLAC and KEK, PEP-II and KEKB, demonstrated the operation with high beam currents of up to a few Ampere, and smooth operation with top-up injection. At DAΦNE the first implementation of crab-waist collisions [7, 8] led to a dramatic luminosity

* This work was supported in part by the European Commission under the FP7 Capacities project EuCARD-2, grant agreement 312453.

[†] frank.zimmermann@cern.ch

increase. SuperKEKB, now being commissioned, will prepare the path for operation at extremely low β_y^* (~ 0.3 mm). It also includes a positron source which would be quite adequate for all operation modes of the proposed Higgs factories. Self-polarized lepton beams were established at HERA and LEP, by means of harmonic spin matching. Operational experience and impressive availability levels (e.g. of the cryogenics systems) from the LHC will also help guide the design of the future machines.

PARAMETERS AND CONSTRAINTS

The beam current is limited by the total synchrotron radiation power per beam P_{SR} ,

$$P_{SR} = n_b N_b \frac{c C_\gamma E^4}{\rho C}, \quad (1)$$

where n_b denotes the number of bunches per beam, N_b the bunch population, c the speed of light, E the beam energy, ρ the bending radius in the arc dipoles, C the ring circumference, and $C_\gamma = (4\pi/3)r_e/(m_e c^2)^3 \approx 8.846 \times 10^{-5}$ m/GeV³, with m_e the electron rest mass and r_e the classical electron radius. All designs assume that other beam power losses, such as those due to higher-order modes or electron cloud, are small compared with the synchrotron radiation power.

Both FCC-ee and CEPC consider two interaction points (IPs) as baseline. The preliminary CEPC design [3] foresees head-on collisions. The FCC-ee design is based on a crossing angle with a crab-waist collision scheme [9].

For collisions with a horizontal full crossing angle θ_c the Piwinski angle is defined as

$$\phi_{piw} \equiv \frac{\sigma_z \theta_c}{2\sigma_x^*}, \quad (2)$$

where σ_z signifies the rms bunch length (in collision), and σ_x^* the horizontal rms beam size at the collision point. Crab-waist collisions increase the luminosity if $\phi_{piw} \gg 1$.

The classical strength of the beam-beam interaction is characterized by the two beam-beam parameters [10]

$$\xi_x = \frac{r_e N_b}{2\pi\gamma} \frac{\beta_x^*}{\sigma_x^{*2} (1 + \phi_{piw}^2)} \quad (3)$$

$$\xi_y = \frac{r_e N_b}{2\pi\gamma} \frac{\beta_y^*}{\sigma_y^* \sigma_x^* \sqrt{1 + \phi_{piw}^2}} \quad (4)$$

where $\gamma = E/(m_e c^2)$ is the relativistic Lorentz factor, and $\beta_{x(y)}^*$ the horizontal (vertical) beta function at the IP. With a large Piwinski angle the vertical beam-beam parameter — a measure of the beam-beam induced tune shift — is much larger than the horizontal one. We may, therefore, expect that beam-beam effects will first be encountered in the vertical plane.

The luminosity per IP is [11]

$$L = \frac{c}{C} \frac{n_b N_b^2}{4\pi\sigma_y^* \sigma_x^* \sqrt{1 + \phi_{piw}^2}} R_{hg}. \quad (5)$$

The luminosity reduction factor due to the hourglass effect, R_{hg} , is important if the rms longitudinal extent of the beam overlap,

$$L_{int} \approx \frac{\sigma_z}{\sqrt{2}} \frac{1}{\sqrt{1 + \phi_{piw}^2}}, \quad (6)$$

becomes comparable to the vertical IP beta function (β_y^*). It can be approximated as [12]

$$R_{hg} \approx \sqrt{\frac{2}{\pi}} \sqrt{a} e^a K_0(a), \quad (7)$$

where

$$a \equiv \frac{\beta_y^{*2} (1 + \phi_{piw}^2)}{2\sigma_z^2}. \quad (8)$$

For example, for $a = 1, 2$ and 5 the luminosity loss due to the hourglass effect amounts to 9%, 5% and 2%, respectively. In the following we assume $R_{hg} \approx 1$.

Using (1) and (4) we can rewrite the luminosity (5) as

$$L = C_{lum} \frac{P_{SR} \rho \xi_y}{\beta_y^* E^3}, \quad (9)$$

where we have introduced a new constant

$$C_{lum} \equiv \frac{3(m_e c^2)^2}{8\pi r_e^2} \approx 4 \times 10^{15} \text{ (TeV)}^2 / (\text{m}^2). \quad (10)$$

In (9) we recognize a decrease of the luminosity with the inverse cubic power of energy, which well matches the energy dependence of the FCC-ee baseline luminosity in Fig. 3. At constant synchrotron radiation power P_{SR} and fixed vertical tune shift ξ_y , the luminosity increases linearly with the bending radius ρ and with the inverse of β_y^* . The luminosity scaling with energy would change if the collider became limited by beamstrahlung instead of by the beam-beam tune shift.

Key parameters for FCC-ee [13] and CEPC [3] are compiled in Table 1.

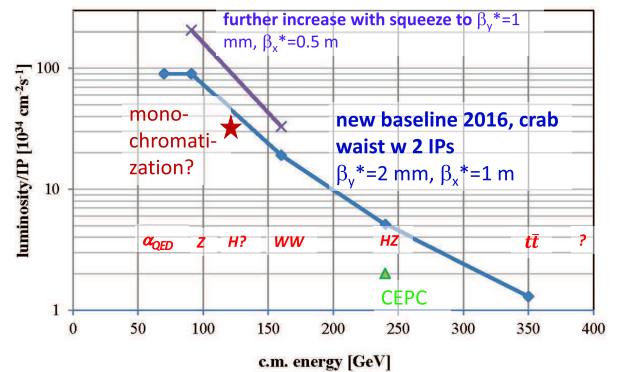


Figure 3: Projected FCC-ee and CEPC luminosity per interaction point (IP) as a function of c.m. energy.

Table 1: Key parameters for the FCC-ee, at three beam energies, and for the CEPC, compared with those achieved at LEP2. The FCC-ee parameters refer to a crab-waist scheme [9], with constant, energy-independent arc-cell length.

parameter	FCC-ee					CEPC	LEP2
circumference	100					54.4	26.7
energy / beam [GeV]	45.6	80	120	175	120	105	
bunches / beam	30180	91500	5260	770	78	50	4
beam current [mA]	1450	152	30	6.6	16.6	3	
luminosity / IP [$10^{34} \text{ cm}^{-2} \text{ s}^{-1}$]	207	90	19	5.1	1.3	2	0.0012
energy loss / turn [GeV]	0.03	0.3	1.67	7.55	3.11	3.11	3.34
total synchrotron radiation power $2P_{\text{SR}}$ [MW]	100	100	100	100	103	103	22
RF voltage [GV]	0.4	0.2	0.8	3.0	10	6.9	3.5
rms horizontal emittance ϵ_x [nm]	0.2	0.1	0.26	0.6	1.3	6	22
rms vertical emittance ϵ_y [pm]	1	1	1	1	2.5	18	250
horizontal IP beta function β_x^* [m]	0.5	1	1	1	1	0.8	1.2
vertical IP beta function β_y^* [mm]	1	2	2	2	2	1.2	50
horizontal IP beam size σ_x^* [μm]	10	9.5	16	25	36	70	182
vertical IP beam size σ_y^* [nm]	32	45	45	49	70	150	3200
rms bunch length (SR) σ_z [mm]	1.2	1.6	2.0	2.0	2.1	2.1	12
rms bunch length (SR+BS) σ_z [mm]	6.7	3.8	3.1	2.4	2.5	2.6	12
horizontal beam-beam parameter ξ_x	0.025	0.05	0.07	0.08	0.08	0.118	0.040
vertical beam-beam parameter ξ_y	0.16	0.13	0.16	0.14	0.12	90.083	0.060
full crossing angle θ_c [mrad]	30	30	30	30	30	0	0
Piwinski angle ϕ_{piw}	10	6	2.9	1.4	1.0	0	0
interaction region length L_{int} [mm]	0.47	0.44	0.71	0.99	1.25	1.84	8.5
longitudinal damping time [turns]	1320	243	72	23	39	39	31
beam lifetime from rad. Bhabha scattering [min]	94	185	90	67	57	61	434

TOP-UP INJECTION

Top-up injection is an essential ingredient of future Higgs factories [14]. It is needed to support the rather short beam lifetime of around 1 hour due to radiative Bhabha scattering in collision (see Table 1), to achieve peak performance and to maximize the integrated luminosity. Using top-up, the collider will operate with constant magnet settings, at stable beam currents, and at a steady temperature. This will also provide optimum conditions for optics fine-tuning.

Top-up injection was successfully employed at both PEP-II and KEKB. For FCC-ee and CEPC, due to the large energy loss per turn, especially at the highest energy, the booster ring providing the injected beam must have a circumference similar to the collider ring itself, and should, for cost reasons, be housed in the same tunnel. The long-standing question of how the booster can bypass the detector has been solved by an asymmetric IR optics of the collider [15]. In this case the top-up booster follows the footprint of the hadron collider, while the e^+e^- collision point is displaced horizontally by, e.g., 9.5 m, larger than, or equal to, the projected half size of the lepton detector. Various options for the actual injection process, including longitudinal injection and multipole-kicker injection, are under study [16].

Intensity rates required from the FCC-ee injector complex are highest at lowest energy (Z pole). The peak rate required for top-up injection is of order $1\text{--}2 \times 10^{12}$ positrons per sec-

ond, which can be delivered already, e.g., by the SuperKEKB injector complex.

TRANSVERSE EMITTANCE

The horizontal emittance is determined by the optics and by the beam energy. It can be written as [17]

$$\epsilon_x = C_q \gamma^5 l_b^3 F / \rho^3 \quad (11)$$

where l_b denotes the length of the bending magnet(s) in a half cell, ρ the bending radius, $C_q = 55/(32\sqrt{3})\hbar c/(m_e c^2) \approx 4 \times 10^{13}$ m for electrons, and F is a form factor depending on the type of arc optics ($F \approx 3$ for a standard FODO lattice with 90 degree phase advance per cell).

The emittance increases with the square of the beam energy, and decreases with the third power of the bending radius. The cell length (dipole length l_b) can be adjusted to obtain the desired emittance. Due to the large bending radius and the shorter cell length (50 m for FCC-ee versus 79 m for LEP) the horizontal emittance of the FCC-ee is much smaller than the emittance at LEP2, at all energies including the $t\bar{t}$ threshold. The vertical emittance is determined by residual errors, in particular spurious vertical dispersion and betatron coupling, which add to the unavoidable small contribution from local vertical design dispersion caused by the horizontal crossing angle together with the detector and compensation solenoid fields around the IP. An emittance

ratio ϵ_y/ϵ_x at the level of 1% is being aimed at. This is much higher than routinely achieved at many storage-ring light sources, but may still be a challenge in the presence of low-beta insertions and with colliding beams.

Figure 4 shows that the target emittance values in the emittance plane are compatible with those of modern light sources and linear-collider damping rings. Figure 5 indicates that given the size of these rings the targeted horizontal emittance — albeit small — should easily be achieved.

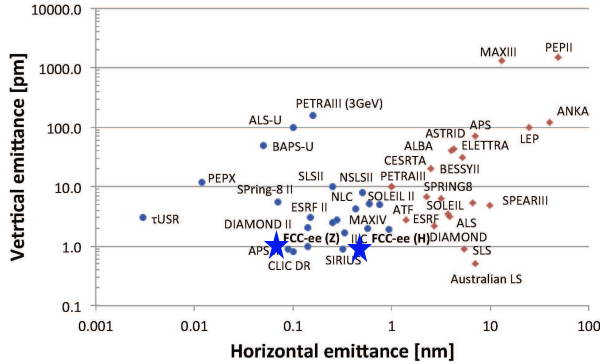


Figure 4: Vertical vs. horizontal emittance for present and future electron storage rings (Courtesy Y. Papaphilippou).

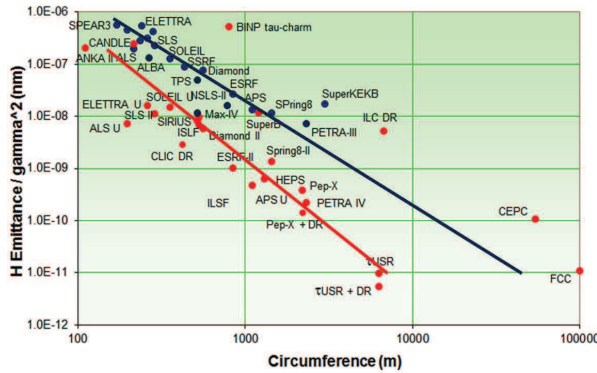


Figure 5: Emittance normalized to beam energy vs. circumference for storage rings in operation (blue dots) and under construction or being planned (red dots). The ongoing generational change is indicated by the transition from the blue line to the red line (Courtesy R. Bartolini).

BEAMSTRAHLUNG

For the first time in a storage-ring collider, beamstrahlung will have a significant impact on the beam parameters and the performance. The term beamstrahlung refers to the synchrotron radiation emitted in the field of the opposing beam during the collision. This can become a limitation on beam lifetime or collider performance for large bunch populations (N_b), small horizontal beam size (σ_x^*) and short bunches (σ_z).

At the highest energy ($t\bar{t}$ running) the hard tail of the beamstrahlung spectrum may limit the beam lifetime due to the fact that electrons or positrons can emit photons of so high an

energy that the emitting particles fall outside the momentum acceptance of the storage ring, The beamstrahlung-limited beam lifetime scales as [9, 18]

$$\tau_{bs} \propto \frac{\rho_{coll}\sqrt{\eta}}{\gamma^2\sigma_z} \exp(A\eta\rho/\gamma^2), \quad (12)$$

where A designates a constant, η the relative momentum acceptance, and the effective bending radius during the collision is

$$\frac{1}{\rho_{coll}} \approx \frac{N_b r_e}{\gamma \sigma_x^* \sigma_z}. \quad (13)$$

For an acceptable lifetime in the $t\bar{t}$ mode of operation the product $\rho_{coll}\eta$ must be sufficiently large. This can be achieved by operating with flat beams ($\sigma_x^* \gg \sigma_y^*$), relatively long bunches, and by designing an optics with large momentum acceptance (typically one is aiming at $\eta \geq 1.5\%$ — a value of 2% has already been demonstrated in simulations without any errors [15]).

At lower energy another effect of beamstrahlung is important. Namely the additional photon emission at the IP increases the equilibrium energy spread and bunch length of the colliding beams. Analytical formulae for this blow up are available [19, 20]. That this indeed is a large effect at low energy can be seen by comparing the value of σ_z from synchrotron radiation alone (SR) with the bunch length expected from the combined effect of synchrotron radiation and beamstrahlung (SR+BS) in Table 1.

NOVEL CONCEPTS

Several novel concepts are either necessary or can further boost the performance. These include an asymmetric IR optics, with low critical photon energies over the last 500 m on the incoming side of the IP, a “virtual crab-waist” scheme, realized by reducing the strength of one of two final-focus sextupoles, and a footprint which matches the footprint of a future hadron collider and allows for the top-up booster injector to bypass the detector. All of these are included in the FCC-ee optics design [15].

FCC-ee consists of two rings with separate beam pipes, which only intersect at the collision points, while the CEPC design is based on a single, common beam pipe. The double ring layout allows for a new efficient measure against the energy sawtooth: “tapering” the strength of all dipoles, quadrupoles, and sextupoles according to the local beam energy. In this way the beam stays nominally centered in all elements, which minimizes the magnitude of beta beating and wake field effects created by orbit offsets from the center of the arc sextupoles or the center of the arc beam pipe, respectively. The RF systems are concentrated in two long straight sections.

CEPC considers a single beam pipe in an attempt to reduce the costs for the arc magnet and vacuum systems. Electron and positron orbits are separated using a pretzel scheme based on electrostatic separators as utilized at CESR, and explored at LEP-1 with fewer bunches. Superimposed on this separation is the energy sawtooth (an inward drift of the

orbit between accelerating sections due to the beam energy loss by synchrotron radiation), which will be different for the two beams. Resulting orbit offsets can lead to significant beta beating [21], which would need to be controlled by sextupoles, independently for the two beams. Off-center beams also excite additional resistive-wall wake fields, which could lead to a unwanted “head-tail” tilts and increase the effective IP beam size [22]. Furthermore, octupole magnets would be required to adjust the chromaticity of either beam, as was the case at the Fermilab Tevatron due to the separation helix. The common beam pipe and its side effects limit the number of bunches which can be stored and significantly reduces the luminosity attainable at the Z pole. One possible mitigation measure is a partial double-ring scheme [23], illustrated in Fig. 6. Partial separation around the two interaction points allows for operation with a bunch train of a certain length (one per beam), which increases the potential luminosity at the Z. However, the transient beam loading of the radio-frequency (RF) cavities could be unacceptably large with a single bunch train. For this reason the simple scheme of Fig. 6 has been extended, to 8 partial separations and 16 RF sections, which enables operation with 4-on-4 bunch trains and, thereby, reduces the magnitude of the transient beam loading to an acceptable value, at the expense of a greater complexity in the layout.

At the highest beam energy, the maximum accelerating voltage is needed. At this energy there are only few bunches in the ring, so that parasitic collisions and impedance effects are less of a concern. For the FCC-ee, sharing the RF system in the two long straights at the $t\bar{t}$ energy saves a factor two in the total number of RF cavities to be installed. The beams are only sharing the two RF straights, but remain in separate beam pipes over the rest of the ring. The sharing of the RF sections can be accomplished with an identical symmetric optics for the two beams [15], and while avoiding any emission of synchrotron radiation on the incoming side of the RF section.

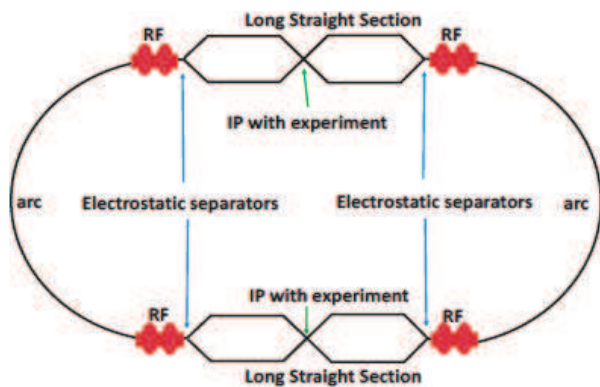


Figure 6: Single ring with partial separation around two IPs (Courtesy M. Koratzinos).

IP BETA FUNCTION

As is evident from (9) a smaller value of β_y^* leads of higher luminosity. Figure 7 shows the historical evolution of β_y^* in e^+e^- colliders. For a long time the minimum β_y^* values were stuck around 1 cm, which was comparable to the bunch length in most of the associated machines. The present β_y^* record in a storage ring, of about 6 mm, is held by the former KEKB. SuperKEKB, presently under commissioning, has a much smaller design value, around 0.3 mm, and will enter a new regime for ring colliders. Therefore, SuperKEKB will pave the way towards the 1–2 mm values of β_y^* targeted for the future Higgs factories.

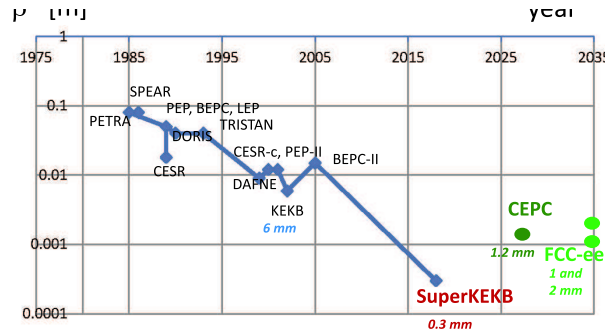


Figure 7: Evolution of β_y^* in e^+e^- colliders over 40 years.

ENERGY EFFICIENCY

The power loss P_{SR} must be constantly sustained by the radio-frequency (RF) system. The associated wall-plug power $P_{wall,SR}$ is equal to P_{SR} divided by the overall efficiency of the RF system, η_{RF} , or

$$P_{wall,SR} = P_{SR}/\eta_{RF} . \quad (14)$$

The various designs are targeting RF efficiencies well above 50%, by use of superconducting cavities at medium gradients (7–10 MV/m), and advanced RF sources, such as highly-efficient “BAC” klystrons [24] or advanced inductive output tubes (IOTs).

In the $t\bar{t}$ mode of operation also the power consumption of the arc magnets becomes significant, scaling with the square of the beam energy. To keep this power as low as possible, for the FCC-ee double-ring arcs novel twin-aperture dipoles, with common Al conductor, and even twin-aperture quadrupoles, with common copper coils, are proposed [25].

Profiting from such innovation, the estimated total power consumption of FCC-ee may stay below 370 MW for the $t\bar{t}$ running, close to 300 MW for the Higgs production mode, and well below 300 MW for the Z and W modes of operation [26].

Considering 200 days of running with 160 days of physics per year the above power levels translate into an annual consumption of about 1400 GWh, which is comparable to the yearly electrical power consumption of the present CERN LHC complex.

MONOCHROMATIZATION

Another possible mode of operation, not yet in any baseline, is monochromatization. Monochromatization could enable an interesting option presently under study for the FCC-ee collider, namely the possibility of direct Higgs production in the s channel, $e^+e^- \rightarrow H$, at a beam energy of 62.5 GeV. This could result in an acceptable Higgs event rate, exactly on the Higgs resonance, and also provide the energy precision required to measure the width of the Higgs particle and the electron Yukawa coupling.

A monochromatized collision can be realized most easily in the case of head-on collisions (i.e. zero crossing angle or nonzero crossing angle with crab cavities), by introducing IP dispersion of opposite sign for the two beams, so that particles with an excess energy ($E + \Delta E$) collide on average with particles of lower energy ($E - \Delta E$) and the spread in the center of mass energy W is reduced by the monochromatization factor λ ,

$$\left(\frac{\sigma_w}{W}\right)_{\text{m.c.}} = \frac{\sigma_\delta}{\sqrt{2}} \frac{1}{\lambda}. \quad (15)$$

For a horizontal IP dispersion $D_x^* \neq 0$, λ is given by

$$\lambda = \sqrt{\frac{D_x^{*2} \sigma_\delta^2}{\epsilon_x \beta_x^*} + 1}. \quad (16)$$

In view of the resonance width of the standard model Higgs of 4.2 MeV and the significantly larger natural rms energy spread of the electron and positron beams at 62.5 GeV of about $\sigma_\delta \approx 6 \times 10^{-4}$ (or $\sigma_\delta E \sim 37$ MeV), the monochromatization factor should be at least 5, which would result in $\sigma_w \leq 10$ MeV.

Simply adding dispersion would not only reduce the effective energy spread, but it would also increase the horizontal beam size and, thereby, lower the luminosity by a factor λ too.

To do better, we need to re-optimize all beam parameters, taking into account both the classical beam-beam limit and the effect of beamstrahlung. In the presence of nonzero IP dispersion, the beamstrahlung will also lead to a blow up of the transverse emittance. The relevant equations were derived in [20] and a partial parameter optimization for monochromatization was reported in [27]. A further refined optimization, varying additional parameters, indicates that for $\lambda \approx 5$ a luminosity of about $4 \times 10^{35} \text{ cm}^{-2} \text{ s}^{-1}$ [28,29] can be attained. Taking into account the standard-model cross section of 1.64 fb for Higgs production in the s -channel, this monochromatization scenario is already of interest for particle physics [30].

SUMMARY

Designing the next generation of circular e^+e^- colliders is a fabulous experience.

The presently proposed designs profit from combining advanced concepts and from the expertise accumulated over the last decades, e.g. concerning optics, collision scheme, high beam currents, polarization, and top-up injection.

Additional novel ideas help optimize the performance and overcome any obstacles encountered. Such new concepts include the virtual crab waist, the asymmetric final focus, the magnet-strength tapering, twin-aperture arc magnets, highly-efficient klystrons, partial double ring, etc.

The next high-energy e^+e^- collider might be the crucial step towards a future 100-TeV hadron collider. It will provide — most importantly — the tunnel, a large part of the infrastructure, the time needed for high-field magnet production, plus additional physics motivation and energy targets for the subsequent hadron machine.

Potentially measuring the Higgs self coupling and Higgs top coupling better than any other proposed facility, this hadron collider may finally become the “ultimate Higgs factory”.

ACKNOWLEDGEMENTS

I am grateful to W. Chou and E. Levichev for inviting this contribution. I would like to thank many colleagues for input and helpful discussions, including M. Aiba, R. Aleksan, A. Apyan, R. Assmann, S. Aull, S. Aumon, R. Bartolini, E. Belli, M. Benedikt, A. Blondel, A. Bogomyagkov, M. Boscolo, O. Brunner, H. Burkhardt, A. Butterworth, Y. Cai, R. Calaga, A. Chao, W. Chou, A. Doblhammer, Z. Duan, J. Ellis, D. d’Enterria, A. Faus-Golfe, Y. Funakoshi, J. Gao, E. Gianfelice-Wendt, B. Haerer, B. Holzer, P. Janot, E. Jensen, I. Koop, M. Koratzinos, E. Levichev, L. Medina, V. Mertens, A. Milanese, A. Novokhatsky, S. Ogur, K. Ohmi, K. Oide, Y. Papaphilippou, P. Piminov, Q. Qin, G. Rumolo, N. Schweg, J. Seeman, D. Shatilov, S. Sinyatkin, G. Stupakov, M. Sullivan, I. Syratchev, L. Tavian, V. Telnov, M.A. Valdivia Garcia, D. Wang, J. Wenninger, U. Wienands, K. Yokoya, J. Zhao and D. Zhou.

REFERENCES

- [1] M. Benedikt, F. Zimmermann, “Towards Future Circular Colliders,” *Journal Korean Physical Society* 69 (6), 893–902 (2016).
- [2] FCC web site <http://cern.ch/fcc>.
- [3] A. Apyan et al., “CEPC-SPPC Preliminary Conceptual Design Report,” IHEP-CEPC-DR-2015-01, IHEP-AC-2015-01 (2015).
- [4] CEPC web site <http://cepc.ihep.ac.cn>.
- [5] M. Bicer et al., *First look at the physics case of TLEP*, JHEP 01 (2014) 164.
- [6] A. Blondel, “Possibilities and Conditions for Very High Precision Electroweak Measurements at TLEP3,” 3rd EuCARD TLEP3 workshop, CERN, 10 January 2013, <http://indico.cern.ch/event/222458>.
- [7] P. Raimondi, “2006 Status on SuperB effort,” at 2nd SuperB Workshop, Frascati, Italy, 16–18 March 2006 (2006).
- [8] M. Zobov et al., “Test of Crab-Waist Collisions at DAΦNE Φ-Factory,” *Phys. Rev. Lett.* 104, 174801 (2010).
- [9] A. Bogomyagkov, E. Levichev, D. Shatilov. “Beam-Beam Effects Investigation and Parameter Optimization for Circular

- e+e- Collider TLEP to study the Higgs Boson,” Phys. Rev. ST Accel. Beams 17, 041004 (2014).
- [10] D.N. Shatilov and M. Zobov, “Beam-Beam Collisions with an Arbitrary Crossing Angl,” ICFA Beam Dynamics Newsletter No. 37 (2005) p. 99.
- [11] F. Ruggiero, F. Zimmermann, “Luminosity Optimization Near the Beam-Beam Limit by Increasing Bunch Length or Crossing Angle,” Phys. Rev. ST Accel. Beams 5, 061001 (2002).
- [12] M.A. Furman, “Hourglass Effects for Asymmetric Colliders,” Proc. PAC91 San Francisco (1991) p. 422.
- [13] J. Wenninger et al., “Future Circular Collider Study Lepton Collider Parameters”, FCC-ACC-SPC-0003, Rev. 3.0, EDMS no. 1346081 (2016).
- [14] A. Blondel, F. Zimmermann, “A High Luminosity e^+e^- Collider in the LHC Tunnel to Study the Higgs Boson,” 12 December 2012, arXiv: 1112.2518 [hep-ex].
- [15] K. Oide et al., “Design of Beam Optics for the Future circular Collider e^+e^- Collider Rings,” presented at FCC Week 2016 Rome, paper submitted to PRAB (2016).
- [16] M. Aiba, A. Saa Hernandez, F. Zimmermann, “Top-up injection for FCC-ee,” CERN-ACC-2015-0065 (2015).
- [17] L. Teng, “Minimizing the Emittance in Designing the Lattice of an Electron Storage Ring,” Fermilab, TM-1269 (1984).
- [18] V.I. Telnov, “Restriction on the Energy and Luminosity of e+e- Storage Rings due to Beamstrahlung,” Phys. Rev. Lett. 110 (2013) 114801.
- [19] K. Ohmi, F. Zimmermann, “FCC-ee/CepC Beam-beam Simulations with Beamstrahlung”, Proc. IPAC14 Dresden (2014).
- [20] M.A. Valdivia Garcia et al., “Effect of Beamstrahlung on Bunch Length and Emittance in Future Circular e^+e^- Colliders”, Proc. IPAC’16 Busan (2016) p. 2438.
- [21] K. Oide, “SuperTRISTAN,” at Workshop on Accelerators for a Higgs Factory: Linear vs. Circular (HF2012), Fermilab 14–16 November 2012 (2012).
- [22] N. Wang et al., “Impedance and Collective Effects Studies in CEPC,” Proc. HF2014, Beijing, 9–12 October 2014 (2014).
- [23] M. Koratzinos et al., “Mitigating Performance Limitations of Single Beam-pipe Circular e^+e^- Colliders,” Proc. IPAC’15 Richmond (2015) p. 2160.
- [24] A.Yu. Baikov, C. Marrelli, I. Syratchev, “Toward High-Power Klystrons With RF Power Conversion Efficiency on the Order of 90%”, IEEE Trans. Electr. Dev., Vol. 62m, No. 10, October 2015 (2015).
- [25] A. Milanese, “Efficient Twin Aperture Magnets for the Future Circular e^+e^- Collider,” to be published in PRAB (2016).
- [26] F. Zimmermann et al., “Electrical Power Budget for FCC-ee,” Proc. IPAC’16 Busan (2016), p. 3828.
- [27] M.A. Valdivia Garcia et al., “Towards a Monochromatization Scheme for Direct Higgs Production at FCC-ee,” Proc. IPAC’16 Busan (2016) p. 2434.
- [28] M.A. Valdivia Garcia, F. Zimmermann, “Towards an Optimized Monochromatization for Direct Higgs Production in Future Circular e^+e^- Colliders,” Proc. CREMLIN funded “CERN-BINP workshop for young scientists in e+e- colliders,” 22–25 August 2016, to be published as CERN Proceedings.
- [29] M.A. Valdivia Garcia, “Monochromatization for Direct Higgs Production in Future Circular e^+e^- Colliders,” Master Thesis, U. Guanajuato, in preparation (2016).
- [30] D. d’Enterria, G. Wojcik, R. Aleksan, “Electron Yukawa from s-Channel Higgs Production at FCC-ee,” FCC-ee Physics Workshop, CERN, 4–5 February 2016 (2016).

IMPLEMENTATION OF ROUND COLLIDING BEAMS CONCEPT AT VEPP-2000

D. Shwartz^{†1}, D. Berkaev, I. Koop¹, E. Perevedentsev¹, Yu. Rogovsky¹, P. Shatunov, Yu. Shatunov¹, Budker Institute of Nuclear Physics, Novosibirsk, Russia
¹also at Novosibirsk State University, Novosibirsk, Russia

Abstract

VEPP-2000 e^+e^- collider at Budker Institute of Nuclear Physics was commissioned in 2009 and collected data during three runs in whole designed energy range of 160–1000 MeV per beam. The Round Colliding Beams concept was implemented at VEPP-2000 to get a significant enhancement in beam-beam limit. The beam-beam parameter value as high as $\xi = 0.12$ per IP was achieved at intermediate energy. To obtain more intensive beams and achieve target luminosity at top energies the injection chain upgrade was done during 2013–2016. Presently VEPP-2000 is recommissioned and ready to start data taking.

ROUND COLLIDING BEAMS

The VEPP-2000 collider [1] exploits the round beam concept (RBC) [2]. The idea of round-beam collisions was proposed more than 25 years ago for the Novosibirsk Phifactory design [3]. This approach, in addition to the geometrical factor gain, should yield the beam-beam limit enhancement. An axial symmetry of the counter-beam force together with the X – Y symmetry of the transfer matrix between the two IPs provide an additional integral of motion, namely, the longitudinal component of angular momentum $M_z = x'y - xy'$. Although the particles' dynamics remain strongly nonlinear due to beam–beam interaction, it becomes effectively one-dimensional. The reduction of degrees of freedom thins out the resonance grid and suppress the diffusion rate resulting finally in a beam-beam limit enhancement [4].

Thus, there are several demands upon the storage ring lattice suitable for the RBC:

1. Head-on collisions (zero crossing angle).
2. Small and equal β functions at IP ($\beta_x^* = \beta_y^*$).
3. Equal beam emittances ($\varepsilon_x = \varepsilon_y$).
4. Equal fractional parts of betatron tunes ($\nu_x = \nu_y$).

The first three requirements provide the axial symmetry of collisions while requirements (2) and (4) are needed for X – Y symmetry preservation between the IPs.

A series of beam–beam simulations in the weak–strong [5, 6] and strong–strong [7] regimes were done. Simulations showed the achievable values of beam–beam parameters as large as $\xi \sim 0.15$ without any significant blow-up of the beam emittances.

First experimental tests of RBC were carried out at CESR collider with use of linear coupling resonance and specially adopted lattice to fulfil mentioned requirements.

The tests showed promising results of beam-beam parameter increase up to 0.09 but could not provide high luminosity due to large β^* value in this test regime [8].

VEPP-2000 OVERVIEW

The layout of the VEPP-2000 complex as it worked before shutdown for upgrade in 2013 is presented in Fig. 1.

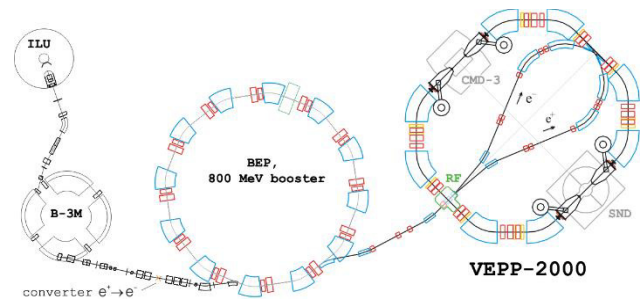


Figure 1: VEPP-2000 complex layout.

VEPP-2000 collider used the injection chain of its predecessor VEPP-2M [9]. It consisted of the old beam transport system and Booster of Electrons and Positrons (BEP) with an energy limit of 800 MeV. Collider itself hosts two particle detectors [10], Spherical Neutral Detector (SND) and Cryogenic Magnetic Detector (CMD-3), placed into dispersion-free low-beta straights. The final focusing (FF) is realized using superconducting 13 T solenoids. The main design collider parameters are listed in Table 1. In Fig. 2 one can find a photo of the collider ring.

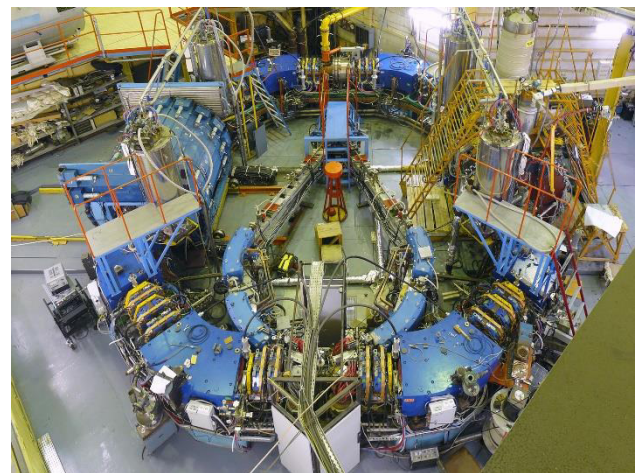


Figure 2: VEPP-2000 collider photo.

The density of magnet system and detectors components is so high that it is impossible to arrange a beam separation in the arcs. As a result, only a one-by-one bunch collision mode is allowed at VEPP-2000.

[†] d.b.shwartz@inp.nsk.su

Table 1: VEPP-2000 Main Parameters (at $E = 1$ GeV)

Parameter	Value
Circumference, C	24.39 m
Energy range, E	150–1000 MeV
Number of bunches	1×1
Number of particles per bunch, N	1×10^{11}
Betatron functions at IP, $\beta_{x,y}^*$	8.5 cm
Betatron tunes, $\nu_{x,y}$	4.1, 2.1
Beam emittance, $\epsilon_{x,y}$	1.4×10^{-7} m rad
Beam–beam parameters, $\xi_{x,z}$	0.1
Luminosity, L	1×10^{32} cm $^{-2}$ s $^{-1}$

Circular Mode Options

The RBC at VEPP-2000 was implemented by placing two pairs of superconducting focusing solenoids into two interaction regions (IR) symmetrically with respect to collision points. There are several combinations of solenoid polarities that satisfy the round beams’ requirements: ‘normal round’ (++) (–), ‘Möbius’ (M) (++) (–) and ‘double Möbius’ (DM) (++) (++) options rotate the betatron oscillation plane by $\pm 90^\circ$ and give alternating horizontal orientation of the normal betatron modes outside the solenoid insertions.

Two ‘flat’ combinations (+– +– or +– –+) are more simple and also satisfy the RBC approach if the betatron tunes lie on the coupling resonance $\nu_x - \nu_y = 2$ to provide equal emittances via X-Y coupling.

All combinations are equivalent in focusing and give the same lattice functions. But the tunes for M and DM options are different due to additional clockwise and counter-clockwise circular mode rotations (see Fig. 3).

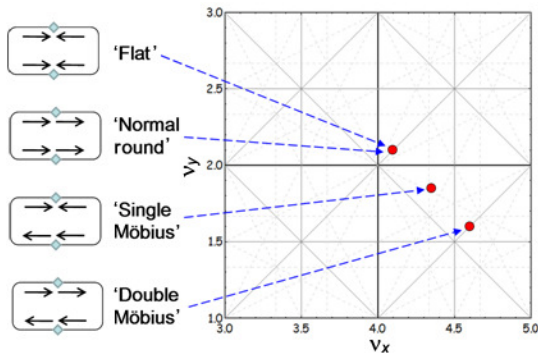


Figure 3: VEPP-2000 round beam options.

Unfortunately, computer simulations showed a serious limitation of the dynamic aperture (DA) for options with mode rotations. A brief experimental study was carried out upon the DM option. At first glance, this case could be preferable, because the tune is a little above 0.5 instead of an integer for the ‘flat’ mode. However, both the simulation and measurement gave a DA of only $\sim 10 \sigma_{x,y}$. In Fig. 4

the measured DA in terms of beam size in M-mode is shown as a function of betatron tune.

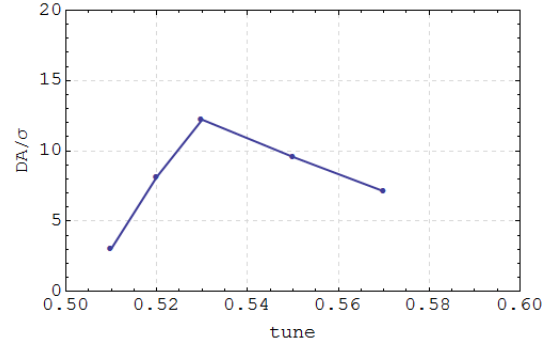


Figure 4: Measured DA in Möbius regime.

The similar problems with DA were reported earlier at CESR collider while trying Möbius regime [11].

Thus hereafter we will suppose conventional ‘flat’ mode (+– –+) with equal emittance due to tunes chosen at the main coupling resonance.

Beam Diagnostics

Beam diagnostics is based on 16 optical CCD cameras that register the visible part of synchrotron light from either end of the bending magnets and give full information about beam positions, intensities, and profiles (see Fig. 5) [12]. In addition to optical beam position monitors (BPM), there are also four electrostatic BPMs in the technical straight sections [13], two photomultipliers for beam current measurements from the synchrotron light intensity, and one beam current transformer as an absolute current monitor.

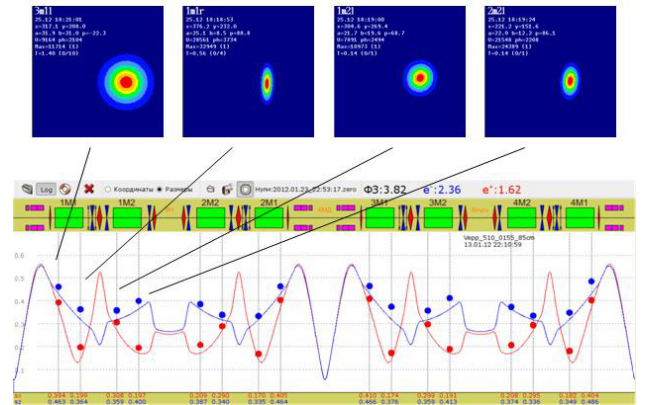


Figure 5: Beam profile measurements.

In addition, VEPP-2000 is equipped with two phi-dissectors – stroboscopic image dissector with electrostatic focusing and deflection. They give information about e $^+$ /e $^-$ longitudinal distribution of particles and bunch length [14].

Beam energy is measured online by the Compton backscattering system [15]. In Fig. 6, one can find the typical edge of the spectrum of scattered photons. The oscillations in the left part are produced by interference of the MeV-scale scattered photons due to interaction of electrons with laser radiation along the curved path inside the dipole.

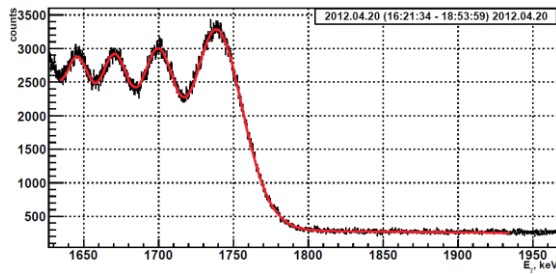


Figure 6: Compton backscattering measurements.

MACHINE TUNING

VEPP-2000 operates in a very wide energy range with strong saturation of magnetic elements at the top energy. For example, the field of conventional iron-dominated bends achieves the value of 2.4 T. In contrast, at low energies the fixed 1.3 T longitudinal field of CMD-3 detector significantly disturbs the focusing. Thus while energy scanning to achieve high luminosity and beam-beam parameter value of great importance is the machine tuning at each energy level. The lattice functions correction is made at VEPP-2000 using Orbit Response Matrix (ORM) analysis [16]. The example of lattice functions before and after correction is presented in Fig. 7.

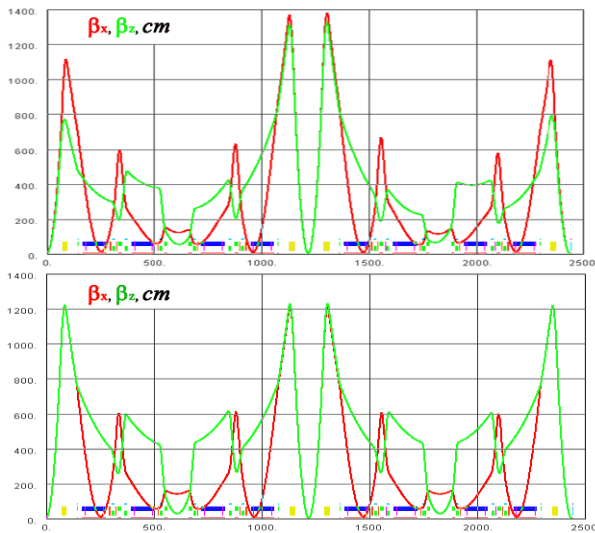


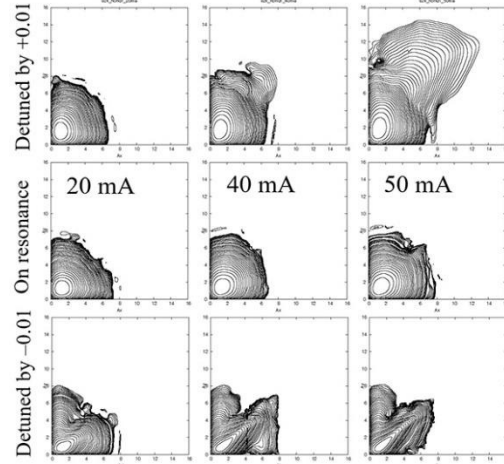
Figure 7: Lattice functions before (up) and after (down) correction.

The ORM is used also to determine and correct closed orbit at quadrupoles by varying their strength, thus using them as additional BPMs. The similar technique is used for final beam-based alignment of solenoids.

Very important it turned out to minimize the dipole correctors' currents, done with help of ORM as well. The reason is poor quality of the steering coils being embedded in quadrupoles due to lack of space.

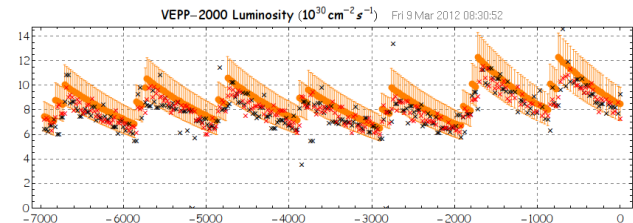
Other parameters need to be tuned carefully are linear coupling in the arcs (tune split < 0.001) [17], and the location of working point (WP) slightly below diagonal of coupling resonance ($\nu_x > \nu_z$). Latter is due to flattening of the beam while shifting from resonance. The tuneshift vector $\{\xi_x, \xi_y\}$ of nonround beam is not parallel with diagonal. If

below diagonal WP self-stabilizes back to resonance, otherwise the shift magnifies itself. In Fig. 8 the results of corresponding *LIFETRAC* [18] simulations are presented. Shown is a transverse beam distribution in terms of normalized amplitudes as a function of counter beam current for three WPs. Beam current of 50 mA corresponds to $\xi \approx 0.11$ at $E = 500$ MeV.

Figure 8: The *LIFETRAC* simulations for on-resonance and detuned WP.

Large number of transverse beam profile measurements along the ring allows us to evaluate the dynamic $\beta_{x,y}^{*+,-}$ values as well as both beam emittances in presence of beam-beam focusing. These measurements by *Lumimetr* software are used routinely to reconstruct luminosity online [19] and serve operator for machine fine-tuning. In Fig. 9 the typical *Lumimetr* predictions (orange dots) together with detectors data (black and red crosses) are shown. Horizontal axis shows the time in seconds.

$$L = 8.477 \times 10^{30} \pm 1.37 \times 10^{30} = 30.52 \text{ nb}^{-1}/\text{hour}$$

Figure 9: Online luminosity monitor @ $E = 800$ MeV.

EXPERIMENTAL RUNS

VEPP-2000 started data-taking with both detectors installed in 2009 [20]. The first runs were dedicated to experiments in the high-energy range [21, 22], while during the last 2012 to 2013 run the scan to the lowest energy limit was done (see Fig. 10). Apart from partial integrability in beam-beam interaction the RBC gives a significant benefit in the Touschek lifetime when compared to traditional flat beams. This results in the ability of VEPP-2000 to operate at an energy as low as 160 MeV — the lowest energy ever obtained in e^+e^- colliders.

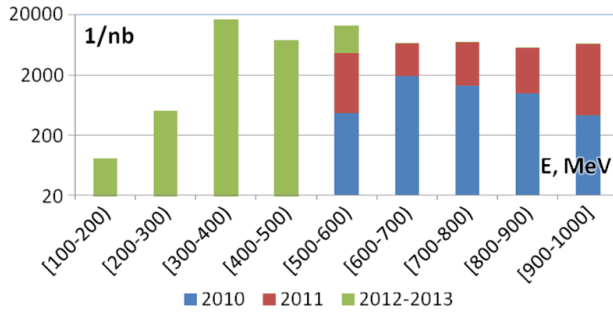


Figure 10: Delivered luminosity in 2010..2013.

The averaged over 10% of best runs luminosity logged by CMD-3 detector during the last three seasons is shown in Fig. 11 with red points. The red lines overestimate the hypothetically achievable peak luminosity with jumps corresponding to possible shortening of FF solenoids by powering only half of coils. The blue dashed line shows the beam-beam limited luminosity for a fixed machine lattice (energy scaling law $L \propto \gamma^4$). It was successfully exceeded due to β^* reduction to 4÷5 cm available at low energies.

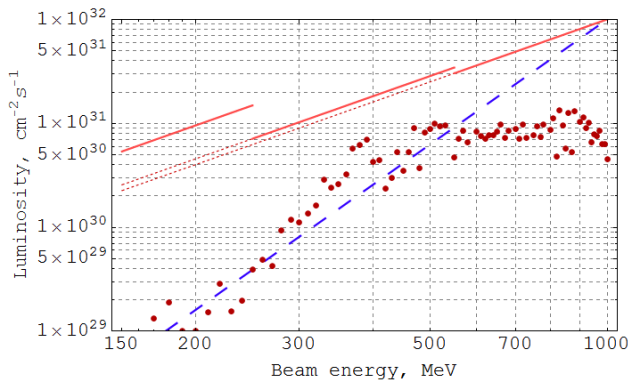


Figure 11: Achieved VEPP-2000 luminosity.

At high energies (> 500 MeV) the luminosity was limited mostly by an insufficient positron production rate (see below). At energies over 800 MeV the necessity of energy ramping in the collider storage ring additionally restricts the luminosity. Only for middle energy range 300÷500 MeV the luminosity is really limited by the beam-beam effects, especially by the flip-flop effect (see below). At the lowest energies the main limiting factors are the small DA, IBS, weak radiation damping, and low beam lifetime as a result.

BEAM-BEAM PARAMETER

We can define the ‘achieved’ beam-beam parameter as:

$$\xi_{\text{lumi}} = \frac{N^- r_e \beta_{\text{nom}}^*}{4\pi\gamma\sigma_{\text{lumi}}^2}, \quad (1)$$

where the beta function is nominal while the beam size is extracted from the fairly measured luminosity.

In Fig. 12 the correlation between achieved and nominal beam-beam parameters is shown for the full data at the

given energy $E = 392.5$ MeV. ‘Nominal’ parameter is defined as (1) but with unperturbed nominal beam size, thus being the measure of beam current. After thorough machine tuning the beam-beam parameter achieves the maximal value of $\xi \sim 0.09$ per one IP during regular work (magenta dots in Fig. 12).

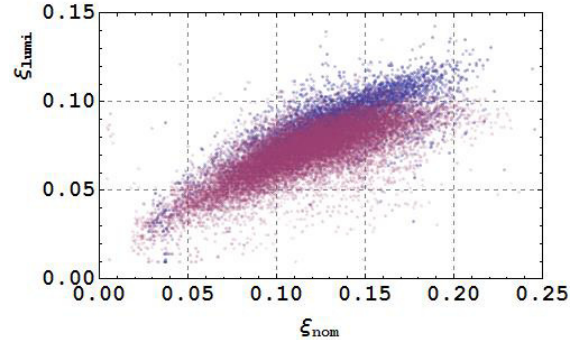
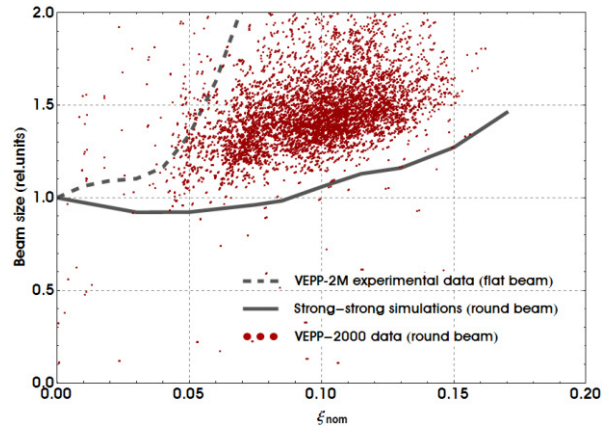


Figure 12: Achieved beam-beam parameter at 392.5 MeV.

Contrary to what the simulations predict (solid line in Fig. 13), the extracted from luminosity beam sizes grow significantly with beam current increase (red dots). However, the emittance grows monotonically, without any blow-up threshold as it happened for flat beam operation at VEPP-2M (dashed line).


 Figure 13: Beam size growth at IP ($E = 537$ MeV).

FLIP-FLOP EFFECT

The beam-beam limit of $\xi_{\text{lumi}} \sim 0.1$ usually corresponds to the onset of a flip-flop effect: the self-consistent situation when one of the beam size is blown-up while another beam size remains almost unperturbed. The simple linear model of flip-flop was discussed earlier [23], with a very high threshold intensity. Observed picture behavior is probably caused by an interplay of beam-beam effects and nonlinear lattice resonances.

In Fig. 14 images from the online control TV camera are presented for the cases of regular beams (a), blown-up electron beam (b) or positron beam (c). The corresponding spectra are shown on the right. One can see in the spectra of a slightly kicked bunch that the shifted tunes (π -mode) jumped to the 1/5 resonance in the case of a flip-flop.

The type of flip-flop effect that has been observed seems to be avoidable by suppressing the resonance driving

terms, as well as by tuning down the working point. Unexpected problems with DA currently prevent us from using the design working point. The acceptable bunch stacking rate and beam lifetime at collision are available only for the betatron tunes of $\{\nu\} \sim 0.13\text{--}0.18$.

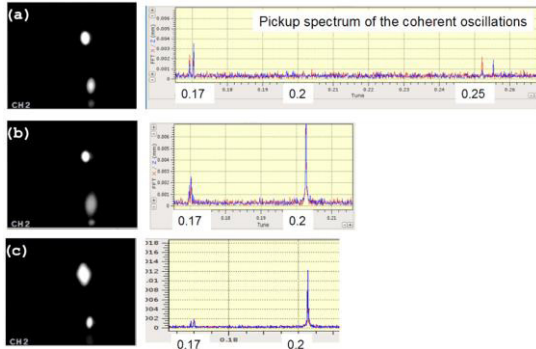


Figure 14: Coherent beam-beam oscillations spectra.

LONG BUNCH

While studying the dependence of beam-beam threshold on bunch length at relatively low energy of 392.5 MeV it was found that the RF voltage decrease from 30 kV to 17 kV gives a significant benefit in the maximal value of ξ (blue dots in Fig. 12) up to $\xi \sim 0.12$ per IP.

The cross-check for beam-beam parameter measurement is the analysis of the coherent beam oscillation spectrum. In Fig. 15 one can find two pairs of σ - and π -modes tunes equal to 0.165 and 0.34, respectively. The total tune shift of $\Delta\nu = 0.175$ corresponds to ξ per one IP equal to:

$$\xi = \frac{\cos(\pi\nu_\sigma) - \cos(\pi\nu_\pi)}{2\pi \sin(\pi\nu_\sigma)} = 0.124. \quad (2)$$

The Yokoya factor here is taken to be equal to 1 due to the fact that oscillations with very small amplitude ($\sim 5 \mu\text{m} = 0.1 \sigma^*$) were excited by a fast kick and the spectrum was investigated for only 8000 turns. During this short time beam distribution is not deformed by an oscillating counter beam and remains Gaussian [24].

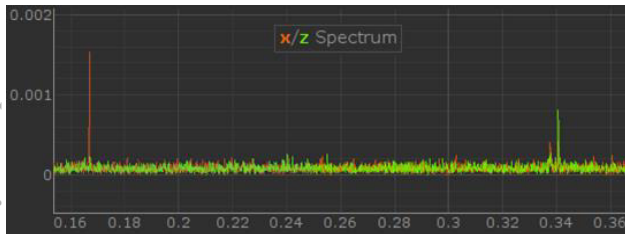


Figure 15: Beam-beam tuneshift @ 392.5 MeV.

The increase of maximal ξ value with lower voltage comes from the bunch lengthening. In our particular case this lengthening is the result of several effects. In addition to regular growth of radiative bunch length two collective effects take place: potential well distortion and microwave instability. The latter one is observed at low energies with a low RF voltage above a certain bunch intensity [14]. In

Fig. 16 the bunch length dependence on beam current is presented for two levels of RF voltage. In Fig. 17 the extracted from horizontal beam size measurements energy spread as a function of intensity is shown. Red points correspond to microwave instability above the threshold.

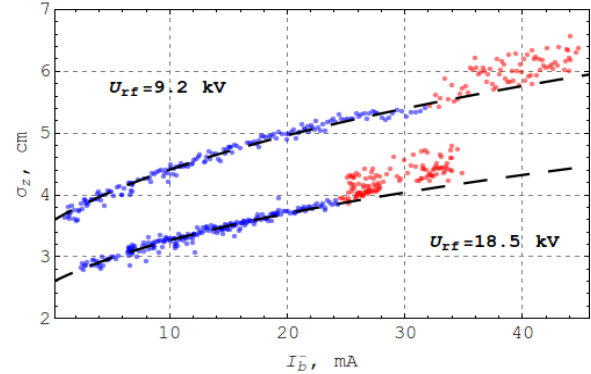


Figure 16: Bunch length as a function of beam current @ $E = 480$ MeV.

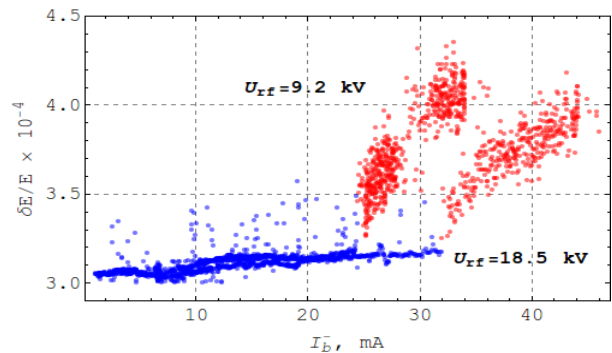


Figure 17: Beam energy spread as a function of beam current @ $E = 480$ MeV.

The observed beam-beam limit enhancement correlated with bunch lengthening firstly believed to be an experimental evidence of predictions [25] of beam-beam interaction mitigation for the bunch slightly longer than β^* due to second integral of motion in addition to the angular momentum. Later it was shown in simulations [26] that finite synchrotron oscillations should prevent full integrability of beam-beam interaction.

Another explanation can come from beam-beam induced resonances suppression due to hour-glass effect [27].

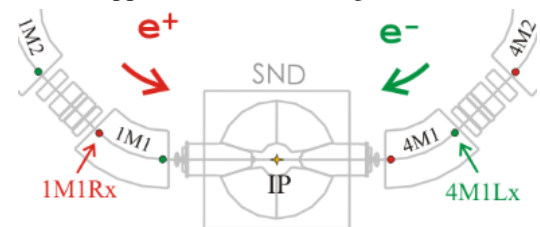


Figure 18: Location of beams size control.

The post-analysis of logged data was done after VEPP-2000 upgrade shutdown had started. At the energy of 392.5 MeV enough data was stored for short (a) and long (b) bunch cases. Only "strong-strong" data was selected, i.e. the beam currents difference does not exceed 10%. In

Fig. 19 the measured horizontal sizes of electron (σ_{4MILx}) and positron (σ_{1MIRx}) beams (see Fig. 18) as a function of beam currents geometric average are shown.

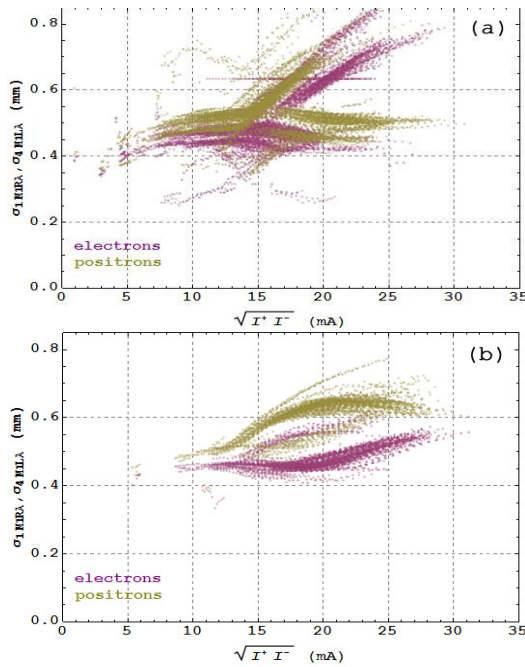


Figure 19: Beam sizes vs. beam current.

These particular sizes (see Fig. 18) are chosen since these observation points are separated from IP by tele-

scopic transformation matrix in horizontal plane and mirror-symmetric to each other. One can see from Fig.19 that in both cases the flip-flop develops (unequal positron and electron beam sizes) for beams intensity higher than 15 mA that corresponds to $\xi_{nom} \sim 0.1$. But the long bunch tends to mitigate this troublesome due to specific luminosity degradation effect for higher intensities.

VEPP-2000 UPGRADE

VEPP-2000 was commissioned and spent three successful runs in 2010-2013 collecting data in the whole energy range of 160÷1000 MeV per beam [28]. In order to achieve the design luminosity the machine was stopped for upgrade of the whole injection chain. Firstly, the complex was linked up via a 250 m beamline K-500 [29] to the new BINP Injection Complex (IC) [30] capable to produce high quality electron and positron beams at energy of 400 MeV (see Fig. 20).

Another VEPP-2000 efficiency limitation came from maximal energy of the booster ring BEP limited at the value of 800 MeV. Even with unlimited e^+/e^- production rate the beam-beam parameter being at the threshold after injection will inevitably decrease after acceleration in the collider ring $\xi \propto 1/\gamma^2$. In addition, the acceleration of colliding beams close to the threshold is very delicate and slow, and leads to a long dead time. As a result, BEP was upgraded to provide top-up injection up to 1 GeV [31]. The transfer channels to VEPP-2000 ring were also reconstructed in order to increase maximal energy.

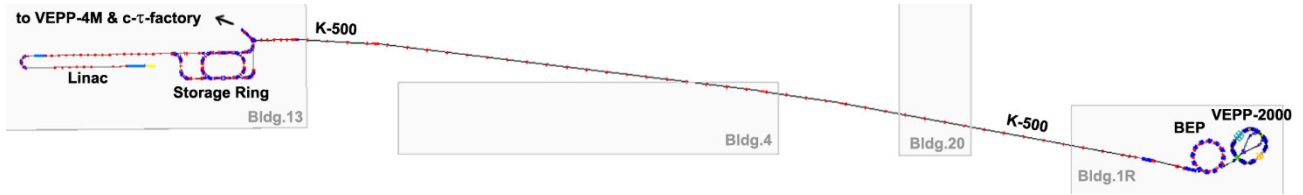


Figure 20: VEPP-2000 linked to the new Injection Complex.

The upgrade was finished in the beginning of 2016. VEPP-2000 injection chain was successfully recommissioned [32]. The achieved positron stacking rate at BEP amounts to $2 \times 10^8 e^+/sec$ that exceeds corresponding value before upgrade in one order of magnitude (see Fig. 21).

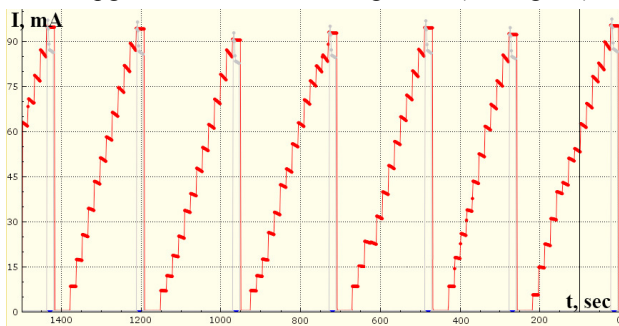


Figure 21: e^+ stacking @ BEP.

Relatively small modifications were done in VEPP-2000 storage ring. Two additional kickers were installed to provide 1 GeV beam injection. All 8 two-sided copper mirrors

used to extract the synchrotron light to CCD cameras were replaced.

In 2016 the collider firstly passed through the beam scrubbing procedure working in so called "warm mode" with switched off SC solenoids. In addition, in this regime two beams e^+/e^- with infinitesimal intensity were obtained to carry out the beam diagnostics alignment and tuning.

During upcoming new run we intend to achieve the target luminosity and start its delivery to detectors with an ultimate goal to deliver at least $1 fb^{-1}$ [33].

CONCLUSION

Round beams give a serious luminosity enhancement. The achieved beam-beam parameter value at middle energies amounts to $\xi \sim 0.1-0.12$. VEPP-2000 was successfully taking data with two detectors across the whole designed energy range of 160–1000 MeV with a luminosity value five times higher than that achieved by its predecessor, VEPP-2M [34]. To reach the target luminosity, injection chain upgrade has been done. Upgraded complex is

now at the finish of the commissioning phase and ready to deliver luminosity at the design level.

ACKNOWLEDGEMENT

We are grateful to M. Achasov, A. Batrakov, E. Bekhtenev, O. Belikov, M. Blinov, D. Burenkov, F. Emanov, K. Gorchakov, G. Karpov, A. Kasaev, A. Kirpotin, I. Korenev, V. Kozak, A. Krasnov, G. Kurkin, P. Logachev, A. Lysenko, S. Motygin, N. Muchnoy, A. Murasev, D. Nikiforov, A. Otboev, V. Prosvetov, A. Romanov, I. Sedlyarov, A. Semenov, A. Senchenko, D. Shatilov, A. Skrinsky, V. Veremeenko, I. Zemlyansky, Yu. Zharinov for continuous support.

REFERENCES

- [1] Yu.M. Shatunov *et al.*, "Project of a New Electron-Positron Collider VEPP-2000", in *Proc. EPAC'00*, Vienna, Austria, 2000, pp. 439-441.
- [2] V.V. Danilov *et al.*, "The Concept of Round Colliding Beams", in *Proc. EPAC'96*, Sitges, Spain, 1996, pp. 1149-1151.
- [3] L.M. Barkov *et al.*, "Phi-Factory Project in Novosibirsk", in *Proc. 14th HEACC'89*, Tsukuba, Japan, 1989, p. 1385.
- [4] K. Ohmi, K. Oide and E.A. Perevedentsev, "The beam-beam limit and the degree of freedom", in *Proc. EPAC'06*, Edinburgh, Scotland, 2006, pp.616-618.
- [5] I. Nesterenko, D. Shatilov and E. Simonov, "Beam-Beam Effects Simulation for VEPP-2M With Flat and Round Beams", in *Proc. PAC'97*, Vancouver, Canada, 1997, p. 1762.
- [6] I.A. Koop, "VEPP-2000 Project", in *Proc. e⁺e⁻ Physics at Intermediate Energies Workshop*, Stanford, 2001, pp. 110-115.
- [7] A.A. Valishev, E.A. Perevedentsev, K. Ohmi "Strong-Strong Simulation of Beam-Beam Interaction for Round Beams", in *Proc. PAC'03*, Portland, USA, 2003, p. 3398.
- [8] E. Young *et al.*, "Collisions of Resonantly Coupled Round Beams at the Cornell Electron-Positron Storage Ring (CESR)", in *Proc. PAC'97*, Vancouver, Canada, 2003, pp. 1542-1544.
- [9] G.M. Tumaikin *et al.*, in *Proc. HEACC'1977*, Serpukhov, USSR, 1977, p.443.
- [10] T.V. Dimova *et al.*, "Recent Results on e⁺e⁻→hadrons Cross Sections from SND and CMD-3 Detectors at VEPP-2000 collider", *Nucl. Part. Phys. Proc.*, vol. 273-275, pp. 1991-1996, 2016.
- [11] S. Henderson *et al.*, "Investigation of the Möbius Accelerator at CESR", in *Proc. PAC'99*, New York, USA, 1999, pp. 410-412.
- [12] Yu.A. Rogovsky *et al.*, "Beam Measurements with Visible Synchrotron Light at VEPP-2000 Collider", in *Proc. DIPAC'11*, Hamburg, Germany, 2011, pp. 140-442.
- [13] Yu.A. Rogovsky *et al.*, "Pickup Beam Measurement System at the VEPP-2000 Collider", in *Proc. RuPAC'10*, Protvino, Russia, 2010, pp. 101-103.
- [14] Yu.A. Rogovsky *et al.*, "Status and Perspectives of the VEPP-2000 Complex", in *Proc. RuPAC'14*, Obninsk, Russia, 2014, pp. 6-10.
- [15] E.V. Abakumova *et al.*, "A system of beam energy measurement based on the Compton backscattered laser photons for the VEPP-2000 electron-positron collider", *Nucl. Instrum. Meth. A*, vol. 744, pp. 35-40, 2014.
- [16] A.L. Romanov *et al.*, "Round Beam Lattice Correction using Response Matrix at VEPP-2000", in *Proc. IPAC'10*, Kyoto, Japan, 2010, pp. 4542-4544.
- [17] I. Koop, E. Perevedentsev, D. Shwartz and A. Valishev, "Correction of the Betatron Coupling and Closed Orbit Distortion at the VEPP-2000 Collider", in *Proc. PAC'01*, Chicago, USA, 2001, pp. 1996-1998.
- [18] D. Shatilov, *Part. Accel.*, vol. 52, p. 65, 1996.
- [19] D. Shwartz *et al.*, "Recent Beam-Beam Effects at VEPP-2000 and VEPP-4M", in *Proc. ICFA Mini-Workshop on Beam-Beam Effects in Hadron Colliders (BB2013)*, Geneva, Switzerland, 2013, CERN-2014-004, pp. 43-49.
- [20] M.N. Achasov *et al.*, "First Experience with SND Calorimeter at VEPP-2000 Collider," *Nucl. Instrum. Meth. A* vol. 598, pp. 31–32, 2009.
- [21] D.N. Shemyakin *et al.*, "Measurement of the e⁺e⁻ → K⁺K⁻π cross section with the CMD-3 detector at the VEPP-2000 collider", *Phys. Let. B*, vol. 756, pp. 153-160, 2016.
- [22] M.N. Achasov *et al.*, "Study of the process e⁺e⁻ → ωηπ⁰ in the energy range $\sqrt{s} < 2$ GeV with the SND detector", *Phys. Rev. D*, 94, 032010, 2016.
- [23] A.V. Otboev and E.A. Perevedentsev. "On self-consistent β-functions of colliding bunches", in *Proc. PAC'1999*, New York, USA, 1999, pp. 1524-1526.
- [24] P.M. Ivanov *et al.*, "Experimental Studies of Beam-Beam Effects at VEPP-2M", in *Proc. Workshop on Beam-Beam Effects in Circular Colliders*, Fermilab, USA, 2001, p. 36.
- [25] V.V. Danilov and E.A. Perevedentsev. "Two Examples of Integrable Systems with Round Colliding Beams", in *Proc. PAC'1997*, Vancouver, Canada, 1997, pp. 1759-1761.
- [26] A. Valishev, S. Nagaitsev, D. Shatilov and V. Danilov, "Beam-Beam Limit in an Integrable System", in *Proc. NaPAC'13*, Pasadena, 2013, pp. 75-77.
- [27] S. Krishnagopal and R. Seeman, "Bunch-length effects in the beam-beam interaction", *Phys. Rev. D*, 41, 2312, 1990.
- [28] A. Romanov *et al.*, "Status of the Electron-Positron Collider VEPP-2000", in *Proc. NaPAC'13*, Pasadena, USA, 2013, pp. 14-18.
- [29] I. Zemlyansky *et al.*, "Electron and Positron Beams Transportation Channels to BINP Colliders", in *Proc. RuPAC'14*, Protvino, Russia, 2014, pp. 462-464.
- [30] A. Starostenko *et al.*, "Status of Injection Complex VEPP-5: Machine Commissioning and First Experience of Positron Storage", in *Proc. IPAC'14*, Dresden, Germany, pp. 538-540.
- [31] D. Shwartz *et al.*, "Booster of Electrons and Positrons (BEP) Upgrade to 1 GeV", in *Proc. IPAC'14*, Dresden, Germany, pp. 102-104.
- [32] D. Berkaev *et al.*, "Commissioning of Upgraded VEPP-2000 Injection Chain", in *Proc. IPAC'16*, Busan, Korea, pp. 3811-3813.
- [33] I. Logashenko *et al.*, "Measurement of hadronic cross-sections with CMD-3 at VEPP-2000", in *Proc. ICHEP'16*, 2016, to be published.
- [34] P.M. Ivanov *et al.*, "Luminosity and the Beam-Beam Effects on the Electron-Positron Storage Ring VEPP-2M with Superconducting Wiggler Magnet", in *Proc. 3rd Advanced ICFA Beam Dynamics Workshop on Beam-Beam Effects in Circular Colliders*, Novosibirsk, USSR, 1989, pp. 26-33.

ISSUES IN CEPC PRETZEL AND PARTIAL DOUBLE RING SCHEME DESIGN

H. Geng*, F. Su, Y. Wang, Y. Zhang, D. Wang, J. Gao, Q. Qin
 Institute of High Energy Physics, Beijing, China

Abstract

IHEP has proposed a circular electron and positron collider (CEPC) to study the properties of the Higgs boson. In the baseline design, the circumference of CEPC will be taken as 50-70 km. The single ring scheme and the partial double ring scheme are now both under study. In the single ring scheme, the electron and positron beam will share the beam pipes, thus a special orbit is needed to avoid the beam colliding at positions except the Interaction Points (IPs). While in the partial double ring scheme, the two beams will be separated into two beam pipes in the parasitic collision positions. This paper will show the latest design of the CEPC lattice, including both the pretzel and partial double ring scheme. Some critical issues that we encountered when designing the lattices will be discussed.

INTRODUCTION

CEPC (a Circular Electron Positron Collider) has been proposed by IHEP to study the Higgs boson [1]. At the end of the 2014, the Preliminary Conceptual Design Report of CEPC was published, with single ring (pretzel) scheme as the baseline design [2]. As the design work move on, especially the demand to increase the luminosity at Z-pole, we started to study a new scheme, e.g. the so called "Partial double ring scheme". Then, the RF system raised that the RF efficiency could be too low to assure a constant voltage at the cavity for all bunches, so another scheme called "Advanced double ring scheme" was proposed to mitigate the low RF efficiency effect.

Another scheme, which is relatively less complicated but more costly, the double ring scheme, is also under study. The pretzel and partial double ring scheme will be introduced in this talk.

PRETZEL SCHEME DESIGN

As described in the Pre-CDR [2], the ring is using 60/60 degrees phase advance FODO cells, with interleaved sextupoles. The pretzel orbit is designed for 50 bunches per beam, every 4π phase advance has one parasitic collision point. A schematic drawing of the pretzel orbit is shown in Fig.1.

In our design, the horizontal separation scheme is adopted to avoid big coupling between the horizontal and the vertical. The orbit is generated such that there is no off-center orbit in RF sections to avoid beam instability and High Order Modes(HOMs) in the cavities. There will be one pair of

electrostatic separators for each arc, and for each arc, the first separator will be placed before the first parasitic collision point in this region to generate the orbit, and the second separator will be placed after the last collision point in this region to remove the orbit.

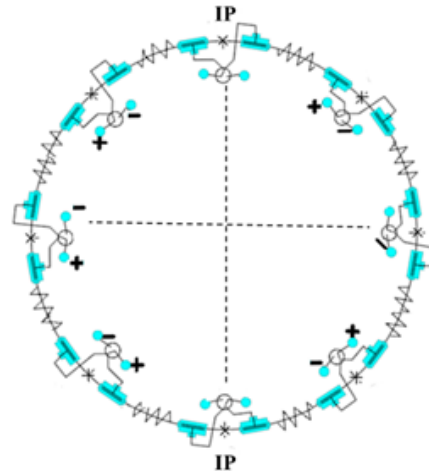


Figure 1: A schematic drawing of the pretzel orbit scheme, the beams are separated by electrostatic separators.

A schematic drawing of the pretzel orbit and the place of electrostatic separators for one arc is shown in Fig.2.

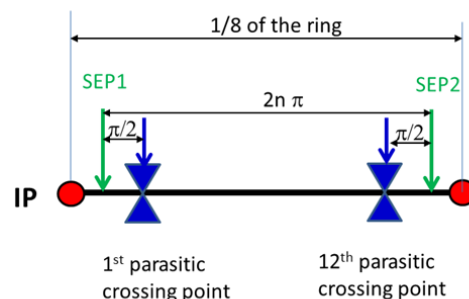


Figure 2: A schematic drawing of the positions of the electrostatic separators for 1/8th of the ring. SEP1 and SEP2 in the drawing means the first and second electrostatic separators.

ISSUES WITH PRETZEL ORBIT

Beams with off-centered orbit, will experience extra fields in magnets. To be specific, in quadrupole magnets, the beam will see an extra dipole field when it is off-centered.

* Email: genghp@ihep.ac.cn. This work was supported by National Natural Science Foundation of China, under contract NO. 11405188.

The dipole strength can be estimated with a simple formula: $\Delta B = K_1 \cdot B\rho \cdot \Delta x$, where K_1 is the normalized quadrupole strength, $B\rho$ is the magnetic rigidity of the beam, and Δx is the orbit of the beam. With a simple calculation, we can see that the extra dipole field seen by the off-centered beam has a strength that is comparable to the strength of the main bending magnets.

In sextupole magnets, the beam will experience extra dipole and quadrupole fields. The field strength can be estimated similarly. These extra fields (dipole field in quadrupoles, and both dipole and quadrupole fields in sextupoles) will break the periodicity and achromatic condition of the lattice, and this effect has to be corrected.

The distortion of pretzel orbit effects on beta functions and dispersion function has to be corrected to have a reasonable dynamic aperture. Also, since the sextupoles are now coupled with quadrupoles, the chromaticity correction and the tune are coupled together, so linear lattice and nonlinear chromaticity has to be corrected at the same time. We try to find a new lattice period by taking 12 FODO cells, with symmetrically placed magnets, and require the phase advance to be 4π and the chromaticity to be zero at the same time. There is no detailed phase advance requirement in each FODO cell in this case. A new lattice can be found accordingly, the new lattice after correction is shown in Fig. 3.

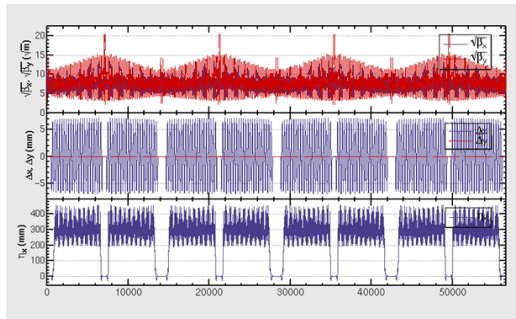


Figure 3: The lattice after correction of off-center orbit effect.

The dynamic aperture of the ring after correction of the pretzel orbit distortion on the lattice has been checked before the insertion of the Final Focus System (FFS). The result is shown in Fig. 4. The working point used here is (.79,.15) in horizontal and vertical planes. The plot shows that the dynamic aperture is $\sim 20\sigma_x \times 150\sigma_y$ in horizontal and vertical planes for on momentum particles, and it is $\sim 16\sigma_x \times 120\sigma_y$ particles with $\pm 2\%$ momentum spread. The tracking has been done with 240 turns, which corresponds to 3 transverse damping times.

COMBINATION WITH FFS

One version of Final Focus System (FFS), which has been optimized for the ring without pretzel orbit, is inserted to the lattice with pretzel orbit, the beta function and dispersion function of the FFS is shown in Fig 5.

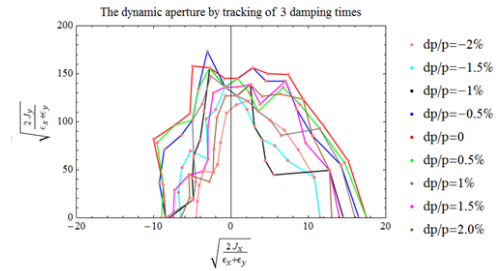


Figure 4: The dynamic aperture of the ring after correction of the pretzel orbit distortion on the lattice has been and before the insertion of the Final Focus System (FFS), the working point used here is (.79,.15) in horizontal and vertical planes.

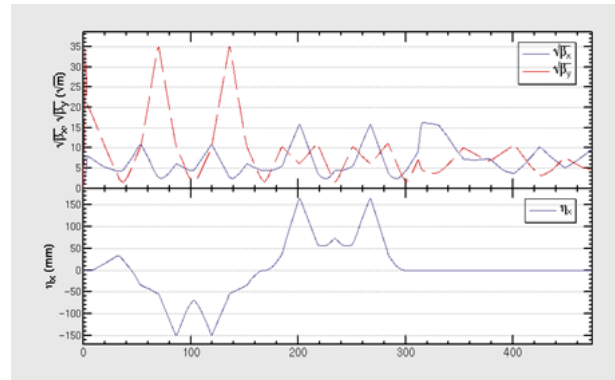


Figure 5: Beta function and dispersion function of Final Focus System to be connected to the ring with pretzel orbit.

In this design, $\beta_y^* = 3$ mm. The dynamic aperture then is optimized with the code MODE (Multi-Objective optimization by Differential Equation). All sextupoles are set free in the optimization. The resulted dynamic aperture is $\sim 16\sigma_x$ in horizontal plane for on momentum particles, and it is $\sim 6\sigma_x$ for particles with $\pm 2\%$ momentum spread, as shown in Fig 6. The tracking has been done with 240 turns, which corresponds to 3 transverse damping times.

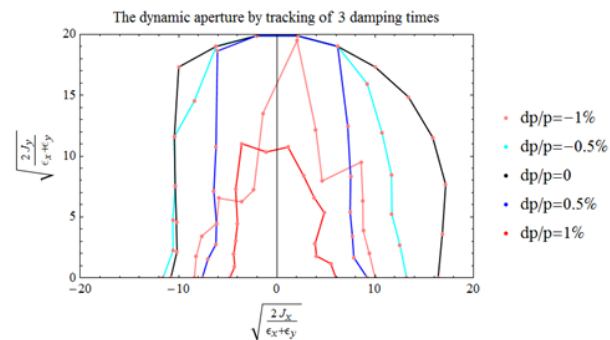


Figure 6: The optimized dynamic aperture with FFS and pretzel orbit.

CEPC PARTIAL DOUBLE RING DESIGN

For the partial double ring design, we choose double ring scheme for e+e- at IP1 and IP3. The total length of this part is about 3 km. The arcs of both sides of IP1 and IP3 are kept the same as the Pre-CDR single ring scheme. The layout of CEPC partial double ring is shown in Fig. 7.

The full crossing angle for CEPC partial double ring scheme is 30 mrad. We assume the final focus system (FFS) length is about 500 m, then the largest distance at the end of FFS is about 7.5 m and between the two separated pipes is about 15 m. At the start of the double ring, we need to use electrostatic separator to separate the electron and positron beams. We choose the parameter of electrostatic separator according to the experience on LEP [3]. The maximum operating field strength is 2 MV/m. The length of electrostatic separator is 4.5 m.

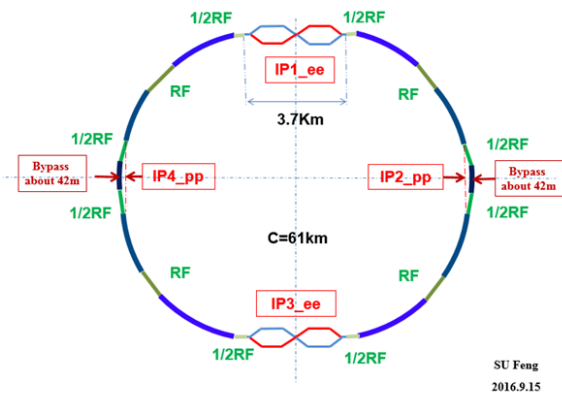


Figure 7: Layout of the partial double ring scheme. The full crossing angle is 30 mrad.

For the beam energy $E_0 = 120\text{GeV}$, the maximum deflection angle per separator is about 66 μrad . We choose 12 electrostatic separators work together to obtain a deflection angle of 0.75 mrad, with each separator deflects the beam by 62.5 μrad . After those separators, we use a pair of septum dipoles to obtain 4.25 mrad and a group of dipole (B1) to acquire the other 10 mrad and suppress the dispersion to zero.

The standard FODO cells here has a phase advance of 90/90 in horizontal and vertical planes, and the chromaticity correction is done with sextupoles and with the non-interleaved scheme, as shown in Fig. 8.

The beta functions at the IP are $\beta_y^* = 1\text{ mm}$ and $\beta_x^* = 0.22\text{ m}$, and for this design $L^* = 1.5\text{ m}$. Local chromaticity correction is done with sextupoles pairs separated by $-I$ transformation. It is expected that 1) all 3rd and 4th order resonance driving terms due to sextupoles are almost cancelled; 2) up to 3rd order chromaticity are corrected with main sextupoles, phase tuning and additional sextupoles; 3) tune shift $dQ(J_x, J_y)$ due to finite length of main sextupoles is corrected with additional weak sextupoles; 4) break down of $-I$, high order dispersion could be optimized with odd dispersion scheme or Brinkmann sextupoles. It is worth

pointing out that the crab sextupoles have not been put into the lattice yet.

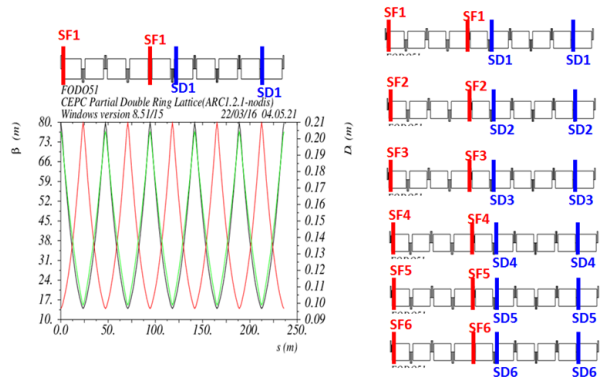


Figure 8: The standard FODO cells with 90/90 degree phase advances in horizontal and vertical planes. The sextupoles are placed using the non-interleaved scheme.

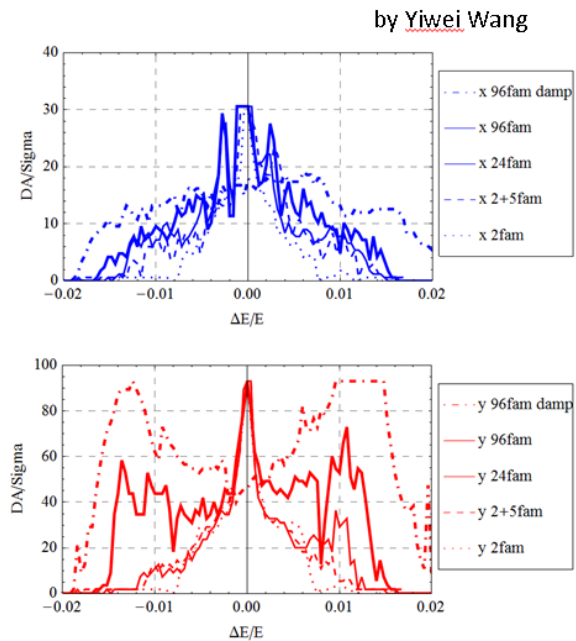


Figure 9: The achieved dynamic aperture after optimization with downhill simplex method, with and without damping.

DA STUDY FOR CEPC PARTIAL DOUBLE RING DESIGN

The dynamic aperture of CEPC partial double ring design has been optimized with the downhill simplex method. Only the bare lattice is considered. The synchrotron motion is considered in the tracking. Tracking has been done for one damping time, with and without damping, respectively. The coupling is assumed to be $\kappa = 0.003$. The working point is taken to be (0.08, 0.22) in horizontal and vertical planes.

The achieved dynamic aperture is $16\sigma_x/45\sigma_y$ for on-momentum particles, and $3\sigma_x/5\sigma_y$ for particles with 2% momentum spread, as shown in Fig. 9.

We think further optimization of the dynamic aperture is possible, by using larger dispersion for IR sextupoles, and increasing β_y^* from 1 mm to 1.3 mm as required in the new parameters, and trying more families of sextupoles in IR.

The study of effects such as quantum excitation, solenoid field, errors and misalignments are under going.

SUMMARY

Several schemes for CEPC are understudy at IHEP. We have described the latest results of the design of the pretzel scheme and partial double ring scheme. A multi-objective code MODE has been developed at IHEP, and it has been proved to be very effective in optimizing dynamic aperture. The dynamic aperture of single ring has been

greatly improved, but has not reached 2% momentum spread. The dynamic aperture for partial double ring achieved $3\sigma_x/5\sigma_y$ @ 2.0% momentum spread after turn damping on. Optimization work are still on-going.

REFERENCES

- [1] A. Blondel *et al.*, "Report of the ICFA Beam Dynamics Workshop - Accelerators for a Higgs Factory: Linear vs. Circular (HF2012)", Fermi National Laboratory, 14-16 November, 2012, Rep. CERN-ATS-2013-032.
- [2] The CEPC-SPPC Study Group, "CEPC-SPPC Preliminary Conceptual Design Report, Vol 2, Accelerator", 2015, Rep. IHEP-AC-2015-001.
- [3] W. Kalbreier, *et al.*, "Layout, design and construction of the electrostatic separation system of the LEP e+e- collider", in *Proc. EPAC'88*, Rome, Italy, June 1988, pp. 1184-1186.

SIMULATIONS OF POLARIZATION LEVELS AND SPIN TUNE BIASES IN HIGH ENERGY LEPTONS STORAGE RINGS*

E. Gianfelice[†], Fermilab, Batavia, USA

Abstract

The use of resonant depolarization has been suggested for precise beam energy measurements in the 100 km long Future Circular Collider e+e-. The principle behind resonant depolarization is that a vertically polarized beam excited through an oscillating horizontal magnetic field gets depolarized when the excitation frequency is in a given relationship with the beam energy. In this paper the possibility of self-polarized leptons at 45 GeV (Z resonance) and 80 GeV (WW physics) in presence of quadrupole vertical mis-alignment is investigated.

INTRODUCTION

e^\pm beams in a ring accelerator may become vertically polarized through the Sokolov-Ternov effect [1]. A small part of the radiation emitted by particles moving in a constant homogeneous field is accompanied by spin flip wrt the field direction. The probability of spin flip in the direction parallel to anti-parallel and from anti-parallel to parallel to the field are slightly different and this results in a polarization of 92.4 %, independently of energy. The polarization rate is given by

$$\frac{1}{\tau_{ST}} = \frac{5\sqrt{3}}{8} \frac{r_0 h}{2\pi m_0} \frac{\gamma^5}{|\rho|^3}$$

which strongly depends upon energy and radius. In actual storage rings there are not only dipoles. Quadrupoles for instance are needed for beam focusing. When a particle emits a photon it starts to perform synchro-betatron oscillations around the machine actual closed orbit experiencing extra possibly non vertical fields. The expectation value \vec{S} of the spin operator obeys to the Thomas-Bargmann-Michel-Telegdi (Thomas-BMT) equation [2] [3]

$$\frac{d\vec{S}}{dt} = \vec{\Omega} \times \vec{S} \quad (1)$$

$\vec{\Omega}$ depends on machine azimuth and phase space position, \vec{u} . In the laboratory frame and MKS units it is given by

$$\vec{\Omega}(\vec{u}; s) = -\frac{e}{m_0} \left[\left(a + \frac{1}{\gamma} \right) \vec{B} - \frac{a\gamma}{\gamma+1} \vec{\beta} \cdot \vec{B} \vec{\beta} - \left(a + \frac{1}{\gamma+1} \right) \vec{\beta} \times \frac{\vec{E}}{c} \right]$$

with $\vec{\beta} \equiv \vec{v}/c$ and $a = (g-2)/2 = 0.0011597$ (for e^\pm).

In a planar machine the *periodic* solution, \hat{n}_0 , to Eq.(1) is vertical and, neglecting the electric field, the number of spin precessions around \hat{n}_0 per turn, the naive ‘‘spin tune’’, in the rotating frame is $a\gamma$. Photon emission results in a

randomization of the particle spin directions (*spin diffusion*). Using a semiclassical approach, Derbenev and Kondratenko [4] found that the polarization is oriented along \hat{n}_0 and its asymptotic value is

$$P_{DK} = P_{ST} \frac{\oint ds < \frac{1}{|\rho|^3} \hat{b} \cdot (\hat{n} - \frac{\partial \hat{n}}{\partial \delta}) >}{\oint ds < \frac{1}{|\rho|^3} \left[1 - \frac{2}{9} (\hat{n} \cdot \hat{v})^2 + \frac{11}{18} \left(\frac{\partial \hat{n}}{\partial \delta} \right)^2 \right] >}$$

with $\hat{b} \equiv \hat{v} \times \hat{v}/|\hat{v}|$ and $\delta \equiv \delta E/E$. \hat{n} the *invariant spin field* [5], i.e. a solution of Eq.(1) satisfying the condition $\hat{n}(\vec{u}; s) = \hat{n}(\vec{u}; s + C)$, C being the machine length. The $\langle \rangle$ brackets indicate averages over the phase space. The term $\partial \hat{n}/\partial \delta$ quantifies the depolarizing effects resulting from the trajectory perturbations due to photon emission.

The corresponding polarization rate is

$$\tau_p^{-1} = P_{ST} \frac{r_e \gamma^3 \hbar}{m_0 c} \oint < \frac{1}{|\rho|^3} \left[1 - \frac{2}{9} (\hat{n} \cdot \hat{v})^2 + \frac{11}{18} \left(\frac{\partial \hat{n}}{\partial \delta} \right)^2 \right] >$$

In a perfectly planar machine $\partial \hat{n}/\partial \delta = 0$ and $P_{DK} = P_{ST}$. In presence of quadrupole vertical misalignments (and/or spin rotators) $\partial \hat{n}/\partial \delta \neq 0$ and it is particularly large when spin and orbital motions are in resonance

$$\nu_{spin} \pm mQ_x \pm nQ_y \pm pQ_s = \text{integer}$$

For FCC- e^+e^- with $\rho \simeq 10424$ m, fixed by the maximum attainable dipole field for the hadron collider, the polarization time at 45 and 80 GeV are 256 and 14 hours respectively.

Here it is assumed that beam polarization of about 10% is sufficient for an accurate depolarization measurement. The time, $\tau_{10\%}$, needed for the beam to reach this polarization level is given by

$$\tau_{10\%} = -\tau_p \times \ln(1 - 0.1/P_\infty)$$

At 80 GeV it is $\tau_{10\%} = 1.6$ hours, but $\tau_{10\%} = 29$ hours at 45 GeV.

At low energy the polarization time may be reduced by introducing properly designed wiggler magnets i.e. a sequence of vertical dipole fields, \vec{B}_w , with alternating signs.

FCC- e^+e^- maximum synchrotron radiation power is set to 50 MW per beam and the beam current at the various energies as been scaled accordingly. This limits the integrated wiggler strength. Moreover the wiggler increases the beam energy spread for which the effect on polarization must be investigated.

At 80 GeV wigglers are not needed. However the energy dependence of the spin motion makes the attainable polarization level more sensitive to machine errors.

Preliminary studies for a FCC- e^+e^- by using a ‘‘toy’’ ring [6] have shown that even in presence of quadrupole vertical

* Work supported by Fermi Research Alliance LLC. Under DE-AC02-07CH11359 with the U.S. DOE

[†] eliana@fnal.gov

misalignments and BPMs errors, useful level of polarization may be obtained at 45 GeV with wigglers and at 80 GeV without.

In this paper a FCC- e^+e^- optics by K. Oide [7] with $\beta_y^*=1$ mm is considered. MAD-X is used for simulating quadrupole mis-alignments and closed orbit correction. The lattice with errors and corrections is dumped to a file which can be read by the SITROS package [8] used for polarization calculations.

THE OPTICS

The optics contains 2 Interaction Points (IPs) based on quadrupole doublets. In the version used in this paper it is $\beta_x^*=0.5$ m and $\beta_y^*=1$ mm. The arcs are based on FODO cells with 90 degrees phase advance in both planes. The large β_y (10 km) at the strong IR quadrupoles makes the closed orbit very sensitive to their vertical misalignment and generates large chromaticity which correction requires strong sextupoles.

The expected rms orbit is given by

$$\langle z_{rms} \rangle = F \delta_{rms}^O$$

with

$$F \equiv \frac{1}{2\sqrt{2}|\sin\pi Q_z|} \sqrt{\langle \beta_z \rangle} \sqrt{\sum_{i=1}^{NQ} \beta_{z,i}(k\ell)_i^2}$$

($z=x$ or y). The orbit response to vertical misalignments for FCC- e^+e^- is summarized in Table 1 for $q_y=0.2$ and $\delta_{rms}^O=200$ μm .

Table 1: Orbit Sensitivity to Misalignments

	F	$\langle y_{rms} \rangle$ (mm)
all quads	613	123
w/o doublets	141	28

The value of 200 μm for δ_{rms}^O may be conservative; in particular one may expect that it will be possible to get a better alignment for the IPs doublets.

For simulating the effect of quadrupole random vertical misalignments and their correction one Beam Position Monitor (BPM) and one vertical corrector (CV) were introduced close to each vertical focusing quadrupole and doublet quadrupoles. The fractional part of the betatron tunes were set to $q_x=0.2$ and $q_y=0.3$ for keeping the vertical tune far from the integer and sextupoles were turned off. Nevertheless it is not possible to get a stable machine when 200 μm rms random offsets are introduced at once. In order to evaluate the achievable polarization for the *already corrected* machine, the sextupoles were switched off and the errors were added in steps of 1 μm for each of the doublet quadrupoles and of 10 μm for all the other quadrupoles at once. By each step the orbit due to each of the doublet quadrupoles was corrected by using the single CV close by, while 500 CVs selected by the MICADO algorithm were used for correcting the orbit due to the other quadrupoles. Evidently such tricks

cannot be played in practice. However the initial machine set-up will take place starting with a more “relaxed” optics and a number of countermeasures can be deployed for establishing a starting closed orbit which analysis is beyond the scope of this paper.

It turned out that for 3 over 13 seeds the MAD-X Twiss module fails right when the sextupoles are turned on at the very end of the procedure.

The reason for this seems to be the relatively large skew quadrupoles created by the SYL and SYR sextupoles at each side of the IPs. The phase advance between SY1L and SY1R and SY2L and SY2R is 180° degrees. As the strengths of the sextupoles on the left side of the IPs have the opposite sign of those on the right side, if the beam offsets in such sextupoles are anti-symmetric, which is likely due to the phase advance, they generate a coupling wave which may be strong enough to cause the optics to become unstable.

POLARIZATION SIMULATIONS

The 45 GeV Case

4 LEP-like wigglers [9] with $B^+=0.7$ T were introduced in dispersion free sections with $\beta_x \approx 50$ -80 m. The time needed to reach 10% beam polarization is about 2.9 h. The horizontal emittance increases from 0.088 nm to 0.5 nm. By using a larger number of poles should be possible to get a smaller emittance increase.

In the absence of BPM errors, after orbit correction it is $y_{rms}=0.05$ mm and the rms value of the polarization axis distortion, $|\delta\hat{n}_0|_{rms}$, is 0.4 mrad. The resulting polarization vs. $a\gamma$ is shown in Fig. 1 for orbital tunes $q_x=0.1$, $q_y=0.2$ and $q_s=0.1$.

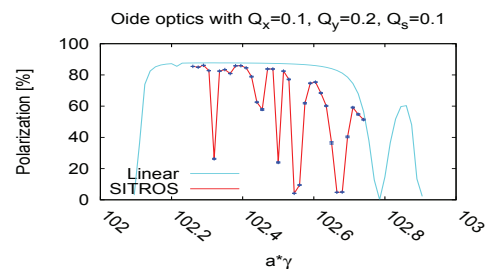


Figure 1: Polarization vs. $a\gamma$ after closed orbit correction for the ring with 4 wigglers; BPMs errors not included.

The 80 GeV Case

The same error realization at 80 GeV results in $|\delta\hat{n}_0|_{rms}=2$ mrad. The corresponding polarization is shown in Fig. 2.

Reducing $\delta\hat{n}_0$ to 1.5 mrad with harmonic bumps [10] gives some improvement (see Fig. 3).

The harmonic bumps increase ϵ_y from 12.8 pm to 19.5 pm and the polarization related to the vertical betatron motion alone is somewhat reduced (see Fig. 4 and 5), indicating

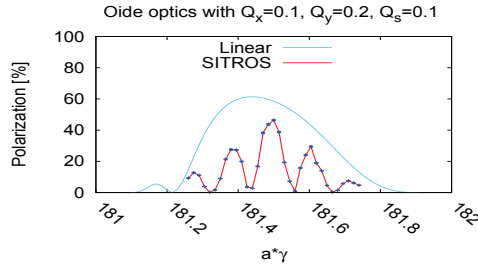


Figure 2: Polarization vs. $a\gamma$ after closed orbit correction for the ring w/o wigglers; BPMs errors not included.

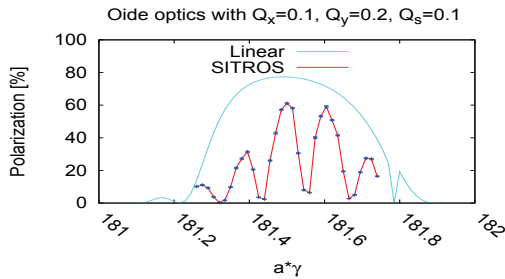


Figure 3: Polarization vs. $a\gamma$ after closed orbit and $\delta\hat{n}_0$ correction for the ring with 4 wigglers; BPMs errors not included.

that there is may be space for improvements in the harmonic bump scheme used.

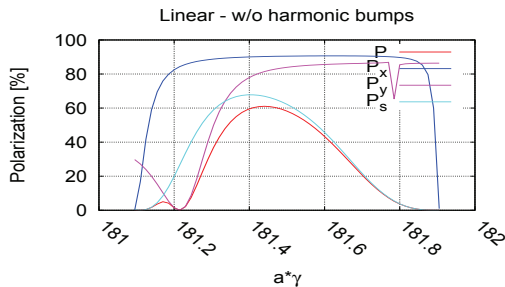


Figure 4: Polarization vs. $a\gamma$ in linear spin motion approximation after closed orbit correction for the ring with 4 wigglers. The blue, magenta and cyan lines show the polarization when only horizontal, vertical or longitudinal motion is considered respectively.

ENERGY MEASUREMENT BIASES

In addition of proving that useful polarization levels may be reached, it must be proved that the required energy measurement precision (better than 100 keV) may be achieved. Some issues such as beamstrahlung limited beam lifetime,

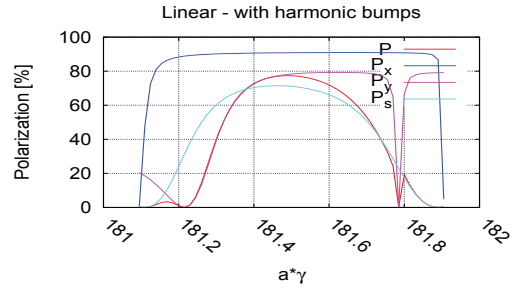


Figure 5: Polarization vs. $a\gamma$ in linear spin motion approximation after closed orbit and $\delta\hat{n}_0$ correction for the ring with 4 wigglers. The blue, magenta and cyan lines show the polarization when only horizontal, vertical or longitudinal motion is considered respectively.

energy sawtooth and synchrotron radiation power budget, set constraints on number of needed measurement stations, measurement scenario and wigglers operation [11]. In addition the relationships $v_{spin} = a\gamma$ strictly holds for a purely planar ring.

The effect of closed orbit distortion has been evaluated for LEP by using a simplified model by R. Assmann [12] who found that for half-integer ν_s^0 it is $\Delta\nu_s=0$ in first and second order in the extra-spin rotations. For $\nu_s^0 \neq 0.5$ it is

$$\langle \Delta\nu_s \rangle = \frac{\cot \pi \nu_s^0}{8\pi} (a\gamma)^2 \left[\langle \Sigma_q (K\ell)_q^2 y_q^2 \rangle + \langle \Sigma_k \theta_k^2 \rangle \right]$$

y_q being the *effective* beam position at the quadrupoles.

The corresponding energy error for FCC- e^+e^- for 10 error realizations is shown in Fig. 6.

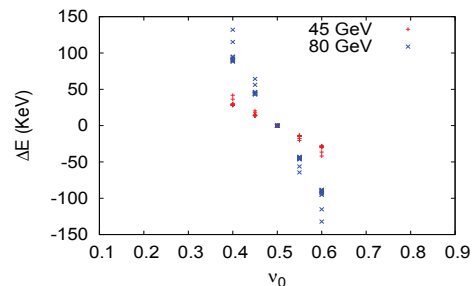


Figure 6: Energy error vs. nominal spin tune for 10 different error seeds.

Analytical expressions (see [13]) shall be implemented and used for comparison.

Finally the energy calibration error due to the angle between RF electric field and beam trajectory at the accelerating cavities [14] is shown in Table 2 where y'_{rms} is the rms vertical slope in mrad.

Table 2: Calibration Error Sensitivity to Orbit in the RF Cavities.

	ΔE (KeV)
45 GeV	$2 \times y'_{rms}$
80 GeV	$16 \times y'_{rms}$

With

$$\langle y'_{rms} \rangle \simeq \sqrt{\frac{\langle \gamma_y \rangle}{\langle \beta_y \rangle}} \langle y_{rms} \rangle \simeq 0.1 \langle y_{rms} \rangle$$

the contribution from the RF electric field should be small.

CONCLUSION

Preliminary studies for the 45 GeV and 80 GeV case have been presented for the current $\beta_y^* = 1$ mm FCC- e^+e^- optics. The large sensitivity of the orbit to vertical misalignment of quadrupoles makes the orbit correction difficult. In particular we learned that the orbit at the SYL and SYR sextupoles on the left and right side of the IPs must be well controlled.

However the goal of this study was to assess the feasibility of self-polarization for energy calibration once a stable closed orbit has been established.

At 80 GeV, $\delta\hat{n}_0$ due to misalignments increases and although the energy spread is the same as at 45 GeV with wigglers, polarization is lower. Large harmonic bumps for correcting $\delta\hat{n}_0$ may cause a vertical emittance increase. With the toy ring it was shown that it is possible, for instance by using dispersion-free 5-coils bumps, to correct $\delta\hat{n}_0$ w/o spoiling the vertical emittance.

The present study has shown that self-polarization for energy calibration should be possible in the $\beta_y^* = 1$ mm FCC- e^+e^- optics. However here only quadrupoles vertical misalignments have been considered and BPMs errors have not been included. The rms misalignment of 200 μm is conservative, a smaller value could be expected in particular for the doublet quadrupoles. The exercise on the “toy” ring had shown the importance of the BPMs errors on the orbit correction quality; however the 10% calibration error there assumed was conservative, 2%-3% should be achievable.

Various additional corrections aiming to preserve the small goal vertical emittance (1 pm at 45 GeV beam energy) have been considered by other contributors [15] [16] at this workshop. Their effect on polarization must be of course studied.

ACKNOWLEDGEMENT

I would like to thank A. Blondel and F. Zimmermann for their encouragement in pursuing this study.

The support of the Workshop organizing committee is warmly acknowledged.

REFERENCES

- [1] A. A. Sokolov and I. M. Ternov, “On Polarization and spin effects in the theory of synchrotron radiation”, *Sov. Phys. Dokl.*, 8 (12) 1203 (1964).
- [2] L. Thomas, “The Kinematics of an electron with an axis”, *Phil. Mag.*, Vol. 3 (1927).
- [3] V. Bargmann, L. Michel and V. L. Telegdi, “Precession of the polarization of particles moving in a homogeneous electromagnetic field”, *Phys. Rev. Lett.*, vol.2, p.435, (1959).
- [4] Ya. S. Derbenev and A. M. Kondratenko, “Polarization kinematics of particles in storage rings”, *Sov. Phys. JETP*, 37, 968 (1973).
- [5] G. H. Hoffstaetter, D. P. Barber and M. Vogt, “Higher order effects in polarized proton dynamics”, *Phys. Rev. ST Accel. Beams*, 2, 114001 (1999).
- [6] E. Gianfelice-Wendt, “Investigation of beam self-polarization in the future e^+e^- circular collider”, *Phys. Rev. ST Accel. Beams*, to be published.
- [7] Personal Communication.
- [8] J. Kewisch, “Depolarisation der Elektronenspins in Speicherringen durch nichtlineare Spin-Bahn-Kopplung”, DESY 85-109 (1985).
- [9] A. Blondel and J. M. Jowett, “Wigglers for polarization”, in *Proceedings of Polarization at LEP*, vol. 2, 216-232 (1987).
- [10] D. P. Barber, et al., *Nucl. Instrum. Meth.*, A338, 166-184, (1994).
- [11] M. Koratzinos, “Polarization: running mode and issues at FCC-ee”, presented at eeFACT2016, Daresbury, UK, Sept.2016, Paper ID: 1681 - TUT1AH3.
- [12] R. Assmann, “Optimierung der transversalen Spin-Polarisation im LEP-Speicherring und Anwendung für Präzisionsmessungen am Z-Boson”, Ph.D.thesis, Phys.Dept., Ludwig-Maximilians-Universität, München, Germany, 1994.
- [13] K. Yokoya, “On multiple siberian snakes”, SSC-189, 1988.
- [14] Y. I. Eidelman, Yu. M. Shatunov, V. E. Yakimenko, “Spin tune shifts in storage rings”, *Nucl.Instrum.Meth.*, A357 (1995).
- [15] S. Sinyatkin, “FCCee Lattice with Errors and Misalignment”, presented at eeFACT2016, Daresbury, UK, Sept.2016, Paper ID: 1302 - MOT3BH2.
- [16] S. Aumon, “Coupling and Dispersion correction in FCC-ee”, presented at eeFACT2016, Daresbury, UK, Sept.2016, Paper ID: 1381 - TUT3BH4.

IDEAS FOR SIBERIAN SNAKES AND SPIN ROTATORS IN VERY HIGH ENERGY e^+e^- RINGS

S. R. Mane*, Convergent Computing Inc., NY, USA

Abstract

The high value of the radiated power in synchrotron radiation in very high energy e^+e^- storage rings presents unique challenges for the design of Siberian Snakes and spin rotators in such machines. This paper presents some ideas which may lead to a feasible design of such devices. The idea is to employ solenoids interleaved with the arc dipoles, to yield a set of noncommuting spin rotations, which can rotate an initially vertical spin to any desired direction. The solenoids should be (approximately) optically transparent, and can be ‘spin matched’ to the ring using known procedures. Preliminary numerical studies indicate the design may be feasible.

SPIN ROTATOR AND SNAKE SCHEMATIC

For a general review of spin dynamics in accelerators and for a review of Siberian Snakes and spin rotators in accelerators, we direct the reader to [1] and [2], respectively. The concern here is e^+e^- rings of very high energy, where the very high synchrotron radiation (SR) radiated power places serious constraints on the design of Siberian Snakes and spin rotators. The subject has of course been studied by others already, see, e. g. [3]. The present work also draws on an analysis by the author for FCC-ee [4]. The prototype ring below is FCC-ee, although the essential ideas apply to any very-high energy e^+e^- collider. The subject of beam polarization in such rings falls naturally into two sections: (i) transverse polarization, for energy calibration, and (ii) longitudinal polarization at the interaction point (IP), for tests of the electroweak theory and other tests/searches for new physics. We discuss these in turn.

For energy calibration via the resonant depolarization (RD) of transversely polarized beams, it is envisaged that a set of ‘pilot’ non-colliding e^+ and e^- bunches will be circulated in each ring. (The colliding bunches for HEP will be unpolarized.) The polarized bunches will be produced at low energy in polarized electron and positron sources and then accelerated to high energy for injection into the main ring. Hence the polarized bunches must be accelerated across a large number of intrinsic and imperfection depolarizing spin resonances. To avoid depolarization via the Froissart-Stora formula [5], one or more Siberian Snakes are required in the booster ring. The basic scenario for FCC-ee is to employ full-energy injection, and this is likely to be case for other rings also. The booster ring will occupy the same tunnel as the main ring, i. e. it will have the same circumference and top energy. Hence the designs of Snakes or spin rotators will apply equally to the booster ring and the main ring.

Longitudinally polarized colliding beams are usually envisaged at the Z^0 peak, to test the electroweak theory. However, they could be useful to explore physics at other energies. It is also possible that, at a later stage, a hadron ring may be installed for an $e-p$ collider option. In such a case, a longitudinally polarized lepton beam would be a natural choice. Longitudinally polarized colliding beams require the e^+ and e^- bunches to be polarized *in situ* in the main rings. This almost certainly requires the use of polarization wigglers, which will increase the SR radiated power. Some details of polarization wigglers for FCC-ee were analyzed in [4]. Since the polarization must be preserved during storage, Siberian Snakes will be required in the main ring. In addition, longitudinally polarized colliding beams require the use of spin rotators.

Hence we are led to consider designs for Siberian Snakes and spin rotators in the booster and/or main ring. We treat a particle of charge e , mass m , with velocity \vec{v} , Lorentz factor $\gamma = 1/\sqrt{1-v^2/c^2}$ and spin \vec{s} . The magnetic moment anomaly will be denoted by $a = \frac{1}{2}(g-2)$. The externally prescribed electric and magnetic fields of the accelerator are denoted by \vec{E} and \vec{B} , respectively. The Thomas-BMT (Bargmann, Michel and Telegdi) equation [6, 7] is given by $d\vec{s}/dt = \vec{\Omega} \times \vec{s}$. Treating only motion in magnetic fields, the spin precession vector is

$$\vec{\Omega} = -\frac{e}{\gamma mc} \left[(\gamma a + 1)\vec{B}_\perp + (a + 1)\vec{B}_\parallel \right]. \quad (1)$$

Here $\vec{B}_\parallel = (\vec{B} \cdot \vec{v})\vec{v}/v^2$ and $\vec{B}_\perp = \vec{B} - \vec{B}_\parallel$ are the components parallel and orthogonal to the particle velocity, respectively. Because of eq. (1), Snakes and rotators built using transverse bending fields have traditionally been considered as the superior choice for use at high energies.

However, the above conclusion is derived by considering only the spin rotation angle in a magnet and neglects the synchrotron radiation generated. The above view is therefore applicable to hadron rings, where synchrotron radiation is negligible, but must be reexamined for very high energy e^+e^- colliders. It was argued in [4] that Snakes and rotators built from transverse field dipoles produce an unacceptable SR load, or else entail unacceptably large beam orbit excursions. This includes the so-called ‘Steffen Snakes’ (see [2] for details) and the Derbenev-Grote Snake/rotator design [8]. The use of helical field Snakes and rotators was analyzed in [4], where it was argued that the closed orbit beam excursions might be tolerable. However, helical field Snakes also generate SR, which is a disadvantage of the design.

Hence in this note, we consider the possibility of employing solenoids to design Snakes and spin rotators. Solenoids do not add to the SR power load. They also have the advantage that they are optically transparent and techniques

* srmanc001@gmail.com

are known for ‘spin matching’ to the optics of the ring [9]. Quadrupoles are placed between two solenoids in series and the entire ‘Snake system’ is both optically transparent and spin transparent. However, solenoids have the disadvantage that their spin rotation axis points along the reference axis only. Hence, for example, a solenoid spin rotator will rotate the polarization from vertical to radial (and vice-versa). A spin rotation through 90° in the horizontal plane is required to attain longitudinal polarization at the interaction point (e. g. see [3, Fig. 3-127]). For example, for FCC-ee at the Z^0 peak, this requires an orbit bend of $(\pi/a)(m_e/M_Z) \simeq 0.015$ rad between a solenoid spin rotator and the IP. The ring geometry must be altered to accommodate this bend. The situation is further complicated if there are vertical bends between the rotator and the IP, which is likely to be the case at FCC-ee. There is the additional undesirable feature that the above angle of 0.015 rad is specific to the energy of the Z^0 peak, and the ring geometry must be modified to operate at other beam energies. For Siberian Snakes, if an even number of solenoids are employed, the fractional spin tune is zero, hence the spin motion is on resonance. If an odd number of solenoid Snakes are employed, the fractional spin tune is $\frac{1}{2}$, but the stable polarization direction lies in the horizontal plane. A circulating beam polarization in the horizontal plane is more susceptible to depolarizing effects than a vertically polarized beam. On the other hand, a pair of diametrically opposed Snakes with orthogonal spin rotation axes yields a fractional spin tune of $\frac{1}{2}$ and the stable polarization is vertical in the arcs, up in one arc and down in the other. See [2] for details.

For all of the above reasons, we are led to consider if it is possible to design a spin rotator using solenoids, which can rotate an initially vertical spin to any desired direction in three dimensions. Clearly this cannot be accomplished using only one solenoid. However, *three* solenoids, interleaved with arc dipoles, *do* have the requisite number of degrees of freedom to rotate an initially vertical spin to an arbitrary final direction. Arc dipoles are employed so that the SR power load is not increased by inserting additional dipoles in the ring. The schematic configuration is displayed below (note that the ‘horizontal bends’ could be several dipoles in series)

$$\text{sol 1} - B - \text{sol 2} - B - \text{sol 3}$$

The solenoid spin rotation angles are $\psi_{1,2,3}$ and the dipole spin rotation angle is ϕ . The bends are considered to be part of the lattice (arc dipoles) hence ϕ is not a free parameter. The free parameters are $\psi_{1,2,3}$. We employ coordinate axes $(\vec{e}_1, \vec{e}_2, \vec{e}_3)$ where \vec{e}_1 points radially outwards, \vec{e}_2 points along the reference axis and \vec{e}_3 points vertically upwards. A positive rotation is counterclockwise. Then the overall spin rotation matrix is

$$M = e^{-i\psi_3\sigma_2/2} e^{-i\phi\sigma_3/2} e^{-i\psi_2\sigma_2/2} e^{-i\phi\sigma_3/2} e^{-i\psi_1\sigma_2/2}. \quad (2)$$

Let the spin rotation matrix be parameterized by

$$M = \xi_0 - i\xi^{\vec{\sigma}} \cdot \vec{\sigma}. \quad (3)$$

Then the matrix M can be simplified to yield

$$\xi_0 = \cos \frac{\psi_1 + \psi_3}{2} \cos \frac{\psi_2}{2} \cos \phi - \sin \frac{\psi_1 + \psi_3}{2} \sin \frac{\psi_2}{2}, \quad (4a)$$

$$\xi_1 = -\cos \frac{\psi_2}{2} \sin \frac{\psi_1 - \psi_3}{2} \sin \phi, \quad (4b)$$

$$\xi_2 = \sin \frac{\psi_1 + \psi_3}{2} \cos \frac{\psi_2}{2} \cos \phi + \cos \frac{\psi_1 + \psi_3}{2} \sin \frac{\psi_2}{2}, \quad (4c)$$

$$\xi_3 = \cos \frac{\psi_2}{2} \cos \frac{\psi_1 - \psi_3}{2} \sin \phi. \quad (4d)$$

Preliminary numerical tests indicate that if we set $\psi_1 - \psi_3 = 0$ or $\psi_1 - \psi_3 = \pi$, we can find values of ψ_1 and ψ_2 to rotate an initially vertical spin to any desired final direction. This is of course a preliminary finding, and further study is required to validate the feasibility of this design. However, it does hold the *tentative* promise that, for transverse polarization, Snakes with orthogonal spin rotation axes can be designed for use in the booster synchrotron. For longitudinal polarization at the interaction point, it may be possible to design spin rotators which can deliver longitudinally polarized colliding beams at any beam energy, *without* modification of the ring geometry.

REFERENCES

- [1] S. R. Mane, Yu. M. Shatunov and K. Yokoya, “Spin-polarized charged particle beams in high-energy accelerators,” Rep. Prog. Phys. **68** 1997–2265, 2005.
- [2] S. R. Mane, Yu. M. Shatunov and K. Yokoya, “Siberian Snakes in high-energy accelerators,” J. Phys. G: Nucl. Part. Phys. **31** R151–R209, 2005.
- [3] SuperB Collaboration, “SuperB: A High-Luminosity Asymmetric e+e- Super Flavor Factory. Conceptual Design Report,” INFN Publishing Services, INFN-Pisa, L.go Pontecorvo, 3, I-56127, Pisa, Italy (2007). Available at arXiv:0709.0451 [hep-ex] <https://arxiv.org/abs/0709.0451>
- [4] S. R. Mane, “Polarization at TLEP/FCC-ee: ideas and estimates,” available at arXiv:1406.0561 [physics.acc-ph] <https://arxiv.org/abs/1406.0561>
- [5] M. Froissart and R. Stora, “Depolarisation d’un faisceau de protons polarises dans un synchrotron,” Nucl. Instrum. Meth. A **7** 297–305, 1960 (in French).
- [6] L. H. Thomas, “The kinematics of an electron with an axis,” Philos. Mag. **3** 1, 1927.
- [7] V. Bargmann, L. Michel and V. L. Telegdi, “Precession of the polarization of particles moving in a homogeneous electromagnetic field,” Phys. Rev. Lett. **2** 435, 1959.
- [8] Ya. S. Derbenev and H. Grote, “Bending Siberian Snake as a Spin Rotator,” CERN SL/Note 95-37 (AP), March 1995. Available at <http://cds.cern.ch/record/703583/files/cer-000415550.pdf>
- [9] I. A. Koop, A. V. Otboev, P. Yu. Shatunov, and Yu. M. Shatunov, “Spin Transparent Siberian Snake And Spin Rotator With Solenoids,” in Proc. SPIN2006 Kyoto, Japan, AIP Conf. Proc. **915**, 948, 2007.

ISSUES ON IR DESIGN AT SuperKEKB

Y. Ohnishi*
KEK, Tsukuba, Japan

Abstract

The design of the interaction region is one of the most important issue in SuperKEKB. The lattice design with the final focus system and the local chromaticity correction as well as the dynamic aperture under the influence of beam-beam interactions are presented.

SUMMARY OF INTERACTION REGION

The machine parameters of SuperKEKB [1] are shown in Table 1. The final focus system is designed to achieve the extremely low beta function at the IP. In order to squeeze the beta functions, doublets of a vertical focusing (QC1) and a horizontal focusing quadrupole magnet (QC2) are adopted. Figure 1 shows the layout of the final focus system. The magnet system consists of superconducting magnets to make strong focusing strength. Those magnets have an iron yoke or a permendure yoke to shield the magnetic field to the opposite beam line except for the most inner magnets QC1Ps in the LER. Cancel coils for the leakage field of sextupole, octupole, decapole, and dodecapole filed from QC1s in the LER are installed in the HER. The dipole and quadrupole leakage fields are used in the lattice design of the interaction region in the HER. The dipole, skew dipole, skew quadrupole coils are quipped with the main quadrupole magnets to adjust X-Y couplings and vertical dispersions induced by solenoid field, although the 1.5 detector solenoid field is almost corrected by compensation solenoid magnets. The octupole coils are also installed to make dynamic aperture large, especially in the transverse direction. In addition to the coils for the lattice design, skew sextupole coils to correct imperfections of the main quadrupole magnet.

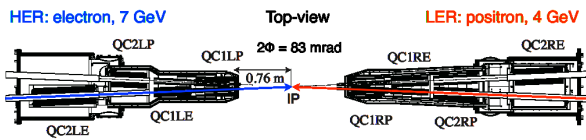


Figure 1: Top View of the Final Focus System.

The natural chromaticity is $\xi_x = -105$ and $\xi_y = -776$ in the LER, $\xi_x = -171$ and $\xi_y = -1081$ in the HER. Since approximately 80 % of the linear chromaticity in the vertical direction is induced in the final focus system, a local chromaticity correction (LCC) is adopted to correct the large chromaticity near the final focus system. There are 2 pairs for the vertical direction (Y-LCC) and another 2 pairs of sextupoles for the horizontal direction (X-LCC) in the IR. The phase advance between QC1 and the Y-LCC is π in the vertical direction and between QC2 and X-LCC is 2π in the horizontal direction for each side of the IP. Horizontal

dispersions are created at the LCC by using several dipole magnets. Figures 2 and 3 show the lattice design of the LCC region.

Table 1: Machine Parameters (with Intra-beam Scattering) for the Final Design of SuperKEKB

	LER	HER	Unit
E	4.000	7.007	GeV
I	3.6	2.6	A
n_b	2500		
C	3016.315		m
ϵ_x	3.2	4.6	nm
ϵ_y	8.64	12.9	pm
β_x^*	32	25	mm
β_y^*	270	300	μm
$2\phi_x$	83		mrad
α_p	3.19×10^{-4}	4.53×10^{-4}	
σ_δ	7.92×10^{-4}	6.37×10^{-4}	
V_{RF}	9.4	15.0	MV
σ_z	6	5	mm
ν_s	-0.0245	-0.0280	
ν_x	44.53	45.53	
ν_y	46.57	43.57	
U_0	1.76	2.43	MeV
τ_x	45.6	58.0	msec
ξ_x	0.0028	0.0012	
ξ_y	0.0881	0.0807	
L	8×10^{35}		$\text{cm}^{-2}\text{s}^{-1}$

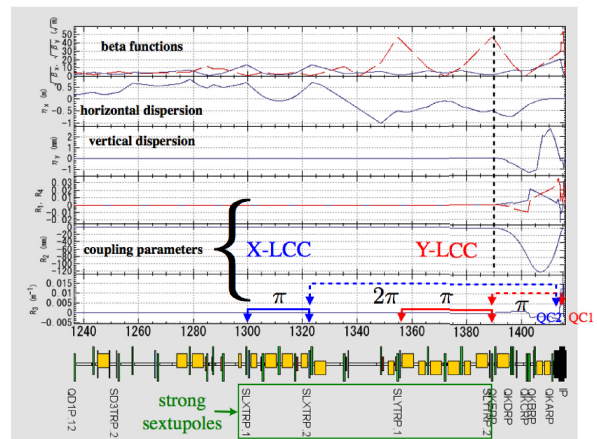


Figure 2: Local Chromaticity Correction in the LER.

NONLINEAR TERM IN FINAL FOCUS

Nonlinear effects in the final focus system decreases the dynamic aperture significantly. In addition to the nonlinear magnetic field, the drift space is not linear system as

* yukiyoshi.ohnishi@kek.jp

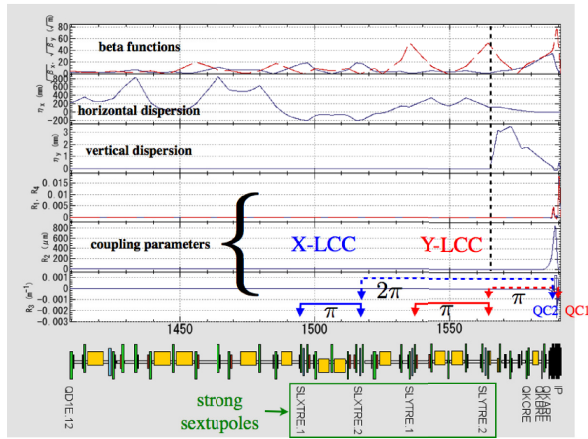


Figure 3: Local Chromaticity Correction in the HER.

shown in a Hamiltonian. Especially, when the beta function is squeezed in the vicinity of the IP and decreased with distance from the IP, the effect cannot be ignored. The aperture of the motion can be described by a simple one-dimensional Hamiltonian [2]. The Hamiltonian of the nonlinear term is expressed by

$$H_{nl} = \left(1 - \frac{2}{3}k_1 L^2\right) \frac{L^*}{\beta_y^*} J_y^2 \cos^4 \psi_y, \quad (1)$$

where

$$k_1 = \frac{1}{B\rho} \frac{\partial B_y}{\partial x}. \quad (2)$$

Table 2 shows the coefficient of the Hamiltonian and related parameters for various machines. The coefficient of the nonlinear Hamiltonian can be used to evaluate the dynamic aperture in SuperKEKB. The coefficient of SuperKEKB is about 200 times larger than that of KEKB [3] and 10 times larger than that of FCC-ee.

Table 2: Coefficient of the Nonlinear Hamiltonian Term. The c indicates $H_{nl}/J_y^2 \cos^4 \psi_y$.

	β_y^* [mm]	k_1 [m^{-2}]	L^* [m]	c [μm^{-1}]
HER	0.30	-3.05	1.22	55.56
LER	0.27	-5.10	0.76	31.25
FCC-ee	1	-0.336	2	3.79
CEPC	1.2	-0.176	1.5	1.32
KEKB	5.9	-1.78	1.76	0.237
DAΦNE	8.66	-9.23	0.2	0.0033

DYNAMIC APERTURE UNDER INFLUENCE OF BEAM-BEAM EFFECT

The dynamic aperture will be reduced under the influence of beam-beam effects in the nano-beam scheme. A particle with a horizontal amplitude collides at a location different from the IP in the longitudinal direction due to the crossing angle of 83 mrad between two beam lines in the horizontal

plane. The deviation along the beam axis is written by

$$\Delta z = \frac{\Delta x}{2\phi_x}, \quad (3)$$

where Δx is the horizontal amplitude and ϕ_x the half crossing angle. The beta function is written by a function of the distance from the IP:

$$\beta_y(\Delta z) = \beta_y^* + \frac{\Delta z^2}{\beta_y^*}. \quad (4)$$

Therefore, the particle with a horizontal amplitude is kicked at a large vertical beta function and the vertical amplitude will increase due to the beam-beam interactions for an initial non-zero vertical amplitude. This behavior is a kind of an hourglass effect. The vertical amplitude given by the beam-beam kick is

$$\Delta y \propto \theta_{bb,y} \sqrt{\beta_y(\Delta z)}. \quad (5)$$

The particle is lost if the vertical amplitude increases and is out of a stable region. In the case of a particle with the horizontal amplitude of $30\sigma_x$ in the LER, the deviation from the IP becomes 3.6 mm in the longitudinal direction where the vertical beta function is 48 mm. The vertical beta function becomes 180 times of the nominal beta function at the IP.

Touschek lifetime in the HER reduces about 10 % due to the beam-beam effect, however, the impact in the LER is much larger than the HER. Figure 4 (b) shows the dynamic aperture in the vertical and the horizontal plane under the influence of the beam-beam effect. The simulation of a particle tracking uses a weak-strong model. The initial momentum deviation is zero in the figure. The transverse aperture is reduced significantly compared with the dynamic aperture without the beam-beam effect (Fig. 4 (a)). The particle with the horizontal amplitude larger than $10\sigma_x$ is lost due to the vertical oscillation even though the initial amplitude is zero in the vertical direction because of the vertical amplitude is induced by nonlinearities such as X-Y coupling originate from the IR.

CRAB-WAIST SCHEME

One of the approaches to compensate the beam-beam effect for the large horizontal amplitude is ‘‘crab-waist scheme’’ [4]. Hamiltonian of the crab-waist term is

$$H_{cw} = \frac{\lambda}{2} x p_y^2, \quad (6)$$

where

$$\lambda = \frac{1}{\tan 2\phi_x}. \quad (7)$$

If we consider the ideal case of the crab-waist scheme, the map of the beam-beam interaction is replaced with

$$f_{BB} \rightarrow f_{cw}(+\lambda) \cdot f_{BB} \cdot f_{cw}(-\lambda), \quad (8)$$

where the map of the crab-waist is

$$f_{cw}(\lambda) : p_x \rightarrow p_x + \frac{\lambda}{2} p_y^2 \quad (9)$$

$$y \rightarrow y - \lambda x p_y. \quad (10)$$

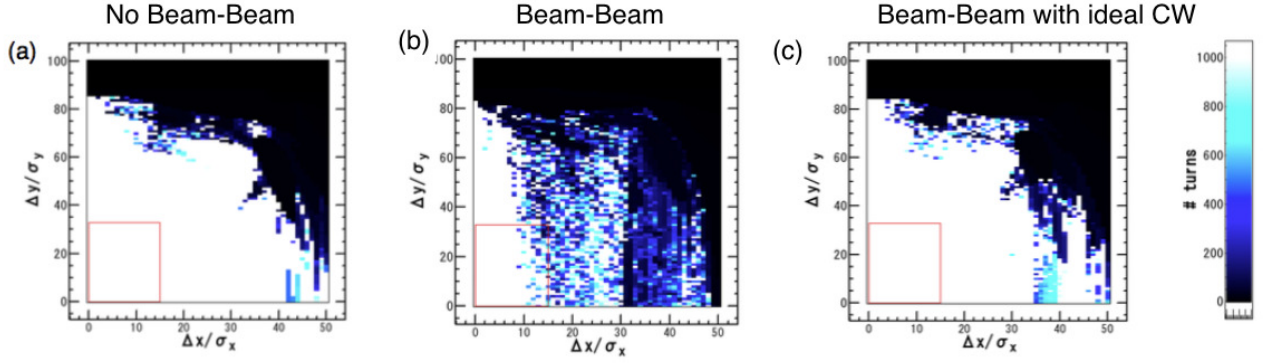


Figure 4: Dynamic Aperture. (a) No Beam-Beam, (b) Beam-Beam Interaction, (c) Crab-Waist Scheme with Beam-Beam. Red Rectangle indicates an Injection Aperture.

A feasibility of the ideal crab-waist scheme has been studied by using tracking simulations. The dynamic aperture is almost recovered by the ideal crab-waist (Fig. 4 (c)). In order to accomplish the crab-waist in the realistic lattice, two sextupole magnets are utilized. In the case of the realistic lattice, the x^3 term comes from the sextupole is added to the crab-waist term in the Hamiltonian. However, it can be ignored by choosing a large ratio of the vertical beta function to the horizontal at the sextupole magnet.

Two sextupole magnets are placed for each side of the IP and shift a waist of colliding particles having a horizontal amplitude to cancel the deviation from the waist. The betatron phase advance between a crab-waist sextupole and the IP is adjusted to be $m\pi$ in the horizontal direction and $(n + 1/2)\pi$ in the vertical direction, where m and n are arbitrary integers. The strength of the crab-waist sextupoles are

$$|K_2| = \frac{1}{\tan 2\phi_x \beta_y^* \beta_{y,s}} \sqrt{\frac{\beta_x^*}{\beta_{x,s}}}, \quad (11)$$

where $\beta_{x,s}$ and $\beta_{y,s}$ are the horizontal and the vertical beta function at the sextupoles, respectively. The sign of K_2 is chosen so as to shift the waist at the IP properly and cancel a nonlinear kick between a pair of the crab-waist sextupoles. The lattice design for the crab-waist scheme in the LER is shown in Fig. 5. The crab-waist sextupole is assumed to be a thin lens to make the model simple in this report. The machine parameters for the crab-waist scheme in the LER are shown in Table 3.

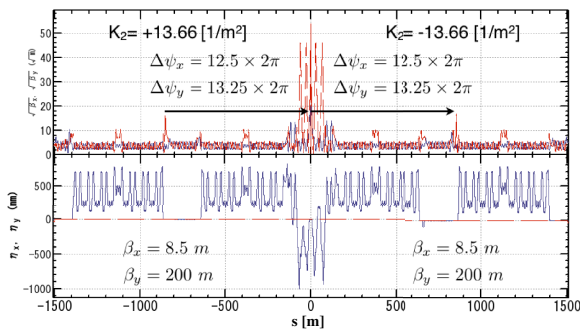


Figure 5: Lattice for the Crab-Waist Scheme in the LER for SuperKEKB.

Table 3: Parameters for the Crab-Waist Scheme in the LER.

	Symbol	LER	Unit
Horizontal beta at the IP	β_x^*	32	mm
Vertical beta at the IP	β_y^*	270	μm
Half crossing angle	ϕ_x	41.5	mrad
Horizontal beta at sextupole	$\beta_{x,s}$	8.5	m
Vertical beta at sextupole	$\beta_{y,s}$	200	m
Horizontal phase advance	$\Delta\psi_x$	25π	rad
Vertical phase advance	$\Delta\psi_y$	26.5π	rad
Nominal field of sextupole	$ K_2 $	13.66	$1/\text{m}^2$

DYNAMIC APERTURE WITH CRAB-WAIST SCHEME

Figure 6 (a) shows transverse dynamic aperture in the LER as a function of K_2 for the crab-waist sextupoles. The initial momentum deviation and the vertical amplitude are zero in the simulations. The dynamic aperture decreases as increasing the strength of the sextupoles. The beam-beam effect is turned off in the simulation. The nonlinear kick due to the crab-waist sextupole can be canceled by another sextupole for the reference particle, however, it cannot be canceled for a particle with a large initial amplitude. The transfer map between two sextupoles which includes the IR with the final focus is no longer the linear map. The term of $\Delta p_y = K_2 xy$ will increase the vertical amplitude, then the particle will be lost and the dynamic aperture will be reduced. Figure 6 (b) shows the transverse dynamic aperture in the LER which is similar to Fig. 6 (a), but the beam-beam effect is turned on. The dynamic aperture is indeed recovered by the crab-waist sextupoles as increasing the field strength until the nonlinear kick from the sextupoles restricts the dynamic aperture. Therefore, it implies the difficulty comes from the cancellation of the nonlinear kick by a pair of crab-waist sextupoles for the large horizontal amplitude of a particle without the beam-beam effect.

In order to investigate the reduction of the dynamic aperture in the crab-waist scheme, a simple model for the IR lattice is considered in the LER as an ideal case. The IR model is simplified to be no solenoid field, no offset of the

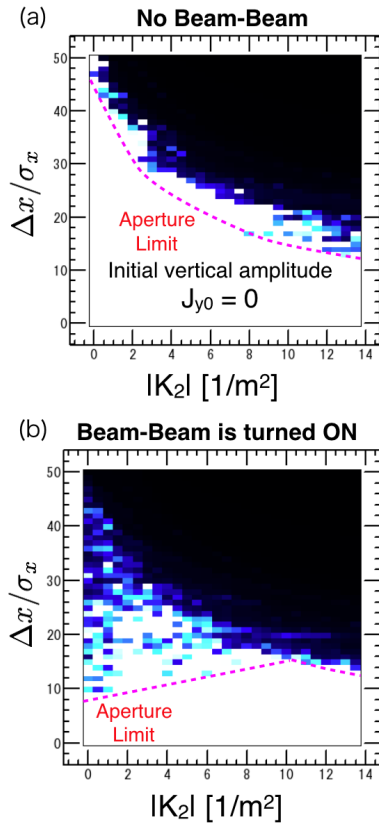


Figure 6: Dynamic Aperture in the Transverse Direction as a Function of the Strength of Crab-Waist Sextupoles for the Crab-Waist Lattice; (a) No Beam-Beam, (b) Beam-Beam interaction.

final focus quadrupole magnets, and no higher-order multipole fields from the IP ($s=0$) to $s=4$ m for each side of the IP. In addition to the simple IR, QC1 and QC2 in which nonlinear Maxwellian fringe fields are turned off are considered to study the dynamic aperture. The transverse dynamic aperture for the on-momentum particle as a function of K_2 for the crab-waist sextupoles is shown in Fig. 7. The dependence of the field strength is almost disappeared for the dynamic aperture without the beam-beam interaction (Fig. 7 (a)). On the other hand, the dynamic aperture is recovered by using the crab-waist sextupoles under the influence of the beam-beam interaction (Fig. 7 (b)). We have also studied the dynamic aperture which depends on the location of the crab-waist sextupoles. In the case of SuperKEKB, there is no dependence of the location outside of the final focus doublets. The reason is that the strength of the nonlinear effect due to the final focus doublets is very strong compared with other machines as shown in Table 3. It is also found that the length of the crab-waist sextupole does not affect the dynamic aperture in this study. Therefore, the issue is how to linearize the lattice between two sextupoles that include the nonlinear IR in the realistic lattice.

CONCLUSIONS

We present the design of the IR at SuperKEKB and the study of the dynamic aperture. The dynamic aperture for

ISBN 978-3-95450-187-8

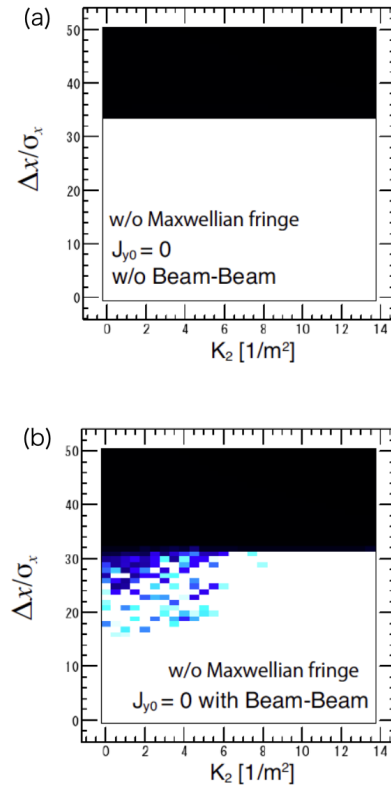


Figure 7: Dynamic Aperture in the Transverse Direction as a Function of the Strength of Crab-Waist Sextupoles for the Crab-Waist Lattice with the Simple IR; (a) No Beam-Beam, (b) Beam-Beam Interaction.

the both of the LER and the HER can be achieved to make Touschek lifetime 600 sec without machine error. However, the dynamic aperture under the influence of the beam-beam interaction will be reduced significantly in the nano-beam scheme. The beam-beam kick will be enhanced because the waist is shifted due to the $x - z$ coordinate exchange. One of the solutions to recover the dynamic aperture is the crab-waist scheme. The interference between the nonlinearity of the final focus doublets and the crab-waist sextupoles reduces the dynamic aperture. The transfer map between the IP and the crab-waist sextupole should be linear to improve the dynamic aperture in the case of SuperKEKB. The development of a cancellation technique for the nonlinearity is under study.

REFERENCES

- [1] Y. Ohnishi *et al.*, *Prog. Theor. Exp. Phys.* 2013 03A011 (2013).
- [2] K. Oide and H. Koiso, *Phys. Rev. E* **47** (1993) 2010.
- [3] T. Abe *et al.*, *Prog. Theor. Exp. Phys.* 2013 03A001 (2013).
- [4] “SuperB Conceptual Design Report”, INFN/AE-07/2, SLAC-R-856, LAL 07-15, March 2007.

DESIGN OF INTERACTION REGION AND MDI AT CEPC*

Q. Xiu[†], S. Bai, J. Gao, X. Lou, D. Wang, Y. Wang, H. Zhu
Institute of High Energy Physics, Beijing, China

Abstract

The CEPC is a proposed circular electron positron collider to study the Higgs boson more accurately. The interaction region and the machine detector interface must be well designed to make sure the machine and the detector can work well after they are integrated together. Important factors that will affect the design of the CEPC interaction region are reviewed, such as the beam induced background, the interference of the magnetic field between the machine and the detector, etc. Several rules are summarized to steer the design of the interaction region. The progress on the machine detector interface of CEPC are presented.

INTRODUCTION

The CEPC [1] is a proposed circular electron positron collider to study the Higgs boson more accurately. It will be operated at the center of mass energy of 240 GeV with an instantaneous luminosity of $2 \times 10^{34} \text{cm}^{-2}\text{s}^{-1}$. One of the most important advantages of the e^+e^- collider is that the produced Higgs events will be much cleaner than those produced at the proton collider, e.g. the LHC. However, if the interaction region (IR) isn't designed well, the potential of the e^+e^- collider will not be fully exploited. For instance, the luminosity might be highly suppressed by the detector solenoid field if the beam coupling is not well cancelled and the Higgs events might be "heavily polluted" by the beam induced backgrounds if the shielding of the IR is not well designed. Thus, the interface between the machine and the detector must be carefully designed to achieve the required luminosity and background level.

Two kinds of problems must be well understood to find reasonable solutions of IR design. Firstly, the mutual influence between the machine and the detector must be well studied. It includes the interference of magnetic field between detector solenoid and machine magnets, the sources of beam induced backgrounds and so on. Secondly, the interface between the machine and the detector, such as the mechanical supporting and the procedure to assemble the interaction region, must be well designed. In this paper, we present the recent progress of the IR design and machine detector interface (MDI) study of CEPC. The dominant sources of beam induced background have been studied and some preliminary results are obtained. A compensating solenoid and anti-solenoid will be used to suppress the influence on the beam status from the detector solenoid. A global design

of the interaction region is undergoing to balance the conflict of performance between the machine and the detector.

MAGNETS AND LAYOUT OF THE INTERACTION REGION

The luminosity is one of the most important parameters of CEPC. The accelerator design are trying to increase the luminosity as much as possible, however, the detector solenoid might decrease the luminosity. The luminosity is given by:

$$L = \frac{N_e^2 n_b f_0}{4\pi \sigma_x^* \sigma_y^*} FH \quad (1)$$

Here, N_e is the bunch population, n_b is the number of bunches, f_0 is the revolution frequency, σ_x^* and σ_y^* are the transverse size of bunches at the interaction point. F is the geometric luminosity reduction factor due to the crossing angle at the interaction point (IP). H is the hourglass factor giving the luminosity reduction due to the change of β^* along the bunch. To improve the luminosity of CEPC, the bunch size should be as small as possible, which means the final focusing magnets should be as close to the IP as possible. At current design, the distance between IP and the final quadrupole magnet L^* is set as 1.5 m. As a result, the final focusing magnets QD0 and QF1 will be inside the field of the detector solenoid. At CEPC, the bunch shape is set to be flat with large horizontal bunch size and very small vertical bunch size, which is helpful to reduced some kinds of beam induced backgrounds such as beamstrahlung meanwhile keep the multiply of σ_x and σ_y to be small. In this case, the detector solenoid will cause the coupling between the horizontal and vertical betatron motion and increase the bunch size in the vertical direction, which will further decrease the luminosity. To achieve the required luminosity, compensating solenoids are designed to cancel the beam coupling before the beam enter quadrupole magnets and anti-solenoids are designed around quadrupole magnets to prevent the beam coupling inside quadrupole magnets. Figure 1 shows the preliminary layout of the interaction region.

BEAM INDUCED BACKGROUNDS

The most important influence on the detector from the machine is the beam induced backgrounds. The major backgrounds at CEPC are the synchrotron radiation, the beam lost particles and the beamstrahlung.

Synchrotron Radiation

Because the beam energy of CEPC is very high and the number of beam particles in one bunch is very large, the synchrotron radiation (SR) emitted from the beam in the dipole and quadrupole magnets will be the most serious

* Work supported by the CAS/SAFEA International Partnership Program for Creative Research Teams, funding from CAS and IHEP for the Thousand Talent and Hundred Talent programs, as well as grants from the State Key Laboratory of Nuclear Electronics and Particle Detectors.

[†] xiuql@ihep.ac.cn

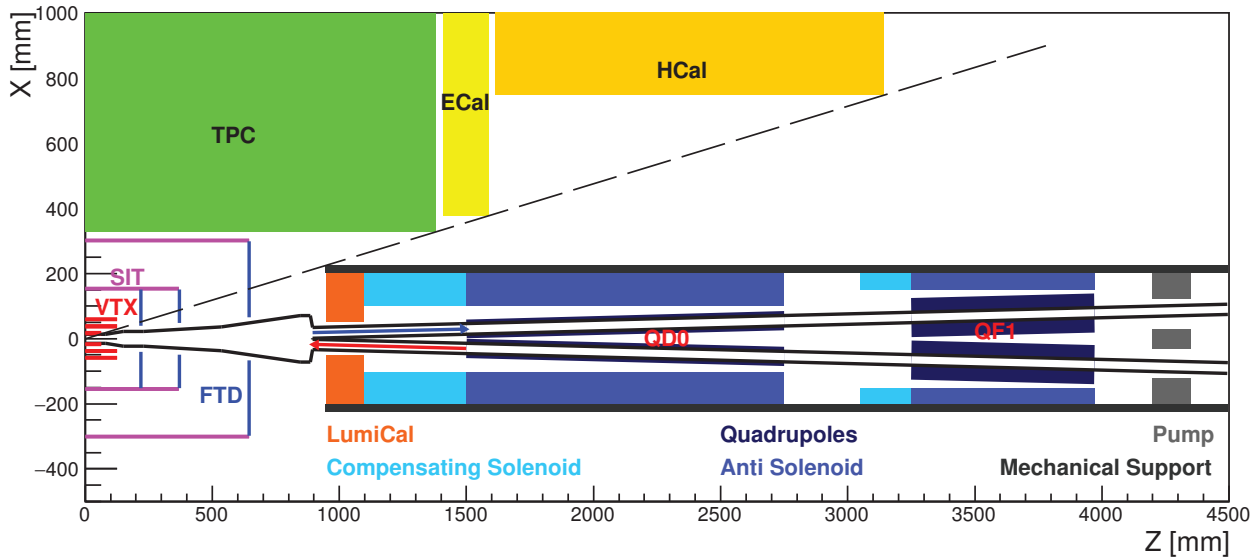


Figure 1: The preliminary layout of the interaction region. The L^* is set as 1.5 m at CEPC. Compensating solenoids are inserted before focusing quadrupole magnets to cancel the beam coupling. Ant-solenoids are around the quadrupole magnets to shield the field of the detector solenoid. There is a virtual boundary between the machine and the detector to suppress their mutual interference.

beam induced background at CEPC. The number and the energy spectrum of the photons that might enter the detector must be well evaluated to check whether the background level is acceptable to the experiments. The synchrotron radiation in the dipole magnets can be easily estimated with analytical formulas of classical electrodynamics. However, it's very difficult to estimate the synchrotron radiation in the quadrupole magnets because the field of the quadrupole magnets are non-uniform and the beam status will affect the radiation power significantly.

To study the synchrotron radiation from the dipole and quadrupole magnets uniformly, a Monte Carlo simulation program is developed based on Geant4 and BDSIM [2] to generate and track photons. In the simulation, the beam particles are generated with specific distributions in the phase space and are tracked along the relevant beam elements in which the SR photons will be emitted. For the synchrotron radiation in the quadrupole magnets, the tails of the beam density distributions should be pay more attention because the tail particles will produce more photons.

Preliminary results show that the SR rate is much higher than that can be tolerated by the detector. To cope with the synchrotron radiation, two kinds of treatments are used. One is to insert some collimator in the IR to absorb the SR radiation before they enter the detector region. Figure 2 shows the effects of preliminary designed collimator. The SR rate can be significantly suppressed by the collimator. The other is to modify the lattice design to reduce the radiation power of the synchrotron radiation in the IR. Further studies of these two methods are undergoing.

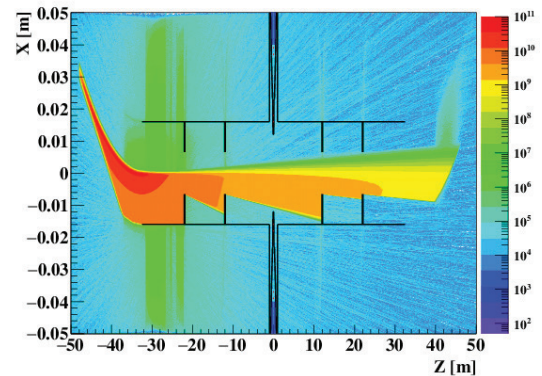


Figure 2: The preliminary design of collimator for the SR. The horizontal bold lines are beam pipe. The vertical line at $Z = 0$ m is the interaction point. Other vertical lines away from IP are collimator. The color represents the spacial distribution of number of photons from the last dipole magnet. The interactions between photon and materials have been considered in this Figure. The number of photons are suppressed by the collimator significantly.

Beam Lost Particles

The beam particles might lose a large fraction of energy through some scattering processes such as the radiative Bhabha, the beam gas scattering and so on. The energy acceptance of CEPC is designed to be 2%. If the relative energy loss of the beam particles are larger than 2%, these particles will be lost from the beam and some of these particles might hit the detector. In order to evaluate the beam lost particles, the energy loss of the beam particles in different

scattering processes are firstly simulated with proper Monte Carlo programs. For instance, the radiative Bhabha events are simulated with BBBREM [3]. Then, the particles with energy loss larger than 2% are tracked with an accelerator simulation program such as SAD [4]. The lost position and the four momentum of the lost particles will be record as the input of the detector simulation. Figure 3 shows the lost position of radiative Bhabha events in the interaction region of CEPC without any collimator. Most particles will loss at the position of final focusing magnets. The energy of these particles are usually very large and lots of secondary particles will be produced. Thus the hit density in the detector will be very high. In order to suppress the lost rate at IR, a set of collimator will be inserted into the main ring to stop the possible lost particles before they enter the IR.

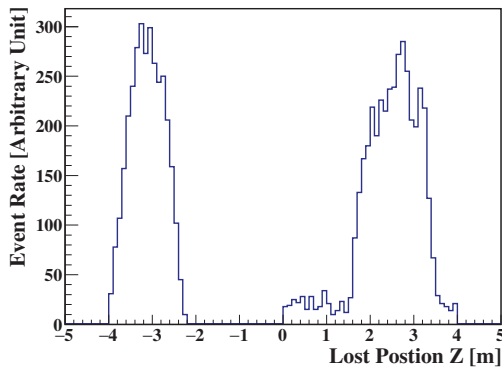


Figure 3: The lost position distribution of radiative Bhabha events at IR without collimator.

Beamstrahlung

To achieve the desired high luminosity, the electron and positron beams will be focused to very small bunch sizes at the IP. Trajectories of the charged particles in one bunch are bent by the induced electromagnetic field of the other crossing bunch of opposite charge. During this process, one kind of synchrotron radiation, called “beamstrahlung”, will be emitted. The beamstrahlung is usually characterised by the beamstrahlung parameter Υ :

$$\Upsilon = \frac{2}{3} \frac{h\omega_c}{E} \quad (2)$$

where $\omega_c = \frac{3}{2}\gamma^3 c/\rho$ denotes the critical energy of synchrotron radiation, ρ the bending radius of the particle trajectory and E the beam particle energy before radiation. The higher the Υ , the more beamstrahlung photons with higher energies will be emitted. Assuming Gaussian charge distribution for the beams, the average Υ [5] can be estimated as:

$$\Upsilon_{av} \approx \frac{5}{6} \frac{Nr_e^2\gamma}{\alpha(\sigma_x + \sigma_y)\sigma_z} \quad (3)$$

where r_e is the classical electron radius, γ the Lorentz factor of the beam particles, α the fine structure constant and σ_z

the bunch length. The value of Υ at CEPC is just about 5×10^{-4} . As a comparison, the Υ at ILC when it's operating at 250 GeV will be about 0.02. Thus, the beamstrahlung effect at CEPC is very small.

The photons emitted by beamstrahlung are usually very forward and will leave the IR along the beam pipe, thus these photons are usually harmless to the detector. However, a fraction of energetic beamstrahlung photons might further produce electron-positron pairs or even hadronic background by proper interactions. These kinds of backgrounds have evaluated with Guinea-Pig++ [6] and detector simulation for CEPC. Figure 4 shows the hit density at the vertex detector caused by the pair and hadronic backgrounds. The results shows that the event rate is acceptable for the CEPC detector.

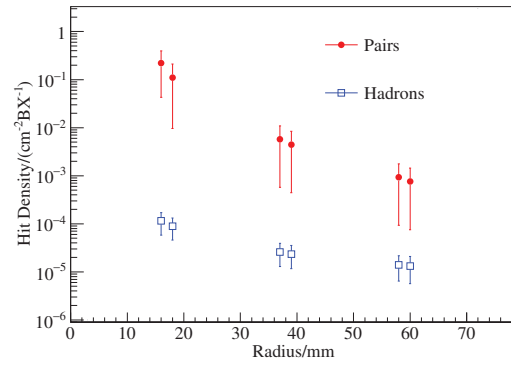


Figure 4: Hit density of pairs and hadronic backgrounds at 6 layers of the vertex detector with radii 16 mm, 18 mm, 37 mm, 39 mm, 58 mm and 60 mm. The hit rate is acceptable for the CEPC detector.

PROGRESS ON THE MACHINE DETECTOR INTERFACE

Besides the mutual influences between the machine and the detector, the mechanical interface between the machine and the detector are also very important. For CEPC, the heavy final focusing quadrupole magnets are very close to the IP. These magnets can't be supported by the detector because the detector will be opened regularly for maintenance. Thus, as shown in Figure 1, the mechanical supporting structure will be designed along the boundary in the accelerator side and the supporting point will be about 6 m (about half length of the detector) away from the IP along the central axis of the detector. It implies that the volume of the supporting structure might be very large and might conflict with the detector in space. To cope with the confliction in space, the final focus elements should be minimized as much as possible. Meanwhile, a global optimization considering the performances of both the machine and the detector is undergoing.

SUMMARY

The MDI problem is the key to make sure the machine and the detector are compatible with each other. The mutual

influence between the machine and the detector must be well understood to design the interaction region reasonable. Preliminary studies on the beam induced background and the magnet design have been done and some results are obtained. The global design of the interaction region that consider both the machine and the detector effects are being under going.

REFERENCES

- [1] CEPC-SPPC Study Group, IHEP-CEPC-DR-2015-01, IHEP-AC-2015-01 (2015).
- [2] S. T. Boogert, S. M. Gibson, R. Kwee-Hinzmann *et al.*, “Beam delivery simulation (BDSIM): a Geant4 based toolkit for diagnostic and loss simulation”, in *Proceedings of IBIC2013*, Oxford, UK, Sep. 2013, paper WEPC46, pp. 799–802.
- [3] R. Kleiss and H. Burkhardt, “BBBREM: Monte Carlo simulation of radiative Bhabha scattering in the very forward direction,” *Comput. Phys. Commun.* 81, 372, 1994.
- [4] K. Hirata, “An introduction to SAD”, CERN 88-04, 1988.
- [5] K. Yokoya, P. Chen, “Beam beam phenomena in linear collider”, *Lect. Notes Phys.*, 400: 415—445, 1992.
- [6] C. Rimbault, P. Bambade, O. Dadoun *et al.*, in *Proceedings of PAC07* (Conf. Proc. C070625, 2007), p.2728.

THE FCC-ee INTERACTION REGION MAGNET DESIGN

M. Koratzinos, University of Geneva, Geneva, Switzerland

Abstract

The design of the region close to the interaction point of the FCC-ee [1] [2] experiments is especially challenging. The beams collide at an angle (± 15 mrad) in the high-field region of the detector solenoid. Moreover, the very low vertical β^* of the machine necessitates that the final focusing quadrupoles have a distance from the IP (L^*) of around 2 m and therefore are inside the main detector solenoid. The beams should be screened from the effect of the detector magnetic field, and the emittance blow-up due to vertical dispersion in the interaction region should be minimized, while leaving enough space for detector components. Crosstalk between the two final focus quadrupoles, only about 6 cm apart at the tip, should also be minimized.

INTRODUCTION

FCC-ee incorporates a “crab waist” scheme to maximize luminosity at all energies [3]. This necessitates a crossing angle between the electron and positron beams which is ± 15 mrad in the horizontal plane in the current baseline design. No magnetic elements can be present in the region approximately ± 1 m from the interaction point (IP) to leave space for the particle tracking detectors and the luminosity counter. Furthermore, the area outside the forward and backward cones of 100 mrad defined from the IP and along the longitudinal axis of the experiment is reserved for detector elements, leaving only the two narrow cones for machine elements. Therefore, beam electrons experience the full strength of the detector magnetic field in the vicinity of the IP. The resulting vertical kick needs to be reversed and this is performed in the immediate vicinity. This vertical bump, however, leads to vertical dispersion and an inevitable increase the vertical emittance of the storage ring. Since FCC-ee is a very low emittance machine (with an emittance budget of the order of 1 pm), the emittance blow-up in the vicinity of the IP needs to be minimized.

THE MAGNETIC ELEMENTS AROUND THE IP

We now have a preliminary conceptual design of the magnetic systems close to the IP which fits our requirements. It comprises the following elements:

The *detector solenoid* is assumed to have a magnitude of 2 T and extend to ± 6 m from the IP.

The *screening solenoid* is a thin solenoid producing a field equal and opposite to the detector solenoid and screens the final focus quadrupoles from the detector solenoid field. It starts at 1.65 m from the IP and extends all the way to the endcap region of the detector. In the current design the screening is such that at the face of the final focus quadrupoles (2.2 m from the IP) the

longitudinal magnetic field strength is 0.013 T (attenuated from 2 T)

The *compensating solenoid* sits in front of the screening solenoid, has a field higher than that of the detector solenoid, so that the magnetic field integral seen by the beam is zero. In our design the length of this solenoid is 0.65 m and its inner edge is at 1.0 m. Its maximum field along the axis is -4.95 T.

The *final focus quadrupoles* in our current design sit at a distance of 2.2 m from the IP and are 3.2 m long. The focusing strength in the current design is 92 T/m at 175 GeV [4]. The distance between the centres of the two quadrupoles is 6.6 cm at the tip closest to the IP and 16.2 cm at the far end.

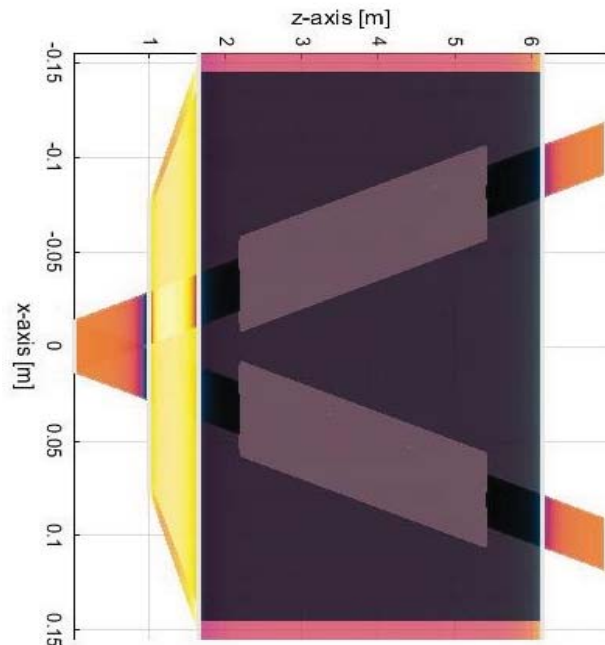


Figure 1: The conceptual design of the magnetic elements close to the IP, looking on the x-z plane. The IP is at (0,0). Please note the elongated scale in x. The opening angle of the (schematic) beam pipes is 30 mrad. The final focus quadrupoles surround the two beam pipes whereas the rest of the elements are aligned to the longitudinal axis of the experiment. The compensating solenoid (yellow) is tapered and is in front of the screening solenoid (pink). The detector solenoid is outside this picture.

The different elements of the design can be seen in Figure 1, as seen from above the detector. Please note the elongated view along the x-axis. Figure 2 shows the magnitude of the magnetic field, whereas Figure 3 shows the components of the magnetic field along the path of the electron. The longitudinal field varies from +2 T to -3 T, whereas the fringe horizontal field varies from +0.26 T to

-0.13 T. All analysis described here was done using the *Field* suite of programs [5].

EMITTANCE BLOW-UP

The vertical emittance increase close to the IP, $\Delta\epsilon_{y,IP}$, is given by

$$\Delta\epsilon_{y,IP} = 3.83 \times 10^{-13} \frac{\gamma^2 I_{5,IP}}{J_y I_2} \quad (1)$$

Where γ is the relativistic γ of the beam, I_2 is the second synchrotron radiation integral which can be approximated by

$$I_2 \cong \frac{2\pi}{|\rho_{bend}|} \quad (2)$$

(equal to about 6×10^{-4} for FCC-ee with bending radius in the arcs $\rho_{bend} = 11$ km). $J_y = 1$. The fifth synchrotron radiation integral is

$$I_{5,IP} = \int_{-d}^d \frac{\mathcal{H}_y(s)}{|\rho|^3} ds \quad (3)$$

where ρ is the bending radius due to the magnetic field along the path of the electrons in the area of interest, $-d$ to d , in our case -3 to 3 m.

$$\mathcal{H}_y(s) = \beta(s)D_y'^2 + 2\alpha(s)D_y D_y' + \gamma(s)D_y^2 \quad (4)$$

where D_y is the vertical dispersion and

$$\alpha(s) = -\frac{1}{2}\beta'(s); \gamma(s) = \frac{1+\alpha(s)^2}{\beta(s)} \quad (5)$$

Where $\beta(s)$ is the vertical beta optics function. Emittance blow up is worse at low energies due to the $\frac{\gamma^2}{|\rho|^3}$ dependence (the magnetic field of the detector is expected not to change at different energies).

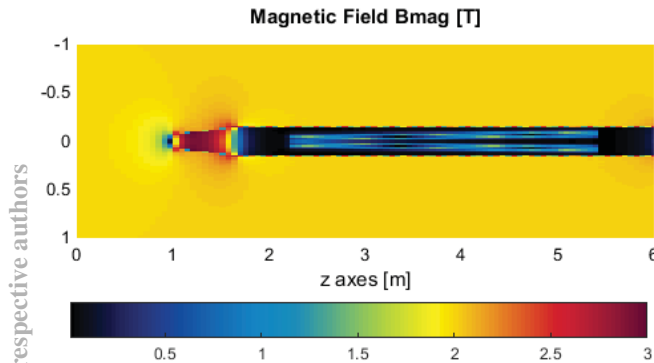


Figure 2: The magnitude of the magnetic field in the region $x=(-1$ m, 1 m) and $z=(0, 6$ m) in the vicinity of the compensating solenoid (red, -3 T), screening solenoid (black, 0 T), final focus quadrupoles (in blue), all in the $+2$ T solenoidal field of the experiment (yellow).

The minimization of the above formula for the emittance blow-up has been done empirically due to the number of parameters. The boundary conditions used were: detector solenoid field of 2 T, magnetic elements should be inside the 100 mrad forward and backward cones, location of closest element to the IP 1 m. The latter is certainly a tight requirement since the luminosity

counter should sit in front of the first magnetic element. The size and position of the different components for the optimal case where the emittance blow-up was the smallest was as follows:

Compensating solenoid: inner edge at 1.0 m, length 0.65 m, diameter 16 to 22 cm (tapered). Current (1000 windings) 2615 A, giving a maximum field along the axis of -4.95 T

Screening solenoid: inner edge at 1.65 m, 4.5 m length, diameter 30 cm and current ($10,000$ windings) 717 A, giving a maximum field along the axis of -2 T.

The resulting emittance blow-up was computed using the SAD suite of programs [6] which gave a result of a total of 0.07 pm of vertical emittance blow up for both sides of the IP and for two identical IPs. Optical functions can be seen in Figure 5.

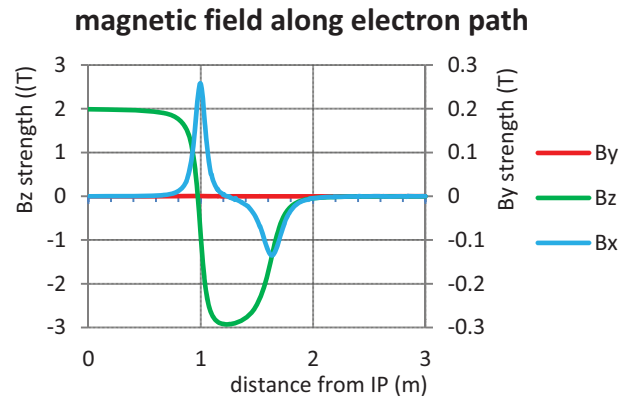


Figure 3: Magnetic field along the electron path: B_z , the longitudinal component of the magnetic field (left axis), B_x , the horizontal component (right axis); B_y , the vertical component, is zero due to symmetry.

FINAL FOCUS QUADRUPOLES

The requirements for the final focus quadrupoles (here we refer to the last elements focusing the beam in y for a resulting β_y^* of 1 mm) are as follows: the beam-stay-clear (b-s-c) area in the vicinity of the quadrupoles has been computed to be ± 12 mm. This allows for a very compact beam pipe. RF beam heating considerations might necessitate a slightly larger beam pipe that the b-s-c suggests, as large as 40 mm diameter. The L^* of these quadrupoles in the current design is 2.2 m and their strength is 92 T/m. Increasing the quadrupole strength would allow for shorter quadrupoles and therefore the L^* requirement can be increased if needed. With a L^* of 2.2 m, the distance between the centre of the quadrupoles is 6.6 cm, calling for a compact design and one that takes into account the cross talk between the two quadrupoles.

One technology that looks promising for such an application is CCT technology.

Canted-cosine-theta (CCT) magnets have been around since the seventies [7], however only recently have they become popular with magnet designers [8] [9], due to the advent of modern manufacturing techniques (CNC

machines and 3D printing). The CCT design offers some advantages over traditional magnet design for certain applications. The main advantages of CCT magnets are

- Accelerator-grade field quality
- Fast prototyping: short turnaround times using 3D printing techniques
- Easy to manufacture with state-of-the-art manufacturing techniques (CNC machines or 3D printing), simple windability and assembly; not labour intensive
- No need for coil pre-stress during assembly; also, reduced coil stresses should improve magnet training
- Total freedom to design any multipole arrangement, therefore capable of producing compact double aperture magnets with the required field quality
- Fewer components and considerably lighter than traditional designs – this might translate to reduced costs (although this currently has not been fully demonstrated)

All of the requirements of the FCC-ee final focus system can be satisfied using a CCT design for the final focus quadrupoles. The design is compact, has a theoretical field quality which is adequate for our stringent requirements, crosstalk can be designed out, and has the added bonus of fast prototyping which ensures fast progress, much greater than what is customary for magnet design. However, the design needs to prove that it can deliver a series of milestones, including adequate field quality and crosstalk correction capability.

FCC-ee is pursuing the CCT option for the final focus quadrupoles, while also keeping the more conventional modified Panofsky lens with twin-aperture and integrated iron yoke style design as an alternative. This design is undertaken at BINP.

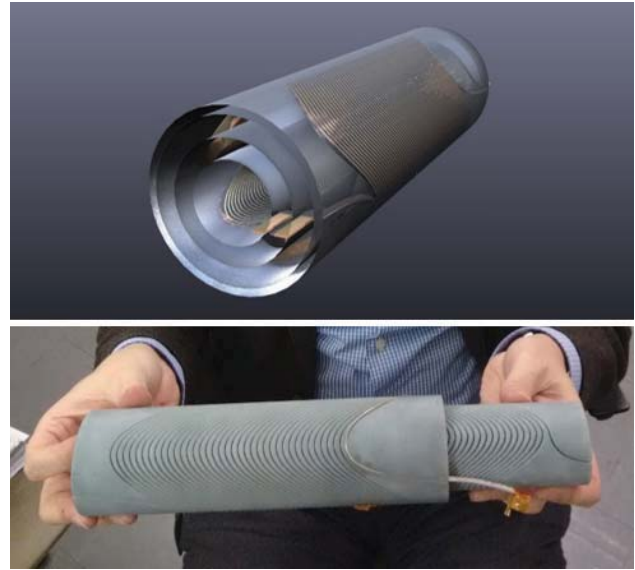


Figure 4: Prototype CCT final focus quadrupole. CAD drawing (top) and 3D printed item (bot).

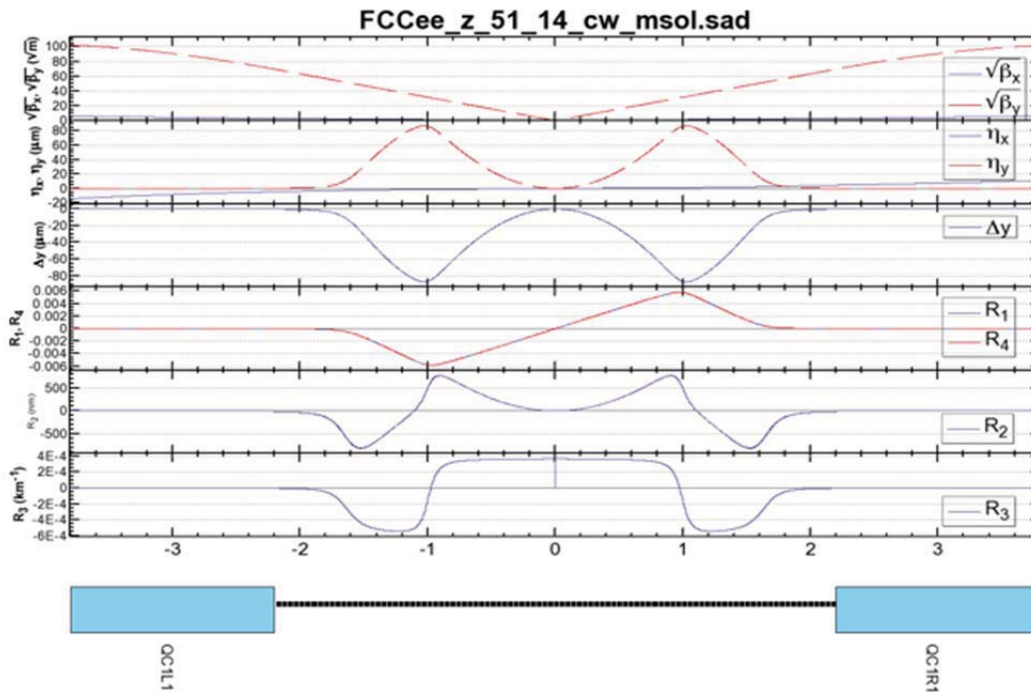


Figure 5: Beam optical functions between the centres of the final quadrupoles of the proposed solution. Columns are, from top to bottom, $\sqrt{\beta_x}$ and $\sqrt{\beta_y}$, x and y dispersion, y orbit, R_1 and R_4 , R_2 , R_3 , where $R_{1,2,3,4}$ are the x-y coupling parameters. The vertical orbit, dispersion, and the coupling parameters are confined within the compensation solenoid

CCT PROTOTYPE

A complete conceptual design of an FCC-ee final focus prototype has been done (Figure 4). The prototype has the final dimensions regarding the bore size, but it is much shorter (20 cm) than the final magnet. The design has been 3D-printed in and awaits winding with an existing NbTi cable and will be ready to be measured for field quality and tested for cryogenic performance.

CONCLUSIONS

We have demonstrated that the very stringent requirements for the magnetic systems around the interaction region of an FCC-ee detector can be met with a system comprising final focus quadrupoles, screening solenoids and compensating solenoids. The emittance blow-up due to two interaction regions is computed to be 0.07 pm, which is less than 10% of the vertical emittance budget of the storage ring. Further improvements and a move to prototyping and technical design will follow.

REFERENCES

- [1] "The FCC-ee study," <http://cern.ch/fcc>
- [2] J. Wenninger *et al.*, "Future Circular Collider Study Lepton Collider Parameters," CERN FCC-1401201640-DSC, updated 2015.
- [3] A. Bogomyagkov *et al.*, "Beam-beam effects investigation and parameters optimization for a circular e+e- collider at very high energies," *Phys. Rev. ST Accel. Beams* **17**, 041004, 2014.
- [4] K. Oide *et al.*, "An asymmetric design of the FCC-ee IP optics," in *Proc. IPAC'16*, paper THPOR022, *this conference*.
- [5] J. van Nugteren, "Internship Report: CERN, Software development for the Science and Design behind Superconducting Magnet Systems," tech. rep., Twente University: Energy Materials and Systems and CERN: ATLAS magnet team, 2011.
- [6] "Strategic Accelerator Design," <http://acc-physics.kek.jp/SAD/index.html>
- [7] D. I. Meyer and R. Flasck, "A new configuration for a dipole magnet for use in high energy physics applications," *NIM A* **80.2** (1970), pp 339-341.
- [8] S. Caspi, "Design, Fabrication and Test of a Superconducting Dipole Magnet Based on Tilted Solenoids," *IEEE Trans. Appl. Supercond.* **17.2** (2007), pp. 2266-2269.
- [9] F. Bosi *et al.*, "Compact Superconducting High Gradient Quadrupole Magnets for the Interaction Regions of High Luminosity Colliders," *IEEE Transactions on Applied Superconductivity*, **VOL. 23, NO. 3**, June 2013.

STUDY OF COHERENT HEAD-TAIL INSTABILITY DUE TO BEAM-BEAM INTERACTION IN CIRCULAR COLLIDERS BASED ON CRAB WAIST SCHEME

K. Ohmi

KEK, 1-1 Oho, Tsukuba, 305-0801, Japan

Abstract

Coherent motion of colliding beam-beam system has been studied mainly for transverse modes. π and σ modes are We dicuss coherent head-tail instability for beam-beam collision with a large Piwinski angle. The instability seems serious for colliders based on the crab waist scheme.

INTRODUCTION

Recent and future e^+e^- colliers adopt collision with large crossing angle $\sigma_z \theta_c \gg \sigma_x$, where θ_c is half crossing angle. The vertical beta function is squeezed smaller than the bunch length, $\beta_y^* < \sigma_z$, while the crossing angle (θ_c : half angle) is chosen $\sigma_x/\theta_c \leq \beta_y$ to avoid the hourglass effect. Crab waist using based on a transformation $H = xp_y^2/2\theta_c$ at collision point suppress hourglass effect for particles with a large horizontal amplitude.

The beam-beam effects in the crab waist collision has been studied using the weak-strong simulation. Strong-strong simulation recently showed a strong coherent head-tail instability in the crab waist collision [?]. The instability is studied in detail in this paper.

STRONG-STRONG SIMULATION

A strong-strong bam-beam simulation code “BBSS” is used to study coherent effects in the crab waist collision. Two colliding bunches are represented by many macro-particles, $\approx 1,000,000$. Each bunch is sliced into several or many pieces, depending on Piwinski angle. Figure 1 shows schematic view of collision simulation for a large Piwinski angle. Typically the number of slices is chosen $n_{sl} \approx 10\sigma_z\theta_c/\sigma_z$. Collision order is given by sorting $z_{+,i} + z_{-,j}$, where z is the arrival time advance of $i(j)$ -th slice of $e^{+(-)}$ beam multiplied by the light speed c . The collision point of a slice pair is given by $s_{\pm} = \pm(z_{+,i} - z_{-,j})/2$ for e^{\pm} beam. A slice pair with $z_{+,i} \approx z_{-,j}$ collides at similar horizontal position, $x_{+,i} \approx x_{-,j} \approx z_{\pm,ij}\theta_c$ at $s \approx s^*$. While a pair with a large difference in z collides at $s = (z_{+,i} - z_{-,j})/2$ deviating from s^* with a large horizontal offset $(s - s^*)\theta_c$.

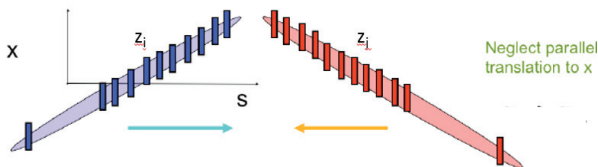


Figure 1: Schematic view of collision simulation for a large Piwinski angle.

In the strong-strong simulation, particles in a beam move with experience of electro-magnetic field induced by another beam. The motion of two beams (slice pair) are solved self-consistently. Strong-strong simulations are performed based on Particle In Cell method usually. The particle distribution is mapped on a transverse grid space (cell). Electric potential due to the particle distribution is calculated by solving Poisson equation in the two dimensional grid space. The potential calculation is simplified by assuming Gaussian distribution in transverse.

The code “BBSS” [3,4] eqipps several options to calculate electro-magnetic force between slice pair.

1. Gaussian approximation using rms value. Transverse Rms sizes of slice pair are calculated at $s_{\pm} = \pm(z_{+,i} - z_{-,j})/2$. Beam-beam force is evaluated by Bassetti-Erskine formula.
2. Gaussian approximation using fitting value. Transverse sizes of slice pair are calculated by Gaussian fitting at $s_{\pm} = \pm(z_{+,i} - z_{-,j})/2$. Beam-beam force is evaluated by Bassetti-Erskine formula.
3. Combined of PIC and Gaussian approximation. PIC is used for collision with small offset, namely $z_{+,i} \approx z_{-,j}$, while Gaussian approximation is used for collision with a large offset.
4. Full PIC using shifted Green function. Every collisions of slice pairs are evaluated by PIC method. Shifted Green function makes possible to evaluate potential for collision with a large horizontal offset.

Computing is harder for later options.

The strong-strong beam-beam simulation has been performed for FCC-ee. We discuss for Z and H, which parameters are listed in Table 1. Coherent instability has been seen in the simulation. Study of the coherent beam-beam instability is main thema of this paper.

Coherent beam-beam mode has been studied for a long time. Typical mode is π and σ modes, in which two beams collide with corrective frequency of transverse betatron frequency shifted by the coherent beam-beam tune shift. Here we discuss head-tail mode induced by beam-beam interaction with a large Piwinski angle. Two beams oscillate coherently with a head-tail mode.

The simulation calculate luminosity and beam distribution turn-by-turn Beam-beam parameter, which is normalized luminosity, is used for index of the beam-beam limit. The

beam-beam parameter is saturated at a certain value at the limit,

$$\xi_L = \frac{2r_e\beta_y}{N_e\gamma f_{rep}} L. \quad (1)$$

COHERENT HEAD-TAIL INSTABILITY IN THE SIMULATION

FCC-ee/H

FCC-ee-H targets beam-beam parameter $\xi_y \sim \xi_L = 0.14$ under radiation damping time 150 turns. FCC-ee has 2IP. In the simulation, we consider a half ring model with the circumference 50,000 km. The effective damping time is 300 turns. Perfect superperiodicity is assumed in this model. Luminosity is converted to 2-IP with 100,000 km circumference.

Figure 2 shows evolutions of the beam-beam parameter and $\langle xz \rangle$ given by full PIC based strong-strong simulation at tune operating point (0.513,0.57). The beam-beam parameter is saturated at around $\xi_L \approx 0.15$. For higher nominal tune shift $\xi_0 \geq .239$, luminosity oscillates turn-by-turn. $\langle xz \rangle$, which also oscillates, seems the source of the beam-beam limit. $\langle xz \rangle$ oscillates in phase for two beams. The beam-beam parameters $\xi_L = 0.11$ and 0.125 are achieved at nominal value $\xi_0 = 0.12$ (design) and 0.179 (1.5x design) without coherent instability. Therefore FCC-ee-H is feasible but somewhat critical for the instability in this operating point (0.513,0.55).

Figure 3 shows evolution of the beam-beam parameter for different conditions. Left plot depicts at operating point (0.54,0.61), and right plot depicts for two times longer damping time ($\tau_x/T_0 = 300$ turns) at tune operating point (0.51,0.55). The coherent oscillation is seen in every x_0 at the operating point (0.54,0.61). The design operating point is (0.54, 0.59-0.61). Therefore operating point should be re-considered in FCC-ee-H. For slower damping time, coherent oscillation is seen at $\xi_0 = 0.12$. The beam-beam parameter is saturated at $\xi_L \approx 0.12$.

Figure 5 shows the beam-beam parameter for Gaussian strong-strong at tune (0.513,0.57). The beam-beam parameter oscillates turn-by-turn, though not seen in the left plot. (the luminosity is calculated every 10 turns.) $\langle xz \rangle$ oscillation is depicted in the right plot. FCC-ee-H is critical for the instability.

Figure 4 summarizes the beam-beam parameter limitation. Three kind of points is depict for operating points (0.51,0.55), (0.54,0.57) and (0.54, 0.61). The error bars correspond to amplitude of coherent fluctuation of luminosity.

Figure 5 shows evolution of $\langle xz \rangle$ and turn-by-turn change of x-z distribution for simulation using the Gaussian option. Luminosity fluctuation is also seen in the Gaussian option. Gaussian approximation is more robust for choice of grid point and treatment of particles outside of grid space.

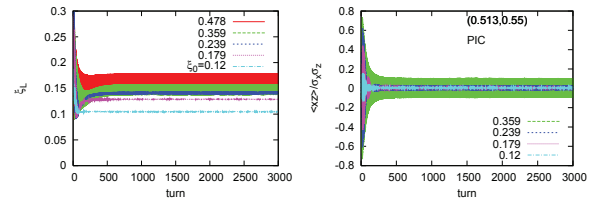


Figure 2: Evolution of the beam-beam parameter (left) and $\langle xz \rangle$ (right) given by strong-strong simulation (full PIC).

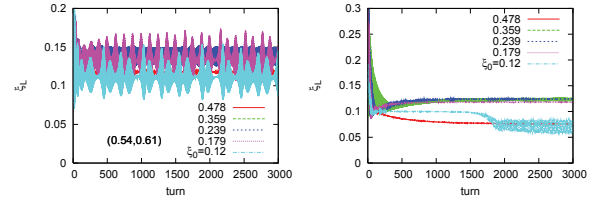


Figure 3: Evolution of the beam-beam parameter for tune (0.54,0.61) in left and twice (slower) damping time 300 turns in right. Both are given by full PIC.

FCC-ee/Z (parameters at Apr 2016)

Z factory was designed larger Piwinski angle $\sigma_z\theta_c/\sigma_x = 2.7$, where the bunch length was $\sigma_z = 2$ mm including beamstrahlung. The design beam-beam parameter is $(\xi_x, \xi_y) = (0.13, 0.17)$ with transverse radiation damping time 3000 turns. Though latest parameter adopts longer bunch length and larger Piwinski angle, systematic studies were performed using the old parameters. Figure 6 shows evolution of the beam-beam parameter for full PIC and fitted Gaussian model. The beam-beam parameter is summarized in Figure 7. The beam-beam parameter is saturated at $\xi_L \approx 0.05$, while the design is 0.17. Approaching half integer, beam-beam parameter increases to 0.07, but still insufficient. Figure 8 shows tune scan for the beam-beam parameter. Two type of tune scan are tried, one is changing tune of both beams, the other is changing electron tune with keeping positron tune $\nu_x = 0.54$. The coherent instability was not suppressed by separation of tune. Even if the coherent instability is weak, the beam-beam parameter is very low.

Figure 9 shows evolution of the beam-beam parameter with chromaticity $\nu'_x = \nu'_y = 5$. Chromaticity little suppresses the oscillation.

SuperKEKB

Strong-strong simulation for SuperKEKB has been done using Gaussian approximation and cobined method with PIC, because Piwinski angle is very large $\sigma_z\theta_c/\sigma_x = 20$. Figure 10 shows evolution of luminosity, horizontal beam size and $\langle xz \rangle$. Very strong coherent head-tail instability is induced by beam-beam interaction at tune (0.525,0.57), where the synchrotron tune is 0.025. The instability arises at the condition, $2(\nu_x - \nu_s) = \text{integer}$. The instability is not seen in design operating point (0.53,0.57). The instability is considered safe for SuperKEKB due to the narrow stop band,

Table 1: Parameters for FCC-ee (ver. 21, June 2016).

Parameter		SuperKEKB	Z	Z	W	H	tt
Energy	E (GeV)	4	45.5	45.5	80	120	175
Bunch population	$N_{\pm}(10^{10})$	9	37.1	3.3	6	8	17
Number of bunch		2500	30180	90150	5260	780	81
Emittance	$\epsilon_{x/y}$ (nm/pm)	3.2/8.64	0.2/1	0.09/1	0.26/1	0.61/1.2	1.3/2.5
Beta at IP	$\beta_{x/y}^*$ (m/mm)	0.032/0.27	0.5/1	1/2	1/2	1/2	1/2
Bunch length	σ_z (mm)	6	6.7	3.8	3.1	2.4	2.5
Energy spread	σ_{δ} (%)	0.08	0.22	0.09	0.10	0.12	0.17
Synchrotron tune	ν_z	0.025	0.036	0.025	0.037	0.056	0.075
Luminosity per IP	L ($10^{34} \text{ cm}^{-2}\text{s}^{-1}$)	80	207	90	19.1	5.1	1.3
Beam-beam	$\xi_{x/y}$	0.0028/0.088	0.025/0.16	0.05/0.13	0.07/0.16	0.08/0.14	0.08/0.12
Piwinski angle	$\sigma_z\theta_c/\sigma_x$	20	10	6	2.9	1.5	1.0

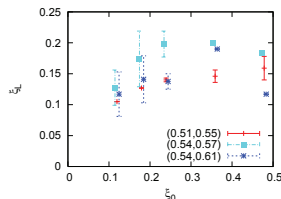


Figure 4: Achieved beam-beam parameter as function of its nominal value.

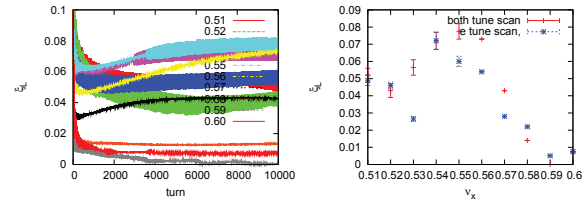


Figure 8: Tune scan for the beam-beam parameter. Right plot summarizes the beam-beam parameter.

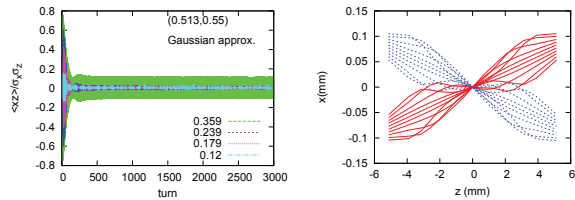


Figure 5: Evolution of $\langle xz \rangle$ given by strong-strong simulation (rms Gaussian).

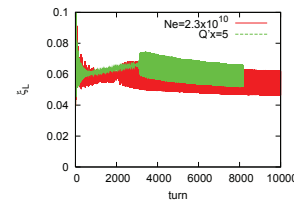


Figure 9: Evolution of the beam-beam parameter with/without chromaticity given by strong-strong simulation (full PIC).

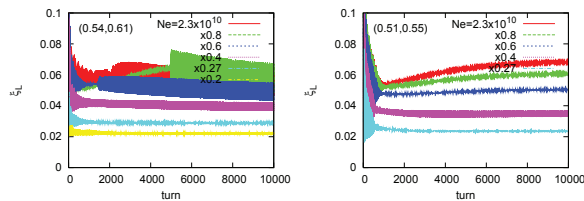


Figure 6: Evolution of the beam-beam parameter given by strong-strong simulation Left and right is given by full PIC and fitted Gaussian, respectively.

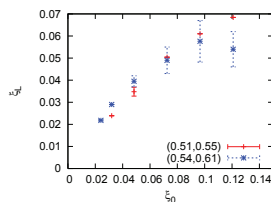


Figure 7: Achieved beam-beam parameter summary for FCC-ee/Z (full PIC).

Figure 11 shows the beam-beam parameter evolution using fitted Gaussian model. The beam-beam parameter behaves well, though it is somewhat lower than the design (0.88).

FCC-ee-Z (parameters June, 2016)

Z factory is proposed larger Piwinski angle $\sigma_z\theta_c/\sigma_x = 6$ or 10. The target beam-beam parameter is 0.13. Fitted Gaussian and full PIC options are used in the strong-strong simulation. Figure 12 shows evolution of the beam-beam parameter. Top two plots depicts for $\sigma_z\theta_c/\sigma_x = 6$. Left and right are given by full PIC and fitted Gaussian, respectively. The behaviors are somewhat different, but the beam-beam parameter is saturated far lower than the design 0.13. Bottom plot depicts for $\sigma_z\theta_c/\sigma_x = 10$. The behavior seemd worse for larger Piwinski angle.

The parameter of Z factory is similar as SuperKEKB. Main difference is target beam-beam parameter is $\xi_L = 0.08$ for SuperKEKB while 0.13 for FCC-ee-Z. We compare simulated beam-beam limit of SuperKEKB and FCC-ee-Z. Choosing half intensity in FCC-ee-Z, initial beam-beam

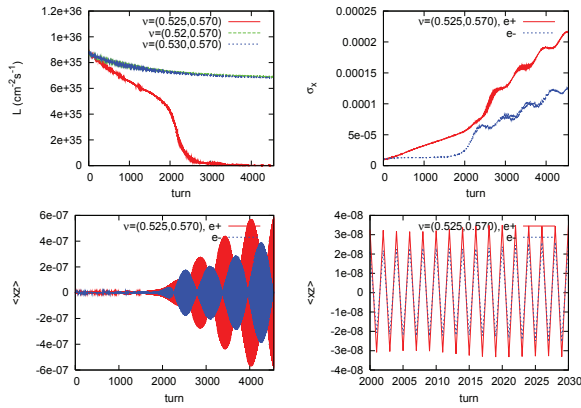


Figure 10: Evolution of luminosity, beam size, $\langle xz \rangle$ in SuperKEKB given by strong-strong simulation (combination of PIC and rms Gaussian).

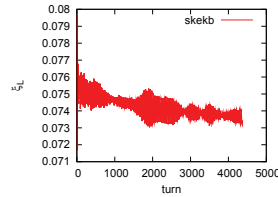


Figure 11: Evolution of the beam-beam parameter in SuperKEKB given by strong-strong simulation (fitted Gaussian).

parameter is similar level as SuperKEKB. Tune is slightly different, thus the same tune is adopted in FCC-ee-Z as SuperKEKB. In SuperKEKB, beam strength is not transparent: tune shift for two beam is different 0.08 and 0.088. Therefore one beam in FCC-ee-Z is decreased 10%. In both cases beam-beam parameter goes down from 0.08 to 0.02 as shown in Figure 13 in contrast with Figs.10 and 11.

Horizontal beam size of SuperKEKB and TLEP-ee-Z is similar, but emittance and β_x are different. They are $\epsilon_x = 3$ nm, $\beta_x = 0.03$ m for SuperKEKB, while $\epsilon_x = 0.09$ nm, $\beta_x = 0.5$ m for FCC-ee-Z. The horizontal tune shift is 0.03 for FCC-ee-Z and 0.0028 for SuperKEKB. We now change emittance and β_x with keeping the horizontal beam size. $\epsilon_x = 0.9$ nm, $\beta_x = 0.05$ m. Figure ?? shows evolutions of beam-beam parameter, beam sizes and $\langle xz \rangle$ for two cases, $\epsilon_x = 0.9$ nm, $\beta_x = 0.05$ m (blue) and $\epsilon_x = 0.09$ nm, $\beta_x = 0.5$ m (red). The behavior is remarkably different and is consistent with SuperKEKB result.

SIMPLIFIED MODELS

For qualitative understanding of the coherent instability, two simplified models were examined. One is one particle-airbag interaction model. One particle (e^+) with the horizontal size $\Sigma_x = \sqrt{\sigma_x^2 + \theta^2 \sigma_z^2}$ interacts with an airbag beam (e^-) which consists of a number of micro bunches. Figure 15 shows the schematic view of the model. We consider linear

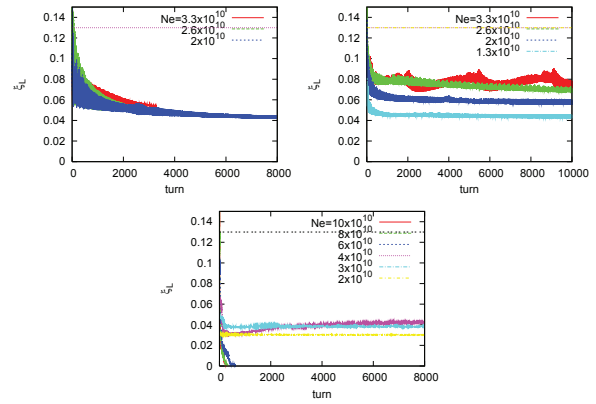


Figure 12: Evolution of the beam-beam parameter given by strong-strong simulation. Top left and right is given by Piwinski angle of $\sigma_x \theta_c / \sigma_z = 6$ using Full PIC Gaussian fitting, respectively. Bottom plot depicts for $\sigma_z \theta_c / \sigma_x = 10$.

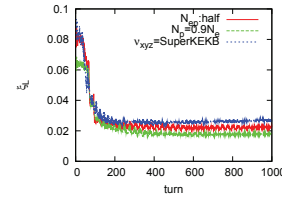


Figure 13: Evolution of beam-beam parameter for half intensity, detuning of transparency condition and SuperKEKB operating point.

force between one particle and airbag. 1,000 micro-bunches are used to represent the airbag beam.

Figure 16 shows a simulation result for the model. Top plot depicts typical horizontal amplitude on longitudinal phase space. The mode number for synchrotron motion is high $m \sim 10$ in the figure. Bottom plot depicts horizontal amplitude at $t=1000$ turn as function of horizontal tune. Three lines are given for beam-beam tuneshift $\xi = 0.03, 0.05, 0.07$. The oscillation is stable at ν_x close to half integer, while it

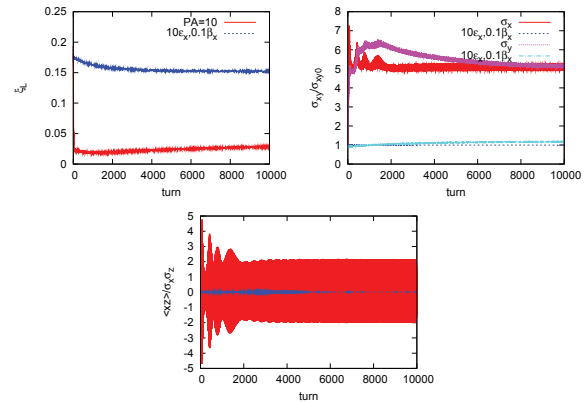


Figure 14: Evolutions of beam-beam parameter, beam sizes and $\langle xz \rangle$ for two cases, $\epsilon_x = 0.9$ nm, $\beta_x = 0.05$ m (blue) and $\epsilon_x = 0.09$ nm, $\beta_x = 0.5$ m (red).

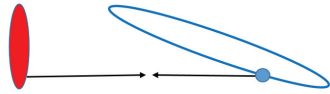


Figure 15: Schematic view of one particle-airbag interaction model.

is unstable leave from half integer. One-two particle model had been studied in Ref. [5]. The one-two particle model take into account only lowest head-tail mode $m = 1$. The model was stable. Now airbag considering higher mode showed contrasted results shown above.

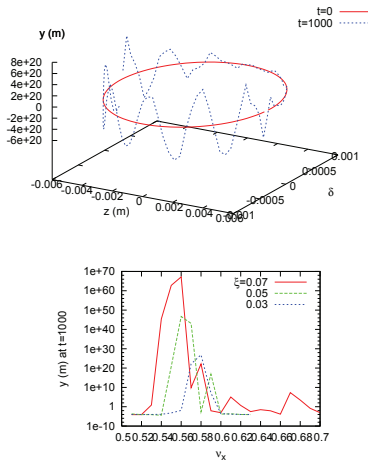


Figure 16: Simple mode simulation. Top and bottom plots are typical horizontal amplitude on longitudinal phase space and horizontal amplitude at $t=1000$ turn as function of horizontal tune, respectively

Figure 17 shows schematic view of the second model; two-airbug interaction model. Each beam is represented by airbag, which consists of a number of micro-bunches. Figure 18 shows bunch shape of airbag after 5, 20, 30, 50 collisions.

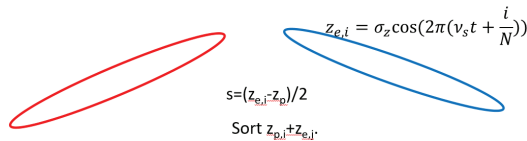


Figure 17: Schematic view of two-airbug interaction model.

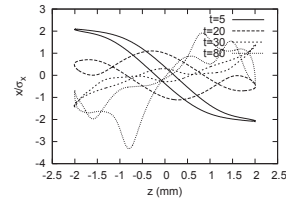


Figure 18: Bunch shape after 5, 20, 30, 50 airbag collision.

SUMMARY

Various kind of strong-strong beam-beam simulation has been performed for FCC-ee. Every simulations show strong coherent beam-beam instability in head-tail mode. The mode is high $m \approx 10$ in simplified mode. Strong-strong simulations also showed complex head-tail motion. The coherent instability seems serious in FCC-ee. Squeezing β_x^* helps the instability. To check feasibility of a design using crab waist collision, strong-strong simulation is inevitable.

The author thanks fruitful discussions with Drs. Y. Cai, K. Oide, D. Shatilov, F. Zimmermann.

REFERENCES

- [1] P. Raimondi, proceedings of the 2nd SuperB workshop, Frascati, March 2006.
- [2] K. Ohmi, "Simulated Beam-beam Limits for Circular Lepton and Hadron Colliders", in *Proc. IPAC2016*, Busan, Korea, May 2016, paper MOZA01, pp. 27–32,
- [3] K. Ohmi, *Phys. Rev.*, **E 62**, 7287 (2000).
- [4] K. Ohmi, M. Tawada, Y. Cai, S. Kamada, K. Oide, and J. Qiang, *Phys. Rev. ST-AB*, **7**, 104401 (2004).
- [5] K. Ohmi and A. W. Chao, *PRST-AB*, **5**, 101001 (2002)

TOP-UP INJECTION FOR A FUTURE ELECTRON-POSITRON COLLIDER*

J. T. Seeman[†], SLAC National Accelerator Laboratory, CA, USA

Abstract

Top-up injection was developed in PEP-II and KEKB both using a linac injector to allow nearly constant luminosity with the BaBar and Belle detectors, respectively, being fully operational in data taking mode during injection [1-13]. This note will cover injection parameters, injection hardware, detector background masking, background detection, and top-up injection commissioning. For this paper top-up injection, continuous injection, trickle injection and trickle charging all refer to the same injection technique.

The positron beam top-off in PEP-II (Figure 1) was first developed in fall 2005. The positron beam lifetime (3 GeV) was the shortest and thus made the luminosity much more constant after top-up injection. Second, the electron beam top-off (9 GeV) was developed making the luminosity fully constant in spring 2006. For PEP-II either electrons or positron could be injection up to 30 Hz each if needed, deciding pulse-by-pulse which beam (i.e. bunch) was desired. The typical injection rate for each beam was a few Hz.

Top-up injection for KEKB (Figure 2) for both electrons and positrons was developed in winter 2005. Which beam was injected was determined by the configuration of the linac and transport lines at the moment. The switching time between injected beams was a about a minute.

REQUIRED INJECTION PARAMETERS FOR A CIRCULAR e^+e^- FACTORY

Future e^+e^- colliders such as CEPC or FCCee will store about 2 to 6 $\times 10^{13}$ e^- and e^+ per beam at the Higgs beam energy. The lifetime is expected to be about 0.5 hr lifetime, thus, needing about 3 to 7 $\times 10^{13}$ e^- and e^+ per hour or about 0.5 to 2 $\times 10^{10}$ e^+ and e^- per second at full energy (75% capture). These rates compare well with previous particle generation rates such as those CERN delivered from the LEP injection complex $\sim 10^{11}$ e^+ per second and SLAC delivered from the SLC injection complex $\sim 6 \times 10^{12}$ e^+ per second.

The requirements for top-up injection involve all aspects of injection and detector operation: One must measure each bunch's charge in real time and determine when it needs refilling. In the injector, the accelerator will initiate a bunch generation to deliver it to the needed particular bunch (bucket) in the ring. Then one must inject the bunch(es) into the collider with very low losses. Then one determines the injected beam backgrounds in the particle physics detector and find cures using

collimation and steering. Next, one develops methods to monitor relevant backgrounds in real time for accelerator operators to tune on. Finally, one develops trigger masking for the detector physics data taking with trigger vetoes by the number of turns and within azimuthal locations within the ring.



Figure 1: PEP-II tunnel with LER above the HER with injection in the vertical plane.

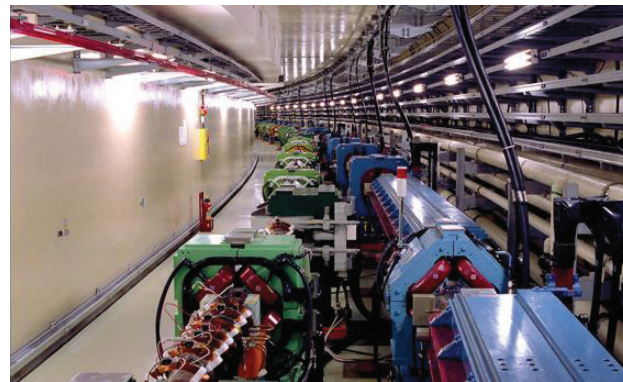


Figure 2: KEKB tunnel with LER and HER side-by-side with injection in the horizontal plane.

Top-up injection into each ring can be provided by stacking into an existing bunch as in PEP-II and KEKB (Figure 3) or by full bunch charge exchange (Figure 4). Most rings use the stacking method but some newer light sources are using charge exchange as the stored dynamic aperture is small making the injection acceptance small.

Listed here are typical lattice parameters at the injection septum for the stacking of bunches in the ring.

$$\beta_x \text{ at injection septum (stored)} = \sim 200\text{m}$$

$$\beta_x \text{ at injection septum (injection)} = \sim 30\text{m}$$

* Supported by US DOE contract DE-AC02-76SF00515.

[†] seeman@slac.stanford.edu

$\epsilon_{x\text{stored}}$ (stored) = 9.4 nm
 $\epsilon_{x\text{inj}}$ (injected) = 50 nm
 $\sigma_{x\text{stored}}$ at septum (stored) = 1.4 mm
 $\sigma_{x\text{inj}}$ at septum (injected) = 1.2 mm
 X_s = Septum blade thickness ≈ 5 mm
 X_c = septum clearance distance = $\sim 6\sigma_x$
 $X_{\text{inj}} < A_x$
 $X_{\text{inj}} = 4 \sigma_{\text{inj}} + X_s + X_c = \sim 18$ mm
 A_x = machine aperture $> \sim 20$ mm

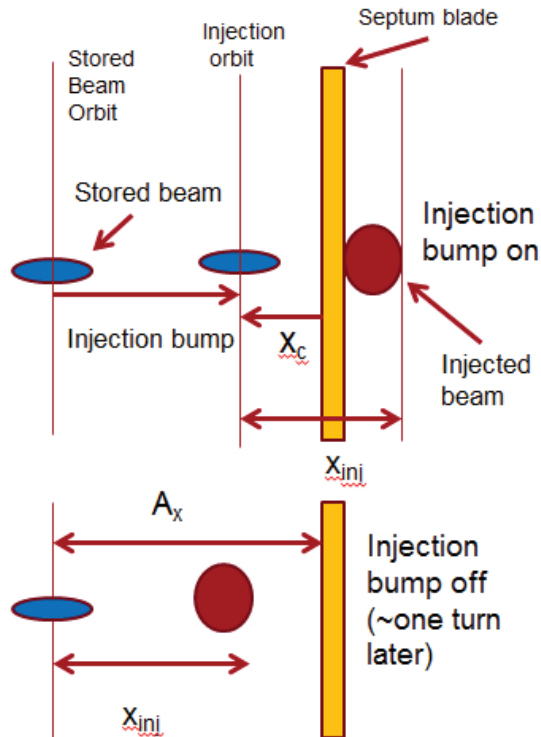


Figure 3: Injection transverse phase space for bunch stacking shown for the horizontal plane but vertical will work as well.

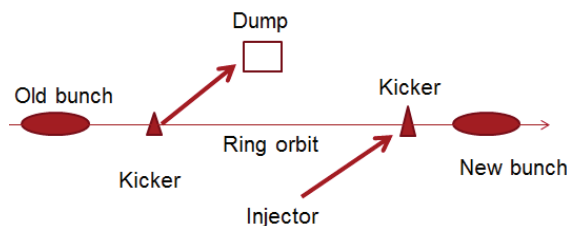


Figure 4: On-axis injection with bunch charge exchange.

PEP-II/BaBar TOP-UP INJECTION

Typical PEP-II stored beam parameters are listed here and shown in Figure 5 and in Table 1. The PEP-II interaction region is shown in Figure 6.

Energy = 3.5 x 9 GeV
 Circumference = 2200 m
 One collision point (IR) at luminosity = 1.2×10^{34}
 Full energy injection from linac and damping rings
 Number of bunches = 1732 / ring

Beam currents = 2.1 A x 3.2 A
 Particles = 1.0 to 1.5 x 10¹⁴ / beam (HER/LER)
 Lifetimes:
 Vacuum = ~ 10 hours
 Touschek = ~ 3 hours (LER)
 Luminosity = ~ 1 hour
 Lost particles per second = 4.2 x 10¹⁰ / second
 Top-up injection = one bunch / pulse, either e⁺ or e⁻
 Injection rate: ~ 3 -15 Hz (30 Hz max)
 Particles per injection: 3 to 9 x 10⁹ / pulse, selectable
 Bunch injection controller: pick the lowest charged bunch
 Injection efficiency = 50 to 90%
 Injection kicker pulse length = 0.4 microsecond
 Ring path length = 7.3 microsecond

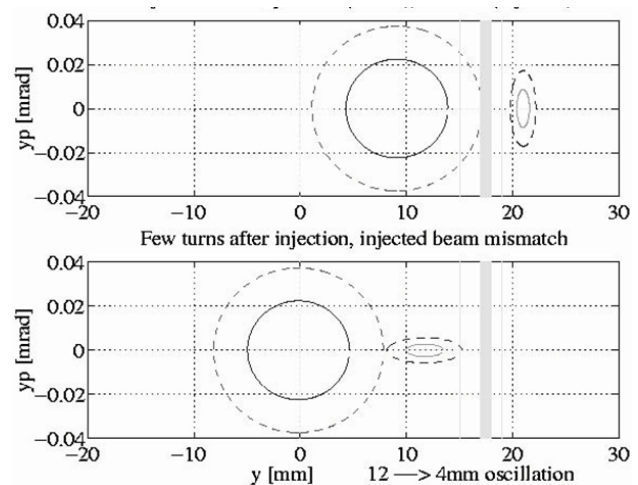


Figure 5: PEP-II injection aperture in the vertical plane with the vertical stored emittance of 3 nm and injected 0.57 nm. The grey area is the 2 mm septum blade.

Table 1: Additional PEP-II Injection Parameters

Parameter	e ⁺	e ⁻
Energy (GeV)	3.1 GeV	9 GeV
1- σ Emittance (x/y)	6.6/0.8 nmr	2.3/0.3 nmr
FWHM energy spread	0.7%	0.7%
Energy acceptance	0.7%	0.7%
1- σ pulse length	1 mm	1 mm

For PEP-II injection the first goal is to set a low injection loss rare to make injection efficient and reduce background in BaBar. The second is the stored beam trajectory (orbit) should not oscillate due to a mismatched injection kicker to avoid luminosity dips and potential abort triggers. There are many issues for the lattice and injection kickers to be considered to make these two goals optimal.

Copyright © 2017 CC-BY-3.0 and by the respective authors

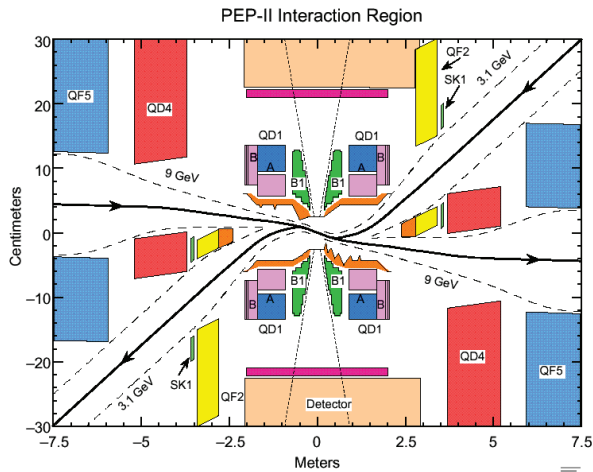


Figure 6: PEP-II interaction region where particle losses affect BaBar's data collection but can be reduced by collimation and trajectory adjustments.

For the lattice constraints, we needed to inject inside the dynamic aperture of both rings of PEP-II, the betatron phase advance between the kickers needed to be adjusted to 180 degrees, the local dispersion of the injection bump was adjusted to acceptable levels after overall ring errors, and the non-linearity of the magnetic field of the septum magnet (steel and blade) corrected or compensated.

For the injection kicker magnets, we needed to adjust the kicker magnet amplitudes to be matched, the kicker timing pulses synchronized, the kicker reflections reduced to acceptable levels or were cancelled, made sure the excitation does not cause aborts, the kicker amplitude not too large and within capabilities of the HV pulser, and the horizontal oscillation due to magnet rolls or coupling fields were within bounds.

During actual top-up injection for PEP-II the charge could be set to about 5 levels but were typically set only to the "smallest quanta" day to day. The maximum top-up injection rate was about 3 per second during set up and collisions. Not all bunches have the same charge loss due to beam-beam and other lifetime effects as shown in Figure 7. The controller to determine which bunch to inject into next is shown in Figure 8. An example of the injection quanta variations with time is shown in Figure 9. With top-up injection the "pseudo beam lifetime" appears to be infinite. However, the real lifetime was calculated using the DCCT-based beam lifetime of bunches that are not being injected into. When the beam currents were very low, for example filling from scratch, the injection rate was set to maximum to reduce the overall time to fill each ring, meaning we avoided "trickling from scratch".

Continuous (trickle charge) (top-up) injection was planned for from the design phase of PEP-II. The LER was accomplished first in 2005 with BaBar taking data. The HER continuous injection was six months later. See Figure 12 before and Figure 13 after top-up. A 40% increase in average integrated luminosity was achieved. The effect of top-up injection was seen immediately with the average length of a fill as shown in Figure 10.

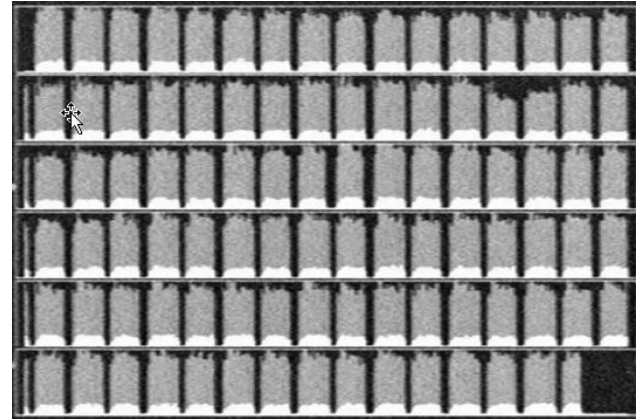


Figure 7: Wrap-around bunch charge plot of the stored bunches in PEP-II with bunch trains in a by-2 bunch pattern with 95 trains of 14-15 bunches in 18 potential bunch locations with 3-4 missing bunches per gap for e⁺ cloud suppression (~2004) and a long gap at the end for potential ions in the electron beam.

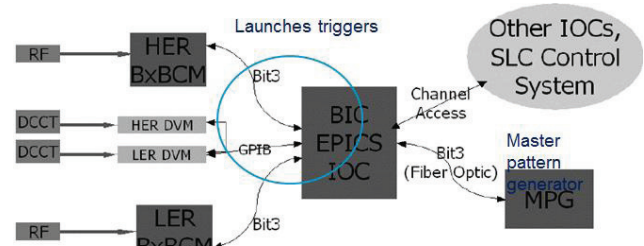


Figure 8: Bunch injection controller BIC that arranged for a bunch to be generated in the injection chain to be delivered to the correct bunch in LER or HER.

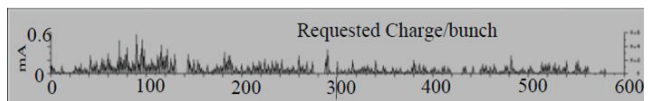


Figure 9: LER injection requests for the first 1/6 of LER versus bunch number. Different bunches have different beam-beam lifetimes and thus injection rates and charge "quanta".

There were several improvements to PEP-II injection that made BaBar backgrounds much better. These improvements took several months to achieve. First, we reduced the rms energy (and phase) jitter of the beam from the damping ring. This allowed the injected beam to fit into the ring energy aperture better, as shown in Figure 11. Second, the bunch charge per bunch was stabilized from the electron gun as shown in Figure 12 allowing fewer injections per ring bunch.

The improvement from top-up injection in the PEP-II integrated luminosity per day is shown in Figure 13 with the corresponding parameters shown in Table 2. Typical

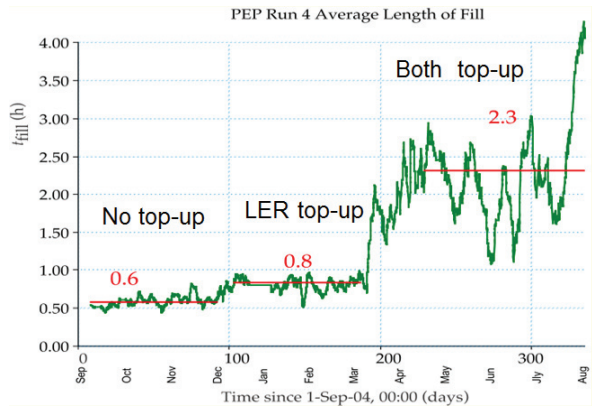


Figure 10: Improvement of PEP-II fill length with LER and then LER+HER top-up injection, giving about x4 gain.

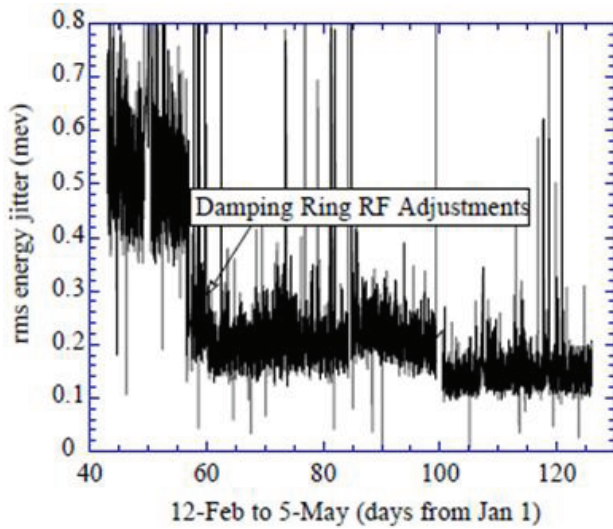


Figure 11: RMS energy jitter reduction into PEP-II to help top-up backgrounds by adjustments to the Damping Ring RF system.

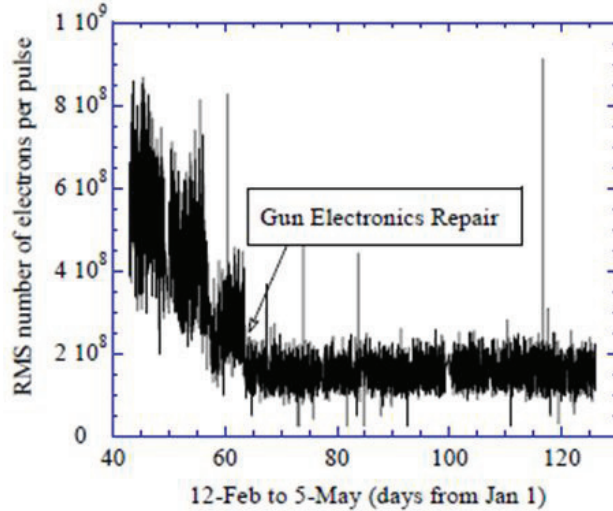


Figure 12: With a repair of the linac electron gun electronics the rms jitter of injected bunches was reduced.

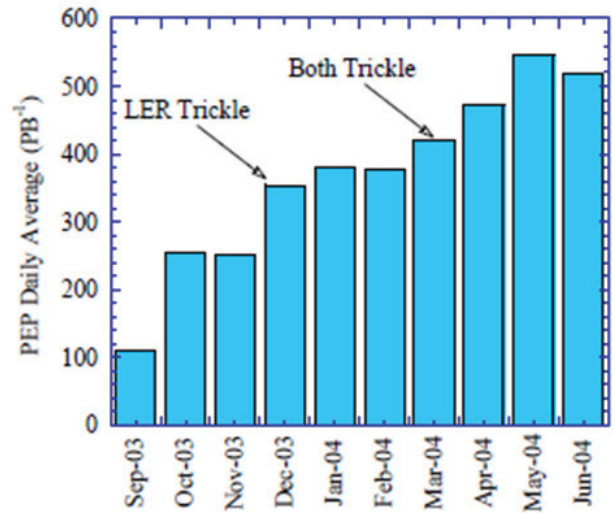


Figure 13: PEP-II integrated luminosity per day increased with top-up injection, first with LER then both rings.

Table 2: PEP-II Top-up Mode Operating Summary

	Top-up	LER trickle	Both trickle
Lum. lifetime	364	560	N/a
Avg./peak ratio	72%	86%	99...100%
Top-ups/shift	10	6	n/a
Gain (expected)	0	15%	29%
Gain (delivery)	0	35%	50%

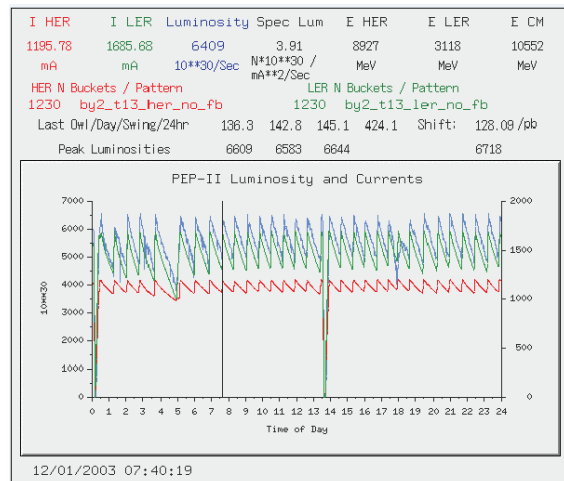


Figure 14: Luminosity and beam currents for 24 hours showing the fill-coast mode of PEP-II in early years.

plots of the daily luminosity and currents before and after top-up injection are shown in Figure 14 and 15, with the improvement in PEP-II efficiencies shown in Figure 16.

KEKB/BELLE TOP-UP INJECTION

The e⁺/e⁻ linac at KEK provides injected beams to four rings (KEKB LER, KEBB HER, Photon Factory and Accumulator Ring). In the original scheme, a transport

line and linac switch was needed every time the injector mode for the different rings changed. All accelerator

succeeded in making the pulse-to-pulse switching injection to the three rings (KEKB LER, KEB HER and PF), which is much faster switching than originally planned. Because of this injection scheme, the accelerator parameter scans at KEB have become much faster with constant beam currents stored in the rings and it has become possible to find better beam-beam machine parameters than before. Another motivation of the introduction of fast switching of the injector mode is related to the beam lifetime issue. They could explore machine parameter space which had not been accessed to due to short beam lifetime before and that they could find better parameter sets which achieved a higher luminosity. This kind of improved machine parameters is expected as well in the new accelerator SuperKEKB.

In the top-up injection scheme, the KEB beams were injected at 10 Hz versus 50Hz in the conventional scheme. After each beam injection, data taking is vetoed for 3.5 msec, which means that the detector dead time is about 3.5% coming from this veto. In the case of KEB, the electron and positron beams cannot be injected simultaneously. The early mode of injection (electron or positron) was switched every 5 minutes. The top-up injection scheme was realized with preparations and trial-and-errors for more than one year. Several serious problems had to be overcome. One was the malfunction of pre-amplifiers of the TOF detector and frequent DAQ (data acquisition) errors of Belle under high beam background conditions. To solve the problem with the pre-amplifiers, Belle modified them so that the circuits could accept a higher noise level. The DAQ problems were overcome by upgrading the DAQ system during the summer shutdown in 2003. On the other hand, efforts were made to decrease the detector backgrounds during beam operations, which was done mainly by optimizing accelerator parameters. The luminosity and beam lifetime were trade-offs which had to be managed. The typical injection parameters for KEB are shown in Figure Table 3. The filling cycle for KEB is shown in Figure 17 before and after top-up injection with a clear improvement in luminosity and average luminosity. The daily luminosity plots for KEB showing luminosity and beam currents before and after top-up are shown in Figures 18 and 19 with the specific luminosity constant to about 5 % with top-up.

The side-by-side comparison of injection parameters are shown in Table 4 with similar results. However, there some differences. PEP-II injected vertically and KEB horizontally. PEP-II had shorter beam lifetimes due to reduced number of particles due to the shorter circumference. BaBar had slightly reduced dead time compared with Belle. KEB had longer fills on average than PEP-II as PEP-II had higher beam currents in the RF systems, thus resulting in increased aborts. Collimation efforts gave somewhat better results in KEB over PEP-II.

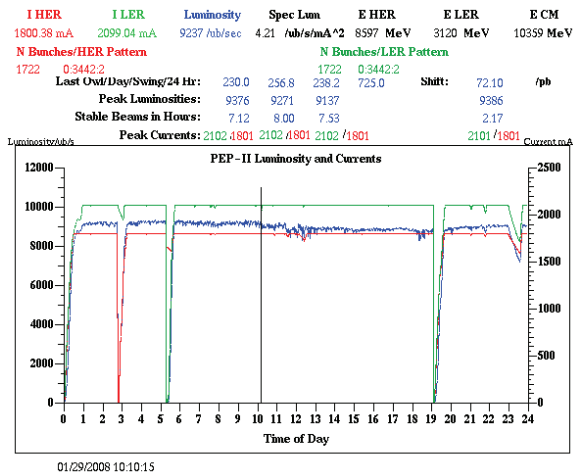


Figure 15: Luminosity with top-up injection for both PEP-II beams.

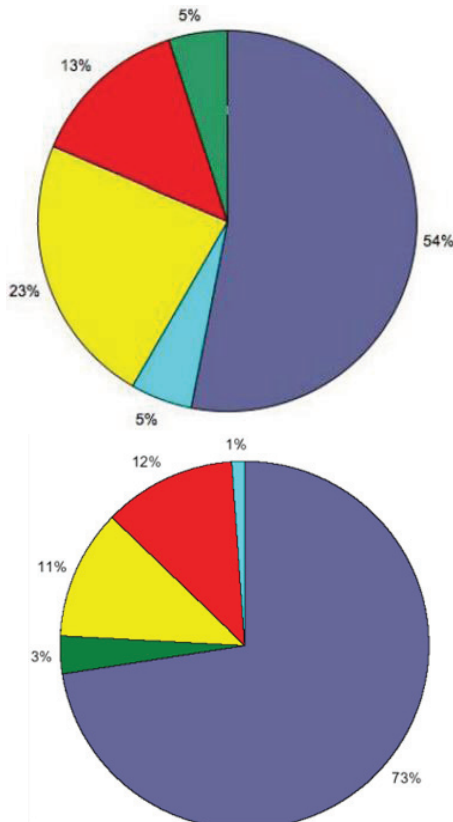


Figure 16: PEP-II run time improvement with no-top-up above and with top-up below. Blue is BaBar data taking, green PEP-II development, yellow tuning and filling, red unscheduled down, and light blue scheduled off.

parameters had to be reloaded, since the beam energies of these rings are different. The switching time was more than 30 seconds. The Linac Group at KEK have been shortening the switching time over many years which took considerable effort. In April 2009, they finally

Table 3: KEKB Injection Parameters

	KEKB HER	KEKB LER
Beam mode	8 GeV e-	3.5 GeV e+
Beam energy	8 GeV e-	3.5 GeV e+
Number of bunch	2	2
Bunch charge	1 nC	1 nC (primary e-)
Maximum beam repetition	50 Hz	50 Hz
Injection per day	> 250	> 500

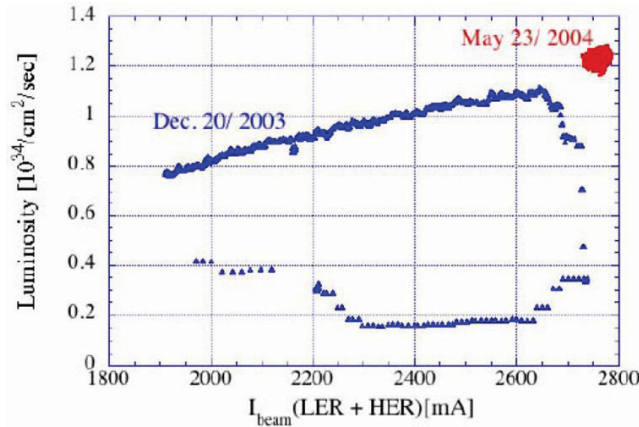


Figure 17: Luminosity during a KEKB fill cycle without top-up injection in blue and the luminosity with top-up in red (small concentrated area.)

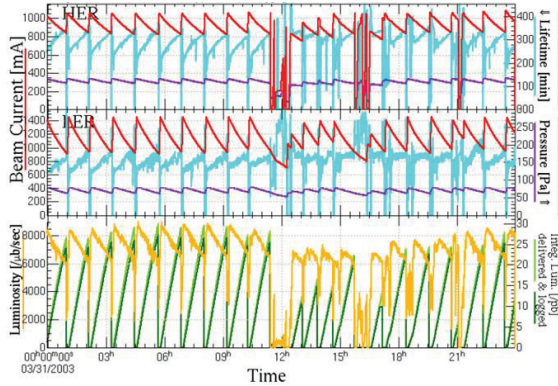


Figure 18: KEKB luminosity versus time over 24 hours before top-up injection.

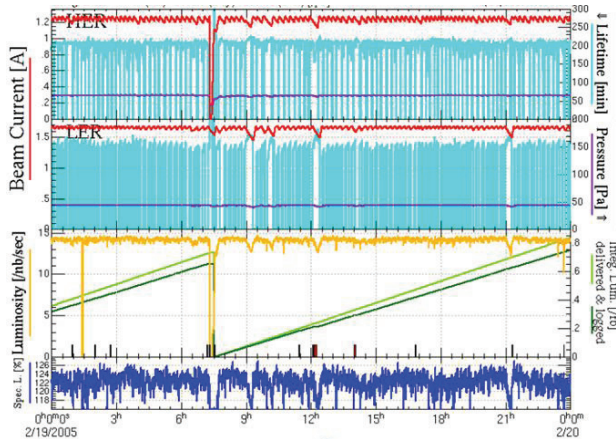


Figure 19: KEKB luminosity in operation after top-up.

Table 4: Summary of KEKB and PEP-II Top-up Injection Parameters

Parameter	KEKB	PEP-II
Injection plane	horiz.	vertic.
Beam lifetime	250/200 m	400/60 m
Gain	30%	30...50%
Detector gate	3.5 ms	15 ms/0.9 μs
Deadtime due to gating	3.5%*	1.8%*
Average length of fill	6...8 h	2.5...4 h
Background reduction by collimation	> 2	≈ 1.5
most important collimation	vertic.	horiz.
Background monitoring	Injection-gated from detector	dto.
Injection control	reduce rate	reduce rate and charge

DETECTOR BACKGROUND MASKING IN BaBar

The backgrounds in BaBar and Belle from top-up injection were dealt with several approaches. The background signals provided to PEP-II by the BaBar detector were gated on immediate injected pulses. The systematic improvements of the e- beam resulted from steady upgrades of the linac injected beams; for example, the systematic reduction of the distance of the injected beam from the closed orbit near the septum reduced backgrounds. The stabilization of the injected beam trajectories through feedback helped. The injection kickers were investigated to make sure the “closed injection bunch” was indeed closed and tuned to the optimum.

There were several improvements that Babar made to improve data collection with top-up. These included smoothing out the trickle-algorithm in Bunch Injection Controller BIC and Master Pattern Generator MPG, avoiding data stoppage including cleaning up BIC-MPG communication. The EPICS bar-chart display showing rate of injection per bunch was updated. There was a desire to display the total injection rate overall. A hardware real-time injection indicator (pulsed LED or counter) was constructed. The accelerator needed to make sure the injection (LER and HER) feedbacks did not stop if too many small quanta were used for a given period from BPM mis-readings. The BIC needed to stabilize the setup of the bunch quanta (intensity, energy). BaBar needed to update its interlocks with time as several were bypassed early on. Finally, BaBar needed to speed up the refresh of injection-trigger histograms.

Several of the injected beam signals are made to be shown in real time as shown in Figure 20. In Figures 21-24 are shown BaBar trigger data indicating real time background signals. Many of the triggers show up around the time of a quarter turn in a synchrotron oscillation in either the LER or HER indicating energy or bunch phase injection errors. Figure 25 shows the masking of the BaBar triggers showing only a partial turn has to be vetoed after a short complete veto. The BaBar trigger includes masking all of ring a few tens of turns and then mask only the injected bunch area. The inhibited area is 600 nsec by 10 msec per 7.33 microseconds times the injection rate which gives about 1% loss at 10 Hz injection rate. The backgrounds increased slowly as a fill progressed. The period from 0 to 240 seconds involved a large quanta injected into HER and LER at 15 Hz each.

The period from 240 to 320 seconds uses small charge quanta injection into HER. The period from 240 to 410 seconds includes 30Hz injection into LER. Finally, the trigger veto provides injection quality feedback to the accelerator operators, identifies possible configuration loss periods, the resetting of the electronic front ends, and then stops data collection when the configuration is being reset.

Likewise, the detectors for FCCee/CEPC will need to mask injection bunches. 1) For a ramped “Storage Ring” style injector (with injection once every 5 minutes), the detector must mask the entire ring for about 10 milliseconds every 5 minutes at injection meaning large injected charge and many bunches (from 50-100) will be entering the ring. The expected integrated luminosity loss will be around 10%. 2) For a ramped “Main Injector” style injector (with injection one every ten seconds or so), the detector must mask the entire ring for about 10 milliseconds every 10 seconds indicating small injected charges and many bunches (from 50 to 100). Here the integrated luminosity loss should be around few %. 3) For a rapid “synchrotron injector” RCS (with injections a few per second), the detector must mask about 1/80 of ring for about 10 milliseconds at 0.1 Hz indicating small injected bunch charges but few bunches (from 1 to 3). Here the integrated luminosity loss will be much less than 1%.

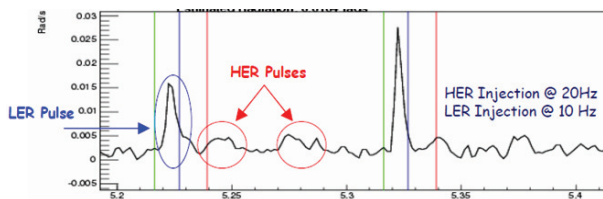


Figure 20: BaBar noise sampling in real time (sec) with HER and LER injections.

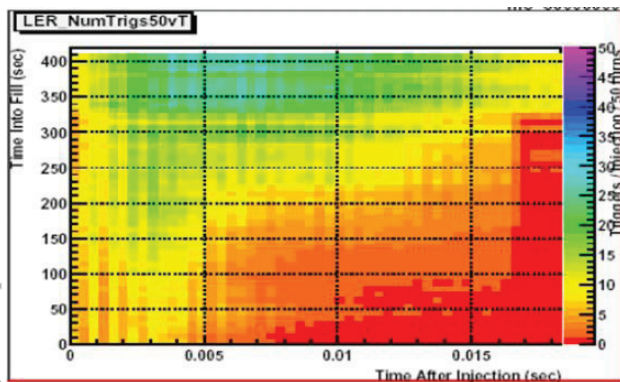


Figure 21: BaBar backgrounds from PEP-II LER injection versus time and time after injection. Red is very low backgrounds.

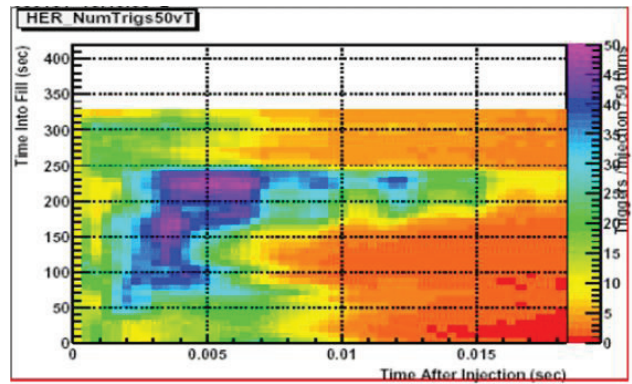


Figure 22: BaBar backgrounds from HER versus time and time after injection. Red is very low backgrounds. The peak backgrounds occur after about 4 msec related to injection energy errors.

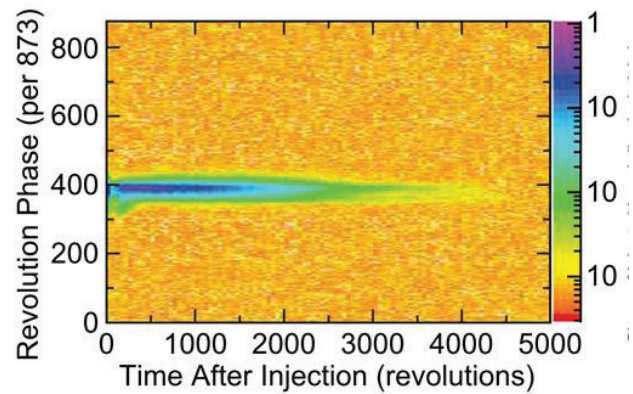


Figure 23: BaBar triggers versus time and bunch number within a turn.

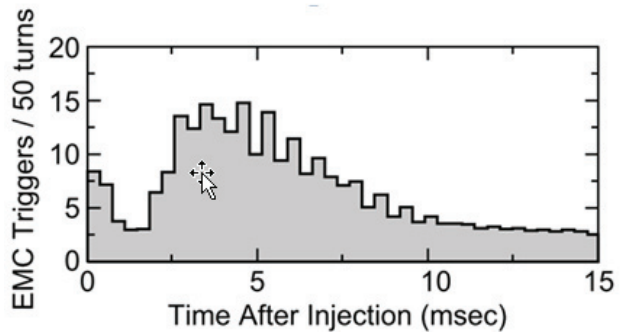


Figure 24: BaBar calorimeter triggers versus time after injection.

TOP-UP INJECTION COMMISSIONING

The commissioning of top-up injection required many shifts and hardware and software improvements prior to actual full time use. After full time use, the tuning for optimum backgrounds took a long period and in some sense is a continuous-ongoing action. Certain radiation detectors can only be used during very high backgrounds including the radiation diodes, vertex tracker signals, and crystal detectors. The injection trigger counters counted the electro-magnetic calorimeter EMC triggers (the most

sensitive BaBar detector component) after every injection pulse and made a histogram of triggers versus time. The EPICS variables with integral counts were shown. Also, an FFT of the background was used to show the effect of accelerator changes with beam-energy deviations as a time display. Everything was normalized to the injection rate. The drift chamber DCH current was good for monitoring the average backgrounds and was not too fast for it could show an assessment of injection spikes. The L3 trigger rate had a similar behavior to the DCH current.

Overall, real time signals from the detector are crucial for making top-up injection function well and for tuning up top-up injection.

A single bunch injection controller needs to be worked out in detail for both the accelerator and the detector.

Finally, commissioning can be complicated as many issues both on the accelerator and detector sides arise mainly with detector backgrounds and masking and have to be worked out in parallel with common purpose.

ACKNOWLEDGEMENTS

The author wishes to thank the following people for discussions on top-up injection. From PEP-II: F.-J. Decker, S. Ecklund, A. Fisher, M. Sullivan, J. Turner, and U. Wienands. From KEKB: Y. Funakoshi, H. Koiso, K. Oide, and S. Uno. From BaBar: S. Curry, W. Kozanecki, A. Perazzo, C. O’Grady, and M. Weaver.

REFERENCES

- [1] “PEP-II an Asymmetric B Factory”, Conceptual Design Report, CALT-68-1869, LBL-PUB-5379, SLAC-418, UCRL-ID-114055, UC-IIRPA-93-01, June 1993.
- [2] J. Seeman *et al.*, “PEP-II at $1.2 \times 10^{34}/\text{cm}^2/\text{s}$ Luminosity”, PAC 2007, p. 37.
- [3] J. Seeman *et al.*, “Last Year of PEP-II Operation”, EPAC 2008, p. 946.
- [4] J. L. Turner *et al.*, “Trickle-charge: A New Operational Mode for PEP-II”, EPAC 2004, p. 881.
- [5] J. Seeman *et al.*, “Performance of the PEP-II B-Factory Collider at SLAC”, PAC 2005, p. 2369.
- [6] U. Wienands *et al.*, “Tracking Down a Fast Instability in the PEP-II LER”, EPAC 2006, p. 658.
- [7] M. Sullivan *et al.*, “Anomalous High Radiation Beam Aborts in the PEP-II B-factory”, EPAC 2006, p. 652.
- [8] Y. Funakoshi *et al.*, “KEKB Performance”, EPAC04, p. 707.
- [9] Y. Funakoshi *et al.*, “Recent Performance of KEKB”, PAC 2009, p. 588.
- [10] F.-J. Decker *et al.*, “Towards Achieving the Design Number of Bunches in PEP-II”, EPAC 2000, p. 403.
- [11] U. Wienands, “Lepton Collider Operation with Constant Currents”, PAC 2005, p. 149.
- [12] F.-J. Decker *et al.*, “Diagnosing the PEP-II Injection System”, EPAC 2004, p. 833.
- [13] J. Seeman, “Top-Up Injection at PEP-II and Applications to a Circular e+e- Higgs Factory”, in Proceedings of HF2014, p. 205.

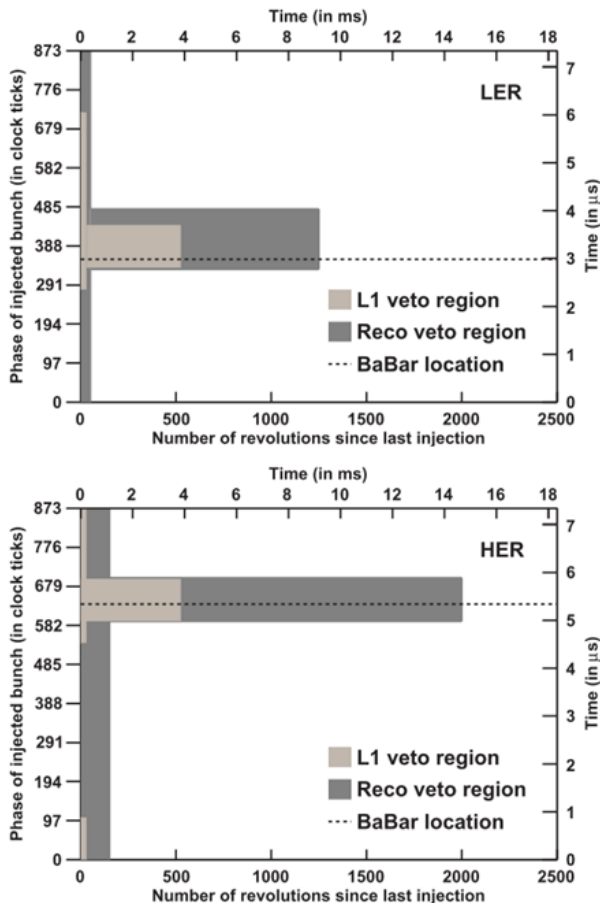


Figure 25: BaBar trigger masking versus time after injection and time in a turn relative to the injected bunch.

CONCLUSIONS

Top-up injection will work and should work well for a future circular e+e-factory. A full energy injector is needed because of the short beam lifetime.

The detectors will need to mask out the buckets being injected into during the damping times of the injected bunches during data taking but not for the whole circumference of the ring (only the injected bunch region).

INJECTOR LINAC UPGRADE AND NEW RF GUN DEVELOPMENT FOR SuperKEKB

Takuya Natsui[†], Daisuke Satoh, Mitsuhiro Yoshida, Rui Zhang, Xiangyu Zhou, KEK, Ibaraki, Japan

Abstract

The SuperKEKB commissioning has finally started. The final goal of luminosity is 40 times higher than KEKB. The injector upgrade is required to obtain the low emittance and high charge beam corresponding to the short beam life and small injection acceptance of the SuperKEKB ring. In the injector linac, several new instruments have been installed. Flux Concentrator (FC) was developed for high charge positron beam capture. The target of positron bunch charge is 4 nC. The new damping ring will be used for positron beam to reduce beam emittance to 10 mm-mrad. However, electron beam must be reached to 20 mm-mrad normalized emittance at 5 nC beam charge without damping ring. Thermionic gun was used for KEKB injector and it was able to generate enough beam charge. However, its emittance is too large. Therefore we developed photo cathode S-band RF gun. This new RF gun has unique accelerating cavity which called quasi-traveling wave side coupled cavity. Laser system for this photo cathode has been also developed. The laser system is constructed with Yb:YAG thin disk for high power and pulse shaping.

INTRODUCTION

The upgrade of KEKB to SuperKEKB is going on. Since high luminosity is required in SuperKEKB, improvement of beam emittance and high charge is necessary. The injector linac has many challenging issues. Table.1 is upgrade parameter of electron and positron beam.

Table 1: Electron and Positron Beam Parameter

	KEKB (e+/e-)	SuperKEKB (e+/e-)
charge [nC]	1 / 1	4 / 5
Emittance [mm-mrad]	2100 / 300	20 / 20

In the positron beam, SuperKEKB beam charge is 4 times higher than KEKB beam charge. Primary electron beam for positron beam generation is 10 nC. It is same charge as KEKB. Therefore new Flux Concentrator (FC) and capture section was developed for efficient positron generation [1]. Since generated positron beam has large emittance, new damping ring has been constructed to reduce beam emittance.

In the other hand, the RF gun is developed to realize both of high charge and low emittance electron beam. Since we have no damping ring for electron beam, high charge beam generation with low emittance is essential in the gun. We are developing a photo cathode S-band RF

gun for high charge (5 nC) low emittance (20 mm-mrad) beam generation. A thermionic cathode DC gun was used in KEKB for both of electron injection beam and positron primary electron beam. However this conventional gun does not have potential of low emittance generation. The new RF gun development is very important issue for electron beam.

Emittance preservation is one of the big issues. Total length of our linac is 600 m. In SuperKEKB, the beam charges are not small enough to ignore wakefield effect. Precise alignment of beam line is required to avoid transverse wakefield effect. However, small misalignment is remained. This small misalignment may be cancelled to using offset injection. The misalignment should be less than 0.1 mm in locally and 0.3 mm in globally. Target value of emittance will be able to be achieved with performing precise alignment and offset injection.

Optimum optics and magnet adjustment is required for both of electron and positron beam offset injection. The KEK injector is required simultaneous injection for HER, LER, PF and PF-AR ring at 50 Hz. The pulse quadrupole magnet and pulse steering magnet has been developed for pulse-to-pulse modulation [2].

Several new devices such as RF gun, FC and pulse magnets have been developed for achieve low emittance high charge electron and positron beam. The SuperKEKB Phase 1 commissioning had been carried out from February to June 2016. We had been able to confirm the performance of the new devices in KEK injector linac.

NEW RF GUN DEVELOPMENT

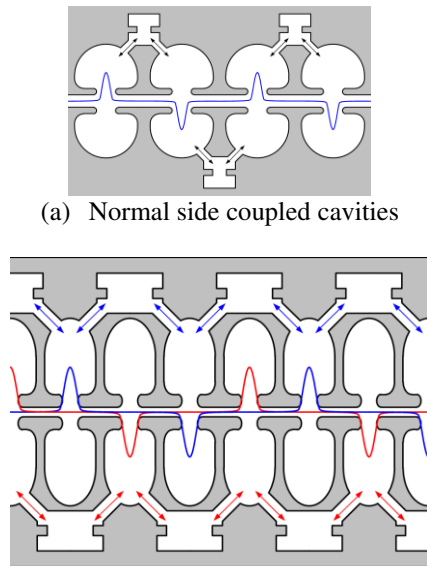
We are developing a photo cathode S-band RF gun for high charge (5 nC) low emittance (20 mm-mrad) beam generation. A thermionic cathode DC gun was used in KEKB. Since it is difficult to make a low emittance beam with the thermionic gun, the new RF gun must be installed to realize required electron beam parameter. However the standard on-axis coupled 1.5 cell RF gun is not suitable for this high charge beam, because standard gun is used up to about 1 nC by ordinary. If we obtain 5 nC in the gun, beam size will be too large. We have to consider both beam focus and emittance preservation. Thus it is necessary to make a focusing field against the space charge in the cavities. In this on-axis coupling cavity, however, it is difficult to arrange the field freely on the axis. Since beam hole is also the coupling hole. Thus annular coupling is required.

We are developing a new advanced RF gun. It has new acceleration scheme, we call it as a quasi-traveling wave. In this method, higher accelerating field and stronger focusing field are expected. It is very efficient accelera-

tion method. This quasi-traveling wave cavity is realized by using a two side couple cavities.

Annular coupled cavities as Disk and Washer (DAW) [3] or side coupled cavities are possible to make narrow acceleration gap. The narrow gap makes the focus field. Our DAW RF gun is using this focus field. Side coupled cavity also can be made the narrow gap. However, these cavities have a long drift space as Fig.1 (a) that shown normal side couple cavities. Due to the long drift space, those RF gun generates beam with a divergence angle.

One solution is to use two standing wave cavities. If two side coupled cavities are arranged staggered, we obtain a double standing wave field as Fig.1 (b). These two standing wave side coupled cavities are independent electromagnetically. If we feed RF power with $\pi/2$ phase difference, acceleration field is similar to traveling wave to accelerated beam. Since two side coupled cavities are possible to place on the same axis, a quasi-traveling wave can be realized. Quasi-traveling wave can realize very efficient beam acceleration and focusing.



(a) Normal side coupled cavities

(b) Quasi traveling wave side coupled cavities

Figure 1: Structure of the quasi traveling wave cavity.

2D Cavity Design

The first cavity of RF gun is most important for beam quality. Since beam energy of cathode cell is still low, space charge affects beam size and emittance. First cavity should be designed to have strong focus field. However nonlinear component of the strong focus field causes emittance growth. In addition, we must avoid the electric field concentration at the cavity surface.

SUPERFISH and GPT (General Particle Tracer) calculation code were used for 2D cavity design. Figure 2 is whole cavities structure design and electric field (SUPERFISH result). This cavity shape is obtained by using automatic downhill simplex method calculation. This RF gun has total of seven acceleration cavities. These are divided into two standing wave structure of 3 and 4 side

coupled cavities respectively. There are no couplings to next cavity on the axis.

Figure 3 shows the beam tracking simulation for 5 nC beam charge result; emittance is 5.5 mm-mrad; beam size is 0.4 mm (standard deviation) at exit of RF gun ($z = 250$ mm). In the Fig.3, we can find that the beam size becomes gradually smaller in the RF gun. This is caused by not additional magnetic field but the focusing electric field of RF gun. Beam energy will be 11.5 MeV with 20 MW RF input. The energy spread is 0.6 %. These results satisfy the requirement in our application.

In addition, we confirm that this gun can generate 10 nC beam generation by calculation; emittance is 10 mm-mrad; beam size is 1.2 mm; energy spread is 1 %. It is enough margins.

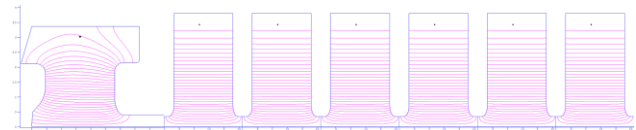


Figure 2: Designed RF gun cavities (SUPERFISH calculation result).

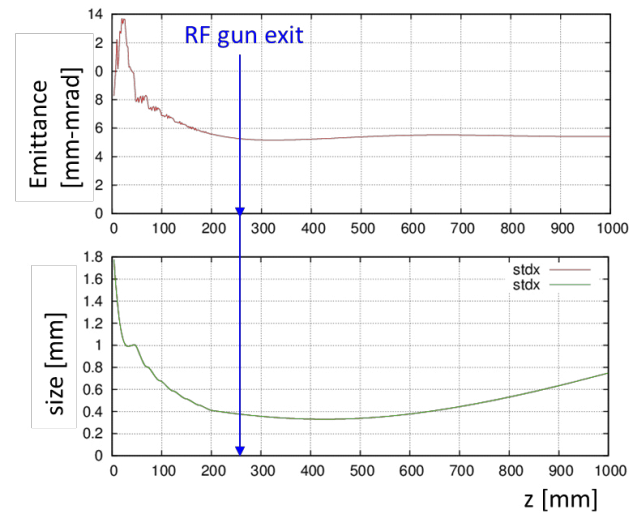
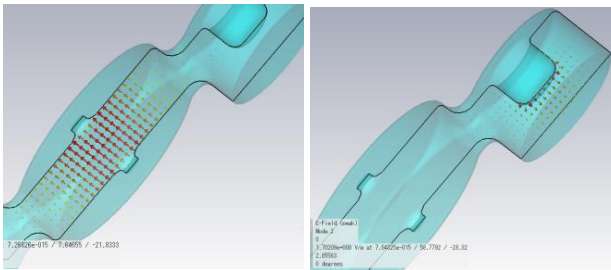


Figure 3: Beam tracking simulation result.

3D Cavity Design

CST MICROWAVE STUDIO was used for 3D cavity design. Figure 4 is the calculation result of the regular cell of a side coupled cavity. The acceleration mode and coupling mode are adjusted to be same frequency. Coupling value k is 3 %. This gun has two standing wave cavities; we designed two types coupler as shown Fig.5.

Figure 6 shows the whole cavity shape. The side couple cavities of the two standing wave cavities are mounted as 90 degrees in the azimuthal angle. It has two ports for RF feed. We use 90 degree hybrid for RF feed. We manufactured a compact 90 degrees hybrid. It will be mounted RF gun directly. We already finished mechanical design as shown in Fig.7.



(a) Accelerating mode (b) Coupling mode
Figure 4: regular cell cavity calculation result.

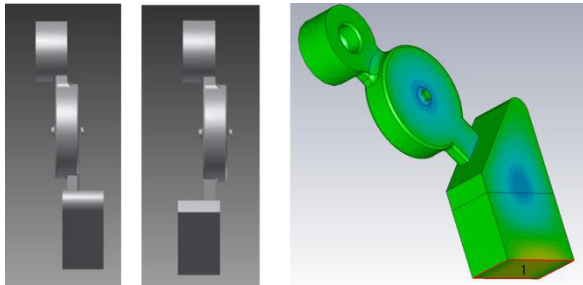


Figure 5: Two type couplers and calculation result.

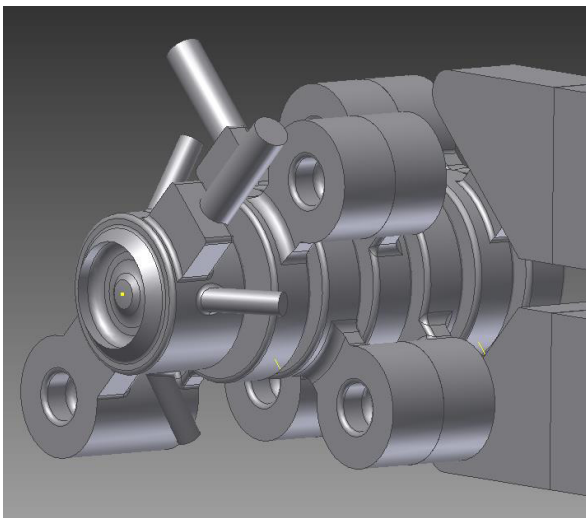


Figure 6: Whole cavity shape.

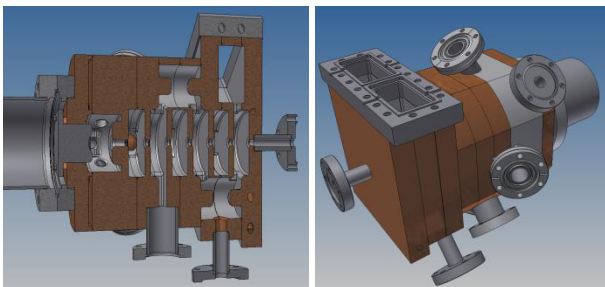


Figure 7: mechanical design.

Laser System and Cathode

The new laser system has been also developed for the RF gun. A schematic diagram of the laser setup is shown in Fig.8. The seed pulse with the pulse energy of 0.2 ns and spectrum of 1025-1070 nm was generated by an Yt-

terbium (Yb) doped fiber ring oscillator. The pulse repetition is 51.9 MHz, synchronized with 51.9 MHz and 2856 MHz RF from master oscillator which is used in linac. After an Yb fiber pre amplifier, the pulse was chirped to ~20 ps by a transmission grating stretcher with a spectral mask. An Yb-doped large-mode-area polarizing double-clad photonic crystal fiber was employed to the first amplification stage. Then, the pulse repetition rate of 25 Hz, double bunch was separated with two Electro Optic (EO) modulators. To increase the pulse energy, another Yb-doped LMA PCF was used. So the pulse was amplified to μJ-level, which was strong enough to be amplified by Yb:YAG thin-disk stage. To obtain the mJ class pulse energy, several multi-pass amplifier stages were employed. Deep UV pulses for the photocathode are generated by using two frequency-doubling stages. High pulse energy and good stability were obtained. Finally, the pulses were injected into RF gun [4].

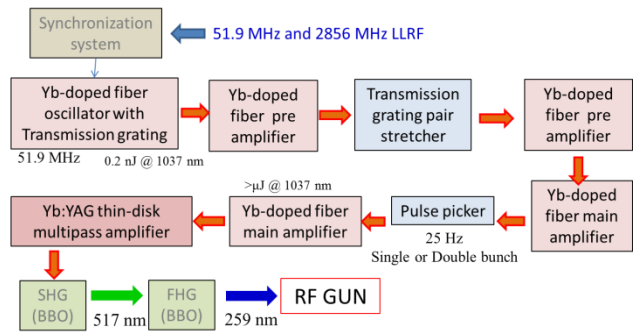


Figure 8: Layout of Laser system.

We succeeded in developing an iridium cerium (Ir₅Ce) photocathode which has a reasonably high QE (~ 9.1×10⁻⁴ at 219 nm at room temperature) and long lifetime (>LaB₆) [5].

RF Gun Install in Injector Linac Beam Line

The new RF gun was installed at A1 sector injector in September 2013. RF power is fed two cavities by using 90 degree hybrid for π/2 phase advance. Laser power is injected from angled laser port. Figure 9 shows installed the RF gun.

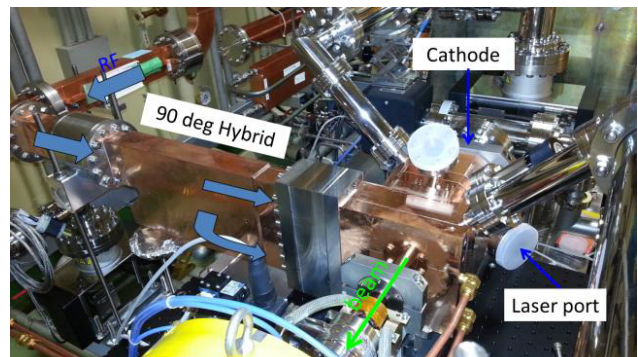


Figure 9: Installed RF gun.

The laser hut was constructed near the RF gun. Injected laser is fourth harmonics. First, laser pulse was converted to second harmonics at laser hut. The second harmonics was used for transportation from laser hut to RF gun. Transported second harmonics was converted to fourth harmonics at near the RF gun. BBO crystal was used for conversion. Optics for injection is shown Fig.10. Injection angle is 60 degree.

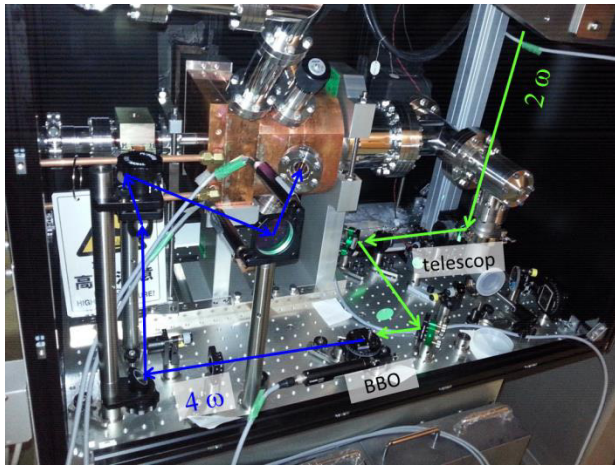


Figure 10: Laser injection component near the RF gun.

In Phase 1 beam operation, conventional thermionic DC gun system was also used. Two electron guns are installed in A1 sector. The conventional thermionic DC gun was being used in KEKB operation. This line was shifted to higher position. Normal beam line is used for study of the new RF gun. This thermionic gun was used for positron primary beam and normal electron beam operation in Phase 1. This short beam line which is used for thermionic gun is merged to normal line by using two bending magnet. RF gun beam line was used for study in Phase1. Figure 11 shows two beam lines of RF gun and thermionic gun.

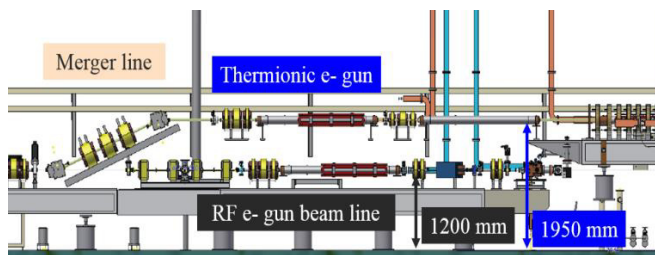


Figure 11: Thermionic gun and RF gun beam line.

RF GUN COMMISSIONING AND PHASE 1

Phase 1 commissioning started at Feb. 2016 and finished at Jun. 2016. Injector linac supplies electron and positron beam with thermionic gun, charge is 1 nC to both of HER and LER. The RF gun study had been carried out on parallel.

RF Gun Study

The RF gun was also operated at 1 nC beam charge. Stability of beam charge is laser power stability. Charge stability of gun exit was less than 5 % at 1.7 nC in 7 hours measurement as shown Fig.12. It is capable for normal operation.



Figure 12: Beam charge stability of RF gun.

Laser spot position on cathode stability is one of the big issues. Beam position is varied by laser position at cathode. Beam position exit of gun is measured with beam position monitor (BPM). As a result, stability is 0.5 mm in horizontal, 0.2 mm in vertical (in sigma). Distance of RF gun is very far (~10 m) from laser hut. Transportation optical line needs precise treatment. It should be improved for Phase 2.

Laser spot profile decides beam quality. We could not realize good Gaussian beam in 4th harmonics. We have to improve laser spot profile till Phase 2.

Normalized emittance at 1 nC beam charge was measured at AB sector in linac. The emittance was about 20 mm-mrad in horizontal and vertical. Measurement emittance is larger than simulated emittance. It might be due to laser pulse quality. We must improve laser spot profile, position jitter and pulse length.

HER Injection with RF Gun

Beam emittance value of RF gun was larger than calculated value. However we attempted to do beam injection to HER with the RF gun. Stability of the RF gun beam was same as the thermionic gun. Certainly, emittance of the RF gun is smaller than emittance of thermionic gun. As a result, we achieved HER injection with RF gun. It was continuous 10 days injection. Injection efficiency and stability were almost same as thermionic gun. Figure 13 is an example of injection history graph with the RF gun injection.

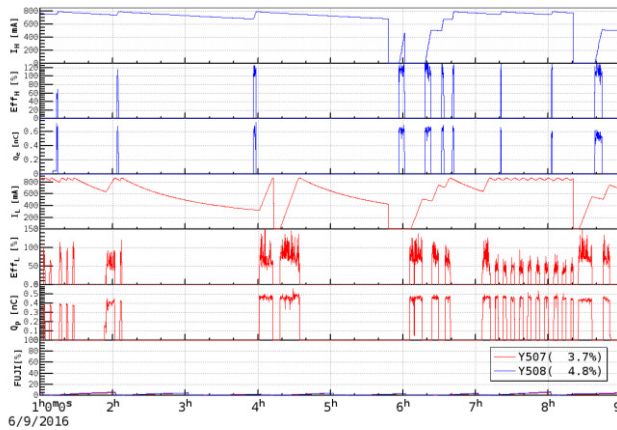


Figure 13: RF gun beam injection history graph.

SUMMARY

KEK injector linac has a lot of mission for SuperKEKB upgrade, such as RF gun development, flux concentrator development, low emittance reservation and others. SuperKEKB Phase1 commissioning was carried out from Feb. to Jun. 2016. Basically, injection beam was generated from conventional thermionic gun. New FC was used for generation of positron. Electron and positron beam injection was achieved. Beam charge was 1 nC in electron and positron for HER and LER. We continued the RF gun beam study during phase1. Beam charge stability was achieved 5 % at 1 nC with the RF gun. We attempted to test injection to HER with the RF gun. As a result, we succeeded in continuous 10 days electron injection to HER with the RF gun. However beam charge and emittance had been not achieved final target with the RF gun. It is required to improve the laser system problems which are less pulse energy, profile and position jitter for SuperKEKB operation.

REFERENCES

- [1] Kamitani, Takuya, "SuperKEKB positron source construction status", MOPRI004, IPAC'14, 2014.
- [2] Furukawa, Kazuro *et al.*, "Pulse-to-pulse beam modulation and event-based beam feedback system at KEKB linac", *arXiv preprint arXiv:1006.2543*, 2010.
- [3] Takuya Natsui *et al.*, "High Charge Low Emittance RF Gun for SuperKEKB", TUPPD057, IPAC'12, Louisiana, USA, 2012.
- [4] Zhou, X *et al.*, "25Hz Sub-mJ Ytterbium Laser Source of RF Gun for SuperKEKB", WEPMA044, IPAC'15, 2015.
- [5] Satoh, Daisuke, "Development of Better Quantum Efficiency and Long Lifetime IrCe Photocathode for High Charge electron RF Gun", MOPFI023, IPAC'13, Shanghai, China, 2013.

DESIGN STUDY OF CEPC BOOSTER*

Bian Tian-Jian[†], Gao Jie, Institute of High Energy Physics, Beijing, China

Cai Yun-Hai, Slac National Accelerator Laboratory, CA, USA

Michael Koratzinos, University of Geneva, GENEVA, Swiss

Zhang Chuang, Cui Xiao-Hao, Wang Yi-Wei, Bai Sha, Wang Dou, Su Feng, Xiao Ming,
Institute of High Energy Physics, Beijing, China

Abstract

CEPC is next generation circular collider proposed by China. The design of the full energy booster ring of the CEPC is especially challenging. The ejected beam energy is 120GeV, but the injected beam only 6GeV. In a conventional approach, the low magnetic field of the main dipole magnets creates problems. we have two ways to solve this problem, Firstly, we propose to operate the booster ring as a large wiggler at low beam energy and as a normal ring at high energies to avoid the problem of very low dipole magnet fields. Secondly, we implement the orbit correction and correct the earth field to make booster work.

INTRODUCTION

CEPC (Circular Electron and Positron Collider) was proposed as an electron and positron collider ring with a circumference of 50-100km to study the Higgs boson[1][2][3]. CEPCB(CEPC Booster) is a full energy booster ring with the same length of CEPC which ramp the beam from 6GeV to 120Gev. At the injected beam energy, the magnetic field of the main dipole is about 30Gs, the low magnetic field will create problems for magnet manufacturing[4].

In the Pre-CDR[5], a preliminary design is proposed, but the problems of earth field correction and dynamic aperture are not solved.

In this paper, we focus on those problems and find a reasonable solution. In the wiggler scheme, which split the normal dipole to several pieces with different magnet field direction to avoid the problem of very low dipole magnet fields[6][7][8], because low field magnet manufacture is difficult.

In the normal bend scheme, we implement the first turn orbit correction and closed orbit correction to correct the earth field effect.

An analytic map method(Differential algebra)[9] is used to derive the twiss functions of arbitrary order of energy spread, such as β function, phase advance function, dispersion function. Those functions are all analytic functions dependent of sextupole strength. Optimize the high order chromaticities, then a good dynamic aperture for both on-momentum and off-momentum particles are got.

* Supported by National Natural Science Foundation of China, Grant No. NSFC 11575218 and No. 11505198

[†] biantj@ihep.ac.cn

DESIGN GOAL

At present, the emittance of CEPC is about $2.0 \times 10^{-9} m \cdot rad$, it is much lower than the Pre-CDR because of the crab waist scheme. That makes the CEPCB harder to design because emittance of CEPCB at high energy is also reduced, which cause the chromaticities much stronger and pose challenges to our design at the same time.

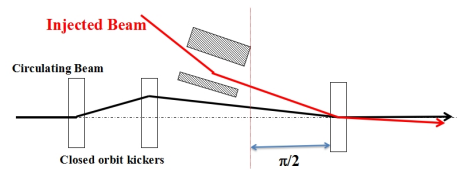


Figure 1: Injection scheme.

Fig. 1 shows the X direction injection scheme for mainring. Assume that the dynamic aperture of CEPC mainring at 0.5% energy spread is 15 times of sigma and the β function is about 200m.

The total space for injection:

$$\begin{aligned} & \sqrt{\epsilon_x \times \beta_x} \times 15 \\ &= \sqrt{2.0 \times 10^{-9} \times 200} \times 15 \\ &= 9.49(mm) \end{aligned}$$

5 sigma is retained for revolution beam to get enough quantum life time:

$$\begin{aligned} & \sqrt{\epsilon_x \times \beta_x} \times 5 \\ &= \sqrt{2.0 \times 10^{-9} \times 200} \times 5 \\ &= 3.16(mm) \end{aligned}$$

Assuming that the emittance of CEPCB at 120Gev is $3.5 \times 10^{-9} m \cdot rad$, and 3 sigma is retained for injection beam to loss less particles:

$$\begin{aligned} & \sqrt{\epsilon_x \times \beta_x} \times 3 \\ &= \sqrt{3.5 \times 10^{-9} \times 200} \times 3 \\ &= 2.51(mm) \end{aligned}$$

The design goals of CEPCB are listed:

1. The emittance of CEPCB at 120Gev is about $3.5 \times 10^{-9} m \cdot rad$.
2. 1% energy acceptance for enough quantum life time.
3. The dynamic aperture results must better than 6 sigma (Normalized by emittance, which is decided by the beam from linac) for both on-momentum and off-momentum(1%) particles.

WIGGLER BEND SCHEME

Linear Lattice

The layout of CEPCB is show in Fig. 2. It is make up by 8 arcs and 8 straight section, and the total length is 63.8 km. The RF cavities are distributed in each straight section. The lattice for CEPCB has been chosen to use the standard FODO cells with 90 degrees phase advances in both transverse planes, which give us smaller emittance and clear phase relationship between sextupoles.

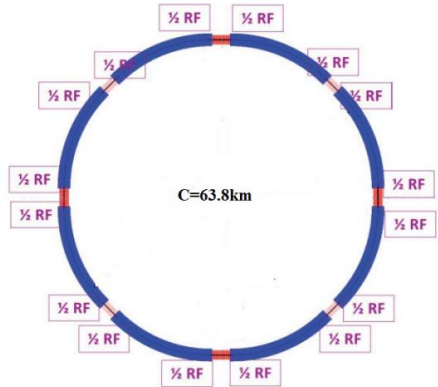


Figure 2: Layout of CEPCB.

A standard FODO cell with 90 degrees phase advance is shown in Fig. 3. The length of each bend is 30.4 m, the length of each quadrupole is 1.2 m, while the distance between each quadrupole and the adjacent bending magnet is 1.7 m. The total length of each cell is 70 m.

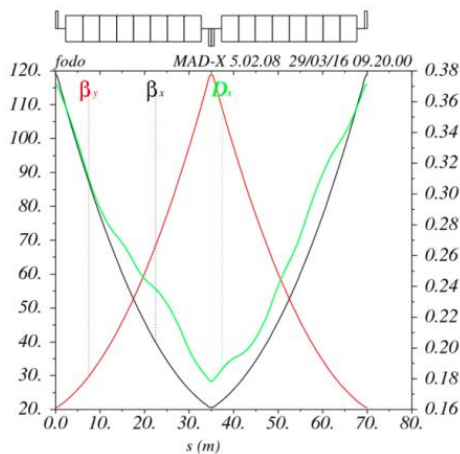


Figure 3: Beta functions and dispersion function of a standard FODO cell with 90/90 degrees phase advance in CEPCB.

In order to make the main dipole stronger to avoid the problem of low magnet field, we split the 30.4 m bend to 8 pieces. The adjacent dipole pieces have different magnet field direction but the integral field strength of dipole is the same as the normal dipole. And we call this scheme “wiggler scheme”, as Fig. 4 shows. The orbit off-set(the red curve in Fig. 4) in dipole is became smaller as the beam ramping up

until the negative dipole change it’s field direction and all the dipole became normal bending magnet at 120 Gev. Fig. 5 shows the bending angle of positive and negative magnet as a function of ramping time.

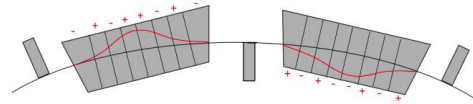


Figure 4: wiggler orbit in a FODO cell.

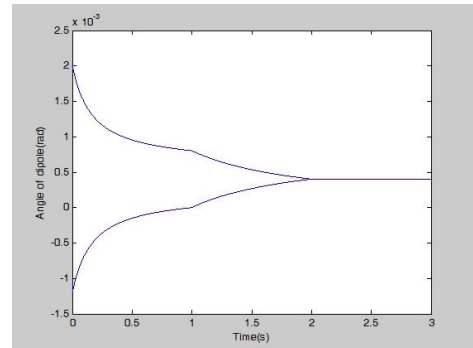


Figure 5: Positive and negative magnet as a function of ramping time.

Sextupole Scheme

The sextupole scheme of CEPCB is shown in Fig. 6. The long space means 180 degree phase advance and the short space means 90 degree phase advance. The FODO in Fig. 6 means to insert a FODO cell in the two repeated sextupole arrangement. In total, 8 families of sextupoles are used.

SF1	SF1	SF2	SF2	SF3	SF3	SF4	SF4
SD1	SD1	SD2	SD2	SD3	SD3	SD4	SD4
FODO							
SF1	SF1	SF2	SF2	SF3	SF3	SF4	SF4
SD1	SD1	SD2	SD2	SD3	SD3	SD4	SD4

Figure 6: Sextupole scheme of CEPCB.

In this scheme, geometric terms are minimized because of the non-interleaved sextupole scheme. Two identical sextupoles apart by 90 degree phase advance to cancel the beta-beat effect of off-momentum particles.

Our goal is reducing the 2nd and 3rd order chromaticities to enlarge the energy acceptance. An analytic map method (Differential algebra)[9] is used to derive the 2nd and 3rd order chromaticities analytically, which contain the information of the 8 sextupole families.

When we optimize the 8 sextupole families using the 2nd and 3rd order chromaticities we have derived, we find it is not enough to make the 2nd and 3rd order chromaticities as small as we expect. So tune shift between ARCs is considered. The analytic map method is also used in finding a right phase

advance between two ARCs, and we find 43.3 degree is a good choice[7]. Fig. 7 shows the tune as a function of energy spread.

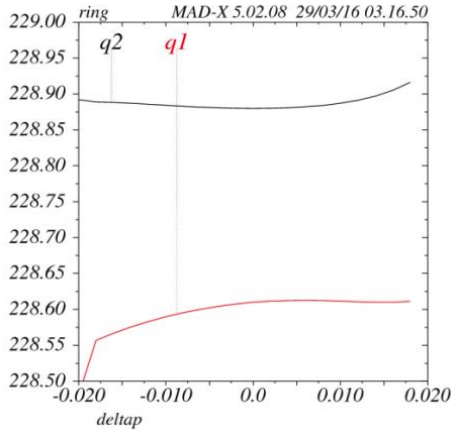


Figure 7: Tune as a function of energy spread.

Dynamic Aperture Results and CEPCB Parameters

To make the CEPCB closer to a real machine, multipole errors are added. We estimate the error of CEPCB is in the same level as LEP[10], the Table 1 shows the error estimation.

Table 1: CEPCB Error Estimate

	Dipole	Quad	Sext
Bend	8×10^{-4}		
Quadrupole	2×10^{-4}	6×10^{-4}	
Sextupole	7×10^{-4}	5×10^{-4}	1.7×10^{-4}

Table 2: CEPCB Parameters@6GeV

6GeV	Unit	Value
offset in bend	cm	1.20
Momentum compaction		2.02E-5
Strength of dipole	Gs	-129/180
NB/beam		50
Beam current/beam	mA	7.50E-1
Bunch population		2.00E10
RF voltage	GV	2.10E-1
RF frequency	GHz	1.30
Synchrotron oscillation		2.10E-1
Energy acceptance RF	%	5.93
SR loss/turn	GeV	5.42E-4
energy spread	%	1.47E-2
Horizontal emittance	m*rad	6.38E-11

The tune we are using here is: 0.61/0.88, because this tune avoid some strong resonance line. But it is just a rough estimation, tune scanning is needed to find a better tune.

Table 3: CEPCB Parameters@120GeV

120GeV	Unit	Value
offset in bend	cm	0
Momentum compaction		2.38E-5
Strength of dipole	Gs	516.71
NB/beam		50
Beam current/beam	mA	7.50E-1
Bunch population		2.00E10
RF voltage	GV	3.5
RF frequency	GHz	1.30
Synchrotron oscillation		1.4E-1
Energy acceptance RF	%	2.46
SR loss/turn	GeV	2.35
energy spread	%	1.20E-1
Horizontal emittance	m*rad	3.62E-9

Table 4: CEPCB Parameters@80GeV

80GeV	Unit	Value
offset in bend	cm	0
Momentum compaction		2.31E-5
Strength of dipole	Gs	344.74
NB/beam		50
Beam current/beam	mA	7.50E-1
Bunch population		2.00E10
RF voltage	GV	1.00
RF frequency	GHz	1.30
Synchrotron oscillation		0.10E-1
Energy acceptance RF	%	2.34
SR loss/turn	GeV	0.46
energy spread	%	7.80E-2
Horizontal emittance	m*rad	1.61E-9

With error, cavity on, 0% and 1% energy spread, the dynamic aperture results are shown in Fig. 8 and Fig. 9. In x direction, dynamic aperture is 0.06 m and 0.04 m, and in the y direction, dynamic aperture is 0.023m and 0.016 m for on-momentum and 1% off-momentum particles. Fig. 8 and Fig. 9 also plot the tune shift depending with amplitude on the tune map, which also constraint in a reasonable range without touch dangous resonance line. The parameters of CEPCB for 6GeV, 120GeV, 80GeV and 45.5GeV are listed in Table 2, Table 3, Table 4 and Table 5.

The normal form parameters for X direction and Y direction are listed in Table 6 and Table 7. Tune is a function of action J_x , J_y and energy spread δ , then Taylor expand it. The first column is the taylor coefficients of tune, the other columns are the exponent of J_x , J_y and δ . The normal form parameters are caculated by LEGO[11].

$$\begin{aligned}
 J_x &= \frac{x^2 + px^2}{2} \\
 J_y &= \frac{y^2 + py^2}{2} \\
 \delta &= \frac{p_0 + \Delta p}{p_0}
 \end{aligned}$$

Table 5: CEPCB Parameters@45.5GeV

120GeV	Unit	Value
offset in bend	cm	0
Momentum compaction		2.38E-5
Strength of dipole	Gs	195.91
NB/beam		50
Beam current/beam	mA	7.50E-1
Bunch population		2.00E10
RF voltage	GV	0.40
RF frequency	GHz	1.30
Synchrotron oscillation		8.80E-2
Energy acceptance RF	%	2.87
SR loss/turn	GeV	4.85E-2
energy spread	%	4.40E-2
Horizontal emittance	m*rad	5.21E-10

Table 6: CEPCB Normal form Parameters for X Direction

Coefficients	J_x	J_x	δ
6.099×10^{-1}	0	0	0
-2.807×10^3	1	0	0
-1.675×10^3	0	1	0
1.452	0	0	1
8.265×10^5	2	0	0
-7.245×10^5	1	1	0
-9.854×10^6	1	0	1
-6.698×10^5	0	2	0
-8.014×10^6	0	1	1
-1.580×10^2	0	0	2
-6.942×10^8	2	0	1
-2.486×10^{10}	1	1	1
5.529×10^7	1	0	2
1.149×10^{10}	0	2	1
-2.303×10^7	0	1	2
1.974×10^3	0	0	3
-6.144×10^9	1	0	3
-1.818×10^9	0	1	3
2.641×10^5	0	0	4
1.793×10^7	0	0	5

NORMAL BEND SCHEME

Earth Magnet Field Correction

In the normal bend scheme, sextupole scheme is the same with the wiggler bend scheme, and linear optics is also similar. The bend strength is very low, which is about 30Gs, because we ramp the beam from 6GeV to 120GeV. As we all know, the earth magnet field is about 0.5Gs. It is just like a big error added on the dipole, about 2 percent. So the earth magnet field must be shielded or corrected.

With the earth magnet field, the booster is a broken ring. The broken ring means the particles in the ring can not find a stable orbit, so the first turn orbit correction is needed. In the first turn orbit correction, we treat the broken ring as linac,

Table 7: CEPCB Normal form Parameters for Y Direction

Coefficients	J_x	J_x	δ
8.800×10^{-1}	0	0	0
-1.675×10^3	1	0	0
-1.114×10^4	0	1	0
-3.391×10^{-3}	0	0	1
-3.622×10^5	2	0	0
-1.340×10^6	1	1	0
-8.014×10^6	1	0	1
-2.520×10^6	0	2	0
-7.542×10^6	0	1	1
1.723×10^2	0	0	2
-1.243×10^{10}	2	0	1
2.297×10^{10}	1	1	1
-2.303×10^7	1	0	2
-4.064×10^9	0	2	1
2.119×10^7	0	1	2
2.195×10^3	0	0	3
-1.818×10^9	1	0	3
-2.907×10^9	0	1	3
2.725×10^5	0	0	4
2.381×10^7	0	0	5

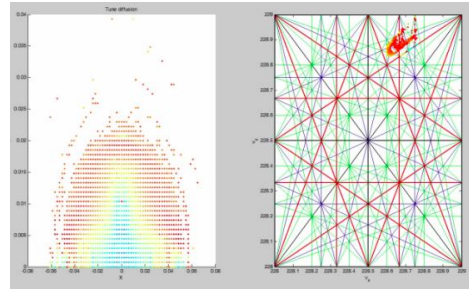


Figure 8: Wiggler bend scheme: Dynamic aperture and tune shift for the on-momentum particles.

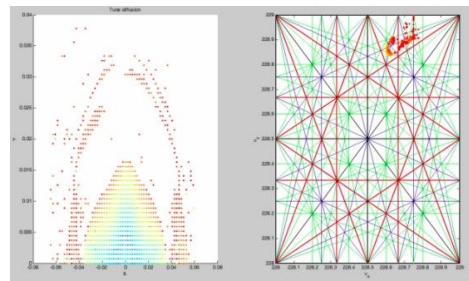


Figure 9: Wiggler bend scheme: Dynamic aperture and tune shift for the 1% off-momentum particles.

propagate the orbit and correct it part by part. As Fig. 10, Fig. 11, Fig. 12, Fig. 13 and Fig. 14 show, we divide the whole booster ring to 8 pieces, correct the orbit part by part. Fig. 14 shows the first turn orbit after whole ring correction.

After the first turn orbit correction, the closed orbit can be found, as Fig. 15 shows, and then we can implement the closed orbit correction. After all the corrections, the orbit

distortion can be limited to 10 micron level. Fig. 16 shows the corrected orbit.

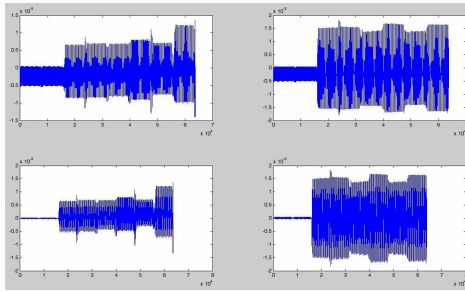


Figure 10: First turn orbit correction for the first part.

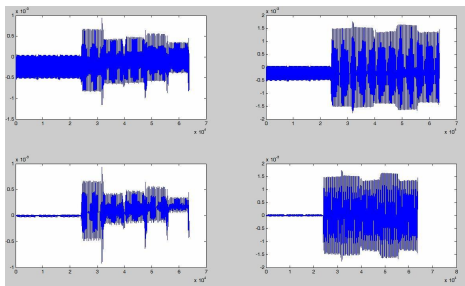


Figure 11: First turn orbit correction for the third part.

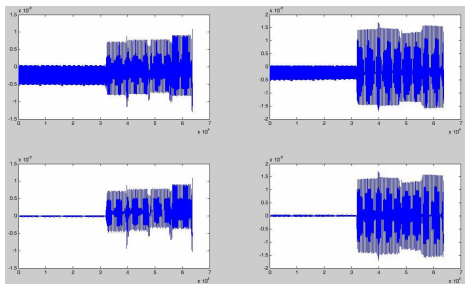


Figure 12: First turn orbit correction for the fourth part.

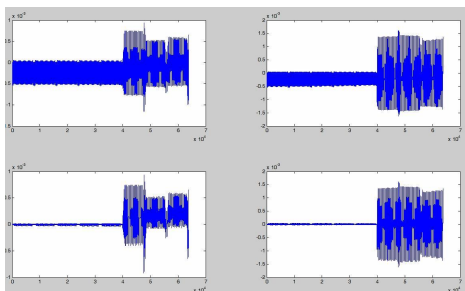


Figure 13: First turn orbit correction for the fifth part.

Dynamic Aperture Results and CEPCB Parameters

With error and orbit correction, Fig. 17 and Fig. 18 show the dynamic aperture result for on-momentum and off-momentum particles. Table 8 shows the wiggler bend scheme parameters at 6GeV.

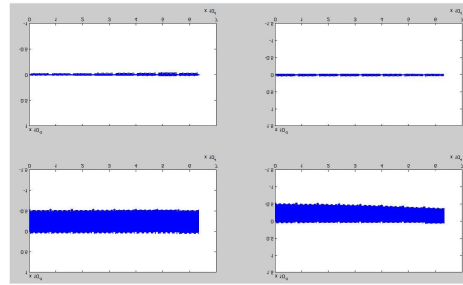


Figure 14: First turn orbit correction for the whole ring.

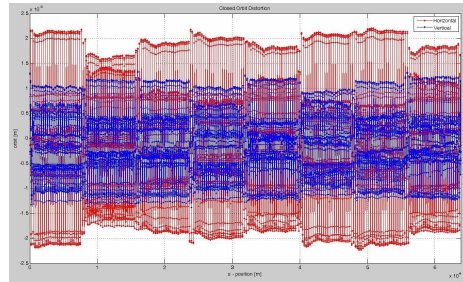


Figure 15: Closed orbit can be found after first turn orbit correction.

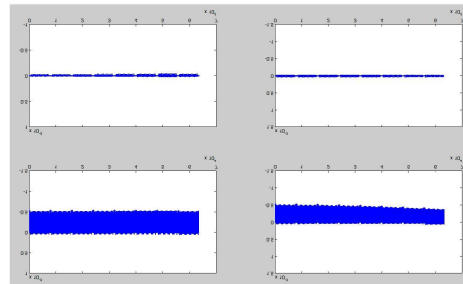


Figure 16: Closed orbit after all the corrections.

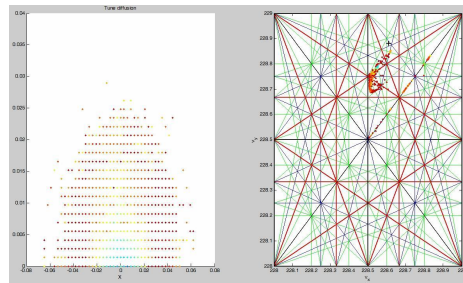


Figure 17: Normal bend scheme: Dynamic aperture and tune shift for the on-momentum particles.

SUMMARY

In this paper, two possible implementations for CEPCB are proposed. The low field problem are solved by the wiggler bend scheme and the method of correcting the earth magnet field is shown in normal bend scheme.

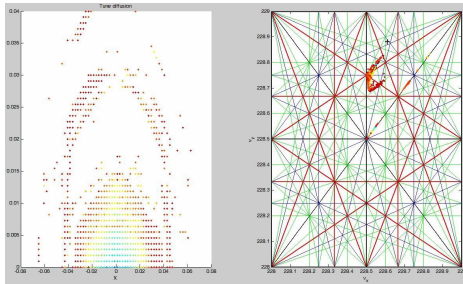


Figure 18: Normal bend scheme: Dynamic aperture and tune shift for the 1% off-momentum particles.

Table 8: CEPCB Parameters@6GeV

6GeV	Unit	Value
offset in bend	cm	0
Momentum compaction		1.91E-5
Strength of dipole	Gs	25.80
NB/beam		50
Beam current/beam	mA	7.50E-1
Bunch population		2.00E10
RF voltage	GV	2.10E-1
RF frequency	GHz	1.30
Synchrotron oscillation		2.10E-1
Energy acceptance RF	%	4.99
SR loss/turn	GeV	1.47E-5
energy spread	%	7.47E-5
Horizontal emittance	m*rad	9.10E-12

Normal scheme:

With error, orbit correction, cavities on and tune 0.61/0.88, x direction dynamic aperture is 8.6 sigma, y direction dynamic aperture is 10.1 sigma @dp=0% for inject beam. With error, orbit correction, cavities on and tune 0.61/0.88, x direction dynamic aperture is 6.7 sigma, y direction dynamic aperture is 6.5 sigma @ dp=1% for inject beam.

Wiggler scheme:

With error, cavities on and tune 0.61/0.88, x direction dynamic aperture is 9.2 sigma, y direction dynamic aperture is 9.6 sigma @dp=0% for inject beam. With error, cavities

on and tune 0.61/0.88, x direction dynamic aperture is 6.6 sigma, y direction dynamic aperture is 6.4 sigma @dp=1% for inject beam.

Contrast with the design goal we have proposed in previous section, both of the two design are reasonable and meet requirements.

ACKNOWLEDGEMENT

The author would like to thank Gang Xu in IHEP and colleagues in BINP for their effort in the CEPC booster design.

REFERENCES

- [1] Gao Jie, "Review of some important beam physics issues in electron-positron collider designs." *Modern Physics Letters A*, vol.30, no.11, pp.1530006, 2015.
- [2] Wang Dou *et al.*, "Optimization parameter design of a circular e+ e- Higgs factory." *Chinese Physics C*, vol.37, no.9, pp.097003, 2013.
- [3] Su Feng *et al.*, "Method study of parameter choice for a circular proton-proton collider." *Chinese physics C*, vol.40, no.1, pp.17001-017001, 2015.
- [4] Kang Wen, "Some Design Considerations and R&D of CEPCB Dipole Magnet", IHEP, Beijing, Apr. 2016.
- [5] The CEPC-SPPC Study Group, "CEPC-SPPC Preliminary conceptual Design Report", IHEP, Beijing, IHEP-AC-2015-01, March. 2015.
- [6] Michael Koratzinos, private communication, Dec. 2015.
- [7] Yunhai Cai, private communication, Feb. 2016.
- [8] Gang Xu, private communication, Feb. 2016.
- [9] Yunhai Cai, "Symplectic maps and chromatic optics in particle accelerators", *Nucl. Instr. Meth.*, vol. 797, pp. 172-181, 2015.
- [10] Sha Bai, "CEPC magnet error study summary", IHEP, Beijing, Dec. 2015.
- [11] Cai, Y., "LEGO - A Class Library for Accelerator Design and Simulation." Icap98 Monterey (1998).

TOP-UP INJECTION SCHEMES FOR HEPS*

Z. Duan[†], J. Chen, Y. Jiao, Y. Peng, Q. Wang, G. Xu, and P. Zhang
 Key Laboratory of Particle Acceleration Physics and Technology,
 Institute of High Energy Physics, Chinese Academy of Sciences,
 Beijing, China

Abstract

Top-up injection has become standard mode of operation for most third generation light sources, and has also been successfully applied in electron-positron circular colliders like KEKB and PEP-II. For next generation ultra-low emittance storage rings approaching the diffraction limit of X-rays, take the High Energy Photon Source (HEPS) for example, top-up injection is a basic requirement but non-trivial to implement. The very small dynamic aperture is insufficient for traditional off-axis injection scheme, instead, a novel on-axis injection scheme was recently proposed for HEPS, based on RF gymnastics of a double-frequency RF system. This paper will describe the physical mechanism of this scheme, related RF issues and the implications for top-up injection.

INTRODUCTION

First implemented in APS [1] and SLS [2] for user experiments, top-up injection has become standard mode of operation in most third generation light sources. Frequent beam injection ensures the relative beam current fluctuation within a few 10^{-3} , which significantly improves the photon beam stability and efficiency in user experiments. This mode of operation was also realized in electron-positron circular colliders KEKB [3] and PEP-II [4], which greatly enhanced the average luminosity and the almost constant beam current made luminosity tuning much easier.

With these success in existing machines, top-up injection is considered to be a basic requirement in the design of next generation electron (positron) storage rings, but this also brings new challenges. In particular, in the next generation synchrotron light sources with ultra-low emittances approaching the diffraction limit of X-rays, the implementation of top-up injection is somewhat non-trivial.

These diffraction-limit storage rings normally adopt multi-bend achromat (MBA) cells [5] in the lattice design, and utilize high-gradient quadrupoles to achieve a ultra-low beam natural emittance of tens of picometers. Therefore, very strong sextupoles are required to compensate for the large natural chromaticities and thus lead to great challenges in optimization of the dynamic aperture (DA) and the momentum aperture (MA). Take the High Energy Photon Source (HEPS), its major parameters are listed in Table 1) for example, a nominal lattice design has achieved a natural emittance of 59.4 pm, while an effective DA of 2.5 mm (horizontal) and 3.5 mm (vertical) and an effective MA of 3.0% are obtained with great effort¹ [6]. Such a small DA is insufficient for tra-

ditional off-axis injection schemes, which typically requires a DA on the order of 10 mm. Therefore, we have to seek alternative on-axis injection schemes.

Inspired by various on-axis injection schemes [7–9] suitable for ultra-low emittance storage rings, we proposed a new injection scheme based on RF gymnastics of an active double-frequency RF system [10] and applied it in HEPS. In this paper, the physical mechanism of this injection scheme will be overviewed, followed by the discussion on the control of RF cavities, finally implications for top-up injection will also be presented.

Table 1: HEPS Parameters [6]

Parameter	Value
circumference C (m)	1295.616
beam energy E_b (GeV)	6
beam current I_0 (mA)	200
natural emittance ϵ_0 (pm)	59.4
betatron tunes ν_x/ν_y	116.155/41.172
momentum compaction α_c	3.74×10^{-5}
rms energy spread σ_ϵ	7.97×10^{-4}
harmonic number h_f/h_h	720/2160
SR energy loss U_0 (MeV/turn) ²	1.995
damping times(ms) $\tau_x/\tau_y/\tau_s$	18.97/25.99/15.95

PHYSICAL MECHANISM OF THE INJECTION SCHEME

Without synchrotron radiation, a particle's longitudinal motion with a double-RF system is described by the Hamiltonian

$$H(\phi, \delta; t) = \frac{h_f \omega_0 \eta}{2} \delta^2 + \frac{e \omega_0}{2\pi E_b \beta^2} \left[\sum_{i=1}^{N_f} V_f^i \cos(\phi + \phi_f^i) + \frac{h_f}{h_h} \sum_{j=1}^{N_h} V_h^j \cos\left(\frac{h_h}{h_f} * \phi + \phi_h^j\right) + \phi \frac{U_0}{e} \right], \quad (1)$$

where ϕ and δ are a pair of canonical variables with respect to the time variable t , $\omega_0 = 2\pi c/C$ is the angular revolution frequency of the synchronous particle, e is the electron charge, γ is the relativistic factor, $\eta = \alpha_c - 1/\gamma^2$,

¹ The "effective" DA (or MA) means the boundary within which, not only particles survive in the ideal lattice tracking, but also the amplitude-dependent tunes are bounded by the nearest integer and half-integer resonances of the nominal tunes.

² Insertion devices are not included.

* Work supported by Natural Science Foundation of China (No.11605212).
[†] duanz@ihep.ac.cn

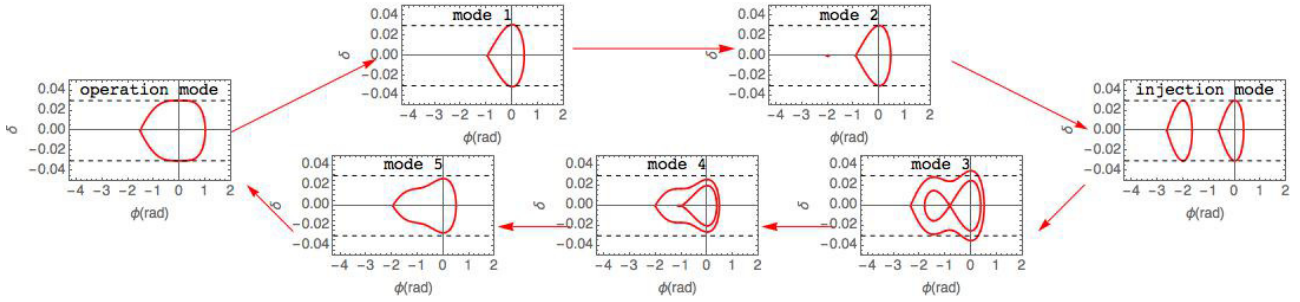


Figure 1: RF gymnastics in a complete injection cycle.

$\beta = \sqrt{1 - \gamma^2}$. Assume there are N_f fundamental cavities of harmonic number h_f and N_h harmonic cavities of harmonic number h_h , V_f^i and V_h^j are the voltages of i -th fundamental cavity and j -th harmonic cavity, respectively; ϕ_f^i and ϕ_h^j are the phase angles of the synchronous particle relative to i -th fundamental cavity and j -th harmonic cavity, respectively. In fact, from the perspective of low-level RF control, both the voltage and phase of an RF cavity can be varied very fast, with a response time of tens of μs . Therefore, to simplify the treatment, we assume cavities of the same frequency share the same setting, and both the voltages and phases are manipulated in the injection, the Hamiltonian can be simplified as

$$H(\phi, \delta; t) = \frac{h_f \omega_0 \eta}{2} \delta^2 + \frac{e \omega_0}{2\pi E_b \beta^2} \left[N_f V_f \cos(\phi + \phi_f) + \frac{h_f}{h_h} N_h V_h \cos\left(\frac{h_h}{h_f} * \phi + \phi_h\right) + \phi \frac{U_0}{e} \right], \quad (2)$$

where $(V_f, V_h, \phi_f, \phi_h)$ are four free knobs in the design of an injection cycle.

The evolution of RF buckets in a complete injection cycle is illustrated in Fig. 1. The parameters of a nominal design of HEPS [6] are used in this calculation, the double-RF system consists of four 166.6 MHz fundamental RF cavities and two 499.8 MHz third harmonic cavities. The ‘‘operation mode’’ corresponds to the settings during the routine operation, it is favored to set the parameters of active RF systems such that the electron bunches are optimally lengthened. As a result, the beam lifetime is increased, the IBS effect and some collective instabilities are also alleviated. On the other hand, we need to generate a second RF bucket near each existing bucket in the operation mode for on-axis accumulation. This is called the ‘‘injection mode’’. Also shown in the figure are 5 intermediate modes, and a complete injection cycle is realized by ramping the four RF knobs between the settings of each two adjacent modes, the evolution of RF parameters is shown in Fig. 2. Note that the bunch length varies a lot, from 32 mm in the operation mode to 2.8 mm in the injection mode, and about 10% increase of beam size is expected due to the intra-beam scattering, which will surely disturb the user experiments. The concrete impact to user experiments is

being evaluated and will be presented elsewhere. Moreover, there might be some beam instability issues at the injection

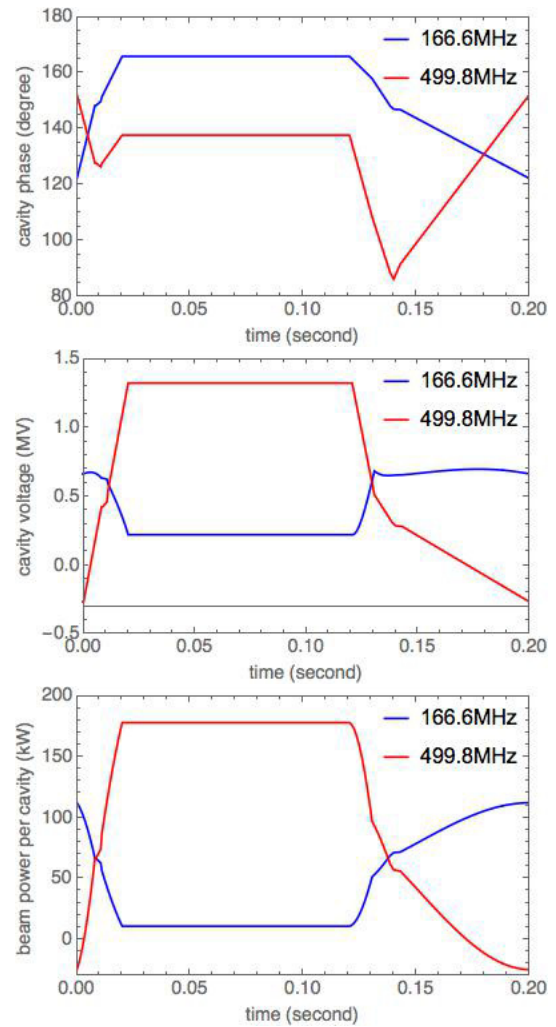


Figure 2: The upper and middle and lower figures show the evolution of RF phases, voltages and beam power per cavity in a complete injection cycle, respectively. Note that beam loading effects and other sources of power consumption are not included in the beam power calculation.

condition due to the very short bunch length, which is also under investigation.

Such an on-axis injection scheme requires the full pulse width of the injection kicker system to be smaller than bunch spacing of the storage ring (6 ns for HEPS), and the kicker pulse fall time to be smaller than the time lag between the injection and circulating bunches in the injection mode (about 2.5 ns for HEPS). These stringent requirements can be realized by stripline kicker systems [11] driven by high voltage fast pulsers [12]. Unfortunately, the readiness of superconducting RF cavities of higher frequencies meets with the technology difficulty in obtaining even faster injection kicker. Therefore, the choice of fundamental RF frequency is a compromise with the choice of injection kicker parameters. Currently, 166.6 MHz superconducting RF cavity and ultra-fast injection kicker are under extensive R&D at IHEP.

RF ISSUES

As illustrated in the previous section, we assumed a complete injection cycle would take 200 ms, and each ramp step would take about 500 μ s. Then the question arises that if the low level RF system can cope with such a fast ramping scenario. Table 2 shows the major parameters of the RF cavities. For each cavity, its coupling parameter and tuning angle are chosen so that there is no reflected power when its beam power is at the maximum value.

Table 2: RF Cavity Parameters

Parameter	fundamental RF cavity	harmonic RF cavity
frequency (MHz)	166.6	499.8
number of cavities	4	2
quality factor Q_0	5×10^8	1×10^9
geometric shunt impedance R/Q (Ω)	135.8	93.5
maximum beam power per cavity (kW)	112.2	178.0
cavity voltage at maximum beam power per cavity (MV)	0.66	1.32
coupling parameter β	17293.4	9490.9
loaded quality factor Q_{load}	28912.8	105364
cavity filling time (μ s)	55	67
optimal tuning angle ψ (degree)	-32.3	-47.8

The low level RF system controls the frequency, amplitude and phase of cavity fields. The latency in control of amplitude and phase can be controlled within tens of microseconds, similar to the cavity filling times. However, the latency of frequency control depends on the type of tuner. Mechanical tuners with a stepper motor normally provide a tuning range of hundreds of kHz at the expense of a slow response on the level of seconds; fast acting piezoelectric tuners can act very fast (in milliseconds) but have limited dy-

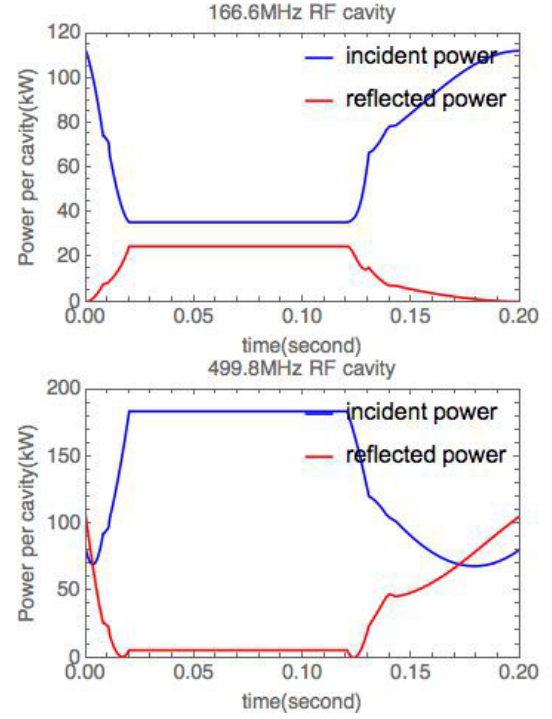


Figure 3: The two plots show incident and reflected RF power of each fundamental and harmonic cavity in a complete injection cycle, respectively.

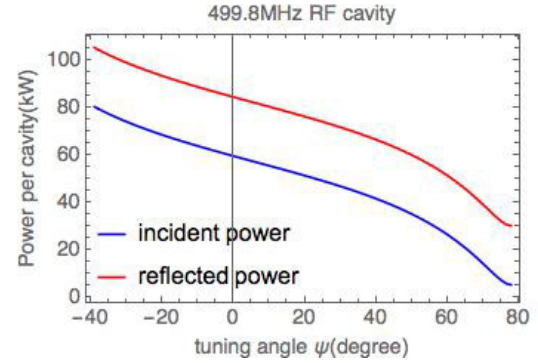


Figure 4: The incident and reflected RF power of a 499.8 MHz cavity versus different tuning angles.

namic range, for example, only about 6 kHz for the 500 MHz superconducting RF cavities in BEPCII. In a complete injection cycle, keeping an optimal tuning angle requires a frequency control range beyond the reach of piezoelectric tuner. As a result, we assume the frequencies of RF cavities are kept fixed according to the setting in Table 2. Then, the incident and reflected RF power for each cavity can be calculated via

$$P_{\pm} = \frac{\beta V_c^2}{8R_s} \left[\left(1 \pm \frac{1}{\beta} \pm \frac{2R_s I_0}{\beta V_c} \cos \hat{\phi} \right)^2 + \left(\tan \psi + \frac{2R_s I_0}{\beta V_c} \sin \hat{\phi} \right)^2 \right], \quad (3)$$

where P_{\pm} denotes the incident and reflected power, respectively, phase $\hat{\phi}$ follows the phasor convention and is related to RF phase in ring dynamics convention via $\cos \hat{\phi} = \sin \phi$. The calculated incident and reflected power of each cavity

are shown in Fig. 3. The incident and reflected powers of the harmonic cavities are quite large at the operation condition, which can be alleviated by ramping the tuning angles to the optimal value for the operation mode using mechanical tuners, as illustrated in Fig. 4, while keeping the voltage and phase fixed. If mechanical tuners can reach the required 18 kHz frequency shift within a few seconds, then ramping the tuning angle before and after each injection cycle will help reduce the power consumption during operation significantly.

TOP-UP INJECTION FOR HEPS

Different from off-axis injection schemes, the time structure of the high voltage pulser driving the injection kicker has a large impact on the design of the injector chain and the operation mode of top-up injection. A qualified pulser model from FID GmbH [13] runs in a bursting mode. As

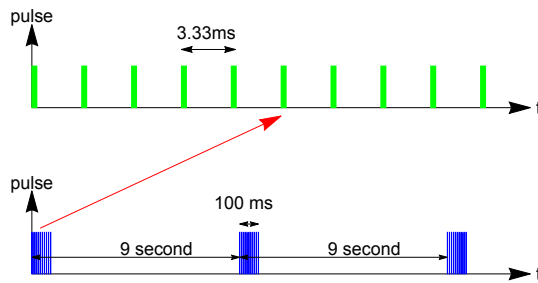


Figure 5: Time structure of the injection kicker pulse.

shown in Fig. 5, a burst pulse has a duration of 100 ms and repeats every 9 s, the spacing between adjacent micro-pulse is 3.33 ms. Therefore, at each injection, a bunch train of no more than 30 bunches following the same time structure can be extracted from the booster and injected into the main ring. To simplify the design, the circumference of the booster is selected to be 1/3 of that of the main ring, and the RF frequency of the booster is 3 times that of the main ring. Since 3.33 ms is much larger than the revolution period, the timing system is capable of selecting a specified bunch to extract from the booster and inject into the corresponding bucket of the main ring. The booster power supply is capable of

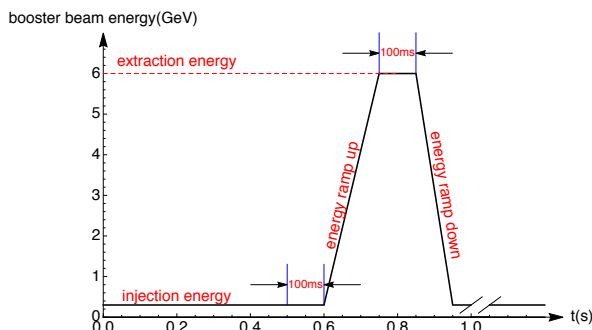


Figure 6: Schematic plot of the booster energy ramp curve.

operating at a repetition rate of 2 Hz. To accord with the time structure of injection kicker and also accommodate the

two different filling patterns, the linac is designed to work at the single bunch mode with a repetition rate of 300 Hz, and the booster ramp curve has a flat bottom of 100 ms to store the injected bunches from the linac, and also a flat top of 100 ms to allow extraction of the bunches, a schematic plot of the booster ramp curve is shown in Fig. 6. Moreover, the 30 bunches can be uniformly distributed in the booster with a spacing of 48 ns, as shown in Fig. 7, and the same kicker systems can be applied in the injection and extraction of the booster, which has the same time structure as that of the main ring injection kicker, but with a micro-pulse full width smaller than 96 ns.

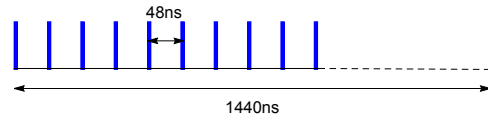


Figure 7: The bunch time structure in the booster.

Top-up injection at HEPS requires a beam current stability of 0.2%. There are two filling patterns under consideration. The first is to uniformly fill 648 bunches, i.e., into 90% of 720 RF buckets, simulations showed the beam lifetime is about 30 hours, and the refill time is about 3.5 min. Since each burst pulse of the injection kicker can inject at most 30 bunches into the main ring, at every refill 120 bunches can be injected with four burst pulses within about 27 s, so that bunch charge uniformity can be ensured. The second is to fill 60 uniform bunches with a bunch charge of about 14 nC while keeping the same average beam current, the beam lifetime can be as short as about 3 hours, and the required refill time is about 20 s. The injection system is capable to refill all the 60 bunches with two burst pulses within about 9 s, which meets the requirements.

OUTLOOK

We reported the recent progress on the study of a novel on-axis injection scheme based on RF gymnastics of a double-frequency RF system for HEPS, and analyzed the RF issues as well as the design of top-up injection for HEPS. More detailed study on injection tolerances as well as possible collective effects are still under way and will be reported in a forthcoming paper.

We would like to thank Dr. Bocheng Jiang from SSRF and experts in HEPS linac group for useful discussions.

REFERENCES

- [1] L. Emery, in *Proc. PAC'01*, pp. 2599–2601.
- [2] A. Lüdeke and M. Muñoz, in *Proc. EPAC'02*, pp. 721–723.
- [3] T. Abe, *et al.*, “Commissioning of KEKB”, *Prog. Theor. Exp. Phys.*, p. 03A010, 2013.
- [4] J. L. Turner, *et al.*, in *Proc. of EPAC'04*, pp. 881–883.
- [5] D. Einfeld, M. Plesko, and J. Schaper, “First multi-bend achromat lattice consideration”, *J. Synchrotron Radiat.*, vol. 21, pp. 856–861, Sep. 2014.
- [6] G. Xu, *et al.*, in *Proc. IPAC'16*, pp. 2886–2888.

- [7] L. Emery and M. Borland, in *Proc. PAC'03*, pp. 256–258.
- [8] M. Aiba, *et al.*, “Longitudinal injection scheme using short pulse kicker for small aperture electron storage rings”, *Phys. Rev. ST Accel. Beams*, vol. 18, p. 020701, Feb. 2015.
- [9] B. C. Jiang, *et al.*, “Using a double-frequency RF system to facilitate on-axis beam accumulation in a storage ring”, *Nucl. Instrum. Meth. A*, vol. 814, pp. 1–5, Apr. 2016.
- [10] G. Xu, *et al.*, in *Proc. IPAC'2016*, pp. 2032–2035.
- [11] B. I. Grishanov, *et al.*, “Very fast kicker with high repetition rate for accelerator applications”, *Nucl. Instrum. Meth. A*, vol. 396, pp. 28–34, Sep. 1997.
- [12] V. M. Efanov, *et al.*, in *Proc. IPPC'97*, pp. 988–991.
- [13] FID GmbH, <http://www.fidtechnology.com>

TOWARDS A PRELIMINARY FCC-ee INJECTOR DESIGN

S. Ogur *, Bogazici University, Istanbul, Turkey & CERN, Geneva, Switzerland

Kazuro Furukawa, Naoko Iida, Fusashi Miyahara, Katsunobu Oide, KEK, Tsukuba, Ibaraki, Japan

Yannis Papaphilippou, Frank Zimmermann, CERN, Geneva, Switzerland

Alexey Barnyakov, Alexey Levichev, Danila Nikiforvo, BINP, Novosibirsk

Abstract

The Future Circular Collider-ee aims to get high luminosity which mainly relies upon high charge and low geometric emittance in the collider. The FCC-ee is a future project of CERN to operate as Z , W , H and tt factories with varying energies between 45.6 to 175 GeV. Among those, the total charge requirement is peaked for Z -operation (i.e. 91500 bunches of electron and positron with 3.3×10^{10} particles per bunch) meanwhile this mode targets the smallest geometric emittance in the Collider. To reach the goal, the normal conducting S-band Linac has been designed to accelerate 4×10^{10} particles in a bunch to 6 GeV and send two bunches per RF pulse within a repetition of 100 Hz. The FCC-ee positrons will also be created inside the linac at 4.46 GeV and accelerated to 1.54 GeV. These positrons are damped at the designed Damping Ring at that energy, and then transferred back to the Linac to meet the same characteristics of electrons. Therefore, in this paper, we'd like to discuss the transmission and robustness of the Linac and the dynamic aperture of the Damping Ring which has to be large enough to accept the incoming beam and cover the probable shrink due to the misalignments.

INTRODUCTION

CERN's leading role over the world in the fields of the particle and accelerator physics has brought about thinking of ambitious post-LHC (Large Hadron Collider) projects. As a 100 km-machine, FCC-ee has been proposed to supply ever increasing demand of high luminosity machines for new physics search and the precision study of the particle physics. Nowadays, FCC-ee is being designed to operate as Z , W , H and tt factories. However, in the design of pre-injectors, the total charge and the equilibrium emittance are determinant. Therefore, we will be following Z -operation which has the highest total charge and lowest final emittance at 45.6 GeV to study pre-injectors, some parameters of Z -operation is tabulated in Table 1.

Table 1: FCC-ee Baseline Parameters for Z -operation Mode

Parameter	Value
Final Energy [GeV]	45.6
Number of Bunches per Beam	91500
Bunch Population	3.3×10^{10}
Horizontal Emittance	0.09 nm
Vertical Emittance	1 pm

* salim.ogur@cern.ch

The detailed version of the table and the preliminary design parameters of the pre-injectors are already discussed in details in our earlier proceedings [1] and [2], respectively. In this paper, however, we'd like to discuss the followings: i) improvements on the Linac transmission, and ii) enlargement of dynamic aperture of the Damping Ring.

IMPROVEMENTS ON LINAC

The designed Linac for FCC-ee is an S-band normal conducting accelerator operating at frequency 2.856 GHz. The optics before the correctors were tightly allocated as presented in Fig. 1.

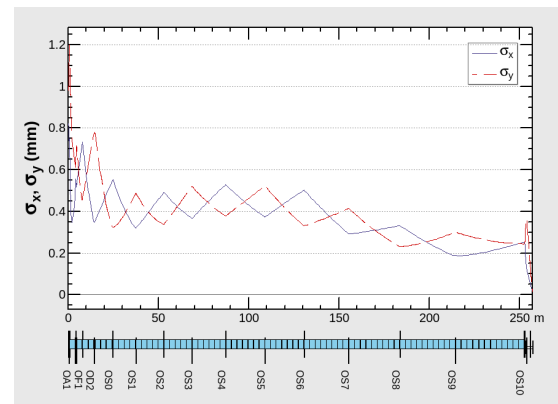


Figure 1: Linac optics before the misalignments.

After the idealistic design of the Linac, the study of errors is crucial in a sense to determine probable and inevitable misalignments through the commissioning of the accelerator. Therefore, we have given some misalignment to the elements both horizontally and vertically as tabulated in Table 2. The study has been done as a Monte-Carlo simulation where the tabulated errors represents one-sigma, and no truncation has been made.

Table 2: Misalignment Study

Element	Simulated Error
Injection Error (h/v)	0.1 mm
Injection Momentum Error (h/v)	0.1 mrad
Quadrupole Misalignment (h/v)	0.1 mm
Cavity Misalignment (h/v)	0.1 mm

After introducing errors, the Linac transmission has dropped dramatically down to 33%. The cavities of the Linac are with length of $28 + 1/3$ wavelengths which correspond to 3 meters approximately. The wakefields of the cavities are similar to ATF-Linac [3] and the cavity geometry

is tapered such a way that 11 mm as an entrance aperture and 9 mm at the exit to keep the field uniformity. For the simplicity, yet the simulations are made for a straight aperture of 10 mm for 3 meter long full length cavity.

The orbit correction is fully automatized by a code written. Firstly, we introduce a steerer magnet before each cavity where the gradients are determined by aligning the orbit of the tracked particles back to the cavity center. The performance of the orbit correction can be seen from the orbit oscillations throughout the accelerator as presented in Fig. 2.

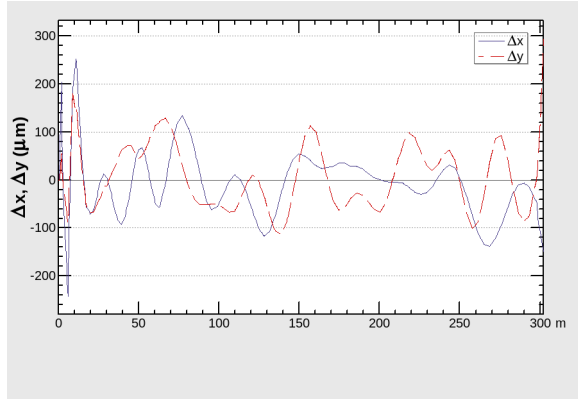


Figure 2: Orbit oscillations.

Actually, this tracking corresponds physically to deploy a Beam Position Monitor before the cavity entrance and the adjusting the steerer magnet accordingly. This adjustment has led the transmission to rise up to 70%, yet the resulting transmission is not sufficient for our requirements. Therefore, we change the optics for the low energy part of the 6 GeV Linac as shown in Fig. 3.

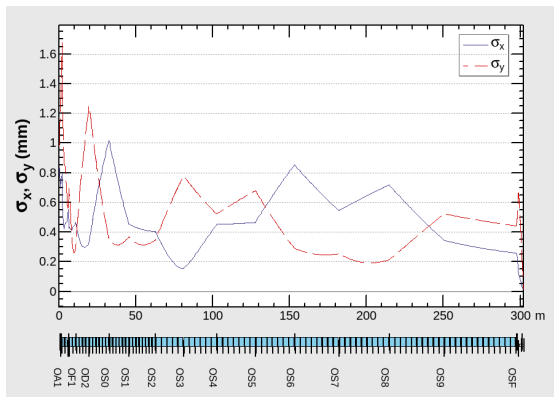


Figure 3: Linac optics after orbit correction elements.

Using the fact that the wakefields are loosen as the cavity aperture widens, we interchange the first 14 full length cavities to 28 half length cavities. The half length cavities are 1.5 m (i.e. $14 + 1/3$ wavelengths) such that their transverse aperture is the twice of the full length (i.e. 20 mm), on the other side, the cavity voltage is still kept below 27 MV/m. Therefore the impact of the wakefields is decreased

significantly. Also, we have become able to steer the beam more frequently due to higher number of dipoles and shorter length to intervene the beam. As a result, the transmission becomes slightly more than 88%. Nevertheless, the wake-fields still affect the beam to shape like *banana* as shown in Fig. 4 which apparently dilates the final emittance.

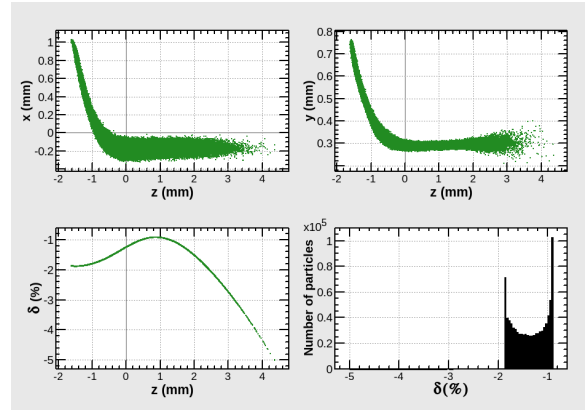


Figure 4: Linac beam profiles after orbit correction.

The overall performance of the orbit correction study can be summarized as in Table 3.

Table 3: Performance of the Misalignment Study

At the end of Linac	Results
Transmission Required	83%
Transmission Provided	88%
Emittance (h/v) Required	0.7/1.0 nm
Emittance (h/v) Provided	60/51 nm

DAMPING RING WITH LARGE DYNAMIC APERTURE

FCC-ee Linac is utilized both for electrons and positrons. The creation of the positrons will be by exposing the electrons at energy of 4.46 GeV to a hybrid (crystal and amorphous) target. Hence, the positrons can be accelerated at 1.54 GeV at the remaining part of the Linac. Yet the positrons do not match the specifications of the electrons at the same energy, this is why they have to be damped. An overview of the damping necessities has been presented in Table 4, in which the positron data of KEK [4] adapted to our parameter selection, and the Booster entrance and exit emittance values are determined by the study of FCC-ee Optics Design team [1].

Table 4: Positron Emittance Evolution

e+ Accelerators	Energy	ϵ_x	ϵ_y
DR Entrance	1.54 GeV	0.76 μm	0.71 μm
DR exit	1.54 GeV	2.66 nm	3.9 nm
Booster exit	45.6 GeV	0.09 nm	0.13 nm

Therefore, the DR is designed to damp μm emittance down to nm level in less than 50 ms, as it is discussed in [2].

The DR design has been altered in a way to cover FCC-ee targets as demonstrated in Fig. 5. Some parameters of the DR has been presented in Table 5.

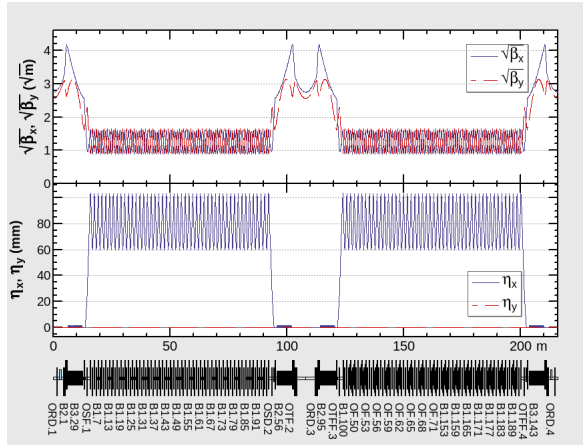


Figure 5: Damping Ring optics.

Table 5: Damping Ring Design Parameters

Parameter	Value
Energy [GeV]	1.54
Number of Trains	3
Bunches/Train	2
Circumference [m]	216
Number of cells	94
Bending Radius [m]	7.7
Bunch Spacing [ns]	120
τ_x [millisecond]	11.0
τ_y [millisecond]	11.4
Horizontal Natural emittance [nm]	1.3
Vertical Natural emittance	-

However, the performance of the Damping Ring is limited by the dynamic aperture provided. The acceptance of a Damping Ring can be calculated as the natural emittance times the square of the dynamic aperture (DA) in that direction. In order to achieve a large DA, we choose lower and closer tune per cells in horizontal and vertical directions, such that we can make the FODO lattice shorter. The DA, presented in Fig. 6, horizontally demonstrates the transverse DA (up to 300 sigmas), whereas the vertical axis shows the longitudinal DA; where each random character should be considered as a flag which indicates that the particle(s) is/are alive for 1000 turns. All in all, we become able to provide 234 sigmas as DA to the on-momentum positrons with respect to the equilibrium emittance of DR.

The resulting performance of DR brings about reaching targets tabulated in Table 4 in 35 milliseconds for horizontal emittance and 29 ms for vertical emittance which both are well-below than the allocated time (i.e. 50 ms) for positrons to spend inside the DR. The acceptance provided for the horizontal direction stated in Table 6.

ISBN 978-3-95450-187-8

92

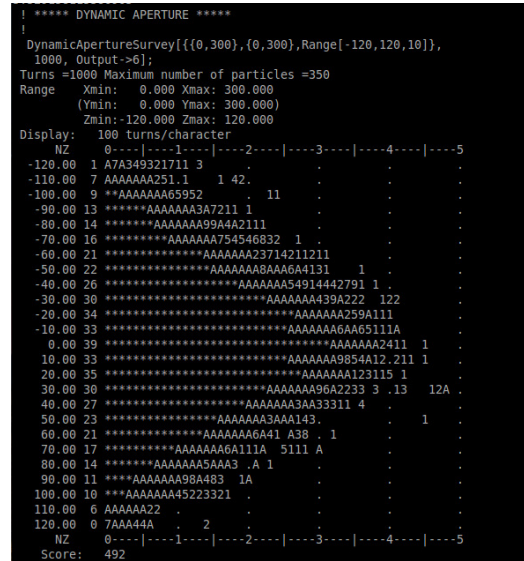


Figure 6: Transverse and longitudinal Dynamic Aperture of the Damping Ring for 1000 turns.

Table 6: Performance of the Damping Ring Design in Transverse Direction

Parameter	Value
Natural Emittance	1.3 nm
Positron Emittance (1-sigma)	0.76 μm
Acceptance needed (3-sigma)	6.84 μm
DA needed (3-sigma)	73 σ
DA provided	234 σ
Acceptance Provided	69.5 μm

Therefore, we can conclude that the DR designed can provide many times larger acceptance than it is required. Similarly, the longitudinal DA enables a wide acceptance, too, as presented in Table 7.

Table 7: Longitudinal Performance of the Damping Ring

Parameter	Value
Natural Emittance	3.6 μm
Positron Emittance (1-sigma)	1 mm
Acceptance needed (3-sigma)	9 mm
DA needed (3-sigma)	50 σ
DA provided	110 σ
Acceptance Provided	43.6 mm

The bucket height ratio is 8.3% and the energy spread is 6.7×10^{-4} for 2 MV cavity voltage which still comprises the longitudinal DA (i.e. 110 σ). Furthermore, the beta function of DR is calculated as the bunch length square divided by the longitudinal emittance as follows:

$$\beta_z = \frac{\sigma_z^2}{\epsilon_z} = \frac{(5.30 \text{ mm})^2}{3.56 \mu\text{m}} = 7.9 \text{ m}. \quad (1)$$

On the other hand, the beta function for the positron data is:

$$\beta_z = \frac{(0.041 \text{ m})^2}{0.001 \text{ m}} = 1.7 \text{ m}. \quad (2)$$

Thus, we conclude that we need an energy compressor which compress the incoming positrons energy dispersion more than to its half.

CONCLUSION

The Linac transmission is increased fairly enough to supply Z-operation, that also means fulfilling all operations of FCC-ee in terms of total charge and emittance in the collider. The introduction of 28 half-length cavities in low energy part with bigger aperture of 20 mm and 92 steerer magnets result 88% of transmission. Cumulatively, the 6 GeV Linac has become 299 meter long, yet still with less than 25 MV/m acceleration gradient throughout the Linac. Despite of the fact that the emittance blow at the exit of the Linac diverges from the goal, the FCC-ee aims not to use an intermediate step to shrink electrons' emittance at the moment. In other words, the Linac will inject 6 GeV electrons directly to 100-km top-up Booster for Z-operation. Therefore, the emittance growth due to the wakefields is going to be studied to be suppressed.

On the other side, the designed Damping Ring covers the FCC-ee positron damping requirements totally thanks to the dynamic aperture which is wider than 200 of sigmas transversely and more than 100 sigmas longitudinally. Moreover, we conclude that an energy compressor is needed before the DR to match the beta functions.

ACKNOWLEDGMENTS

The authors are thankful to K. Furukawa, N. Iida, F. Miyahara from KEK, Japan; A. Barnyakov, A. Levichev, E. Levichev, D. Nikiforov from BINP, Russia; Y. Papaphilipou from CERN, Switzerland for their fruitful discussions and contributions.

REFERENCES

- [1] K. Oide *et al.*, "Design of Beam Optics for the FCC-ee Collider Ring", Proceedings of IPAC16, Busan, South Korea, THPOR022, 2016.
- [2] S. Ogur *et al.*, "FCC-ee Pre-Booster Accelerators", Proceedings of CERN-BINP Workshop, Geneva, Switzerland, 2016.
- [3] K. Yokoya, "Short-Range Wake Formulas for Infinite Periodic Pill-Box", 1998.
- [4] N. Iida *et al.*, Proc. IPAC2011, THYA01, pp.2857-2861.

ELECTRON SOURCES AND POLARIZATION

R.Xiang[†], J.Teichert, Helmholtz Zentrum Dresden Rossendorf, Dresden, Germany

Abstract

In this presentation the present electron sources and the relevant issues will be discussed. For the electron positron colliders and accelerator based light sources, the electron gun and injector design, are arguably the most critical part. There are a variety of electron source designs: DC guns, normal-conducting RF guns, superconducting RF gun and hybrid guns. All variants have their own advantages and difficulties. We will overview the typical sources around the world, and compare their advantages and main challenges. The polarization production will also be discussed.

INTRODUCTION

For most of the electron accelerator facilities, design of electron gun and injector is arguably the most critical work. The quality of guns determines the ultimate performance of whole machine: current, bunch charge, bunch structure, repetition rate, transverse and longitudinal emittance. Certain applications require polarized electron beams. These parameters can only be degraded in subsequent beam line, will never become better [1].

High brilliant beams are required by electron based colliders and high energy free electron lasers (FELs) [2]. Obviously, higher bunch charge in smaller transverse phase space and in smaller longitudinal phase space leads to higher brilliance. This gun must not work in continuous wave mode (CW), but provide very high electrical field at emission to overcome the space charge effect in the low energy stage.

Energy Recovery Linac (ERL), high power FELs and some other accelerator-based facilities place extra emphasis on high average current and low emittance, which needs robust cathodes with high emission efficiency, and high acceleration field in CW or high duty factor pulsed mode [1].

For microscopes and some accelerator applications, cold beams with extremely low emittance are request. Thermal emittance of the emitted electrons determines the limit of the lowest emittance of the beam. During the acceleration and transportation the emittance can only be degraded. So it is important to modify the cathode emission process and to optimize the accelerating structure to maintain the low emittance in the electron source [3].

Polarized beams are required by some high energy particle physics experiments, thus the spin-polarized electron sources are specially stimulated by the application of e^+e^- colliders and electron-hadron colliders. For this case cathode materials with high spin-polarization rate and the good operation vacuum are the essential issue [4].

The main challenges of electron sources are to provide

high efficient emitters, to deal with severe space charge effect and normally to work in the limited space. Although different facilities have their own focus, stability and reliability are the common requirement to ensure the routine operation, and also low dark current is request to reduce the damage risk and radiation doses for the downstream beam line.

EMITTERS

According to the different electron emitters, electron sources can be classified as thermal emission sources, photoemission sources, field emission sources and hybrid sources.

Thermionic cathodes, like Hexaborides, will emit when the temperature reach the threshold, when thermalized electrons can overcome the work function and finally escape the cathode surface [5]. Because of the high working temperature (for example 2500 K for LaB6), thermal emitters can only work in direct current (DC) guns and in normal conducting radio frequency (NC RF) guns. With high electric fields, they are able to produce high current, but the time structure of bunches cannot be as short as those from photo-emitters and the emittance will be high due to the thermal emission process.

Photo-induced emission is up to now the best candidate for low emittance sources. Photocathodes can locate in DC guns, NC RF guns and lately in Superconducting RF guns (SRF guns). Photo-guns have produced beams with sufficient quality for many accelerator facilities [6]. But the critical gun vacuum and the expensive drive lasers increase greatly machine cost. In the next section the photo emission sources will be discussed.

Electron sources with cold field emission cathodes, like diamond field emitter and multiwall carbon nanotubes, are very common used in the field of electron microscopy, Gabor holography and also the accelerator facilities [7]. Due to the Fowler-Nordheim theory, the high fields built at the tips of emitter surface will induce stable field emission [8]. There are some new ideas inspired from field emission, for example, photo-induced field emission cathode or field enhanced photocathode [9], thermal field emission cathode [10], Schottky emission cathode [11], combining two emission models by using one method to reduce the work function of material and then extract the electrons with another method.

AVAILABLE ELECTRON SOURCES

Photoemission based electron sources (photo guns) have reached the best beam quality. For electron positron colliders, photo guns have the biggest potential to produce high current and low emittance beam. In this section we will overview the various on-going photo gun types, DC guns, NC RF guns and SRF gun projects.

[†] r.xiang@hzdr.de

DC Guns

This type of sources consists of a photocathode, an anode and a high voltage between cathode and anode. DC guns are mature technique and have been used in many research accelerators since 1977, for instance, at Cornell [12], JAEA[13], KEK[14], Jlab [15], Daresbury [16] and so on. The state-of-art DC guns with negative electron affinity (NEA) cathodes deliver ~10 mA average current and hundreds of Coulombs from one single activated cathode [12].

Besides the mature technology, the main advantages of the DC guns include high average current, good vacuum 10-11 mbar for sensitive high QE photocathodes and arbitrarily high repetition rates. But the major challenges are obvious also: the limitation of the field on cathode surface, ion back bombardment limiting the cathode lifetime, dark current and space charge effect. The voltage between the cathode and anode are normally 300 - 500 kV, and very high voltage (500-750kV) is still essentially difficult.

As an example, Fig.1 shows the DC gun developed by JAEA and then operated and modified at KEK for ERL. In this design, chemically polished titanium is used for gun chamber and electrodes, and totally 14, 000 l/s NEG pumps are equipped in the vacuum chamber. This gun has been successfully operated at 500 kV for more than 8 hours without voltage breakdown [17].

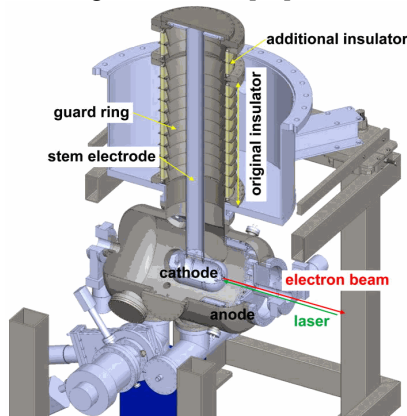


Figure 1: 500 kV DC gun at KEK. [17]

Normal Conducting RF Guns

There are two types of normal conducting RF guns: the first type is high frequency guns in L-band, S-band and even X-band and the other is low frequency guns in VHF or UHF range for potential CW operation.

NC RF guns with high frequency resonant cavities are successfully operated at CERN [18], FLASH [19], LCLS [20], etc. This is a mature technique producing the highest gradient (>100 MV/m) on cathode and the highest brilliance beam in pulsed mode. Also the application of a solenoid around the gun cavity makes the emittance compensation possible. The main limitations are bad vacuum during operation and low repetition rate. Also due to impedance and ohmic losses on the cavity wall, water cooling system is very demanding for the stable operation. High dark current from field emission is another

problem for the beam application. The typical vacuum of 10^{-9} mbar restricts the choice of photocathodes. Only very robust cathode materials like Cu, Mg, Cs₂Te can be used. Sensitive NEA photocathodes and Cs₂K₂Sb photocathodes are not suitable for RF guns at normal temperature. The dark current is another limiting factor in the RF guns operation at high accelerating gradients [21].

DESY RF gun is a very successful design. Fig. 2 shows the cross-sectional view of this gun. The operation gradient is up to 60 MV/m producing high brightness beams with 1 nC electron bunch and transverse normalized rms emittance as low as 1.26 ± 0.13 mm mrad [22].

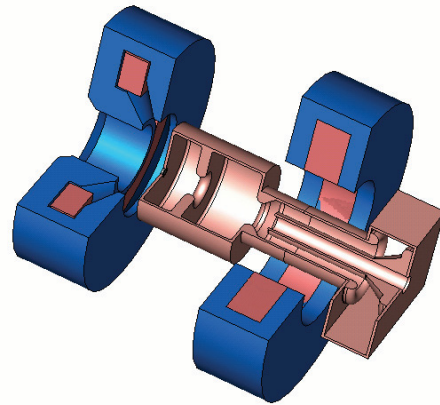


Figure 2: The transverse cross-sectional view of DESY normal conducting RF gun [23]. The 1.6 cell copper cavity produces 60 MV/m at emission.

The other type of NC RF guns are low frequency guns for CW mode operation. Good examples are LBNL 186 MHz gun [24], LANL/AES 700 MHz gun [25] and Boeing 433 MHz RF gun. Boeing RF gun has reached duty factor of 25 % and produced 32 mA average current with a K₂CsSb photocathode driven by 532 nm green laser [26].

Figure 3 is the cross view of the APEX RF gun developed at LBNL. The 186 MHz RF field provides a gradient on cathode of 20 MV/m in 4 cm gap. With Cs₂Te photocathode it succeeded to produce 0.3 mA average current in 1 MHz repetition rate [27].

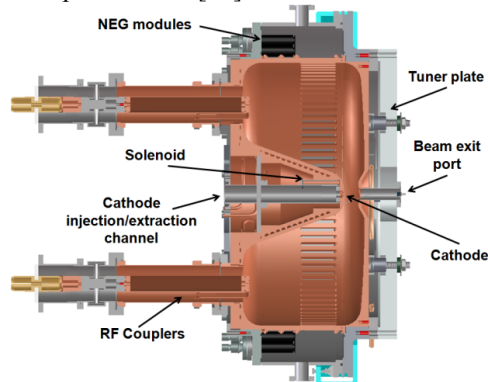


Figure 3: The cross-section view of the APEX RF gun developed at LBNL [27]. The 186 MHz RF field provides a gradient on cathode of 20 MV/m, and the powerful pumps around the cavity maintain good vacuum for alkali photocathodes.

Superconducting RF Guns

There are several ongoing and proposed accelerator projects using SRF guns. The advantages of SRF guns are the high bunch repetition rate, high fields (>20 MV/m) on cathode surface and excellent vacuum environment for the sensitive cathode materials. SRF guns are suitable for CW operation with medium bunch charge (hundreds of pC). But the sensitivity of the superconducting cavity and the compatibility of the cavity and high QE photocathodes are the major challenges for this type sources in the practical operation. On the other hand, how to reduce the dark current from the field emission is also a question. According to the combination methods of RF fields and photocathodes there are four types of SRF guns.

Elliptical cavity + NC cathode is a classic design. The elliptical cavity is based on TESLA technology, able to build high field at emission up to 40 MV/m, which can compare favorably with NC RF guns. Since 1998 HZDR has been devoting to two generations of $3+1/2$ cell SRF guns [28]. And since 2008 HZB is working on a 1.4 cell SRF gun for 100 mA high current for the ERL project [29]. Recently KEK tested a $1+1/2$ cell SC cavity for the SRF gun prototype, which has a feature: the excitation laser injects from backside of the photocathode. These cavities have resonant frequency of 1.3 GHz. There is also design with low frequency elliptical cavity. The cavity of the BNL/AES SRF gun is 703.75 MHz. Cylindrical protrusions on the outside of the cavity's back wall and on the cathode stalk form a folded RF choke joint with four gaps, where unexpected multipacting appeared during operation. This gun has generated the first beams from CsK₂Sb photocathodes [30].

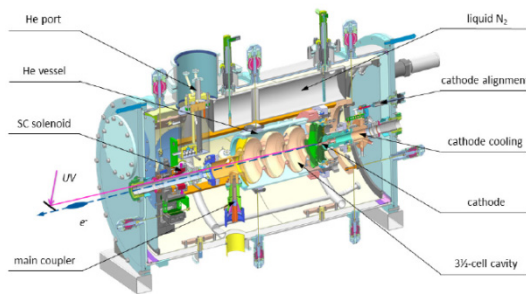


Figure 4: SRF gun-II cryomodule at HZDR. Normal conducting photocathode is inserted into the SC elliptical cavity. A SC solenoid is installed in the cryomodule for emittance compensation.

As an example, Fig. 4 shows the SRF gun II developed by HZDR [31]. The normal conducting photocathode is cooled with liquid nitrogen, surrounded by a SC cavity as RF choke filter. Between the $3+1/2$ cell Nb cavity and the NC photocathode there is a vacuum gap to isolate the cathode to SC cavity. The cathode structure allows to load a DC voltage to suppress the possible multipacting. Copper, Magnesium and Cs₂Te can be used as photo emitter driven by a UV laser. A SC solenoid is installed in the gun cryomodule, used to compensate the transverse emittance [32]. Due to the strong field emission led by the

contamination during the cathode exchange, the field was restricted to 7 MV/m. However it should be still able to generate a bunch charge up to 500 pC.

Quarter wave resonator + NC cathode is another variant. The advantages of the quarter wave resonator (QWR) are low RF losses, small HOM effect, long bunch allowed due to the relative constant field in the acceleration gap.

The 200MHz QWR SRF gun built in University of Wisconsin-Madison has achieved 20 MV/m in CW operation with the cathode inserted. Bunch charges of ~ 100 pC have been delivered [33]. As the second example, the Naval Postgraduate School (NPS) has built a 500 MHz QWR SRF gun as electron beam source, which has a photocathode with adjustable position and uses a unique cascaded RF coupler design [34].

In 2014 a 112-MHz superconducting QWR electron-gun cryomodule was developed in a collaboration between BNL and Niowave, Inc. as part of testing the concept of coherent electron cooling. The gun is designed to deliver electrons with a kinetic energy of 2 MeV. Fig. 5 shows the layout of the 112 MHz gun, recently generating 3 nC bunches at 1.7 MeV from an CsK₂Sb driven by a green laser of 532 nm [35].

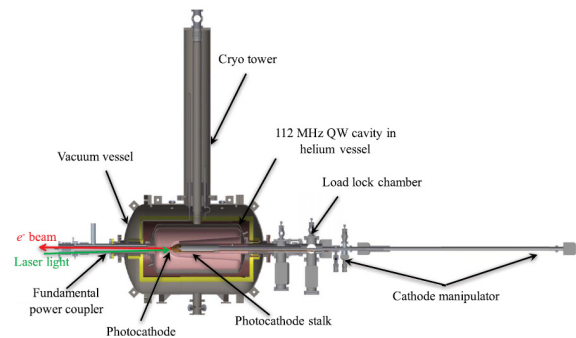


Figure 5: Cross section of the 112 MHz SRF gun (elevation view) at BNL [35].

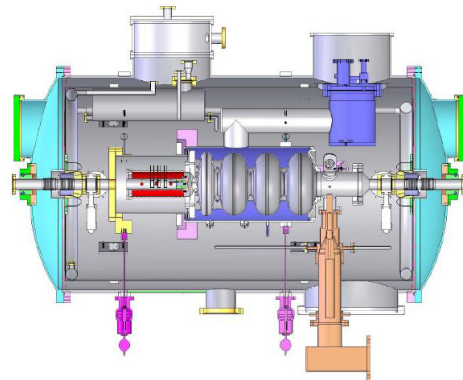


Figure 6: the cross section of PKU DC-SRF gun [36].

Elliptical cavity + DC pierce + NC cathode is a kind of hybrid gun, combining low voltage DC gun and SRF gun. Peking University has successfully developed the DC-SRF gun consisting of a nominal 45 kV DC Pierce gun and a 1.3GHz 3.5 cell superconducting RF cavity.

The normal conducting Cs_2Te cathode is installed in the DC pierce structure. Extracted electrons are accelerated in DC field, and then float through a centimeters gap into RF field, so the danger of contamination due to cathode exchange is reduced. However, because of the low field on cathode and the floating gap, the bunch charge and the transverse emittance are strictly limited (Fig. 6). E_{acc} of the gun reached 8.5 MV/m, and produced electron beam of 1mA at 81.25 MHz with normalized transverse emittance 2.0 mm-mrad [36].

All SC gun can avoid the compatibility problem of the NC cathode and SC cavity, and reduce the contamination risk for the SC cavity. The development of the SC gun is an on-going R&D program at DESY since 2006. Recently, the 1.6-cell niobium cavity was tested in a vertical cryostat with exchangeable plug, reaching 63 MV/m with Nb-plug and 32 MV/m with Pb-coated plug. The limitation of this SC gun is the bunch charge because of the very low QE of superconducting photocathodes [37].

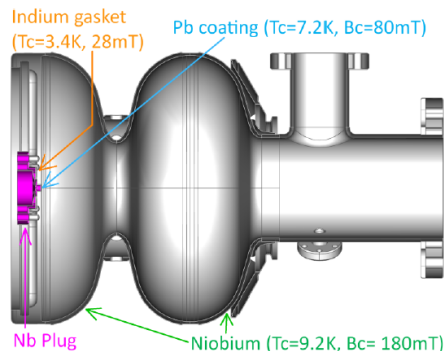


Figure 7: Design concept of the SC gun at DESY [37].

POLARIZED ELECTRON SOURCES

Polarized beams play a crucial role in the experimental programs of RHIC (Relativistic Heavy Ion Colliders), HERA (Hadron-Elektron-Ring-Anlage), as well as in the e^+e^- collider program.

In 1970s, there are several early polarized electron sources for accelerators: Yale / Stanford source based on the photoionization of 6Li atoms, the source for Bonn synchrotron based on Fano effect, and Bielefeld source based on field emission from W-EuS. After 1974, benefit from the contribution of material scientists, GaAs(Cs) photocathodes illuminated with circularly polarized light become the most popular method to produce polarized electron beam for accelerators [38]. This method keeps state-of-art with DC guns [39]. Moortgat-Pick and the co-authors have introduced the polarized electron sources and positron sources in detail in reference [40].

As for the gun construction, the only special requirement is the extremely high vacuum (XHV) during the operation. Thus the polarized electron sources presently in operation are based on DC guns with semiconductor photocathodes. There is argument to use RF guns (SRF

gun or RF gun in cryogenic temperature) with GaAs-based photocathodes for polarized electron guns [41]. However, up to now no successful operation has been reported.

The most important element for polarized electron sources is polarized photocathodes. The bulk-GaAs crystal can reach polarization up to 50% with high QE. The QE is mainly determined by the property of the NEA surface. It is realized by using a combination of two techniques; band-bending due to the heavily p-doped surface layer, and the monolayer formation of alkali (e.g. Cs) and oxidant (O) on the semiconductor surface [42].

Higher polarization is an ongoing R&D aim. Researchers at several laboratories, including Nagoya University and KEK[43], St. Petersburg Technical University [39], and ISP Novosibirsk [44] etc. have been searching for a cathode structure that would yield electron beams with a higher polarization while maintaining a high QE. The strained layer InGaP- or GaAsP-cathodes can reach polarization of 70-80% and QE of 0.1-0.4%. Today the most promising photocathode structure is the superlattice with strain pioneered by the Nagoya-KEK collaboration [42] and St Petersburg [39]. The maximal polarization of 92% with quantum efficiency of 0.85% at room temperature has been reported in St Petersburg with superlattices with strained QW AlInGaAs/AlGaAs, shown in Fig. 8.

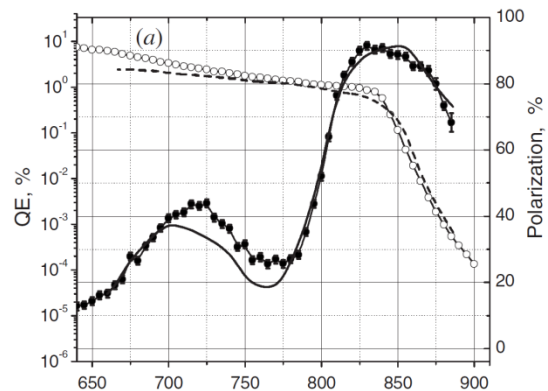


Figure 8: Polarization (solid symbols) and quantum efficiency (circle symbols) spectra of the emitted photoelectrons from a strained AlInGaAs/AlGaAs superlattice sample [39].

The main challenges for polarized sources come from the photocathodes. The short life time due to harmful rest gases and ion back bombardment during the operation in DC field. At JLab, ion back bombardment is the predominant mechanism limiting the operational lifetime of the cathodes during electron emission [45]. Note to this point, in RF field there is no reported problem of ion back bombardment to photocathodes.

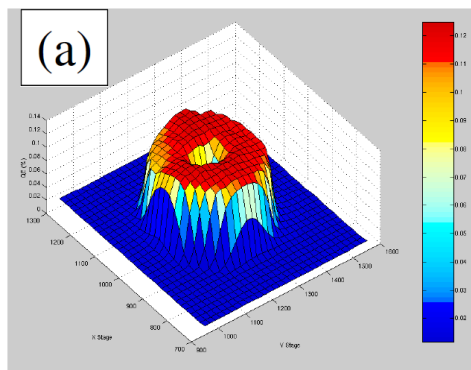


Figure 9: QE scan of a photocathode obtained over many weeks of continuous operation. The pattern of QE degradation indicates damage from ion back bombardment [45].

Another problem faced by polarized electron sources is the response time of GaAs-based photocathodes slower than that of metallic and alkali cathodes. For bulk GaAs, the response time is measured as 1.8 ps with 400nm and 2.8ps with 800nm [46] (shown in Fig. 10). Response time of semiconductor AlInGaAs/AlGaAs superlattices was reported also in level of several picoseconds [47]. Compared with sub-ps response time of metal and alkali photocathode, GaAs produce a tail of bunches or longitudinal halo.

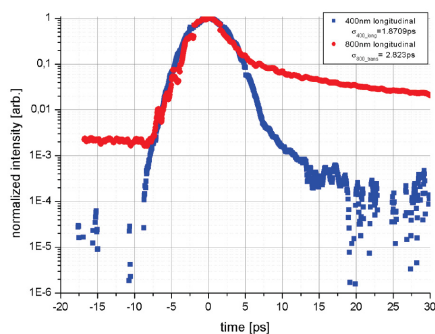


Figure 10: The response time of NEA GaAs photocathode measured in Mainz [46].

CONCLUSION

Many groups around the world are intensively working on different schemes and technologies potential for achieving the required electron beams: bunch charge density, brilliance, average current, bunch structure, repetition rate, transverse and longitudinal emittance and polarization. Gun structure design has to promise high field for acceleration and good gun lifetime. Suitable electron emitters have to be chosen to fulfil the requirements of endurance in high field, low thermal emittance, prompt response time and high polarization for colliders and certain applications.

- choose appropriate emitter for more electrons
- build high field for acceleration for better beam quality
- build an accurate diagnostic beam line

Attention must be paid also on the study of beam dynamics in the gun and injector, where electron beams have only low energy and suffer strong space charge effect. Modeling and computational issues are greatly important for conceptual design. A number of simulation codes, EGUN, ASTRA, PARMELA...can help to optimize the field. Careful simulation is needed for emittance compensation and nonlinear effect in the high density bunches.

ACKNOWLEDGEMENT

The work is supported by the European Community under the FP7 programme (EuCARD-2, contract number 312453, and LA3NET, contract number 289191) and by the German Federal Ministry of Education and Research (BMBF) grant 05K12CR1.

REFERENCES

- [1] I. Ben-Zvi and IV Bazarov, *Nuclear Instrum. Methods*, A 557 (2006) 337-344.
- [2] D.C. Nguyen, *et al.*, *Nuclear Instrum. Methods*, A 528.1 (2004): 71-77.
- [3] D.B. Williams, & C. B. Carter, The transmission electron microscope. In *Transmission electron microscopy* (pp. 3-17). Springer Us.1996.
- [4] J. Wenninger, *et al.*, "Future Circular Collider Study Lepton Collider Parameters." CERN EDMS no 1346082 (2014).
- [5] J.D. Buckingham, "Thermionic emission properties of a lanthanum hexaboride/rhenium cathode." *British Journal of Applied Physics*, 16.12 (1965): 1821.
- [6] J.G. Power, "Overview of photoinjectors." *ADVANCED ACCELERATOR CONCEPTS: 14th Advanced Accelerator Concepts Workshop*. Vol. 1299. No. 1. AIP Publishing, 2010.
- [7] J.D. Jarvis, *et al.*, *Journal of Applied Physics*, 108, 094322 (2010).
- [8] K.L. Jensen, "General formulation of thermal, field, and photoinduced electron emission." *Journal of Applied Physics*, 102.2 (2007): 024911.
- [9] S. Kher, *et al.*, *Applied Physics Letters*, 96.4 (2010): 044101.
- [10] Z. W.Chen & J. Dou, U.S. Patent Application No. 12/972, 299 (2011).
- [11] S. Hiroyuki, *et al.* U.S. Patent No. 5,616,926. 1 Apr. 1997.
- [12] B. Dunham, *et al.* "Record high-average current from a high-brightness photoinjector," *Applied Physics Letters*, 102.3 (2013): 034105.
- [13] T. Nishitani, *et al.*, "JAEA photocathode DC-gun for an ERL injector," in *Proc. FEL2006*, p. 319 (2006).
- [14] R. Nagai, *et al.*, "High-voltage testing of a 500-kV dc photocathode electron gun," *Review of Scientific Instruments*, 81.3 (2010): 033304.

- [15] C. Hernandez-Garcia, *et al.*, "A high average current DC GaAs photocathode gun for ERLs and FELs," in *Proc PAC'05*, Knoxville, TN, USA, May 2005, paper WPAP050, pp. 3117-3119.
- [16] S. L. Smith, *et al.*, "The status of the Daresbury energy recovery linac prototype," in *Proc. PAC'07*, Albuquerque, NM, USA, May 2007, paper TUPMN083, pp. 1103-1105.
- [17] M. Yamamoto and N. Nishimori, *Applied Physics Letters*, 109, 014103 (2016)
- [18] R. Losito, *et al.*, "The PHIN photoinjector for the CTF3 drive beam," in *Proc EPAC'06*, Edinburgh, UK, June 2006, paper WEPLS059, pp. 2517-2519.
- [19] M. Vogt, *et al.*, "Status of the free-electron laser FLASH at DESY," in *Proc. IPAC'11*, San Sebastián, Spain, September 2011, paper THPC081, pp. 3080-3082.
- [20] R. Alley, *et al.*, "The design for the LCLS RF photoinjector," *NIM*, A 429.1 (1999): 324-331.
- [21] L. Monaco, *et al.*, "Dark current investigation of FLASH and PITZ RF Guns," in *Proc. EPAC'06*, Edinburgh, UK, June 2006, paper WEPLS051, pp. 2493-2495.
- [22] F. Stephan *et al.*, *Phys. Rev. ST Accel. Beams*, 13, 020704.
- [23] F. Stephan, presentation on LA3NET Workshop, 2013
- [24] F. Sannibale, *et al.*, "Advanced photoinjector experiment photogun commissioning results," *Phys. Rev. ST Accel. Beams* 15.10 (2012): 103501.
- [25] D. Nguyen, "Development of High-average-current RF Injectors," in *Proc. FEL'08*, Gyeongju, Korea. August 2008, paper THCAU02, pp. 511-516.
- [26] D.H. Dowell *et al.*, *Applied Physics Letters*, 63, 2035 (1993).
- [27] F. Sannibale, *et al.*, *Phys. Rev. ST Accel. Beams*, 15, 103501 (2012).
- [28] A. Arnold, *et al.*, *Nuclear Instrum. Methods*, A 593.1 (2008): 57-62.
- [29] A. Neumann *et al.*, "CW Superconducting RF Photoinjector Development for Energy Recovery Linacs," in *Proc. LINAC10*, Tsukuba, Japan, September 2010, paper THP112, pp. 998-1000.
- [30] S. Belomestnykh, *et al.*, "Commissioning of the 112 MHz SRF Gun," in *Proc. SRF'2015*, Whistler, BC, Canada, September 2015, paper THPB058, pp. 1240-1242.
- [31] P. Lu, *et al.* "Simulation of ELBE SRF gun II for high-bunch-charge applications." *Nuclear Instrum. Methods*, A 830 (2016), 536-544.
- [32] H. Vennekate *et al.*, "ELBE SRF Gun II - Emittance Compensation Schemes," in *Proc SRF'2015*, Whistler, Canada, September 2015, paper THPB057, pp.1235-1237.
- [33] J. Bisognano, *et al.*, "Wisconsin SRF Electron Gun Commissioning," in *Proc. NAPAC'13*, Pasadena, CA USA, September 2013, paper TUPMA19, pp. 622-624.
- [34] A.D. Holmes, "Characterization of the First SRF Electron Beam Source at the Naval Postgraduate School," in *Proc. IPAC'12*, New Orleans, Louisiana, USA, May 2012, paper MOPPP047. pp. 667-669
- [35] T. Xin *et al.*, *Review of Scientific Instruments*, 87, 093303 (2016)
- [36] K. Liu, *et al.*, talk at SRF2015, FRAA05, http://accelconf.web.cern.ch/Accelconf/SRF2015/talks/fraa05_talk.pdf
- [37] D. Kostin, *et al.*, "SRF Gun Cavity R&D at DESY," in *Proc. SRF'2015*, Whistler, BC, Canada, September 2015, paper THPB056, pp. 1231-1233.
- [38] D.T Pierce, *et al.*, *Review of Scientific Instruments*, 51.4 (1980): 478-499.
- [39] Mamaev *et al.*, *Appl. Phys. Lett.*, 93, 081114 (2008).
- [40] G. Moortgat-Pick *et al.*, *Physics Reports*, 460 (2008) 131-243.
- [41] R. Xiang, *et al.*, "Low Emittance Polarized Electron Source Based on FZD Superconducting RF Gun", in *Polarized Sources, Targets & Polarimetry*, published by World Scientific. 2009.
- [42] T. Nakanishi, K. Togawa, T. Baba, *et al.*, *Nuclear Instrum. Methods*, A 455 (2000) 109-112.
- [43] T. Nishitani, *et al.*, "Highly polarized electrons from GaAs-GaAsP and InGaAs-AlGaAs strained-layer superlattice photocathodes," *Journal of Applied Physics*, 97.9 (2005): 094907.
- [44] D. Dmitriev, *et al.*, "Transport relaxation time and quantum lifetime in selectively doped GaAs/AlAs heterostructures," *JETP Letters*, 95.8 (2012): 420-423.
- [45] C.K. Sinclair, *et al.*, *Phys. Rev. ST Accel. Beams*, 10, 023501 (2007)
- [46] M.A. Dehn, *et al.*, "Pulse Response Measurements of NEA Photocathodes at Different Laser Wavelengths," in *Proc. IPAC'16*, Busan, Korea, paper THPOW004, pp. 3931-3933.
- [47] L.G Gerchikov, *et al.*, *St. Petersburg State Polytechnical University Journal. Physics and Mathematics* No. 4-2(182) 2013, 66-75.

COLLECTIVE EFFECTS ISSUES FOR FCC-ee

M. Migliorati^{1*}, E. Belli^{1,2}, G. Castorina³, S. Persichelli⁴, B. Spataro³, M. Zobov³

¹ University of Rome 'La Sapienza' and INFN Sez. Roma1, Rome, Italy

² CERN, Geneva, Switzerland

³ INFN-LNF - Frascati - Roma - Italy

⁴ LBNL - Berkeley - CA - USA

Abstract

The Future Circular Collider study, hosted by CERN to design post-LHC particle accelerator options in a worldwide context, represents a great challenge under several aspects, which require R&D on beam dynamics and new technologies. One very critical point is represented by collective effects, generated by the interaction of the beam with self-induced electromagnetic fields, called wake fields, which could produce beam instabilities, thus reducing the machines performance and limiting the maximum stored current. It is therefore very important to be able to predict these effects and to study in detail potential solutions to counteract them. In this paper the resistive wall and some other important geometrical sources of impedance for the FCC electron-positron accelerator are identified and evaluated, and their impact on the beam dynamics, which could lead to unwanted instabilities, is discussed.

INTRODUCTION

The new CERN project, called High Luminosity LHC [1], aims to increase the number of collisions accumulated in the experiments by a factor of ten from 2024 onwards. While the project is well defined for the next two decades, CERN has started an exploratory study for a future long-term project based on a new generation of circular colliders with a circumference of about 100 km. The Future Circular Collider (FCC) study [2] has been undertaken to design a high energy proton-proton machine (FCC-hh), capable of reaching unprecedented energies in the region of 100 TeV, and a high-luminosity e+e- collider (FCC-ee), serving as Z, W, Higgs and top factory, with luminosities ranging from about 10^{34} to 10^{36} cm⁻²s⁻¹ per collision point as a potential intermediate step towards the realization of the hadron facility. The design of the lepton collider complex will be based on the same infrastructure as the hadron collider.

At high beam intensity, necessary to reach the high luminosity foreseen for FCC-ee, the electromagnetic fields, self-generated by the beam interacting with its immediate surroundings and known as wake fields [3], act back on the beam, perturbing the external guiding fields and the beam dynamics. Under unfavorable conditions, the perturbation on the beam further enhances the wake fields; the beam-surroundings interaction then can lead to a reduction of the machine performance and, in some cases, also to instabilities.

The theory of collective beam instabilities induced by the wake fields is a broad subject and it has been assessed over many years by the work of many authors, such as F. Sacherer [4], A. W. Chao [5], J. L. Laclare [6], B. Zotter [7], C. Pellegrini [8], M. Sands [9] and others [10].

To simplify the study of collective effects, in general it is convenient to distinguish between short range wake fields, which influence the single bunch beam dynamics, and long range wake fields, where high quality factor resonant modes excited by a train of bunches can last for many turns exciting, under some conditions, coupled bunch instabilities. In both cases the bunch motion is considered as a sum of coherent oscillation modes perturbed by these wake fields.

In this paper we will focus on the FCC-ee collective effects induced by wake fields. In particular we will first evaluate the wake fields induced by the finite resistivity of the beam vacuum chamber (resistive wall). Due to the 100 km length of the beam pipe, the resistive wall plays a non negligible role among the sources of wake fields for this accelerator, and the choice of the pipe geometry, material, and dimensions is particularly important. We then discuss the collective effects induced by the resistive wall for both the short range and long range wake fields, and for both longitudinal and transverse planes. For some instabilities we will resort to the linear theory, while for other cases and for more accurate predictions, we need to use simulation codes.

We finally dedicate the last part of the paper to other important sources of wake fields, such as the RF system, the synchrotron radiation absorbers, and smooth transitions, in order to reduce their impact on the beam dynamics. Finally, concluding remarks and outlook will end the paper.

For reference we report in Table 1 the list of beam parameters for the two lowest energies that we have used for evaluating the effects of wake fields on the beam dynamics. At the 45.6 GeV energy, two options are foreseen, with the same total beam current and a different bunch spacing, 7.5 ns and 2.5 ns. It is important to observe that the 7.5 ns option is more critical, from the single bunch point of view, with respect to the 2.5 ns option, having a triple bunch current and a shorter bunch length.

RESISTIVE WALL WAKE FIELDS, IMPEDANCES, AND EFFECTS ON BEAM DYNAMICS

The electromagnetic interaction of the beam with the surrounding vacuum chamber, due to its finite resistivity, produces unavoidable wake fields, which, for FCC-ee, result

* mauro.migliorati@uniroma1.it

Table 1: Parameter List used to Evaluate the Beam Dynamics Effects of Wake Fields

Circumference (km)	100	100	100
Beam energy (GeV)	45.6	45.6	80
Beam current (mA)	1450	1450	152
Mom. compaction (10^{-5})	0.7	0.7	0.7
Betatron tune	350	350	350
RF frequency (MHz)	400	400	400
Bunch spacing (ns)	7.5	2.5	50
RF voltage (GV)	0.4	0.2	0.8
Bunch length (mm)*	1.2	1.6	2.0
Energy spread (10^{-3})*	0.37	0.37	0.65
Synchrotron tune	0.036	0.025	0.037
Bunches/beam	30180	91500	5260
Bunch population (10^{11})	1.0	0.33	0.6

* without beamstrahlung (no collision, worst case)

to be of particular importance. If we consider a beam pipe with circular cross section and a single material of infinite thickness, the longitudinal monopolar ($m = 0$) coupling impedance is given by [11]

$$\frac{Z_{||}(\omega)}{C} = \frac{Z_0 c}{\pi} \frac{1}{[1 + i \operatorname{sgn}(\omega)] 2bc \sqrt{\frac{\sigma_c Z_0 c}{2|\omega|}} - ib^2 \omega} \quad (1)$$

and the transverse dipolar ($m = 1$) one by

$$\frac{Z_{\perp}(\omega)}{C} = \frac{Z_0 c^2}{\pi} \frac{2}{[\operatorname{sgn}(\omega) + i] b^3 c \sqrt{2\sigma_c Z_0 c |\omega|} - ib^4 \omega^2} \quad (2)$$

where C is the machine circumference, Z_0 the vacuum impedance, c the speed of light, b the pipe radius, and σ_c the material conductivity. The above expressions are valid in a frequency range defined by

$$\frac{\chi c}{b} \ll \omega \ll \frac{c \chi^{-1/3}}{b} \quad (3)$$

with $\chi = 1/(Z_0 \sigma_c c b)$. The corresponding wake functions are given by [12]

$$\frac{w_{||}(z)}{C} = \frac{4Z_0 c}{\pi b^2} \left[\frac{e^{-z/s_0}}{3} \cos\left(\frac{\sqrt{3}z}{s_0}\right) - \frac{\sqrt{2}}{\pi} \int_0^{\infty} dx \frac{x^2 e^{-zx^2/s_0}}{x^6 + 8} \right] \quad (4)$$

and

$$w_{\perp}(z) = \frac{2}{b^2} \frac{dw_{||}(z)}{dz} \quad (5)$$

with $z > 0$ and $s_0 = [2b^2/(Z_0 \sigma_c)]^{1/3}$.

By considering a beam pipe of 35 mm of radius made by copper (conductivity of about 5.9e7 S/m) or aluminium (conductivity of about 3.8e7 S/m), eqs. (1) and (2) are valid in a

very large range of frequency. In addition, it is important to observe that the last term in the denominator of eqs. (1) and (2) is negligible up to high frequencies, giving then the possibility to easily evaluate the scale of the impedance with the pipe radius. Indeed the longitudinal impedance is inversely proportional to the beam pipe radius, and the transverse one to the inverse of the third power of b . This scaling can be used to find a compromise for the pipe geometry. By reducing the radius it is possible to reduce the power required for the magnets, but this would increase in particular the coupling impedance and then reduce transverse instability thresholds.

The discussion on the vacuum chamber shape and material choice can be found in ref. [13]. In the following, for the beam dynamics studies, we will consider a circular beam pipe having 35 mm inner radius with three layers [14], a first layer of aluminium of 4 mm, then 6 mm of dielectric and finally iron with resistivity of $10^{-7} \Omega\text{m}$. In this case, the impedance has been evaluated with the code Impedance-Wake2D [15]. Even if the above equations are valid only for a single thick layer, for which the skin depth is much smaller than the wall thickness, the difference with respect to the code results starts to show up only below very low frequency. As a conclusion we can say that all the considerations derived from eqs. (1) and (2) are essentially valid also for the multilayer case.

Fig. 1 shows the total transverse and longitudinal resistive wall impedance as a function of frequency. This impedance is used in the following section for evaluating the resistive wall effect on beam dynamics.

Single Bunch Effects

One important effect of the resistive wall on the single bunch dynamics is related to the transverse mode coupling instability, or strong head tail instability [5]. The frequencies of the coherent modes are here calculated with DELPHI [15] code, which considers Laguerre polynomials. In Fig. 2 we show the real part of the frequency (tune shift) of the first two radial coherent oscillation modes, with the azimuthal number going from -2 to 2, as a function of the bunch population for 45.6 GeV, 2.5 ns of bunch spacing, and 80 GeV. As expected, the worst scenario is at the lowest energy, where we find an instability threshold that is a factor of about 6 higher than the nominal bunch population. However, if we consider the 7.5 ns bunch spacing case, the scenario can be worse due to the higher bunch current and lower bunch length. The higher energy cases, not shown here, give higher thresholds. In this situation we can see that, if other contributions to the transverse impedance do not exceed the resistive wall, we have a good margin of safety for this kind of instability. However, a more detailed study of transverse mode coupling instability with a more detailed transverse impedance is necessary.

For what concerns the longitudinal beam dynamics, one main problem caused by the resistive wall is related to the longitudinal potential well distortion and the evaluation of the microwave instability threshold. The microwave insta-

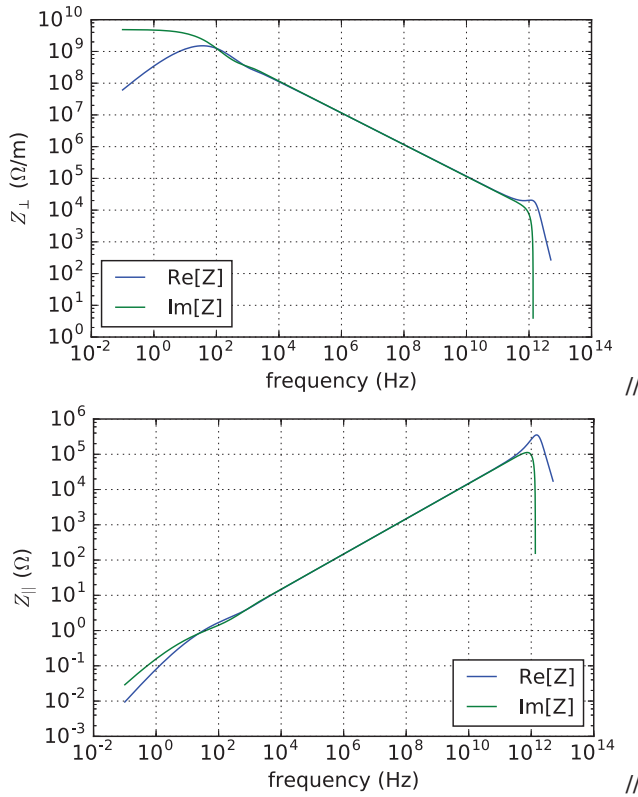


Figure 1: Real and imaginary part of transverse (top) and longitudinal (bottom) impedance of resistive wall as a function of frequency.

bility does not produce a bunch loss, but the consequent longitudinal emittance increase and possible bunch internal oscillations that cannot be counteracted by a feedback system, make the microwave instability an effect that has to be studied with care. In addition to that, there are no reliable analytical expressions that can be used to easily evaluate the instability threshold. For these reasons we have performed a series of simulations by using a tracking code, which we refer here as SBSC [16], initially developed to study the longitudinal beam dynamics in DAΦNE damping and main rings [17], and successively developed and adapted to other machines [18].

In Fig. 3 in red and blue we show the wake potentials of 2 mm and 4 mm Gaussian bunches as given by the equation [19]

$$W_{||}(z) = \int_{-\infty}^{\infty} \lambda(z') w_{||}(z - z') dz' = \frac{cC}{8\sqrt{2}\pi b\sigma_z^{3/2}} \sqrt{\frac{Z_0}{\sigma_c}} F(z/\sigma_z) \quad (6)$$

with

$$F(x) = |x|^{3/2} e^{-x^2/4} (I_{1/4} - I_{-3/4} \pm I_{-1/4} \mp I_{3/4}) \quad (7)$$

where I_n are the modified Bessel functions, the upper signs in eq. (7) are for positive z , $\lambda(z)$ is the longitudinal distribution function, and $w_{||}(z)$ is the wake function given by eq. (4).

ISBN 978-3-95450-187-8

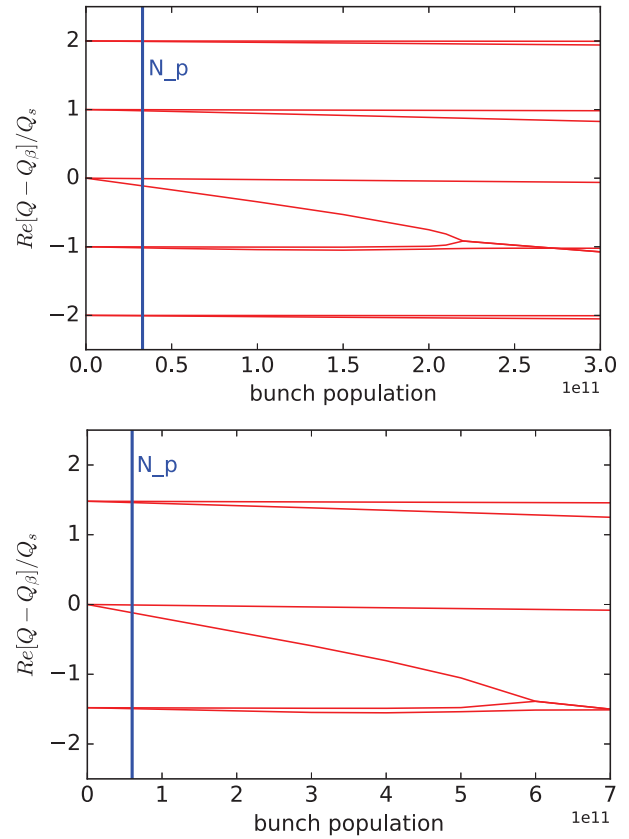


Figure 2: Real part of the frequency of the first coherent oscillation modes as a function of bunch population for the 45.6 GeV case (top) and the 80 GeV case (bottom).

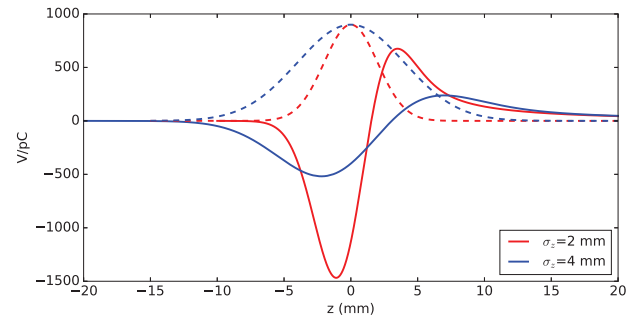


Figure 3: Resistive wall longitudinal wake potentials of 2 mm and 4 mm Gaussian bunches.

In order to perform a test of the code, and to evaluate the effect of the resistive wall on the longitudinal beam dynamics, we have first solved the Haissinski integral equation [20], which is able to predict the bunch length and the distortion from a Gaussian distribution for intensities below the microwave instability threshold. The equation can be written as

$$\lambda(z) = \lambda_0 \exp \left[\frac{1}{E_0 \eta \sigma_{\varepsilon 0}^2} \Psi(z) \right] \quad (8)$$

with λ_0 a normalization constant, E_0 the collider energy, η the slippage factor, σ_{e0} the natural RMS energy spread, and

$$\Psi(z) = \frac{1}{C} \int_0^z [eV_{RF}(z') - U_0] dz' - \frac{e^2 N_p}{C} \int_0^z dz' \int_{-\infty}^{z'} \lambda(z'') w_{||}(z' - z'') dz'' . \quad (9)$$

where V_{RF} represents the total RF voltage, U_0 the energy lost per turn due to the synchrotron radiation, and N_p the bunch population.

The bunch shapes for different bunch populations at the lowest energy of 45.6 GeV for 2.5 ns bunch spacing are shown in Fig. 4.

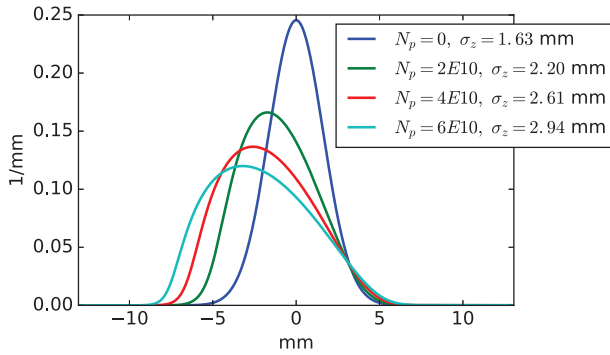


Figure 4: Longitudinal distribution for different bunch population as given by Haïssinski equation.

The bunch length is about 2.4 - 2.5 mm at the nominal current, but we have to remind that only the resistive wall effect has been taken into account for the moment. For the three shown bunch populations the tracking code gives exactly the same distribution.

The potential well distortion theory described by the Haïssinski equation predicts a bunch length increasing with current and a constant energy spread up to a given threshold, called microwave instability threshold, above which also the energy spread increases. In the microwave instability regime, even if the bunch is not lost, it could be characterized by internal turbulent motion which would compromise the machine performances. Several papers have been written to determine the microwave instability threshold [21]. In particular, in ref. [22], the microwave instability due to the resistive wall wake fields was analyzed giving a criterion for the threshold evaluation. Applied to the FCC-ee case, it gives a threshold value of $N_p = 8.1 \times 10^{10}$, a factor slightly higher than 2 with respect to the nominal bunch population for 2.5 ns bunch spacing.

This value can be compared with the results of the tracking code. From Fig. 5, where we represented the RMS energy spread given by the code as a function of the bunch population, we can see that the energy spread starts to increase at about $8 - 10 \times 10^{10}$. This is in a good agreement with the above analytical estimate. Even if there is a margin of safety

for the 2.5 ns bunch spacing, for the 7.5 ns case, the nominal bunch current is found in a weak microwave instability regime.

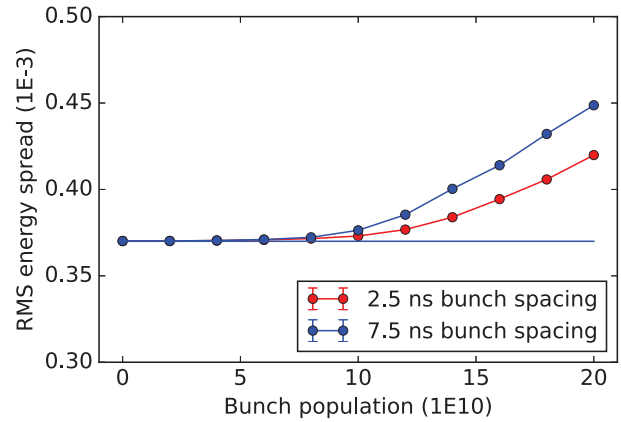


Figure 5: RMS energy spread as a function of bunch population given by the simulation code with only the resistive wall impedance for 2.5 ns and 7.5 ns bunch spacing.

As a further check of the tracking code results, a Vlasov-Fokker-Planck solver [23] has also been used for 2.5 ns bunch spacing, showing that up to a bunch population of 8×10^{10} the beam is stable and giving the onset of the instability at about $10 - 12 \times 10^{10}$.

Finally, Fig. 6 shows the RMS bunch length, obtained with the simulation code, as a function of the bunch population up to an intensity of 2×10^{11} for the two bunch spacing cases.

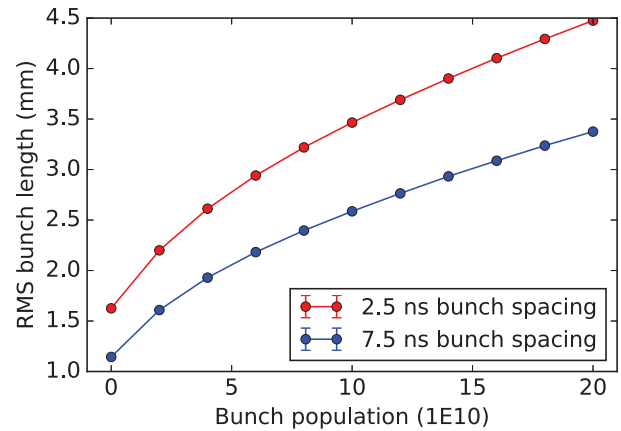


Figure 6: RMS bunch length as a function of bunch population as given by the simulation code with only the resistive wall impedance for 2.5 ns and 7.5 ns bunch spacing.

Multi-bunch Effects

A more critical situation is related to the transverse coupled bunch instability due to the long range transverse wake fields. In this case the study can be performed by considering the motion of the entire beam (not of the single bunch) as a sum of coherent oscillation modes, with coupled bunch

modes to be taken into account. By considering the lowest azimuthal mode $m = 0$ and a Gaussian bunch, the real part of the coupling impedance can produce stability or instability depending on the sign of the growth rate

$$\alpha_{\mu,\perp} = -\frac{cI}{4\pi(E_0/e)Q_\beta} \sum_{q=-\infty}^{\infty} \text{Re}[Z_\perp(\omega_q)] G_\perp(\sigma_\tau \omega'_q) \quad (10)$$

where I the total beam current, Q_β the betatron tune, σ_τ the RMS bunch length in time, G_\perp a form factor which, for our case, is about 1, and

$$\omega_q = \omega_0(qN_b + \mu + Q_\beta) \quad \omega'_q = \omega_q + \omega_0\xi \frac{Q_\beta}{\eta} \quad (11)$$

with N_b the number of bunches, ξ the chromaticity, and ω_0 the revolution frequency.

In the above equations, μ represents the μ^{th} coupled bunch mode, which goes from 0 to $N_b - 1$. When α_μ is positive, the corresponding mode is unstable. If we consider, as transverse impedance, the resistive wall one given by eq. (2), and ignore the term $-ib^4\omega^2$, we observe that $\text{Re}[Z_\perp(\omega)]$ depends on the sign of the frequency ω . Negative frequencies produce unstable modes with an exponential growth given by eq. (10), while positive ones give rise to damped oscillations. In addition to that, the resistive wall impedance grows approximately with the inverse of the square root of the frequency, determining the most dangerous coupled bunch mode when ω_q is as close to zero as possible. If we consider, as an example, the parameters given by Table 1 for the lowest energy and 2.5 ns bunch spacing, with $q = -1$, by denoting with Q_0 the integer part of the betatron tune, that is $Q_\beta = Q_0 + \nu_\beta$, with ν_β the fractional part of the tune, which plays a crucial role for this kind of instability, it comes out that the most dangerous coupled bunch mode is $\mu = N_b - Q_0 - 1 = 89949$, and this mode has its lowest negative frequency at $\omega_q = -\omega_0(1 - \nu_\beta)$.

Fig. 7 shows the beam spectrum of three coupled bunch modes and the real part of the resistive wall impedance of a circular pipe of aluminium, with radius of 35 mm and three layers, close to zero frequency for two extreme cases of fractional part of the betatron tune, $\nu_\beta = 0.05$ (red lines) and $\nu_\beta = 0.95$ (black lines), and we see that a smaller fractional tune is preferred to alleviate the transverse coupled bunch instability because the impedance has a lower value. Due to dynamic aperture and beam-beam issues, and since FCC-ee has 2 interaction points, the fractional tunes are indeed just above the integer [24], and therefore its fractional part is close to zero, mitigating the instability growth rate.

If we consider, as an approximation, not a sum of the impedance over frequency in eq. (10), but the coupling with a single betatron frequency line of the coupled bunch modes, the most dangerous unstable mode has a growth rate given approximately by

$$\alpha_\perp = \frac{cI}{4\pi(E/e)Q_\beta} \frac{C}{2\pi b^3} \sqrt{\frac{CZ_0}{\pi|1 - \nu_\beta|\sigma_c}} \quad (12)$$

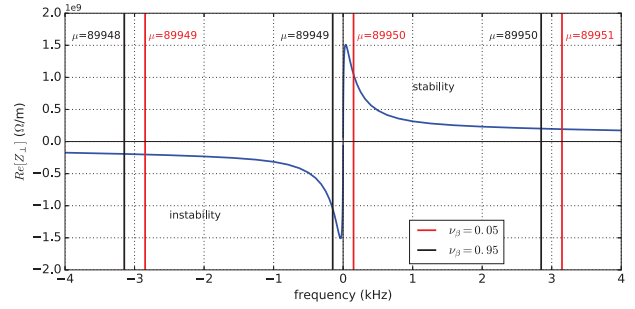


Figure 7: Coupled bunch spectrum and real part of the resistive wall impedance as a function of frequency around $f = 0$ for fractional tune $\nu_\beta = 0.05$ (red line) and $\nu_\beta = 0.95$ (black line).

which, for the best case with $\nu_\beta = 0.05$, gives a growth rate of about 432.4 s^{-1} , corresponding to a rise time of approximately 2.3 ms, that is about 7 machine turns. If the fractional tune increases, the situation worsens because the most dangerous spectrum line couples a higher impedance.

A more precise calculation by considering the sum in eq. (10) and by using the Laguerre polynomials with the DELPHI code confirms the values of the growth rates. Even if the rise times are in the range of few milliseconds, which are not typically a concern for an accelerator machine, due to the large circumference, the rise times correspond to very few turns, making very challenging the realization of a feedback system. Some schemes that could deal with this problem have been proposed in ref. [25].

For what concerns possible longitudinal coupled bunch instabilities excited by HOMs, at this stage it is not possible to quantify their impedance contribution, but we can estimate the maximum shunt impedance giving a growth rate that can be compensated by the natural radiation damping.

Similarly to the transverse case, by considering only the lowest longitudinal azimuthal mode $m = 1$, it is possible to show that the real part of the HOM impedance can produce stability or instability depending on the sign of the growth rate

$$\alpha_{\mu,\parallel} = \frac{\eta I}{4\pi(E_0/e)Q_s} \sum_{q=-\infty}^{\infty} \omega_q \text{Re}[Z_{\parallel}(\omega_q)] G_{\parallel}(\sigma_\tau \omega_q) \quad (13)$$

with Q_s the synchrotron tune and $\omega_q = \omega_0(qN_b + \mu + Q_s)$. Stability in this case occurs for negative frequencies because the real part of the longitudinal impedance is always positive, and the worst and simplest unstable case is when the HOM has its resonant angular frequency ω_r equal to $\omega_q > 0$. If we consider, as an approximation, not a sum of the impedance over frequency, but the coupling with a single synchrotron frequency line of the coupled bunch modes, the most dangerous unstable mode has a growth rate given approximately by

$$\alpha_{\parallel} = \frac{\eta I}{4\pi(E_0/e)Q_s} \omega_r R_s \quad (14)$$

with R_s the HOM shunt impedance. Also in this case $G_{||}(x) \approx 1$, if $f_r \ll 25$ GHz. This growth rate has to be compared with the natural damping rate due to the synchrotron radiation, which, for the lowest energy machine, is about 1320 turns. In Fig. 8, we have represented the maximum HOM shunt impedance of eq. (14) as a function of the resonance frequency, such that the corresponding growth rate is exactly balanced by the radiation damping. Of course, also here a feedback system has to be developed as a further safety knob.

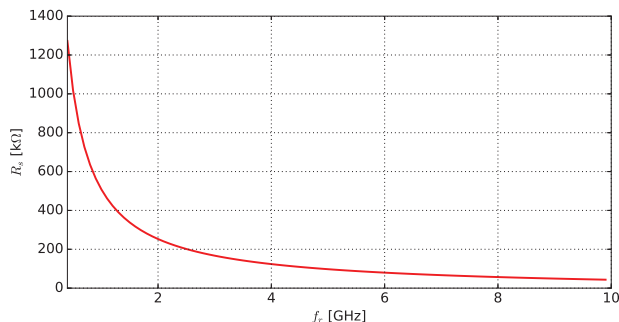


Figure 8: Maximum shunt impedance of a HOM as a function of its resonance frequency, producing a growth rate that is compensated by the natural radiation damping.

OTHER IMPORTANT IMPEDANCE SOURCES

In the previous section, by discussing the effects of the resistive wall, we have seen that its impact on the beam dynamics is very important, requiring, in some cases, active feedback systems to keep under control beam instabilities. In addition to that, other machine devices can be sources of high impedance, and their evaluation is paramount.

Let us first estimate the impact of the synchrotron radiation absorbers. For FCC-ee a synchrotron radiation absorber will be installed every 4-6 meters, with the purpose of intercepting the radiation that, otherwise, would impact on the beam chamber. Due to their large number, the absorbers represent a very important source of machine impedance.

A proposed design foresees a modification of the circular pipe with winglets on both sides, as the one of SuperKEKB [26].

The absorbers are metallic devices shaped like a trapezoid, with a total length of 30 cm, and they are inserted inside the chamber winglets, at about 42.5 mm from the beam axis. Placing slots for vacuum pumps just in front of the absorber allows efficient capturing of the synchrotron radiation and the molecule desorption. The pumping slots have a racetrack profile, length of 100-120 mm and width of 4-6 mm. Behind the slots, a cylindrical volume and a flange will be installed to support a NEG pump [27].

Impedance studies of the beam chamber profile with one absorber insertion have been performed using CST Particle Studio [28]. In Fig. 9, the geometry of the FCC-ee beam chamber used in CST simulations is shown to-

gether with a detail of the absorber inside the beam chamber. Pumping slots and pumps are not included in this simplified model. Preliminary simulations show that below about 3 GHz the longitudinal impedance is purely inductive, giving, for 10000 elements, a longitudinal broadband impedance Z/n of about 1 mΩ.

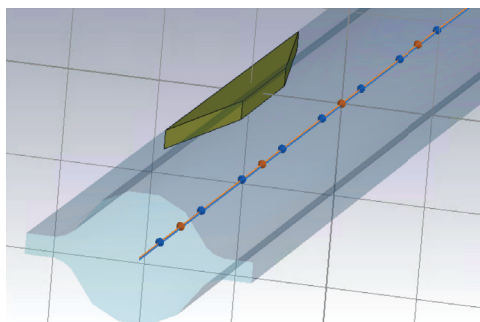


Figure 9: 3D model of the FCC-ee vacuum chamber with winglets and a synchrotron radiation absorber used for CST simulations.

In Fig. 10, the wake potentials for 2 and 4 mm Gaussian bunches for 10000 elements are shown. Even if further analysis is needed, and this first evaluation could overestimate the impedance, we can see that these wake potentials are not negligible. As for the transverse impedance of a single absorber, this is so low that, up to now, we did not manage to obtain reliable results.

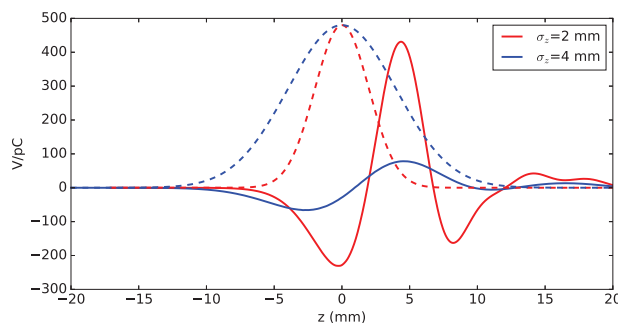


Figure 10: Wake potential of 10000 absorbers for 2 and 4 mm RMS bunch length from CST code.

In FCC-ee there will be many straight sections used for installation of RF systems, quadrupoles with attached BPMs, diagnostics etc. Due to the particular shape of the dipole vacuum chambers with winglets, gradual transitions (tapers) are to be foreseen to connect these chambers to the circular pipes of the straight sections. A possible design of such transitions is shown Fig. 11. The total number of double tapers is estimated to be around of 4000. Their total longitudinal wake potentials for 2 mm and 4 mm bunch lengths are shown in Fig. 12.

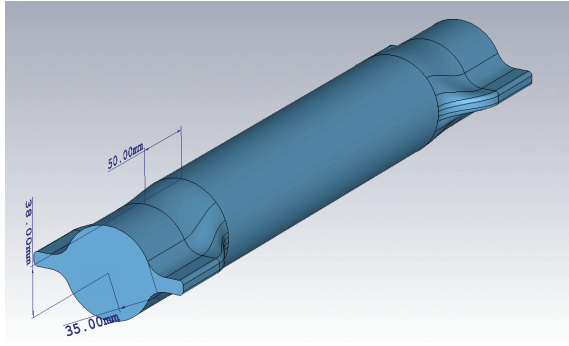


Figure 11: Taper connecting the vacuum chamber with walingets to the circular pipe.

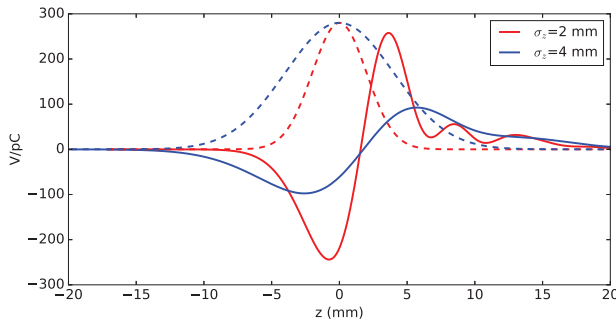


Figure 12: Wake potential of 4000 double tapers for 2 and 4 mm RMS bunch length from CST code.

The RF system is another important source of the beam coupling impedance. Several options of the system are under investigation [29]. For our study we consider the use of 100 single cell 400 MHz cavities, similar to those used in LHC. We assume that, like in LHC, these cavities are separated in groups composed of 4 cavities, placed in common cryostats and connected by tapers to the beam pipe. As a consequence, in addition to the 100 single cell cavities, also the impedance contribution of 25 double tapers has to be taken into account. The wake potentials for the single cells have been obtained with the ABCI code [30], and the results can be very well approximated by the analytical expression [3]

$$W(x) = \tilde{W}|x|^{1/4} e^{-x} [I_{-1/4}(x) + \text{sign}(z)I_{1/4}(x)] \quad (15)$$

with $x = [z/(2\sigma_z)]^2$ and $\tilde{W} = 1.92 \times 10^6 / \sqrt{2\pi\sigma_z/c}$.

The impedance produced by the tapers strongly depends on their length, which we have considered here to be 500 mm. The wake potential of the total RF system under these assumptions is shown in Fig. 13.

If we consider the longitudinal wake potentials of the absorbers, the smooth transitions and the RF system, we see that their sum cannot be neglected with respect to the resistive wall. Even if the contribution of a single element is negligible, due to their high number, the effect on the beam dynamics could be important. In Fig. 14 we show the total wake potential for 2 mm and 4 mm bunch lengths, given by the contributions evaluated so far. We can see that there has been an increase of about 50% with respect to the resistive

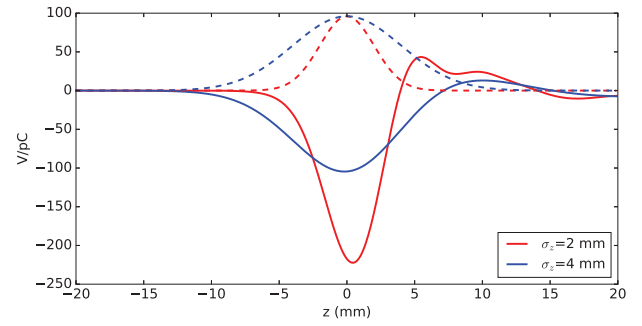


Figure 13: Wake potentials of the RF system for 2 and 4 mm RMS bunch length.

wall contribution. Beam dynamics studies are in progress to evaluate the impact of such wakes on coherent instabilities.

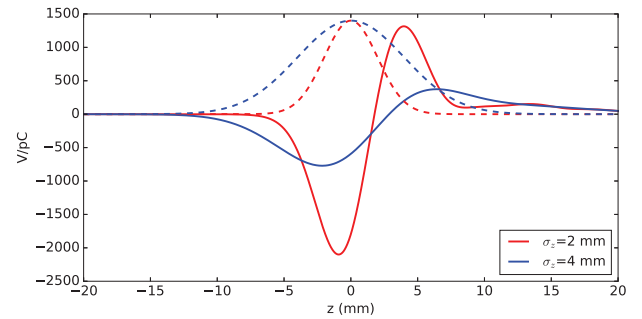


Figure 14: Total wake potentials for 2 and 4 mm RMS bunch length given by the contributions of resistive wall, synchrotron radiation absorbers, RF system and tapers.

Of course, also the transverse contribution of the previous devices has to be taken into account to determine the impact of the impedance on the TMCI. In addition, there are several other sources of impedance, such as the bellows, RF fingers, BPMs and other devices for diagnostics, and their impact on beam dynamics has to be carefully evaluated. Also possible trapped modes in the interaction region deserve special studies, and work on other collective effects, such as the fast ion and the electron cloud instabilities, is in progress.

CONCLUSIONS AND OUTLOOK

In this paper we have discussed single beam collective effects in FCC-ee due to the beam coupling impedance. In particular we focused our study primarily on the resistive wall effects because this is, up to now, the main source of impedance.

We have found that, in the single bunch case, the transverse mode coupling instability threshold due to the resistive wall is by about a factor 6 higher than the nominal bunch population at the lowest energy (45.6 GeV) for 2.5 ns bunch spacing, and even higher for other collider energies. In turn, the microwave instability threshold has a safety margin of 2.4 with respect to the nominal bunch population for the 2.5 ns bunch spacing, while for the 7.5 ns option the threshold is equal to the nominal bunch intensity. Besides, the resistive

wall results in the bunch shape distortion and substantial bunch lengthening (see Fig. 4 and Fig. 6).

Regarding the multi-bunch effect, we have concluded that the resistive wall transverse coupled bunch instability has to be counteracted by a feedback system, which requires innovative ideas for its design. For the longitudinal case, at this stage, it is not possible to evaluate the characteristics of trapped HOMs, but an estimate of the maximum allowed shunt impedance as a function of the resonant frequency has been given.

In addition to the assessment of the resistive wall effects, we have started the evaluation of the impedance budget for other devices, with the goal of designing them in order to reduce their impact on the beam dynamics. With an accelerator of 100 km of length, this is a long work, and the strategy is to identify the most important sources of impedance. We have started with the synchrotron radiation absorbers, the RF system, and smooth transitions from the beam pipe with winglets to the circular one. The results show that the total wake potential is increased of about 50% with respect to the resistive wall one.

ACKNOWLEDGEMENTS

We acknowledge many helpful and stimulating discussions with R. Calaga, R. Kersevan, K. Oide, E. Shaposhnikova, G. Stupakov, J. Wenninger, and F. Zimmermann.

REFERENCES

- [1] The HiLumi LHC Collaboration, CERN-ACC-2014-0300, CERN, Geneva, Switzerland (2014).
- [2] <https://fcc.web.cern.ch/>
- [3] L. Palumbo, V. G. Vaccaro, M. Zobov, CERN 95-06, pp. 331-390, CERN, Geneva, Switzerland (1995), and arXiv: physics/0309023 LNF-94-41-P.
- [4] F. Sacherer, IEEE Trans. Nucl. Sci. 20, 825 (1973); IEEE Trans. Nucl. Sci. 24, 1393 (1977).
- [5] A. W. Chao, *Physics of Collective Beam Instabilities in High Energy Accelerators*, John Wiley & Sons, (1993).
- [6] J. L. Laclare, CERN 87-03, Vol. I, p. 264, CERN, Geneva, Switzerland (1987).
- [7] B. Zotter, CERN-SPS/81-18, 81-19, 81-20, (DI), CERN, Geneva, Switzerland (1981).
- [8] C. Pellegrini, AZP Proc. 87, Phys. High Energy Part. Accel., Fermilab, p. 77 (1981).
- [9] M. Sands, SLAC-TN-69-8, and SLAC-TN-69-10 (1969).
- [10] see, e. g., T. Suzuki and K. Yokoya, Nucl. Instr. and Meth., 203, p. 45 (1982), or K. Y. Ng, *Physics of Intensity Dependent Beam Instabilities*, World Scientific, (2005).
- [11] K. Y. Ng and K. Bane, SLAC-PUB-15078, (2010).
- [12] K. Bane and M. Sands, SLAC-PUB-95-7074, (1995).
- [13] E. Belli, M. Migliorati, S. Persichelli, M. Zobov, CERN-ACC-2016-0111 (2016), and arXiv:1609.03495 (2016).
- [14] R. Kersevan, private communication.
- [15] N. Mounet, Ph.D. thesis, École Polytechnique Fédérale de Lausanne (EPFL), Lausanne, Switzerland, 2012.
- [16] M. Migliorati, L. Palumbo, Phys. Rev. ST Accel. Beams, 18, 031001 (2015).
- [17] R. Boni, et al., NIMA 418, p. 241 (1998); M.Zobov et al., e-print: physics/0312072.
- [18] M. Migliorati, et al., Phys. Rev. ST Accel. Beams, 16, 031001 (2013).
- [19] A. Piwinski, DESY Report 72/72 (1972).
- [20] J. Haïssinski, Il Nuovo Cimento, Vol. 18 B, N. 1, (1973).
- [21] see, e. g., Y. Cai, Phys. Rev. ST Accel. Beams, 14, 061002 (2011).
- [22] K. L. F. Bane, Y. Cai, and G. Stupakov, SLAC PUB -14150, June 2010.
- [23] R. Warnock and J. Ellison, SLAC-PUB-8404, (2000).
- [24] see, e. g. K. Oide, presentation at the FCC Week 2016 - 11 April 2016, Rome - https://indico.cern.ch/event/438866/contributions/1085096/attachments/1255571/1853343/Optics_KO_160411a.pdf
- [25] see A. Drago, presentation at the FCC Week 2016 - 11 April 2016, Rome - https://indico.cern.ch/event/438866/contributions/1085137/attachments/1257184/1857470/Drago_fb_fcc_ee.pdf
- [26] Y. Suetsugu et al, *Design and construction of the SuperKEKB vacuum system*, J. Vac. Sci. Technol. A 30, 031602 (2012).
- [27] R. Kersevan, Proceedings FCC Week 2016 - 14 April 2016, Rome - <https://indico.cern.ch/event/438866/contributions/1085121/>
- [28] <https://www.cst.com/>
- [29] S. Aull, et al., Proceedings of IPAC2016, Busan, Korea, p. 3828 (2016).
- [30] Y. H. Chin, KEK Report 2005-06, KEK, Tsukuba, Japan (2005).

INSTABILITY ISSUES IN CEPC*

N. Wang[†], D.J. Gong, H. J. Zheng, Y. Zhang, Y.S. Sun, G. Xu, Y.W. Wang, D. Wang, Q. Qin, J. Gao, W. Chou, J. He, Key Laboratory of Particle Acceleration Physics and Technology, Institute of High Energy Physics, Beijing 100049, China
D. Zhou, K. Ohmi, KEK, Ibaraki, Japan

Abstract

The CEPC is a high-energy circular electron-positron collider under design. Large bunch population is required to achieve the design luminosity. Instabilities driven by the coupling impedance are possible limitations for reaching high machine performance. An updated impedance model, including the resistive wall and the main vacuum components, has been obtained for the main ring. Based on the impedance model, the collective instability issues of the beam with the partial-double ring design are discussed.

INTRODUCTION

In high-energy circular e⁺e⁻ colliders, large efforts have been made to increase the bunch intensity in order to reach high luminosity. Meanwhile, large circumferences are often chosen due to restricted synchrotron radiation power, which means a further enhancement of the machine impedance. The interaction of the beam with the impedances may lead to collective instabilities, which can induce beam quality degradation or beam losses. Moreover, the large bending radius and small horizontal dispersion in dipoles will generate small momentum compaction factor, which can make the beam more sensitive to the collective instabilities. Therefore, collective instability becomes a potential restriction for the machine performance. In this paper, the instability issues for the partial double ring design of CEPC are studied. The impedance budget for the CEPC main ring is first given. Based on the impedance studies, the single bunch and coupled bunch instabilities are investigated. The main parameters used in the calculation are listed in Table 1.

Table 1: Main Parameters

Parameter	Symbol, unit	Value
Beam energy	E , GeV	120
Circumference	C , km	54
Beam current	I_0 , mA	16.9
Bunch number	n_b	50
Bunch length	σ_z , mm	4.1
RF frequency	f_{RF} , GHz	0.65
Energy spread	σ_e	1.3E-3
Slipping factor	α_p	2.5E-5
Betatron tune	ν_x/ν_y	319.21/318.42
Synchrotron tune	ν_s	0.08
Damping time	$\tau_x/\tau_y/\tau_z$, ms	14/14/7

* Work supported by NSFC (11205171), NKPSTRD (2016YFA0400400)
† wangn@ihep.ac.cn

IMPEDANCE BUDGET

The impedance and wake are calculated with both analytical formula and numerical simulations. The vacuum components considered in the calculation include resistive wall, RF cavities, flanges, shielded bellows, BPMs and pumping ports. The short range wake at nominal bunch length is shown in Fig. 1. The impedance budget of the objects considered is listed in Table 2, where $Z_{||}/n$ is the longitudinal effective impedance, k_l is the loss factor, R and L are effective resistance and inductance of the components obtained by fitting the wake potential with the analytical formula [1]

$$W(s) = -Rc\lambda(s) - Lc^2\lambda'(s). \quad (1)$$

Here, c is the speed of light, and $\lambda(s)$ is the bunch line density.

Table 2: Summary of Impedance Budget

Objects	R , k Ω	L , nH	$Z_{ }/n$, m Ω	k_l , V/pC
Resistive wall	6.7	487.7	17.0	138.4
RF cavity	14.9	-132.7	-	307.5
Flange	0.7	165.5	5.8	15.1
Bellows	5.9	331.5	11.6	122.3
BPM	0.6	21.4	0.7	11.6
Pumping port	0.007	3.1	0.1	0.1
Total	28.8	876.5	35.2	595.0

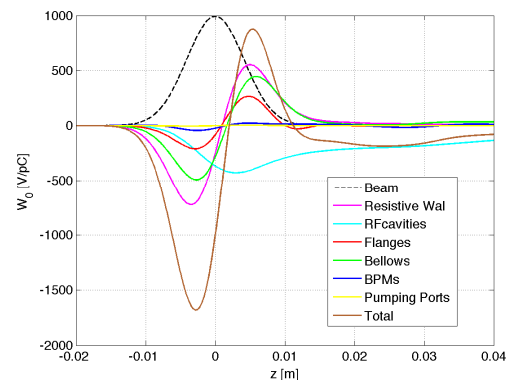


Figure 1: Longitudinal wake potential at nominal bunch length of 4.1 mm.

From the impedance budget we can conclude that the longitudinal impedance is dominated by the resistive wall and the vacuum components with large quantity, such as flanges and bellows. A more complete impedance budget

will be obtained as more vacuum components are designed.

SINGLE BUNCH EFFECTS

Broadband impedance can induce single bunch instabilities, which will result in emittance blow-up, bunch lengthening or beam losses. Since the bunch intensity is quite high in CEPC, the single bunch instability is more critical compare to the coupled bunch instability. The instabilities are evaluated base on the beam parameters listed in Table1.

Microwave Instability

The longitudinal microwave instability is estimated according to the Boussard or Keil-Schnell criterion [2, 3]. With a longitudinal impedance of $|Z_{||}/n|=35$ m Ω , the threshold bunch current is around 0.17 mA, which is lower than the design current of 0.25mA. This instability will rarely induce beam losses, but may reduce the luminosity due to the deformed beam distribution and increase of the energy spread. For short bunches, the impedance seen by the beam is dominated by the high frequency resonances, therefore the analytical criteria is often believed to be too passive. However, the high frequency part of the impedance may lead to turbulent distributions in the longitudinal phase space. More detailed simulation studies are required.

CSR

The coherent synchrotron radiation (CSR) is generated when beam pass through the bending magnets. It can induce microwave instability with high bunch intensity. With the linear theory, the shielding parameter is [4]

$$\chi = \sigma_z \rho^{1/2} / h^{3/2}. \quad (2)$$

where σ_z is the rms bunch length, ρ the bending radius, and h the distance between the parallel plates. For the case of CEPC, the shielding parameter is much higher than 2. According to the studies in Ref. [4], the coasting beam theory with the shielding impedance should be used for estimating the threshold. The beam becomes unstable when [4]

$$I_b > \frac{3\sqrt{2}\alpha_p \gamma \sigma_e^2 I_A \sigma_z}{\pi^{3/2} h}. \quad (3)$$

where α_p is the momentum compaction, γ the relativistic energy, σ_e the relative energy spread, and $I_A=17045$ A.

The instability threshold given by Eq. (3) is about 30 times higher than the design bunch population. Therefore, CSR is not a concern in the present design.

Transverse Beam Tilt

In the transverse plane, when a beam passes through an impedance with a transverse offset, the tail particles will receive transverse kicks, which can lead to a transverse

displacement of the bunch tail at the interaction point and increase the beam emittance. With the parameters of CEPC, the kick angle along the bunch due to a single RF cavity is shown in Fig. 2. The maximum kick angle at the bunch tail is 1.2 nrad. As there are 384 cavities located in 8 places in the ring, the displacement at IP is around 23 nm, which is about one fifth of the beam size at the IP.

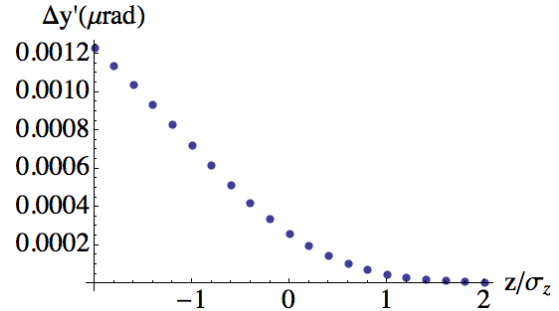


Figure 2: Transverse kick angle along the bunch due to single RF cavity in CEPC ring.

Transverse Mode Coupling Instability

The threshold of the transvers mode coupling instability is estimated with both analytical formula and Eigen mode analysis. For a Gaussian bunch, the threshold intensity can be expressed with the transverse kick factor [5, 6]

$$I_0^{th} = \frac{2\nu_s \omega_0 E / e}{\sum_j \beta_{y,j} \kappa_{y,j}} \Theta. \quad (4)$$

where ν_s the longitudinal tune, ω_0 the angular revolution frequency, E the beam energy, $\beta_{y,j}$ the betatron function at the j th impedance element, $\kappa_{y,j}$ the transverse kick factor, and $\Theta \approx 0.7$. With the impedance model considered, the total kick factor is 18.9 kV/pC/m. The analytical criterion gives threshold bunch current of 0.9mA.

The Eigen mode analysis gives the dependences of the head-tail mode frequencies on the bunch current as shown in Fig. 3. The Eigen mode analysis shows the threshold bunch current is around 1.9 mA, which is about two times higher than the analytical formula. Both analyses leave us with an enough safety margin to avoid transverse mode coupling instability.

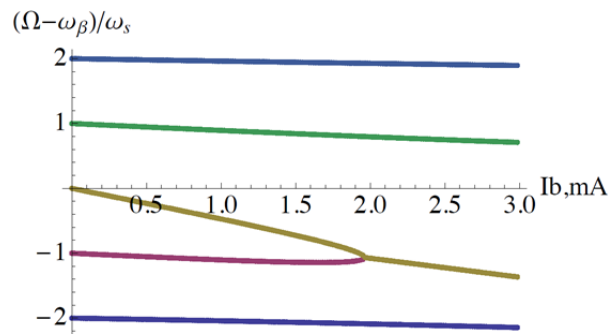


Figure 3: Dependences of the head-tail mode frequencies on the bunch current.

MULTI-BUNCH EFFECTS

In large-scale circular colliders, the revolution frequency is considerably low, which will generate dense beam spectra and is more easily to be coupled with the narrow-band impedances. The interaction of the beam with the narrowband impedances may induce coupled bunch instabilities.

In the present design of CEPC, a partial double ring design is proposed. The electron and positron beam will share the beam pipe except in the collision region. Each beam has a long bunch train of 67 bunches, which will be filled in about 3.2 km in the ring circumference. So that there is a long gap of around 50 km. Therefore, the multi-bunch effects with uneven fills are investigated.

Coupled Bunch Instabilities with Uneven Fills

Coupled bunch instabilities are commonly studied with equal bunch spacing [7]. In the general frame of uneven filled ring, there are two effects due to the uneven fill: damping from the additional tune spread and modulation coupling of the strong even-fill eigenmodes. Here, only the second effect is investigated.

Consider a long bunch train of M identical bunches with bunch spacing of T_b , the longitudinal and transverse beam oscillation with rigid bunch model can be described as

$$\ddot{z}_n(t) + \omega_s^2 z_n(t) = -\frac{Nr_0\alpha_p c}{\gamma T_0} \sum_{m=0}^{M-1} \sum_{k=0}^{\infty} W'_0(-kC - (m-n)T_b c + z_n(t) - z_m(t - kT_0 - (m-n)T_b)) \quad (5)$$

and

$$\ddot{y}_n(t) + \omega_\beta^2 y_n(t) = -\frac{Nr_0 c}{\gamma \beta T_0} \sum_{m=0}^{M-1} \sum_{k=0}^{\infty} y_m(t - (kT_0 + (m-n)T_b)) W_1(-kT_0 + (m-n)T_b) \quad (6)$$

respectively, where N is the bunch intensity, r_0 the critical radius of the electron, T_0 the revolution time, β the relativistic velocity, and C the circumference.

By solving the equation above, the tune shift can be expressed in form of impedances as

$$\Delta\Omega = \Omega - \omega_s = \frac{iNM r_0 \alpha_p}{2\gamma T_0^2 \omega_s} \quad , \quad (7)$$

$$\Delta\Omega = \Omega - \omega_\beta = -\frac{iNM r_0 c}{2\gamma \beta T_0^2 \omega_\beta} \sum_{p=-\infty}^{\infty} Z_1(\omega_0(p + \frac{\mu}{M})M' + \omega_\beta) \quad , \quad (8)$$

where $M' = T_0/T_b$.

Transverse Resistive Wall Instability

One dominant contribution to the coupled bunch instability is the resonance at zero frequency of the transverse resistive wall impedance. Figure 4 shows the growth rate of the transverse resistive wall instability with different mode numbers. The growth rate for the most dangerous instability mode is 3.1 Hz, which is much lower than the transverse radiation damping. So the beam should be safe from the resistive wall coupled bunch instability.

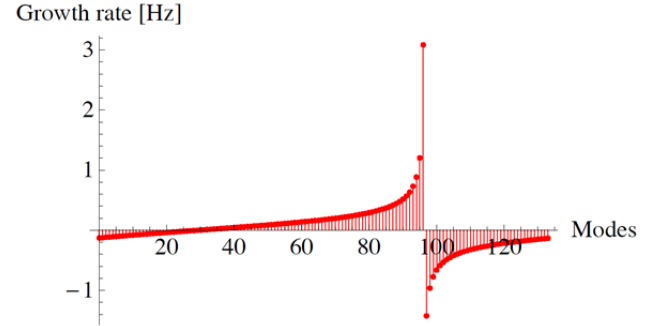


Figure 4: Growth rate of the transverse resistive wall instability with mode numbers.

RF HOMs

Another important contribution to the coupled bunch instability is the HOMs of the accelerating cavities. To keep the beam stable, the rise time of any oscillation mode should be larger than the radiation damping time. In resonant condition, the threshold for the shunt impedances of any HOMs are given by

$$\frac{R_L^{thresh}}{M\Omega} \frac{f_L}{\text{GHz}} < \frac{2(E/e)v_s}{N_c I_0 \alpha_p \tau_z} = 16.9. \quad (9)$$

and

$$\frac{R_T^{thresh}}{M\Omega/m} < \frac{2(E/e)}{N_c f_{rev} I_0 \beta_{x,y} \tau_{x,y}} = 17.6. \quad (10)$$

where N_c is the cavity number along the ring, f_L the frequencies of the HOMs, f_{rev} the revolution frequency of the ring, I_0 the beam current, $\tau_{x,y,z}$ the damping time in transverse and longitudinal directions, and $\beta_{x,y}$ the transverse beta functions. With two counter-rotating beam sharing the RF cavities, the threshold impedance could be further reduced by a factor of two.

However, considering the whole RF system, the threshold value greatly depends on the actual tolerance of the cavity construction. Assuming the resonant frequencies of the RF cavities have a Gaussian distribution with rms frequency spread of 0.5MHz, the threshold shunt impedance considering the whole RF system can be increased by a factor of 50.

CONCLUSION

An updated impedance model is derived for the CEPC main ring. Based on the impedance model, the potential instability issues with the partial double ring design are investigated. The impedance budget shows a total longitudinal effective impedance of 35.2 m Ω , and a total transverse kick factor of 18.9 kV/pC/m. Single bunch instability is more critical compare to coupled bunch instability, especially the microwave instability. Bunch lengthening is expected to happen. Bunch shape distortion due to the transverse wake is another potential restriction to the high luminosity.

REFERENCES

- [1] K. Bane *et al.*, “PEP-X impedance and instability calculations”, SLAC-PUB-14151, 2010.
- [2] D. Boussard, “Observation of microwave longitudinal instabilities in the CPS”, CERN LabII/RF/Int. 75-2, 1975.
- [3] E. Keil and W. Schnell, “Concerning longitudinal stability in the ISR”, CERN ISR-TH-RF 69/48, 1969.
- [4] Y. Cai, “Theory of microwave instability and coherent synchrotron radiation in electron storage rings”, in *Proc. IPAC'11*, San Sebastián, Spain, September 2011, paper FRXAA01, pp. 3774-3778.
- [5] S. Krsinsky *et al.*, “Collective effects in the NSLS-II storage ring”, in *Proc. PAC'07*, Albuquerque, NM, USA, June 2007, paper TUPMS074, pp1344-1346.
- [6] L. Wang and G. Stupakov, “Transverse single bunch instability in PEP-X”, SLAC-PUB-13658, 2009.
- [7] A. Chao, *Physics of Collective Beam Instabilities in High Energy Accelerators*, Wiley-Interscience Publication, John Wiley & Sons, Inc., 1992.

BEAM-BASED IMPEDANCE MEASUREMENT TECHNIQUES *

V. Smaluk[†],

NLSLS-II, Brookhaven National Laboratory, USA

Abstract

Characterization of a vacuum chamber impedance is necessary to estimate stability conditions of a particle beam motion, to find a limit of the beam intensity and characteristic times of single-bunch and multi-bunch instabilities. For a new accelerator project, minimization of the impedance is now the mandatory requirement for the vacuum chamber design. For an accelerator in operation, the impedance can be measured experimentally using various beam-based techniques. The beam-impedance interaction manifests itself in measurable beam parameters, such as betatron tunes, closed orbit, growth rates of instabilities, bunch length and synchronous phase. The beam-based techniques developed for measurement of the longitudinal and transverse impedance are discussed, including theoretical basics and experimental results.

WAKE FUNCTIONS AND IMPEDANCES

In a theory of collective effects, the interaction of a particle beam with electromagnetic fields induced by the beam itself is described in terms of wake functions. These electromagnetic fields are called wake fields because they never propagate ahead of a relativistic particle. The wake function is defined as a normalized integral of the Lorentz force that acts on a test particle moving behind a leading particle which excites the wake fields. To analyze the beam stability in most practical cases, it is enough to consider only monopole longitudinal W_{\parallel} and dipole transverse W_{\perp} wake functions. The longitudinal wake function is obtained by integrating the electric field component E_z , which is parallel to the velocity \mathbf{v} ($|\mathbf{v}| = c$) of the particles moving on the same trajectory [1]:

$$W_{\parallel}(\tau) = -\frac{1}{q} \int_{-\infty}^{\infty} E_z(t, \tau) dt, \quad (1)$$

where q is the charge of leading particle, $\tau = s/c$, s is the distance between the leading and trailing particles, c is the speed of light. The dipole transverse wake function is determined similarly to the longitudinal one as an integral of transverse electromagnetic forces normalized by the dipole moment qr of the leading particle (r is the transverse offset); it is a vector with horizontal and vertical components:

$$\mathbf{W}_{\perp}(\tau) = -\frac{1}{qr} \int_{-\infty}^{\infty} [\mathbf{E}(t, \tau) + \mathbf{v} \times \mathbf{B}(t, \tau)]_{\perp} dt. \quad (2)$$

The longitudinal and transverse wake functions are related to each other by the Panofsky-Venzel theorem [1, 2].

For a beam with arbitrary charge distribution, its interaction with wake fields is described by the wake potential V , which is a convolution of the wake function W and the longitudinal charge density $\lambda(t)$:

$$V(\tau) = \int_0^{\infty} W(t) \lambda(\tau - t) dt, \quad (3)$$

where $\lambda(t)$ is normalized as $\int_{-\infty}^{\infty} \lambda(t) dt = 1$.

In the frequency domain, each part of the vacuum chamber is represented by a frequency-dependent impedance. Longitudinal Z_{\parallel} and transverse Z_{\perp} impedances are defined as Fourier transforms of the corresponding wake functions:

$$\begin{aligned} Z_{\parallel}(\omega) &= \int_{-\infty}^{\infty} W_{\parallel}(\tau) e^{-i\omega\tau} d\tau, \\ Z_{\perp}(\omega) &= i \int_{-\infty}^{\infty} W_{\perp}(\tau) e^{-i\omega\tau} d\tau. \end{aligned} \quad (4)$$

The main contributors to the total impedance of the vacuum chamber are: finite conductivity of the walls (resistive-wall impedance), variations of the chamber cross section, high-order modes of accelerating RF cavities, electrostatic pickup-electrodes, strip-lines, flanges, bellows, synchrotron radiation ports, etc. If there is no interference of the wake fields excited by the beam in different components of the vacuum chamber (the components are far away from each other or the wake fields are rapidly damping), the impedances are additive at any frequency. In this case, the total impedance of the vacuum chamber can be represented as a sum of impedances of its components. For almost any component of a vacuum chamber, the impedance can be approximated by equivalent resonators with proper resonance frequencies, shunt resistances and quality factors. Since a narrowband oscillation mode is more long-living than the broadband mode, the beam interaction with the narrowband impedance and with the broadband one can be analyzed separately. We can assert that the narrowband impedance leads to the bunch-by-bunch interaction and can result in multi-bunch instabilities, whereas the broadband impedance leads to the intra-bunch interaction and can cause single-bunch instabilities. The beam stability is analyzed using the computed impedance or its simplified representation by resonators and resistive-wall impedance calculated analytically.

To compute the impedance of complex components of vacuum chambers, 3D finite-difference simulation codes [3, 4] are used. These codes solve Maxwell equations with the boundary conditions determined by the chamber geometry. The fields are excited by a bunched beam with pre-defined charge distribution, usually Gaussian. The simulation code

* Work supported by DOE under contract No.DE-AC02-98CH10886.

[†] vsmaluk@bnl.gov

output is a wake potential (3) which is a convolution of the wake function and the longitudinal bunch profile. Taking into account that the convolution of two time-domain functions is equivalent to the product of their Fourier transforms, the impedance is calculated as

$$Z(\omega) = \frac{\tilde{V}(\omega)}{\tilde{\lambda}(\omega)}, \quad (5)$$

where \tilde{V} and $\tilde{\lambda}$ are the Fourier transforms of the wake potential and the longitudinal charge density, respectively. So the bandwidth of the impedance derived from the simulated wake potential is limited by the bunch spectrum width which is inversely proportional to the bunch length defined for the simulation. The mesh size of the solver is essential, it should be small enough to get reliable results for a given bunch spectrum. For a typical bunch length of few millimeters, full 3D simulation of wake fields in a big and complex structure is quite difficult because huge memory and processor time are required.

The beam-impedance interaction manifests itself in several effects of beam dynamics, some of these effects can be measured quite precisely using modern beam diagnostic instruments and measurement techniques.

LONGITUDINAL BROADBAND IMPEDANCE

For a beam-based measurement of longitudinal broadband impedance, we need to understand what can be measured. The measurable effects such as current-dependent bunch lengthening, synchronous phase shift, and energy spread growth due to microwave instability are dependent on integral parameters combining the impedance and the bunch spectrum. These parameters are the effective impedance and the loss factor. The normalized effective impedance $(Z_{\parallel}/n)_{\text{eff}}$ is defined as

$$\left(\frac{Z_{\parallel}}{n}\right)_{\text{eff}} = \frac{\sum_{p=-\infty}^{\infty} Z_{\parallel}(\omega_p) \frac{\omega_0}{\omega_p} h_l(\omega_p)}{\sum_{p=-\infty}^{\infty} h_l(\omega_p)}, \quad (6)$$

where $Z_{\parallel}(\omega)$ is the frequency-dependent longitudinal impedance, $n = \omega/\omega_0$ is the revolution harmonic number, $\omega_p = p\omega_0 + l\omega_s$, ω_0 is the revolution frequency, ω_s is the synchrotron frequency,

$$h_l(\omega) = (\omega\sigma_t)^{2l} e^{-\omega^2\sigma_t^2}, \quad (7)$$

is the spectral density of l -th Hermite mode (for a Gaussian bunch), $\sigma_t = \sigma_z/c$, σ_z is the bunch length. If the low-frequency longitudinal impedance is assumed as inductive, the normalized impedance Z_{\parallel}/n is frequency-independent.

The coherent loss ΔE of the beam energy caused by the beam-impedance interaction is

$$\Delta E = k_{\parallel} q^2, \quad (8)$$

where q is the bunch charge, k_{\parallel} is the loss factor

$$k_{\parallel} = \frac{\omega_0}{2\pi} \sum_{p=-\infty}^{\infty} Z_{\parallel}(\omega_p) h(\omega_p) = \frac{\omega_0}{\pi} \sum_{p=-\infty}^{\infty} \text{Re} Z_{\parallel}(\omega_p) h(\omega_p), \quad (9)$$

$h(\omega) = \tilde{\lambda}(\omega)\tilde{\lambda}^*(\omega)$ is the bunch power spectrum, $h(\omega) = e^{-\omega^2\sigma_t^2}$ for a Gaussian bunch. The second equality in (9) is valid because $\text{Re} Z_{\parallel}(-\omega) = \text{Re} Z_{\parallel}(\omega)$ and $\text{Im} Z_{\parallel}(-\omega) = -\text{Im} Z_{\parallel}(\omega)$. If $\sigma_t\omega_0 \ll 1$, the sum can be replaced with the integral:

$$k_{\parallel} = \frac{1}{\pi} \int_{-\infty}^{\infty} \text{Re} Z_{\parallel}(\omega) h(\omega) d\omega. \quad (10)$$

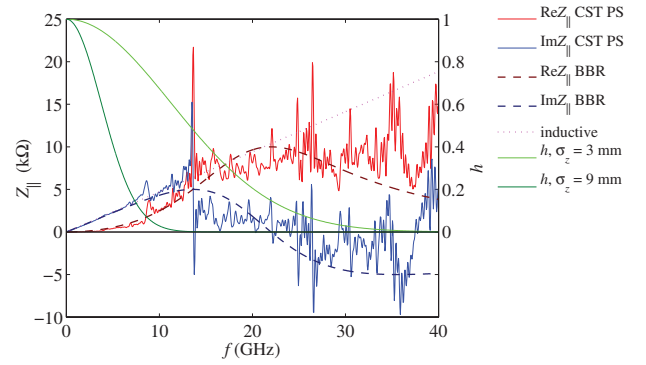


Figure 1: Longitudinal impedance and bunch spectra.

Figure 1 shows an example of the longitudinal impedance calculated by a 3D Maxwell equation solver CST Particle Studio together with a broadband resonator model and pure inductive impedance ($Z_{\parallel}/n = \text{const}$). The Gaussian bunch spectra are also shown for two bunch lengths: $\sigma_z = 3$ mm and $\sigma_z = 9$ mm. The measurable integral parameters, effective impedance and loss factor calculated using the simulated impedance and two simplified models are summarized in Table 1.

Table 1: Longitudinal Effective Impedance and Loss Factor

	$\sigma_z = 3$ mm		$\sigma_z = 9$ mm	
	$(Z_{\parallel}/n)_{\text{eff}}$ Ω	k_{\parallel} V/pC	$(Z_{\parallel}/n)_{\text{eff}}$ Ω	k_{\parallel} V/pC
Simulation	0.21	82	0.24	2.2
BBR	0.20	77	0.24	2.9
Inductive	0.25		0.25	

As one can see, the measurable single-bunch effects resulted from the beam interaction with a rather complex impedance such as the example shown in Figure 1 can be described with reasonable accuracy using a simple broadband resonator model. For longer bunches, even the simplest inductive model could be acceptable.

The reactive part of normalized effective impedance $\text{Im}(Z_{\parallel}/n)_{\text{eff}}$ can be estimated by measuring the r.m.s. bunch

length σ_t as a function of beam current I_b . The bunch length can be directly measured using a streak-camera, a dissector tube or, indirectly, by measuring the bunch spectrum width from a button-type pickup electrode. Interaction of a bunched beam with broadband impedance deforms the longitudinal bunch profile $\lambda(t)$, which is Gaussian for a zero-intensity bunch. At small beam currents, the energy spread of a relativistic electron beam is independent of its intensity and $\lambda(t)$ as a function of the average bunch current I_b can be described by the Haissinski integral equation [5]. The Haissinski equation can be solved numerically for a certain impedance model (i.e. broadband resonator) and the model parameters can be found by fitting the measured beam profile with the equation solution [6].

For a positive momentum compaction α , the intensity-dependent deformation of the longitudinal bunch profile $\lambda(t)$ causes the bunch lengthening, which can be approximately described by a cubic equation [7]:

$$\left(\frac{\sigma_t}{\sigma_{t0}}\right)^3 - \frac{\sigma_t}{\sigma_{t0}} = \frac{I_b \alpha}{\sqrt{2\pi} v_s^2 (\omega_0 \sigma_{t0})^3 E/e} \operatorname{Im}\left(\frac{Z_{\parallel}}{n}\right)_{\text{eff}}. \quad (11)$$

Formula (11) has been derived for the bunch lengthening of a relativistic electron or positron bunch caused by potential well distortion below the microwave instability threshold. The microwave instability results from the interaction between a large number of bunch oscillation modes growing and damping with their characteristic time constants. If the impedance can be considered as inductive, then to estimate the peak value of the threshold current I_p^{mwi} , the simple criterion [8] is applicable:

$$I_p^{\text{mwi}} = \frac{\alpha E/e}{|Z_{\parallel}/n|} \left(\frac{\Delta p}{p}\right)_{\text{FWHM}}^2, \quad (12)$$

where $\frac{\Delta p}{p} = \frac{\gamma^2}{\gamma^2-1} \frac{\Delta E}{E}$ is the momentum spread, which is equal to the energy spread $\Delta E/E$ for ultra-relativistic ($\gamma \gg 1$) beams.

The dynamics of longitudinal motion above the microwave instability threshold is characterized by the energy spread growth and a turbulent bunch lengthening with the beam current increase. The relative energy spread $\delta \equiv \sigma_E/E$ can be estimated from a measured transverse beam size which is determined by the combination of betatron and synchrotron contributions:

$$\sigma_x^2 = \beta_x \varepsilon_x + (\eta_x \delta)^2, \quad (13)$$

where β_x is the beta function, ε_x is the transverse emittance, η_x is the dispersion. The transverse beam size is usually measured by a visible light monitor or a pin-hole X-ray camera located in a dispersive section.

Figure 2 shows an example of the measured bunch length (upper plot) and energy spread (lower plot) as functions of the beam current, the measurement was done at APS [9]. As one can see, it is practically impossible to find the microwave instability threshold from the bunch lengthening although

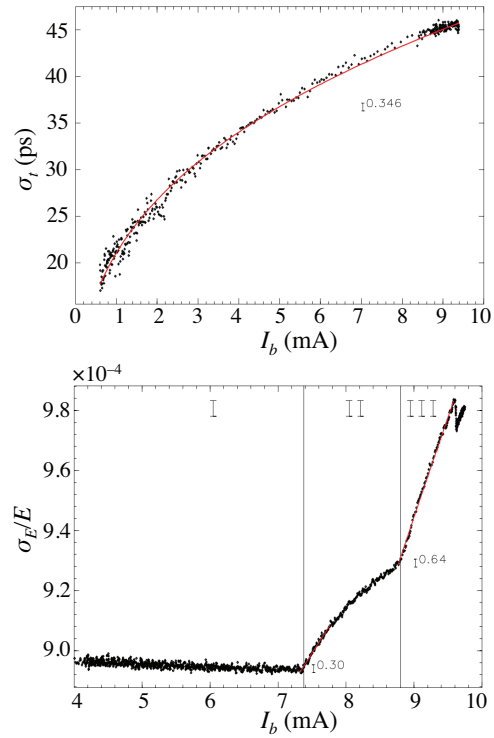


Figure 2: Measured bunch length (upper plot) and energy spread (lower plot) as functions of the beam current.

it is clearly visible on the energy spread graph, this is also confirmed by numerical simulations [10]. This means that formula (11) could be useful to fit the bunch lengthening even if the beam current exceeds the microwave instability threshold.

The coherent energy loss is compensated in the accelerating RF cavities every beam turn, as well as the energy loss caused by synchrotron radiation. The coherent energy loss leads to the current-dependent shift $\Delta\phi_s$ of the synchronous phase, which can be derived from the energy balance of the bunch:

$$\Delta\phi_s = \frac{I_b k_{\parallel}}{f_0 V_{\text{RF}} \cos \phi_{s0}}, \quad (14)$$

where V_{RF} is the RF voltage, ϕ_{s0} is the synchronous phase at zero current. The phase shift is proportional to the beam current I_b and the loss factor k_{\parallel} , which in turn depends on the bunch length growing with the beam current, so the phase shift as a function of the beam current is non-linear. For small beam current, we can neglect the bunch lengthening and, with this approximation, the phase shift $\Delta\phi_s$ can be assumed proportional to the zero-current loss factor.

The current-dependent shift of synchronous phase can be measured directly using synchrotron light diagnostics (streak camera, dissector tube) or RF system diagnostics. To reduce the systematic error resulted from the drift or jitter of the diagnostic instruments, the two-bunch technique is useful. The longitudinal profiles of two bunches are measured simultaneously, one bunch has variable intensity, whereas

the other bunch with a fixed intensity is the reference. Figure 3 shows an example of two bunch profiles measured by a streak camera.

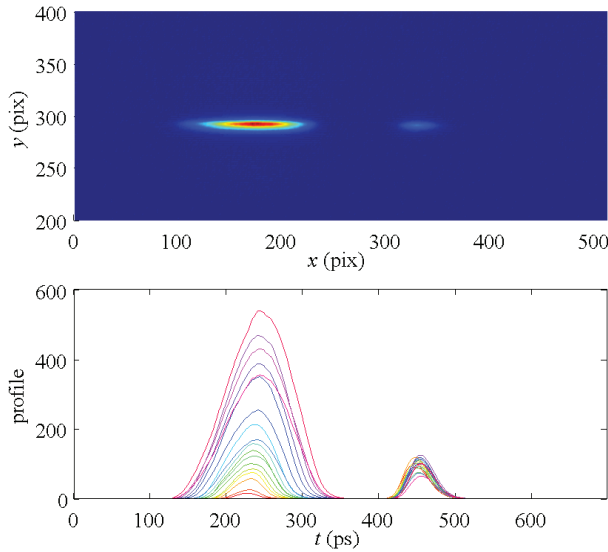


Figure 3: Reference bunch technique: bunch profile measured by a streak camera.

The other measurement technique is based on measuring the closed orbit deviation caused by the coherent energy loss [11]. If the dispersion and its derivation is zero in the accelerating RF cavities, the orbit deviation $x(s)$ can be assumed proportional to the dispersion $\eta(s)$:

$$x(s) \approx \eta(s)\delta_c(s). \quad (15)$$

The relative energy loss per particle $\delta_c \equiv \Delta E/E$ is distributed along the ring as

$$\delta_c(s) = \frac{q}{E/e} \int_{s_{\text{RFC}}}^s k'_{\parallel}(\zeta) d\zeta, \quad (16)$$

and the orbit deviation caused by this energy loss, when the beam current $I_b = qf_0$ is changed by ΔI_b , is:

$$\Delta x(s) \approx \eta(s) \frac{\Delta I_b}{f_0 E/e} \int_{s_{\text{RFC}}}^s k'_{\parallel}(\zeta) d\zeta, \quad (17)$$

where k'_{\parallel} is the specific loss factor per length unit of the beam orbit, s_{RFC} is the position of the accelerating RF cavity. The loss factor k_{\parallel} can be estimated by measuring the closed orbit deviation as a function of the beam intensity [12]:

$$k_{\parallel} = \frac{f_0}{\Delta I_b} \frac{E}{e} \frac{\Delta x(s)}{\eta(s)}. \quad (18)$$

If the RF cavities are located in several places, this method can be used to measure the longitudinal loss factor of a section between the cavities. For every modern synchrotron,

high-precision beam position monitors (BPMs) are now a standard component of beam diagnostics, so the beam orbit can be measured very precisely.

An example of the measured deviations of the horizontal and vertical orbits depending on the beam current is presented in Figure 4 [13]. Before the measurement, the orbit was corrected globally to minimize the influence of the transverse impedance. The intensity-dependent errors of the BPMs introduce a systematic error in the measurement results. We can assume that this error is of the same order for both horizontal and vertical planes. So, taking the vertical orbit deviation, which is less than 10% of the horizontal one (see Figure 4), and assuming zero dispersion in the vertical plane, we can conclude that the BPM-caused errors does not exceed 10%.

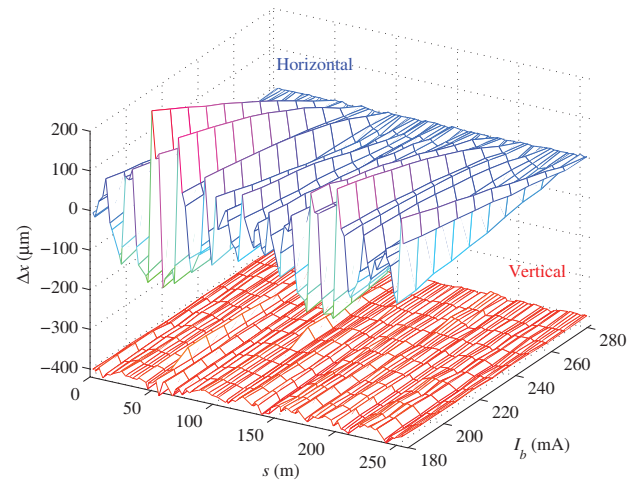


Figure 4: Orbit deviation as a function of beam current.

TRANSVERSE BROADBAND IMPEDANCE

For the transverse broadband impedance, the measurable effects are current-dependent shift of betatron tunes and rising/damping time of chromatic head-tail effect. Similar to the longitudinal impedance case, these effects are dependent on integral parameters combining the impedance and the bunch spectrum: transverse effective impedance and dipole kick factor. The transverse effective impedance $Z_{\perp\text{eff}}$ is defined as

$$Z_{\perp\text{eff}} = \frac{\sum_{p=-\infty}^{\infty} Z_{\perp}(\omega_p) h_l(\omega_p - \omega_{\xi})}{\sum_{p=-\infty}^{\infty} h_l(\omega_p - \omega_{\xi})}, \quad (19)$$

where $Z_{\perp}(\omega)$ is the frequency-dependent transverse impedance, $\omega_p = p\omega_0 + \omega_{\beta} + l\omega_s$, $h_l(\omega)$ is the spectral density of l -th Hermite mode (7), $\omega_{\xi} = \xi\omega_0/\alpha$, $\xi = dv_{\beta}/(dE/E)$ is the chromaticity, $\omega_{\beta} = v_{\beta}\omega_0$ is the betatron frequency.

The transverse dipole kick $\Delta x'$ caused by the beam-impedance interaction is

$$\Delta x' = \frac{q}{E/e} k_{\perp} x, \quad (20)$$

where x is the beam transverse offset, k_{\perp} is the dipole kick factor

$$k_{\perp} = \frac{\omega_0}{2\pi} \sum_{p=-\infty}^{\infty} Z_{\perp}(\omega_p) h(\omega_p) = \frac{\omega_0}{\pi} \sum_{p=-\infty}^{\infty} \text{Im} Z_{\perp}(\omega_p) h(\omega_p), \quad (21)$$

$h(\omega)$ is the bunch power spectrum. If $\sigma_t \omega_0 \ll 1$, the sum can be replaced with the integral:

$$k_{\parallel} = \frac{1}{\pi} \int_{-\infty}^{\infty} \text{Im} Z_{\perp}(\omega) h(\omega) d\omega. \quad (22)$$

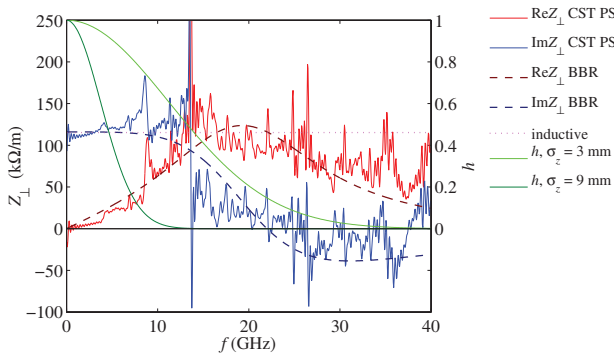


Figure 5: Transverse impedance and bunch spectra.

Figure 5 shows an example of the transverse impedance: result of wake field simulation, a broadband resonator model, and a pure inductive impedance ($Z_{\perp} = \text{const}$). The Gaussian bunch spectra are also shown for two bunch lengths: $\sigma_z = 3$ mm and $\sigma_z = 9$ mm. The measurable integral parameters, transverse effective impedance and dipole kick factor calculated using the simulated impedance and the simplified models are summarized in Table 2. As one can see, the measurable transverse single-bunch effects can be also described using the simplified models such as broadband resonator or pure inductive impedance for longer bunches.

Table 2: Transverse Effective Impedance and Kick Factor

	$\sigma_z = 3$ mm		$\sigma_z = 9$ mm	
	$Z_{\perp \text{eff}}$ $k\Omega/m$	k_{\perp} $V/(pC m)$	$Z_{\perp \text{eff}}$ $k\Omega/m$	k_{\perp} $V/(pC m)$
Simulation	101	2836	117	1083
BBR	97	2710	116	1075
Inductive	115		115	

Interaction of a bunched beam with short-range wake fields characterized by the broadband impedance, results in

the transverse mode coupling. The wake fields induced by the bunch head act on particles of its tail part (a head-tail effect) and the head and tail of the bunch exchange places periodically due to synchrotron oscillations. If the chromaticity is zero, a fast head-tail instability occurs when the beam current exceeds a certain threshold. In the frequency domain, the instability threshold is reached when the coherent (center-of-mass) mode is coupled with the lowest (-1) head-tail mode. If the chromaticity is non-zero, a chromatic head-tail effect occurs. The coherent mode damps upon the positive chromaticity and becomes unstable when the latter is negative, and the higher-order head-tail modes behave oppositely. The rising/damping rates decrease rapidly with the mode number, and the higher-order modes are usually not dangerous for beam stability, since they are suppressed by the radiation damping. Since only a few of the lowest modes are essential, the eigenmode analysis is quite efficient for study of the head-tail effect. The complex frequency $\Omega = \omega + i/\tau$ of l -th head-tail mode can be found solving the eigenvalue problem [14]

$$\det \left[\left(\frac{\Omega - \omega_{\beta}}{\omega_s} - l \right) \mathbf{I} - \mathbf{M} \right] = 0, \quad (23)$$

where ω_{β} is the unperturbed betatron frequency, τ is the rising/damping time, \mathbf{I} is the unity matrix. The matrix elements are

$$M_{lk'} = I_b \frac{\beta}{2\gamma_s E/e} \sum_{p=-\infty}^{\infty} Z_{\perp}(\omega_p) g_{lk}(\omega_p - \omega_{\xi}) g_{lk'}(\omega_p - \omega_{\xi}), \quad (24)$$

where β is the average beta function. The functions g_{lk} characterizing oscillation modes of the Gaussian bunch are:

$$g_{lk}(\omega) = \frac{1}{\sqrt{2\pi} k! (|l| + k)!} \left(\frac{\omega \sigma_t}{\sqrt{2}} \right)^{|l|+2k} \exp\left(-\frac{\omega^2 \sigma_t^2}{2}\right). \quad (25)$$

If the frequency shift of coherent (0-th) mode is small compared with the synchrotron frequency ω_s , the linear approximation [14] is applicable:

$$\frac{d\Omega}{dI_b} = i \frac{\beta Z_{\perp}^{\text{eff}}}{4\sqrt{\pi} \sigma_t E/e}. \quad (26)$$

If the chromaticity is positive, the frequency shift $\Delta\omega = \text{Re}\Omega - \omega_{\beta}$ and chromatic damping time $\tau = 1/\text{Im}\Omega$ of the coherent ($l = 0$) mode can be obtained by spectral analysis of beam oscillations registered by a turn-by-turn beam position monitor. Figure 6 shows the current-dependent shift of vertical betatron tune $\nu_y = \omega_y/\omega_0$ (upper plot) and damping rate $1/\tau_y$ (lower plot) [6]. The measured values are shown by blue points with errorbars, red lines represent the eigenvalues of (23) calculated for 3 values of chromaticity according to the measurements, the green lines represent the tracking results. The betatron tune graphs corresponding to different values of chromaticity are manually separated for better visibility.

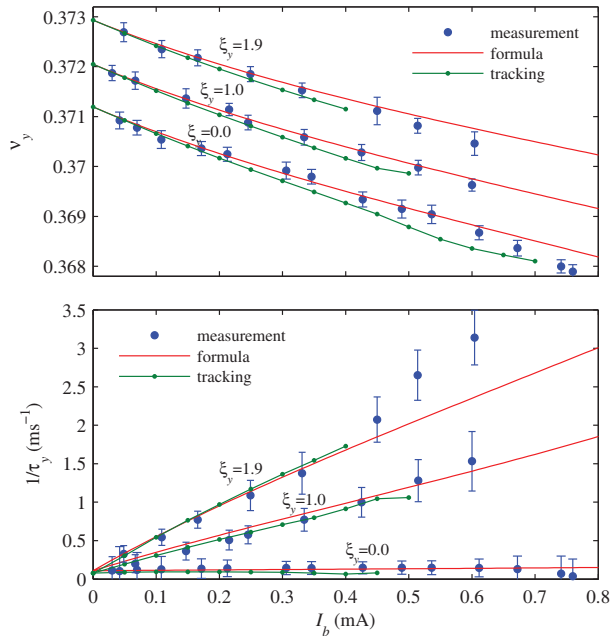


Figure 6: Vertical betatron tune ν_y (upper plot) and damping rate $1/\tau_y$ (lower plot) vs bunch current I_b . Measurement, formula and tracking.

LOCAL IMPEDANCE

Measurement of the betatron phase advance along the ring allows determining the contributions of different sections of the vacuum chamber into the coherent shift of betatron tune. In such a way, one can obtain the azimuthal distribution of the transverse impedance [12].

$$\Delta\mu(s) = -\frac{\Delta I_p}{8\pi C E/e} \int_0^s \beta(\zeta) \text{Im}Z_{\perp}(\zeta) d\zeta, \quad (27)$$

where I_p is the peak bunch current ($I_p = \frac{\sqrt{2\pi}}{\omega_0 \sigma_t} I_b$ for a Gaussian bunch), C is the ring circumference. Accuracy of this technique is determined by the single-turn resolution of the beam position monitors, the signals of which are used to calculate the betatron phase. A typical coherent betatron tune shift is of the order of 0.001 per 1 mA of the beam current and the BPM-to-BPM phase advance is much smaller, so this technique requires very good turn-by-turn resolution of BPMs.

The orbit bump technique [15, 16] is more sensitive because the BPMs are used in the narrowband orbit mode rather than in the broadband turn-by-turn mode and the noise is much smaller. This technique is based on the fact that an off-axis beam passing through the vacuum chamber section with a non-zero transverse impedance is deflected by the wake-fields. The beam-impedance interaction results in the transverse kick x' (20) proportional to the bunch charge q and its transverse position x at the location of the transverse impedance. If two closed orbits are measured with different

beam intensity, the orbit deviation is:

$$\Delta x(s) = \frac{\Delta q}{E/e} k_{\perp} x_0 \frac{\sqrt{\beta(s)\beta(s_0)}}{2 \sin \pi \nu} \cos(|\mu(s) - \mu(s_0)| - \pi \nu), \quad (28)$$

where x_0 is the orbit bump height, s_0 is the transverse impedance location, Δq is the bunch charge variation, ν is the betatron tune, β is the beta function, and μ is the betatron phase advance. This wave-like orbit deviation can be measured using beam position monitors, and the wave amplitude is proportional to the kick factor at the bump location. To reduce the systematic error caused by intensity-dependent behavior of the BPM electronics, this error is also measured and then subtracted. First of all, after the initial correction of the orbit to zero, two reference orbits x_{01} and x_{02} are measured at the high and low values of beam current. Then, after creating the orbit bump, again two orbits x_1 and x_2 are measured at the same beam current values. In the four-orbit combination $\Delta x = (x_2 - x_1) - (x_{02} - x_{01})$, the systematic error is eliminated, as well as the bump itself.

Rapid evolution of BPM electronics allows us to improve much the sensitivity of this technique. Now we can measure the orbit deviation of the order of several micrometers [17] compared to 100 micrometers orbit deviation measured at the very beginning of the bump method development [15], see examples in Figure 7.

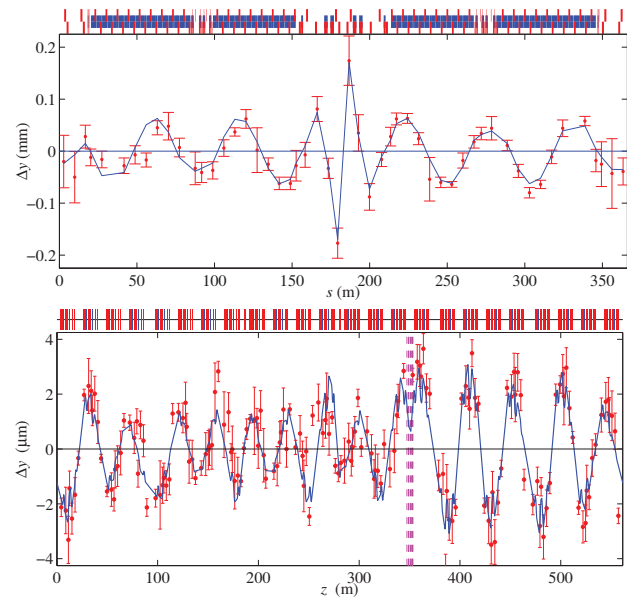


Figure 7: Measured orbit waves caused by a local impedance. Upper plot: VEPP-4M, 1998, lower plot: Diamond Light Source, 2014

To measure the impedance of a vacuum chamber component with variable geometry such as beam scrapers or in-vacuum undulators, both orbit and turn-by-turn techniques are effective. Using the reference bunch technique and high-precision BPMs, a contribution of the movable element to

the total shift of betatron frequency (26) can be measured quite accurately [18].

TRANSVERSE NARROWBAND IMPEDANCE

The motion of a multi-bunch train can be expanded in Fourier series, so we describe the motion in terms of multi-bunch modes. For a uniform fill pattern, if every RF bucket is occupied by a bunch with the same bunch current I_b , M bunches correspond to M modes, where M is the RF harmonic number. Without bunch-to-bunch interaction all bunches oscillate independently with the betatron frequency ω_β . Transverse multi-bunch instability is driven by long-range wake fields (narrowband impedance), usually trapped modes in cavity-like strictures in the vacuum chamber or resistive-wall impedance. If the bunches are coupled by the wake fields, each bunch oscillates with the frequency Ω , which becomes complex. For M bunches with finite length and internal modes, the complex frequency shift $\Delta\Omega = \Omega - \omega_\beta$ of the mode n is [14]:

$$\Delta\Omega_n = -\frac{i}{4\pi} \frac{\omega_0\beta}{E/e} MI_b \sum_{p=-\infty}^{\infty} Z_{\perp}(\omega_{pn}) h_l(\omega_{pn} - \omega_{\xi}), \quad (29)$$

where $\omega_{pn} = (pM + n)\omega_0 + \omega_\beta + l\omega_s$. The coherent frequency shift and growth rate are $\text{Re}\Delta\Omega$ and $\text{Im}\Delta\Omega$, respectively.

Almost all modern synchrotrons are equipped with transverse multi-bunch feedback systems (TMBF). These systems can be used as powerful beam diagnostic instruments. Using TMBF, we can excite the mode n by a stripline kicker driven at the frequency $\omega_{pn} = (pM + n)\omega_0 + \omega_\beta$, then stop the excitation and measure free oscillations (damped or anti-damped) and finally run the feedback to suppress any residual oscillation.

Figure 7 shows an example of vertical damping rates measured at Diamond light source [19]. The fit curve is calculated using formula (29). The resistive-wall impedance is calculated with the analytical formula

$$\frac{Z_y^{\text{rw}}(\omega)}{L} = (\text{sign}\omega + i) \frac{Z_0\delta_s(\omega)}{2\pi b^3} G_{1y}, \quad (30)$$

where $\delta_s(\omega)$ is the skin depth

$$\delta_s(\omega) = \sqrt{\frac{2c}{\mu_r\sigma_c Z_0|\omega|}}, \quad (31)$$

c is the speed of light, μ_r and σ_c are the relative permeability and conductivity of the chamber material, respectively; Z_0 is the free space impedance; b is the half-aperture, G_{1y} is the form-factor for an elliptical vacuum chamber [20]. The resonance peaks are fitted by narrowband resonators

$$Z_{\perp}^{\text{res}}(\omega) = \frac{\omega_r}{\omega} \frac{R_s}{1 + iQ\left(\frac{\omega}{\omega_r} - \frac{\omega_r}{\omega}\right)}, \quad (32)$$

where R_s is the shunt impedances, ω_r is the resonance frequency, and Q is the quality factor. Two of these resonances ("3" and "4" shown in Figure 8) can be attributed to the in-vacuum undulators. The effect of the undulator gaps closing was observed on the damping rates including both geometric impedance and contribution to the resistive wall impedance. Three other peaks ("1", "2", and "5") can be likely attributed to the beam position monitors (BPMs), this conclusion is based on comparison of the resonators fitting the measured data with the impedance obtained from wake field simulations.

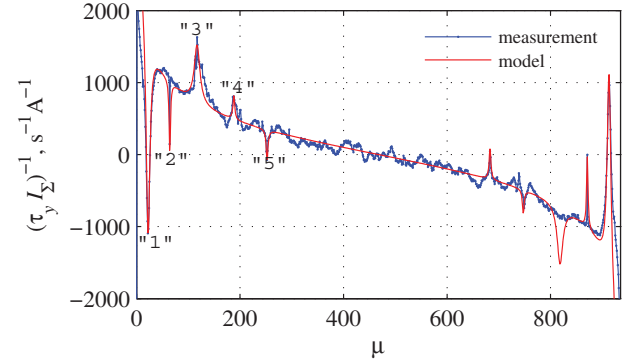


Figure 8: Vertical damping rates normalized by the beam current after subtraction of radiation damping (measured data in blue, fit in red).

CONCLUSION

Knowledge of impedances is necessary to understand collective effects of beam dynamics in accelerators. The most significant result of the collective effects is instability of longitudinal or transverse motion leading to deterioration of the beam quality or even to beam loss. Studies of collective effects are important both for designing new accelerators and for understanding the beam dynamics in the accelerators in operation. Calculation of impedance budget is an essential stage of a new accelerator design. There is a limited number of analytical formulae to calculate impedances of simplest vacuum chamber components but real vacuum chambers of modern accelerators usually have a complex geometry. Practically, finite-difference simulation codes are used for estimation of the impedance budgets. The problem is that the wake function is not calculated directly, the simulation code output is a wake potential which is a convolution of the wake function with longitudinal bunch profile. So the bandwidth of the impedance derived from the simulated wake potential is limited by the bunch spectrum width which is usually limited by computing capabilities. The impedance of an accelerator in operation can be studied experimentally using beam-based methods because the beam-impedance interaction manifests itself in various physical effects. The total frequency-dependent impedance is usually very complex so it is practically impossible to obtain its fine structure from the beam-based measurements. The measurable values

are integral parameters combining the impedance and the bunch spectrum, such as effective impedance, longitudinal loss factor or transverse kick factor. Using these measured parameters, simplified impedance models are usually developed to characterize and predict collective effects of beam dynamics.

REFERENCES

- [1] B.W. Zotter and S.A. Kheifets, *Impedances and Wakes in High-Energy Particle Accelerators*, Singapore: World Scientific, 1998.
- [2] W.K.H. Panofsky, W.A. Wenzel, *et al.*, "Some considerations concerning the transverse deflection of charged particles in radio-frequency fields", *Rev. Sci. Instrum.*, vol. 27, p. 967, 1956.
- [3] W. Bruns, *The GdfidL Electromagnetic Field simulator*, <http://www.gdfidl.de/>
- [4] Computer Simulation Technology, *CST Particle Studio*, <http://www.cst.com/Products/CSTPS>
- [5] J. Haissinski, "Exact Longitudinal Equilibrium Distribution of Stored Electrons in the Presence of Self-Fields", *Nuovo Cimento*, vol. 18B, No. 1, 1973.
- [6] V. Smaluk, I. Martin, R. Fielder, R. Bartolini, "Beam-based model of broadband impedance of the DIAMOND Light Source", *Phys. Rev. ST Accel. Beams*, Vol. 18, 064401 (2015).
- [7] B. Zotter, "Potential-Well Bunch Lengthening", Rep. CERN SPS/81-14 (DI), Geneva, Switzerland, 1981.
- [8] D. Boussard, "Observation of Microwave Longitudinal Instabilities in the SPS", Rep. CERN II/RF/Int.75-2, Geneva, 1975.
- [9] Y.-C. Chae *et al.*, "Measurement of the Longitudinal Microwave Instability in the APS Storage Ring", in *Proc. PAC'01*, Chicago, USA, June 2001, paper TPPH068, pp. 1817-1819.
- [10] A. Blednykh *et al.*, "A Numerical Study of the Microwave Instability at APS", in *Proc. NA-PAC'2016*, Chicago, October 2016, paper TUPOB51.
- [11] J.P. Koutchouk, "Trajectory and closed orbit correction", Rep. CERN LEP-TH/89-2, Geneva, Switzerland, 1989.
- [12] D. Brandt *et al.*, "Measurement of Impedance Distribution and Instability Threshold in LEP", in *Proc. PAC'95*, Dallas, Texas, USA, May 1995, paper RAA20, pp. 570-572.
- [13] E. Karantzoulis, V. Smaluk, L. Tosi, "Broad Band Impedance Measurements on the Electron Storage Ring ELETTRA", *Phys. Rev. ST Accel. Beams*, Vol. 6, 030703 (2003).
- [14] A. Chao, *Physics of Collective Beam Instabilities*, Wiley, New York, 1993.
- [15] V. Kiselev, V. Smaluk, "Experimental Study of Impedances and Instabilities at the VEPP-4M Storage Ring", in *Proc. EPAC'98*, Stockholm, Sweden, June 1998, paper THP09F, pp. 1005-1007.
- [16] V. Kiselev, V. Smaluk, "Measurement of Local Impedance by an Orbit Bump Method", *Nucl. Instr. and Meth. A* 525 (2004).
- [17] V. Smaluk *et al.*, "Coupling impedance of an in-vacuum undulator: Measurement, simulation, and analytical estimation", *Phys. Rev. ST Accel. Beams*, Vol. 17, 074402 (2014).
- [18] B. Podobedov *et al.*, "Novel Accelerator Physics Measurements Enabled by NSLS-II RF BPM Receivers", in *Proc. IBIC2016*, Barcelona, Spain, 2016, paper TUCL02.
- [19] R. Bartolini *et al.*, "Analysis of Multi-bunch Instabilities at the Diamond Storage Ring", in *Proc. IPAC'16*, Busan, Korea, May 2016, paper TUPOR013, pp. 1685-1687.
- [20] R.L. Gluckstern, J. van Zeijts, B. Zotter, "Coupling Impedance of Beam Pipes of General Cross Section", *Phys. Rev. E* vol. 47 No. 1, 1993.

ELECTRON CLOUD AND ION EFFECTS AND THEIR MITIGATION IN FCC-ee

K. Ohmi, M. Tobiyama, H. Fukuma
KEK, 1-1 Oho, Tsukuba, 305-0801, Japan

Abstract

High current and high repetition beam causes electron cloud and ion build-up, which result in two stream type of instability. We discuss build-up of electron cloud and ion, and related instabilities in FCC-ee. Latest result of ion instability in SuperKEKB is reported.

INTRODUCTION

Electron cloud and ion effects in FCC-ee is presented in this paper. These effect is serious for storage rings operated with high current and high repetition beam. FCC-ee is designed so that total synchrotron radiation loss is 50 MW. The effects in FCC-ee Z is most serious, because bunches are stored every 2.5 or 7.5 ns with total current of 1.45 A. In high energy FCC-ee; H and t options, the number of bunch is limited by hundreds due to the total radiation loss. These instability is less serious in W, H and t options.

Ion effects in SuperKEKB is discussed, while electron cloud effects in SuperKEKB is discussed in Ref. [1].

ELECTRON CLOUD EFFECTS

We first evaluate threshold of fast head-tail instability caused by electron cloud, and then how the electron cloud build-up compare with the threshold value.

Threshold of Electron Density for Fast Head-Tail Instability

The fast head-tail instability is caused by the electron cloud moving in a positron bunch with a frequency

$$\omega_e = \sqrt{\frac{\lambda_p r_e c^2}{\sigma_y (\sigma_x + \sigma_y)}}, \quad (1)$$

where λ_p is a positron line density in a bunch, namely $\lambda_p = N_p / (\sqrt{2\pi} \sigma_z)$. Beam, which is modulated by the electron oscillation, experiences the fast head-tail instability above a threshold density of the electrons. The threshold density of electron cloud is expressed by [2]

$$\rho_{e,th} = \frac{2\gamma v_s \omega_e \sigma_z / c}{\sqrt{3} K Q r_e \langle \beta_y \rangle L}, \quad (2)$$

where $K = \omega_e \sigma_z / c$ and $Q = \min(\omega_e \sigma_z / c, 7)$. Table 1 shows beam parameters, the frequency in Eq.(1) and the threshold density in Eq.(2) for FCC-ee.

Coherent Head-Tail Instability in the Simulation

The fast head-tail instability caused by the electron cloud is simulated by a code ‘‘PEHTS’’ [3]. Electrons with a density

distribution are placed in a beam line, and interaction with beam is calculated in every passage of a bunch. The bunch is transferred by a revolution matrix for the next interaction. Figure 1 shows evolution of the vertical beam size and the beam-electron centroid along a bunch after 500 turns at the electron density $\rho_e = 1.0 \times 10^{10} \text{ m}^{-3}$. The threshold density in the simulation, $\rho_{e,th,sim} = 0.8 \times 10^{10} \text{ m}^{-3}$, agrees with that in Table 1.

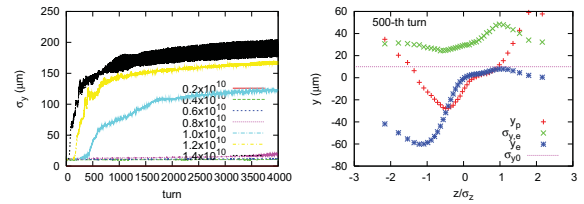


Figure 1: Evolution of the vertical beam size (left) and beam-electron centroid along a bunch after 500 turn (right).

Electron Cloud Build-up

We next discuss how high density of the electron cloud is built-up. The electron cloud is formed by photo-electrons and their secondary electrons. Photon production rate per revolution per positron is given by

$$n_\gamma = \frac{5}{2\sqrt{3}} \frac{\alpha \gamma}{\rho_{bend}}, \quad (3)$$

where $\alpha = 1/137$ is the fine structure constant. The critical energy is

$$u_c = \frac{3\hbar c}{2} \frac{\gamma^3}{\rho_{bend}}. \quad (4)$$

Electrons are created by photons hitting a chamber wall with a quantum efficiency around $Y_1 \approx 0.1$. Electron production by a bunch per meter passage is given by

$$n_{e,1} = n_\gamma Y_1 N_p \quad (5)$$

For FCC-ee-Z, $\rho_{Bend} = 11.3 \text{ km}$ and $N_+ = 3.3 \times 10^{10}$, the electron production is $n_{e,1} = 1.8 \times 10^8 \text{ m}^{-1}$. Assuming the chamber cross section of 0.005 m^2 , increment of the electron density by a bunch passage is $\Delta\rho_e = 3.5 \times 10^{10} \text{ m}^{-3}$. This density after a passage of a bunch is already 4.4 times higher than the threshold $\rho_{e,th} = 0.8 \times 10^{10} \text{ m}^{-3}$ in Table. 1. An ante-chamber protect the density increment, because most of electrons are produced at the chamber slot. The effective increment of the density near the beam is order of 1% of the above value. Secondary emission amplifies the electrons even the number of initial electrons are small. To evaluate the electron density more precisely, a simulation in which

Table 1: Parameters for Electron cloud instability.

Parameter		CEPC	FCC-ee-Z	FCC-ee-W	FCC-ee-H	FCC-ee-t
Energy	E (GeV)	120	45.5	80	120	175
Bunch population	$N_{\pm}(10^{10})$	37.1	3.3	6	8	17
Number of bunch	N_b	50	90300	5162	770	78
Beam size	σ_x/σ_y (μm)	583/32	95/10	164/10	247/11	360/16
Bunch length	σ_z (mm)	2.6	5	3	2.4	2.5
Averaged vert. beta	β_y (m)	50	100	100	100	100
Synchrotron tune	ν_z	0.216	0.015	0.037	0.056	0.075
Electron frequency	$\omega_e/2\pi$ (GHz)	137	127	171	174	171
Electron osc. period	$\omega_e\sigma_z/c$	7.5	13	11	8.7	9.0
Threshold density	$\rho_{e,th}$ (10^{10} m^{-3})	104	0.8	3.4	7.7	15

electron motion is simulated with considering beam force and magnetic field, is used.

Electron cloud build-up is simulated using a code ‘‘PEI’’ [4] for FCC-ee. Maximum secondary emission yield is assumed $Y_{2,max} = 1.8$ at $E_e = 300$ eV. This number is somewhat pessimistic. The best number is around $Y_{2,max} \sim 1$. Figure 2 shows the electron line density in every passages of bunches. For uniform distribution, the electron density is given by dividing the chamber cross section. Actually the electron density near the beam is several or 10 times higher than the averaged density. The central density m^{-3} is estimated to be 10^3 times larger than the line density m^{-1} . Top left plot in Fig.2 depicts the electron density for FCC-ee-Z. The density is several times 10^{13} m^{-3} . Even if the density is reduced by 1% using the antechamber, it is difficult to achieve the threshold density $0.8 \times 10^{10} \text{ m}^{-3}$. Very careful cure is necessary, for example, using weak magnets, grove, coating and so on. Top right plot depicts the electron density for W. The density is 10 times higher than the threshold. 1/10 reduction of electron cloud is not difficult. In FCC-ee-W the electron cloud effects are critical, but are manageable. In H and t, the density is lower than the threshold; they are safe for the instability.

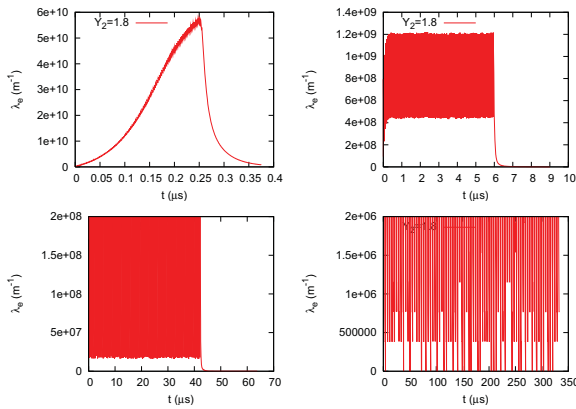


Figure 2: Electron cloud build-up in FCC-ee. Top left, right, bottom left and right are given for Z, W, H and t, respectively.

CEPC is designed as a single ring collider. To get gain in a Z factory, a partial double ring is proposed. Bunches

are injected in a train with the length of 3,000 m. Bunch spacing is much narrower than that with uniform filling in the initial design. In Higgs operation, a bunch train contains 50 bunches with 50 m spacing. Figure 3 shows electron cloud build-up for $Y_{2,max} = 1.8$ and 2.2. The density is $\rho_e \sim 1 \times 10^{12}$ and 4×10^{13} for $Y_{2,max} = 1.8$ and 2.2, respectively, where $\rho_{e,th} = 1 \times 10^{12} \text{ m}^{-3}$. The electron cloud instability may be critical, but not very serious for H.

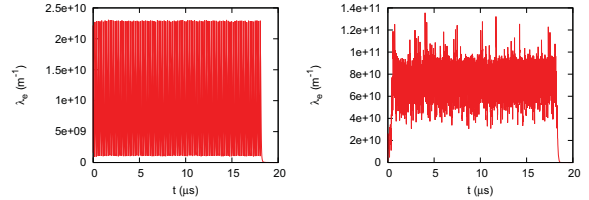


Figure 3: Electron cloud build-up in CEPC. A bunch train contains 50 bunches with 50 m spacing.

ION INSTABILITY

Ion instability can be serious in high current and high repetition electron storage rings [5]. Ions, which are trapped in a electron bunch train, oscillate with a frequency

$$\omega_{i,x/y} = \sqrt{\frac{\lambda_e r_i c^2}{\sigma_{x/y}(\sigma_x + \sigma_y)}}, \quad (6)$$

where the ion frequency is far slower than that of electrons, because $r_i = e^2/(4\pi\epsilon_0 M_i c^2)$ is smaller than r_e due to the mass ratio m_e/M_i . The oscillation is not inside a bunch, but is along a bunch train. The electron line density is now that of the bunch train, $\lambda_e = N_e/L_{Sp}$.

There is no stabilization due to the synchrotron oscillation. The bunch train is basically unstable for ion instability; no threshold exists. The threshold is determined by other damping mechanisms like head-tail damping, feedback damping time, and so on.

A simulation code based on a rigid bunch model has been used for studying the ion instability in both of trapping and fast instability [7].

Ion Instability in FCC-ee-Z

We focus on the Z factory. FCC-ee uses 400MHz cavities, thus bunch spacing is 2.5 ns. Using parameters in Table 1, the ion frequency is given by $\omega_i = 2\pi \times 87$ MHz and $\omega_i L_{sp}/c = 1.4$, where $\beta_{xy} = 50$ m. The horizontal beam size is assumed to be $\sigma_x = \sqrt{2\varepsilon_x \beta_x}$ by taking into account of dispersion. The number $\omega_i L_{sp}/c = 1.4$ is critical to judge whether ions are trapped or not in the bunch train. A simulation based on a rigid bunch model [7] is performed. The simulation calculates betatron amplitude of every bunches interacting with an ion cloud in turn-by-turn. The betatron amplitude grows when the ion instability arises, while the bunch-by-bunch feedback, which is implemented in the simulation, suppress the betatron oscillation. Figure 4 shows the growth of the vertical betatron amplitude due to the ion instability. 100, 200, 400 and 800-th bunch. Ions are kept and drift after interaction with the end of bunch train. Top left depicts growth of the ion instability. The growth time is around 20 turns. Top right and bottom plots shows the growth with the bunch-by-bunch feedback with the damping time 10 and 50 turns, respectively. The betatron motion is suppressed by the feedback with 10 turns of damping time, but not suppressed by that with 50 turn.

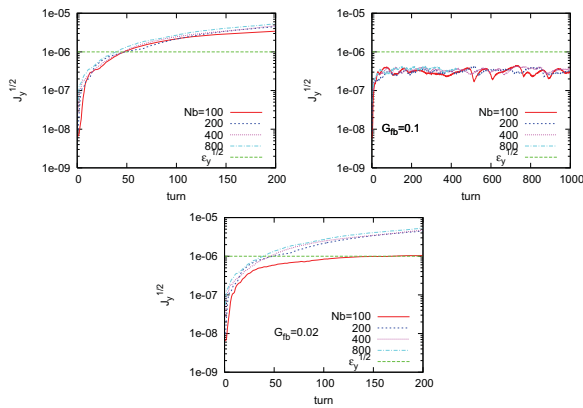


Figure 4: Evolution of the vertical betatron amplitude of 100,200,400 and 800-th bunch. Top left, top right and bottom plots depict the growth without feedback, with feedback damping time 10 and 50 turns, respectively.

Ion Instability in SuperKEKB

An instability, which seems to be caused by ions, has been observed in SuperKEKB. Figure 5 shows growth time for horizontal and vertical unstable mode. The instability is suppressed by the bunch-by-bunch feedback system normally. The measurement was done by recording motion of every bunches after switch off of the feedback. The beam condition, which is date, current and the number of bunches, is written in the right part of the plots.

The mode number is defined by

$$\text{Mode} = 5120 - \frac{\omega_i}{\omega_0}, \quad (7)$$

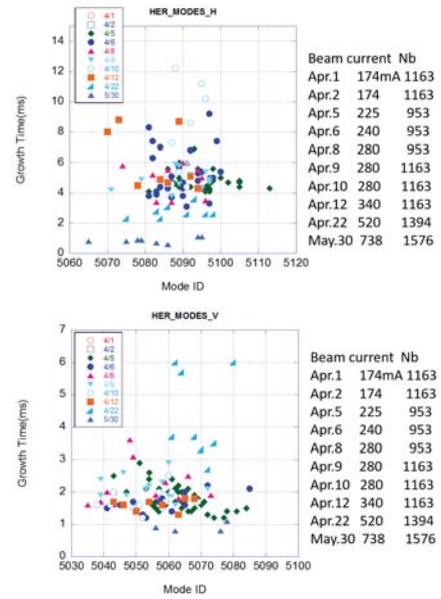


Figure 5: Unstable mode and their growth time in HER. Top and bottom plot are horizontal and vertical mode, respectively.

where ω_i is given by Eq.(6) as in the usual theory. The measurement gave $\omega_{i,x} = 2\pi \times 3$ MHz and $\omega_{i,y} = 2\pi \times 6$ MHz. Figure 6 shows the vertical mode number as a function of the beam current, Carbon monooxide (CO) is dominant in SuperKEKB [6]. The horizontal mode which is drawn by the cyan lines is consistent with the measurement. Vertical mode is drawn by blue lines for various vertical emittance. The design emittance is $\varepsilon_y = 11$ pm.

The frequency ratio of vertical/horizontal in Fig.5 is 60/30=2. This means emittance coupling is 25%, if beam size ratio equal to ion size ratio in a naive theory. If ion size is large, beam size ratio is not necessary so large as shown later.

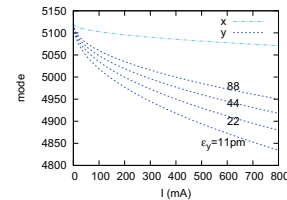


Figure 6: Mode number as function of beam current estimated by Eq.(6) for various vertical emittance.

Ion density can be estimated by measuring the tune shift. To measure the bunch-by-bunch tune, ion induced coherent motion is suppressed by the bunch-by-bunch feedback system. The tune of each bunch is measured by frequency response in the gated excitation of the bunch. Figure 7 shows the tune shift along a bunch train. The tune shift increases along the train. The last point of the tune shift is given for the pilot bunch separated 23 buckets (46ns) from the train end. We note the horizontal tune shift is roughly twice larger than

the vertical one. Tune shift due to the ion cloud is expressed by

$$\Delta\nu_x + \Delta\nu_y = \frac{\rho_i r_e \beta_{x,y}}{\gamma} L. \quad (8)$$

The tune shift sum is 0.0022 as shown in Fig.7. The ratio of the vertical/horizontal tune shifts is equal to the aspect ration of the ion size, $\Delta\nu_x/\Delta\nu_y = \sigma_{i,y}/\sigma_{i,x}=2$. For $\beta_{x,y} = 12$ m, ion density is obtained as $\rho_i = 2.8 \times 10^{11} \text{ m}^{-3}$.

Vacuum pressure in SuperKEKB is about 10^{-7} Pa for CO [6]. The number of created ions is 90 m^{-1} for the bunch population $N_e = 2 \times 10^{10}$. The line density of ion at the last bunch passage is $\lambda_i = 90 \times 1576 = 1.4 \times 10^5 \text{ m}^{-1}$. Since ions are trapped by the bunch train, ions are expected to be located at the beam position. The density should be $\rho_i = \lambda_i/(2\pi\sigma_{e,x}\sigma_{e,y}) = 7.4 \times 10^{12} \text{ m}^{-3}$, therefore the tune shift sum should be $\Delta\nu_x + \Delta\nu_y = 0.057$, where the beam size is $\sigma_{e,x} = 0.25 \text{ mm}$ and $\sigma_{e,y} = 0.012 \text{ mm}$.

Considering the tune shift ratio and density reduction, ion cloud size is estimated as $\sigma_{i,x} = 0.28 \text{ mm}$ and $\sigma_{i,y} = 0.56 \text{ mm}$. This ion size can not be explained by a simple theory.

We attempt to reproduce the measurement of mode spectra mentioned above using a simulation, where $I=600 \text{ mA}$, 1576 bunches by 3 buckets. Figure 8 shows growth of betatron amplitude with the feedback. Green and blue lines of the left plot correspond to for the feedback damping time, 1ms and 0.5ms, respectively. Ion instability is suppressed by the feedback with 0.5ms damping time. The feedback is cut off after 1,000 turn (0.5ms damping). Right plot depicts unstable bunch oscillation in vertical after the feedback OFF, at 1250-th turn. The frequency is around $f_{sim} = 13 \text{ MHz}$, that is slower than $\omega_i/2\pi = 25 \text{ MHz}$ in Eq.(6) but is faster than that in mode spectra ($f_{mes.} \sim 6 \text{ MHz}$).

Figure 9 shows ion distribution along the bunch train, where bunch motion is suppressed by the feedback but remains $\sim 10\%$ as shown in Fig.8. The ion cloud is enlarged due to interaction with the beam. The vertical size seems to be still smaller than horizontal one. In a bending magnet, since only vertical ion size increase, better agreement with the experiment may be expected.

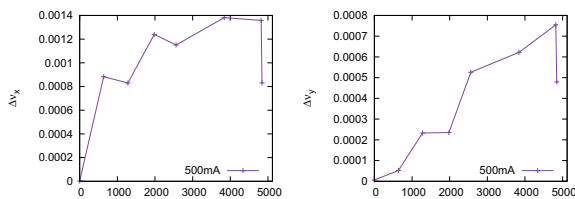


Figure 7: Horizontal and vertical tune shift along a bunch train. The last bunch is separated from train end by 23 buckets.

SUMMARY

Electron cloud build-up and the threshold of the electron density were evaluated for FCC-ee. The electron density

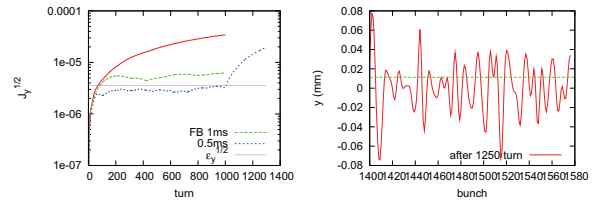


Figure 8: Left plot depicts evolution of vertical amplitude for No feedback (red), feedback with 1ms and feedback with 0.5ms. Feed back is OFF at 1000-th turn (blue line). Right plot depicts bunch oscillation pattern after OFF (1250-th turn).

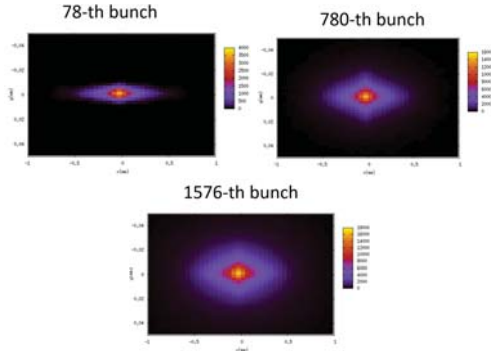


Figure 9: Ion distribution along the bunch train. Top left, right and bottom are ion distributions when 78, 780 and 1576-th bunches pass, respectively.

produced by a bunch is $\rho_e = 3.5 \times 10^{10} \text{ m}^{-3}$ per bunch passage, while the threshold is $\rho_{e,th} = 0.8 \times 10^{10} \text{ m}^{-3}$ for FCC-ee Z. In SuperKEKB, $\rho_e = 1.5 \times 10^{11} \text{ m}^{-3}$ per bunch passage and $\rho_{e,th} = 1 \times 10^{11} \text{ m}^{-3}$. FCC-ee Z is harder than SuperKEKB to suppress the instability. Antechamber suppresses the primary photo-electrons to 1%. Ante-chamber is indispensable to suppress the electron cloud. Further cures, such as weak magnets, groove, coating etc., are necessary. Comparison of the measurement with simulation/theory is being performed in SuperKEKB.

Ion instability should be serious in FCC-ee Z. In simulation, vacuum pressure 10^{-8} Pa and the bunch-by-bunch feedback with 10 turns damping time are required. Ion instability has been observed in SuperKEKB. There are several unintelligible facts:

- Unstable mode (frequency) is slower than the prediction in Eq.(6).
- Tune shift is far smaller than a prediction from ion production rate.
- Horizontal tune shift is larger than vertical one.

They can be solved partially in simulation. Anyway the ion density is far smaller than the prediction, therefore ion instability may not be serious in high intensity electron storage rings.

The author thanks fruitful discussions with Drs. Y. Suet-sugu and F. Zimmermann.

REFERENCES

- [1] H. Fukuma, K. Ohmi, Y. Suetsugu, M. Tobiyama, "Electron cloud at superKEKB", presented at eeFACT2016, Daresbury, UK, September 2016, paper TUT3AH6.
- [2] K. Ohmi, F. Zimmermann, E. Perevedentsev, *Phys. Rev.*, E65, p. 016502, 2001.
- [3] K. Ohmi, "Particle-in-cell simulation of beam-electron cloud interactions", in *Proc. PAC'01*, Chicago, USA, June 2001, paper TPPH096, pp. 1895-1897.
- [4] K. Ohmi, *Phys. Rev. Lett.*, 75, p. 1526, 1995.
- [5] T. Raubenheimer, F. Zimmermann, *Phys. Rev.*, E52, p. 5487, 1995.
- [6] Y. Suetsugu, private communications, 2016.
- [7] K. Ohmi, *Phys. Rev.*, E 55, p. 7550, 1997.

ELECTRON CLOUD AT SuperKEKB

H. Fukuma[#], K. Ohmi, Y. Suetsugu, M. Tobiya, High Energy Accelerator Research Organization (KEK), Tsukuba, Japan

Abstract

Several measures such as TiN coated aluminum ante-chambers, clearing electrodes and grooved structure have been taken to mitigate the electron cloud effects in the SuperKEKB positron ring. During phase 1 operation of SuperKEKB, where solenoid windings were not applied as a measure against the electron cloud, the electron cloud effects such as the beam size blowup, the nonlinear pressure rise, the betatron tune shift along a bunch train and the transverse coupled bunch instability were observed. Permanent magnets attached at aluminum-bellows-chambers that generate longitudinal magnetic field in the chambers were effective to reduce the electron cloud. In case of no solenoid windings, the threshold linear current density of the blowup was increased from 0.04mA/RF bucket in KEKB to 0.17mA/RF bucket in SuperKEKB owing to the measures mentioned above. This paper covers following subjects about the electron cloud at SuperKEKB, 1) mitigation methods against the electron cloud, 2) observation of the electron cloud effects in phase 1 operation and 3) measures against the EC toward phase 2 operation which will start in the late FY2017.

MEASURES AGAINST THE ELECTRON CLOUD IN SUPERKEKB

SuperKEKB is the upgraded electron-positron collider of the KEKB B-factory [1]. The design luminosity of $8 \times 10^{35} \text{ cm}^{-2}\text{s}^{-1}$ will be achieved by so called nano-beam scheme. Machine upgrades include the replacement of round copper chambers in LER to aluminum TiN coated ante-chambers so as to withstand large beam currents and mitigate the electron cloud effects.

A threshold electron density of the strong head-tail instability caused by the electron cloud (EC) in SuperKEKB Low Energy Ring (LER) is estimated to be $2.7 \times 10^{11} \text{ m}^{-3}$ by an analytic estimate [2]. A threshold electron density of $2.2 \times 10^{11} \text{ m}^{-3}$ calculated by a simulation [3] is consistent with the analytic estimate. Growth time of the coupled bunch instability (CBI) due to the EC is estimated to be 50 turns at the threshold electron density of the single bunch instability [3], which is larger than an expected damping time of the transverse bunch by bunch feedback system. Thus the target electron density near the beam against the EC instabilities was taken to be less than $1 \times 10^{11} \text{ m}^{-3}$.

The electron density near the beam in SuperKEKB was estimated to be $5 \times 10^{12} \text{ m}^{-3}$ based on results from measurements at KEKB assuming a round copper

chamber with a diameter of 94 mm, no solenoid field, 4 ns bunch spacing and the bunch current of 1 mA [4]. Main contribution comes from the drift space. Based on studies at KEK following measures were considered at the SuperKEKB LER [4], TiN coated aluminum ante-chambers and solenoid windings in the drift space in arc sections, TiN coated aluminum ante-chambers with grooved surface in dipole chambers and copper ante-chambers with clearing electrodes in wiggler chambers. Taking these measures, the electron density near the beam is expected to be less than $1.0 \times 10^{11} \text{ m}^{-3}$ [4].

OBSERVATION OF THE ELECTRON CLOUD EFFECTS IN PHASE 1

Phase 1 operation of SuperKEKB was carried out from February 2016 to June 2016 without final focus quads and the Bell-II detector. The main purposes of the phase 1 were vacuum scrubbing, optics tuning to achieve small emittance beams and a background study with Beast detectors. Measures against the EC taken until the start of phase 1 operation were TiN coated aluminum ante-chambers, grooved surface in dipole chambers and clearing electrodes in wiggler sections. Solenoid windings which were assumed at the initial design were not applied in this stage of the commissioning.

EC Related Events

The vertical beam size blowup was observed at LER by an x-ray beam size monitor. At the same time, pressures at whole LER ring showed a nonlinear behavior against the beam current above $\sim 500 \text{ mA}$ [5]. The fill pattern was one long train of 1576 bunches with average bunch separation of 3.06 RF buckets. A separation of adjacent

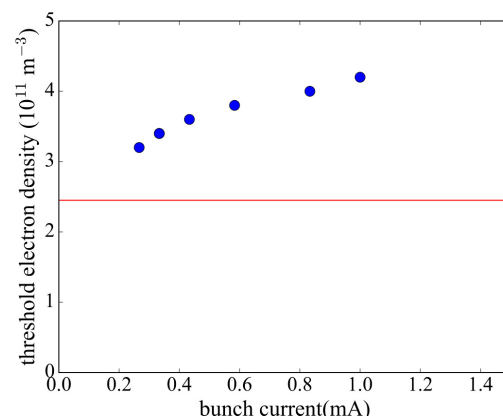


Figure 1: Simulated threshold electron density of the strong head-tail instability caused by the electron cloud as a function of the bunch current. A red line shows an analytic estimate.

[#] hitoshi.fukuma@kek.jp

two RF buckets is 2 ns. The behavior was quite similar to that of electron current measured at an aluminum chamber without TiN coating. Aluminum bellows-chambers without TiN coating were suspected to be a source of the nonlinear pressure rise which would be caused by the electron stimulated desorption in the aluminum bellows-chambers by the EC. The bellows-chamber has a length of 0.2 m and located every 3 m on average. They cover $\sim 5\%$ of the ring in length.

An axial magnetic field was applied by solenoids or permanent magnets at nine aluminum bellows-chambers in a section of ~ 30 m long. The field strength is 40 \sim 100 G near the inner wall at the center of bellows. The rate of the pressure rise at this section was relaxed after the application of the magnetic field. The solenoids and the permanent magnets had nearly same effect on the pressure. Then permanent magnets of ~ 800 sets were

installed at most aluminum-alloy bellows-chambers. The rate of pressure rise was relaxed in whole ring and threshold current of the beam size blowup was increased. However the nonlinear pressure rise and the beam size blowup are still remain at high beam current.

Measurement of the Threshold of Beam Size Blowup

A vertical beam size was measured by an x-ray monitor [6] as a function of the beam current in various fill patterns. Threshold points of the blowup coincided if the beam size was plotted as a function of linear current density which is defined as the bunch current divided by the bunch separation in RF bucket. This scaling behavior was observed in KEKB [7].

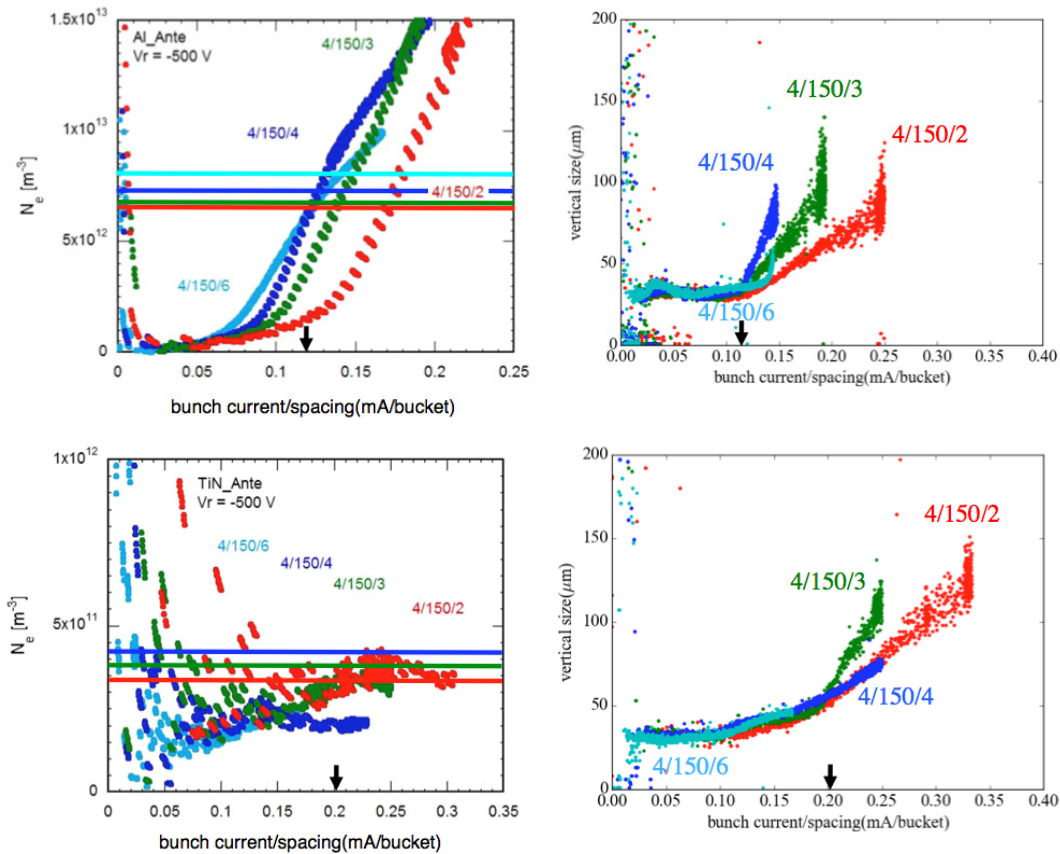


Figure 2: Electron density (left column) and vertical beam size (right column) as a function of the linear current density before (1st row) and after (2nd row) the installation of the permanent magnets. The upper-left figure shows the electron density measured at a bare aluminum ante-chamber, while the lower-left figure shows that measured at a TiN coated aluminum ante-chamber. Black arrows show the threshold of the blowup. Colored solid lines are the threshold electron density of the blowup obtained by the simulation. Since the total length of the bellows-chambers is about 5% of the circumference, the electron density that is 20 times as large as the simulated threshold electron density is plotted as the colored line in the upper-left figure. XXX/YYY/ZZZ represents a fill pattern, i.e. the number of trains/the number of bunches per train/bunch separation or spacing in RF bucket.

Threshold increased by 1.7 after installation of the permanent magnets as shown in Fig 2. The blowup was not seen up to 1A in one long train of 4 RF buckets separation. Beam size seems slowly increase with the beam current.

Measurement of Electron Density

The electron density was measured by retarding field analyzers (RFA) [8]. One RFA was installed at a bare aluminum chamber, while another RFA at a TiN coated chamber. Electron density on the bare aluminum chamber was 50 times larger than that on the TiN coated aluminum chamber in 3 RF bucket separation at 350mA.

Figure 1 shows the threshold electron density as a function of the bunch current simulated by PEHTS [9]. The solid line is an analytic estimate of the threshold [3] which is constant if $\omega_e \sigma_z / c > Q$ in which $Q=6$, while it increases with increasing bunch current in the simulation, where ω_e , σ_z and c are the angular oscillation frequency of electrons, the bunch length and the speed of light respectively. Q characterizes damping of electron coherent motion due to the nonlinear interaction with the beam.

Figure 2 shows the measured electron density and the beam size as a function of the linear current density before and after installation of permanent magnets. Before the installation of the permanent magnets the electron density at the blowup threshold is consistent with the simulation in 3, 4 and 6 RF bucket separation. For 6 RF bucket separation the threshold linear current density is higher than that of other bucket separations, which is probably due to higher bunch current as suggested by the simulation. After the installation of the permanent magnets the electron density at the blowup threshold is consistent with the simulation in 2 and 4 RF bucket separation. No blowup was observed up to 1A in a long train with 1200 bunches and 4 RF bucket separation, which is consistent with the simulation.

Laboratory measurements of the maximum secondary emission yield (SEY) δ_{max} of TiN coated surface is 0.9 to 1.2 at the estimated electron dose (5×10^{-4} C mm⁻²) in phase 1. On the other hand an EC buildup simulation by CLOUDLAND suggests δ_{max} of 1.4. The reason of difference between the laboratory measurements and the simulation is not clarified yet. Possible reasons would be high maximum SEY in the actual machine, insufficiently conditioned sections such as far downstream of bends or inside bends, high SEY at non-coated parts and better conditions of materials at the laboratory such as the good pressure and baking of sample. Further investigation is required in phase 2 operation.

Tune Shift Along a Bunch Train

Tune shift along a bunch train was measured after the installation of the permanent magnets with an iGp12 digital filter by kicking a specific bunch by a strip-line kicker of the bunch by bunch feedback system [10]. The fill pattern was 4 trains, 150 bunches in a train and bunch separation of 3 RF buckets. Figure 3 shows a measured

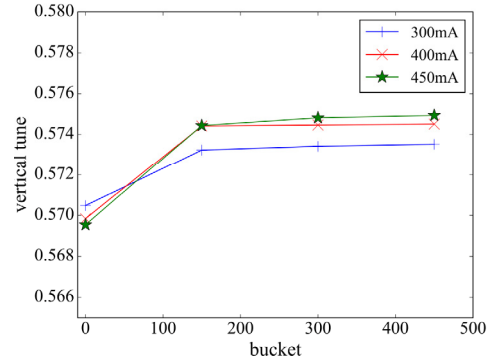


Figure 3: Vertical tune shift along a bunch train.

vertical tune shift along the train. The tune shift saturates at about 0.005. A simple analytic formula gives the tune shift caused by the EC [11] as

$$\Delta \nu_y = \frac{\rho_e r_e \beta_y}{k \gamma} C,$$

where ρ_e is the electron density, r_e the classical electron radius, β_y the vertical beta function, C the ring circumference and k is 1 or 2 for flat or round EC distribution respectively. The estimated tune shift is 8×10^{11} m⁻³ or 4×10^{11} m⁻³ if the EC distribution is round or flat respectively. The measured electron density at the tune shift measurement was 3.5×10^{11} m⁻³. The tune shift is consistent with the measurement of the electron density if the EC is flat.

Coupled Bunch Instability

Bunches can oscillate by coupled bunch motion mediated by the EC. A sideband spectrum of bunch oscillation reflects the motion of the EC [12]. Electrons in drift space cause a short range wake whose range is ~10ns. Electrons in a solenoid slowly rotate around a chamber surface (magnetron motion). Measurements in KEKB showed totally different sideband spectra, i.e. drift mode and solenoid mode with and without the solenoid field respectively [13]. In phase 1 operation the sideband spectrum was measured by the bunch by bunch feedback system. Figure 4 shows the measured vertical sideband spectrum before and after the installation of the permanent magnets. It clearly shows the drift and solenoid mode before and after the installation of the permanent magnets respectively. Growth time was measured in the fill pattern of 4 trains, 150 bunches in a train and bunch separation of 2, 3 and 4 RF buckets. Growth time was larger than 0.8ms after the installation of the permanent magnets.

Remaining Electron Cloud

The blowup and the nonlinear pressure rise are still observed in a fill pattern in the vacuum scrubbing (one train, 1576 bunches in a train, average bunch separation of 3.06 RF buckets) after the installation of the permanent magnets. The drift mode in a sideband spectrum still

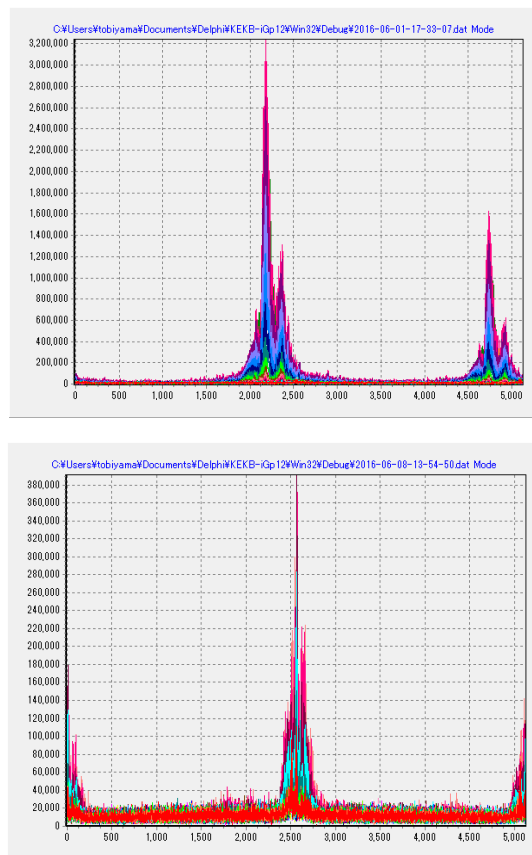


Figure 4: Vertical sideband spectrum before (top) and after (bottom) the installation of the permanent magnets. Bunch separation is two RF buckets. The number of trains is four. The number of bunches in a train is 150. Beam current is 300mA.

appeared at high current after the installation of the permanent magnets in 2 RF bucket separation where electron density is larger than that in other fill patterns. A test installation of the permanent magnets in a long straight section improved pressure in that region. These facts suggest the EC still remains in drift regions.

EC AT HIGH BETA SECTIONS

The EC in high beta function regions might give strong impact on the blowup because of a large kick to the beam by the EC. To investigate this effect, cloud densities were estimated in two cases, 1) high density in high beta section and 2) low density in high beta section and then the threshold electron density was compared by a simulation. It shows the threshold electron density in the case 1 is lowered by $\sim 70\%$ compared with the case 2 [14].

It was pointed out that if photon scattering on a chamber wall is considered, the number of synchrotron light photons incident on a chamber of a final focus quadrupole QC1RP is 30 times larger compared with the case without photon scattering [15]. Since the vertical beta function is very large ($\sim 3000\text{m}$), the EC in the quad could be a source of the blowup.

PLAN TOWARD PHASE 2

Tentative parameters in phase 2 operation of SuperKEKB [16] with final focus quads and the Belle II detector being installed are,

Target luminosity : $1 \times 10^{34} \text{ cm}^{-2} \text{ s}^{-1}$,

Target values of IP beta functions :

β_x^* : 4 times the design, β_y^* : 8 times the design,

Beam current : 1 / 0.8 A (LER/HER).

At the end of phase 1, the blowup started at the linear current density of $\sim 0.2\text{mA}/\text{RF bucket}$. This means total current at the threshold will be $h x I_b / s_b = 1024\text{mA}$, where h is the harmonic number, i.e. 5120, I_b the bunch current and s_b the bunch separation in RF bucket. The threshold is marginal in the phase 2 operation.

The maximum growth rate of the CBI due to the EC is proportional to the bunch current if the wake affects only next bunch [12]. Fill pattern of 4 RF buckets separation fits this condition since range of the wake is $\sim 10\text{ns}$. Growth time of the CBI at phase 1 was 0.8ms to 1ms at the bunch current of 1mA in the fill pattern of 4 trains, 150 bunches in a train and bunch separation of 4 RF buckets. The damping time of bunch by bunch feedback system was about 0.5 ms near 1A [10]. If the bunch separation is 4 RF buckets, the present feedback system would suppress the CBI at phase 2 where the maximum bunch current will be around 1mA.

Budget has been requested to install permanent magnets in most drift sections (mainly arc sections) until phase 2 to keep an enough margin for the blowup.

SUMMARY

In order to reduce the EC, many measures such as the TiN coated aluminum ante-chamber, the grooved surface and the clearing electrode have been applied in SuperKEKB. Measurements in phase 1 operation without solenoid winding show the evidence of the EC effects such as nonlinear pressure rise, the beam size blowup, the sideband spectrum of the coupled bunch instability and the tune shift along a bunch train. The permanent magnets at the bellows-chambers were very effective in reducing the EC. In case of no solenoid windings, the threshold linear current density of the blowup was increased from $0.04\text{mA}/\text{RF bucket}$ in KEKB [7], where round copper chambers were equipped, to $0.17\text{mA}/\text{RF bucket}$ in SuperKEKB owing to the measures mentioned above.

At the end of the phase 1 no blowup is observed up to 1A in 4 RF bucket separation without solenoid windings. However, measurements of the electron density and the CBI sideband spectrum suggest the EC still remains in drift regions if the current increases further. Installation of the permanent magnets in drift regions before phase 2 is proposed.

The EC effects in high beta sections will be studied in phase 2.

ACKNOWLEDGMENTS

The authors would like to thank the member of the SuperKEKB operation group for their help in machine studies.

REFERENCES

- [1] Y. Funakoshi *et al.*, in proceedings of IPAC 2016, paper TUOBA01, pp. 1019-1021.
- [2] K. Ohmi, talk given at a seminar in Fermilab, June 14, 2011.
- [3] Y. Susaki and K. Ohmi, in proceedings of IPAC'10, paper TUPEB014, pp. 1545-1547.
- [4] Y. Suetsugu *et al.*, JVST A, 34 021605 (2016).
- [5] Y. Suetsugu *et al.*, in proceedings of IPAC2016, paper TUOCB01, pp. 1086-1088.
- [6] E. Mulyani and J.W. Flanagan, in proceedings of IBIC2016 (2016), paper TUPG72, to be published.
- [7] H. Fukuma *et al.*, in proceedings of EPAC'00, paper WEP5A12, pp. 1122-1124.
- [8] K. Kanazawa *et al.*, in proceedings of PAC'05, paper FPAP007, pp. 1054-1056.
- [9] K. Ohmi, Proc. in proceedings of PAC2001, paper TPPH096, pp. 1895-1897.
- [10] M. Tobiyama *et al.*, in proceedings of IBIC 2016, paper MOAL03, to be published.
- [11] K. Ohmi *et al.*, in proceedings of APAC'01, Paper WEP056, pp. 445-447.
- [12] S. S. Win *et al.*, PRST-AB 8, 094401 (2005).
- [13] M. Tobiyama *et al.*, PRST-AB 9, 012801 (2006).
- [14] K. Ohmi, a talk given at the 19th KEKB Accelerator Review Committee (2014).
- [15] J.A. Crittenden, in proceedings of IPAC2015, paper TUPTY079, pp. 2218-2221.
- [16] Y. Funakoshi, a talk given at the 18th KEKB Accelerator Review Committee (2013).

ELECTRON CLOUD AND COLLECTIVE EFFECTS IN THE INTERACTION REGION OF FCC-ee

E. Belli^{1,2*}, M. Migliorati¹, G. Rumolo²

¹ University of Rome 'La Sapienza' and INFN Sez. Roma1, Rome, Italy

² CERN, Geneva, Switzerland

Abstract

The FCC-ee is an e^+e^- circular collider designed to accommodate four different experiments in a beam energy range from 91 GeV to 350 GeV and is a part of the Future Circular Collider (FCC) project at CERN. One of the most critical aspects of this new very challenging machine regards the collective effects which can produce instabilities, thus limiting the accelerator operation and reducing its performance. The following studies are focused on the Interaction Region of the machine. This paper will present preliminary simulation results of the power loss due to the wake fields generated by the electromagnetic interaction of the beam with the vacuum chamber. A preliminary estimation of the electron cloud buildup is also reported, whose effects have been recognized as one of the main limitations for the Large Hadron Collider at CERN.

INTRODUCTION

The Future Circular Lepton Collider FCC-ee has been designed as an e^+e^- collider with a centre-of-mass energy from 91 to 350 GeV and 100 km circumference. In this paper we will focus on the Interaction Region (IR) of the machine, whose proposed layouts are shown in Fig. 1. While the symmetric layout [1] has synchrotron radiation (SR) masks to shield the two final focusing quadrupoles and a 12mm pipe radius, the asymmetric layout [2] presents two ingoing pipes with 13mm radius and two outgoing pipes with a larger radius of 20mm. In particular, this latter design will allow high order modes that remain trapped in the IR to escape to the outside through the outgoing pipes, whose cutoff frequency is the same as the IP. Moreover, in the asymmetric optics the final quadrupole closer to the IP is thinner and stronger. High Order Modes (HOMs) and electron cloud studies presented in this paper will be focused on both the layouts, since there are still many open questions. Regarding all the FCC-ee beam pipes (including those at IR), it was decided to use them at room temperature as in the case of KEKB, SuperKEKB and other lepton colliders. However, even if there will be no cryogenic systems, the beam heat load represents one of the major issues to be analyzed in the machine, in order to avoid extra heating and eventual damage of the background.

By considering a uniformly filled machine, i.e. a train of M bunches covering the full ring circumference ($M = h$ with h the harmonic number) with bunch spacing $\tau_b = \frac{2\pi}{h\omega_0}$ where ω_0 is the revolution frequency, the total power loss of

the beam depends only on the real part of the longitudinal component of the coupling impedance [3]:

$$P_{loss} = I^2 \sum_{p=-\infty}^{+\infty} |\Lambda(pM\omega_0)|^2 \text{Re}[Z_{\parallel}(pM\omega_0)] \quad (1)$$

where Λ is the bunch spectrum, $\text{Re}[Z_{\parallel}]$ is the real part of the longitudinal impedance and $I = \frac{MNe}{T_0}$ is the average beam current with N the bunch population and T_0 the revolution period of the machine.

Possible beam heat load sources in the IR are the resistive wall wake fields, geometric wake fields due to the step transitions of the SR masks, the HOMs that remain trapped in the IR and the electron cloud in the two final focusing quadrupoles.

IMPEDANCE STUDIES

This section will present preliminary results of the power losses due to geometrical and resistive wall impedances and trapped modes carried out by analytical tools and simulation codes.

Heat Load due to Resistive Wall Impedance

The resistive wall impedance is produced by the finite resistivity of the beam pipe. If we consider a circular pipe with radius b the classic analytic formula for the power loss per unit length due to resistive wall is given by:

$$\frac{P_{loss}}{L} = \frac{1}{T_0} \frac{N^2 e^2 c}{4\pi^2 b \sigma_z^{\frac{3}{2}}} \sqrt{\frac{Z_0}{2\sigma_c}} \Gamma\left(\frac{3}{4}\right) n_b \quad (2)$$

where N is the bunch population, e the elementary charge, σ_z the bunch length, σ_c the conductivity of the material, Z_0 the vacuum impedance and n_b the number of bunches. In the evaluation of the resistive wall impedance, we considered a beam pipe with 12mm radius and three layers: a first layer of aluminum or copper with 2mm thickness, then 2mm of dielectric and finally stainless steel with resistivity $6.89 \cdot 10^{-7} \Omega m$. Simulations were performed by using the Impedancewake2D code [4] and results are shown in Fig. 2, for both the aluminum (with a conductivity $\sigma_{Al} = 3.77 \cdot 10^7 S/m$) and copper (with conductivity $\sigma_{Cu} = 6 \cdot 10^7 S/m$). The results for the power loss are summarized in Table 1 for the two energy cases of 45.6 GeV and 175 GeV at the nominal beam parameters.

* eleonora.belli@cern.ch

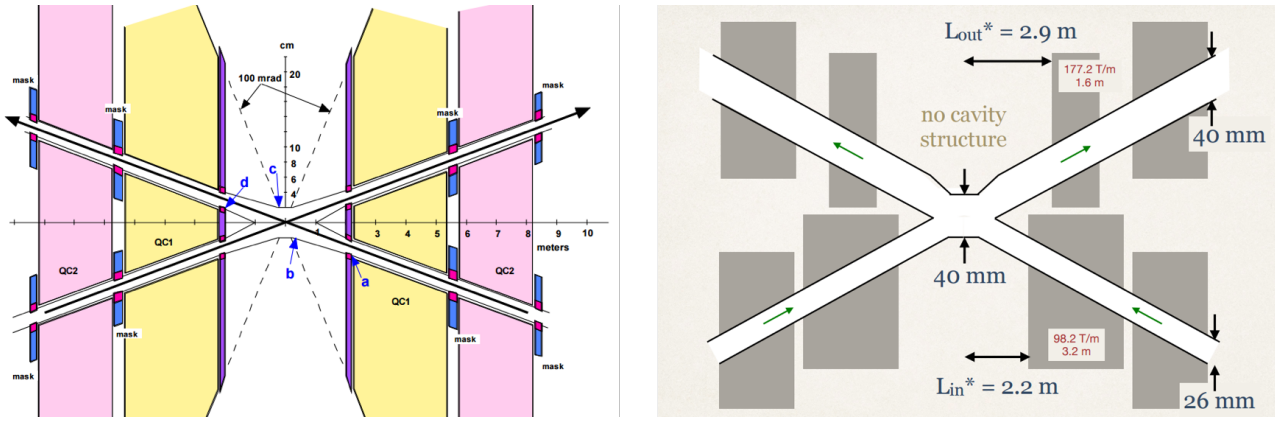


Figure 1: The IR symmetric layout [1] (on the left) and the IR asymmetric layout [2] (on the right).

Table 1: Power Loss Due to Resistive Wall Impedance

Energy [GeV]	45.6		175
Bunch spacing [ns]	7.5	2.5	4000
Bunch population [10^{11}]	1.0	0.33	1.7
Bunches/beam	30180	91500	81
Bunch length [mm]	6.7	3.8	2.5
P_{loss} [W/m](Al)	74.11	57.25	2.52
P_{loss} [W/m](Cu)	59	45.58	2

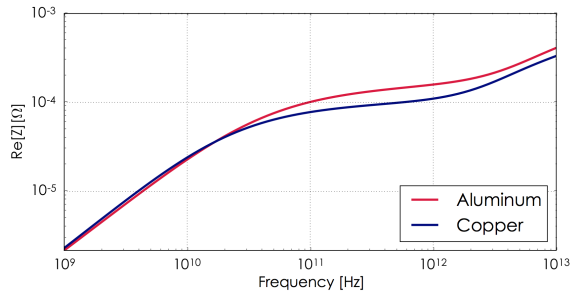


Figure 2: Resistive wall impedance for aluminum (in red) and copper (in blue).

Heat Load due to Geometric Impedance

When there is a geometric variation of the vacuum chamber and the beam passes through a section of a circular pipe from a radius a to a radius b , wake fields are produced at the edges of the discontinuity to satisfy the new boundary conditions. In particular, when the beam goes into a narrower pipe (step-in transition), the real part of the impedance is negative and shows a peak at the cutoff frequency of the larger pipe, while it vanishes above cutoff. On the other hand in the step-out case, i.e. when the beam enters a larger pipe, the real part of the impedance is mostly resistive with a peak at cutoff and then it reaches an asymptotic value. Thus, above cutoff the real part of the impedance is:

$$\text{Re}[Z^{in}] \approx 0$$

$$\text{Re}[Z^{out}] \approx \frac{Z_0}{\pi} \ln\left(\frac{b}{a}\right) \quad (3)$$

Theoretical studies [5] show that at low frequencies the geometric impedance is purely inductive (the real impedances of the step-in and the step-out cancel out) and in the case of step length l greater than the pipe radius b , the impedance is given by the contribution of two independent transition steps:

$$Z(\omega) = 2j\omega \frac{Z_0}{4bc} \left[h^2 + \frac{lh}{\pi} \left(2\ln\left(\frac{8\pi l}{h}\right) - 3 \right) \right] \quad (4)$$

where h is the difference between the two pipe radii. As shown in the symmetric layout in Fig. 1, masks are placed after each quadrupole to shield the magnet from synchrotron radiations. These masks are 20cm long and produce a variation of 2mm in the pipe radius (from 12mm to 10mm). Geometric impedances and wake potentials have been computed with the ABCI code [6]. In particular Fig. 3 shows the wake potential obtained from ABCI for the lowest energy case: by considering a circular pipe of 12mm radius and the nominal bunch length $\sigma_z = 3.8\text{mm}$, we obtain a loss factor $k_l = 6.386 \cdot 10^{-2} V/pC$ which corresponds to a power loss per bunch of $P_{loss} = 5.4\text{mW}$. Table 2 shows the total power loss due to geometric impedance for the lowest and highest energy cases at the nominal bunch length.

Table 2: Power Loss due to Geometric Impedance

Energy [GeV]	45.6		175
Bunch population [10^{11}]	1.0	0.33	1.7
Bunches/beam	30180	91500	81
Bunch spacing [ns]	7.5	2.5	4000
Bunch length [mm]	6.7	3.8	2.5
k [V/pC]	$8.077 \cdot 10^{-3}$	$6.38 \cdot 10^{-2}$	$1.93 \cdot 10^{-1}$
P_{loss} [W]	189.1	493.2	35

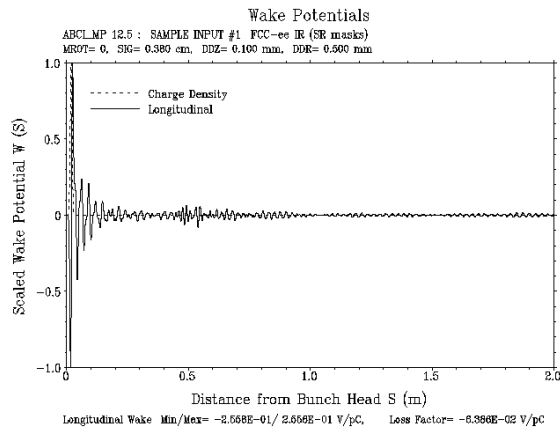


Figure 3: Wake potential of $\sigma_z=3.8\text{mm}$ bunch at 45.6 GeV given by SR masks.

Heat Load due to Trapped Modes

It is well known from the theory [7] that small variations in the beam pipe geometry can generate accidental cavities and produce trapped modes, i.e. resonance peaks with frequencies below the cutoff frequency of beam pipe. These modes cannot propagate into the pipe and remain localized near the discontinuity, representing another possible source of heating that must be analyzed with particular care. As mentioned at the beginning of this paper, the final choice of the FCC-ee Interaction Region layout will be mainly based on HOMs considerations. The asymmetric design proposed in [2] will allow the trapped modes to escape to the outside through the outgoing pipes, thanks to the same radius of the IP. CST eigenmode and impedance simulations in the frequency domain confirmed the presence of a large number of trapped modes in the interaction region. In this section, we will present preliminary simulation results for TM modes trapped in the IR and the resulting power loss. A general method that can be followed to study the HOMs in the IR is the following:

- Build a CST 3D model of the interaction region
- Wakefield simulations (time domain)
- Eigenmode simulations (frequency domain)
- For each excited mode, extract parameters (resonance frequency ω_r , shunt impedance R_s and quality factor Q) and evaluate the real part of the impedance as:

$$Z(\omega) = \frac{R_s}{1 + iQ\left(\frac{\omega_r}{\omega} - \frac{\omega}{\omega_r}\right)} \quad (5)$$

- Compute the power loss by following the model given by equation 1

Fig. 4 shows the real part of the longitudinal impedance obtained from CST wakefield simulations for the symmetric layout. The peaks of impedance correspond to the modes excited in the pipe below the cutoff frequency of the outgoing

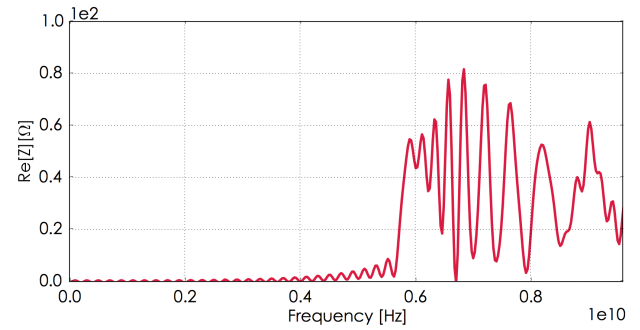


Figure 4: Real part of the longitudinal impedance in the symmetric layout case.

pipes that could remain trapped in the interaction region and represent an issue in terms of extra heating. In the symmetric layout case, the cutoff frequency of the outgoing pipes with 12mm radius is around $f_{cutoff} = 9.57\text{GHz}$ for TM_{01} modes. By assuming that all the TM modes below this cutoff are excited and remain trapped in the IR, we obtain a total power loss (given by the contribution of each mode) $\approx 2.74\text{W}$. In the case of the asymmetric layout, the cutoff frequency of the outgoing pipes with 20mm radius is around $f_{cutoff} = 5.74\text{GHz}$ for TM_{01} modes. As expected, eigenmode simulations showed that there are no longitudinal modes below cutoff trapped in the interaction region and this was also confirmed with wakefield simulations.

Trapped modes can also excite longitudinal coupled bunch instabilities. Fig. 5 shows the maximum shunt impedance of a HOM as a function of its resonance frequency giving an instability growth rate which is compensated by the natural radiation damping [8].

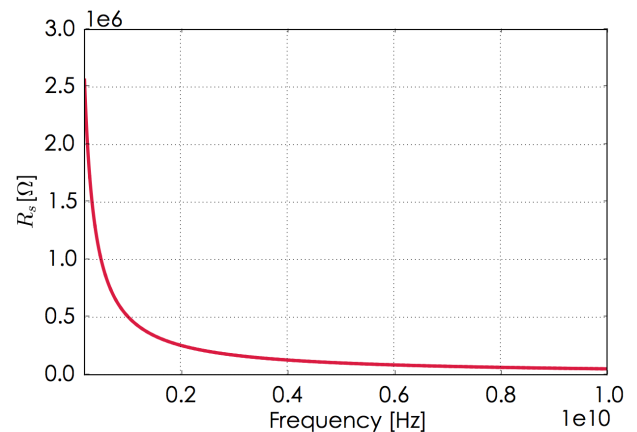


Figure 5: Maximum HOM shunt impedance producing a growth rate of the instability compensated by the natural radiation damping.

ELECTRON CLOUD STUDIES

Electron cloud (EC) has been recognized as one of the main limitations in the performance of the Large Hadron

Collider at CERN [9]. In the FCC-ee case, when the positron beam passes through a section of the accelerator, primary electrons can be produced by ionization of the residual gas in the beam pipe or by photoemission due to synchrotron radiations (photoelectrons). These primaries are attracted and accelerated by the beam up to energies of several hundreds of eV: when they impact the pipe walls with this energy, they produce secondary electrons that in turn, depending on their energy, can be absorbed, reflected, or accelerated again by the following bunch, thus producing an avalanche of electron multiplication. This accumulation of electrons in the beam chamber can represent another source of heat load and produce instabilities and emittance blow up. In this paper we will focus on the fast-head tail instability and on the heat load caused by the electron cloud in the two final focusing quadrupoles of the interaction region.

Heat Load due to Electron Cloud

In order to evaluate the EC build up in FCC-ee, we used the PyELOUD code [10]. Table 3 shows the beam and magnet parameters used for electron cloud studies at 45.6 GeV. In particular, by assuming an initial uniform distribution of electrons in the vacuum chamber, we simulated the following cases at 45.6 GeV:

- a train of 300 bunches with 2.5ns bunch spacing in both the symmetric and asymmetric layouts
- 30 trains of 8 bunches with 10ns gap and 2.5ns bunch spacing in the symmetric layout

Table 3: Beam and IR Magnet Parameters for FCC-ee at 45.6 GeV

Energy [GeV]	45.6			
Bunch spacing [ns]	7.5	2.5		
Bunch population [10^{11}]	1.0	0.33		
H emittance [nm]	0.2	0.09		
V emittance [pm]	1	1		
Bunch length [mm]	6.7	3.8		
Filling pattern	300b (8b+4e)x30			
	L[m]	G[T/m]	β_x [m]	β_y [m]
Quadrupole QC1R	3.2	26.6	53.3	8934
	1.6	46.2	34.6	10265
Quadrupole QC2R	2.5	18.7	341	4488
	2.5	16.3	297	4082

Fig. 6 shows the EC induced heat load for the two final magnets as a function of the Secondary Electron Yield for all the test cases. The multipacting threshold is ≈ 1.1 for both quadrupoles which means that we need a $SEY < 1.1$ to run the machine without electron cloud.

Simulations show that the heat load is up to three times lower for the quadrupole QC1R in the case of asymmetric

layout while results in quadrupole QC2R confirmed that the presence of gaps in the bunch train allows to mitigate the electron cloud, with a heat load up to two times lower. One possible strategy to avoid electron cloud in the machine will be the choice of a proper filling pattern that will depend also on HOMs considerations, as mentioned in the previous section.

Photoemission due to SR When charged particles are subject to a transverse acceleration, they emit photons that can have enough energy to extract electrons from the walls when hitting the pipe. Photoelectrons usually represent the main source of primaries in the EC build up. The number of photoelectrons that are generated per beam particle and per unit length is given by:

$$N_{ph} = N_{\gamma} Y \quad (6)$$

where

$$N_{\gamma} = \frac{5\alpha}{2\sqrt{3}} \frac{\gamma}{\rho} \quad (7)$$

is the number of photons per beam particle per unit length and Y is the Photoelectron Yield, i.e. the probability of electron emission per impinging photon. For FCC-ee, with a bending radius $\rho = 11.3$ km, the number of photons per positron per meter is $N_{\gamma} = 0.085$ at 45.6 GeV, a number three times higher than LHC at 7 TeV and roughly twice higher than FCC-hh at collision. Another fraction of photoelectrons is produced by the scattered photons and is associated to the photon reflectivity parameter R . The photoelectron yield and the photon reflectivity depend both on the pipe materials and synchrotron radiation properties. Since no experimental data exist for these parameters, simulations were performed by scanning Y and R in the following ranges: $Y = [0.05, 0.2, 0.3]$ and $R = [2\%, 50\%, 80\%]$. Results are shown in Fig. 7 for both quadrupoles by considering the 2.5ns beam at 45.6 GeV in the symmetric case.

Electron Density Threshold for the Single Bunch Head-tail Instability

The single bunch head-tail instability is the direct consequence of the interaction of the bunch with the electron cloud: if the bunch enters the e-cloud with the head slightly displaced from the beam axis, electrons will be attracted towards the head centroid position and there will be an accumulation of electrons in this region. Following particles of the bunch will be attracted by this new electron distribution and after few passages through the electron cloud the tail will be completely deflected [11].

Electron cloud acts as a short range wake field with frequency

$$\omega_e = \sqrt{\frac{2\lambda_p r_e c^2}{\sigma_y(\sigma_x + \sigma_y)}} \quad (8)$$

where $\lambda_p = \frac{N}{4\sigma_z}$ is the line density with N bunch population and σ_z bunch length, r_e is the classical electron radius

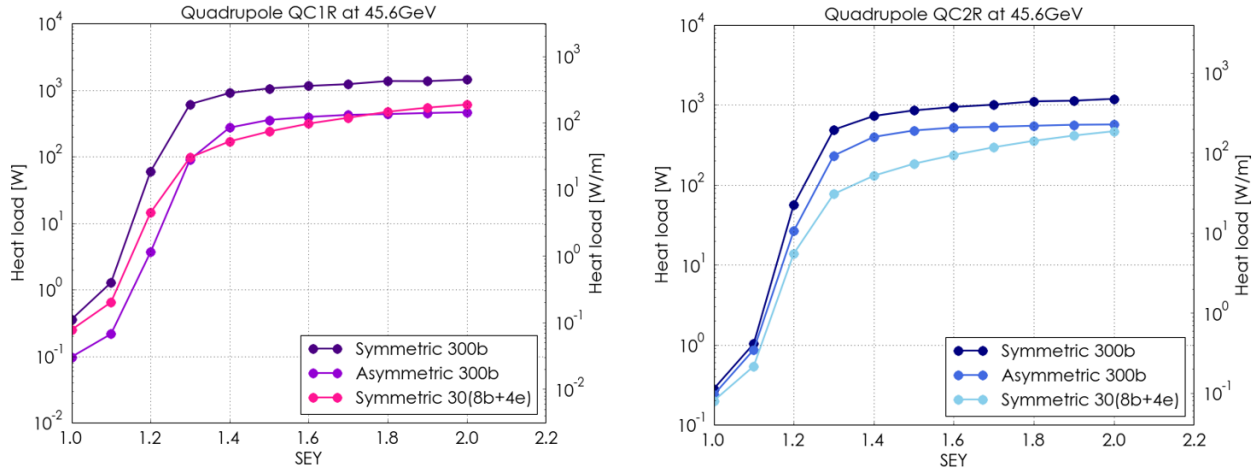


Figure 6: Heat load in the two final FCC-ee quadrupoles as a function of the SEY parameter at 45.6 GeV with 2.5ns bunch spacing.

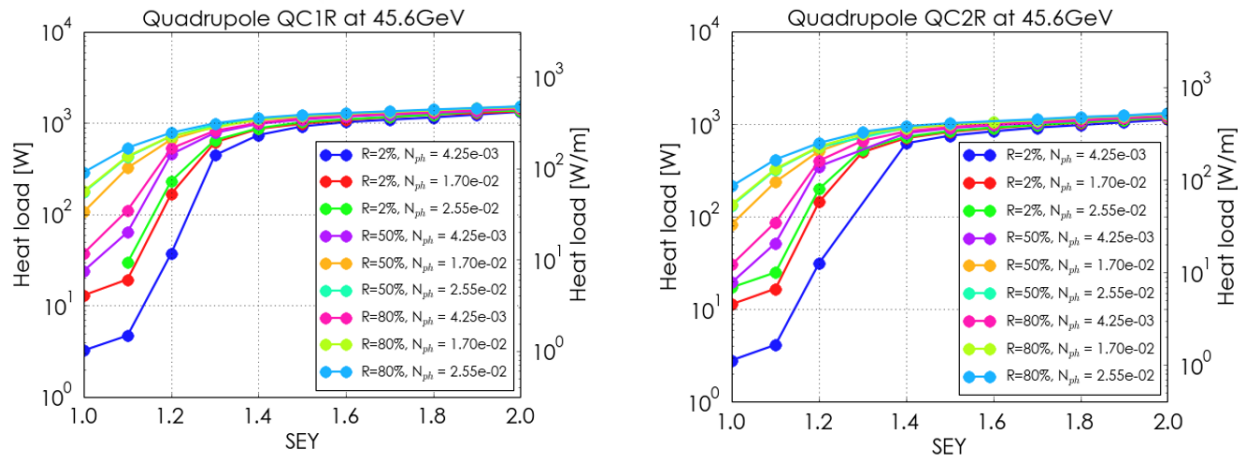


Figure 7: EC induced heat load as a function of the SEY for different values of the photon reflectivity and the photoelectron yield, for quadrupole QC1R (on the left) and quadrupole QC2R (on the right) at 45.6 GeV with 2.5ns bunch spacing.

and $\sigma_{x,y}$ are the transverse beam dimensions.

The threshold density for the single bunch head - tail instability is given by

$$\rho_{th} = \frac{2\gamma v_s \frac{\omega_e \sigma_z}{c}}{\sqrt{3} K Q r_0 \beta C} \quad (9)$$

where v_s is the synchrotron tune, C the machine circumference and we assumed $K = \frac{\omega_e \sigma_z}{c}$ and $Q = \min(7, \frac{\omega_e \sigma_z}{c})$. Table 4 shows the parameters of FCC-ee for the lowest and highest energy cases and the corresponding density thresholds.

CONCLUSIONS

Simulation results of the beam heat load contribution due to resistive wall and geometric impedances have been presented for the interaction region of FCC-ee. For the estimation of the power loss due to the resistive wall impedance we considered a pipe of aluminum and copper and in this

Table 4: FCC-ee Parameter List for Electron Density Threshold Evaluation

Energy [GeV]	45.6		175
Bunch spacing [ns]	7.5	2.5	4000
Bunch population [10^{11}]	1.0	0.33	1.7
Horizontal emittance [nm]	0.2	0.09	1.3
Vertical emittance [μm]	1	1	2.5
β [m]	100	100	100
Bunch length [mm]	6.7	3.8	2.5
Synchrotron tune	0.036	0.025	0.075
Elec. frequency $\frac{\omega_e}{2\pi}$ [GHz]	177.8	163	191.4
Elec. oscillation $\frac{\omega_e \sigma_z}{c}$	25	13	10
Density threshold [10^{10}]	1.88	1.3	15

latter case the losses are lower for all energies and below 60W/m (for the entire beam). ABCI simulations of the loss

factor of the synchrotron radiation masks have also been performed, showing that the power loss is below 1W for all the energies. CST simulations in both time and frequency domains were performed to study high order modes in the IR, in particular the TM modes that remain trapped and can cause extra heating. In this context, the asymmetric layout seems to be the best choice, even if further studies are needed. Electron cloud induced heat load as a function of the SEY was estimated in the two final focusing quadrupoles of the interaction region by performing numerical simulation with the PyECLoud code. Simulation results showed that the presence of gaps in the bunch train allows to mitigate the electron cloud in the machine. Moreover, the heat load is up to three times lower for both quadrupoles in the asymmetric layout case. The heat load was also estimated by scanning the photoelectron yield and the photon reflectivity. The multipacting threshold has been localized at 1.1 for both quadrupoles. An estimation of the electron density threshold of the single bunch head-tail instability was also presented. Further studies are needed to identify a possible strategy to mitigate the electron cloud: a scan of the bunch spacing and the use of different filling patterns will be analyzed more in detail.

ACKNOWLEDGEMENT

The authors would like to thank G. Iadarola, L.Mether, A.Romano, F. Zimmermann, K.Oide, K. Ohmi, M. Zobov, B. Salvant, N. Biancacci, E. Shaposhnikova, for their contribution and their valuable comments and discussions.

REFERENCES

- [1] M.Sullivan, "FCC-ee Interaction Region Layout" FCC Week 2016, Rome, April 2016, <http://indico.cern.ch/event/438866/contributions/1085089/>
- [2] K.Oide, "FCC-ee machine layout and optics" FCC Week 2016, Rome, April 2016, <http://indico.cern.ch/event/438866/contributions/1085096/>
- [3] G. Rumolo, "Beam instabilities", Proceedings of the CAS-CERN Accelerator School: Advanced Accelerator Physics, Trondheim, Norway, 19–29 August 2013.
- [4] N. Mounet, https://impedance.web.cern.ch/impedance/Codes/ImpedanceWake2D/user_manual_todate.txt
- [5] Palumbo, L., Vittorio G. Vaccaro, and M. Zobov. "Wake fields and impedance." Arxiv preprint physics/0309023 (2003).
- [6] <http://abci.kek.jp/abci.htm>
- [7] A. Chao, et al., "Handbook of accelerator physics and engineering", World scientific, 2013.
- [8] E.Belli, M.Migliorati, et al. "Single beam collective effects in FCC-ee due to beam coupling impedance." arXiv preprint arXiv:1609.03495 (2016).
- [9] G. Iadarola, "Electron Cloud studies for CERN particle accelerators and simulation code development", PhD Thesis, Università degli Studi di Napoli Federico II, 2014
- [10] <https://github.com/PyCOMPLETE/PyECLoud>
- [11] G. Rumolo and F. Zimmermann, "Theory and Simulation of the Electron cloud instability." Proceedings of the LHC Workshop Chamonix XI. 2001.

FEEDBACK SYSTEMS FOR FCC-EE

Alessandro Drago

Istituto Nazionale di Fisica Nucleare, Laboratori Nazionali di Frascati

Via Enrico Fermi 40, Frascati, Italy

Abstract

In this paper, some preliminary considerations on the feedback systems for FCC-ee are developed. Bunch-by-bunch feedback systems have been designed in the last years for other e^+/e^- colliders like PEP-II, KEKB, DAFNE, SuperB and SuperKEKB. In all these cases, similar approaches have been implemented, even if some design variations have been suitable or necessary for different reasons. Bunch-by-bunch feedback systems are based on the concept that the barycenter of each bunch moves with harmonic motion around the equilibrium point in three planes (L, H, V). The feedback copes with the forcing excitation by producing damping correction for each individual bunch. This is possible managing every single bunch by a dedicated processing channel in real time. For FCC-ee the very high number of stored bunches requires much more power in terms of processing capability for the feedback systems. Ring length (100 Km) and very low fractional tunes must be also considered requiring for a more effective strategy in the feedback system design.

INTRODUCTION

A new tunnel with a circumference of 100 Km around the CERN area could host the proposed FCC-ee (Future Circular Collider e^-/e^+), in the past also called TLEP (Triple LEP). As alternative, the tunnel can host FCC-hh, a 100 TeV center-of-mass energy-frontier hadron-hadron collider or FCC-he, a proton-electron collider. Beside the lepton accelerator, the hadron one faces additional challenges, such as high-field magnet design, machine protection and effective handling of large synchrotron radiation power in a superconducting machine [1] [2].

FCC-ee [3][4], operating at four different energies for precision physics of Z, W, and Higgs boson and top quark, represents a significant push in terms of technology and design parameters. Pertinent R&D efforts include the RF system, top-up injection scheme, optics design for arcs and final focus, effects of beamstrahlung, beam polarization, energy calibration, and power consumption. Finally, feedback systems in the three oscillation planes (H, V, L) are necessary, and some preliminary considerations are carried on in this paper.

To achieve this goal, in the following a fast sketch of the foreseen instabilities impacting the possible design of the FCC-ee feedback systems is reported.

In the past two decades, bunch-by-bunch feedback systems have been designed for several e^+/e^- colliders like PEP-II [5] [6] [7], DAFNE [8], KEKB [9] and more recently for SuperB [10] (feedback built and installed at DAFNE [11]) and SuperKEKB [12].

In all these cases, very similar or identical approaches have been implemented, even if some design variations have been possible for technological progress or convenient for specific reasons.

All these feedback systems are based on the concept that the barycenter of each bunch moves with harmonic motion around the equilibrium point in each of the three planes (H, V, L).

The feedback copes with the forcing excitation by calculating individual damping correction kicks for each bunch. This is possible by managing in real time every single bunch by a dedicated processing channel implementing a FIR (Finite Impulse Response) filter at n taps, with n from 1 to 32, chosen by the operator. In each system, the phase response must be found experimentally with great care to give the best correction kick for each bunch. Betatron and synchrotron phase advance at pickups and kickers determines the filter setup along with other parameters.

For the FCC-ee feedback systems, a similar design is proposed in this paper taking also in consideration the peculiarities of the collider: a very high number of stored bunches and a huge harmonic number, fast instability growth rates and remarkable ring length.

Figure 1: Parameter list from FCC Week 2015 M.Migliorati's talk with arrows indicating the most relevant parameters for a feedback design point of view.

Parameter list - FCC-ee Z-pole, crab waist, 2 IPs

parameter	Z	W	H	t
Circumference (km) →	100	100	100	100
Beam energy (GeV)	45.5	80	120	175
Beam current (mA) →	1450	152	30	6.6
RF frequency (MHz) →	400	400	400	400
RF Voltage (GV)	0.2	0.8	3	10
Mom compaction [10^{-5}]	0.7	0.7	0.7	0.7
Bunch length [mm](*)	1.63	1.98	2.0	2.1
Energy spread(*)	3.7×10^{-4}	6.5×10^{-4}	1.0×10^{-3}	1.4×10^{-3}
Synchrotron tune	0.025	0.037	0.056	0.075
Bunches/beam →	90300	5162	770	78
Bunch population [10^{11}]	0.33	0.6	0.8	1.7
Betatron tune	350	350	350	350

(*) without beamstrahlung (no collision)

vanant parameters for a feedback design point of view.

FORESEEN INSTABILITIES

The preliminary evaluation of the foreseen instabilities is based on the talks held by M. Migliorati at the FCC Week 2015 (First Annual Meeting of the Future Circular Collider Study) [13] and in a March 2016 CERN meeting (First Annual Meeting of the Future Circular Collider Study) [14]. In the following Fig. 1 a parameter list is shown with the arrows indicating the most relevant parameters for a feedback design point of view.

Coupled bunch instability – transverse RW

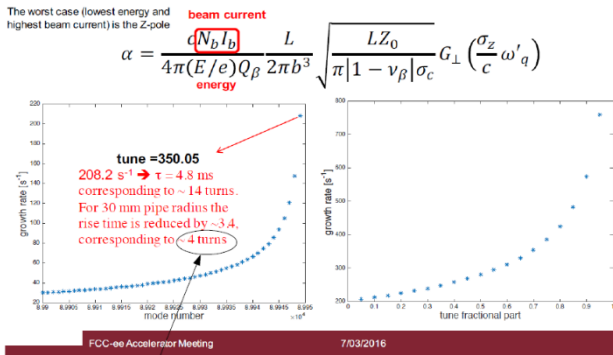


Figure 2: RW instability growth rate is evaluated in four turns (from M. Migliorati's talk during the March 2016 CERN meeting). Fractional tune is 0.05.

The harmonic number H is 133600. Usually the bunch-by-bunch feedback systems process all the buckets without selecting the full and the empty ones. This is a design choice that simplifies and makes faster the data processing.

A preliminary evaluation of RW (resistive wall) instability growth rate has been discussed in the March 2016 meeting and one of the results is shown in the Fig. 2.

From the transverse point of view the most important instability is due to RW. The value computed from the impedance model gives a growth rate of 4 turns, that is an extremely fast value from a feedback performance point of view. Nevertheless, if we consider the e-cloud effects expected in the positron ring, the growth rates could be even much worst. Furthermore, the fractional tune is 0.05, that is a very low frequency.

If we consider the DAFNE case, the resistive wall instability is faster in the e+ ring than in the e- ring by a

factor 10. The more relevant instability effect is in the horizontal plane [15] [16].

FEEDBACK BASICS

To introduce a possible design, the feedback system description is organized in several main blocks as shown in the Fig. 3.

The blocks are: pickups, analog front-end, DPU (digital processing unit), including analog to digital converter working with at least 12 bits, better if 14 or 16, multiplexer, FIR filter for each bunch, demultiplexer, digital to analog converter, analog back end, timing including also delay lines, power amplifiers, kickers, and operator interface for remote control.

Analyzing more in depth every block and starting from the pickups, there are no special requirements, apart a very good H/V beta to increase the signal to noise ratio.

In the transverse plane, usually this condition requires to use different BPM (beam position monitor) as feedback horizontal and vertical pickups.

The kickers are different for the two cases: cavity type kicker [17] should be implemented for the longitudinal plane while stripline type kickers for transverse planes. For both cavity and stripline kicker, the impedance needs to be carefully evaluated. As in the previous e+/e- colliders, a high beta (H/V) is required for the transverse kickers to have the best feedback performance. Implementing separate kickers for the horizontal and the vertical case helps to have a high beta in both the cases.

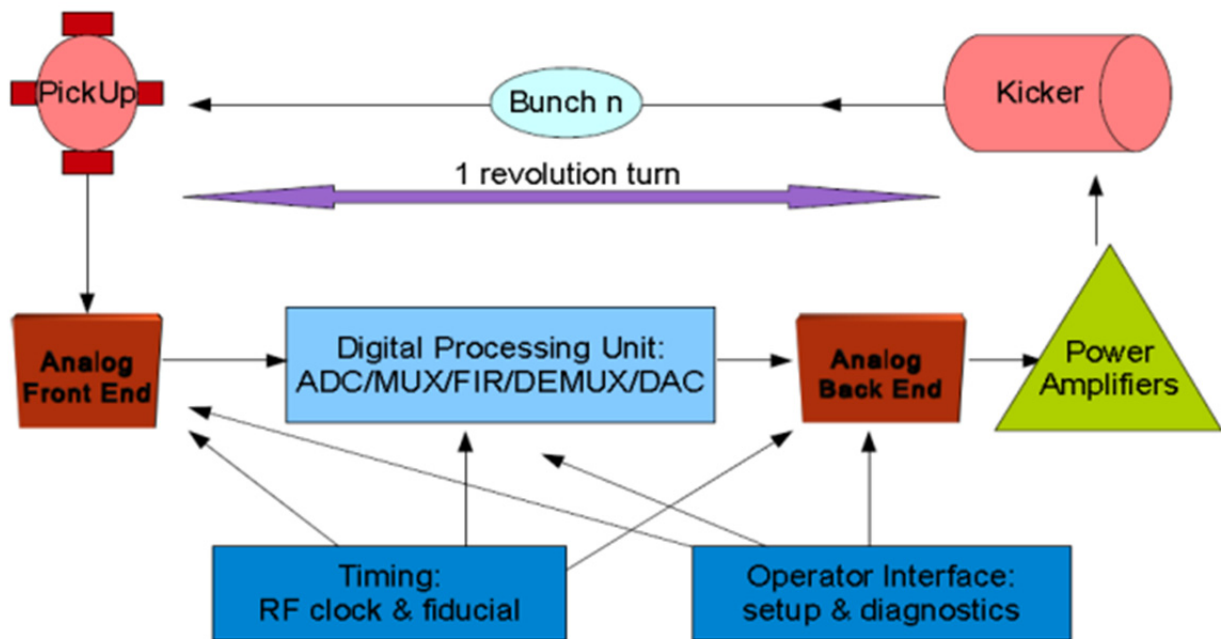


Figure 3: Feedback main blocks. They can differ if transverse or longitudinal system.

Copyright © 2017 CC-BY-3.0 and by the respective authors

Both kinds of kicker should assure adequate performance with signals having very low frequencies, even of the order of one Hertz. This is because the stripline kicker has a bandwidth starting from dc and the cavity kicker requires a signal modulated at 1-1.5 G Hertz, allowing to manage even dc voltage.

The **Analog Front End** differs partially from the longitudinal and the transverse cases. Basically, it is designed around custom PCB comb filters at $4 \cdot RF$ (H, V) or $6 \cdot RF$ (L). The same scheme has been implemented for SuperB (installed at DAFNE) and SuperKEKB. In both cases the modules have been assembled in-house.

Regarding the **DPU** and considering the complexity of this block, it will be convenient to implement the same type of unit for all the feedback types (H, V, L) to reduce design and fabrication efforts. There is a warning about the very high number of processing channels. This point will be discussed in the next paragraph. Note that in the DPU the signal propagation delay is of the order of 600 ns. The DPU has the goal to implement the FIR filters that compute the correction signal for each bunch.

The **Analog Back End** for the transverse feedback systems will work in base band, so usually only a level adapter (pre-amplifier stage with splitters) is necessary. For the longitudinal feedback, as in the previous designs, a double modulation scheme is proposed, both AM and QPSK. To make effective these modulations on each bunch, a precise analog delay line with high bandwidth must be included. In both cases, transverse and longitudinal, the modules can be assembled in-house.

About the **power amplifiers**, there are models with an adequate bandwidth that of course will be different for transverse and longitudinal cases. Typically, they have between 250W and 2kW power and they are commercially available (though very expensive). The pulse response must be evaluated to avoid cross-talk between adjacent bunch. Note that the performance at very low frequency needs to be checked to manage correctly the bandwidth.

Timing specifications are like for the other colliders considered previously, that means a jitter within 10 ps. However, the transmission over such distances, of the order of tens of Km, needs to be managed by an adequate technology mainly to maintain jitters in the specification.

The **operator interface** takes care of the correct running of the systems, the real time and off line diagnostics, the verification and the implementation of the best setup. In general, the setup will be different for each individual feedback system and it must be checked with single and multiple bunches.

The First Critical Point

As said above, the number of bunches is very high, furthermore the bunch-by-bunch feedback systems currently implemented do not use a lookup table to select the filled and the empty buckets, so they must process all the H buckets (H =harmonic number=133600) even if empty. Changing this strategy in the design can be feasible but not necessarily convenient from a design point of view.

By the way, at the present the SuperKEKB feedback processes 5120 bunches, that is the highest harmonic number for currently operative lepton colliders.

Note that the damping ring of ILC, still not approved, should have $H \approx 7000$ and CepC proposal should have $H = 118800$ but with few bunches.

In conclusion for FCC-ee, each feedback system needs a processing power such as $133600 / 5120 = 26$ times the SuperKEKB systems. An advantage is the much slower revolution frequency of FCC-ee that compensates partially the high number of processing channels.

Concluding, the DPU design is not trivial, requiring an extremely high computing power that must be implemented by custom modules based mostly on FPGA technology.

Luckily the FPGA technology is growing fast, so the goal is demanding but feasible. Of course, a new DPU design is necessary.

The Second Critical Point, Fb Damping Capability

It is a common point of view and an experimental result too that a bunch-by-bunch feedback in e+/e- collider can damp the instabilities up to 10 revolution turns, even if, at very low fractional tunes, this result ought to be checked. However, reporting this evaluation in terms of revolution turns helps to correlate the feedback performance for very different length accelerator rings.

Anyway, if the oscillation frequency is very low, for example with fractional tune < 0.09 , difficulties can arise to damp very fast instabilities in only 10 revolution turns.

The "standard" performance can be achieved by installing one feedback system for relatively high beam currents (1-3A) with an amplifier section of the order of 1 or 2 kW total power.

The limit to increase the feedback gain is basically due to the noise present in the loop that in large part comes outside the system, from the pickup, and only in small part from inside the feedback. In this case it is due to analog electronics and quantization noise.

DAFNE 2008 Experiment

About the previous topic in the year 2008 at DAFNE the author did an experiment by implementing two separate feedback systems working in the same plane (horizontal e+) [18].

This was necessary for damping a very fast horizontal mode induced by e-clouds and waiting for the fabrication of a new feedback stripline kicker with a much better shunt impedance.

Having the availability of a second kicker in the ring (see Fig. 4) installed to be used as test injection kicker, a new transverse horizontal feedback was put in operation in the positron ring. To avoid managing too complicate timing setup including also difficulties to check the feedback performance, two complete loops were implemented including a second pickup and another DPU. A big advantage of the double feedback strategy is the capability

to check easily and separately the correct setup and performance of each system by turning off the other one.

The “trivial” result obtained was that the damping times of the two feedback systems add up about linearly within the measurement error (10-20%). Growth and damping rate are computed by fitting routines running off-line to analyze the stored bunch-by-bunch data. An example of this data analysis done in the 2008 runs is shown in the Fig. 5.

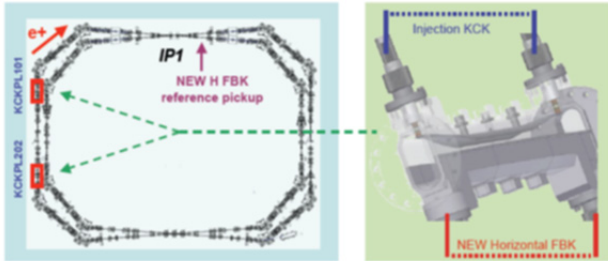


Figure 4: The injection kicker used as horizontal feedback kicker (on the right) and the placements in the e+ ring (on the left).

The modal instability growth rates for the positron beam were 34.5 ms⁻¹ at 560 mA and 712 ms⁻¹ at 712 mA of beam current.

The damping rates measured for mode 119 (=120-1 that is -1 mode as computed by the e-cloud DAFNE model) are also shown in the same fig. 5 and were:

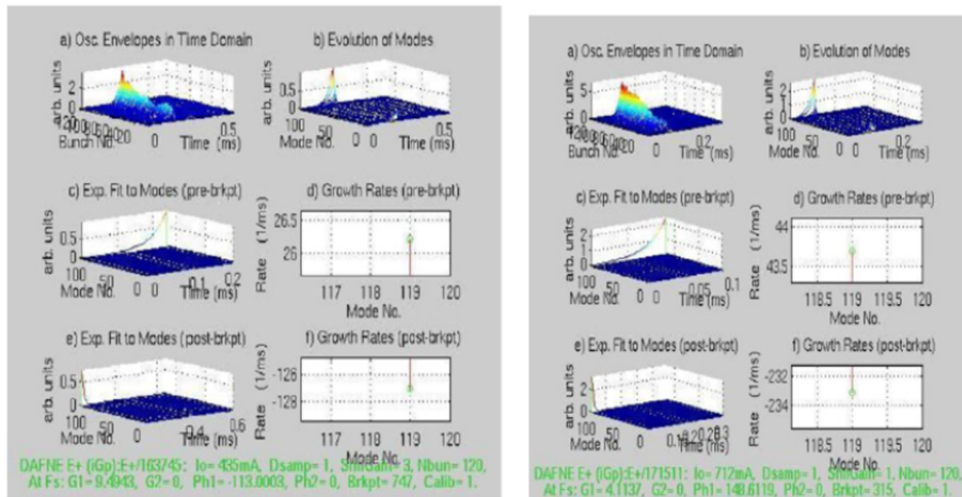
-127 ms⁻¹ for a single feedback loop, that means damping in 24 revolution turns (=7.8 microseconds)

-233 ms⁻¹ by using two cooperating feedback systems that means damping in 13 revolution turns (= 4.3 microseconds).

Note that in DAFNE the harmonic number is 120 and one revolution period (turn) is 324 ns. It should be remembered also that having a DPU propagation delay of 400-600 ns makes impossible to kick the bunch after just one turn and two turns are necessary. This gives a little loss of performance evaluated in about 15%. In conclusion, there is a clear experimental demonstration that the damping rate of the feedback has been doubled by doubling systems and power. Nevertheless, a simulation model could clarify better range and performance of the linearity of the behavior. More important is that two feedback systems in the same ring and plane have worked very well together cooperating perfectly without loss of power. Furthermore, during May 2016, the double feedback technique has been implemented again and tested with same results at SuperKEKB by M. Tobiyaama confirming the approach validity.

Single horizontal feedback
 I=560mA, mode -1 [=119],
 grow=34.5 ms⁻¹, damp=-127 ms⁻¹

Double horizontal feedback:
 I=712mA, mode -1 [=119],
 grow=43.7 (ms⁻¹), damp=-233 (ms⁻¹)



Damping time
 in 4.3 microsecond
 i.e. in ~13
 revolution turns

International Linear Collider Workshop 2008
 LCWS08 & ILC08
 ILC08 Damping Ring session

Note: in DAFNE, the mode 119=-1 is the Mode of the resistive wall instability

Figure 5: Growth rates and damping rate measured at DAFNE in the year 2008 in the e+ horizontal plane by using one and two feedback systems.

It must be noted that having more kickers placed in different parts of the ring requires for a complete duplicate of the feedback to simplify the setup because both timing and phase response of the systems are different.

In the previous case (year 2008) the systems used 2x250W amplifiers for each feedback. After implementing a new kicker with a much better shunt impedance, there was no more need of the second system.

FCC-EE FEEDBACK PROPOSAL

In order to perform an effective feedback scheme able to give solution to the FCC-ee beam dynamics problems as outlined in the second chapter, a multiple and distributed feedback approach is proposed. The scheme can be implemented in two different proposals, the first one by maintaining the usual feedback scheme even if updated, the second one by implementing an innovative and more complicate design of DPU to apply correction signal by shortening the loop delay.

A question could arise: why do not implement only one feedback loop with a very high gain by using a big number of power amplifiers to have a faster damping time?

The answer, based on the experience, is: because the noise entering in the pickup cannot be filtered completely and increasing gain and power makes an enlargement effect of the bunches, that could become very evident in the vertical size, and could also push feedback to performance saturation.

Proposal 1: Cooperating Feedback Systems

Considering a damping time of about 10 turns for each feedback system (feasibility already demonstrated in other lepton colliders with tune > 0.09), it will be necessary to implement more feedback stations, most likely between 4 and 6.

There are some drawbacks in this strategy because a larger number of kickers and pickups increases the ring impedance. Another minor drawback is in the more complicated timing and setup operations.

An important advantage will be to have the possibility to apply correction kicks distributed along the ring. A second advantage is the following: by implementing this strategy it could be possible to achieve, if necessary, the theoretical damping limit of 1 revolution turn by installing more feedback stations, maybe by implementing 10-12 loops. As said previously very low tune frequencies can lower the feedback performance in any case.

Evaluating this scheme, it is obvious that a damping rate faster than 1 turn cannot be not achieved. This is because the correction kick can be applied only with 1 turn delay after processing the acquired signal. The DPU propagation delay cannot allow to kick faster. In the Fig. 6 an example of cooperating feedback scheme is shown. It is implemented by 4 stations placed along the 100 Km long FCC ring. The foreseen damping rate is 2.5 revolution turns.

4 Feedback systems (4 stations)

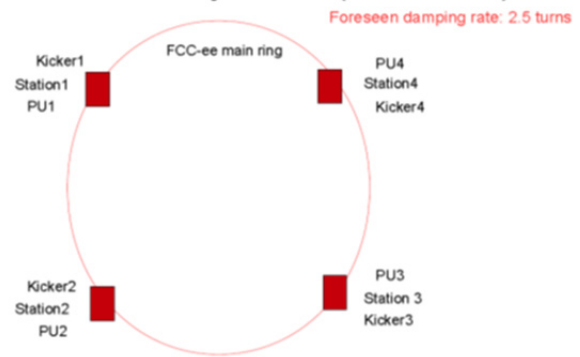


Figure 6: Example of cooperating feedback scheme implemented by 4 stations placed along the 100 Km long FCC ring. The foreseen damping rate is 2.5 revolution turns.

Proposal 2: Cooperating And “Feeding Forward” Systems

Of course, the ring length is a critical point for managing the feedback in terms of timing and control of the correct performance of the system. Nevertheless, a 100 Km ring length is also a very interesting opportunity to design an innovative scheme of feedback system [19] that is not convenient and neither possible in shorter rings. The idea is to make shorter than 1 turn the correction signal path. In this way, it will be feasible to achieve damping rates even faster than 1 revolution turn.

The “feeding forward” approach will somewhat change the usual system scheme, however not as much as it would seem. The phase response will be controlled by individual bunch FIR filter inside the DPU in this case too.

The implementation would be a big challenge from a technological point of view: it will be necessary to send the correction signal in a way to arrive to the kicker location before the arrival of the bunch that must be corrected. As example, few cases are analyzed below.

First, a “feeding forward” system can be designed that takes the input signal at the pickup 1 (PU1) and, after processing it in the station 1, sends the correction signal to the station 2 where kicker and power amplifier section are placed. The correction signal path follows the main ring diameter and hence it is 31.8 km long. The foreseen damping rate is 5 turns, the half of the standard approach.

In the Fig. 7 the “feeding forward” system is implemented by two stations and two loops. The system 1 takes the input signal at the pickup 1 (PU1) and, after processing in the station 1, sends the correction signal at the station 2 where kicker 1 and power section 1 are placed. Vice versa the system 2 takes the input signal at the pickup 2 (PU2) and, after processing it in the station 2, sends the correction signal to the station 1 where kicker 2 and power amplifier section 2 are placed. The correction signal path is along the main ring diameter and it is 31.8 km long. The foreseen damping rate is 2.5 turns.

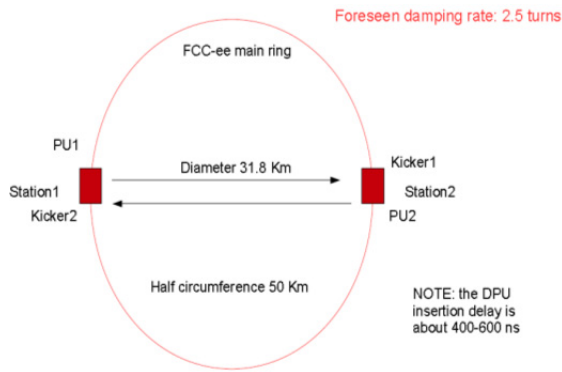


Figure 7: “Feeding forward” system implemented by two stations and two loops. The system 1 takes the input signal at the pickup 1 (PU1) and, after processing it in the station 1, sends the correction signal to the station 2 where kicker 1 and power section 1 are placed. Vice versa the system 2 takes the input signal at the pickup 2 (PU2) and, after processing it in the station 2, sends the correction signal to the station 1 where kicker 2 and power amplifier section 2 are placed. The correction signal path is on the main ring diameter and it is 31.8 km long. The foreseen damping rate is 2.5 turns.

In the Fig. 8 a “feeding forward” system is implemented by one station and one loop. The system 1 takes the input signal at the pickup 1 (PU1) and, after processing it in the station 1, sends the correction signal to the station 2 where kicker 1 and power section 1 are placed. The correction signal path is on the chord related to a quarter of circumference arc and it is 22.5 km long. The foreseen damping rate is 2.5 turns.

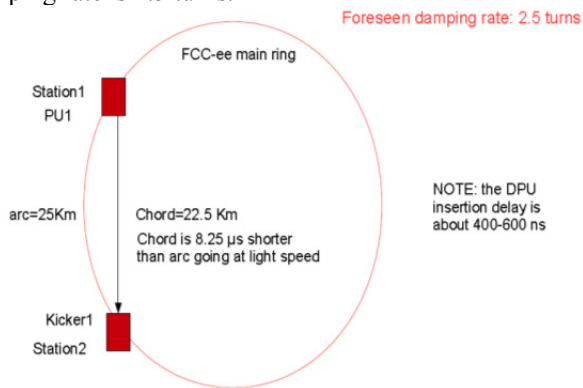


Figure 8: “Feeding forward” system implemented by one station and one loop. The system 1 takes the input signal at the pickup 1 (PU1) and, after processing it in the station 1, sends the correction signal to the station 2 where kicker 1 and power section 1 are placed. The correction signal path is on the chord related to a quarter of circumference arc and it is 22.5 km long. The foreseen damping rate is 2.5 turns.

In the Fig. 9 the “feeding forward” system is implemented by four stations and four loops. The system 1 takes the input signal at the pickup 1 (PU1) and, after processing it in the station 1, sends the correction signal

to the station 2 where kicker 1 and power section 1 are placed.

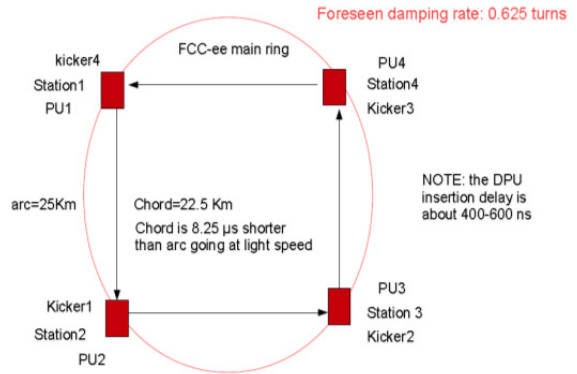


Figure 9: “Feeding forward” system implemented by four stations and four loops. The system 1 takes the input signal at the pickup 1 (PU1) and, after processing it in the station 1, sends the correction signal to the station 2 where kicker 1 and power section 1 are placed. The correction signal path is on the chord related to a quarter of circumference arc and it is 22.5 km long. The systems 2, 3 and 4 similarly take the input signals at the PU2, PU3, PU4 and after processing them in the station 2, 3 and 4 they send the correction signal to the station 3, 4 and 1 where kickers and power sections are placed. The foreseen damping rate is 0.625 turns.

The correction signal path is on the chord related to a quarter of circumference arc and it is 22.5 km long. The system 2, 3 and 4 similarly take the input signals at the PU2, PU3, PU4 and, after processing them in the station 2, 3 and 4, they send the correction signals to the station 3, 4 and 1 where kickers and power sections are placed. The foreseen damping rate in this case is 0.625 turns breaking the 1 turn limit with only four systems.

How to Transmit the Correction Signal

Efficient correction data transmission is not a simple task. A very preliminary idea could be to transmit correction signals by using lasers, with transmission lines in the vacuum, but the alignment, for distances of 22 or 32 km, is not easy. This technique seems also very expensive.

In theory the chord length could be shorter than 22 km, but the arc path should be long enough to recover the DPU insertion delay of 400-600 ns plus cable delays.

Radio-frequency transmission can also be considered [20] but it should be evaluated if it will be affected by noises caused by bad weather or of other natural or artificial origin.

A simpler solution seems to be the transmission of the digital data by optical fibers, compacting the correction signals by an efficient code, maybe treating them in blocks. In this way, the data should be applied to the kicker before the arrival of each bunch that needs to be corrected. A study on the possible codes should start taking as example the well-known MP3 coding.

CONCLUSION

The feedback systems for FCC-ee can be based on the designs developed for other previous e+/e- colliders as PEP-II, KEK, DAFNE, SuperB and SuperKEKB. The same DPU (digital processing unit) can be used for longitudinal and transverse systems, while analog modules and kickers need to be different in the transverse or longitudinal cases.

A DPU managing more than 100k separated bunch/bucket signals is feasible but it requires efforts for redesigning the present systems in a more compact design.

By implementing multiple cooperative feedback systems and maintaining the "traditional" design scheme it will be possible to damp up to 1 revolution turn, considering fractional tunes > 0.09 . This approach has been tested at DAFNE in the year 2008 with very good results. For lower fractional tunes some R&D is necessary.

Damping in less than one revolution turn is possible only changing the usual feedback strategy and implementing an innovative "feeding forward" strategy.

This new approach can be implemented because of course a chord or the diameter are shorter than the related arc and in this way, it is possible to compensate the DPU insertion delay (400-600 ns). Note that this scheme is feasible and convenient only for very long accelerator rings.

A "feeding forward" system, very challenging to implement, requires strong technological efforts to modify (partially) the DPU and to find an extremely fast data transmission method for distances in the range of 22-32 km. A strong R&D program should be planned.

REFERENCES

- [1] F. Zimmermann, M. Benedikt, D. Schulte, J. Wenninger, CERN, Geneva, Switzerland, "Challenges for the highest energy circular colliders", MOXAA01, in *Proceedings of IPAC2014*, Dresden, Germany.
- [2] F. Zimmermann *et al.*, "Beam dynamics issues in the FCC", in *Proceedings of HB2016*, Malmoe, Sweden, July 2016.
- [3] Michael Benedikt and Frank Zimmermann, "Outline and Status of the FCC-ee Design Study", ICFA, *Beam Dynamics Newsletter No. 67.*, Issue Editor: Y. Funakoshi, Editor in Chief: W. Chou. August 2015.
- [4] Michael Benedikt, Katsunobu Oide, Frank Zimmermann, Anton Bogomyagkov, Eugene Levichev, Mauro Migliorati, Uli Wienands, "Beam Dynamics Challenges for FCC-ee", ICFA, *Beam Dynamics Newsletter No. 67.*, Issue Editor: Y. Funakoshi, Editor in Chief: W. Chou. August 2015.
- [5] J.D. Fox *et al.*, "Programmable DSP Based Multibunch Feedback: Operational Experience from Six Installations". BIW 2000, Cambridge, Mass., May 2000, SLAC-PUB-8410.
- [6] D.Teytelman, "Architectures and Algorithms for Control and Diagnostics of Coupled-Bunch Instabilities in Circular Accelerators", Stanford Univ. PhD thesis, SLAC-R-633, June 2003.
- [7] S. Prabhakar, "New Diagnostics and Cures for Coupled-Bunch Instabilities", Stanford Univ. PhD thesis, SLAC-R-554, August 2001.
- [8] M. Zobov *et al.*, "Test of crab-waist collisions at DAFNE Phi factory", *Phys.Rev.Lett.*, 104 (2010) 174801.
- [9] E.Kikutani, M.Tobiyama, "Strategy for developing fast bunchfeedback systems for KEKB", May 1997, PAC97, Vancouver, Canada.
- [10] "SuperB: A High-Luminosity Asymmetric e+ e- Super Flavor Factory. Conceptual Design Report", e-Print: arXiv:0709.0451 [hep-ex].
- [11] A.Drago, "SuperB Fast Feedback Systems", in *PAC'09 Proceedings*, 4-8 May 2009. Vancouver, BC, Canada.
- [12] Y. Funakoshi *et al.*, "Beam Commissioning of SuperKEKB", in *Proceedings of IPAC 2016*, 08-13 May 2016. Busan, Korea.
- [13] <http://indico.cern.ch/event/340703/>
- [14] <http://indico.cern.ch/event/509631/>
- [15] A. Drago, M. Zobov, INFN-LNF; Dmitry Teytelman, "Recent Observations on a Horizontal Instability in the DAFNE Positron Ring", in *Proceedings of the 2005 Particle Accelerator Conference (PAC2005)*, Knoxville, Tennessee, USA - May 16-20, 2005.
- [16] A. Drago, "Horizontal Instability and Feedback Performance in DAFNE e+ Ring", LNF-04/18(P), 30/07/04. EPAC-2004. -THPLT056, Oct 2004. 3pp. In *Proceedings of 9th European Particle Accelerator Conference (EPAC 2004)*, Lucerne, Switzerland, 5-9 Jul 2004. In *Proceedings of EPAC 2004*, Lucerne, Switzerland: 2610-2612, 2004.
- [17] A.Gallo, F. Marcellini, A. Ghigo, R.Boni, "An overdamped Cavity for the DAFNE Longitudinal feedback", DAFNE Technical Note RF-17, 6/8/1995.
- [18] A.Drago, "Fast feedbacks for diagnostics and mitigation of e-cloud instability", oral presentation at International Linear Collider Workshop 2008, LCWS08 & ILC08, ILC08 Damping Ring session. Nov. 16-20, 2008. Univ. of Illinois at Chicago, USA.
- [19] A.Drago, talk held at the FCC Week 2016, Rome, April 2016.
- [20] A.Hutton, private communication.

OPTICS CORRECTION AND LOW EMITTANCE TUNING AT THE PHASE 1 COMMISSIONING OF SuperKEKB

Y. Ohnishi*, Y. Funakoshi, H. Koiso, A. Morita, K. Oide, and H. Sugimoto
KEK, Tsukuba, Japan

Abstract

The SuperKEKB collider has finally come to the first commissioning, Phase 1 without the final focus system and before Belle II detector roll-in. In order to accomplish an extremely high luminosity of $8 \times 10^{35} \text{ cm}^{-2} \text{ s}^{-1}$, the nano-beam scheme is adopted. Since the vertical emittance is one of the keys in this scheme, optics corrections for low emittance tuning are applied. The non-interleaved sextupole scheme is utilized in the arc section. Skew quadrupole-like corrector is equipped for each sextupole. These skew quadrupole-like correctors can correct both X-Y coupling and physical vertical dispersions which induce the vertical emittance. Beta function and physical horizontal dispersion are corrected by fudge factors of quadrupoles and/or horizontal orbit bumps at the sextupoles. Overall optics performance as well as the strategy of low emittance tuning is also presented.

Table 1: Machine Parameters in Phase-1 (Without Intra-beam Scattering)

	LER	HER	Unit
E	4.000	7.007	GeV
I	1.01	0.87	A
n_b	1576		
ε_x	1.8	4.6	nm
α_p	2.45×10^{-4}	4.44×10^{-4}	
σ_δ	7.52×10^{-4}	6.30×10^{-4}	
V_{RF}	7.56	12.61	MV
σ_z	4.6	5.3	mm
ν_s	-0.0192	-0.0253	
ν_x	44.53	45.53	
ν_y	46.57	43.57	
U_0	1.76	2.43	MeV
τ_x	46	58	msec

INTRODUCTION

The SuperKEKB collider [1] is an asymmetric-energy and a double-ring electron-positron collider. The energy of the electron ring is 7 GeV(HER) and the positron ring is 4 GeV(LER). The collision point is one and the circumference is 3 km. The target luminosity is $8 \times 10^{35} \text{ cm}^{-2} \text{ s}^{-1}$, which is 40 times as high as the predecessor KEKB collider [2]. In order to accomplish the extremely high luminosity, a nano-beam scheme [3] is adopted.

There are three stages for the commissioning of SuperKEKB; Phase-1, Phase-2, and Phase-3. The initial commissioning was done during Phase-1 without the final focus system before Belle II roll-in. The Phase-1 commissioning was started in February 2016 and operated until the end of June 2016 for about 5 months. The commissioning for Phase-2 will start in November 2017 and will operate for 5 months with the final focus system and Belle II detector. The first collision will be performed in Phase-2, however, the vertex detector will not be installed. The physics run with the full detector in Phase-3 will start October 2018, then the luminosity will increase gradually by squeezing the beta function at the IP and increasing the beam currents toward the target luminosity.

The vertical emittance is one of the most important issues in Phase-1 since the luminosity performance significantly depends on the coupling parameter in the nano-beam scheme. Table 1 shows machine parameters in Phase-1.

OPTICS MEASUREMENTS AND CORRECTIONS

The lattice for Phase-1 is the same lattice as those of Phase-2 and Phase-3 except for the interaction region(IR). Since there is no final focus magnet in the vicinity of the IP, the field strengths of quadrupole magnets in the IR are adjusted so as to connect the arc lattice. The optics tuning [4] without the final focus, the solenoid field, and the local chromaticity corrections can be performed for Phase-1. The lattice designs of the so-called interaction region in the LER and the HER are shown in Fig. 1.

The optical functions such as beta functions, dispersions, and X-Y couplings were measured and corrected in the LER and HER, respectively. The beta functions are obtained by orbit responses induced by six kinds of dipole correctors for each x and y direction [5]. The physical dispersions are measured by orbit displacements for the rf frequency shifts between -500 Hz and +500 Hz. Note that the dispersions are physical and different from normal mode dispersions. In the case of the X-Y couplings, vertical leakage orbits from horizontal orbits induced by six kinds of horizontal dipole correctors are used to correct the X-Y couplings instead of four X-Y coupling parameters of $r_1 - r_4$. The number of BPMs is 438 in the LER and 460 in the HER to measure closed orbits. The BPM gain mapping and the beam based alignment(BBA) have been performed before the optics tuning.

In order to correct the beta functions, the measured beta functions and phase-advance are compared with those calculated by the reference optics and amount of the correc-

* yukiyoshi.ohnishi@kek.jp

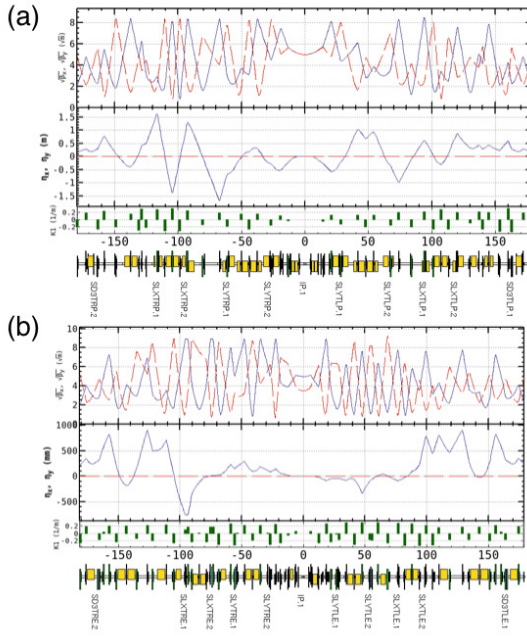


Figure 1: Lattice Design of “Interaction Region” in Phase-1; (a) LER and (b) HER.

tion of field strength for each quadrupole magnets are estimated. Correction coils are installed for each quadrupole magnet, however, the correction was performed by families of quadrupole magnets during the Phase-1 commissioning. The arc lattice adopts non-interleaved sextupole correction scheme and two identical sextupoles are connected by $-I'$ transfer matrix. The dispersions and X-Y couplings are corrected by using this specialty. The horizontal dispersions are corrected by using asymmetric local bumps in the horizontal direction at pairs of two horizontal focusing sextupoles(SF). The horizontal offset of the sextupole generates quadrupole field, however, this quadrupole field is localized between two identical sextupoles then only horizontal dispersions can be corrected. The vertical dispersions and the X-Y couplings are corrected by using skew quadrupole-like correctors at the sextupole magnets. The opposite sign of the skew quadrupole field can correct only the vertical dispersions, on the other hand, the same sign can correct only the X-Y couplings. Because of the non-interleaved sextupole scheme, the corrections of vertical physical dispersions and X-Y couplings can be solved independently for each other.

Table 2 shows the results of optics corrections. After these optics corrections, the vertical emittance has achieved 8 pm in the LER which was measured by an X-ray beam size monitor. The vertical emittance is derived by $\varepsilon_y = \sigma_y^2/\beta_y$. Figure 2 shows the history of the vertical emittance and the vertical physical dispersion in the LER. In another way, the vertical emittance can be estimated by measured optical functions and magnet configurations;

$$\varepsilon_y = C_q \gamma^2 \frac{I_{5,y}}{I_2}. \quad (1)$$

The normal dispersions can be derived by X-Y coupling parameters and transfer matrix between neighboring two BPMs in the model. The vertical emittance of 8 pm in the LER is obtained by this estimation which is consistent with the X-ray measurement. On the other hand, the measured vertical beam size in the HER was $30 \mu\text{m}$ for $\beta_y = 7.6 \text{ m}$ without any corrections, which corresponds to the vertical emittance of 40 pm when corrections for the X-ray measurement was applied. This value seems to be too large because the optics tuning is the same level between the LER and HER as shown in Table 2. A simulation assuming a mis-alignment of the sextupoles which reproduces the measured optical functions provides the vertical emittance of 5 – 20 pm. We consider that the calibration issues of X-ray monitor still remains. The vertical emittance is indirectly estimated to be 6 pm by using the measured optical functions in the HER.

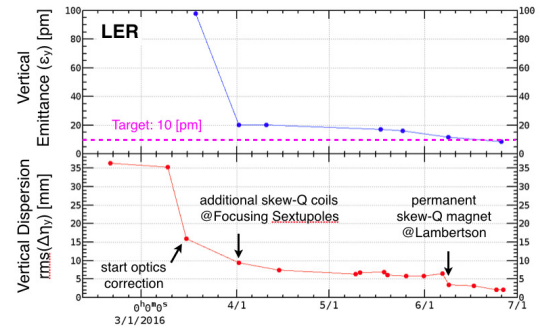


Figure 2: History of Vertical Emittance and Vertical Physical Dispersion in the LER.

Table 2: Results of the Optics Tuning in Phase-1. X-Y coupling* refers an average value of $\text{rms}(\Delta y)/\text{rms}(\Delta x)$ induced by six kinds of horizontal dipole correctors. Dispersions are physical variables in the table.

Items	Symbol	LER	HER
Coupling strength	$ C^- (\times 10^{-3})$	1.2	2.0
X-Y coupling*	$\text{rms}(\Delta y)/\text{rms}(\Delta x)$	0.9 %	0.6 %
Hor. dispersion	$\text{rms}(\Delta \eta_x)$	8 mm	11 mm
Ver. dispersion	$\text{rms}(\Delta \eta_y)$	2 mm	2 mm
Hor. β function	$\text{rms}(\Delta \beta_x/\beta_x)$	3 %	3 %
Ver. β function	$\text{rms}(\Delta \beta_y/\beta_y)$	3 %	3 %
Hor. tune	$\Delta \nu_x (\times 10^{-4})$	2	5
Ver. tune	$\Delta \nu_y (\times 10^{-4})$	5	1

OFF-MOMENTUM OPTICS

The dynamic aperture for a particle without a momentum deviation is almost recovered by the optics correction when machine errors decrease the dynamic aperture. However, the dynamic aperture with momentum deviations decreases compared with the ideal lattice even though the optics correction is performed. It is necessary to correct the

off-momentum optics in order to recover the dynamic aperture. The optical parameters, a chromatic phase-advance and a chromatic X-Y coupling are expected to be useful to accomplish this purpose. The chromatic phase-advance is adjusted by using sextupole magnets. The chromatic phase-advance in the horizontal and the vertical direction are expressed as

$$\chi_i(x) = \frac{1}{2\pi} \frac{\partial \Delta\psi_{x,i}}{\partial \delta} \quad (2)$$

$$\chi_i(y) = \frac{1}{2\pi} \frac{\partial \Delta\psi_{y,i}}{\partial \delta}, \quad (3)$$

where

$$\Delta\psi_{x,i} = \psi_{x,i} - \psi_{x,i-1} \quad (4)$$

$$\Delta\psi_{y,i} = \psi_{y,i} - \psi_{y,i-1}. \quad (5)$$

The number of locations is about 450 for each ring which corresponds to the neighboring BPMs. In order to correct the chromatic phase-advance, the field gradient of the sextupole magnets, ΔK_2 , are obtained by solving these equations:

$$\begin{pmatrix} \chi_{1,m}(x) - \chi_{1,d}(x) \\ \vdots \\ \chi_{N,m}(x) - \chi_{N,d}(x) \\ \chi_{1,m}(y) - \chi_{1,d}(y) \\ \vdots \\ \chi_{N,m}(y) - \chi_{N,d}(y) \\ \xi_{x,m} - \xi_{x,d} \\ \xi_{y,m} - \xi_{y,d} \end{pmatrix} = M_{resp} \begin{pmatrix} \Delta K_{2,1}/K_{2,1} \\ \Delta K_{2,2}/K_{2,2} \\ \vdots \\ \Delta K_{2,M}/K_{2,M} \end{pmatrix}, \quad (6)$$

where m indicates the measurements, d indicates the model calculation, M_{resp} is a response matrix calculated by the model lattice, N is the number of BPMs, and M is the number of families of the sextupole magnets. In the Phase-1 commissioning, M is 50. The measurements of the phase advance for each momentum deviations are similar to the beta measurement with the frequency shift between -500 Hz and +500 Hz. The corrections for the sextupole families in the LER are shown in Fig. 3. The field gradient, K_2 , which corresponds to the rated current for the defocusing sextupole(SD) is -8.2 1/m^2 and 5.0 1/m^2 for the focusing sextupole(SF). The amount of the sextupole correction is within 5 % of the rated current.

Figure 4 (a) shows the chromatic phase-advance before the correction and Fig. 4 (b) shows after the correction in the LER. The blue plots indicate the measured values and the green plots indicate the model calculations. The motivation of analysis for the off-momentum optics comes from the discrepancy of the chromaticity between measurements and the model lattice. Table 3 shows the measured chromaticity and calculated values by using the model lattice in the LER. The betatron tunes as a function of the momentum deviations, δ , are also shown in Fig. 5.

Although the phase advance and the beta function are derived by the model independent, one of the Twiss parameters, $\alpha_{X,y}$ is obtained by using a transfer matrix between

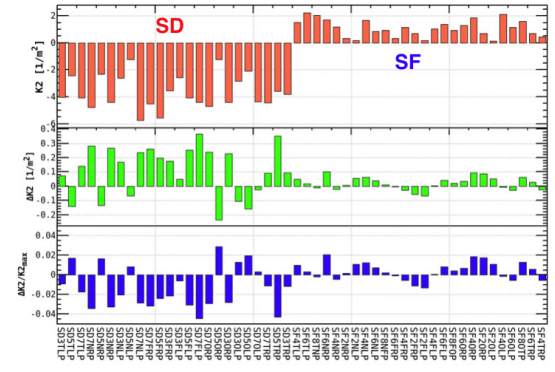


Figure 3: Corrections for the Field Gradient of the Sextupole Families in the LER.

Table 3: Chromaticity in the LER.

Symbol	Meas.	Model before	Model after
ξ_x	2.97	0.87	3.00
ξ_y	1.88	5.78	2.15

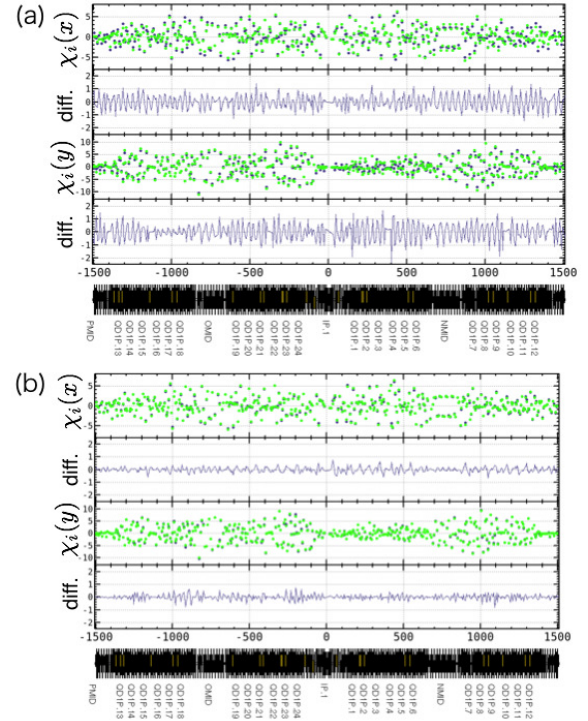


Figure 4: Chromatic Phase-Advance in the LER; (a) Before Correction and (b) After Correction. Measurements(blue) and Model(green).

neighboring two BPMs with the model and measured β functions and phase advances. The chromatic functions, $W_{X,y}$ can be defined by

$$W_{x,y} = \sqrt{\left(\frac{1}{\beta_{x,y}} \frac{\partial \beta_{x,y}}{\partial \delta} \right)^2 + \left(\frac{\partial \alpha_{x,y}}{\partial \delta} - \frac{\alpha_{x,y}}{\beta_{x,y}} \frac{\partial \beta_{x,y}}{\partial \delta} \right)^2}. \quad (7)$$

Figure 6 shows the chromatic functions for the measurements and the model after the correction in the LER. The

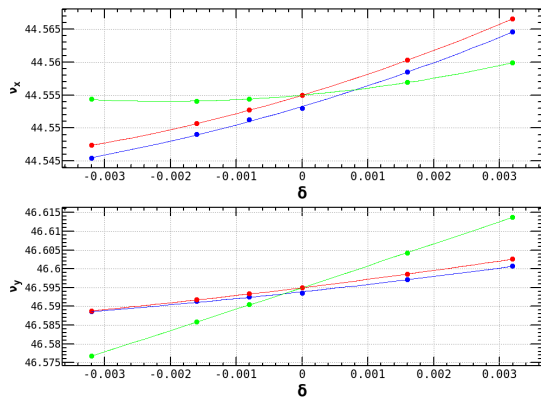


Figure 5: Chromaticity in the LER. Measurement(blue), Model before correction(green), Model after correction(red)

chromatic functions calculated by the model lattice can also reproduce the measured chromatic functions well after the correction in the LER.

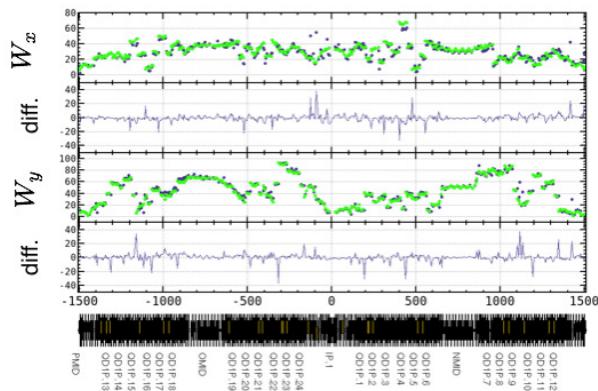


Figure 6: $W_{x,y}$ Function in the LER. Measurements(blue) and Model(green) after Correction.

CONCLUSIONS

The optics measurements and corrections have successfully been worked during Phase-1. The vertical emittance of 8 pm has been achieved in the LER which is smaller than the tentative target value at this stage. The value of the vertical emittance measured by X-ray beam-size monitor and the estimation from the measured optical functions are consistent with each other in the LER. However, the vertical emittance in the HER is still discrepancy between the X-ray measurement and the estimation from the optical functions. The reason is under study so far.

The analysis of the off-momentum optics has been performed. Understanding of the off-momentum optics is necessary to optimize the dynamic aperture. Measurements of the chromatic phase-advance and the correction of the field gradient for the sextupole magnets are presented. The correction of the sextupole magnets is less than 5% of the rated current. Consequently, the chromatic phase-advance, chromaticity, and the chromatic functions, $W_{x,y}$, can be adjusted on the model lattice.

REFERENCES

- [1] Y. Ohnishi *et al.*, *Prog. Theor. Exp. Phys.* 2013 03A011 (2013).
- [2] T. Abe *et al.*, *Prog. Theor. Exp. Phys.* 2013 03A001 (2013).
- [3] “SuperB Conceptual Design Report”, INFN/AE-07/2, SLAC-R-856, LAL 07-15, March 2007.
- [4] Y. Ohnishi *et al.*, in *Proceedings of IPAC2016*, Busan, Korea, May (2016), paper THPOR007.
- [5] A. Morita *et al.*, *Phys. Rev. ST-AB*, vol. 10, p. 072801, 2007.

LUMINOSITY TUNING AT KEKB

Y. Funakoshi*, KEK, Tsukuba, Japan

Abstract

KEKB achieved the world's highest luminosity. One of the key issues for the high luminosity at KEKB was a luminosity tuning which was done almost all the time even during the physics run to suppress the beam-beam blowup. In this talk, those experiences are summarized.

factors are not much different from unity. Therefore, the luminosity is almost determined by the three parameters; *i.e.* the beam current (I), the beam-beam parameter (ξ_y) and the vertical beta function at the IP (β_y^*). Table 1 shows machine parameters of KEKB at the time when the highest luminosity was achieved.

INTRODUCTION

KEKB [1] was an energy-asymmetric double-ring collider for B meson physics. KEKB consisted of an 8-GeV electron ring (the high energy ring: HER), a 3.5-GeV positron ring (the low energy ring: LER) and their injector, which is a linac-complex providing the rings with both of the electron and positron beams. The construction of KEKB started in 1994, utilizing the existing tunnel of TRISTAN, a 30 GeV \times 30 GeV electron-positron collider. The machine commissioning of KEKB started in December 1998. The physics experiment with the physics detector named Belle was started in June 1999. The peak luminosity surpassed the design value of $1.0 \times 10^{34} \text{cm}^{-2}\text{s}^{-1}$ in May 2003. The maximum peak luminosity of KEKB is $2.11 \times 10^{34} \text{cm}^{-2}\text{s}^{-1}$, which was recorded in June 2009. This value has been the world-record since then. The KEKB operation was terminated at the end of June 2010 for the works to upgrade KEKB to SuperKEKB. The total integrated luminosity collected by the Belle detector was 1041fb^{-1} . The history of KEKB is shown in Figure 1. In this report, some experiences at KEKB are described. An emphasis is placed on the experiences on the luminosity tuning. Some of them may be useful in future colliders such as SuperKEKB or a high-luminosity circular e+e- Higgs factory. Achievements of KEKB and details of commissioning are described elsewhere [2] [3].

Table 1: Machine Parameters of KEKB

Parameters	LER	HER	Units
Energy	3.5	8.0	GeV
Circumference	3016		m
I_{beam}	1.637	1.188	A
# of bunches	1585		
I_{bunch}	1.03	0.75	mA
Ave. Spacing	1.8		m
Emittance	18	24	nm
β_x^*	120	120	cm
β_y^*	5.9	5.9	mm
Ver. Size@IP	0.94	0.94	μm
RF Voltage	8.0	13.0	MV
ν_x	.506	.511	
ν_y	.561	.585	
ξ_x	.127	.102	
ξ_y	.129	.090	
Lifetime	133	200	min.
Luminosity	2.108		$10^{34} \text{cm}^{-2}\text{s}^{-1}$
Lum/day	1.479		fb^{-1}

MACHINE PARAMETERS RELATED TO LUMINOSITY

As is well known, the luminosity is expressed as

$$L = \frac{\gamma_{\pm}}{2er_e} \left(1 + \frac{\sigma_y^*}{\sigma_x^*} \right) \frac{I_{\pm} \xi_{y\pm}}{\beta_{y\pm}^*} \frac{R_L}{R_{\xi_y}}$$

Here, γ and r_e are the Lorentz factor and the electron classical radius and the index of \pm denotes the positron or electron. σ_y^* and σ_x^* are the vertical and horizontal beam sizes at the IP, respectively. I , ξ_y and β_y^* denote the total beam current, the vertical beam-beam parameter and the vertical beta function at the IP, respectively. R_L and R_{ξ_y} are the reduction factors for the luminosity and the vertical beam-beam parameter due to the hourglass effect and the crossing angle, respectively. In usual cases, the beam size ratio is much smaller than unity and the two reduction

BEAM CURRENTS AND VERTICAL BETA FUNCTIONS AT THE IP

The HER beam current of 1.188 A in Table 1 is near the hardware limit. The design beam current of HER was 1.1 A. On the other hand, the design beam current of LER was 2.6 A and there was large room to increase LER beam current from the viewpoint of the hardware limit. There are evidences that this saturation of the luminosity against the LER beam current is caused by the effects of the electron clouds [3]. Based on these experiences, we will take more fundamental countermeasures against the electron clouds effect at SuperKEKB such as adoption of antechambers with TiN coating. As for the vertical beta function at the IP (β_y^*), the minimum values are determined by the hourglass effect. Although lower values than 5.9 mm were possible from the viewpoint of the dynamic aperture and the detector beam background, the lower β_y^* did not bring a higher luminosity.

* yoshihiro.funakoshi@kek.jp

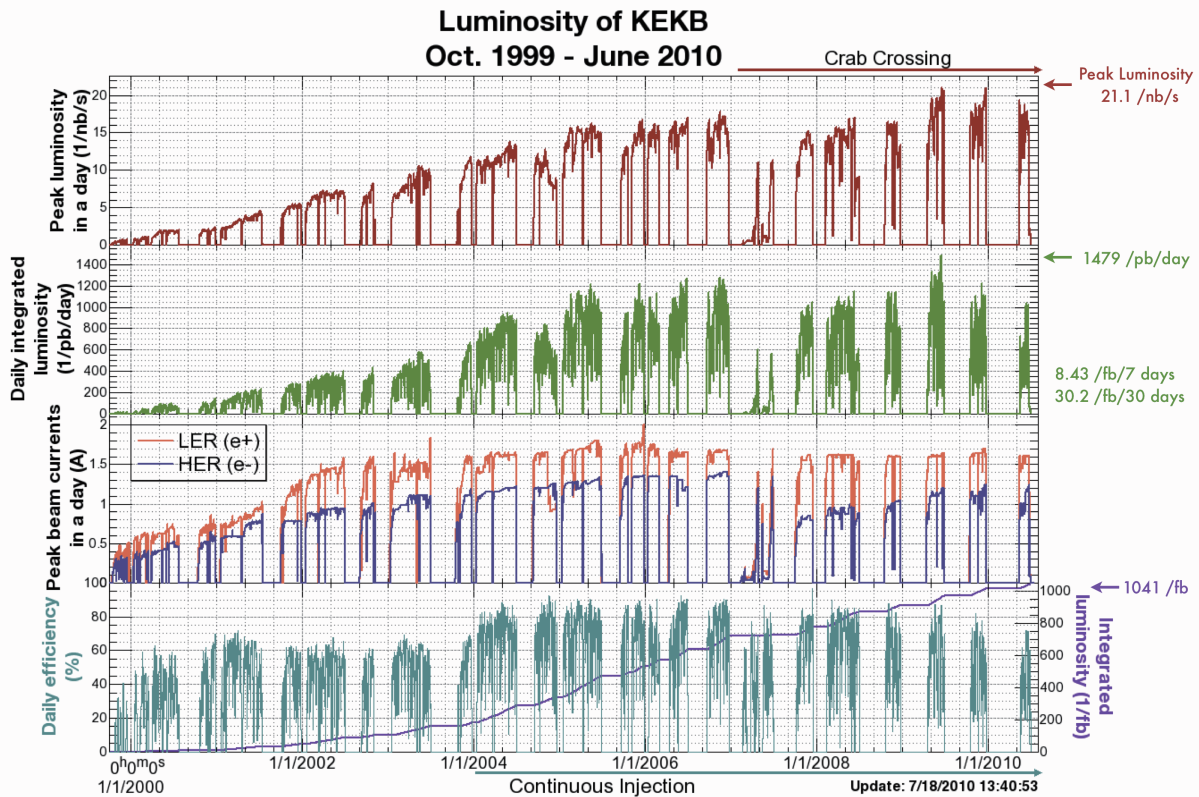


Figure 1: History of the performance of KEKB from October 1999 to June 2010. The rows represent (top to bottom) the peak luminosity in a day, the daily integrated luminosity, the peak stored currents in the LER and HER in a day, the daily efficiency, and the total integrated luminosity at Belle, respectively. The integrated luminosities are the numbers recorded by Belle. The daily efficiency is defined as (Daily integrated luminosity)/(Peak luminosity times 1 day), and was boosted in January 2004 by the continuous injection. The crab crossing scheme had been in use since February 2007.

SUPPRESSION OF THE BEAM-BEAM BLOWUP

In early days of KEKB, we experimentally found that a horizontal tune closer to half-integer gives a higher luminosity. This tendency is confirmed later by the beam-beam simulation. This issue was also studied theoretically later and the reason for the high luminosity with the horizontal tune close to the half-integer is explained in the context of the degree of the freedom of the dynamical system [4]. Figure 2 shows a history of the horizontal tune of KEKB.

There are a number of knobs to tune up the luminosity. Only a few of them can be tuned up with independent observables besides the luminosity. Table 2 lists the tuning parameters and its observables. Tuning parameters related to the crab cavities are not listed in the table. We found that the liner optics correction is important for suppressing the beam-beam blowup. In usual beam operation, we frequently (typically every 2 weeks) made optics corrections where we corrected global beta functions, x-y coupling parameters and dispersions [5]. Sometimes, the optics corrections were

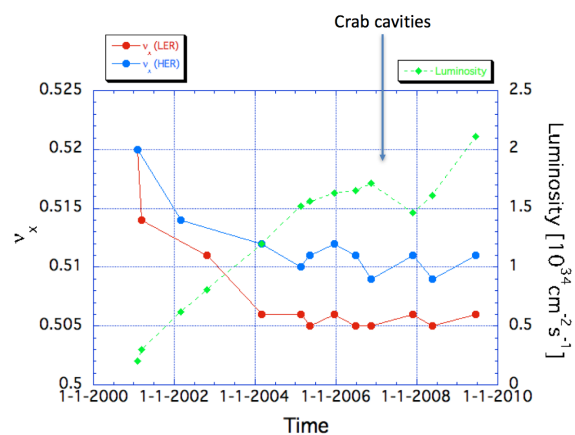


Figure 2: History of horizontal tune of LER and HER together with the luminosity.

done with a different set of strength of the sextupole magnets to narrow the stop-band of the resonance ($2\nu_x + \nu_s = \text{integer}$) or ($2\nu_x + 2\nu_s = \text{integer}$). The optics correction is the

basis of the luminosity tuning. On this basis, we carried out tuning on the other parameters in Table 2. At KEKB, we found that the local x-y coupling and the vertical dispersion at IP are very important for increasing the luminosity. We have developed tuning knobs to adjust those parameters. In the conventional method of tuning at KEKB, most of these parameters (except for the parameters optimized by observing their own observables) were scanned one by one just observing the luminosity and the beam sizes. As a more efficient method of the parameter search, we introduced in autumn 2007 the downhill simplex method for twelve parameters of the x-y coupling parameters at IP and the vertical dispersions at IP and their slopes, which are very important for the luminosity tuning from the experience of the KEKB operation. These twelve parameters can be searched at the same time in this method. We had been using this method since then. However, even with this method an achievable specific luminosity had not been improved, although the speed of the parameter search seemed to be rather improved.

For the luminosity tuning, only the luminosity monitor [7] and the beam size monitor based on the SR interferometer [6] are used and so these monitors are particularly important at KEKB. Also, the continuous injection scheme (top-up injection) made the luminosity tuning easier through more stable beam conditions [3]. With the scheme, the beam currents were almost constant and heating effects by the beams were saturated at some points. Generally speaking, a machine has a tendency that its operation becomes more stable with operation conditions unchanged. As an example in the KEKB operation, in the conventional injection scheme we used different working points during the injection and the physics run and the beam abort sometimes occurred in changing the tunes due to wrong setting of the tunes. We can avoid this problem with the continuous injection. Of course, the direct motivation of the continuous injection was to increase the integrated luminosity. Roughly speaking, the gain of the continuous injection in the integrated luminosity was about 30%. One third of it came from elimination of the loss time, while two third from keeping the maximum beam currents. We started the beam operation with the continuous injection scheme in the middle of January 2004. Since then, this scheme had been very successfully applied to the KEKB operation and brought an enormous gain in the integrated luminosity to Belle. In Table 3, we show a comparison of luminosity performance before and after the continuous injection. For comparison, we took two shifts that were stable and gave record integrated luminosities. The beam operations of the two shifts are shown in Fig. 3 and 4.

Some Experience of Luminosity Tuning at KEKB

In the following, some experiences of luminosity tuning at KEKB are summarized.

- The KEKB luminosity had been increased by many and continuous parameter scans.
 - The machine operators performed almost always (even in physics run) parameter scans. (scan, scan,

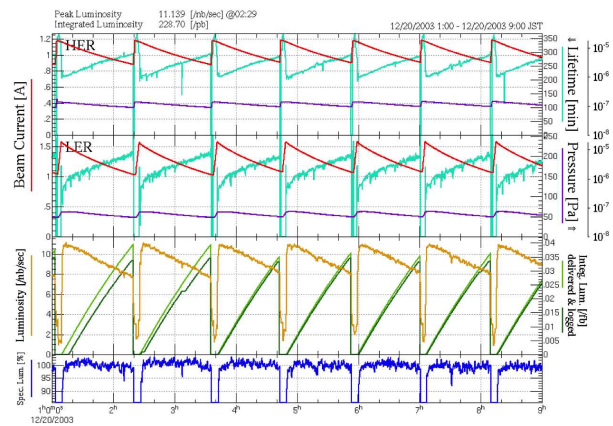


Figure 3: Beam currents and luminosity trend before continuous injection.

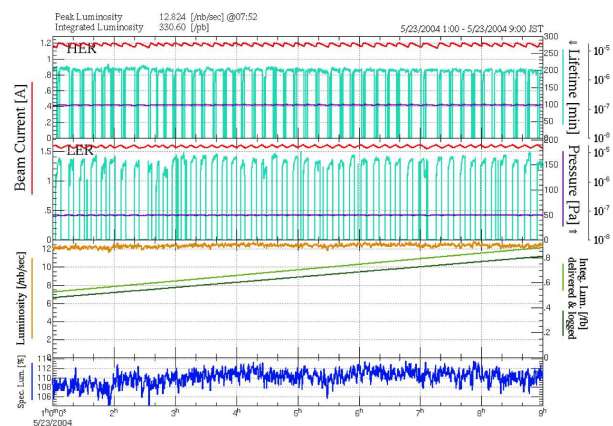


Figure 4: Beam currents and luminosity trend after continuous injection.

scan...). In almost all cases, scans are done in vain. But sometimes, we got an improvement in the luminosity. It was important to continue the scans.

- An introduction of downhill simplex method for the parameter search speeded up the parameter search. However, the achievable luminosity was not increased with this method.
- Most of the luminosity tuning used the luminosity monitors and the beam size monitor (SR interferometer) as observables. Reliability of those monitors were important.
- The continuous injection scheme (top-up injection) made the luminosity tuning easier through more stable beam conditions.

Table 2: Tuning knobs for the luminosity and their observables. We relied also on the beam size at the synchrotron radiation monitor (SRM), besides the luminosity.

Knob	Observable	frequency
Beam offset at IP (orbit feedback)	Beam-beam kick (BPMs)	~1 s
Crossing angle at IP (orbit feedback)	BPMs	~1 s
Target of orbit feedback at IP (offset)	vertical size at SRM, luminosity	~1/2 day
Target of orbit feedback at IP (angle)	vertical size at SRM, luminosity	~1/2 day
Global closed orbit	BPMs	~ 20 s
Betatron tunes	tunes of non-colliding bunches	~ 20 s
Relative RF phase	center of gravity of the vertex	~ 10 min
Global coupling, dispersion, beta-beat	orbit response to kicks, RF freq.	~ 14 days
Vertical waist position	vertical size at SRM, luminosity	~ 1/2 day
x-y coupling and dispersion at IP	vertical size at SRM, luminosity	~ 1/2 day
Chromaticity of x-y coupling at IP	vertical size at SRM, luminosity	~ 1/2 day

Table 3: Comparison of the continuous injection with the conventional injection scheme.

Injection mode	Continuous	Conventional	
Reference shift	Dec. 20 2003 owl	May 23 2004 owl	
Integrated luminosity per shift	330.6	228.7	pb ⁻¹
Peak luminosity	12.824	11.139	nb ⁻¹ s ⁻¹
Loss time*	0	~13.4	%
Veto time during injection	3.5	0	ms
Increase of dead time due to Veto	~2.3	0	%
Linac repetition rate	10	50	Hz
Injection rate (e+)	~0.39	~3.1	mAs ⁻¹
Injection rate (e-)	~0.71	~4.5	mAs ⁻¹
Peak beam current (e+)	1600	1570	mA
Peak beam current(e-)	1200	1175	mA

* due to injection and HV up/down

OTHER EFFORTS TO INCREASE THE LUMINOSITY

Skew-sextupole Magnets

Ohmi et al. showed that the chromaticity of x-y coupling parameters at the IP could degrade the luminosity, if the residual values, which depend on machine errors, are large [8]. To control this chromaticity, skew sextupole magnets, 10 pairs for HER and 4 pairs for LER, were installed during winter shutdown 2009. It turned out that the skew sextuples are very effective to raise the luminosity at KEKB. The knobs to control the chromaticity of the x-y coupling were introduced for beam operation on May 2 2009. The gain of the luminosity by these magnets was about 15~17% [3].

Crab Cavities

20 years after they were initially proposed, in February 2007 crab cavities are for the first time installed in an operating collider, KEKB. It was expected that the beam-beam parameters (ξ_y) and the luminosity would be doubled with the crab cavities. Actually achieved luminosity gain with crab was about 30~40 % including the effect of the skew-sextupoles. The beam-beam parameter was increased from

~0.06 to ~0.09, while ~0.15 had been expected. The discrepancy between the simulation and the experiment has not been understood yet [3].

REFERENCES

- [1] KEKB B-Factory Design Report, KEK-Report 95-7, 1995.
- [2] T. Abe *et al.*, *Prog. Theor. Exp. Phys.* (2013) 2013 (3), 03A001.
- [3] T. Abe *et al.*, *Prog. Theor. Exp. Phys.* (2013) 2013 (3), 03A010.
- [4] K. Ohmi, K. Oide and E. A. Perevedentsev, "Beam-beam Limit and the Degree of Freedom", in *Proc. EPAC06*, Edinburgh, Scotland (2006), paper MOPLS032.
- [5] K. Akai *et al.*, *Nucl. Instrum. Methods A* 499, 191 (2003).
- [6] M. Arinaga *et al.*, *Nucl. Instrum. Methods Phys. Res., Sect. A* 499, 100 (2003).
- [7] V. Zhilich, *Nucl. Instrum. Methods Phys. Res., Sect. A* 494, 63 (2002).
- [8] D. Zhou, K. Ohmi, Y. Seimiya, Y. Ohnishi, A. Morita, and H. Koiso, *Phys. Rev. Special Topics, Accelerator and Beams*, **13**, 021001 (2010).

COUPLING AND DISPERSION CORRECTION FOR THE TOLERANCE STUDY IN FCC-EE

S. Aumon *, B. Holzer, CERN , Geneva , Switzerland, Katsunobu Oide, KEK, Japan
 A. Doblhammer (Technische Universität Wien, Austria), B. Haerer (KIT, Karlsruhe, Germany)

Abstract

The FCC-ee study is investigating the design of a 100 km e+/e- circular collider for precision measurements and rare decay observations in the range of 90 to 350 GeV center of mass energy with luminosities in the order of $10^{35} \text{ cm}^{-2} \text{ s}^{-1}$. In order to reach such performances, an extreme focusing of the beam is required in the interaction regions with a low vertical beta function of 2 mm at the IP. Moreover, the FCC-ee physics program requires very low emittances never achieved in a collider with 1.3 nm for ϵ_x and 2 pm for ϵ_y at 175 GeV, reducing the coupling ratio to around 2/1000. With such requirements, any field errors and sources of coupling will introduce spurious vertical dispersion which degrades emittances, limiting the luminosity of the machine. This study describes the status of the tolerance study and the impact of errors that will affect the vertical emittance. In order to preserve the FCC-ee performances, in particular ϵ_y , a challenging correction scheme based on dispersion free steering and linear coupling correction is proposed to keep the coupling and the vertical emittance as low as possible.

INTRODUCTION

Electron-positron circular colliders profit from small vertical beam size due to vertical emittances close to the quantum excitation. The FCC-ee machine is foreseen to run at 4 different energies in order to perform precision measurements of the Z and W resonance and the Higgs and top. In order to produce a high luminosity, an extreme focusing of the beam is required in the interaction regions with a low vertical beta function of 2 mm at the IP. The baseline foresees very low emittance never achieved in a collider with 1.3 nm for ϵ_x and 2 pm for ϵ_y at 175 GeV, bringing down the coupling ratio to 2/1000. The main parameters are presented in Tab. 1. With such performances, the chromaticities reach several hundred units and the high beta functions in the interaction regions cause the machine to be very sensitive to lattice errors, resulting in large distortion of the vertical dispersion. As a consequence, the vertical emittance will be enlarged, since

$$\epsilon_y = \left(\frac{dp}{p} \right)^2 (\gamma D^2 + 2\alpha DD' + \beta D'^2) \quad (1)$$

where D is the vertical dispersion, D' the dispersion derivative with s , $\frac{dp}{p}$ the momentum spread, γ, β, α are the lattice parameters. This article present the status of the tolerance of the FCC-ee lattice to errors such as magnet misalignments, rolled angles, which are the main cause of vertical dispersion and emittance blowup. The main challenge is to

establish an optics correction methodology suitable for large machines with such challenging beam parameters baseline such as FCC-ee.

FCC-EE RACETRACK LAYOUT

The FCC-ee machine is foreseen to run at 4 different energies and in term of tolerance, the biggest challenge comes from the 175 GeV case, due the 8 GeV energy loss per turn by synchrotron radiation, as shown in Tab. 1. A constraint being that the lepton and hadron collider layout should fit together, several lattice scenarios with different interaction regions and sextupole layouts are under study (See [1] [2]). This paper will show mainly results about a racetrack lattice, with 2 RF sections and a LEP-like interaction region, where the final doublet quadrupoles focus the beam down to 2 mm β_y^* . The IR and arc optics are shown in Fig. 1. In this lattice, the chromaticity is corrected with sextupoles in the arcs including a matching from arc to IP of the Montague functions, whereas another lattice option provides as well a local chromaticity correction at the IPs [2]. The two layouts are shown in Fig. 2 for a lattice with the LEP-like IR and chromaticity correction in the arcs and Fig. 3 for a lattice with a local chromaticity correction at the IPs.

Table 1: Baseline Beam Parameters in FCC-ee

Beam Energy (GeV)	120	175
Beam current (mA)	30	6.6
Bunch/beam	780	81
Bunch population (10^{11})	0.8	1.7
Horizontal ϵ (nm)	0.61	1.3
Vertical ϵ (nm)	0.0012	0.0025
Momentum compaction (10^{-5})	0.7	0.7
Hor. β^* at the IP (mm)	1000	1000
Vert. β^* at the IP (mm)	2	2
Energy loss/turn (GeV)	1.67	7.55
Total RF Voltage (GV)	3	10

For FCC-ee, the so-called sawtooth effect is particularly important at 175 GeV: with 8 GeV of energy loss per turn, the off-momentum particles are following the dispersive orbit until they reach the next RF section. This effect causes an orbit distortion of about 1.5 millimeter, which is very problematic when the beam goes off center through the strong sextupoles. Two options are foreseen to alleviate this problem: the FCC-ee lattice can be tapered either fully or partially. In the fully tapered option, every magnet strength (dipole, quadrupole, sextupole) is adapted to the current energy loss. In the partially tapered option - or sectorwise version- the machine

* sandra.aumon@cern.ch

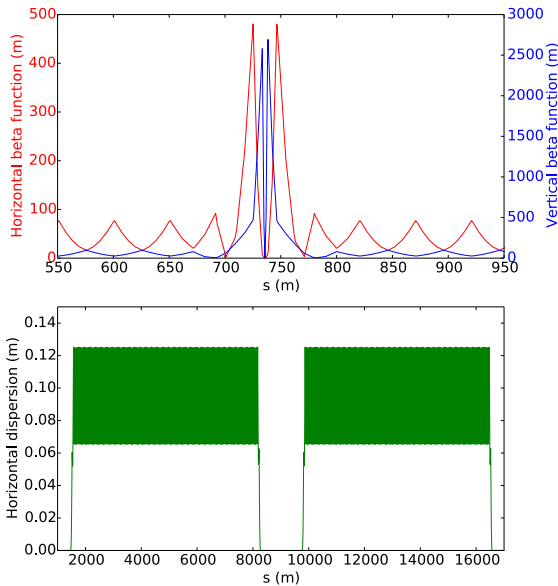


Figure 1: Beta functions (upper figure) in the IR and in the arcs and horizontal dispersion (lower figure).

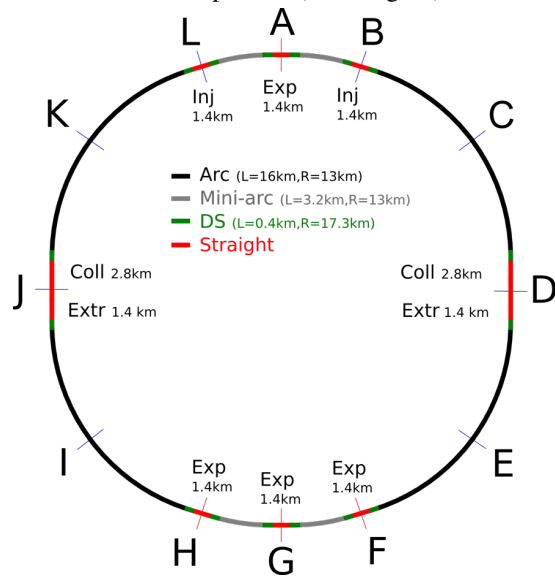


Figure 2: Racetrack layout with chromaticity correction in the arcs [1].

provides a tapering to the dipoles only, leaving therefore a remaining horizontal orbit as shown in Fig. 4 [3].

Therefore, with targeted emittances of the order of nm and pm, FCC-ee is a collider with foreseen performances of light sources (ESRF, SLS).

AMPLIFICATION FACTOR BY ERROR TYPE

In this section, amplification factors on the orbit and/or the vertical dispersion are computed by errors type. For emittance tuning purposes, any source of vertical dispersion and coupling has to be identified and should be corrected as much as possible. Let consider the most important errors to consider.

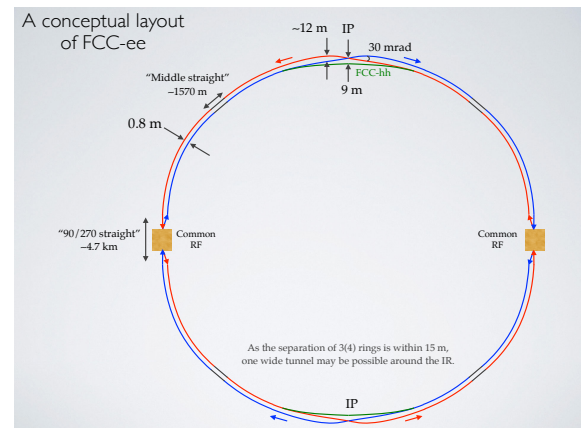


Figure 3: Racetrack layout with local chromaticity correction at the IR [2].

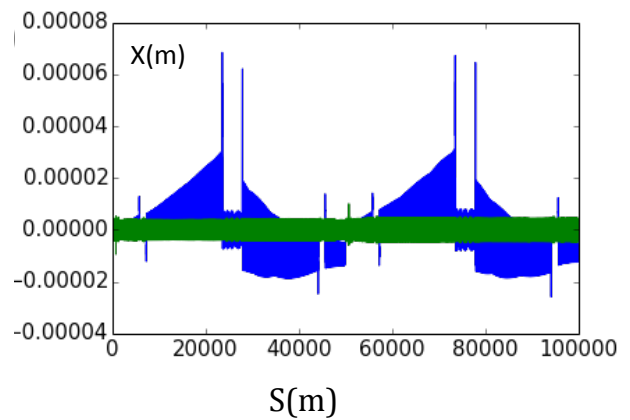


Figure 4: In green, typical horizontal orbit remaining after correction without synchrotron radiation, in blue [3]

A vertical offset Δy in the quadrupole provides a dipolar kick since [4],

$$B_x = k(y + \Delta y) = ky + k\Delta y \quad (2)$$

with k the normalised quadrupole strength. The constant term $k\Delta y$ provides a vertical dipole component and therefore vertical dispersion. Sextupole offsets produce coupling and vertical dipole kick since,

$$\begin{aligned} B_x &= kxy + kx\Delta y \\ B_y &= k(x^2 - y^2) - 2k\Delta y - (\Delta y)^2 \end{aligned} \quad (3)$$

Quadrupole roll angles produce a skew strength, generating betatron coupling and transferring horizontal emittance to vertical emittance. The resulting vertical dispersion change due to a skew strength component is

$$\Delta D_y = -(\Delta J_w) D_x \frac{\sqrt{\beta_y \beta_{y0}}}{2 \sin(\pi Q)} \cos(\pi Q - |\phi_{y0} - \phi_y|) \quad (4)$$

where J_w is the skew strength, D_x is the horizontal dispersion, β_y and β_{y0} are respectively vertical beta function at the measurement point and at the location of the skew

Table 2: Amplification Factor by Error Type on Vertical Closed Orbit (Vert. CO) and Vertical Dispersion Dy

Error type	Vert. CO	Dy
Quad. Vert. displ. (2 μm)	300	1.0e6
Roll quad (10 μrad)		25 (0.2mm RMS)
Sextupole V. displ.(1 μm)	$\ll 1$	80

quadrupole component. ϕ and ϕ_0 are the phase advance at the measurement point and at the skew quadrupole.

Applying 2 μm vertical displacement gaussian distributed truncated at 3 sigma amplifies the vertical orbit by 300 and gives a vertical orbit amplitude of 0.3mm RMS. The most problematic consequence is the impact on the vertical dispersion, which is amplified by a factor 10^6 , scaling values of the vertical dispersion to 2 m RMS in the arcs and 20 m at the IPs. Therefore, the vertical quadrupole misalignments have to be treated very carefully.

CORRECTION METHODS

So far, MADX has been used in combination with Python to apply the different correction methods of the vertical dispersion and of the betatron coupling. All the optics corrections are done without RF activated and energy loss by synchrotron radiation in the magnets, that approach being valid only for fully or sector-wise tapered machine. The EMIT command from MADX allows to finally compute the equilibrium emittances after correction: EMIT [5] is based on the Chao formalism and takes into account the energy loss via synchrotron radiation in dipoles, quadrupoles, sextupoles etc. This paper mainly concentrate transverse displacements of the quadrupoles and their tilt angles.

The following method has been used:

1. Applying alignment errors in the lattice, gaussian distributed around the ring and truncated at 2 sigma.
2. Rough orbit corrections without sextupoles in the lattice.
3. Local vertical dispersion correction at the IPs without sextupoles in the lattice.
4. Dispersion Free Steering with orbit correctors without sextupoles in the lattice.
5. Correction of the chromaticity.
6. Local vertical dispersion correction at the IPs with sextupoles in the lattice.
7. Dispersion Free Steering with orbit correctors with sextupoles in the lattice.
8. Coupling correction and vertical dispersion correction with skew quadrupoles.
9. Tapering
10. Optics and tune matching.
11. RF cavity voltage switch on in the lattice, energy loss via synchrotron radiation

12. Emittance computation with EMIT.

In principle, an orbit correction after introducing errors helps to reduce the vertical dispersion due vertical dipolar kicks. However, in presence of BPM reading errors, the orbit correction might produce higher vertical dispersion. The next section will present the effect of BPM errors in FCC-ee and justify to use the Dispersion Free Steering correction method rather than an orbit correction to reduce the vertical dispersion.

BPM ERROR TOLERANCE

In order to be consistent with the layout of the FCC-hh project, a racetrack layout ([1], [2]) was adopted. With only 2 RF sections, the magnets need either a fully or a sectorwise tapering at 175 GeV [3]. The BPM tolerance was evaluated at 175 GeV for both options by introducing BPM reading errors, the "wrong" orbits are then corrected with an orbit correction algorithm (MICADO+SVD), creating then vertical dispersion, and the equilibrium vertical emittance is evaluated. The results are shown in Fig. 5 and Fig. 6.

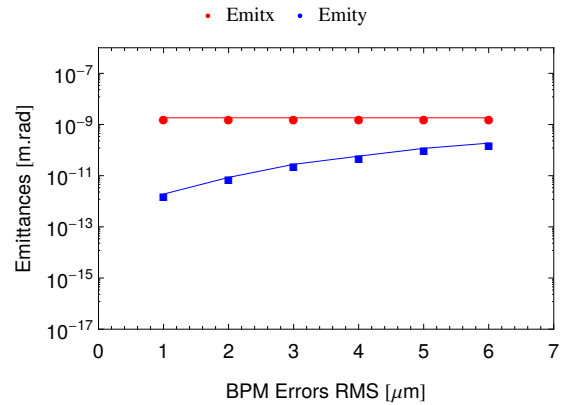


Figure 5: Resulting RMS vertical dispersion with the presence of BPM error readings.

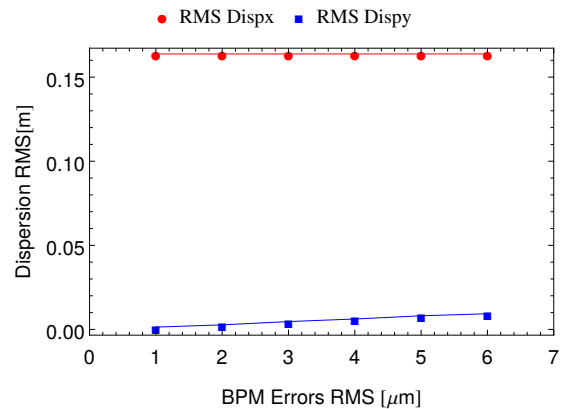


Figure 6: Resulting emittances with the presence of BPM error readings.

Relying only on orbit corrections to reduce the vertical dispersion increases of the vertical emittance when BPM

errors are taken into account. LEP and light sources used to minimize ϵ_y by rather correcting the vertical dispersion than the orbit via a method called Dispersion Free Steering (DFS). This method allows to overcome the problem of BPM errors and put more weight on the vertical dispersion correction.

DISPERSION FREE STEERING

Dispersion Free Steering (DFS) is an efficient method which was used in LEP to minimize the vertical emittance [6]. Response matrices for orbits and dispersions are established with correctors with and without sextupoles, and the following system has to then to be solved [6].

$$\begin{pmatrix} (1-\alpha)\vec{y} \\ \alpha\vec{D}_y \end{pmatrix} + \begin{pmatrix} (1-\alpha)\mathbf{A} \\ \alpha\mathbf{B} \end{pmatrix} \vec{\theta} = 0 \quad (5)$$

where \mathbf{A} , \mathbf{B} are the response matrices of the orbit and the dispersion due to a corrector kick, θ is the corrector strength, α is a weight. When α is 0, the correction is only on the orbit. With $\alpha = 1$, the correction is purely dispersive. A singular value decomposition (SVD) is then applied

$$T = UWV^t \quad (6)$$

where W is a diagonal matrix, composed by the singular values w_i , on which a cut-off has to be applied to optimize the efficiency of the correction. More singular values means more local correction but more noise, while less singular values will put the emphasis onto more global correction: a compromise has to be found between noise and local correction, in particular in a machine with large distortion of the orbit and of the dispersion which would then necessitate local correction at the IPs. As a first approach, a pure dispersion correction was used on a $2\mu\text{m}$ vertical displacement in the quadrupoles of the lattice, with random gaussian distribution cut at 3 sigma. The response matrices with and without sextupoles are very large, with a dimension of (2006x2006), and a scan of the number of singular values taken into account was performed in order to identify a minimum in emittance. Depending to the seed, 5 or 6 μm are enough to reach the foreseen vertical emittance without DFS. This tight tolerance also comes from the high vertical dispersion at the IPs, and any errors in the quadrupoles at the final focus are amplified.

In order to reduce the vertical emittance, the vertical dispersion at the IPs has to be locally corrected and treated separately from the arcs. Four correctors around the IPs are used to create a vertical dispersion dump in order to minimize D_y at places where the β_y is the largest. Combining the DFS method with a local vertical dispersion correction at the IPs after a rough orbit correction allows to decrease the vertical dispersion from some centimeters to 10^{-5}m RMS, as shown in Fig. 7.

Combining the Dispersion Free Steering first without sextupoles, then with sextupoles with the local vertical dispersion correction at the IPs increase the tolerance limit for quadrupole misalignments to 20/30 μm instead of 5, Fig. 8 and Fig. 9.

ISBN 978-3-95450-187-8

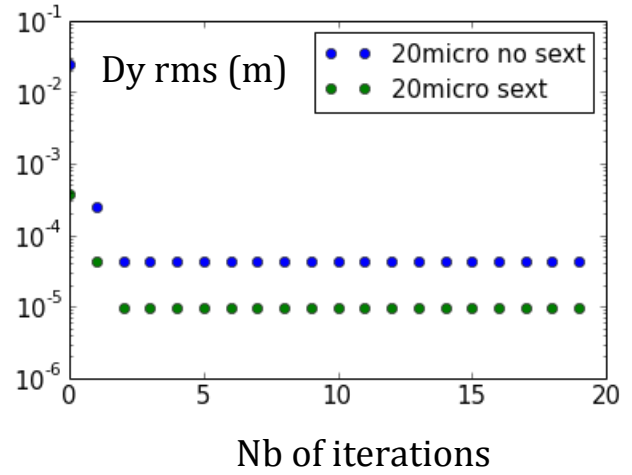


Figure 7: RMS vertical dispersion for several iterations of Dispersion Free Steering first without sextupole and then with sextupoles.

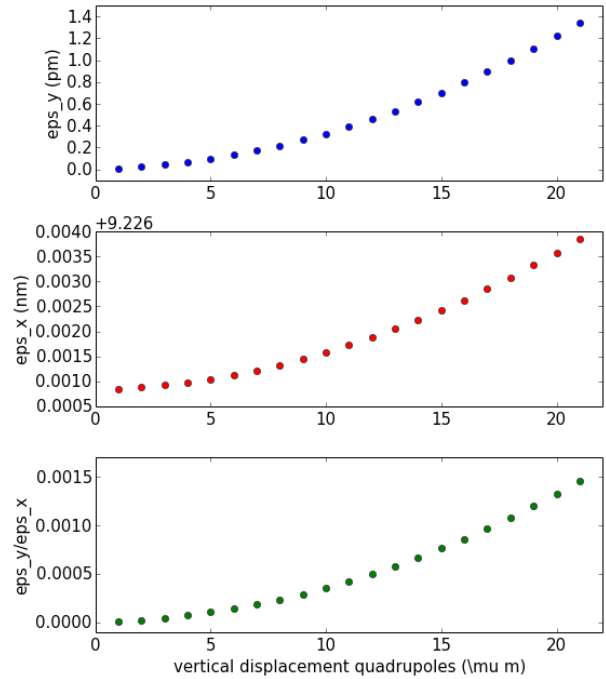


Figure 8: Vertical, horizontal emittance and coupling ratio as a function of the misalignments in the quadrupoles.

The same method can be applied to the BPMs errors for which the tolerance goes from 5 to 30 μm Fig. 10.

ROLLS IN QUADRUPOLES AND COUPLING CORRECTION

Current Skew Quadrupole Correctors Scheme for FCC-ee

In order to correct the betatron coupling, one skew quadrupole has been installed every 6 FODO cells, with a horizontal and vertical phase advance of $\Delta\phi_x = 540$ and

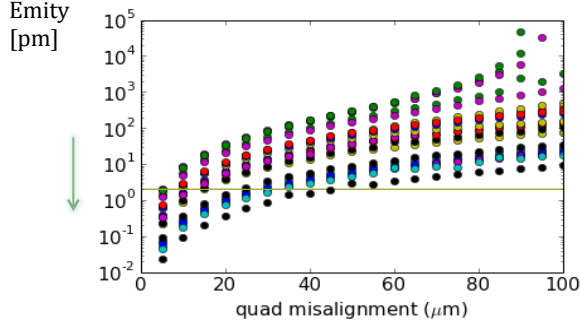


Figure 9: RMS vertical dispersion for several iterations of Dispersion Free Steering first without sextupole and then with sextupoles.

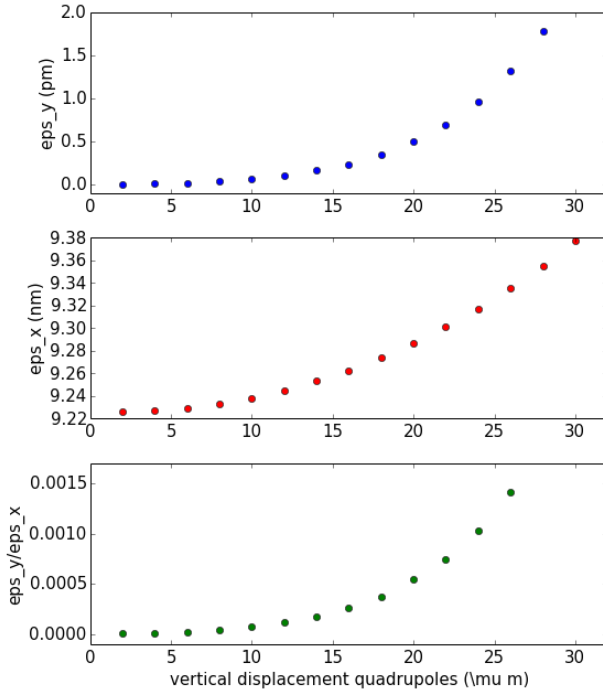


Figure 10: Vertical, horizontal emittance and coupling ratio as a function of the errors in the BPMs.

$\Delta\phi_y = 360$ degrees, since the lattice has a 90/60 degrees phase advance per cell. Therefore the total amount of skews in the machine is 272, installed in dispersive places. Currently, they are used to correct both betatron coupling and vertical dispersion. No local correction of the coupling at the IPs is performed, but is foreseen as next step in order to compensate the coupling generated by the roll angles of the final focus doublets. To correct the betatron coupling, the coupling resonance driving terms, so called f_{1001} for difference resonance and f_{1010} for the sum resonance, are mitigated, as successfully applied in LHC and at the ESRF [7] [8].

The closest tune approach is related to the complex coupling parameter, C^- - here the difference coupling parameter - which is directly a function of the coupling resonance driv-

ing terms (RDT) as [7] [8] [9]

$$\Delta Q_{min} = |C^-| = \left| \frac{4\Delta}{2\pi R} \oint ds f_{1001} e^{-i(\phi_x - \phi_y) + is\Delta/R} \right| \quad (7)$$

The resonant driving terms f_{1001} and f_{1010} can be computed from several ways, here the analytical formula

$$f_{1010}^{1001} = \frac{\sum_w J_w \sqrt{\beta_x^w \beta_y^w} e^{i(\Delta\phi_{w,x} - / + \Delta\phi_{w,y})}}{4(1 - e^{2\pi i(Q_u - / + Q_v)})} \quad (8)$$

where J are the skew strength, $\beta_x^w \beta_y^w$ are the horizontal and vertical beta function at the location of the skew strength, $\Delta\phi_{w,x}$, $\Delta\phi_{w,y}$ are the phase advance between the observation point and the skew component.

Using the matrix formalism, a response matrix of the RDT using the quadrupole skews of the lattice can be computed,

$$(f_{1001})_{meas} = -M\vec{J} \quad (9)$$

where J are the vector of the skew, f_{1001} are the complex coupling RDT at the BPMs, M is the response matrix of the RDT to skew quadrupole kicks. f_{1010} is neglected to the distance of the working point with respect to the sum coupling resonance.

Coupling Correction for a Lattice with Roll Angles in the Quadrupoles

The roll quadrupole tolerances are much less tight compared to the transverse displacement with an amplification factor of 25 on the vertical dispersion. Let us consider the FCC-ee lattice at 175 GeV with 50 μ rad roll angle gaussian distributed cut at 2 sigma. Since no other error is considered in this simulation, the coupling mainly comes from the tilted quadrupoles.

The coupling RDT at the BPMs are computed and corrected with the corresponding response matrix after a SVD, and skew quadrupoles strength are then applied. The resulting RDT is compared to the initial RDT. The successive corrections allow to correct by a factor 10 the RDT f_{1001} .

This correction can be combined with a response matrix of the vertical dispersion to the skew quadrupoles:

$$(\vec{D}_y) = -M\vec{J} \quad (10)$$

where \vec{D}_y is the vertical dispersion measured at the BPMs, M is the response matrix of the RDT to the skews, J are the skew strength. While introducing roll angles in the quadrupoles of the lattice, dispersion is transferred from the horizontal plane to the vertical one Eq. 4. The correction of the vertical dispersion with the skew quadrupoles allows to bring it down from 3.5 mm RMS to 0.5 mm.

Fig. 11 shows the real part of the coupling RDT before coupling correction in blue with 0.010 RMS, the RDT after coupling correction with 0.001 RMS in red, and finally in green, the RDT when the RF cavities are on with synchrotron damping in the simulation and with a sector wise tapering

Fig.4. This latter brings extra source of coupling which was not present before switching on the RF cavities. A possible explanation is the coupling of the remaining sawtooth to the vertical plane, exciting a vertical orbit, which would then create additional coupling through the sextupoles.

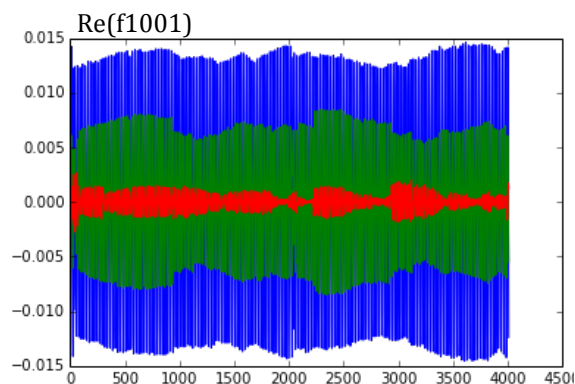


Figure 11: Real part of the coupling RDT at the BPMs before coupling correction in blue, after correction in red, with RF cavities and synchrotron damping in green.

Combining $20 \mu\text{m}$ misalignments in the quadrupoles with $50 \mu\text{m}$ roll angles is acceptable for the tolerances for a sector wise tapered lattice.

SUMMARY-CONCLUSION

Lattice errors have a very large impact on the vertical dispersion and emittance due the high beta functions in the interaction regions. The challenges come from the the very low emittances of the order of pm in vertical plane with a very strong focus at the IPs resulting in a β_y^* of 2mm, which makes the machine very sensitive to alignment errors. In order to alleviate BPM errors and maximize the vertical dispersion correction, a Dispersion Free Steering algorithm was implemented without and with sextupoles combined with a local correction of the dispersion at the IPs. The tolerances could then be increased by a factor 4 and 20/30 μm

misalignments with $50 \mu\text{rad}$ roll angles is an acceptable tolerance for a sector wise tapering machine at 175 GeV. Further studies will focus on the tolerance to errors of a lattice fully tapered which might relax the tolerances. An implementation of a local correction of the coupling at the IPs is also required, and further investigations to improve the coupling correction needed.

ACKNOWLEDGEMENT

The authors would like to acknowledge Frank Zimmermann, Jorg Wenninger and Simone Liuzzo for fruitful discussions.

REFERENCES

- [1] B. Haerer *et al.*, "Chromaticity compensation schemes for the arc lattice of the FCC-ee collider", in *Proc. 7th Int. Particle Accelerator Conf. (IPAC'16)*.
- [2] K. Oide *et al.*, in *Proc. IPAC'16*, paper THPOR022, pp. 3821-3823.
- [3] A. Doblhammer *et al.*, "Tapering options and emittance fine tuning for the FCC-ee collider", *Proc. 7th Int. Particle Accelerator Conf. (IPAC'16)*.
- [4] A. Wolski, "Coupling and Alignment.", *US Particle Accelerator School*.
- [5] MADX manual, "Methodical Accelerator Design", <http://madx.web.cern.ch>
- [6] R. Assmann, P. Raimondi,* G. Roy, and J. Wenninger, "Emittance optimization with dispersion free steering at LEP", *PRSTAB*, Volume 3, 121001 (2000).
- [7] T. Persson *et al.*, "Improvement control of the betatron coupling in the Large Hadron Collider", *PRSTAB*, Volume 17, 051004 (2014).
- [8] T. Persson *et al.*, "Chromatic coupling correction in the Large Hadron Collider", *PRSTAB*, Volume 13, 081003 (2013).
- [9] A. Franchi *et al.*, "Vertical emittance reduction and preservation in electron storage rings via resonance driving terms correction", *PRSTAB*, Volume 14, 034002 (2011).

BEAM INSTRUMENTATION NEEDS FOR A FUTURE ELECTRON-POSITRON COLLIDER BASED ON PEP-II OBSERVATIONS*

J.T. Seeman[†], SLAC National Accelerator Laboratory, CA, USA

Abstract

Instrumentation for e+e- colliders is very important to monitor collider operations, detector data taking quality, accelerator physics, hardware status, and beam error analysis. The required instrumentation grows with the complexity of the collider and must be constantly advanced to higher functionality.

Future e+e- colliders will operate with many bunches, short bunch lengths, small emittances, high currents, and small interaction point betas. The stability of the colliding beams with these characteristics will depend on detailed, high precision, and continuous measurements. The various beam measurement requirements and techniques will be discussed with using PEP-II observations [1-13].

The parameters of PEP-II are shown in Table 1. PEP-II operated until April 2008. The general layout of the instrumentation in the HER ring is shown in Figure 1. The LER layout is similar but reversed relative to IR 2 where the BaBar detector was located. The instrumentation needs of PEP-II covered every possible beam and accelerator parameter and most were crucial to the ultimate operation of the accelerator and the detector. During the design of PEP-II, the instrumentation was integrated into the collider design. For construction, the desire was to be as inexpensive as possible but as broad as possible. For operations, the need was for low power costs, reliable running, and low maintenance costs with as many standard units as possible.

PEP-II BEAM MEASUREMENTS

The topics covered will be:

- Beam parameter overview
- Beam position (single pass and stored)
- Bunch transverse and longitudinal instabilities
- Beam tunes
- Beam size
- Bunch length
- Beam loss rates
- Beam lifetime
- IP luminous size
- HOM measurements
- Chamber vacuum pressure

Table 1: PEP II Parameters and Ultimate Potential

Parameter	Units	Design	April 2008 Best	2008 Potential
I+	mA	2140	3210	3700
I-	mA	750	2070	2200
Number bunches		1658	1722	1740
β_y^*	mm	15-25	9-10	8.5
Bunch length	mm	15	11-12	9
ξ_y		0.03	0.05-0.06	0.07
Luminosity	$\times 10^{33}$	3	12	20
Int lumi / day	pb ⁻¹	130	911	1300

*Supported by US DOE contract DE-AC02-76SF00515.

[†]seeman@slac.stanford.edu

BEAM POSITION

The beam position monitors BPM for PEP-II were button type feedthroughs as shown in Figure 2. The diameter was 15 mm and resolution 20 microns. They worked well except at the highest currents (>3 A) as the button heads could fall off. The BPMs were used to make many measurements: initial turn observations (Figures 3 and 4), tune measurements in the longitudinal and transverse planes of stored beams (Figures 5 and 6), orbit corrections and feedback, and feedback of the tunes with beam current (Figure 7) which was done automatically by computer.

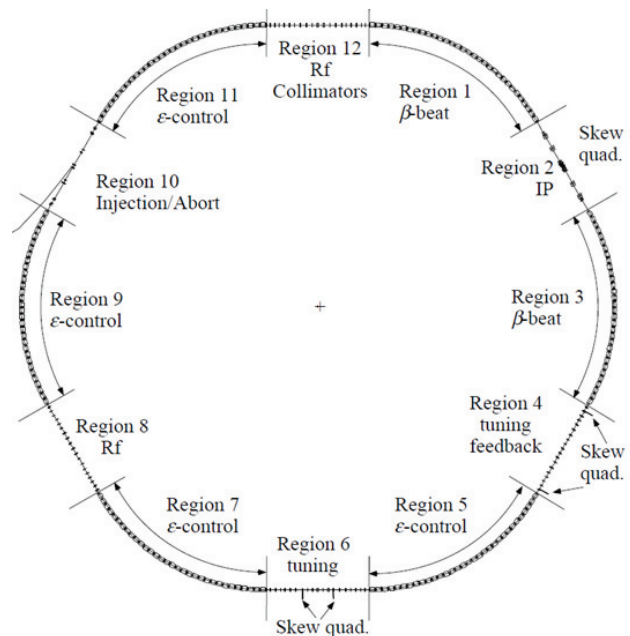


Figure 1: PEP-II layout with instrumentation.

ISBN 978-3-95450-187-8



AF_002 Pick-up Buttons for the Beam-Position Monitors 8-19-97

Figure 2: PEP-II BPM buttons and HER Cu chamber.

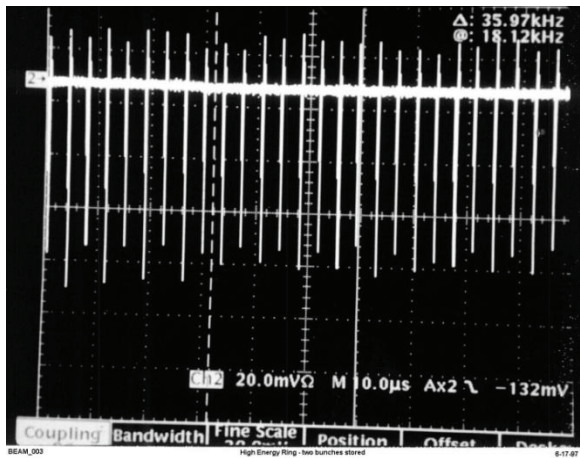


Figure 3: HER BPM signals showing the first few turns.

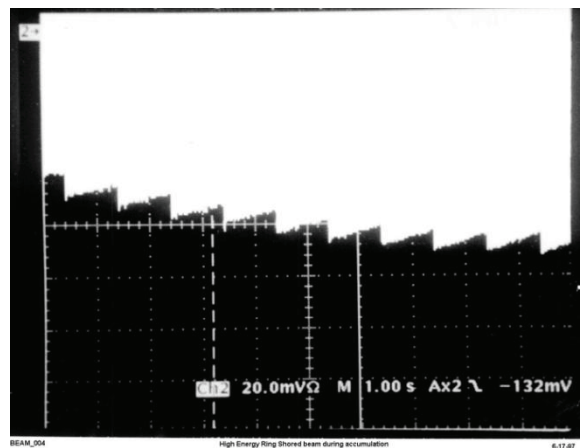


Figure 4: HER BPM signals indicating initial storage and stacking with beam current accumulation. A new injection was about every 10 seconds.

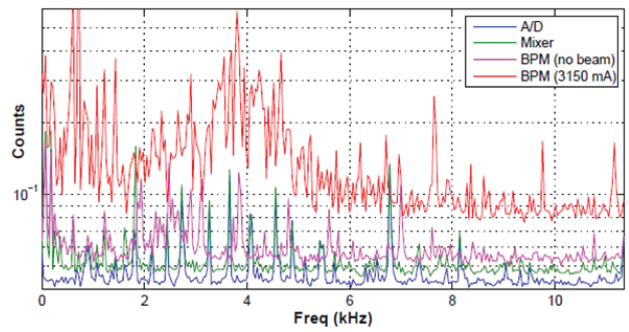


Figure 5: LER tune spectrum from a BPM showing the synchrotron frequency of about $4\text{ kHz} = 0.028$.

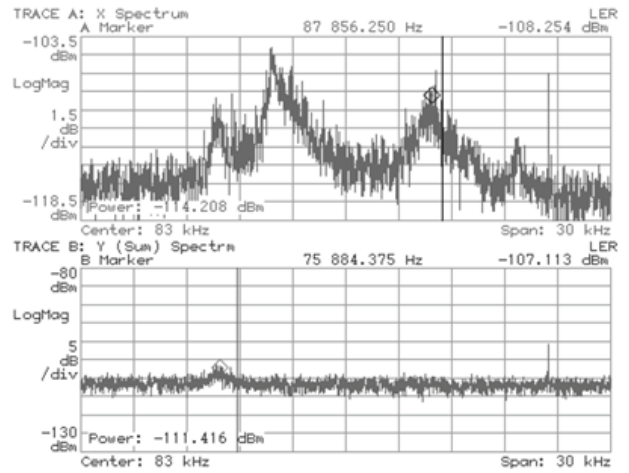


Figure 6: LER tune spectrum with colliding beams with 1550 mA (LER) on 850 mA (HER). The spectrum shows a lot of tune structure which makes it hard to use as a feedback to align the two beams.

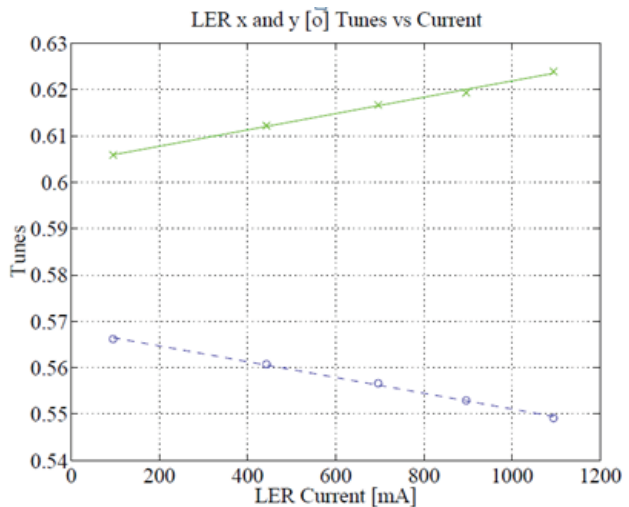


Figure 7: LER tune variation versus beam current with 700 bunches in a by-4 pattern. The measured x and y and following tune compensation adjustments have about the same values with opposite signs. Slope about 0.017 per A.

The BPMs were used in the bunch-by-bunch feedback systems to control instabilities at high currents. A schematic of the feedback is shown in Figure 8. The feedback

could not only control the instabilities but used to determine the causes as well as, as shown in Figure 9 and 10. When the instabilities are large the beam tails could scrape, get lost on the vacuum chambers and then detected by the fast (~1 microsecond) loss monitors (Figure 11) which feeds into the abort system input triggers.

The loss monitors and lifetime calculation can be used to measurement transverse tails of the beams as shown in Figure 12. Here the effect of the beam-beam interaction on the transverse beam size can be quite significant and leads ultimately to a strong limit of the beam-beam parameter and luminosity. As the beam currents are raised the beam parameter increases and then saturates followed by beam size enlargement and finally beam loss. PEP-II had vertical beam-beam parameters on the order of 0.08 to 0.09 in HER and LER respectively.

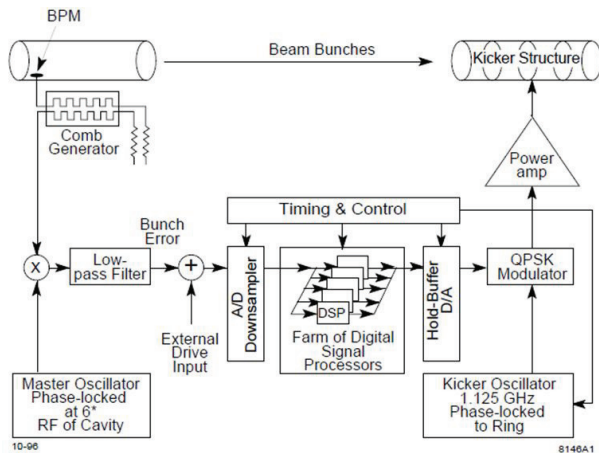


Figure 8: Longitudinal feedback system for 4 nsec spaced bunches showing BPM pickups, digital signal processing, high power amplifiers and kicker structures.

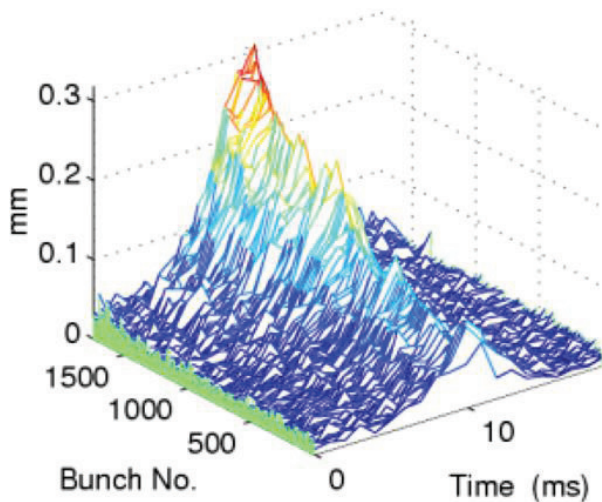


Figure 9: Time domain plot from the digital feedback system showing mode development with time in the HER after the feedback was turned off at $t=0$. Bunch 0 is just after the ion gap. Later bunches show larger growth. The HER beam had 1087 mA in 1740 bunches.

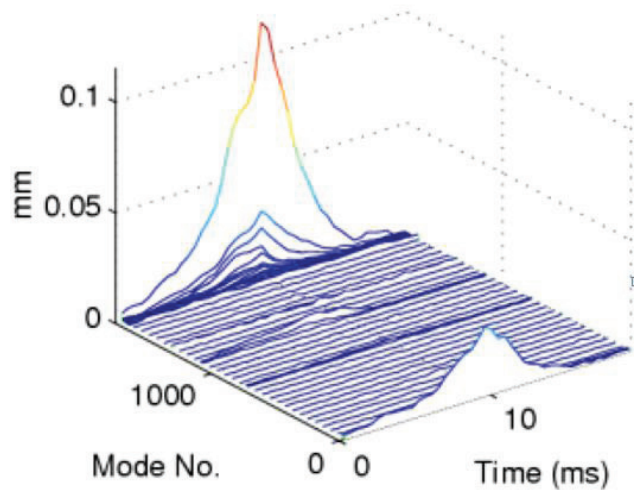


Figure 10: Evolution of modes in HER from the data from Figure 9 indicating low order and very high order modes.

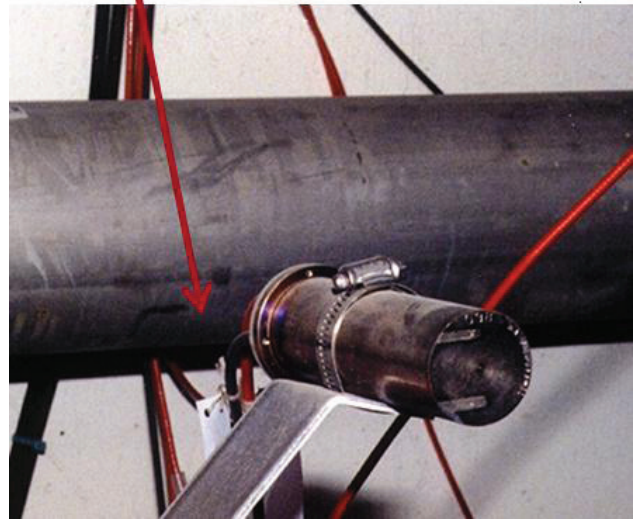


Figure 11: PEP-II beam loss monitor using PMT and SiO₂.

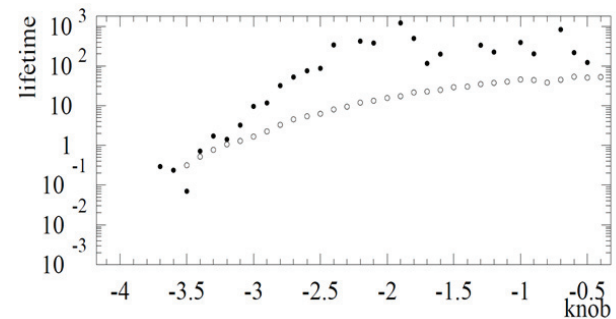


Figure 12: Results of scraping measurements in LER with colliding beams. Open circles are with high currents and bullets with low. The knob settings are in mm of the collimator position setting. Inward is negative. Lifetime measurements are in minutes. The HER data is similar.

Copyright © 2017 CC-BY-3.0 and by the respective authors

SYNCHROTRON LIGHT BEAM SIZE MONITORS

The synchrotron light monitor was used to measure the transverse and longitudinal beam sizes (at 600-200 nm). The main parameters are shown in Table 2 and the hardware in Figures 13 and 14. With multi-ampere beams the synchrotron light mirrors used to extract the light needed to handle high concentrated power. HER used a slotted water cooled polished mirror inside the vacuum. Both the HER and LER beam signals were put on to the same analysis table under the HER to reduce construction costs.

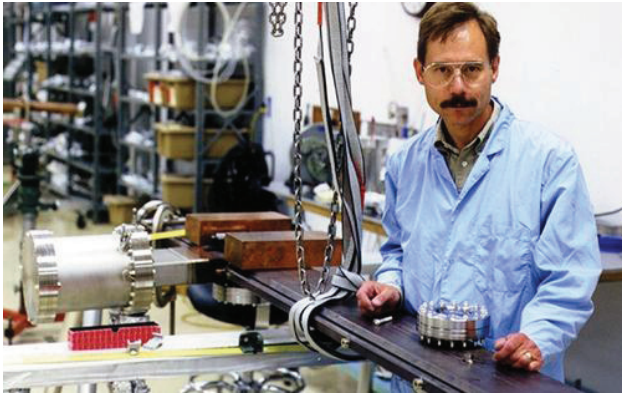


Figure 13: HER synchrotron light monitor in the lab.



Figure 14: HER synchrotron light mirror with main power slot down the center to reduce mirror distortions.

Table 2: PEP-II SLM Synchrotron Monitor Parameters

Parameter	HER	LER
Circumference [m]	2199.318	
Revolution time [μ s]	7.336	
RF frequency [MHz]	476	
Harmonic number	3492	
Number of full buckets	1658	
Bunch separation [ns]	4.20	
Nominal current [A]	0.99	2.16
Maximum current [A]	3	3
Nominal energy [GeV]	9.01	3.10
Maximum energy [GeV]	12 (at 1 A)	3.5
Bend radius in arc dipoles [m]	165	13.75
Critical energy in dipoles [keV]	9.80	4.83

The light monitor signals were gated so we could observe the bunch sizes of individual bunches spaced 4 nsec apart. In Figure 15 are shown bunch sizes along the train showing the effects of the mini-gaps and the electron cloud effect (LER). As the size signals were weak, the size measurements had to be averaged over a few hundreds of turns to get these measurements.

A streak camera was used to measure the bunch lengths. The calibration of the bunch length measurements was done with an etalon as shown in Figure 17. In Figure 18 are shown measurements of the bunch length

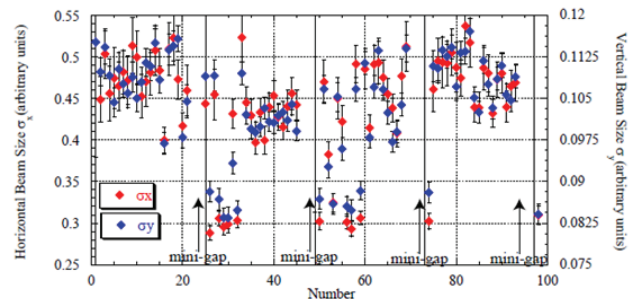


Figure 15: Vertical and horizontal bunch sizes versus bunches along the train. The bunch gaps reduce the electron cloud allowing bunches to have smaller sizes and higher luminosity, thus, indicating strong e- cloud effect in the LER.

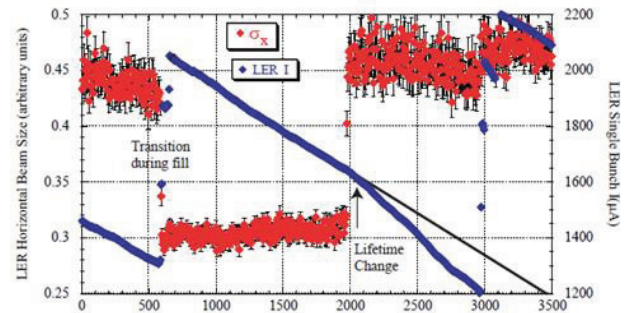


Figure 16: The LER beam current and horizontal beam size as a function of time for a single colliding bunch during transition between the flip-flopped states.

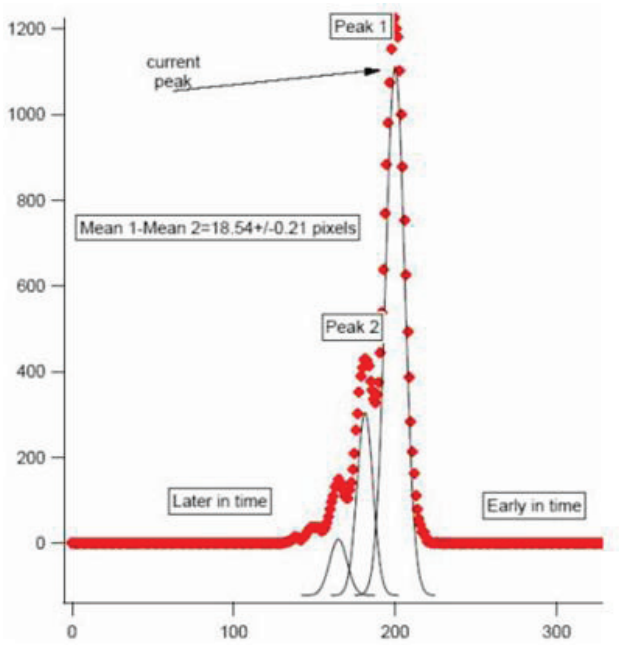


Figure 17: A streak-camera scan of a light pulse that was transmitted through an etalon and projected onto the camera's time axis with strength versus pixel number. The distance between reflections indicates the calibration.

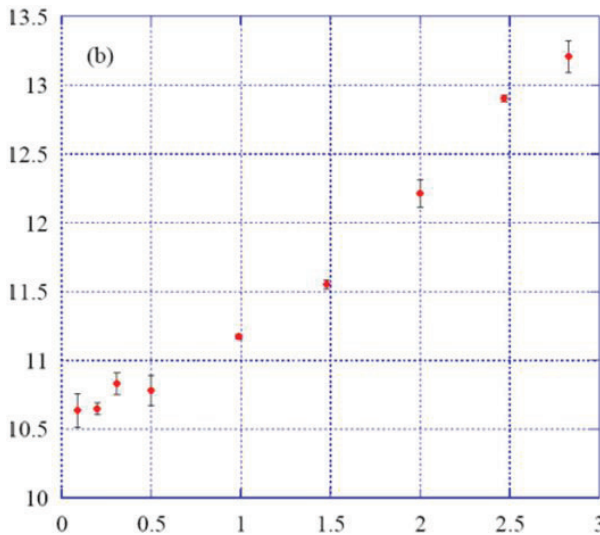


Figure 18: Streak camera measurements of the LER bunch length (mm) versus bunch current (mA) indicating growth in bunch length due to the ring longitudinal impedance.

with beam current showing an increase with current. The individual bunch lengths along the train could also be measured as shown in Figure 19.

LUMINOSITY MEASUREMENTS

The luminosity was measured using straight ahead gammas produced by beam-beam collisions from the LER beam measured in the upstream HER as shown in Figure 20. The gammas exited the HER chamber about 4 m from

the IP and entered a hodoscope and PMT array as shown in Figure 21. Average luminosity and the luminosity from single bunches could be measured and then calibrated with the wide angle Bhabbas in BaBar. The hodoscopes could give information on the angular divergence of the LER IP spot size and the centering of the beams in the IR. The luminosity for each bunch could be measured as shown in Figure 22. The overall luminosity could be measured to about 1% in about one second and was used extensively as a tuning aid for improving the luminosity.

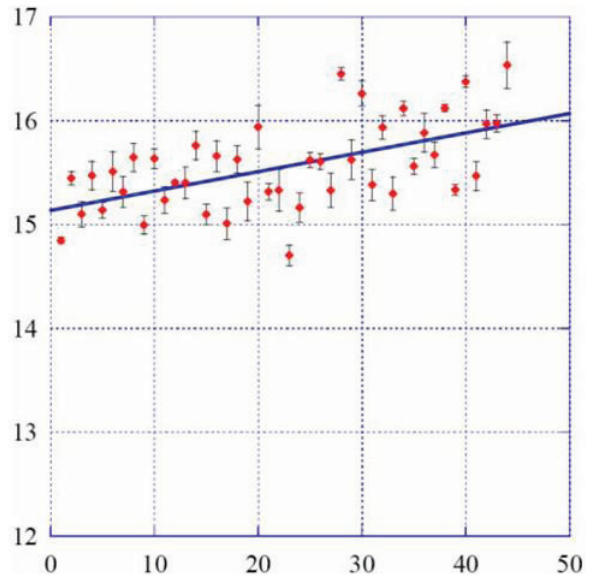


Figure 19: Streak camera measurements of the LER bunch length (mm) versus bunch number along the twentieth bunch train with 1.4 mA per bunch and 3.8 MW in the RF cavities.

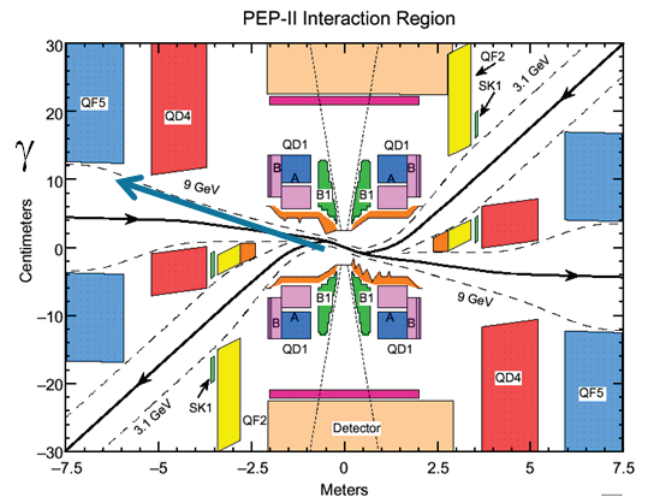


Figure 20: The PEP-II interaction region showing the beam-beam $e^+e^- \rightarrow e^+e^- \gamma$ emission to the upper left for luminosity measurements using the LER γ s.

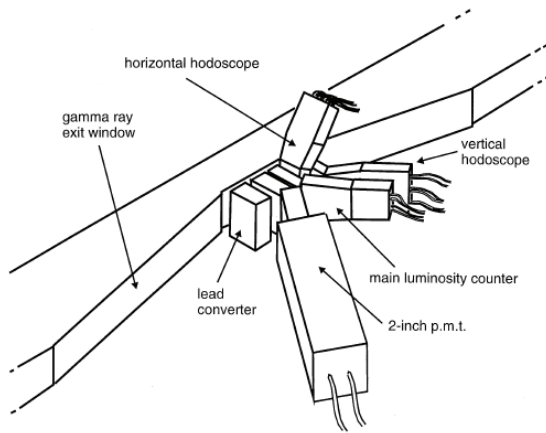


Figure 21: Luminosity monitor using γ s with position hodoscopes in the horizontal and vertical and an integrating 2 inch photomultiplier tube.

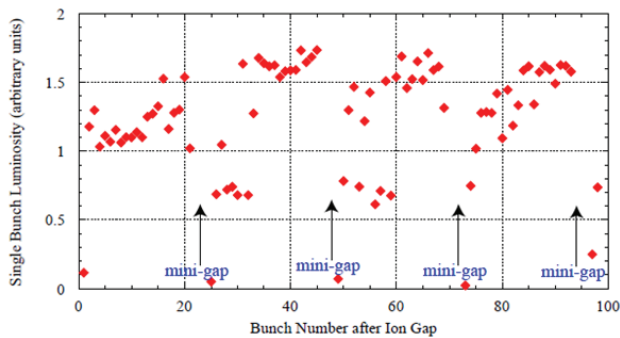


Figure 22: Bunch-by-bunch luminosity measurements of the first four mini-trains after the ion gap.

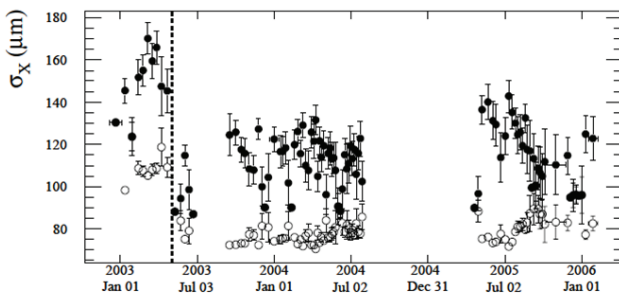


Figure 23: History of the horizontal combined IP beam size at the IR luminous region as measured by BaBar over several years. The dotted line indicates the time when both x tunes were moved close to the half integer resulting in a sizable luminosity improvement. HER indicated by black dots and LER open circles.

BABAR IP ACCELERATOR MEASUREMENTS

The BaBar detector used the recorded particle physics events to measure accelerator parameters at the IP taking several thousand events to make a measurement. Examples of the horizontal luminous beam size at the IP are

ISBN 978-3-95450-187-8

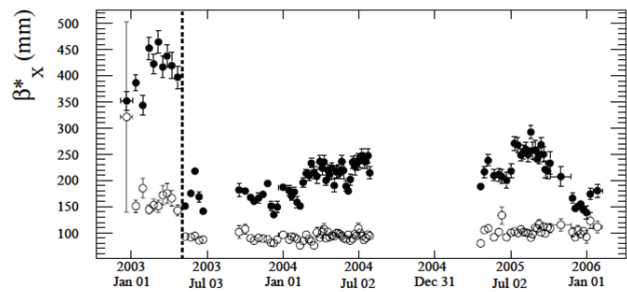


Figure 24: Horizontal beta function at the IR luminous region as measured by BaBar over several years. The dotted line indicates the time when both x tunes were moved close to the half integer resulting in a sizable luminosity improvement. HER indicated by black dots and LER open circles.

shown in Figure 23. Assuming an emittance from other beam measurements, the IP collective horizontal beta function can be calculated as displayed in Figure 24.

VACUUM MEASUREMENTS

The vacuum pressure was measured at several thousand locations in the rings and RF systems. Real time recorded signals allowed investigation of vacuum events that correlated with other beam related signals. An example is shown in Figure 25 with an RF arc and correlated pressure and IP background spikes.

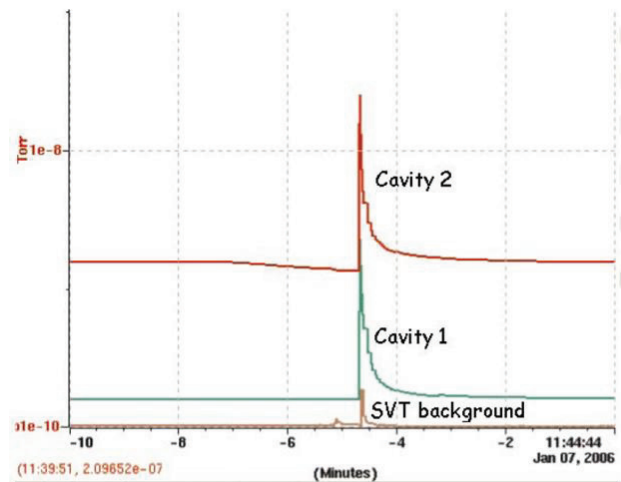


Figure 25: A cavity vacuum spike caused by an RF vacuum arc in the RF station 4-2 cavity in LER. The following vacuum pressure and associated background event in BaBar resulting in a beam abort.

RF SPECTRAL MEASUREMENTS

The RF spectrum of the beam could be measured in several devices, e.g. as shown in Figure 26. These measurements could be used to calculate the longitudinal length of the bunch producing these RF signals. The HER and LER bunch lengths were measured by their RF spectra are shown in Figure 27 which can be correlated with streak camera measurements such as in Figure 18.

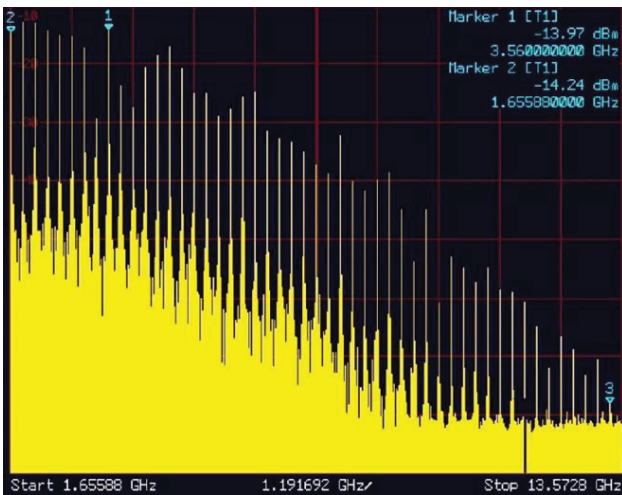


Figure 26: Measured RF spectrum of the LER positron beam for the bunch pattern of by-2 and 12 mm bunch length. The horizontal scale is 1.2 GHz per division. The spectrum fall off is related to the bunch length.

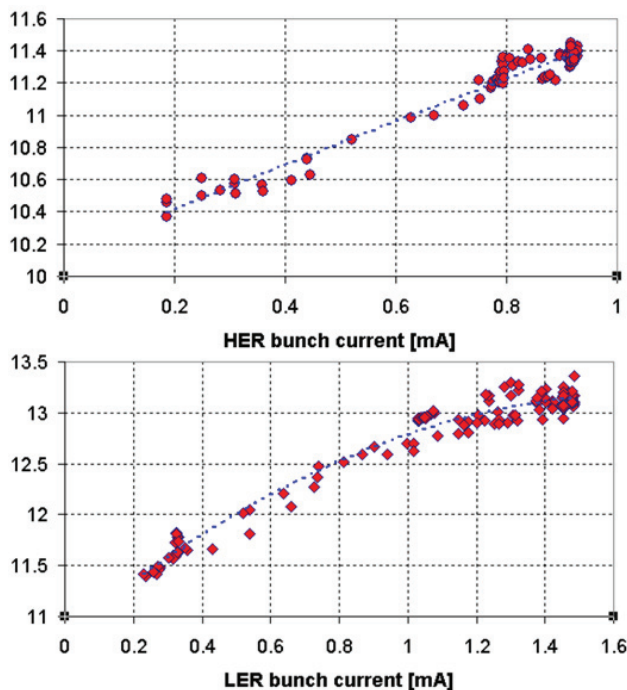


Figure 27: Bunch length (mm) measurements using the RF spectra for HER (16.5 MV) (above) and LER (3.8 MV) (below) as a function of bunch current (mA) in a colliding multi-bunch pattern.

CONCLUSIONS

Many complicated measurements are needed in a high-power, high-current collider to make it function well. The accelerator control system must measure and record versus time as many parameters as possible to diagnose issues. The commissioning team must find new and innovative measurement techniques. Many of the measurements relate to potential hardware damage to the accelerator. As many as possible of the measurements need to be automated and computer monitored to make the accelerator operation safe and allow pushing the luminosity limit.

ACKNOWLEDGMENT

The author would like to thank the PEP-II design and operations staff including A. Fisher, J. Fox, W. Kozan-ecki, S. Ecklund, A. Kulikov, N. Kurita, M. Nordby, A. Novokhatski, M. Sullivan, D. Teytelman, M. Weaver, and U. Wienands for many conversations on PEP-II instrumentation.

REFERENCES

- [1] “PEP-II an Asymmetric B Factory”, Conceptual Design Report, CALT-68-1869, LBL-PUB-5379, SLAC-418, UCRL-ID-114055, UC-IIRPA-93-01, June 1993.
- [2] J. Seeman *et al.*, “PEP-II at $1.2 \times 10^{34}/\text{cm}^2/\text{s}$ Luminosity”, PAC 2007, p. 37.
- [3] J. Seeman *et al.*, “Last Year of PEP-II Operation”, EPAC 2008, p. 946.
- [4] U. Wienands, “Vacuum Performance and Beam Lifetime in the PEP-II Storage Rings”, PAC 2001, p. 597.
- [5] U. Wienands *et al.*, “Tracking Down a Fast Instability in the PEP-II LER”, EPAC 2006, p. 658.
- [6] M. Sullivan *et al.*, “Anomalous High Radiation Beam Aborts in the PEP-II B-factory”, EPAC 2006, p. 652.
- [7] A. Fisher, “Status Report and Future Plans for the PEP-II B-Factory,” SLAC-PUB-8815, April 2001.
- [8] A. Fisher *et al.*, “Turn-by-Turn Imaging of the Transverse Beam Profile in PEP-II”, Twelfth Beam Instrumentation Workshop AIP, 2006, p. 303.
- [9] A. Fisher *et al.*, “Bunch Length Measurements in PEP-II, PAC 2005, p. 1934.
- [10] D. Teytelman *et al.*, “Injection Diagnostics using Triggered Bunch-by-Bunch Data Acquisition”, DIPAC 2005, p. 2369.
- [11] A. Novokhatski *et al.*, “Loss Factor of the PEP-II Rings”, EPAC 2008, p. 1670.
- [12] A. Beven *et al.*, “Combined Phase Space Characterization at the PEP-II IP Using Single-Beam and Luminous-Region Measurements”, EPAC 2006, p. 655.
- [13] A. Fisher, “Instrumentation and Diagnostics for PEP-II”, CPI451 Beam Instrumentation Workshop, 1998, p. 95.

BEAM INSTRUMENTATION IN SUPERKEKB

H. Fukuma[#], High Energy Accelerator Research Organization (KEK), Tsukuba, Japan

Abstract

SuperKEKB is the upgraded collider of the KEK B-factory (KEKB). Beam instrumentation of KEKB has been commissioned in phase 1 operation which has just finished in this June. A beam position monitor system consists of super heterodyne detectors, turn by turn log-ratio detectors with fast gates and detectors for the orbit feedback to maintain stable collision. New x-ray beam profile monitors with the coded aperture method are installed. A bunch-by-bunch feedback system is upgraded using low noise frontend electronics and new 12 bits iGp digital filters. An introduction of instrumentation of SuperKEKB and its performance in phase 1 operation will be given here briefly.

INTRODUCTION

SuperKEKB is the upgraded electron-positron collider of the KEKB B-factory [1]. The design luminosity of $8 \times 10^{35} \text{ cm}^{-2}\text{s}^{-1}$ will be achieved using so-called nano-beam scheme. Main machine upgrades include the replacement of cylindrical copper chambers in LER to those with aluminum TiN coated ante-chambers so as to withstand large beam current and also mitigate the electron cloud effect, a new final focus system in order to adopt the nano-beam scheme and the construction of a positron damping ring. Phase 1 operation has just finished in June 2016 [1].

This paper introduces the beam instrumentation in SuperKEKB and shortly comments on its performance in phase 1 operation. Detailed reports to which this paper often refers are appeared in [2, 3, 4, 5] and their references.

BEAM POSITION MONITOR SYSTEM [2,3]

The number of beam position monitors (BPMs) in SuperKEKB is 445 in the low energy ring (LER) and 466 in the high energy ring (HER). The BPM chambers and button electrodes in HER are reused from KEKB. New button electrodes whose diameter is 6mm are installed on new LER vacuum chambers. The electrode is a flange type for easy replacement. A pin-type inner conductor is adopted for tight electrical connection.

A narrowband detector system which follows that in KEKB is a main detection system. A new narrowband detector with a detection frequency of 509 MHz has been developed and used in LER since the cutoff frequency of the new LER ante-chamber is below the detection frequency of the KEKB detector of 1 GHz. Analogue

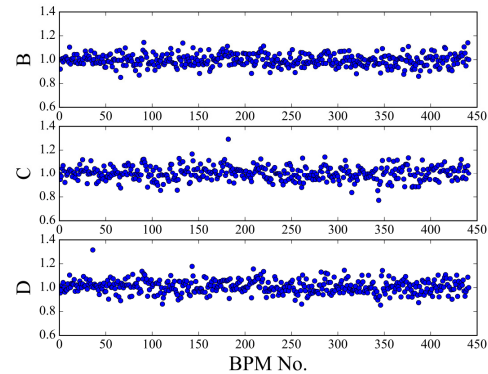


Figure 1: BPM gain mapping of LER relative to electrode A [3].

circuits are housed in an aluminum shield case. An isolator is put in front of a variable attenuator to reduce change of signal level upon switching of the attenuator. Discrete PIN diodes with DC coupling are used in a multiplexer and the attenuator to improve transient characteristics such as spike and ringing. S/N ratio larger than 90 dB is achieved by 2048 points FFT and averaging of 8 points data with CW signal, which corresponds to position resolution better than $0.5\mu\text{m}$.

Gain calibration [6] has been applied by the narrowband detection system. Imbalance of signal level of four channels was measured by beam and then corrected in position calculation. Figure 1 shows measured relative signal levels with respect to that of the electrode A. Dispersion of the LER gain is slightly larger than that of HER, which probably reflects the difference of flange-type connection (LER) and brazing (HER) to fix the BPM to the chamber.

Beam based alignment [7] has been applied to measure the BPM position offset against the center of an adjacent quadrupole. The rms values of the measured offset (x/y) were 0.570 mm/0.222 mm in LER and 0.505 mm/0.392 mm in HER [8]. Rotation angle of BPMs was measured prior to the operation to correct the position data of the beam. The rms values of rotation were 0.62 mrad and 0.78 mrad in HER and LER respectively.

Position resolution of the narrowband system was measured by the three BPM method. The obtained resolution is better than $3\mu\text{m}$ and $5\mu\text{m}$ in LER and HER, respectively, for most of the BPMs. The result represents upper bound of the resolution because the measurement could be affected by beam movement between switching interval of a multiplexer. The beam current dependence of BPM resolution was small because signal voltage was adjusted by the variable attenuator as a function of the beam current. Anti-correlation between resolution and signal level was seen.

[#]hitoshi.fukuma@kek.jp

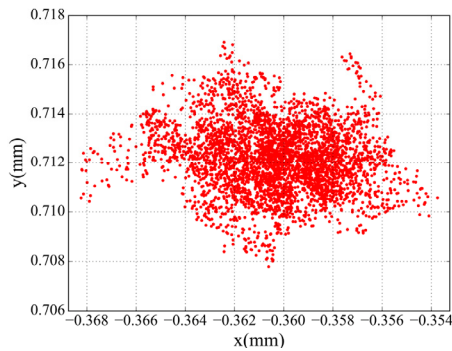


Figure 2: Transverse beam positions measured by a prototype detector for the orbit feedback at IP (preliminary).

One hundred seventeen gated turn by turn detectors (GTBT) are installed at selected BPMs to measure the optics during collision. A non-colliding pilot bunch is kicked by the bunch-by-bunch feedback system and then the GTBT measures turn by turn position of the pilot bunch using a fast gate to select the signal of the pilot bunch. The gated signal is processed by a log-amp then sent to an ADC. Signals of remaining bunches are sent to the output port of the detector which is connected to the narrowband detector in order to allow the simultaneous measurement of the narrowband detector and the GTBT. Optics parameters such as beta functions and coupling parameters can be obtained from the bunch oscillation data. The GTBT is also available for injection tuning.

FFT spectrum of orbit vibration in HER was measured by the GTBT from 1.3s, i.e. 131k turns data in phase 1. The peaks at 9.1 Hz and 16.68 Hz were found with amplitude of around 5 μm . The oscillation could affect the resolution of the narrow band measurement.

A special wideband detector is to be installed at four BPMs closest to the collision point (IP) for orbit feedback to maintain stable collision. Tentative specifications for the detector are resolution less than 1 μm , repetition from 5k to 32kHz, bandwidth of 1kHz. It down-converts 508.8MHz component of the beam signal to intermediate frequency (IF) of 16.9 MHz with an analog mixer. IF signal is supplied to a low pass digital filter with a cut off frequency of 2kHz which consists of two CICs and one FIR. The digital part is implemented in a μTCA board developed for the SuerKEKB LLRF system. EPICS is embedded in the board.

A prototype model was tested by the beam in phase 1 operation. Figure 2 shows preliminary data of the beam position measurement in LER.

A displacement sensor monitors the change of the distance between a BPM and an adjacent sextupole because orbit change at the sextupoles causes vertical emittance growth and tune change. The displacement sensors used in KEKB are re-installed at BPMs near every sextupoles in SuperKEKB. Special sensor supports made of Metal Matrix Composites with low thermal expansion coefficient of $3 \times 10^{-6} \text{ K}^{-1}$ are used in the sensors near rotatable sextupoles in LER. The support has a long

pillar fixed to a base of the sextupole because the sensor can't be mounted on the movable sextupole.

BUNCH-BY-BUNCH FEEDBACK SYSTEM

A transverse feedback system [3, 9] consists of BPMs, frontend electronics, a digital filter, backend electronics, power amplifiers and stripline kickers. To ensure a fast response of the feedback two sets of short stripline kickers which cover two feedback loops with 90 degrees phase difference between monitor chambers are installed in each ring.

The button electrode has a glass-type sealing with low relative dielectric constant (~ 4) which has good time and frequency response. The detection frequency is 2 GHz. A difference signal is mixed with LO with frequency of 4 x RF frequency, amplified to increase gain, fed to a 600 MHz Bessel LPF then amplified by a DC amp.

The design of the kicker is similar to that of the KEKB kicker. Eight power amps with power of 500W or 250W are used to drive the kickers in each ring.

A digital filter adjusts a gain so as to maximize it at betatron frequency and also adjusts a phase shift between the kicker and the pickup to 90 degrees. The iGp12 processor [10] is a baseline system of the digital filter. It was developed under US-Japan collaboration (KEK-SLAC). Main features of the iGp12 are 12 bit ADC and DAC, FPGA of Vertex-5 (VSX95T, VSX50T), 10 to 20 tap FIR filter, 12MB memory to analyze instabilities and availability for single bunch excitation by PLL.

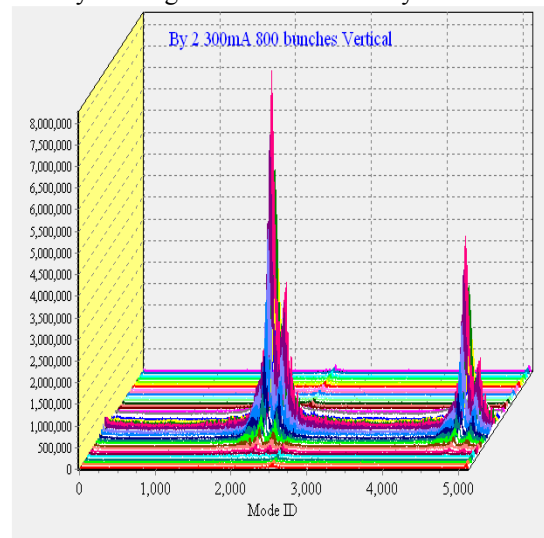


Figure 3: Evolution of vertical unstable modes with by-2 fill pattern in LER at a current of 300 mA [3].

Strong transverse coupled-bunch instability was observed in both horizontal and vertical planes in both rings at very early stage of the phase 1 commissioning as shown in Fig. 3 [3]. The instability was successfully suppressed by the feedback up to maximum beam current (1A in LER, 0.87A in HER) with minimum bunch spacing of 4 ns. Transverse feedback damping time around maximum beam current was about 0.5 ms (i.e. 50 turns).

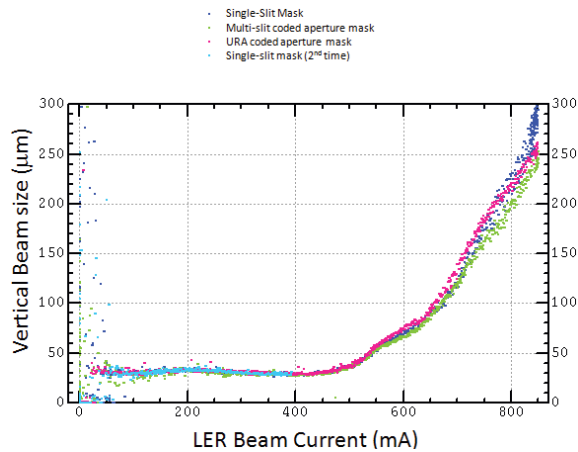


Figure 4: LER Vertical beam size as a function of beam current. Different colors represent data taken with different x-ray optical elements [3].

A growth rate of the longitudinal coupled bunch instability due to the impedance of ARES cavities in LER is estimated to be 15 ms which is shorter than the longitudinal radiation damping time of 22 ms. Thus the longitudinal feedback system is prepared in LER. Four DAFNE type kickers, with 2-input and 2-output ports are used to get larger capture range. A calculated shunt impedance and a quality factor are $\sim 1.6\text{k}\Omega$ and ~ 5 respectively. Two 500W power amps per kicker are used. The frontend electronics and the digital filters are same as those of the transverse system.

Unexpected longitudinal instability starting at beam current larger than 660mA in a by-3 fill pattern was found in phase 1. Growth time was about 15ms. It was successfully suppressed up to 1A by the feedback.

PHOTON MONITORS

Three kinds of photon monitors, x-ray beam size monitors (XRM), visible synchrotron radiation monitors (SRM) and large angle beamstrahlung monitors (LABM) are installed in SuperKEKB [2].

The XRM uses coded aperture imaging to measure the vertical beam size. Light from an object is modulated by a mask. The resulting image is calculated through mask response including diffraction and spectral width by Kirchhoff integral over mask for various beam sizes to make a template assuming a Gaussian profile. The beam size is determined by a template fit to a measured image. Large open aperture of 50 % gives high flux throughput for bunch-by-bunch measurements. Three masks (a single slit mask, a multi-slit mask and a URA mask) are installed.

The vertical size measurement by the XRM in LER in phase 1 shows good fill-to-fill repeatability and good agreement between different masks, especially below 150 μm as shown in Fig. 4. On the other hand large difference between the measured HER vertical beam size via the XRM and the estimated beam size from optics correction was found [4]. Systematic study to clarify this discrepancy is under way.

We developed a diamond mirror [11] in the SRM that would not deform as much under the heat load by synchrotron light, since the heat deformation was a problem at KEKB. Good heat conductance and low thermal expansion coefficient of diamond make apparent change in magnification smaller than that of Be mirrors used at KEKB.

The SRM was used mainly to measure the bunch length by streak cameras in phase 1. An unsolved problem is that the measured magnification factor is more than twice as large as that of the design in both rings. The check of the alignment of a light transport and deformation of optical elements are underway.

The LABM measures relative offset and size ratio of the beams at the IP. Beamstrahlung is the radiation of the particles of one beam due to the bending force by the electromagnetic field of the other beam. Beamstrahlung polarization at specific azimuthal points provides information about the beam-beam geometry.

The LABM in SuperKEKB is being built in US, mostly at Wayne State University. The monitor consists of four viewports. Light is transported through an optical channel to an optics box where light is separated into two transverse polarizations and four different wavelength bands before sent to photomultipliers.

LABM beam lines and optics boxes were installed at interaction region in phase 1 even without beam collision. Measurements were made with the beam using synchrotron light from far side of the IP to refine models of the beam line.

LOSS MONITOR

The loss monitor system [5] provides a trigger to the beam abort system. Abort request signals from each hardware component are collected at twelve local control rooms, and then sent to the abort kicker within 20 msec. The sensors of the loss monitors are coaxial ion chambers and PIN photo-diodes. Several selected signals are logged by four data loggers to analyze abort events.

The total number of beam aborts was about 1500 in phase 1, among them about 95% were recorded. Main causes of the aborts were manual aborts (53% in the total), beam loss aborts (27%) and RF Aborts (10%). Manual aborts were triggered for optimization of kicker timing, beam study of beam instability, beam size measurement, detector background study and so on. Beam loss aborts were caused by a trouble of software of injection trigger system and a vacuum spike occurred at higher current operation. RF Aborts were caused by troubles of a frequency tuner and beam instability by HOM.

OTHERS

A bunch current monitor measures the bunch current of all bunches with a fast ADC. The recording stops by the injection trigger. The ADC data are sent to the bucket selection system via a reflective memory [3].

The global tune meter uses a tracking method in which all bunches are excited by the feedback kicker by the signal from a tracking generator of a spectrum analyzer.

In the single bunch tune measurement, the iGp12 is used to close the PLL excitation of a selected bunch without feedback damping. The betatron frequency is directly measured by the excitation frequency of the loop [3].

DCCTs for beam current measurement are reused from KEKB.

[10] DimTel, <http://www.dimtel.com>

[11] J. W. Flanagan *et al.*, in *proceedings of IBIC2012*, p.515, 2012.

SUMMARY

The electron-positron collider KEKB B-factory is being upgraded to SuperKEKB. The BPM system in SuperKEKB is equipped with the super-heterodyne detectors, the gated turn-by-turn log ratio detectors and the IP orbit feedback detectors. New x-ray beam profile monitors based on the coded aperture imaging method are installed. The large angle beamstrahlung monitor detecting polarization of the synchrotron radiation generated by beam-beam interaction is installed near the IP. The diamond mirror has been developed for the visible light monitors. The bunch-by-bunch feedback system is upgraded using low noise frontend electronics and new 12 bits iGp2 digital filters. The loss monitor system provides a trigger to the beam abort system and is used to analyze the performance of the machine.

Phase 1 operation without Belle II and final-focus quads continued from this February to June. Most of the beam instrumentations prepared for phase 1 are working well.

ACKNOWLEDGMENTS

The author would like to thank all the members of the KEKB beam monitor group for their help to prepare this paper. He also would like to thank Prof. M. Tobiyama for careful reading of the manuscript.

REFERENCES

- [1] Y. Funakoshi *et al.*, in *proceedings of IPAC2016*, p.1019, 2016.
- [2] M. Arinaga *et al.*, in *proceedings of IBIC2012*, p.6, 2012.
- [3] M. Tobiyama *et al.*, "Beam commissioning of SuperKEKB rings at phase I", in *proceedings of IBIC2016*, 2016.
- [4] E. Mulyani and J. W. Flanagan, "Calibration of x-ray monitor during the phase I of SuperKEKB commissioning", in *proceedings of IBIC2016*, 2016.
- [5] H. Ikeda *et al.*, "Beam loss and abort diagnostics during SuperKEKB phase-I operation", in *proceedings of IBIC2016*, 2016.
- [6] M. Arinaga *et al.*, *Prog. Theor. Exp. Phys.*, 03A007 (2013).
- [7] M. Masuzawa *et al.*, in *proceedings of EPAC2000*, p.1780, 2000.
- [8] The data was taken by the SuperKEKB operation group.
- [9] M. Tobiyama *et al.*, "Bunch by bunch feedback systems for SuperKEKB rings", in *proceedings of 13th Annual Meeting of Particle Accelerator Society of Japan*, 2016.

MEASUREMENT OF BEAM POLARISATION AND BEAM ENERGY IN ONE DEVICE*

N. Yu. Muchnoi[†], Budker Institute of Nuclear Physics & Novosibirsk State University, Russia

Abstract

Electron beam interaction with the monochromatic laser radiation produces scattered photons and electrons due to the Compton effect. Both types of scattered particles carry the information about the polarisation (if any) and the energy of initial electrons in the beam. In this report we focus on the properties of the scattered electrons. After a bending magnet these electrons leave the beam and their X-Y space distribution is measured by the 2D pixel detector. We show that if the electron beam vertical emittance is sufficiently small, the shape of this distribution is an ellipse. Measurement of the length of the X-axis of this ellipse allow to calibrate accurately the bending field integral seen by the beam. The distribution of the electrons within the ellipse depends on the initial beam polarisation, allowing to measure its degree and direction. So we propose a universal Compton polarimeter with a unique feature of precise calibration of the LEP-style beam energy spectrometer. The approach is thought to be useful for the future high-energy e+/e- colliders, while the feasibility tests may be performed on existing accelerators.

INTRODUCTION

An illustration for the process of Inverse Compton Scattering (ICS) is presented in Fig. 1:

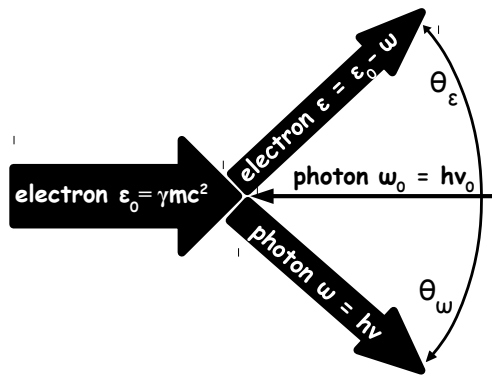


Figure 1: Inverse Compton scattering: the thickness of the arrows qualitatively represents the energies of the particles.

Considering the case when $\varepsilon_0, \varepsilon, \omega \gg \omega_0$ let's introduce the scattering parameter

$$u = \frac{\omega}{\varepsilon} = \frac{\theta_\varepsilon}{\theta_\omega} = \frac{\omega}{\varepsilon_0 - \omega} = \frac{\varepsilon_0 - \varepsilon}{\varepsilon}, \quad (1)$$

* This work was supported by Russian Science Foundation (project N 14-50-00080)

[†] muchnoi@inp.nsk.su

where $u \in [0, \kappa]$ and $\kappa = 4\omega_0\varepsilon_0/mc^2$ is twice the ratio between the photon and electron energies in the electron rest frame. The photon and electron scattering angles are:

$$\eta_\omega \equiv \gamma\theta_\omega = \sqrt{\frac{\kappa}{u} - 1}; \quad \eta_\varepsilon \equiv \gamma\theta_\varepsilon = u\sqrt{\frac{\kappa}{u} - 1}. \quad (2)$$

Further we consider an ICS of monochromatic laser radiation on the beam of ultra-relativistic electrons. ICS cross section is sensitive to the polarisation of initial electron and photon beams:

$$\frac{d\sigma}{du d\varphi} = \frac{r_e^2}{\kappa(1+u)^2} \times \quad (3)$$

$$\times \left\{ \left(2 + \frac{u^2}{1+u} + 4\frac{u}{\kappa} \left[\frac{u}{\kappa} - 1 \right] \left[1 - \xi_\perp \cos(2(\varphi - \varphi_\perp)) \right] \right) + \right. \\ \left. + \xi_\cup \left(\zeta_\parallel \frac{u(u+2)(\kappa-2u)}{\kappa(1+u)} - \zeta_\perp \frac{2u^2\sqrt{\kappa/u-1}}{\kappa(1+u)} \sin\varphi \right) \right\},$$

where

- φ is the azimuthal angle of scattered electron relative to horizon,
- ξ_\perp and φ_\perp are the degree and direction of laser beam linear polarisation,
- ξ_\cup is the degree and sign of laser circular polarisation,
- ζ_\parallel and ζ_\perp are the signs and degrees of longitudinal and vertical transverse electron beam polarisations.

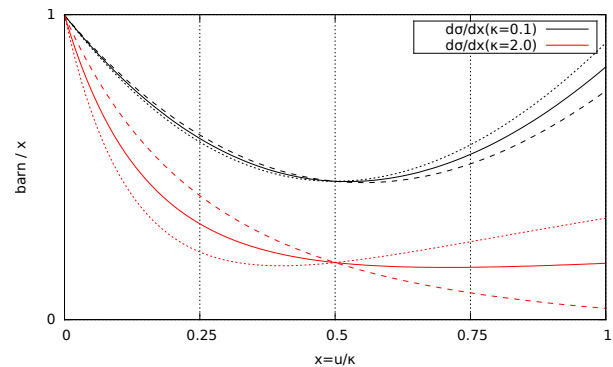


Figure 2: ICS cross section for small and large κ . The dashed lines illustrate the influence of $\xi_\cup\zeta_\parallel$.

Experiments with polarised e[±] beams were performed at many facilities (ACO, VEPP-2, SPEAR, DORIS, TRISTAN, VEPP-4, CESR, LEP, HERA...). Compton polarimeters usually dealt with scattered photons. General layout of ICS

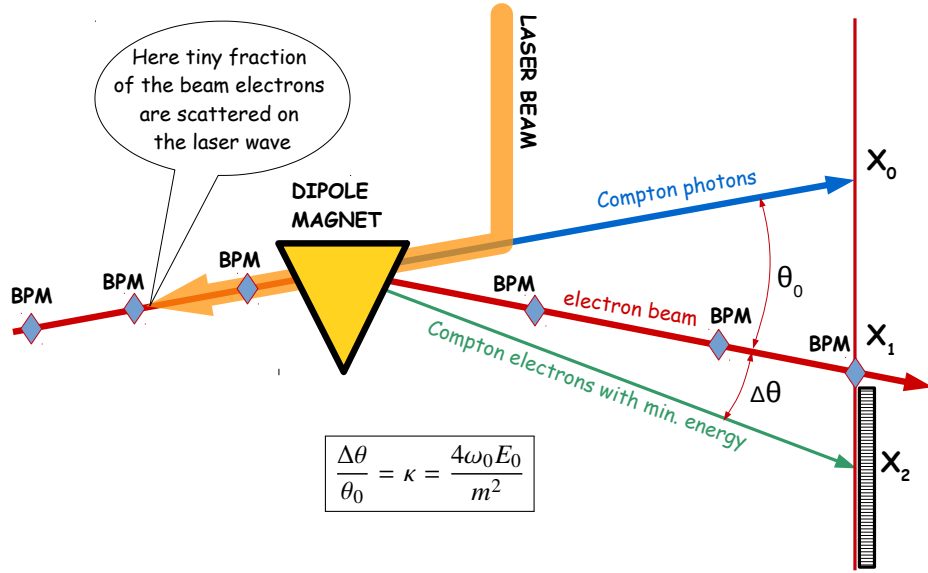


Figure 3: The general layout of ICS experiments.

experiments is shown in Fig. 3. At higher electron energies the divergence of γ -beam is small, high energy SR photons appear, etc. So it is reasonable (like ILC) to look at the scattered electrons. Maximum electron scattering angle: $\max(\theta_\varepsilon) = 2\omega_0/m$, see Eq. (2). It means that with $\omega_0 = 2.33$ eV one has $\max(\theta_\varepsilon) \approx 10$ μrad . In order to distinguish kinematics of electrons at this angular range, the beam angular spread $\sigma'_y = \sqrt{\epsilon_y/\beta_y}$ should be much smaller than $\max(\theta_\varepsilon)$. For example, the parameters $\epsilon_y = 100$ pm and $\beta_y = 100$ m gives $\sigma'_y = 1$ μrad . It's also important that the dimension of scattered electrons angular distribution does not depend on beam energy.

SCATTERED ELECTRONS AFTER A BENDING DIPOLE

An energy of a scattered electron depends on u as:

$$\varepsilon(u) = \varepsilon_0/(1+u). \quad (4)$$

This electron will be bent to the angle

$$\theta_s = \frac{c \int B dl}{\varepsilon_0} (1+u), \quad (5)$$

where $\int B dl$ is the field integral along the dipole (assuming it does not depend on electron energy). Let

$$\eta_s \equiv \gamma\theta_s = \eta_0 + u\eta_0, \quad (6)$$

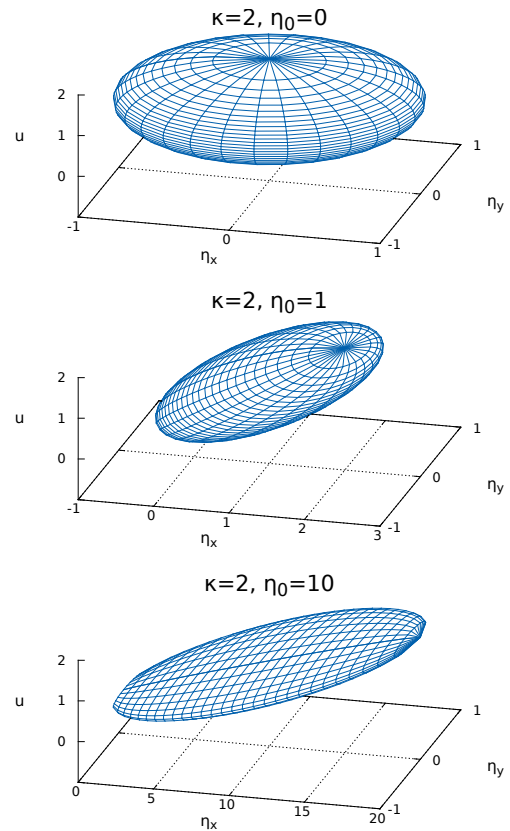
where $\eta_0 = \int B dl / B_c \lambda_c$ and $B_c \lambda_c$ is the product of Schwinger field and the Compton wavelength of an electron: $B_c \lambda_c = \frac{mc}{e} \approx 1.7 \times 10^{-3}$ [T m]. With the scattered electron angles defined as

$$\begin{cases} \eta_x \equiv \eta_s - \eta_0 = u\eta_0 + u \sqrt{\kappa/u - 1} \cos \varphi \\ \eta_y = u \sqrt{\kappa/u - 1} \sin \varphi \end{cases} \quad (7)$$

one gets the equation:

$$(\eta_x - u\eta_0)^2 + \eta_y^2 = u(\kappa - u). \quad (8)$$

Equation 8 describes surface of determination for the ICS cross section, shown in Fig. 4 for $\kappa = 2$ and various η_0 .


 Figure 4: ICS surface in (u, η_x, η_y) space.

The scattered electrons distribution in the η_x, η_y plane can be obtained by Monte Carlo method, using Eq. (3) for generation and Eq. (7) for tracking the scattered electrons through a dipole magnet. In Fig. 5 the results of such MC simulations are presented, and the shape of the ICS electrons in the η_x, η_y plane is an ellipse with certain dimensions. These dimensions, expressed in radians, are:

$$O_y = \frac{4\omega_0}{m}, \quad O_x = \frac{4\omega_0}{m} \sqrt{1 + \eta_0^2} \quad (9)$$

$$\kappa = 3.26, \eta_0 = 500, P = [0.0, 0.0, -0.5, 0.0]$$

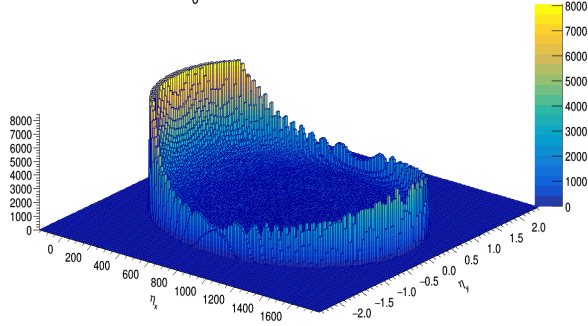


Figure 5: The scattered electrons distribution in η_x, η_y plane. $\kappa = 3.26$ when $\varepsilon_0 = 45.5$ GeV and $\omega_0 = 4.68$ eV. P is the polarisation vector and does not matter here. $\eta_0 = 500$ means that the electron beam was turned to an angle of $500 \cdot 1/\gamma$. Electron beam is located at $\eta_x = \eta_y = 0$.

In Ref. [1] there is a study about application of silicon pixel detector to measure the distribution of scattered electrons, similar to one shown in Fig. 5, in order to determine the transverse polarisation of an electron beam in ILC. Based on this work is our assumption that there are existing apparatus allowing to measure such a distribution, and we're not going into details about it. In this report we want to show that the analysis of this distribution allows to measure whatever possible polarisation as well as to perform a precise calibration of magnetic spectrometer.

Our analysis is based on the procedure of fitting the 2D distribution of scattered electrons by the theory function. The cross section itself, according to Eq. (3), consists of three parts. The new variables for the ICS cross section will be x and y , obtained by transformation of an ellipse, Eq. (9), to a circle where $x = y = 0$ is the centre of the circle. After some analytical calculations, Fig. 6 presents their results in graphical way. Three components of ICS cross section, according to Fig. 6 and its caption, are \mathcal{U} , \mathcal{L} and \mathcal{T} . The distribution of scattered electrons in x, y coordinates is expressed by the convolution of

- a) the cross section

$$f(x, y) = \mathcal{U} + \xi_{\cup} (\xi_{\parallel} \mathcal{L} + \xi_{\perp} \mathcal{T}) \quad (10)$$

- b) transverse distributions (σ_x, σ_y) of beam electrons.

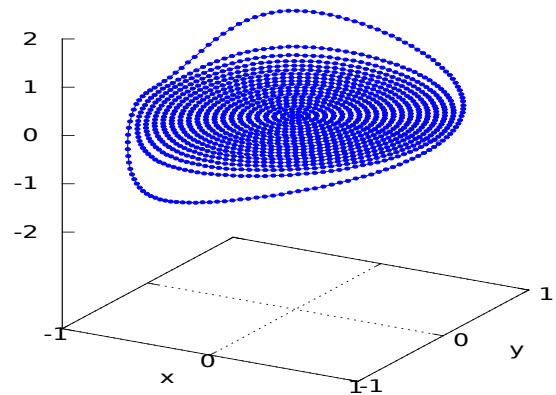
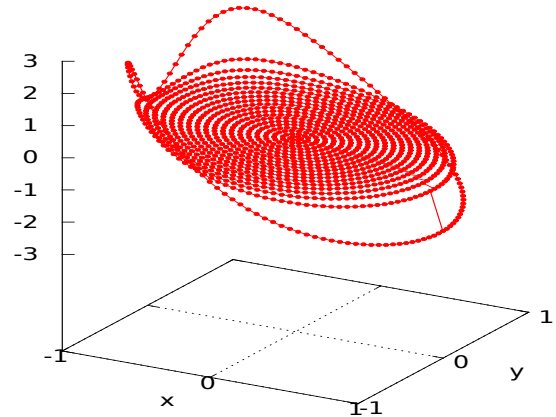
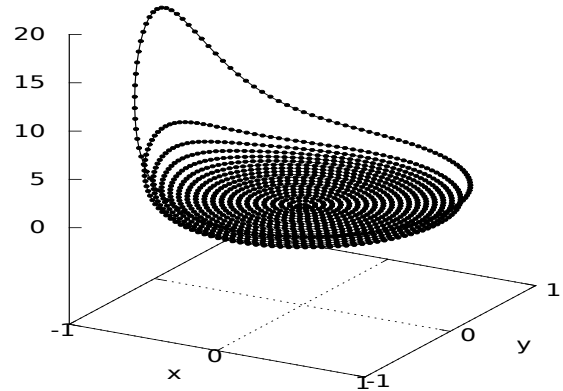


Figure 6: From top to bottom: three ICS cross section components: \mathcal{U} - unpolared (black), \mathcal{L} - 100% longitudinal (red), \mathcal{T} 100% transverse vertical (blue) e^- spin polarisation. Vertical scale (arbitrary units) is the same for all of the plots.

The horizontal (x) and vertical (y) dimensions of the components \mathcal{U} , \mathcal{L} and \mathcal{T} in Eq. (10) could be scaled to any real values of ω_0 and η_0 according to Eqs. (9). The only value, depending on the beam energy ε_0 is the value of the cross section at each point in Fig. 6. This dependence is relatively weak, see Fig. 2, so 10% accuracy in beam energy knowledge is more than enough for the fit success.

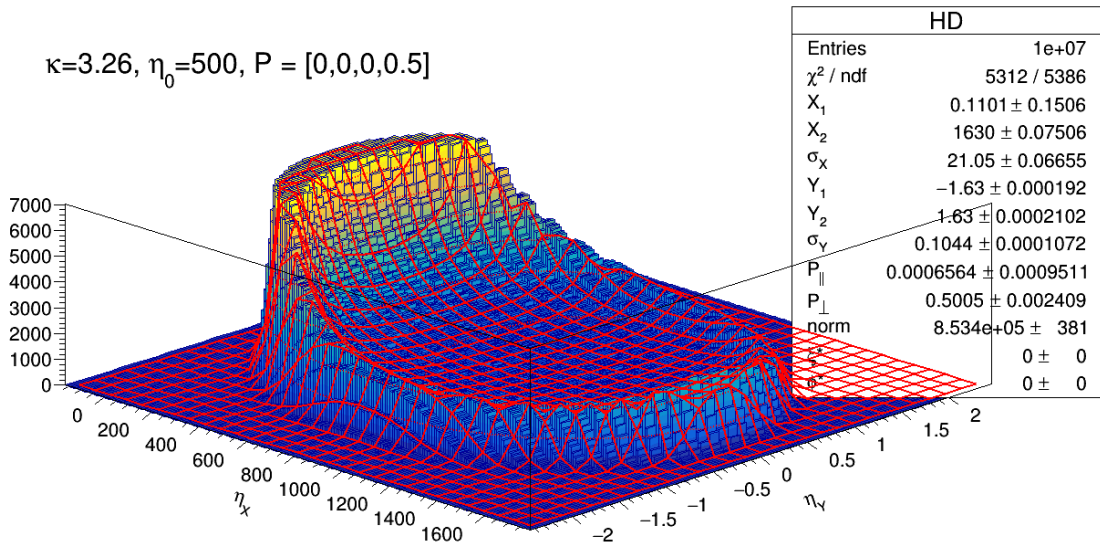


Figure 7: The MC distribution of scattered electrons with the fit function and fit results.

The example of fitted distribution is presented on Fig. 7. The initial conditions are:

- The horizontal size of an ellipse fixed by MC generator O_x equals $\kappa\eta_0 = 3.26 \cdot 500 = 1630$.
- $P = [0,0,0,0.5]$ is the polarisation vector meaning that $\xi_{\perp} = \varphi_{\perp} = \xi_{\cup}\zeta_{\parallel} = 0$ and $\xi_{\cup}\zeta_{\perp} = 0.5$.
- The histogram has 100 bins in η_x and 50 bins in η_y . In our consideration this is an equivalent of the number of detector pixels.
- The 10^7 scattered electrons were generated.
- Fit range in η_x is starting from $\eta_x = 200$, assuming that the smaller values of η_x are not available for measurement cause these electrons propagate too close to the beam. The electron beam itself is located at $\eta_x = \eta_y = 0$, see Fig. 3.
- the transverse horizontal and vertical sizes of the electron beam are described by Gaussian distributions with parameters $\sigma_x = 20$ and $\sigma_y = 0.1$ in the same units as η_0, η_x and η_y .

The fit results are shown in the parameters table in Fig. 7. The essential results are:

- $P_{\parallel} \equiv \xi_{\cup}\zeta_{\parallel} = 0.0007 \pm 0.0009$.
- $P_{\perp} \equiv \xi_{\cup}\zeta_{\perp} = 0.501 \pm 0.002$.
- $O_x \equiv X_2 - X_1 = (1630.02 \pm 0.08) - (0.110 \pm 0.151)$.

The polarisation parameter P_{\perp} “was measured” with 0.4% accuracy. Note that X_1 is the beam position, which in principle can be also measured by beam position monitors, see Fig. 3. The relative error $\Delta X_2/(X_2 - X_1) \approx 5 \cdot 10^{-5}$ in our

example is twice better than the $\Delta X_1/(X_2 - X_1) \approx 10^{-4}$. This is because the detector can not measure the part of the scattered electrons distribution close to the main beam, i. e., again, the fitting range in η_x is started at $\eta_x = 200$. We claim again that the O_x measurement is the measurement of the parameter $\eta_0 = \int Bdl/B_c \lambda_c$, i. e. the bending field integral. From the statistical point of view such measurement is evidently much more efficient to be compared to one-dimensional measurements of η_x only. The relative error in O_x measurement obviously depend on the number of detected particles (statistics) and the ratio between the overall size of the distribution and number of histogram bins (i. e. detector pixels). In this sense, the absolute value of $\kappa\eta_0 = 1630$ in our example, does not matter at all, the similar accuracy can be obtained for any other case.

The difference in trajectories of scattered and unscattered electrons

In all of the above considerations we have implicitly believed that the beam electrons and the scattered electrons are bent by the dipole in such a way, that all of these electrons experience the same bending force defined by the only one parameter $\eta_0 = \int Bdl/B_c \lambda_c$. However this is only an approximation, and electrons with different energies are propagating with individual trajectories. It is very important to understand the accuracy of this approximation. To do this, let us consider the possible difference of η_0 for the beam electrons with energy ε_0 , and the scattered electrons with minimal energy $\varepsilon_{min} = \varepsilon_0/(1 + \kappa)$. The bending radii of these electrons in the same bending field are related by:

$$R_{min} = R_0/(1 + \kappa). \quad (11)$$

In Fig. 8 the geometry of bending dipole is presented. By

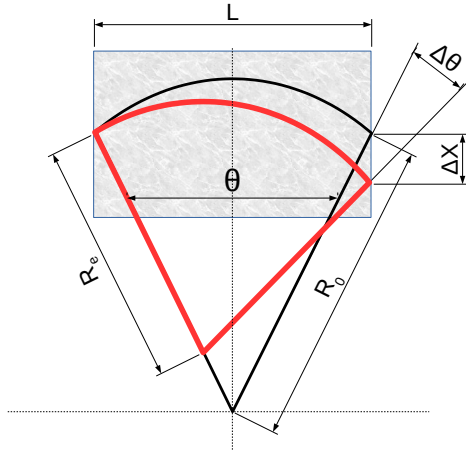


Figure 8: Bending of electrons with different energies. Black upper arc – the trajectory of an electron with ε_0 energy, red lower arc – the trajectory of an electron with ε_{min} energy.

simple trigonometry calculations one obtains:

$$S_0 = 2R_0 \arcsin \left[\frac{L}{2R_0} \right], \quad (12)$$

$$S = 2R_{min} \arcsin \left[\frac{\sqrt{L^2 + \Delta X^2}}{2R_{min}} \right], \quad (13)$$

where

$$\Delta X = \sqrt{R_{min}^2 - \left[\frac{LR_{min}}{2R_0} \right]^2} - \sqrt{R_{min}^2 - \left[L - \frac{LR_{min}}{2R_0} \right]^2}.$$

We are going to compare the length of the trajectories $\Delta S = (S - S_0)/2S_0$ and the maximum transverse distance ΔX between trajectories in the spectrometer, illustrated by Fig. 9.

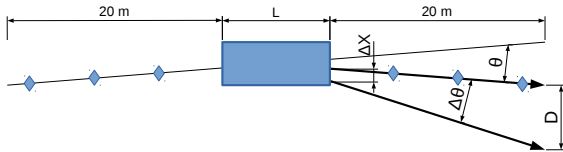


Figure 9: Sketch of spectrometer.

Table 1: Calculations by Eqs. (12, 13)

θ mrad	$\Delta\theta$ mrad	L m	ΔX mm	$\Delta S/S$	D mm
1	1.53	10	3.83	$2.59 \cdot 10^{-7}$	46
2	3.06	10	7.65	$1.04 \cdot 10^{-6}$	92
1	1.53	5	1.91	$2.59 \cdot 10^{-7}$	46
2	3.06	5	3.83	$1.04 \cdot 10^{-6}$	92

The results of calculations for various parameters are presented in Table 1, where D is the horizontal size of the distribution of scattered electrons at the detector. From Table 1 we see that our main approximation about the equality of η_0 for all electrons could be made rather strict by appropriate design of the spectrometer. It is also important to mention that

$$\Delta S/S \propto \kappa\theta, \quad \Delta X \propto \kappa\theta L, \quad D \propto \kappa\theta L_{arm}.$$

Since everything is proportional to $\kappa\theta$, our approximation is valid for any electron beam energy range. At high electron beam energies, implying circular machines, the value of θ is naturally small and the value of κ is naturally large. At low energies we can afford larger θ and will have smaller κ .

CONCLUSION

Inverse Compton scattering of laser radiation is a currently available reliable method for beam polarisation [2, 3] and energy [4–6] determination. The future high energy lepton colliders require polarised beams and polarimetry, inter alia for application of resonant depolarisation technique for precise beam energy calibration at circular machines. Analysis of 2D-distribution of ICS electrons allows to measure beam polarisation degree and direction as well as to provide a unique way for accurate calibration of the $\int Bdl$ exactly along a beam trajectory in a conventional magnetic spectrometer. Such a spectrometer was installed at LEP [7] and no doubt it should be implemented at future high-energy colliders, either linear or circular. The proposed approach has no limitations in beam energy, the only thing it requires is a small value of vertical emittance of the electron beam. Now it's a good time to start the proof-of-principle project at one of the existing low-emittance facilities. Another subject for further studies should be a possibility to measure the position of backscattered photons with high accuracy, see Fig. 3. This seems to be not an easy task, but it allows to build the completely independent beam energy measurement approach for arbitrary beam energies.

REFERENCES

- [1] Itai Ben Mordechai and Gideon Alexander. ILC Note: LC-M-2012-001 (2012).
- [2] M.Placidi, R.Rossmannith, Nucl. Instr. Meth. A274 (1989) 79-94.
- [3] S.Boogert *et al.*, JINST 4 P10015 (2009).
- [4] V.E.Blinov *et al.*, Nucl. Instr. Meth. A598 (2009) 23-30.
- [5] E.V.Abakumova *et al.*, Nucl. Instrum. Meth. A659 (2011) 21-29.
- [6] E.V.Abakumova *et al.*, Phys. Rev. Lett. 110 (2013) 140402.
- [7] R.Assmann *et al.*, Eur. Phys. J. C39 (2005) 253-292. SLD

NEW CAVITY TECHNIQUES AND FUTURE PROSPECTS*

P. Sha[†], J. Y. Zhai, Institute of High Energy Physics, CAS, Beijing, China

Abstract

In the recent decades, Superconducting cavities have been widely used to accelerate electron, positron, and ions. Most SRF cavities are made from bulk niobium till now, which has developed fast in the past years and is hard to advance more. Take 1.3 GHz 9-cell cavity for example, the quality factor (Q) can keep above $1e10$ when the accelerating field (E_{acc}) reach 40 MV/m, which nearly touch the theoretical limitation of Q and E_{acc} for bulk niobium. For large superconducting accelerators in future (FCC, CEPC, etc), Q and E_{acc} should be increased significantly compared to now, which can reduce the cryogenic power and use fewer cavities. So new cavity material and techniques are being studied at accelerator laboratories, while Nitrogen doping (N-doping) and Nb_3Sn have developed quickly and been paid attention to mostly [1]. N-doping can increase Q by one time for 1.3 GHz 9-cell cavity, which have been adopted by Linac Coherent Light Source II (LCLS-II) at SLAC [2].

INTRODUCTION

In recent years, N-doping technology has been proposed and proven to increase Q of superconducting cavity obviously, which lowers the BCS surface resistance. It was discovered in 2012 at FNAL, which has been promoted by FNAL, JLAB and Cornell together. Since 2013, there have been over 60 cavities nitrogen doped in USA laboratories. After N-doping, Q of 1.3 GHz 9-cell cavities increased to $3 \cdot 10^{10}$ at $E_{acc}=16$ MV/m, while $1.5 \cdot 10^{10}$ without N-doping [3].

Besides, thin film technologies have also developed very quickly, which include Nb_3Sn/Nb , Nb/Cu et al. There've been many good results of vertical tests. And superconducting cavities made of thin film would be more practical in future.

RESEARCH OF N-DOPING

Theory

N-doping of niobium can create a niobium nitride layer, which is about 2-micron deep and harmful to Q value. So this layer is removed by 5-micron electro polishing. Then, the diffraction pattern of transmitted electron microscope shows only clean niobium phase without nitride. It indicates that the interstitial nitrogen contributes to the increase of Q value.

N-doping has been proven to prevent Q-slope at medium accelerating fields for superconducting cavities, which is found to reduce the BCS surface resistance compared to ILC/XFEL standard by 50%. The non-trapped flux related

residual resistance can also be reduced to $2 \text{ n}\Omega$ with N-doping [4]. But it also results to undesirable lower quench field. The levels of N-doping affect R_{BCS} , R_0 , R_{MAG} and quench field, which is important and needs deeper research.

Achievements

The experiments of N-doping succeeded on the 1.3 GHz cavities firstly. And then it was applied to 650 MHz cavities.

Based on the research achievements above, the N-doping technique has been adopted by the LCLS-II project. To transfer it to industrial vendors, the protocol of N-doping has been optimized, as Table 1 [5].

Table 1: N-doping Parameters

Step	Temperature (°C), Pressure (Pa)	Duration (min)
Hydrogen degassing	$800 \pm 10, 0$	180 ± 5
N-doping	$800 \pm 10, 3.5 \pm 10$	2 ± 0.1
Vacuum annealing	$800 \pm 10, 0$	6 ± 0.1

Table 1 shows the latest recipe of N-doping adopted by LCLS-II, which is known as “2/6”. It stands for 2-minute nitrogen injection and 6-minute annealing, both at 800C. Then, 5 microns of cavity inner surface are removed by electro polishing [6]. So it's different from the standard protocol of 1.3 GHz 9-cell cavities for XFEL. The 120C baking is cancelled, which may cause a decrease in Q and quench fields for cavities nitrogen doped.

Details of N-doping for LCLS-II are deeply analysed in [7]. Figure 1 shows the vertical test results of LCLS-II cavities adopted 2/6 recipe at FNAL and JLAB. All cavities meet the design target of $2.7e10@16MV/m$ at 2K. Average Q is $3.5e10@16MV/m$ at 2K, and average quench field reach 22 MV/m [2, 4].

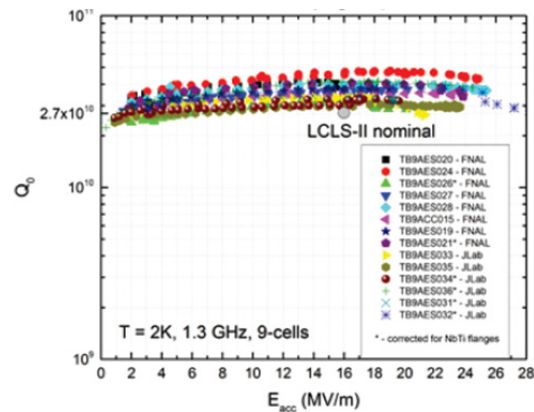


Figure 1: Performance of 1.3 GHz 9-cell cavities for LCLS-II.

* This study was supported by National Key Programme for S&T Research and Development (Grant NO.: 2016YFA0400400) and National Natural Science Foundation of China (Grant NO.: 11505197)

[†] shapeng@ihep.ac.cn

The same recipe is adopted by 650 MHz single-cell cavities for PIP-II, too. The vertical test results adopted 2/6 recipe and standard 120C baking are compared, as Figure 2 [8, 9]. The Q value increases by 100% and reaches $7e10@17MV/m$ at 2K, which is the world record at this frequency.

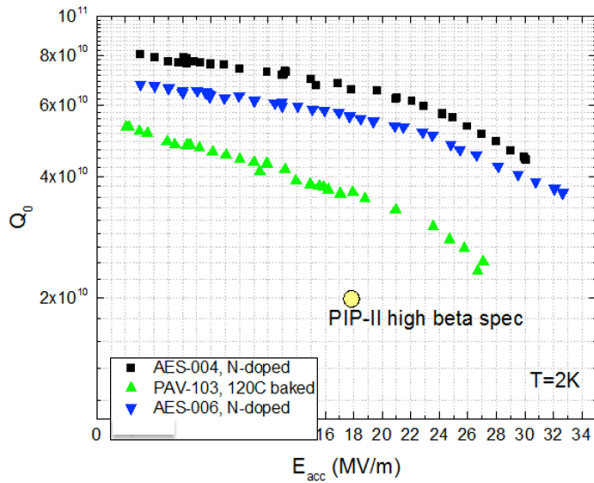


Figure 2: Performance of 650 MHz cavities for PIP-II.

N-doping at IHEP

Recently, the Circular Electron Positron Collider (CEPC) was proposed by Chinese high energy physicists, which contains more than 600 superconducting cavities (1.3 GHz and 650 MHz). So it's eager to increase Q value of cavities to minimize cryogenic capital and operating cost, as Table 2 [10].

Table 2: Target of Q Value for CEPC Cavities

Cavity	Qualification	Operation
650MHz 2-cell	4e10@22MV/m (VT), 2e10@20MV/m (HT)	2e10@16.5MV/m
1.3GHz 9-cell	3e10@25MV/m (VT)	2e10@20MV/m

It's hard to achieve such target with ILC/XFEL standard, while N-doping is a good choice. So research of N-doping was begun by IHEP in cooperation with Peking University in early 2015.

Firstly, niobium samples were nitrogen doped both at IHEP and Peking University, as Figure 3. Different methods were used to achieve that nitrogen enters into niobium surface and exists for long. To verify that, experiments of secondary ion mass spectrometry (SIMS) and auger electron spectroscopy (AES) were done, as Figure 4. Then, one method of N-doping was found to be useful.

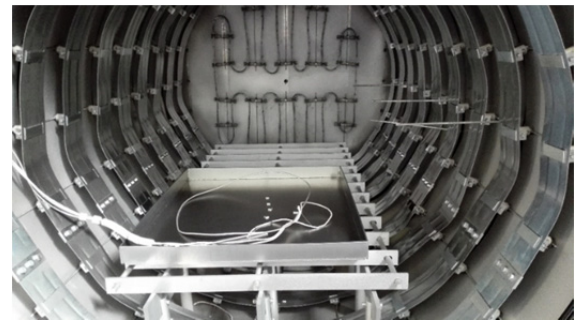


Figure 3: Niobium samples for N-doping in the furnace at IHEP.

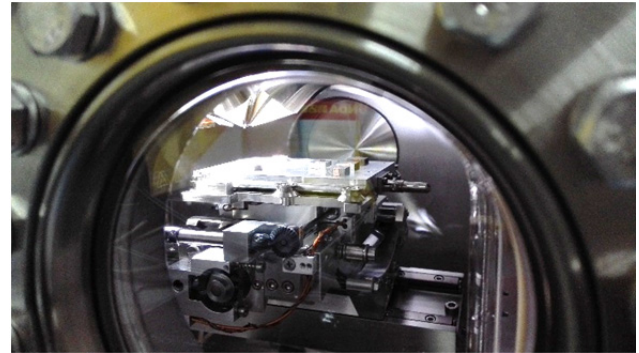


Figure 4: SIMS of niobium samples at Tsinghua University.

Secondly, a single-cell 1.3 GHz cavity was N-doped adopting the same technique. Afterwards, vertical test was held. But the performance of cavity N-doped was bad. The reasons are being investigated at present.

Low Temperature N-doping

Experiments show that N-doping can cause the decrease of quench field (23 MV/m for 1.3 GHz 9-cell cavities), which is unwelcome for superconducting cavity. In order to achieve both high Q and high field, low temperature (120C-160C) N-doping is being studied right now [11], which realizes very high Q at both medium and high accelerating field. The quench field limitation increases to 45 MV/m for 1.3 GHz 9-cell cavities, as Figure 5.

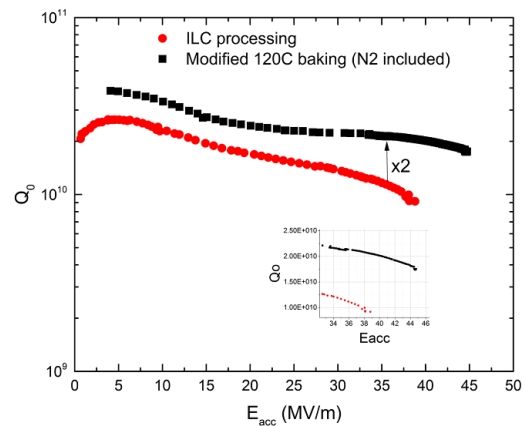


Figure 5: Vertical test result for low temperature N-doping (120C N₂ baking).

High temperature (800C) N-doping is proven to manipulate mean free path with several microns throughout. With contrast, low temperature N-doping manipulates mean free path at very near surface of bulk niobium. The actual regime of low temperature N-doping is still being studied.

RESEARCH OF THIN FILM

Figure 6 shows possible alternative materials for superconducting cavity [13].

Material	Critical Temp. T_c [K]	Normal-state resistivity $\rho_n(\mu\Omega\text{cm})$	Critical Field $H_{c1}(0)$ [T]	Lower Critical field $H_{c1}(0)$ [T]	Upper Critical field $H_{c2}(0)$ [T]	Penetration depth $\lambda(0)$ [nm]	Δ [meV]	Type
Nb	9.23	2	0.2	0.18	0.28	40	1.5	II
Pb	7.2		0.08	N/A	N/A	48		I
NbN	16.2	70	0.23	0.02	15	200-350	2.6	II, B1 comp.
NbTiN	17.3	35		0.03		150-200		II, B1 comp.
Nb ₃ Sn	18	20	0.54	0.05	30	80-100	3.1	II, A15
V ₃ Si	17				24.5	179		II, A15
Mo ₃ Re	15		0.43	0.03	3.5	140		II, A15
MgB ₂	40	0.1-10	0.43	0.03	3.5-60	140	2.3/7.2	II- 2 gaps
YBCO	93		1.4	0.01	100	150	20	d-wave
Pnictides	30-55		0.5-0.9	30	>100	200	10-20	

Figure 6: Possible alternative materials for superconducting cavity.

Among these materials, Nb₃Sn has shown great potential for operation at medium gradients at 4.2 K. Cornell has completed several vertical tests of Nb₃Sn cavities (niobium cavities coating with Nb₃Sn), as Figure 7 [14]. Besides, MgB₂ may have even better performance, which is not as technologically ready yet.

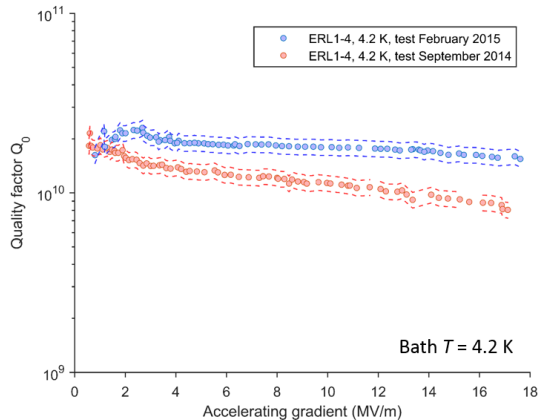


Figure 7: Vertical test results for Nb₃Sn cavities.

CONCLUSION

There've been many new superconducting cavity technologies for the large accelerators under planning, while N-doping technique is developing very fast. It has been applied in the LCLS-II project. Besides, cavity coating with Nb₃Sn is also very promising.

ACKNOWLEDGEMENT

Colleagues of IHEP, Peking University, FNAL, JLAB, Cornell, CERN and TRIUMF also contribute to this paper. Thanks for them!

REFERENCES

- [1] Alexander Romanenko, "Bulk Nb Based SRF Technology", FCC Week 2016.
- [2] C. M. Ginsburg *et al.*, "LCLS-II Cryomodules at FNAL & JLAB", TTC Meeting 2016.
- [3] A. Romanenko, "Breakthrough technology for very high quality factors in SRF cavities", in Proceedings of LINAC14, Sep 2014.
- [4] A. Grassellino *et al.*, "N-doping: progress in development and understanding", in Proceedings of SRF2015, Whistler, BC, Canada.
- [5] C. E. Reece *et al.*, "The transfer of improved cavity processing protocols to industry for LCLS-II: N-doping and electropolishing", in Proceedings of SRF2015, Whistler, BC, Canada.

- [6] M. Checchin, INFN-SSSA Summer Internship Final Report, Fermilab, USA, 2013.
- [7] A. Romanenko, A. Grassellino, *Appl. Phys. Lett.*, 102, 252603, 2013.
- [8] L. Ristori, Cavity, “Test Results for PIP-II”, TTC Meeting 2016.
- [9] P. Sha *et al.*, “Research of nitrogen doping in IHEP”, in *Proc. IPAC’16*, Busan, Korea, 2016.
- [10] P. Sha, CEPC “Nitrogen doping study”, CEPC-SppC Study Group Meeting, Beijing, China, 2-3 Sep, 2016.
- [11] M. Martinello, “N-doping: a breakthrough technology for SRF cavities”, presented at LINAC2016, East Lansing, USA, 28 Sep, 2016.
- [12] A. Grassellino *et al.*, “New Low T Nitrogen Treatments Cavity Results with Record Gradients and Q”, TTC 2016.
- [13] T. Junginger, “RF Superconductivity”, IHEP 2016 RF lecture series, Sep, 2016.
- [14] D. Hall, “Next Generation Nb₃Sn cavities: Current performance, limitations, and considerations for practical use”, TTC 2016.

LLRF CONTROLS INCLUDING GAP TRANSIENTS AT KEKB AND PLANS FOR superKEKB

T. Kobayashi[†] and K. Akai, KEK, Tsukuba, Japan

Abstract

Features of LLRF control systems in KEKB and SuperKEKB will be reviewed, and the evaluation of the bunch gap transient effect on beam phase will be presented for SuperKEKB. The RF systems of KEKB are being reinforced to handle triple as large beam power for upgrade to SuperKEKB. Furthermore, a new LLRF control system, which is based on a recent digital control technique, has been developed. They were worked successfully in the Phase-1 commissioning.

Bunch phase shift along the bunch train due to a bunch gap transient is a concern in a high intensity circular collider. In KEKB operation, a rapid phase change was observed at the leading part of the train in the bunch phase measurement, which was not predicted. Our new simulation study of the bunch gap transient effect on beam phase clarified that the rapid phase change is caused by a transient loading in the three-cavity system of ARES. The new simulation for SuperKEKB shows that the phase change due the bunch gap will be significantly large at the design beam current operation. The main issue is the difference in beam phase change between the two rings for the asymmetry colliding. The measures for mitigation of the relative beam phase difference between the two rings will be also suggested.

INTRODUCTION

KEKB is an asymmetric energy collider consisting of an 8 GeV electron ring (high-energy ring, HER) and a 3.5 GeV positron ring (low-energy ring, LER), which was operated from 1998 to 2010 [1]. It obtained the world record in luminosity of $2.11 \times 10^{34} \text{ cm}^{-2}\text{s}^{-1}$. To increase the luminosity, a high-current beam is needed in both rings, which is accomplished by filling bunches into a number of buckets. One serious concern for high-current storage rings is the coupled-bunch instability caused by the accelerating mode of the cavities. This issue arises from the large detuning of the resonant frequency of the cavities that is needed to compensate for the reactive component of the beam loading [2]. Two types of cavities that mitigate this problem are used in KEKB [3, 4]: one is the ARES normal conducting three-cavity system [5, 6] and the other is the superconducting cavity (SCC) [7, 8]. The detuning frequency of these cavities is reduced owing to the high stored energy in these cavities.

The ARES is a unique cavity, which is specialized for KEKB. It consists of a three-cavity system operated in the $\pi/2$ mode: the accelerating (A-) cavity is coupled to a storage (S-) cavity via a coupling (C-) cavity as shown in Fig. 1 [9]. The A-cavity is structured to damp higher-order modes (HOM). The C-cavity is equipped with a damper to damp parasitic 0 and π -modes. The $\pi/2$ mode

has a high Q-value even with a C-cavity with a very low Q-value of about 100. In LER, where a higher beam current is stored than in HER, only the ARES cavities were used. For details regarding the RF systems of KEKB, see Refs. [3, 4]. The RF issues to be considered for the heavy-beam current storage are summarized in Ref. [10].

KEKB is being upgraded to SuperKEKB, which is aiming at a 40 times higher luminosity than KEKB [11, 12]. The RF related machine parameters are shown in Table 1. The RF systems are being reinforced to handle twice as large stored beam currents in both rings and much higher beam power (compared to KEKB) [13]. ARES and SCC will be reused with the reinforcements. The RF power source systems, including klystrons, waveguides, and cooling systems, also need to be reinforced to increase the driving RF power to provide larger beam power. Furthermore, a new low-level RF (LLRF) control system, which is based on a recent digital control technique using field-programmable gate arrays (FPGAs), has been developed to realize higher accuracy and greater flexibility [14]. For nine RF stations, among a total of thirty, the LLRF control system used in KEKB has been replaced with new ones.

The first beam commissioning of SuperKEKB (Phase-1) was accomplished in 2016. The RF systems and the new LLRF control systems were soundly worked. The desired beam current of 1A for Phase-1 was successfully achieved and the vacuum scrubbing was sufficiently progressed.

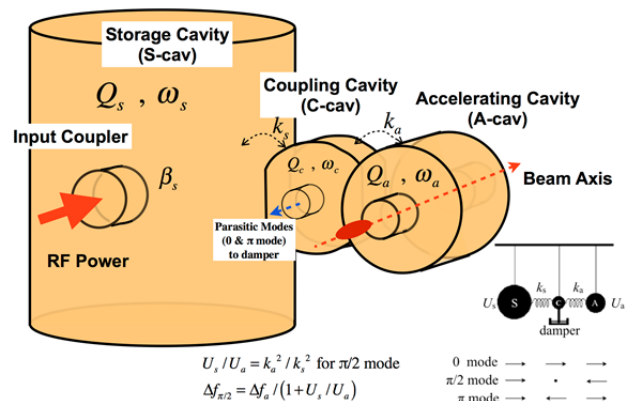


Figure 1: Illustration of the ARES cavity structure.

RF SYSTEM ARRANGEMENT

RF related parameters of SuperKEKB are shown in Table 1 in contradistinction with those of KEKB. The RF system layout of KEKB is shown in Fig. 2. The planed arrangement for SuperKEKB at the design beam current is also shown in the figure (lower side). We have about

thirty stations of the RF power source (klystron and the LLRF control). SCC's are used in HER. Eight modules of SCC are installed at Nikko section. For the other section, ARES cavity units are used. In LER, all cavities are the ARES type. In the KEKB operation, one klystron has driven two ARES units. On the other, in SuperKEKB, one klystron should drive only one ARES unit (so called "one-to-one configuration" is necessary), because the beam power per ARES will be three times higher than that of KEKB (see Table 1). The cavity input power will be about 750 kW (cavity wall loss + beam power) in SuperKEKB, while the maximum klystron output power is about 1MW. Accordingly additional klystrons are needed for the upgrade. The input coupler of ARES has been already reinforced for the increased input power.

For Phase 1 as a first step, six ARES units of OHO-D5 section were relocated from HER to LER, and the configuration of them was changed to the one-to-one configuration. Additionally the configuration of D7-C, D7-D, D8-C and D8-D stations was also changed to the one-to-one configuration for Phase-1.

Table 1: RF related parameters of KEK and SuperKEKB

Parameter	unit	KEKB (achieved)		SuperKEKB (design)					
		HER	LER	HER	LER	HER	LER		
Ring		HER	LER	HER	LER	HER	LER		
Energy	GeV	8.0	3.5	7.0	4.0	7.0	4.0		
Beam Current	A	1.4	2	2.6	3.6	2.6	3.6		
Number of Bunches		1585	1585	2500	2500	2500	2500		
Bunch Length	mm	6-7	6-7	5	6	5	6		
Total Beam Power	MW	~5.0	~3.5	8.0	8.3	8.0	8.3		
Total RF Voltage	MV	15.0	8.0	15.8	9.4	15.8	9.4		
		ARES		SCC		ARES			
Number of Cavities		10	2	8	20	10	8	8	14
Klystron : Cavity		1:2	1:1	1:1	1:2	1:1	1:1	1:2	1:1
RF Voltage (Max.)	MV/cav.	0.5	1.5	0.5	0.5	0.5	1.5	0.5	0.5
Beam Power (Max.)	kW/cav.	200	550	400	200	600	400	200	600

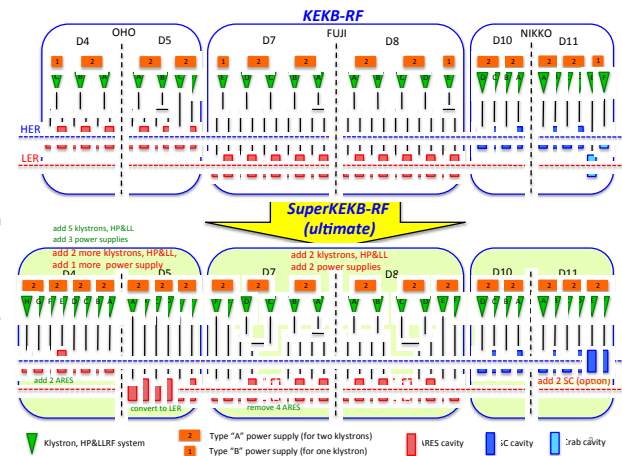


Figure 2: RF system arrangement of KEKB and plan for SuperKEKB ultimate stage.

LLRF CONTROL SYSTEM

Accuracy and flexibility in accelerating field control are very essential for storage of high-current and high-quality beam without instability. Therefore, new low level RF (LLRF) control system, which is based on recent digital architecture, was developed for the SuperKEKB. Figure 3 shows a picture of a mass-production model of the new LLRF system for the SuperKEKB. A block diagram of an ARES cavity driving system is shown Fig. 4. The principal functions of this system are performed by five FPGA boards which work on MicroTCA platform as advanced mezzanine cards [15]: Vc-FB controller (FBCNT), cavity-tuner controller (TNRcnt), inter-lock handler (INTLCNT), RF-level detector for the interlock and arc-discharge photo-signal detector. As shown in Fig. 4, the new LLRF control system handles I/Q components of controlling signals in the FPGAs. For slow interlocks (e.g. vacuum, cooling water) and sequence control, a PLC is utilized. EPICS-IOC on Linux -OS is embedded in each of the FPGA boards and the PLC [16].

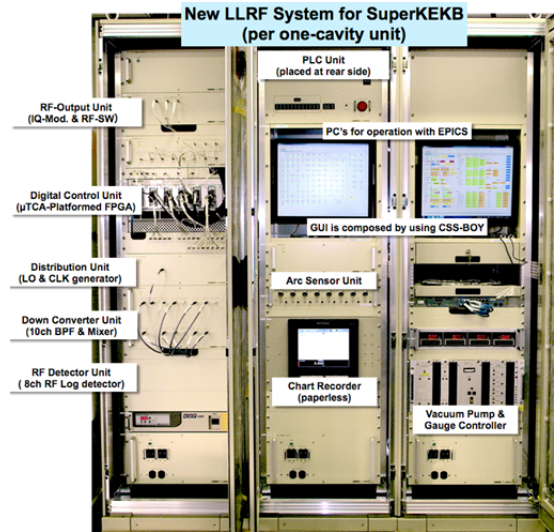


Figure 3: LLRF control system for SuperKEKB.

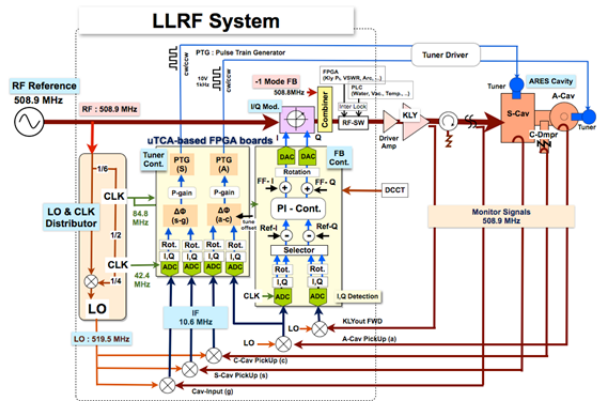


Figure 4: Block diagram for ARES cavity control.

At 9 stations of Oho D4&D5 (6@D5 + 3@D4), the LLRF control systems were replaced with new digital control systems for Phase-1 as shown Fig. 5 and Fig. 6.

All of new systems successfully worked well without problem. Some software bugs found during the operation were fixed. The DR-LLRF control system has already installed in DR control room. It is almost the same as MR one, except 3-cavity vector-sum control is needed. In the present stage, the number of cavities is two.

On the other hands, the other stations were still operated with existing (old analogue) LLRF control systems, which had been used in the KEKB operation. These systems are composed of combination of NIM standard analogue modules as shown in Fig. 7. They are controlled remotely via CAMAC system. All systems also soundly worked as well as operated in the KEKB operation, although many old defective modules were replaced with spares in the maintenance works.



Figure 7: Old LLRF control system, which was used in KEKB operation, continues in use for SuperKEKB.

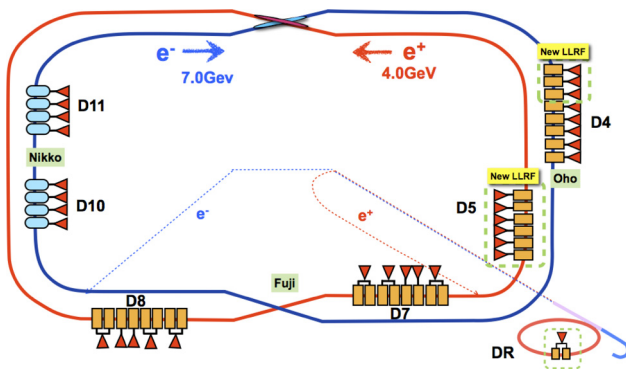
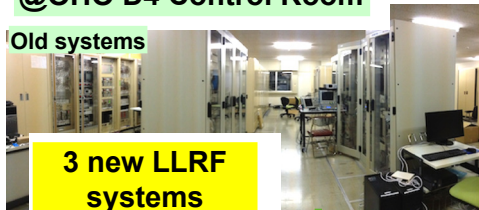


Figure 5: RF system layout for the Phase-1. Nine LLRF stations were replaced with the new ones. DR-LLRF control system was also newly installed.

RF reference distribution system was also upgrade for SuperKEKB [17]. RF reference signal is optically distributed into 8 sections by means of “Star” topology configuration from the central control room (CCR). “Phase Stabilized Optical Fiber”, which has quite small thermal coefficient ($< 1\text{ppm}/^\circ\text{C}$), is adapted. For the thermal phase drift compensation, optical delay line is controlled digitally at CCR for all transfer lines as shown in Fig 8. The short term stability (time jitter) is about 0.1 ps (rms), and the long term stability (pk-pk) is $\pm 0.1^\circ = \pm 0.55$ ps at 508.9MHz (expected by the optical delay control).

@OHO D4 Control Room

Old systems



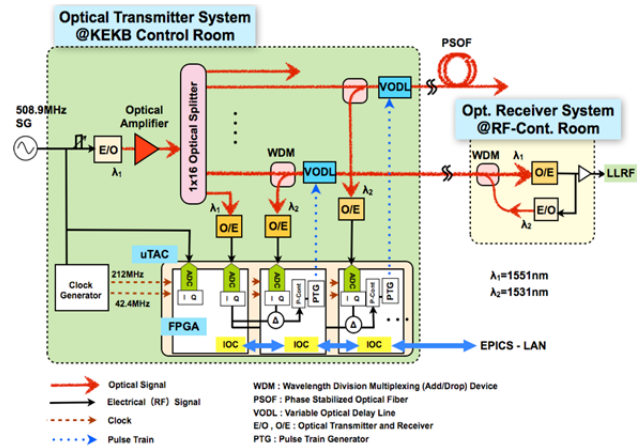
3 new LLRF systems

@OHO D5 Control Room



6 new LLRF systems

Figure 6: Installation appearance of the new LLRF control systems in the RF control rooms at D4 (upper) and D5 (lower) section.



Variable Optical Delay Lines (VODLs) for 8 transmissions

uTCA-platformed FPGAs for the VODLs control

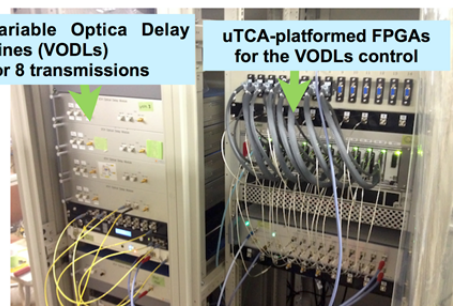


Figure 8: New RF reference signal distribution system for SuperKEKB. Block diagram of the reference distribution (upper side) and the photo of VODL control system (lower side) are shown.

The Phase-1 commissioning result is shown in Fig. 9. History of the stored beam current with beam dose (upper side) and the total acceleration voltage called total-Vc (lower side) of the both ring during Phase-1 is plotted in the figure. RF systems worked well without serious trouble. Target beam current of ~1A for Phase-1 was successfully achieved in both ring and vacuum scrubbing has been sufficiently progressed.

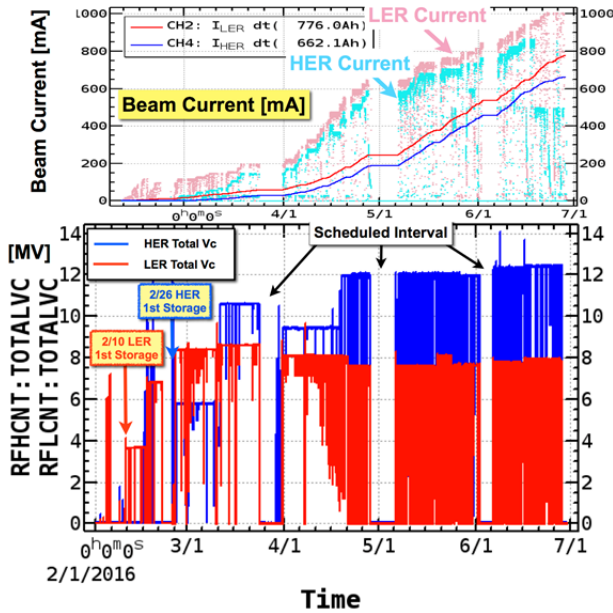


Figure 9: History of the stored beam current, the beam dose (upper side), and the total acceleration voltage called Total-Vc (lower side) for the both ring.

COUPLER BUNCH INSTABILITY DUE TO ACCELERATING MODE

In HER, over the 400-mA beam current, the $\mu=-1$ mode instability due to the detuned cavities (parked with some reasons) was excited. It could not be suppressed by the tuner adjustment. Consequently, the $\mu=-1$ mode damper system, which had been used in KEKB operation as shown in Fig. 10, was applied to the D4 station. It worked well to suppress the $\mu=-1$ mode successfully and the beam current could be increased.

Figure 11 shows estimation of the growth rates of the couple bunch instability due to the accelerating mode plotted as function of the stored beam current for SuperKEKB LER (left side) and HER (right side) [18]. The threshold current of the $\mu=-1$ is about 1.8 A for LER and 1.2 A for HER. In Phase-1, at an earlier stage than expected, the $\mu=-1$ mode damper became needed due to the detuned cavities. At the design beam current of SuperKEKB, the growth rate of the $\mu=-2$ mode instability will be close to the radiation damping rate. Therefore, the $\mu=-2$ mode damper system is additionally necessary for Phase-2. New damper system with new digital filters is now under development for Phase-2 [18]. It will be avail-

able for $\mu=-2, -1, -2$ and -3 modes in parallel as shown in Fig. 12. Respective feedback phase for each mode can be adjusted independently in the digital filter.

Block diagram of the -1 Mode Damping System

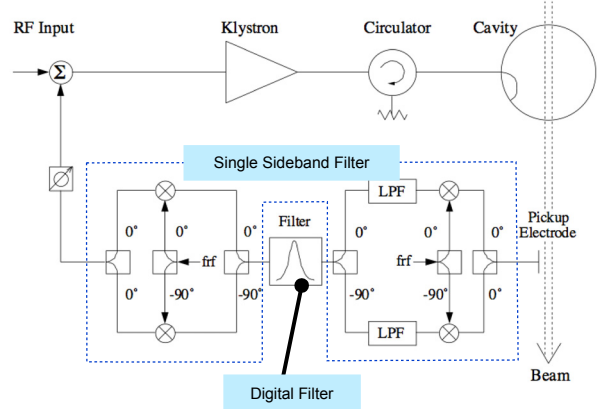


Figure 10: Block diagram of the $\mu=-1$ mode damping system, which had been used in KEKB operation. The $\mu=-1$ mode digital feedback selectively reduces impedance at the driving frequency.

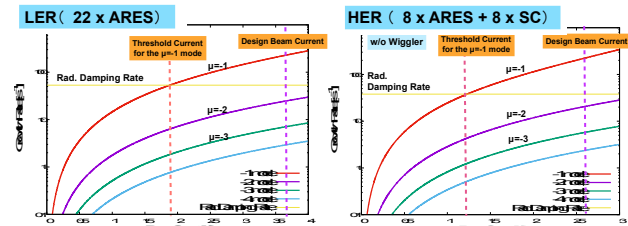


Figure 11: Estimation of the growth rate of the couple bunch instability due to the accelerating mode for SuperKEKB.

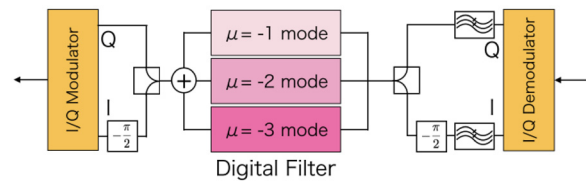


Figure 12: Design concept of the new digital filter with single sideband filter for the couple bunch instability damping system. The digital filter is available for the $\mu=-1, -2$ and -3 modes in parallel.

BUNCH GAP TRANSIENT EFFECT ON BEAM PHASE

In generally, for a high-current multi-bunch storage ring, a bunch train has a gap of empty buckets in order to allow for the rise time of a beam abort kicker. The empty gap is also effective in clearing ions in electron storage rings. However, the gap modulates the amplitude and phase of the accelerating cavity field. Consequently, the

longitudinal synchronous position is shifted bunch-by-bunch along the train, which shifts the collision point of each bunch in a collider.

Figure 13 shows the beam phase measured along the bunch train in KEKB operation. The abscissa axis indicates the bucket ID. The measured phase shift along the train agreed well with a simulation (solid line) and a simple analytical form given by [19] in most part of the train. However, a rapid phase change was observed at the leading part of the train, which was not predicted by the simulation or by the analytical form. In order to understand the cause of this observation, we have developed an advanced simulation, which treats the transient loading in each of the three cavities of ARES [20], instead of the equivalent single cavity used in the previous simulation. The new simulation result shown Fig. 13 as dashed line reproduces well the observed phase modulation. Accordingly it clarifies that the rapid phase change at the leading part of the train is caused by a transient loading in the three-cavity system of ARES: the rapid phase change is attributed to the parasitic ($0\&\pi$) mode of ARES.

Figure 14 shows RF phase modulation of the accelerating cavity of ARES. It was measured by the new digital LLRF control system in the Phase-1 commissioning. The abscissa axis is time in microseconds. The time interval of 10 microseconds is the revolution period. Similarly, the rapid phase change is observed at the leading part of the train. The simulation result (dashed red line) agrees well with the measurement. In the simulation, function of feedback control for cavity voltage regulation by LLRF control system is also included. However, at the leading part of the train, the behaviour of the phase ringing after the rapid phase rising disagrees with the simulation. It is considered that the sampling rate of the LLRF system, which is about 10MHz, might not be enough to catch this rapid change of the phase ringing. On another front, the behaviour of this phase ringing at the leading of the bunch train depends strongly on Q-value of the coupling cavity of ARES. The ARES cavity parameters used for the simulation are shown in Table 2. There is possibility that the practical Q-value of the C-cavity in this measurement is lower than 100.

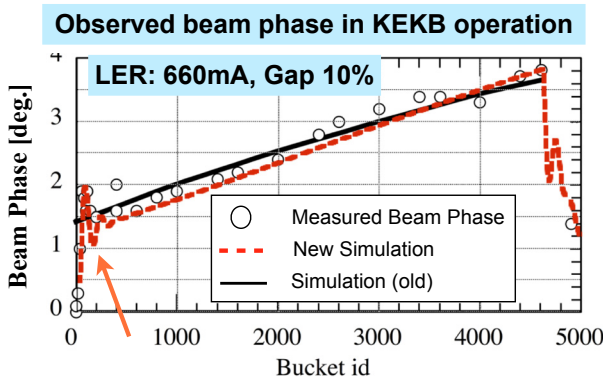


Figure 13: Observed beam phase along the bunch train in the KEKB operation and simulation results.

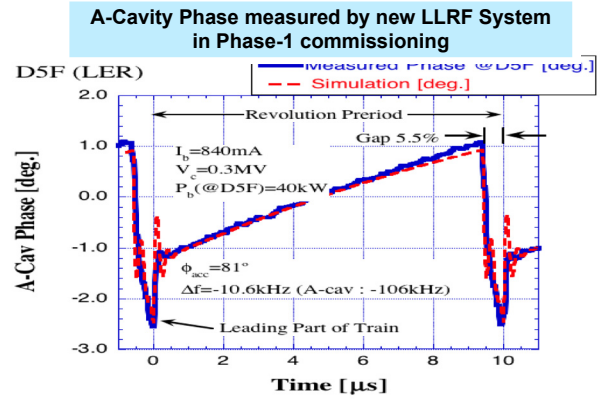


Figure 14: RF phase modulation in the accelerating cavity of ARES, which measured by new LLRF control system in Phase-1 commissioning, and the new simulation result are plotted during the revolution period.

Table 2: ARES cavity parameters used for the simulation

Q-value of A-cavity (Q_a)	26000
Q-value of C-cavity (Q_c)	100
Q-value of S-cavity (Q_s)	180000
Coupling between A and C cavity (k_a)	5%
Coupling between S and C cavity (k_s)	1.6%

ESTIMATION OF BUNCH GAP TRANSIENT EFFECT FOR superKEKB

The phase modulation caused by the bunch gap transient was estimated for SuperKEKB by using the new simulation. The operation parameters used for the simulation are shown in Table 3. The length of the bunch gap will be reduced to 2% of the ring in SuperKEKB by improving the rise time of the abort kicker.

Figure 15 shows the simulation results of the phase modulation caused by the bunch gap transient in LER (left side) and HER (right side). The revolution frequency is set to 100 kHz instead of 99.4 kHz to simplify the abscissa axis of time. In the figure, the periodic interval of time 0 to 10 μ s corresponds to one revolution, including the 2% empty gap. The time 0 corresponds to the head bunch of the train, and the empty gap is located from 9.8 to 10 μ s. For the HER simulation, the vector sum of ARES and SCC was calculated. On the other hand, LER is operated with only ARES type cavities. Accordingly a rapid phase change with a ringing following the gap is clearly found. As mentioned in the previous section, the rapid phase change with ringing is attributed to the parasitic modes of ARES. Figure 16 shows a plot of Fig. 15 zoomed in around the empty gap. A rapid phase change at the leading part of the train is 6.5 degrees (pk-pk). In Fig. 15, except the leading part, a phase modulation of about 2

degrees due to the bunch gap transient is found along the train, which agrees with the simple analytical estimation.

From the simulation results shown in Figs. 15 and 16, the rapid phase change in the leading part of the bunch train due to the bunch gap will be significantly larger in SuperKEKB. Figure 17 shows the phase difference between LER and HER ($\Delta\phi_{\text{HER}} - \Delta\phi_{\text{LER}}$), obtained from Fig. 15. In the figure, a plot zoomed in around the gap is presented and the solid red line indicates the relative phase. As seen in the figure, the maximum phase difference will be 5.5 degrees at the leading bunches. Besides the leading bunches, the phase difference along the train is not so large. The relative phase shift at the interaction point (IP) will be $\pm(\Delta\phi_{\text{HER}} - \Delta\phi_{\text{LER}})/4 = \pm 1.4$ degrees, excluding the leading part of the bunch train. The 1.4-degree phase shift corresponds to a longitudinal displacement of $0.44 \sigma_z$ at the IP, where the bunch length (σ_z) is 5 mm (rms).

Table 3: SuperKEKB parameters for the estimation of the bunch gap transient effect

Parameter	LER	HER
Beam energy [GeV]	4	7
Beam current [A]	3.6	2.6
Bunch gap length [%]	2	2
Beam power [MW]	8	8.3
Bunch length [mm] (rms)	6	5
RF frequency [MHz]		508.887
Harmonic number		5120
Revolution frequency [kHz]		99.4
Cavity type	ARES	SCC/ARES
Number of cavities	22	8/8
Total RF voltage [MV]	10~11	15~16
Loaded Q of cavity [$\times 10^4$]	2.4	7.0/2.0
Coupling factor (β)	4.3	-/5
RF voltage/cavity [MV]	0.48	1.5/0.5
Wall loss/cavity [kW]	140	-/150
Beam power/cavity [kW]	460	400/600
Cavity detuning [kHz]	-28	-18/-44
(A-Cav detuning of ARES)	(-280)	(-180)
Number of klystrons	18	8/8
Klystron power [kW]	~600	~450/~800

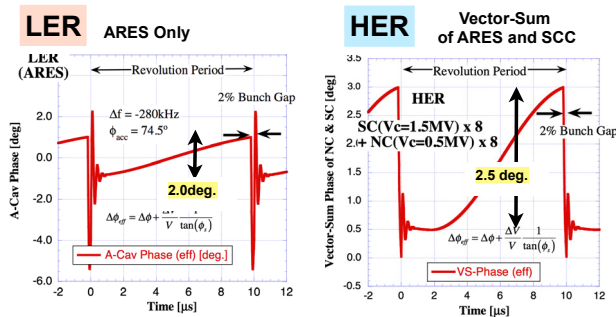


Figure 15: The simulation results of the phase modulation caused by the bunch gap transient in LER (left side) and HER (right side) for SuperKEKB design current.

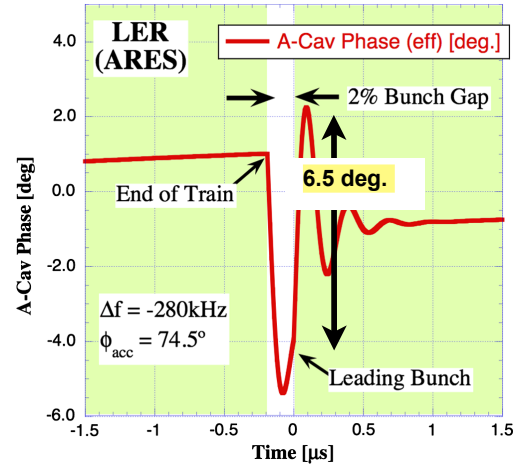


Figure 16: A plot of the simulated phase modulation shown in Fig. 15, enlarged to show the empty gap region.

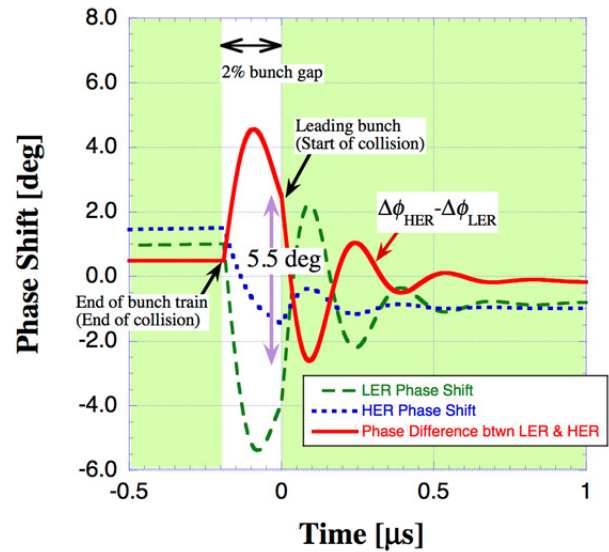


Figure 17: Plot of the phase difference between LER and HER (red solid line = $\Delta\phi_{\text{HER}} - \Delta\phi_{\text{LER}}$), which is zoomed in around the gap.

MITIGATION OF THE RELATIVE PHASE DIFFERENCE FOR superKEKB

In the KEKB operation, no degradation was observed of the luminosity due to the bunch gap transient. However, in the SuperKEKB operation, the beam phase difference due to the gap transient will be much larger than that of KEKB, as presented in the previous section. Because the crossing angle between the two beams at the collision point is larger in SuperKEKB and the vertical beta function (β_y^*) is much smaller than for KEKB, the effect of the large phase difference on the colliding beams might be a crucial issue to achieve high luminosity.

We propose measures to mitigate the phase difference between the colliding beams as a cure if the beam-beam interaction effect turns out to be critical [20]. It should be

noticed that feed-forward control cannot be available in our RF system for the measures to reduce the phase modulation due to the gap transient, because the klystron performance (bandwidth, output power) is not enough to cancel the rapid phase modulation. Consequently, we investigated the method of changing the bunch fill pattern and gap delay for the mitigation of the phase difference between two rings. The mitigation method is that LER bunch train is to be filled up in two steps with making a delay of the HER gap timing with respect to the LER gap at the cost of a reduced number of colliding bunches as shown in Fig. 18. For the simplest case, the first step increase (b_s) is set to half of the nominal bunch current. Then, the HER gap delay (d_g) and the time interval of the first step (w_s) are parameters to be optimized.

Simulation result for the best case of the fill pattern is shown in Fig. 19 and 20. In this case, the length of the initial step (w_s) is 140 ns and the delay of the HER gap (d_g) is 160 ns. In this optimization, d_g was decided to synchronize the LER phase ringing with the HER phase change, and w_s was optimized to mostly cancel the phase change each other after the second step. As the result, the phase difference between two rings is significantly reduced to 0.4 degrees at the leading part of the collision as shown in Fig. 20, while the entire phase difference along the train is kept sufficiently small as shown in Fig. 19.

The effects of the proposed mitigation method are summarized in Table 4. From this summary, it is found that the fill pattern change with a HER gap delay gives a more effective mitigation compared with only the gap delay cases. However, it should be noted that this result here is an example of certain conditions. In reality, the optimization depends on strongly operation conditions. The operation conditions will be optimized for the luminosity in future SuperKEKB. The best optimization for the fill pattern and gap delay will be investigated based on the best operation conditions.

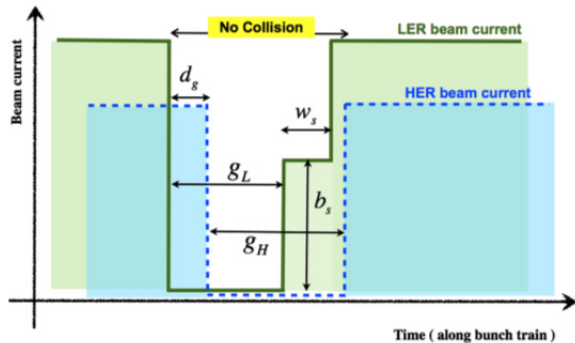


Figure 18: Illustration of a bunch fill pattern for effective mitigation. The bunch current at the leading part of the LER train is increased in two steps with a time interval w_s and the bunch current at the first step by b_s . The gap lengths are g_L and g_H for LER and HER, respectively, and the HER gap is delayed by d_g .

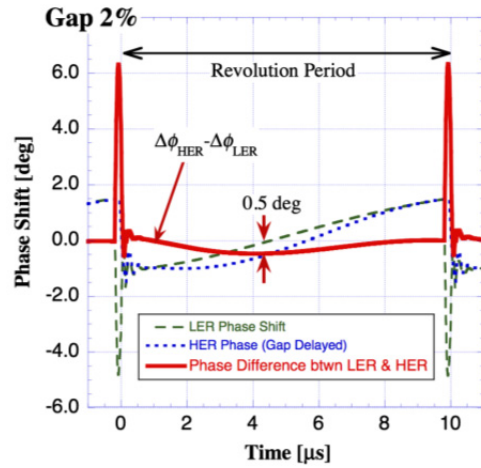


Figure 19: Simulation result of phase difference for the best case of the fill pattern shown in Fig. 18. The gap length of both rings is 2% (200 ns), the current height at the initial step of the LER leading part (b_s) is half of the nominal current, the length of the initial step (w_s) is 140 ns and the delay of the HER gap (d_g) is 160 ns.

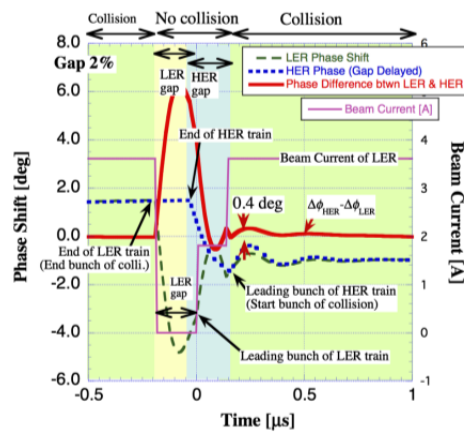


Figure 20: Zoomed plot of Fig. 19, which shows the vicinity of the gap region.

SUMMARY

Phase-1 Beam Commissioning of SuperKEKB was successfully accomplished. Desired Beam current in the two rings was achieved and sufficient vacuum scrubbing was progressed.

Newly developed digital LLRF control systems are applied to 9 stations at OHO section, and successfully worked in Phase-1.

The $\mu=-1$ mode damper is applied to HER, and the coupled bunch instability due to detuned cavities is suppressed successfully. The $\mu=-2$ and -3 mode damper system is now under development for Phase-2.

Phase modulation due to bunch gap transient effect will be too large at the leading part of the bunch train for design beam current. Simulation study proposes the measures to mitigate the phase difference: the relative phase change at the IP can be reduced by optimization of the gap delay and bunch fill pattern of LER.

Table 4: Effects of the proposed mitigation methods on reducing the phase difference between colliding beams.

Method	Bunch Gap	HER delay	Relative Phase Difference		Longitudinal displacement @IP ($\sigma_z = 5$ mm)	Rate of num. of colliding bunches
			Leading Part	The rest of train		
HER Gap Delay Only	2%	no delay	5.5 [deg.]	0.9	$0.44 \sigma_z$	-
	2%	200 ns	2.4	0.9	$0.19 \sigma_z$	-2%
	3%	300 ns	< 0.2	1.6	$0.13 \sigma_z$	-4%
LER 2-step fill up + HER Gap Delay	2%	160 ns	0.4 [deg.]	0.5	$0.07 \sigma_z$	-1.6%

REFERENCES

- [1] T. Abe, et al., “KEKB Accelerator,” Prog. Theor. Exp. Phys. 2013, Special Section (2013)
- [2] P. B. Wilson, “Beam Loading in High Energy Storage Rings,” PEP-Note 37, SPEAR-163 (1973)
- [3] K. Akai, et al., “RF systems for the KEK B-Factory,” Nucl. Instrum. Meth. A 499, 45–65 (2003)
- [4] T. Abe, et al., “Performance and operation results of the RF systems at the KEK B-Factory”, Prog. Theor. Exp. Phys. 2013, 03A006 (2013)
- [5] Y. Yamazaki and T. Kageyama, “A Three-Cavity System which Suppresses the Coupled-Bunch Instability Associated with the Accelerating Mode,” Part. Accel., 44, 107 (1994)
- [6] T. Kageyama, et al., “The ARES cavity for KEKB,” Conf. Proc. of APAC98, pp. 773-775 (1998)
- [7] T. Furuya, et al., “A Prototype Module of a Superconducting Damped Cavity for KEKB,” Conf. Proc. of EPAC96, pp. 2121-2123 (1996)
- [8] S. Mitsunobu, et al., “Superconducting cavities for KEK B factory,” Adv. Cryog. Eng. 45A, 861-870 (2000)
- [9] T. Kageyama, et al., “ARES Cavity System for SuperKEKB,” Proc. of the 8th annual meeting of Particle Accelerator Society of Japan, pp. 1245-1249 (2011)
- [10] K. Akai, “RF Issues for High Intensity Factories,” Conf. Proc. of EPAC96, pp. 205-209 (1996)
- [11] Y. Ohnishi, et al., “Accelerator design at SuperKEKB,” Prog. Theor. Exp. Phys. 2013, 03A011 (2013)
- [12] T. Abe, et al., “Belle II Technical Design Report,” KEK Report 2010-1 (2010)
- [13] K. Akai, et al., “RF system for SuperKEKB,” Proc. of the 7th annual meeting of Particle Accelerator Society of Japan, pp. 1232-1236 (2010)
- [14] T. Kobayashi, et al., “Development and Construction Status of New LLRF Control System for SuperKEKB,” Conf. Proc. of IPAC2014, pp. 2444-2446 (2014)
- [15] M. Ryoshi et al., “LLRF Board in Micro-TCA Platform,” Proc. of the 7th Annual Meeting of Particle Acc. Society of Japan, p. 668 (2010).
- [16] J. Odagiri et al., “Fully Embedded EPICS-Based Control of Low Level RF System for SuperKEKB,” Proc. of IPAC’10, p. 2686 (2010).
- [17] T. Kobayashi, et al., “RF Reference Distribution System for SuperKEKB,” Proc. of the 10th Annual Meeting of Particle Accelerator Society of Japan, pp. 1159-1163 (2013)
- [18] K. Hirose, et al., “Development of a Coupled Bunch Instability Damper Caused by the Acceleration Mode for SuperKEKB,” Proc. of the 13th Annual Meeting of Particle Accelerator Society of Japan, TUP012 (2016)
- [19] D. Boussard, “RF Power Requirements for High Intensity Proton Collider,” Conf. Proc. of PAC91, pp. 2447-2449 (1991)
- [20] T. Kobayashi and K. Akai, “Advanced simulation study on bunch gap transient effect” Phys. Rev. Accel. Beams 19, 062001 (2016)

HIGH EFFICIENCY KLYSTRON DEVELOPMENT FOR PARTICLE ACCELERATORS

D. A. Constable^{†1}, G. Burt¹, V. C. R. Hill¹, C. Lingwood¹, Lancaster University, Lancaster, United Kingdom

A. Yu. Baikov, Moscow University of Finance & Law, Moscow, Russia

I. A. Guzilov, JSC Vacuum Devices Basic Technologies, Moscow, Russia

A. Jensen, SLAC, Stanford, California, United States of America

R. Kowalczyk, L-3 Communications, San Carlos, California, United States of America

R. Marchesin, Thales Group, Cannes, France

C. Marrelli, ESS, Lund, Sweden

I. Syratchev, CERN, Geneva, Switzerland

¹also at Cockcroft Institute, Daresbury, United Kingdom

Abstract

Presently, state-of-the-art klystrons operate at efficiencies of up to 65%. Through the use of novel bunching mechanisms, it is possible to improve the efficiency towards 90%, which will be beneficial for reducing the power consumption of future particle accelerators. An overview of these bunching schemes, supported by results from numerical simulation and experiment are presented.

INTRODUCTION

Upcoming large scale particle accelerators, such as the Future Circular Collider (FCC-ee) [1], the Compact Linear Collider (CLIC) [2,3], the International Linear Collider (ILC) [4], and European Spallation Source (ESS) [5] are expected to require RF powers in the 10-100 MW range. For comparison, the currently operational, Large Hadron Collider (LHC) [6], has a total RF drive of 5 MW. Due to the significant increase in RF power, it is advantageous to maximise the efficiency of the RF source, in order to reduce their running costs.

Klystrons are an attractive RF source for such applications, owing to their stability, operating frequencies, output powers, and efficiencies. In terms of efficiency, current state of the art klystrons can deliver a maximum of approximately 65%. The limiting factor lies with the profile of the electron bunch, as it approaches the output cavity of klystron, as well as the velocity of the slowest electron leaving the output gap. In order to maximise the efficiency of the tube, the spatial and phase profile of the bunch should be such, that, after it is decelerated by the output gap, each electron has identical velocity.

The High Efficiency International Klystron Activity (HEIKA) collaboration seeks to make improvements to the overall efficiency of klystrons by considering these issues. To that end, a number of novel electron bunching mechanisms have been proposed. In this paper, a brief discussion, along with numerical and experimental results of these novel schemes in operation, will be presented.

BUNCHING MECHANISMS

In traditional klystrons, electrons are monotonically brought towards the centre of a single bunch along the length of the device. At the output gap, the final bunch does not contain all available electrons within it, with some being contained in a so called ‘anti-bunch’. Therefore, these electrons do not provide any energy to the output RF signal. As a result, the overall efficiency of the device is limited by the number of un-bunched electrons contained in the anti-bunch. The novel bunching mechanisms investigated by HEIKA will be discussed.

Core Oscillation Method (COM)

The core oscillation method (COM) [7,8] is based on the non-monotonic bunching technique, where, along the length of the klystron, electrons at the periphery of the bunch gradually approach the bunch centre. Simultaneously, the core of the bunch experiences an oscillation in its phase, due to its space charge causing it to expand, and the momentum delivered by successive bunching cavities causing it to contract. The cavity RF fields have a weak effect on the periphery electrons (phase of $\pm\pi$ with respect to the core); therefore, COM klystrons require a substantial increase in their interaction length to capture all electrons in the bunch. However, very high efficiencies ($> 90\%$) have been observed in 1-D simulations.

This process can be seen in Figure 1, which shows electron trajectories in phase space, modelled in AJDISK [9]. Here, the de-bunching of the core can be observed between successive cavities (shown by vertical lines in Figure 1), as a contraction and expansion of the centre of the beam, while the outlier electrons move into the bunch.

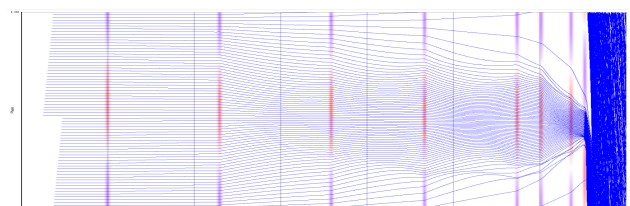


Figure 1: Electron phase profile of an 800 MHz klystron employing the Core Oscillation Method (COM).

[†] d.constable@lancaster.ac.uk

Numerical simulations of eight cavity, 800 MHz klystrons employing COM have been performed [10]. These designs primarily examined electron beams with relative perveances of 0.213 μK , with the length of the devices being approximately 6 m. Good agreement was observed across MAGIC2-D, TESLA, KLYS2-D and KlypWin, predicting a stable klystron with efficiencies greater than 80%. Subsequent optimisation finally established a design with a power production efficiency of 84.64%, with the output power from MAGIC2-D shown in Figure 2.

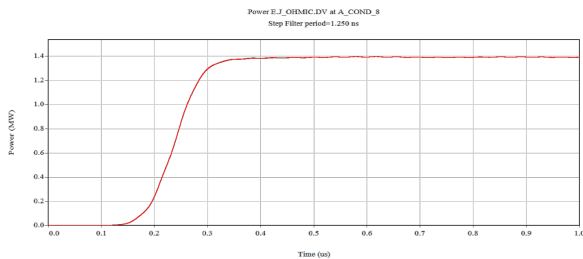


Figure 2: Output power of an 800 MHz klystron employing COM, with efficiency of 84.64%.

On examining the electron bunch profile prior to the output cavity, it can be seen that the bunch is triangular in shape (Figure 3a), with a pedestal close to the axis. This effect (radial bunch stratification) is due to the radial mismatch between the space charge forces and RF impedance of the klystron. This effect can be mitigated by employing a hollow beam [11]. In this case, the absence of electrons on axis allows the formation of a slab-like bunch prior to the output gap (Figure 3b). Numerical simulations of this configuration predict stable operation, with efficiencies of greater than 86%.

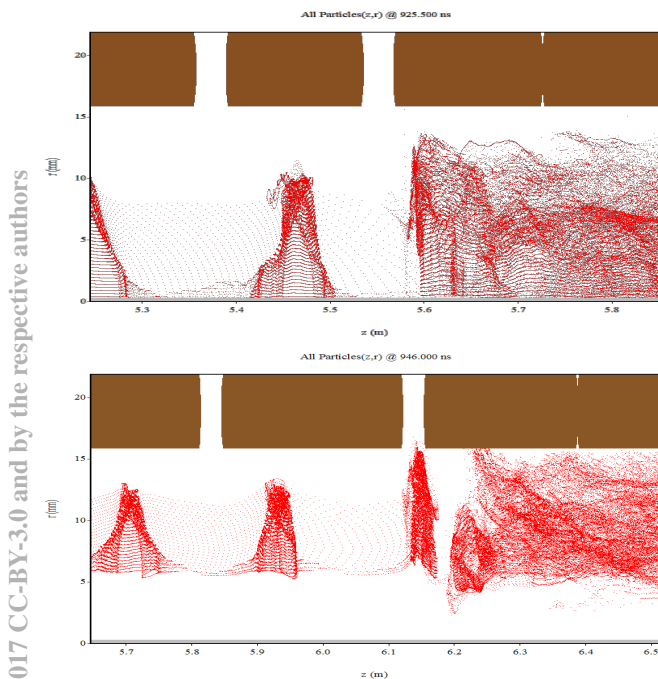


Figure 3: Electron bunch profile in a) cylindrical beam, and b) hollow beam, simulated by MAGIC2-D.

The X-band 50 MW, 12 GHz XL-5 klystron has previously been reported to have an efficiency of 40% [12]. Early AJDISK simulations of a modified XL-5 design employing COM, predict output power of 40 MW, with efficiencies in excess of 70%. This design, although increasing in length over the original (~ 35 cm) is only on the order of 50 cm in length.

Bunching-Alignment-Collection (BAC) Method

The BAC method [13] is a technical extension of the COM method, allowing a reduction in the klystron length by a factor of two, while preserving the high efficiency. In this scheme, a set of three cavities is used to “bunch, align, and collect” (BAC) the electron bunch. Here, the first cavity serves as a “traditional” bunching cavity; the second aligns the electron velocities, while the third cavity (set at the 2nd harmonic) primarily effects the particles in the anti-bunch, causing them to be directed more rapidly towards the core of the bunch.

AJDISK was used to re-design the existing SLAC 5045 S-band, 65 MW pulsed klystron, with the introduction of a BAC section [14]. The existing tube has an efficiency of 45%. With the addition of two BAC sections, the predicted efficiency (in simulations) is expected to be as high as 65%.

BAC has also been implemented in a prototype of an S-band multi-beam klystron (MBK) developed at VDBT (Russia). This is a retrofitted design of an existing tube, which has efficiency of 42%. By adding BAC sections, the simulated efficiency was above 65%, while maintaining the length of the klystron. The klystron has been constructed and tested at CERN [15], demonstrating an efficiency of 60%, as shown in Figure 4.

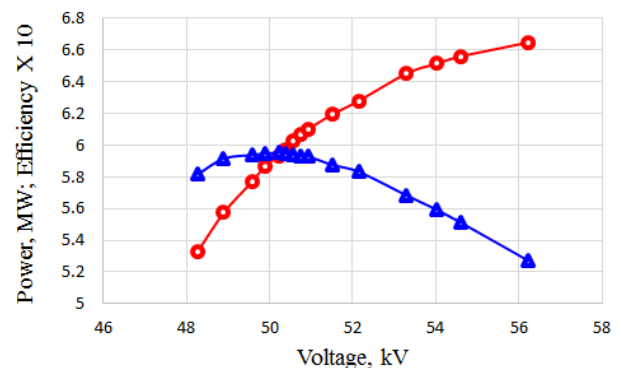


Figure 4: Efficiency (triangles) and RF power (circles) of the VDBT klystron at 2.99855 GHz, in saturation.

Third Harmonic Cavities (F-type Tubes)

On introducing a third harmonic cavity, the advantages of COM and BAC can be extended further. The presence of the third harmonic creates three “virtual” cores within the electron bunch, which due to the space charge forces created, allows the electrons in the anti-bunch to move into the central bunch. This behaviour is shown in the phase diagrams in Figure 5, where the third and fourth

cavities (vertical lines), are 2nd and 3rd harmonics, respectively.

An initial numerical study of a 1 GHz, six cavity F-Tube in AJDISK [16], predicted efficiencies of up to 88%. A subsequent re-design of the F-Tube to 800 MHz in AJDISK has predicted an efficiency of 80.25%. The inclusion of two additional fundamental harmonic cavities (FG-Tube), results in a smoother phase profile for the final bunch, with an improvement in efficiency to 80.87%. MAGIC2-D simulations of both designs are currently in progress.

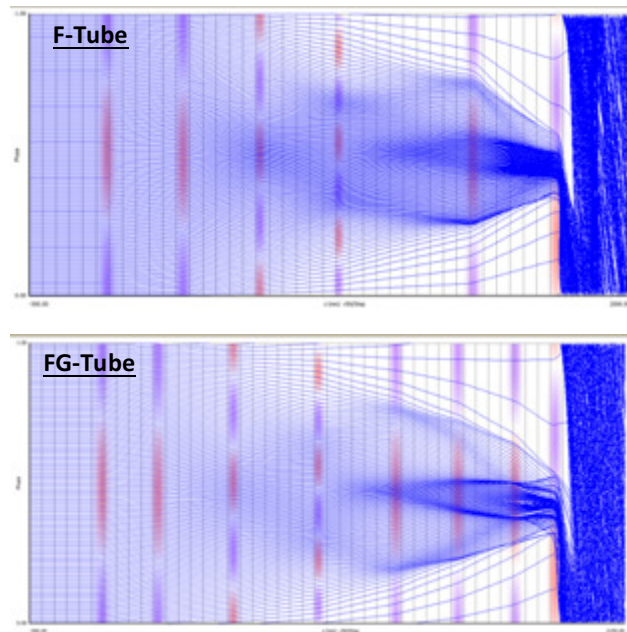


Figure 5: Electron phase profiles of the F-Tube and FG-Tube, from AJDISK.

CONCLUSIONS

Through numerical investigations, the core oscillation method (COM), bunching-alignment-collection (BAC) and use of third harmonic cavities have been shown to improve on the efficiency offered by current state of the art klystrons. Early experimental testing of klystrons employing COM and BAC have demonstrated the strength of these bunching schemes, offering increases in efficiency when implemented in existing devices.

ACKNOWLEDGEMENT

The authors would like to thank the members of the High Efficiency International Klystron Activity (HEIKA) collaboration.

REFERENCES

- [1] M. Koratzinos, “FCC-ee accelerator parameters, performance and limitations”, in *Proc. 37th Int. Conf. on High Energy Physics (ICHEP’14)*, Valencia, Spain, July 2014, arXiv: 1411.2819.
- [2] M. Aicheler *et al.*, “A multi-TeV linear collider based on CLIC technology: CLIC conceptual design report”, CERN, Geneva, Switzerland, Rep. CERN-2012-007, Oct. 2012.
- [3] M. J. Boland *et al.*, “Updated baseline for a staged Compact Linear Collider”, CERN, Geneva, Switzerland, Rep. CERN-2016-004, Aug. 2016.
- [4] C. Adolphsen, “ILC RF system R&D”, in *Proc. 2007 IEEE Particle Accelerator Conf. (PAC ’07)*, Albuquerque, New Mexico, USA, June 2007.
- [5] C. Darve *et al.*, “Requirements for ESS superconducting radio frequency linac”, in *Proc. 11th International Particle Accelerator Conf. (IPAC ’14)*, Dresden, Germany, June 2014, paper THPME039, pp. 3311-3313.
- [6] E. Ciapala *et al.*, “Commissioning of the 400 MHz LHC RF System”, in *Proc. 11th European Particle Accelerator Conf. (EPAC ’08)*, Genoa, Italy, June 2008, paper MOPPI24.
- [7] A. Yu. Baikov, O. A. Grushina and M. N. Strikhanov, “Simulations of conditions for the maximal efficiency of decimetre-wave klystrons”, *Technical Physics*, vol. 59(3), pp. 421-427, Mar. 2014.
- [8] A. Yu. Baikov, C. Marrelli, I. Syratcev, “Toward high-power klystrons with RF power conversion efficiencies on the order of 90%”, *IEEE Trans. Elec. Dev.*, vol. 62(10), pp. 3406-3412, Oct. 2015.
- [9] A. J. Jensen *et al.*, “Developing sheet beam klystron simulation capability in AJDISK”, *IEEE Trans. Elec. Dev.*, vol. 61(6), pp. 1666-1671, Jan. 2014.
- [10] D. A. Constable *et al.*, “2-D Particle-in-Cell Simulations of High Efficiency Klystrons”, in *Proc. 2016 Int. Vacuum Electronics Conference. (IVEC ’16)*, Monterey, USA, April 2016.
- [11] D. A. Constable *et al.*, “MAGIC2-D simulations of high efficiency hollow beam klystrons”, presented at the 2016 National Vacuum Electronics Conference (NVEC ’16), Lancaster, United Kingdom, unpublished.
- [12] D. Sprehn *et al.*, “A 12 GHz 50 MW klystron for support of accelerator research”, in *Proc. 7th International Particle Accelerator Conf. (IPAC ’10)*, Kyoto, Japan, June 2010, paper THPEB065, pp. 4020-4022.
- [13] I. A. Guzilov, “BAC method of increasing the efficiency in klystrons”, in *Proc. 10th Int. Vacuum Elec. Sources Conf. (IVESC ’14)*, Saint Petersburg, Russia, July. 2014.
- [14] A. Jensen *et al.*, “Increasing klystron efficiency using COM and BAC tuning and application to the 5045 klystron”, in *Proc. 2016 Int. Vacuum Electronics Conference. (IVEC ’16)*, Monterey, USA April 2016.
- [15] I. A. Guzilov *et al.*, “Commercial prototype of high efficiency S-band pulsed BAC MBK”, in *Proc. 11th Int. Vacuum Elec. Sources Conf. (IVESC ’16)*, Seoul, South Korea, Oct. 2016.
- [16] V. C. R. Hill *et al.*, “Particle-in-cell simulation of the third harmonic cavity F-Tube klystron”, in *Proc. 2016 Int. Vacuum Electronics Conference. (IVEC ’16)*, Monterey, USA, April 2016.

EXTRACTION LINE AND BEAM DUMP FOR THE FUTURE ELECTRON POSITRON CIRCULAR COLLIDER*

Armen Apyan[†], ANSL, Yerevan, Armenia

Katsunobu Oide, KEK, Tsukuba, Japan

Frank Zimmermann, CERN, Geneva, Switzerland

Abstract

The conceptual design of an extraction line and beam dump for the future electron positron circular collider is presented. The proposed extraction line, consisting of abort kicker system, spoilers and beam diagnostics apparatus transports the electron and positron beams to the main beam dumps. The beam must be spread over a large surface in order not to damage the beam dump and the window, which separates the ring from the dump. The extraction line redistributes bunches at different location on the face of beam dump. Monte Carlo simulations using FLUKA have been performed to estimate the distribution of energy deposition on the window and beam dump to find the optimal absorber and its dimensions.

INTRODUCTION

The Future Circular Collider (FCC) is a high-luminosity and high-precision e^+e^- storage ring collider. The FCC-ee study includes the design of a high-luminosity e^+e^- collider serving as Z, W, Higgs and top factory, with luminosities ranging from $\approx 10^{36}$ to $\approx 10^{34} \text{cm}^{-2}\text{s}^{-1}$ per collision point at the Z pole and $t\bar{t}$ threshold, respectively. The design of FCC-ee provides separate e^+e^- channels allowing very large luminosities to be considered in up to four interaction points. In a 100 km tunnel, the accessible centre of mass energy range spans from the Z pole (90 GeV) to above the top pair threshold (350 GeV) [1].

The key part of modern high energy colliders operation is the machine-protection system. Safe operation requires systems for beam dumping, beam instrumentation and absorbers, etc. One of the important collider systems is the extraction line directing the particle bunches to the beam dump. It is important to be able to dump the electron and positron beams in a controlled way in the main collider. The function of the beam dump system is to reliably absorb the power from the electron and positron beams. For safe, long-term operation, the beam dump must be able to withstand the thermal stress and possible fatigue stress.

We have considered several actually implemented or proposed concepts of beam dump systems for various past and future e^+e^- colliders, such as LEP [2], KEK [3] and CLIC [4]. Both solid [2, 3] and water based [4] absorbers are considered for use in the FCC-ee beam dump system.

The FCC-ee design is a part of the global Future Circular Collider (FCC) study. The FCC-ee will be a potential

* This work was supported in part by the European Commission under the FP7 Capacities project EuCARD-2, grant agreement 312453.

[†] aapyan@gmail.com

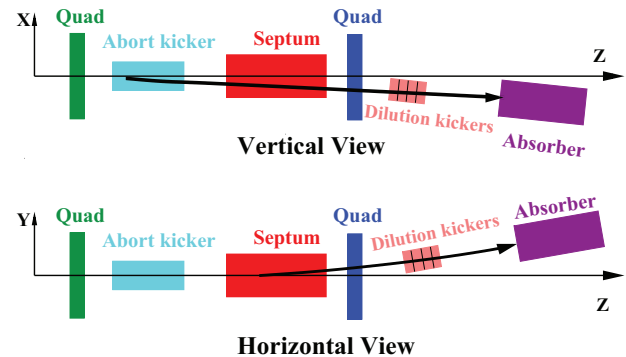


Figure 1: Schematic layout of the extraction system. The horizontal extraction kicker and vertical bending septum magnet are marked in yellow and red, respectively.

intermediate step towards a 100 TeV hadron collider, FCC-hh, sharing the same tunnel infrastructure. Therefore, it is reasonable to assume that part of the FCC-hh beam dump infrastructure [5], e.g. the tunnel for the extraction line or galleries hosting powering systems, may be shared with the FCC-ee beam extraction system. Also key concepts of the existing LHC beam dump [6] may be adopted and adapted for the FCC-ee.

The proposed FCC-ee beam dump system must have the capability to absorb an energy ranging from 0.4 MJ/beam (for $t\bar{t}$) to 22 MJ/beam (for Z factory). A preliminary beam dump design for the lower current operation mode of FCC-ee (Higgs factory) was discussed at the FCC Week 2016 [7]. In this paper, we include the most challenging operation mode, namely the Z factory. After discussing the components and the magnet parameters of the extraction line, we will present results of Monte-Carlo shower simulations, comparing the energy deposition in various beam-absorber candidate materials.

EXTRACTION LINE

The extraction line is designed to transport the electron and positron beams from the main ring to the main beam dump. The concept of the beam dump system has been adopted from CERN LHC [6] as baseline for the FCC-ee dumping system where energy of 22 MJ of high current beam must be absorbed. We can use one of the six straight sections with a length of 1.4 km for the extraction line. The layout of the extraction line system consists of abort kicker, septum magnet, dilution kickers system and absorber as shown in Fig. 1.

Table 1: Beam Parameters used in Monte-Carlo Simulations

FCC-ee	Units	Z	\bar{t}
Beam Energy	GeV	45.5	175
Beam current	mA	1450	6.6
Bunches\beam		16 700	98
Bunch population	10^{11}	1.8	1.4
ϵ_x	nm	0.2	1.3
ϵ_y	pm	1.0	2.6
σ_x	mm	0.45	1.15
$\sigma_{x'}$	μ rad	0.45	1.15
σ_y	μ m	32	51.0
$\sigma_{y'}$	μ rad	32	51.0
σ_p	%	0.1	0.2

A set of special magnets can be pulsed very rapidly to kick the whole beam out of the machine in a single turn. The revolution time for FCC-ee is 333 μ sec. During this time the whole beam should be removed from the main ring. A fast pulsed kicker magnet deflects the beam in the horizontal (or vertical) direction by about 0.37 mrad. For a kicker length of 1 m, this deflection would correspond to a magnetic field required of 56 mT or to an electric field of 17 MV/m. After 135 m, this deflection angle would shift the beam transversely by 50 mm, which is enough to move the beam outside of circulating beam aperture and into the high-field aperture of a septum magnet. The septum magnet provides a strong vertical (or horizontal) deflection, which after a further distance of 100 m, the extracted beam is sufficiently separated from the collider storage ring that dilution kickers can be installed. The septum magnet deflects the beam vertically (or horizontally) by 2.4 mrad. Assuming a septum-magnet length of 3 m, the required magnetic field strength is about 120 mT. The extracted beam is transported through a 600 m long vacuum line to increase its beam size, and it is then deposited on dedicated absorber blocks, specially designed to take the enormous power.

In order not to melt the absorber material, the beam is spread over the front surface of the dump, by means of horizontal and vertical dilution kicker magnets, located about 100 m downstream of the septum [5,6]. Dilution kickers are used to distribute the bunches on the face of beam dump. These kickers should deflect the beam by up to ± 90 cm in the horizontal and vertical direction, if we assume cylindrical beam dump with a diameter of 100 cm. With a distance between the dilution kicker and the beam dump of 600 m, the deflection angle required from the dilution kicker system is 1.5 mrad. This angle can be obtained by means of kickers with a length 3 m and a magnetic field strength of 75 mT, or from 9-m long kickers with an effective electric field of 22 MV/m.

BEAM DUMP

The important and sensitive component of the beam dumping system is the absorber. We have examined several ma-

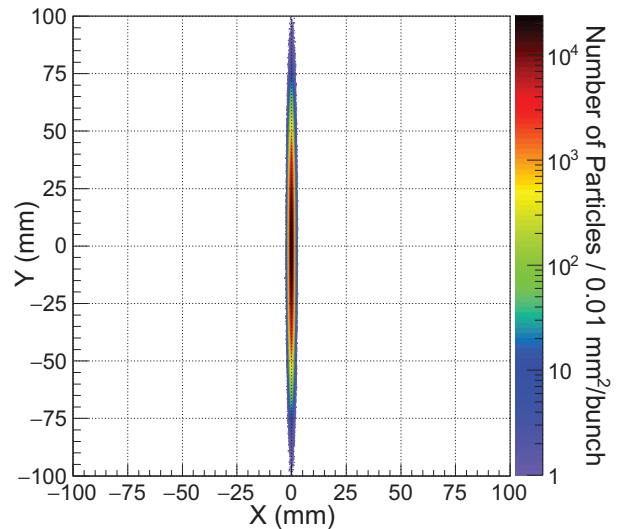


Figure 2: Beam spatial distribution on the face of the beam dump.

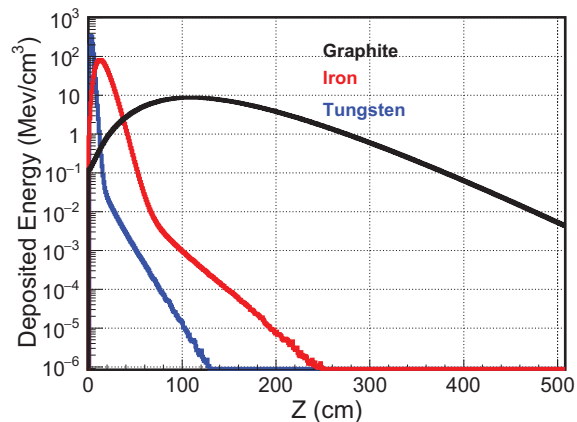


Figure 3: Longitudinal distribution of the deposited energy in graphite (black), iron (red) and tungsten (blue) absorbers.

terials from low to high Z as a possible absorbers, taking into account the critical properties of melting temperature, etc. We considered dumps made from one block of a single material. Both low-Z and high-Z materials are considered. For our simulation study reported in the following, we have chosen graphite, iron and tungsten as candidate absorber materials.

Monte Carlo simulations were carried out to investigate the energy deposition in the absorber and, then, to estimate the resulting temperature rise in the absorber. This procedure allow us to compare various media and to determine the optimal dimensions of the absorber.

More specifically, the energy deposition by the primary beam on the dump was calculated using the FLUKA Monte Carlo simulation code [8]. We consider a scenario with a realistic beam. The present optics easily allows for beta functions between 100 m to 2000 m, both in x and y, in any of the straight sections. If we assume $\beta_x = \beta_y = 1000$ m, we

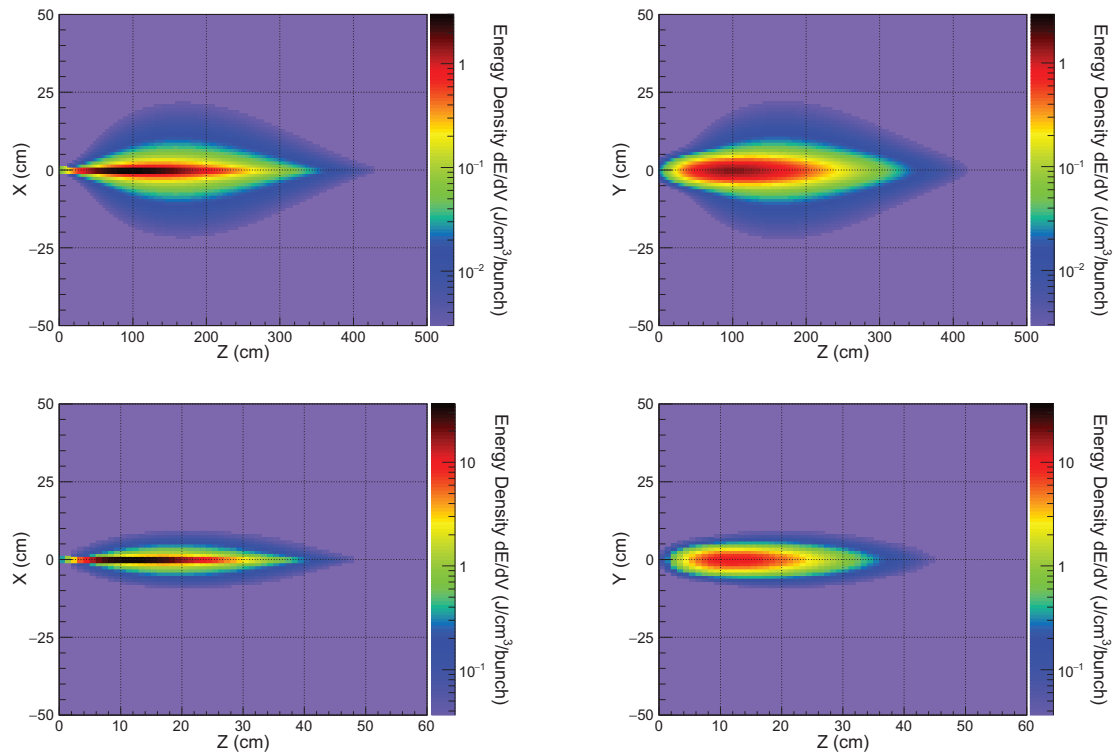


Figure 4: The deposited energy density in the graphite (top plots) and iron (bottom plots), on the $X - Z$ and $Y - Z$ plane, respectively.

obtain the beam parameters listed in Table 1. The simulations were performed for the highest-current beam, i.e. for Z-production.

A cylinder with 100 cm radius and a length of 500 cmh was chosen as shape of the absorber. One electron bunch containing 1.8×10^{11} particles, with an energy of 45.6 GeV, initiates a shower inside the absorber made from different materials. The spatial distribution of the electron beam in front of the beam-dump face is shown in Fig. 2. One can see that after 600 m drift through the extraction line the beam area amoputns to about 10 mm², largely increased from the initial value 0.0144 mm² at the location of the abort kicker.

The electron bunch with a distribution as shown above hits, and penetrates into, the beam dump, causing an electromagnetic shower and deposits energy in the dump medium. The energy penetration depths for graphite, iron and tungsten absorbers are compared in Fig. 3. The maximum of the energy deposition occurs at a depth of 110 cm for graphite, 14 cm for iron and 4 cm for tungsten.

Figure 4 presents the deposited energy density contours for the graphite and iron absorbers. We remark that the main energy deposition is concentrated within a narrow cylinder around the beam trajectory. The transverse sizes of the energy deposition, obtained from a Gaussian fit, are compiled in Table 2. In the future this table will be used as an input for the detailed design of the beam dilution kicker system.

We can estimate the temperature rise ΔT in the beam dump, corresponding to the beam parameters of Table 1. Namely, the maximum energy deposition density by one

Table 2: Transverse Extent of the Simulated Energy Deposition Obtained from a Gaussian Fit.

Material	σ_x (cm)	σ_y (cm)
Graphite	1.1	2.6
Iron	0.68	2.2
Tungsten	0.58	2.0

bunch of electrons in the graphite is found to be 0.54 J/cm^3 , which is equivalent to 0.24 J/g . The associated peak temperature rise in the graphite due to the impact of one bunch of electrons is $0.5 \text{ }^\circ\text{C}$. The peak temperature rise for iron is $2.0 \text{ }^\circ\text{C}$, and for tungsten it is $13.0 \text{ }^\circ\text{C}$. These results show that all three materials would melt when a full electron beam consisting of 16700 bunches hits the same locations on the dump. Thus a beam dilution system will be an essential component for the extraction line of the FCC-ee.

CONCLUSION

Preliminary considerations for the FCC-ee beam dump system were reported, for the most challenging operation scenario of the Z factory. The FCC-hh infrastructure may be used to extract beams from the FCC-ee. Tentative parameters for the kicker and the septum magnets are proposed. Monte-Carlo simulations have examined the energy deposition in different candidate absorber materials. The simulation results reveal the necessity of a kicker-based dilution system,

as is being used at the LHC, for safe beam-dump operation. Detailed design studies have started for the FCC-ee main dump, which needs to withstand the full beam power ranging from 0.4 MJ/beam (for $\bar{t}t$) to 22 MJ/beam (for Z factory).

REFERENCES

- [1] F. Zimmermann, High-energy physics strategies and future large-scale projects, *Nucl. Instr. Meth.*, vol. 335, pp. 4–10, 2015.
- [2] E. Carlier *et al.*, The LEP Beam Dumping System, CERN, Geneva, Switzerland, CERN-SL-94-49, 1994.
- [3] N. Iida *et al.*, Abort Systems for the KEKB, in *Proc. 7th European Particle Accelerator Conf. (EPAC 2000)*, Vienna, Austria, June 2000, paper THP1A09, pp. 2423–2425.
- [4] E. Gschwendtner *et al.*, The CLIC Post-Collision Line, in *Proc. 1st Int. Particle Accelerator Conf. (IPAC 10)*, Kyoto, Japan, May 2010, paper WEPE019, pp. 3386–3388.
- [5] T. Kramer *et al.*, Considerations for the Beam dump system of a 100 TeV Centre-of-Mass FCC hh Collider, in *Proc. 6th Int. Particle Accelerator Conf. (IPAC 15)*, Richmond, VA, USA, May 2015, paper TUPTY050, pp. 2132–2135.
- [6] Z. M. Zazula *et al.*, LHC Beam Dump Design Study, CERN, Geneva, Switzerland, LHC Project report 80, Nov.1996.
- [7] A. Apyan *et al.*, Beam Dump for FCC-ee Collider, presented at FCC week 2016, Rome, Italy, Apr. 2016, unpublished.
- [8] T. T. Bohlen *et al.*, The FLUKA Code: Developments and Challenges for High Energy and Medical Applications, *Nuclear Data Sheets*, vol. 120, pp. 211–214, 2014.

IMPROVEMENT OF EFFICIENCY OF KLYSTRON TO APPLY THE CPD METHOD

K. Watanabe, KEK, Tsukuba, Japan

Abstract

A high power RF system for the particle accelerators needs large electrical power in the operation. Improvement of efficiency is also always required as a technology component for the energy saving.

To improve efficiency of a high-power rf source, the CPD (Collector Potential Depression) method already was applied a Gyrotron to recover the electrical energy form the dissipated power in the collector. The CPD is an energy-saving scheme that recovers the kinetic energy of the spent electrons after generating rf power. A proto-type klystron (E37703 CPD) was fabricated at 2013, to recycle an existing klystron of Toshiba E3786. The purpose of our study is to demonstrate the proof-of-principle of the CPD method to apply a klystron. A plane of R&D at KEK is reported in this meeting.

INTRODUCTION

Two examples to obtain the high efficiency of the klystron are shown as following, (1) more strong bunching on the output cavity to optimize rf design (increase number of cavities compare with existing model) and electron gun (chose multi-beam gun)[1], (2) dissipated power on the collector reuses to do the energy recovery by CPD (Collector Potential Depression) method. The CPD method already was applied a Gyrotron to recover the electrical energy form the dissipated power in the collector. It was worked very well [2].

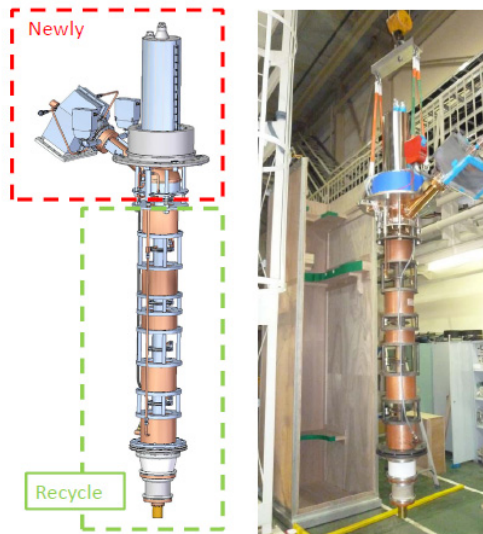


Figure 1: the proto-type CPD klystron (E37703 CPD).

At KEK, a proto-type CPD klystron (CW, 508.88 MHz) was fabricated using by existing klystron (it was used at TRISTAN and KEKB.) at 2013, to demonstrate the proof-of-principle of this method to apply a klystron

(see figure 1). In the fabrication, the recycled components were the electron gun, the input cavity and the middle cavities in drift tube. Newly fabricated components were the output cavity, the output coupler and the collector with CPD gap. These parts were bonded by brazing. The parameters of the existing and newly klystrons are shown in Table 1. The range to apply CPD for a klystron is restricted to the un-saturate situation. Then, the efficiency of klystron has the possibility that 10~20 % is improved. However, at present three issues are assumed for the operation. We must design and build an experiment setup in consideration of the health hazards by exposure of the electromagnetic wave and the radiation. We are estimating the amount of field level of rf leakage from the proto-type klystron to design rf shield with some access port by the CST-studio (Particle studio). Moreover, commercial viability of CPD klystron is required development of KPS (Klystron Power Supply) to optimize it. At present, it is not the category of this examination. This is a future task.

Table 1: Parameters compared with E3732 and E37703 CPD

Item	E3732 (E3786)	E37703 CPD
Frequency	508.89 MHz	508.89 MHz
Maximum rf output power	1.2 MW (saturation)	500 kW (un-saturation)
Efficiency	20~65%	w/o CPD 20~60% w/ CPD 40~80%
Collector	1 MW	500 kW
Cooling method of collector	Vapor cooling (130 l/min + AFC)	Water cooling (360 l/min)
Cooling items	Klystron body Output coupler Focusing coil	Klystron body Output coupler Focusing coil Ceramics insulator Microwave absorber
KPS	B-type x 1	B-type x 1 PS for CPD
V _k	47~90 kV	47~90 kV
V _a	25~60 kV I _b max = 20 Adc	25~60 kV I _b max = 20 Adc
V _c (CPD)	none	0 ~ -50 kV

HOW TO APPLY THE CPD METHOD TO KLYSTRON

Figure 2 shows a schematic diagram of conventional design and one for CPD to apply klystron. An insulator needs to insert between the body and the collector to isolate the collector from body (ground). High voltage (V_c) is applied to the gap between collector and body to recovery as electrical energy form spent electron beam after generating rf power.

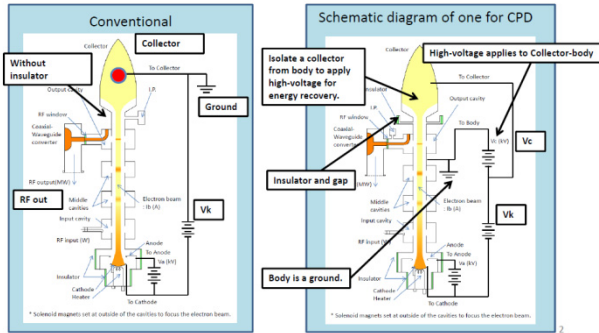


Figure 2: Schematic diagram of the conventional and one of CPD to apply klystron.

In case of the klystron, the spent electron beam has large energy spread through electromagnetic interaction in the cavities at the saturated operation. Therefore, the collector potential cannot be increased beyond the lower limit of distribution of the spent electron beam, otherwise backward electrons hit the cavities. To apply the potential which can obtain satisfactory effect, the operation mode of klystron is restricted to the un-saturate situation with high cathode voltage ($V_k = 90$ kV).

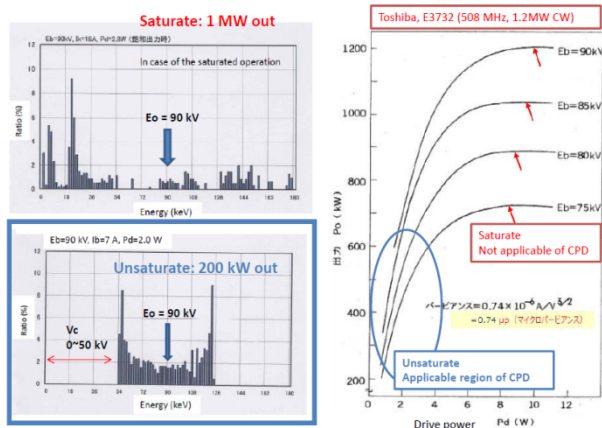


Figure 3: Energy distribution of the spent electron beams after pass through the output cavity of the klystron.

Figure 3 shows the energy distribution of the spent electron beams after pass through the output cavity of the klystron. The improved efficiency is defined by ratio of V_k and V_c . The amplitude of V_c is depend on the energy distribution of the spent electron beam, then the amplitude of V_c must be controlled to keep the maximum efficiency for all power range.

ISSUES MUST BE ADDRESSED FOR CPD KLYSTRON

The structure around CPD gap is used only dielectric materials to isolate between the collector and the body. In the operation, the high voltage of V_c is applied to physical gap. In this case, three issues must be addressed for the operation. That is; (a) the corona discharge and breakdown around ceramics insulator and the outside of klystron, (b) the rf leakage from the physical gap include the dielectric materials and (c) the structure of the radiation shield to cover top of klystron. Figure 4 shows the cross-section drawing at the gap.

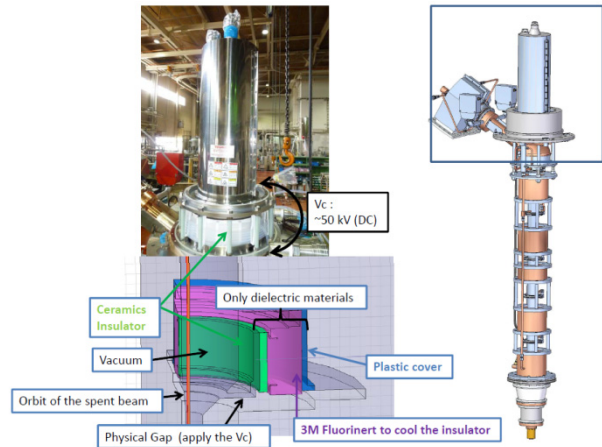


Figure 4: The structure around CPD gap.

RF Leakage from CPD Gap

The amount of field level of rf leakage exciting by spent electron beam is under estimating by HFSS and CST-studio (PCI solver) to design the rf shield for the health hazards by exposure of the electromagnetic wave. Figure 5 shows an example of the calculation result using by HFSS. This result shows the rf leakage to pass through drift tube and CPD gap at 1 MW rf output power form output cavity to check the cut-off frequency of drift tube. The leakage field level of fundamental mode (500 MHz) and 2nd order mode (1000 MHz) are very small, it fills the regulation value of the low (28 V/m at UHF).

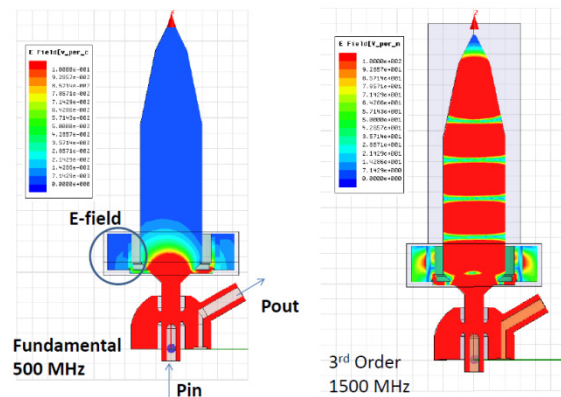


Figure 5: Calculation result to check the performance of cut-off frequency of drift tube for each mode.

The 3rd order mode (1500 MHz) must be care because of the field level of rf leakage has possibility over the regulation value.

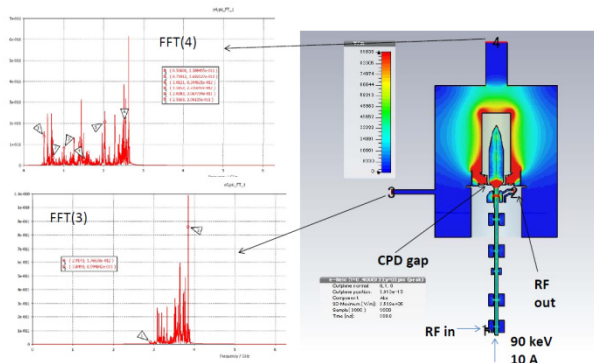


Figure 6: The amount of wake field level excited by modulated electron beam.

Figure 6 shows the calculation result using by CST-studio. This result shows that when the modulated electron beam passes through at CPD gap, the strong leakage field excites from klystron. The rf shield and some access ports must be built around the klystron in consideration of the cut-off frequency. In the DC aging of the klystron, the rf leakage does not generate from the gap.

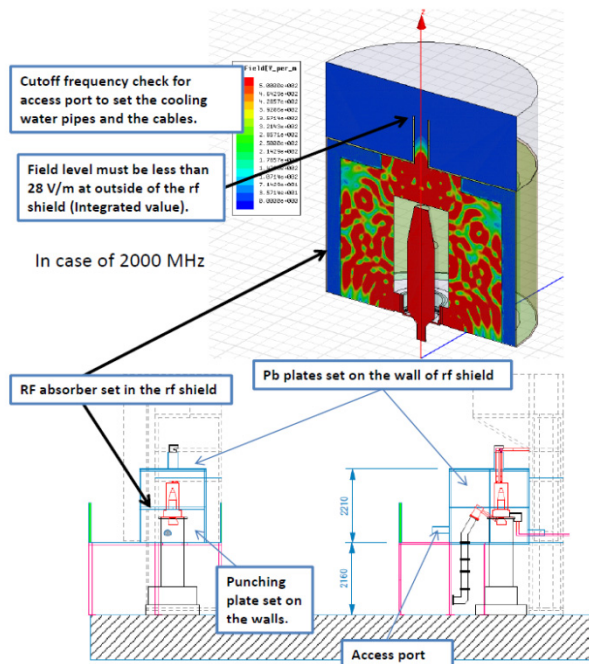


Figure 7: Structure of the rf and radiation shield.

Structure of RF and Radiation Shield

Figure 7 shows a drawing of rf and radiation shield. The klystron will be installed in metal box. The high power type microwave absorber is put in the rf shield to reduce the field level of rf leakage. And some components in the shield are also protected using by microwave absorber from exposure to rf leakage.

FUTURE PLANS

We are planning three stages to demonstrate the proof-of-principle of the CPD method for klystron after Phase 2 of SuperKEKB. First stage is to check whether to drive as normal klystron include DC aging and RF output. And the amount of field level of rf leakage and the radiation level are also measured in this stage. Second stage is the measurement of the output signal from collector without Vc under the condition of small collector loss. The output signal from collector will be terminated to the water cooling type high-power dummy load. Third stage is the measurement of recovery power from the collector with Vc. Another klystron with Marx-circuit will be used as the high-power dummy load to terminate recovery power.

We must be considered that how to design the KPS to optimize the CPD klystron. Figure 8 shows a schematic diagram of KPS.

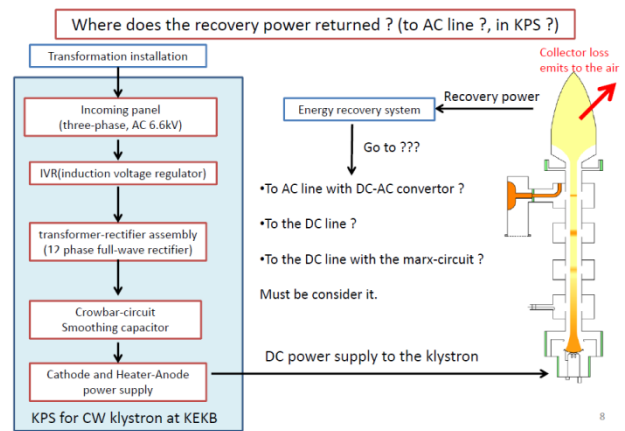


Figure 8: Schematic diagram of KPS.

CONCLUSION

A proto-type CPD klystron was fabricated at 2013 to recycle an existing klystron of Toshiba E3786. (It was used to TRISTAN and KEKB.) Target is a proof-of-principle of CPD to apply CW klystron in the unsaturated region. Now, we are doing the design of rf and radiation shield to optimize the CPD klystron. The test to demonstrate the proof-of-principle of the CPD method for klystron is planning to after Phase2 of SuperKEKB. This CPD klystron will not be installed in SuperKEKB in the future. Commercial viability of it is required development of KPS (Klystron Power Supply) to optimize it. At present, this is a future task.

REFERENCES

- [1] D. Constable, "High Efficiency Klystron Development for Particle Accelerators", presented at eeFACT2016, Daresbury, UK, October 2016, paper WET3AH2.
- [2] K. Sakamoto *et al.*, "Major Improvement of Gyrotron Efficiency with Beam Energy Recovery", *Phy. Rev. Lett.*, vol. 73, no. 26, p. 3532, Dec. 1994.

SUMMARY OF DESIGN CONCEPTS*

R. Aßmann, DESY, Hamburg, Germany;
 A. Blondel, U. Geneva, Switzerland;
 F. Zimmermann[†], CERN, Geneva, Switzerland

Abstract

This paper summarizes the session on design concepts at the ICFA workshop on future circular electron-positron factories “eeFACT2016” [1] held at the Cockcroft Institute, Daresbury, from 24 to 27 October 2016.

OVERVIEW

The eeFACT2016 [1] session on design concepts featured the following four presentations:

1. Crab Waist Concept [2], by Pantaleo Raimondi, ESRF;
2. Higgs Factory Concept [3], by Frank Zimmermann, CERN;
3. Implementation of Round Colliding Beams Concept at VEPP-2000 [4], by Dmitry Shwartz, BINP; and
4. New Concept of a very Compact e^+e^- Collider with Monochromatization and Maximum Beam Energy of around 200 MeV [5], by Anton Bogomyagkov, BINP.

Another important design concept is maximizing the synergies between kepton and hadron colliders, which was highlighted by Alain Blondel, U. Geneva, during the summary session.

CRAB WAIST CONCEPT

The crab-waist scheme overcomes, or exploits, the classical limitations from hourglass and beam-beam effect, allowing for much lower values of β^* and gaining luminosity with a large Piwinski angle [2]. Its key feature is the crab-waist compensation, a new idea from 2006. Positive and useful experience comes from an actual implementation at the DAFNE collider, where the crab-waist scheme significantly increased the luminosity, as is illustrated in Figs. 1 and 2. The price to pay is a more challenging final-focus system design/construction, in particular the realization of particular phase advances and the possible impact of crab waist sextupoles on the dynamic aperture. Regardless, DAFNE experience and several designs for future have proven the feasibility of this novel approach. Now crab waist is a key concept for the next generation of high luminosity colliders, such as FCC-ee or the Super charm-tau factory at BINP.

At eeFACT2016, the possible conversion of DAFNE into a test facility for studies on the large Piwinski angle and the crab waist scheme was discussed. While this would be useful, it was not entirely clear if there was an added value

* This work was supported in part by the European Commission under the FP7 Capacities project EuCARD-2, grant agreement 312453.

[†] frank.zimmermann@cern.ch

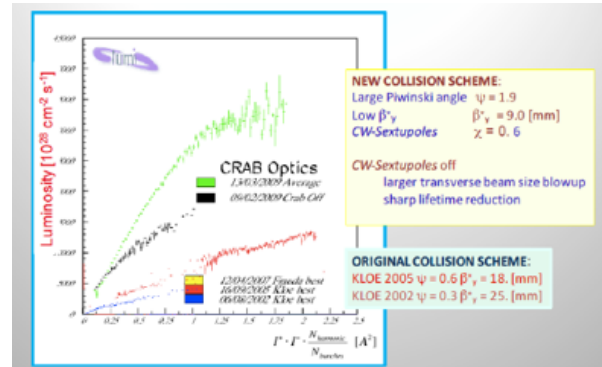


Figure 1: DAFNE luminosity versus product of beam currents for the classical and crab-waist collision scheme [2].

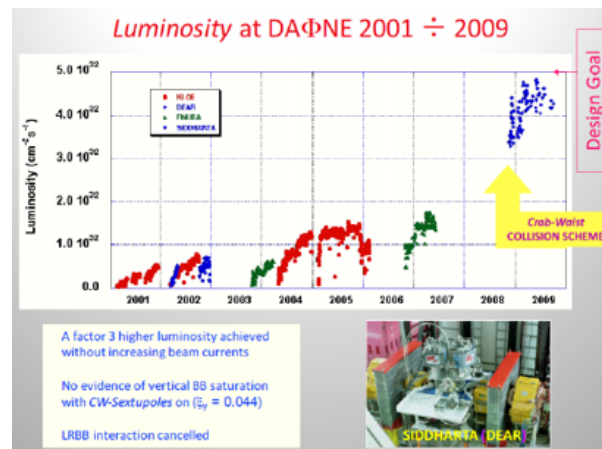


Figure 2: DAFNE luminosity versus time, showing a step-like increase at the moment the crab-waist was introduced, together with a photograph of the DAFNE installation [2].

beyond the SuperKEKB experience and whether this would not interfere with the DAFNE physics programme. The resource needs and the benefits would need to be analysed.

Discussion: The limit on β^* in the crab waist scheme was addressed including the question whether such limit would be consistent with the FCC-ee design. The subsequent discussion revealed that other limits in the final focus design (e.g. dynamic aperture) must also be considered.

HIGGS FACTORY CONCEPTS

The designs of FCC-ee & CEPC exploit lessons or recipes from past and present e^+e^- and pp colliders: combining successful ingredients of recent colliders leads to extremely high luminosity at high energies (Fig. 3), up to and beyond $10^{36} \text{ cm}^{-2} \text{ s}^{-1}$ [3]. Crab waist is successfully implemented in the design of the proposed new machines. Obtaining a low

emittance is “easy” for large rings. Limitations are being carefully studied: particle loss from beamstrahlung [6, 7], energy sawtooth, luminosity lifetime, synchrotron-radiation fans in the interaction region, the “Talman barrier” for β_y^* , electrical power consumption, emittance growth from beamstrahlung [8], etc. Mitigations and innovative schemes are being implemented, including double ring, partial double ring, magnet tapering, top-up injection, weak bends, asymmetric interaction-region optics, monochromatization [9], improved klystron efficiency, and 2-in-1 arc magnets.

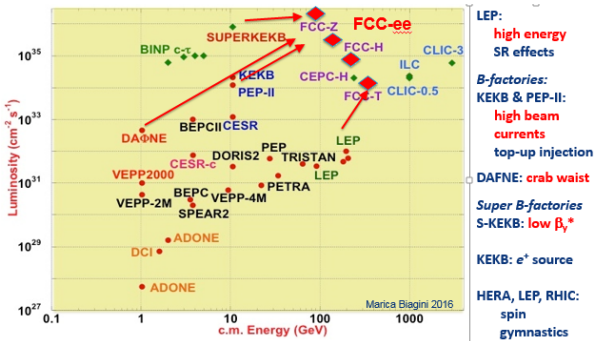


Figure 3: Luminosity vs. c.m. energy for past, present and future e^+e^+ colliders, sketching the paths to FCC-ee/CEPC and the origins of some of the key ingredients [3].

Discussion: The question was raised when FCC-ee could start operation. The answer was not before 2035–2037 given the present schedule of the HL-LHC. Also, the technical readiness for a large e^+e^- collider like FCC-ee or CEPC was discussed. It was concluded that the required technologies exist today, feasibility is guaranteed and performance estimates are realistic. Ongoing R&D will improve the power efficiency.

IMPLEMENTATION OF ROUND COLLIDING BEAMS CONCEPT AT VEPP-2000

Round beams offer advantages in the geometric luminosity factor, an enhanced beam-beam limit thanks to a reduction in the degrees of freedom [10], and suffer less from intrabeam scattering and Touschek effect [4]. Lattice requirements for round beams are summarized in Fig. 4. Round beams were implemented in VEPP-2000. Different modes are possible. Round beams on the coupling resonance are operational at VEPP-2000. The round beam configuration with a Möbius ring has insufficient dynamic aperture. Machine tuning is essential: orbit correction, beta functions, betatron coupling, and betatron tunes. VEPP-2000 achieved a measured coherent beam-beam tune shift of 0.175, corresponding to a beam-beam parameter of 0.125 per IP, as is indicated in Fig. 5. This value of beam-beam parameter was confirmed independently from luminosity-monitor data. Issues studied at VEPP-2000 include the microwave instability and coherent oscillations. The injection chain of VEPP-2000 has recently been upgraded to remove a limitation on the

e^+ intensity. This should allow obtaining the round-beam target luminosity also at higher VEPP-2000 energies [4].

Lattice requirements:

- Head-on collisions!
 - Small and equal β -functions at IP: $\beta_x = \beta_y$
 - Equal beam emittances: $\epsilon_x = \epsilon_y$
 - Equal fractional parts of betatron tunes: $\nu_x = \nu_y$
- Round beam
 $M_x = M_y$

Figure 4: Lattice requirements for round beams [4].

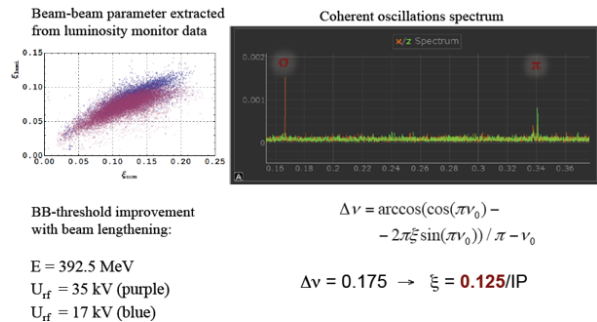


Figure 5: Beam-beam parameter extracted from luminosity-monitor data (left) and from the coherent beam-beam oscillation spectrum (right) [4].

Discussion: It was discussed whether the dynamic aperture can be improved in VEPP-2000, such that the Möbius scheme can also be investigated. This is not possible, however, due to missing space for sextupoles. The reason for missing a factor 10 from the design luminosity (at high energy) while reaching a beam-beam tune shift of about 0.1 was discussed.

VERY COMPACT e^+e^- COLLIDER WITH MONOCHROMATIZATION

A new concept of an e^+e^- double-ring collider with monochromatization and maximum beam energy of 200–300 MeV for true muonium production has been developed. Exciting physics can be explored at such a machine, as is sketched in Figs. 6 and 7.

- The first production and observation of true muonium (bound state of $\mu^+\mu^-$).
- Spectroscopic study of true muonium, Lamb shift measurement, etc.
- Pion form factor measurement at the production threshold.
 - Cross sections of rare decays ($e^+\mu^- \rightarrow \pi^0 \gamma, 2\pi^0, 3\pi^0, 4\pi^0 \dots$).
- Electron width of eta meson ($e^+\mu^- \rightarrow \eta$).
- ??? (Other proposals are welcome)

Figure 6: Possible physics programme for a compact monochromatized collider operating at 200–300 MeV [5].

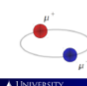
True muonium: smallest QED system

Fundamental physics could be described as having a muon problem. Discrepancies between theory and experiment in a number of muonic measurements (r_{μ} , a_{μ} , $H \rightarrow \mu\tau$, R_{K^*} , R_{K^*}) have been observed in the last decade that demand explanation. True muonium, the bound state of a muon and its antiparticle, has the potential to put strong constraints on any beyond standard model physics that affects the muon sector. To

Henry Lamm, arXiv 1509.09306v1, 30 Sep 2015

Why is True Muonium Interesting?

- Detection of true muonium would be a significant discovery and would constitute a further important test of QED.
- Unique as a laboratory for precision QED tests, and as tests of muon properties
- Further measurements of muon properties could be useful – cross-check possible explanations of the proton charge radius measurement using muonic hydrogen, and perhaps the g-2 anomaly.



Jefferson Lab UNIVERSITY of NEW HAMPSHIRE

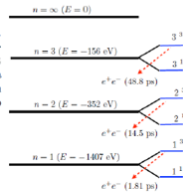


FIG. 1: True muonium level diagram (spacings not to scale).

S. Brodsky, R. Lebed, Phys.Rev.Lett. vol. 102, no. 21, 2009

$$M\mu\mu \approx 2 \times 105 \text{ MeV},$$

$$\sigma(e^+e^-) = 0.33 \text{ barn},$$

$$\Gamma_{\mu\mu} = 0.37 \times 10^{-3} \text{ eV}.$$

Figure 7: Production of true muonium as key study element for a compact monochromatized collider at 200–300 MeV [5]. The left-bottom picture is from S. Philips, U. New Hampshire, 2012.

All dipoles, quadrupoles could be made without cooling, rendering them simple and cheap. The synchrotron radiation energy loss is small. Therefore, the vacuum chambers need not have radiation absorbers and cooling. The RF system is straightforward and inexpensive too. For the proposed double-ring mirror-symmetric double-ring layout (Fig. 8), electrostatic separator plates are required: 1 m long with 100 kV voltage. The only more complicated element is the wiggler ($B=5 \text{ T}$, $\lambda=10 \text{ cm}$, $L=1.8 \text{ m}$), but BINP has already developed and produced several of such wigglers.

Two mirror symmetrical rings with electrostatic separators. Damping wiggler: $B=5 \text{ T}$, $\lambda=10 \text{ cm}$, $L=1.8 \text{ m}$. RF frequency 180 MHz (long bunch for IBS suppression), 10-15 bunches.

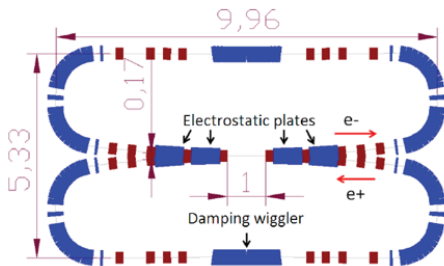


Figure 8: Proposed layout of compact monochromatized collider [5].

Discussion: It was pointed out that the collider would be quite compact, but the required e^+ generation chain providing 11 mA of e^+ current might not be compact at all. Fortunately, at BINP a powerful e^+ injector exists, which could be used to inject into the compact collider.

LEPTON-PROTON SYNERGIES

A future large e^+e^- collider like FCC-ee and CEPC will prepare the tunnel, infrastructure, time and physics case for a subsequent highest-energy hadron collider, just as LEP did for the LHC [11] (Fig. 9), or as had been proposed, in the

U.S., for both a 50 TeV 513 km hadron collider [12] (Fig. 10) and, later, for the 200 km VLHC [13]. Conversely, had its first stage been an e^+e^- factory, the SSC project in Texas might not have been cancelled and would have discovered the Higgs boson long before the LHC.

-- LHC was in the plans since 1983...

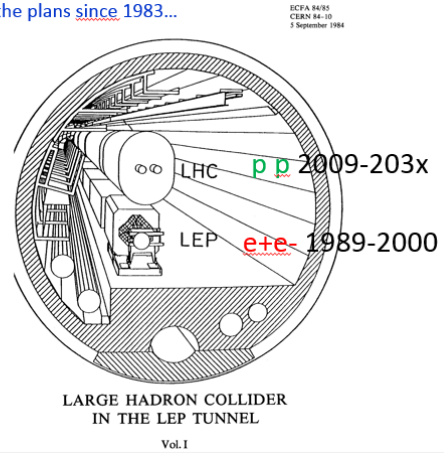


Figure 9: ECFA/CERN LEP-LHC project proposal from 1984, highlighting the historical synergy [14].

AN e^+e^- TOP FACTORY
IN A 50 + 50 TeV HADRON COLLIDER TUNNEL

J. Norem, J. Jagger, S. Sharma, Argonne National Laboratory, Argonne IL 60439 USA
E. Keil, CERN, CH-1211 Geneva 23 Switzerland
G. W. Foster, E. Malamud, Fermilab, Batavia IL 60510 USA
E. Chojnacki, Cornell University, Ithaca NY 14853
D. Winn, Fairfield University, Fairfield CT 06430 USA
Snowmass 1996 & IPAC 97 Vancouver 1997

513km single ring, no top-up, $L=10^{35}$ @ top quark

Figure 10: Promising but failed attempt to invoke lepton-hadron synergies for a 500 km machine, after the top-quark discovery at the Tevatron [14].

CONCLUSIONS

Circular colliders have been a frontier technology for over 50 years, with more than a factor 10 luminosity increase every 10 years. SuperKEKB will be the next step. Super-charm-tau, CEPC and FCC-ee are being designed.

The session on “design concepts” showed that there continues to be a high level of innovation in collider concepts despite the maturity of the collider field. Several game-changing schemes were proposed during the last 10 years (e.g. crab waist, large Piwinski angle, low emittance). The novel schemes give access to uncharted regimes in luminosity and performance. Upcoming colliders like SuperKEKB will probe the potentials and limits of these new concepts, and will demonstrate their positive impact.

The upgraded VEPP-2000 collider will push the concept of round beams. The large future collider concepts FCC-ee and CEPC build on the recent innovations, and plan to exploit their full potential at the precision frontier, exploring the Higgs and other high-energy particles.

New ideas for low energy colliders are emerging as well. They might offer attractive alternative paths for research and science. Continuing investigation of their potential is very interesting and exciting.

REFERENCES

- [1] Joint ICFA/EuCARD-2 Workshop on future circular electron-positron factories “eeFACT2016”, Cockcroft Institute, Daresbury, 24–27 October 2016; <https://eventbooking.stfc.ac.uk/news-events/eefact2016-349> .
- [2] P. Raimondi, “Crab Waist Concept,” presented at eeFACT216, Cockcroft Institute, Daresbury, 23-27 October 2016 [1].
- [3] F. Zimmermann, “Higgs Factory Concepts,” in *Proc. eeFACT2016*, Cockcroft Institute, Daresbury, 23-27 October 2016 [1].
- [4] D. Shwartz, “Implementation of Round Colliding Beams Concept at VEPP-2000,” in *Proc. eeFACT216*, Cockcroft Institute, Daresbury, 23-27 October 2016 [1].
- [5] A. Bogomyagkov, “e+e- Collider with Monochromatization and Maximum Beam Energy of 200-300 MeV for True Muonium Production and Other Experiments,” in *Proc. eeFACT216*, Cockcroft Institute, Daresbury, 23-27 October 2016 [1].
- [6] V.I. Telnov, “Restriction on the Energy and Luminosity of e+e- Storage Rings due to Beamstrahlung,” *Phys. Rev. Lett.*, 110 (2013) 114801.
- [7] A. Bogomyagkov, E. Levichev, and D. Shatilov, “Beam-Beam Effects Investigation and Parameter Optimization for Circular e^+e^- Collider TLEP to study the Higgs Boson”, *Phys. Rev. ST Accel. Beams*, 17, 041004 (2014).
- [8] M.A. Valdivia Garcia, F. Zimmermann, “Effect of Beamstrahlung on Bunch Length and Emittance in Future Circular e^+e^- Colliders,” in *Proc. IPAC’16*, Busan (2016), pp. 2438-2441.
- [9] M.A. Valdivia Garcia, A. Faus-Golfe, F. Zimmermann, “Towards a Monochromatization Scheme for Direct Higgs Production at FCC-ee,” in *Proc. IPAC’16*, Busan (2016), pp. 2434–2437.
- [10] V.V. Danilov et al., “The Concept of Round Colliding Beams,” in *Proc. EPAC’96*, Barcelona, (1996) p. 1149.
- [11] A. De Rujula, R. Ruckl, “Large Hadron Collider in the LEP Tunnel,” ECFA 84/85, Rep. CERN 84-10 (1984).
- [12] J. Norem et al., “An e^+e^- Top Factory in a 50+50 TeV Hadron Collider Tunnel,” presented at Snowmass 1996 and Proc. PAC’97 Vancouver (1996). in *Conf. Proc. C970512*, (1997) pp. 363–368.
- [13] T. Sen, J. Norem, “A Very Large Lepton Collider in the VLHC Tunnel,” *Phys. Rev. ST Accel. Beams*, 5 (2002) 031001.
- [14] P. Raimondi, “Important Synergy of Lepton and Hadron Colliders,” comment at eeFACT216, Cockcroft Institute, Daresbury, 23-27 October 2016 [1].

SUMMARY OF OPTICS ISSUES

K. Oide*, KEK, Oho, Tsukuba, Ibaraki 305–0801, Japan

There were three talks in this session:

1. “Review of IR Designs with CW” by Anton Bogomyagkov – Budker Institute of Nuclear Physics,
2. “FCCee La5ce with Errors and Misalignment” by Sergey Sinyatkin – Budker Institute of Nuclear Physics
3. “Issues in CEPC pretzel and parAal double ring scheme design” by Huiping Geng – Institute of High Energy Physics,

The first talk by A. Bogomyagkov analyzes the nonlinearities associated with a crab-waist optics, evaluated the effects on the dynamic aperture. It can explain the reduction of the dynamic aperture due to crab-waist sextupoles in many machines. Then he proposes a new layout for the location of the crab-sext to reduce those nonlinearities. This idea can help the issue on any machines, including SuperKEKB.

The second talk by S. Sinyatkin will be summarized in the Machine Tuning session.

The third talk by H.P. Geng introduces the progress of the lattice design for CEPC, since single-ring pretzel to the partial double ring scheme. Now they have a consistent design that involves the arc, IR, RF, etc. They have optimized the dynamic aperture using an advanced multi-objective optimization method, then it nearly reaches the goal. They are still in progress.

* Katsunobu.Oide@kek.jp

SUMMARY OF IR AND MDI SESSION

Y. Funakoshi*, KEK, Tsukuba, Japan

Abstract

A brief summary of talks in IR and MDI session is given. Also features and issues on the IR design in the future colliders are summarized.

INTRODUCTION

In this session, 5 talks were given on 4 colliders; *i.e.*, SuperKEKB, CEPC, FCC-ee and eRHIC. The talks are listed below.

- "Issues on IR Design at SuperKEKB" by Yukiyoishi Ohnishi (KEK)
- "IR Design and MDI at CEPC" by Qinglei Xiu (IHEP)
- "FCC-ee Interaction Region Magnet Design" by Michael Koratzinos (Unige)
- "The eRHIC Interaction Region Magnets and Machine Detector Interface" by Brett Parker (BNL)
- "FCC-ee MDI" by Manuela Boscolo (INFN-LNF)

In this summary, a brief summary for each talk is given firstly and then a summary of the whole session is given.

SUMMARY OF EACH TALK

Issues on IR Design at SuperKEKB

SuperKEKB has a relatively large (full) crossing angle of 83 mrad to squeeze the IP vertical beta function down to ~ 0.3 mm with "Nano-Beam Scheme". L^* is chosen as ~ 0.76 m. The strength of the detector solenoid is 1.5 T and the field is cancelled with compensation solenoid magnets so that the integral of the field along the beam line is zero on both sides of the IP. A challenge is to keep enough dynamic aperture and the enough Touschek beam lifetime with the extremely small IP beta functions. For this purpose, many corrector coils are installed in IR including the cancelling coils of the leakage field from the opposite beam. Octupole and skew-sextupole coils are also wound for wider dynamic aperture. In the simulation, the target beam lifetime of ~ 600 s from the Touschek effect has been obtained for both rings without the beam-beam effect by optimizing many parameters including the octupole, skew-sextupole and sextupole magnets. A serious issue presented is that the dynamic aperture in the horizontal direction shrinks largely with the beam-beam effect particularly in LER. The beam lifetime can be decreased down to less than 100 s. A particle with a large horizontal offset collides with the other beam at the position where the vertical beta function is large and the vertical oscillation is induced when the particle is lost

in the simulation. This phenomena can be suppressed with the crab waist scheme. But the nonlinearity of the sextupoles for the crab waist scheme reduces the dynamic aperture very seriously combined with other IR nonlinearity particularly with the fringe field of the final focus quadrupoles. This is an unsolved problem and the conclusion of the speaker is "The transfer map between the IP and the crab waist sextupole should be linear. Development of a cancellation technique for the nonlinear field is necessary."

IR Design and MDI at CEPC

A preliminary IR design of CEPC was shown. The (full) crossing angle is 30 mrad. The vertical beta function at the IP is 1.2 \sim 1.3 mm. The strength of the detector solenoid is 3.5 T and the field is cancelled with compensation solenoid and is shielded with the screening solenoid. L^* is chosen as ~ 1.5 m. A preliminary design of the final focus quadrupole (QD0) with Serpentine coil layers was shown. The problem with the present design is the cross talk of the two QD0's for the two beams. The cross talk should be decreased by adding shield coils. The simulations on the beam background were done on the three types of the background, the synchrotron radiation (SR), the beam loss and Beamstrahlung. Of the 3 types of background, the SR background is the most serious. The critical energy of SR is assumed to be ~ 1 MeV. If this value is for the SR from the last bending magnet, this seems too high considering the experiences at LEP. Collimators for synchrotron radiation from the dipole are designed. The particle loss from the radiative Bhabha process was simulated and the preliminary design of collimator for this background was made. The energy deposition to the collimator should be estimated. In the talk, it was stressed that the mechanical support may be a new challenge for IR design due to the limited space for the support.

FCC-ee Interaction Region Magnet Design

The IR magnet design of FCC-ee was shown. The (full) crossing angle is 30 mrad. The vertical beta function at the IP is 1 \sim 2 mm. The strength of the detector solenoid is 2 T. L^* is chosen as ~ 2.2 m. A border between the accelerator and the detector has been set at ± 100 mrad. Two big challenges for the IR magnet design are vertical emittance creation from the IR vertical dispersion and very tight space for two final focus quadrupoles sitting ~ 6 cm apart. As for the vertical emittance, the emittance budget is very tight and is 1 pm for most of energies. By introducing two magnetic elements; *i.e.* the screening solenoid and compensating solenoid and localizing the dispersion near the IP as much as possible, the emittance blowup has been successfully suppressed to only 10 % of the emittance budget for 2 IPs. As for very tight space for the final focus quadrupoles, the influence of one quadrupole to the other beam might be problem. To

* yoshihiro.funakoshi@kek.jp

cope with this problem, two options of magnets have been proposed; *i.e.* Modified Panofsky type quadrupole and a Canted-Cosine-Theta (CCT) magnet. The former has a disadvantage that no correction coils can be inserted. The latter seems to fulfill all requirements as the final focus quadrupole; (1) Compact design, (2) Correction coils can easily be incorporated and (3) Can be designed so that the twin aperture design can each have a pure quadrupole component. For further study, a prototyping work is needed for the final focus quadrupole.

The eRHIC Interaction Region Magnets and Machine Detector Interface

At eRHIC, they plan to collide an electron beam against a hadron beam. The electron beam energy is 2~18 GeV. For the hadron beam, up to 275 GeV polarized protons or 110 GeV/u Au ions will be used. While a ring or an ERL will be newly constructed for the electron beam, one of present RHIC rings will be used for the hadron beam. The crossing angle is 22 mrad for the electron ring option or 14 mrad for the ERL option which can create a lower emittance electron beam. In both options, the crab crossing is assumed. L^* is about 5 m. The target luminosity is $\sim 10^{32-33}\text{cm}^{-2}\text{s}^{-1}$ (initial) and $\sim 10^{33-34}\text{cm}^{-2}\text{s}^{-1}$ (after upgrade). A big challenge for the eRHIC IR magnet design is that the two step separation (electrons/hadrons and then charged hadrons/neutrons) and large required apertures. Solutions to this challenge are to use active shields for the e-ring option or sweet spot coils for the ERL option to minimize the leakage field from the final focus magnets for the hadron beam to the electron beam. The sweet spot coil technique seems very elegant in the sense that the coils contribute to $\sim 1/3$ of the quadrupole field for the hadron beam. At present, they are midway through production of a 1 m long dipole sweet spot coil prototype in order to gain experience with such coil configurations.

FCC-ee MDI

The present status of the study on MDI for FCC-ee is reviewed. An emphasis was placed on the beam background due to SR. SR is the main constraint for the IR design and it drives the IR optics and the IR layout at FCC-ee. To mitigate the serious SR background to the detector, an asymmetric IR optics has been worked out. In this optics, the last bending magnets are located ~ 100 m upstream the IP and ~ 42 m downstream the IP. By placing the upstream bending magnet farther from the IP, the SR background was drastically decreased compared with the case of the 42 m distance. They consider this asymmetric optics as a baseline optics for the MDI studies. Requirements to the critical energy of SR have been set based on the LEP experiences. The critical energy of photons from the weak bending magnet (last bending magnet) should be less than 100 keV. Those for the other magnets in whole ring should be less than 1 MeV to minimize the neutron production. For the simulation of the SR background, several software tools have been developed. The beam-pipe geometry and their material have been de-

signed. Detailed SR shielding and collimation studies have been being done. The studies of the SR background from far bending magnets have started. In the collider in this energy region, the luminosity detection is very important. Its design and integration to the IR design is a challenge. The study on the optimization of the position, size and optimal coverage of the luminosity detector, which could influence the choice of L^* , is going on.

SUMMARY OF SUMMARY

In the future e^+e^- (ep) colliders including SuperKEKB which has just finished non-beam-collision tuning, the IR design has become more difficult than the existing colliders. Since a much higher luminosity is required, the IP beta functions are much smaller and the final focus doublets are placed much closer to the IP. These requirements or constraints make the IR design much more difficult. In the following, features and issues on the IR design in these colliders are summarized.

Crossing Angle

All of the four colliders in the session have the horizontal crossing angle. In SuperKEKB, CEPC and FCC-ee, a large Piwinski angle is essential to squeeze the vertical beta function beyond the limit from the hourglass condition. eRHIC also needs a crossing angle instead of IR separator dipoles, since the dipoles would create a serious SR background, interfere with the physic detector and affect acceptance for forward neutrons and charged particles. The crab waist scheme will be adopted in FCC-ee and CEPC and the crab cavity scheme will be introduced in eRHIC. Motivations of both schemes are to compensate some harmful effects arisen from the crossing angle.

Lattice Nonlinearity from IR

One of the hard challenges for the IR design in the future colliders is to keep sufficient dynamic aperture. In CEPC and FCC-ee, a momentum acceptance of $\pm 2\%$ at 175 GeV is required to hold the large energy spread caused by Beamstrahlung. In SuperKEKB, the Touschek effect is important for the lifetime and so both a large momentum acceptance and an enough horizontal acceptance are required. By optimizing related parameters, required dynamic aperture is achieved in the simulation for a perfect machine at FCC-ee. Dynamic aperture at CEPC is under study. At SuperKEKB, a target beam lifetime from the Touschek effect of 600 s was achieved in the simulation without the beam-beam effect. However, the dynamic aperture shrinks largely with the beam-beam effect. If the crab waist scheme works, this shrinkage can be reduced. At SuperKEKB, however, nonlinearity of the crab waist sextupoles combined with the fringe field of the final focus quadrupoles reduces dynamic aperture seriously. In a talk in the optics issues session, Anton Bogomyagkov compared IR nonlinearity of several colliders as is shown in Table 1. In the table, μ'_y , α_{yy}^k , α_{yy}^k and α_{yy}^S denote the chromaticity by the final focus quadrupoles,

the detuning coefficient (amplitude dependent tune shift) from the kinematic term, that from the fringe field of the quadrupoles and that from the -I sextupole pairs, respectively. As is seen in the table, nonlinearity from the fringe field of the final focus quadrupoles of SuperKEKB is remarkably large compared with other colliders. To make the crab waist scheme work in SuperKEKB, reducing IR nonlinearity seems important. One possibility is to remake the final focus quadrupoles (QCS) with less nonlinear fringe field in future by making the length of the quadrupoles longer. They may need such kinds of upgrade plans. In FCC-1, nonlinearity from the sextupoles of the local chromaticity correction was very large. This nonlinearity comes from thickness of the sextupoles. This nonlinearity was drastically reduced by adopting thin superconducting sextupoles.

Table 1: Comparison of IR Nonlinearity of Several Colliders

	μ'_y	$\alpha_{yy}^k [m^{-1}]$	$\alpha_{yy}^k [m^{-1}]$	$\alpha_{yy}^S [m^{-1}]$
DAΦNE	-61	694	218	
Super-KEKB	-5400	1.8×10^6	9.8×10^6	-7×10^5
SuperB	-1060	1×10^6	2.8×10^5	-5.4×10^6
C Tau	-700	1.3×10^5	7.7×10^5	-7.2×10^5
FCC-1	-2800	4.5×10^5	1.9×10^5	-1.2×10^7

Vertical Emittance

In SuperKEKB, CEPC, FCC-ee, the design value of the vertical emittance is very small and then the emittance budget is very tight. In this situation, the vertical emittance created in the IR region should be minimized. In principle, it is inevitable that the detector solenoid plus the horizontal crossing angle cause the vertical kick particularly in the fringe region and the vertical dispersions. It is important to minimize the resultant vertical emittance by cancelling the detector solenoid properly. At SuperKEKB, they took a special care of the design of the compensation solenoid magnets. Since the vertical kick by the solenoid fringe is proportional to the derivative of B_z (solenoid field) in the longitudinal direction, the compensation solenoid was design so that the slope of B_z along the beam orbits in the fringe region should be sufficiently gentle. In the FCC-ee design, they carefully designed the compensation solenoid and the screening solenoid to minimize the vertical emittance. In this manner, the low emittance requirement poses some constraint to the IR design.

IR Magnet Design

One of the challenges for the IR design is the IR magnet design. The difficulty in the design comes from many functions

packed within the very limited space, mutual interference of magnetic fields for the two beams, mutual interference of accelerator components and detector components and others. At SuperKEKB, in addition to the main quadrupole coils, many corrector coils were designed and fabricated. As of November 2016, the fabrication has almost finished. Many corrector coils are needed to compensate fabrication errors of the main quadrupoles and alignment errors or cancel the leakage field from the quadrupoles for the other beam. In the extreme machine like SuperKEKB, such compensation is very important. Some coils such as the octupole coils are used to improve dynamic aperture. All of the corrector coils except for the main quadrupole coils have been fabricated at BNL. The IR and magnet design at eRHIC is much different from that of e^+e^- colliders due to asymmetry of the hadron and lepton beams. The sweet spot coil technique seems a very unique and elegant solution for the ring-ERL option. BNL is one of the technical leader in the field of the superconducting magnet in the world. Its accumulated experiences should be learnt by other laboratories. The next step of the IR magnet design of FCC-ee is R&D works with a prototype magnet.

Detector Beam Background

The detector beam background is a very important issue related to the IR design. At FCC-ee and CEPC, the SR background is most important. It gives a strong constraint to the IR optics design. The tolerance to the SR has been determined considering the experiences at LEP. This should be confirmed by realistic simulations. Considering its big impact on the accelerator design, efforts on the detector side to increase tolerance of the detector against SR should be made. At SuperKEKB, the beam background from the Touschek effect, the Coulomb scattering and the radiative Bhabha process are important. To reduce the detector background, setting the collimators in the rings properly is very important. In Phase 2 commissioning, it is very important to validate the simulation tools.

Others

In CEPC and FCC-ee, the design of the luminosity detector is a big challenge. If the distance of the detector from the IP is short, the lack of knowledge of the precise position of the detector degrade the accuracy of the luminosity measurement. A careful attention should be paid to its design. Heating of the IR components due to SR and HOM is also important issue in the IR design. More engineering issues such as how to support the IR components or how to assemble them are important and should be studied in future for FCC-ee and CEPC.

SUMMARY BEAM-BEAM SESSION, eeFACT2016 WORKSHOP

Alex Chao, SLAC National Accelerator Laboratory, CA, USA

Abstract

There are two talks in the beam-beam session. But beam-beam is an issue that permeates in several other sessions. So in this summary I have taken the liberty to include some materials extracted also from other sessions.

FLIP-FLOP

The first talk was “Flip-flop instability in FCC-ee at low energies” by Dmitry Shatilov.

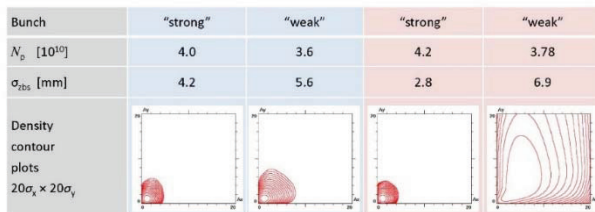
The old flip-flop as we know it is a 1D effect. A new intriguing 3D flip-flop is now discovered for strong-weak cases when the beam intensity asymmetry exceeds ~10%. The instability mechanism is rather involved, requiring several ingredients. Missing one of them removes the instability. Ingredients include:

1. asymmetry in beam intensities
2. beamstrahlung
3. crossing beams
4. x-y coupling

This flip-flop instability has a beam intensity threshold. Below a certain threshold, even asymmetric beams do not become unstable. The threshold can be increased by lowering β_x^* (and raising β_x holding luminosity fixed).

A slide from Dmitry Shatilov:

3D Flip-Flop triggered by beamstrahlung (asymmetry 10%)



The flip-flop threshold depends on asymmetry in the bunch currents. But even in symmetrical case the flip-flop was observed (with larger bunch population).

SIMULATIONS

The second talk was “FCC-ee beam-beam strong-strong simulations for all working and mitigation” by Kazuhito Ohmi.

For FCCee at Higgs energy, it was found that the beam-beam limit behaves rather differently for a strong-weak case and a strong-strong case. For a strong-weak case, it was found that the beam-beam limit ξ depends sensitively on the choice of the working point. For one working point, it can be as high as $\xi = 0.6$, while for

another working point it is 0.2. Two observations can be made:

- The fact that a strong-weak case can have large beam-beam limit is in sharp contrast with the prediction by 3D flip-flop (as in the previous talk), where it was observed that a small asymmetry in beam intensities leads to a strong instability. The present-day beam-beam is a subtle subject involving multiple parameters and multiple physical mechanisms. Careful and complete considerations are necessary to draw final conclusions.
- The sensitivity to working point apparently appears when the working point is in the proximity to $\frac{1}{2}$ tunes.

In contrast to the strong-weak case, the strong-strong cases seem to converge to a beam-beam limit $\xi = 0.2$ at the Higgs energy, insensitive to the choice of working point. Very interesting is the observation that in the FCCee case with crossing beams, there is a strong beam-beam-induced high-mode coherent x-z oscillation, while the lowest x-z mode is stable. This oscillation becomes more serious at the Z energies, when the beam-beam limit is reduced to 0.06. It was further observed that these x-z oscillations can be removed by substantially lowering β_x^* and raising ϵ_x , curiously the same trick to cure the 3D flip-flop instability.

Two slides from Kazuhito Ohmi showing the beam-beam limits:

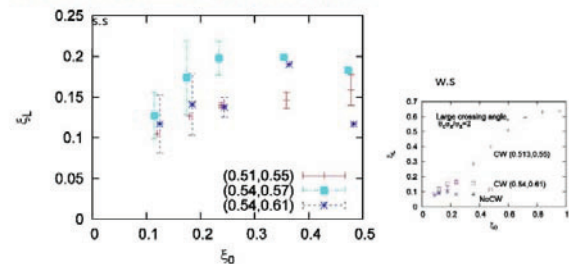
ξ limit for FCC-ee H

No clear difference for (0.54,0.61) from weak-strong $\xi_{lim}=0.2$.

Big difference for (0.51,0.55), the limit in weak-strong is extremely high $\xi_{lim}=0.6$ (ws), $\xi_{lim}=0.2$ (ss).

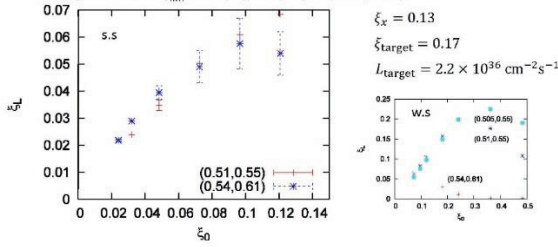
ξ limit is weakly dependent of tune in Strong-strong simulation.

It is possible to achieve $\xi_L=0.15$ for tlep-H.



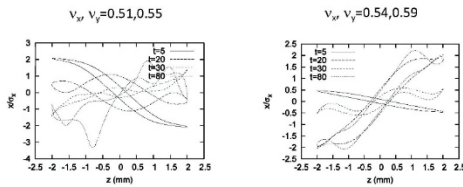
ξ limit in Z factory

- Error bar is fluctuation due to coherent motion
- The beam-beam parameter is limited 0.06, and coherent oscillation
- Big difference from the weak-strong results ξ_{lim}=0.2 at (0.51,0.55).
- No big difference ξ_{lim}=0.06(ss), 0.1(ws) in (0.54,0.61).



One more slide from Kazuhito Ohmi showing the beam-beam induced high-mode x-z oscillation:

Simulated Beam distribution using simple model II



Lab frame (not collision frame)

BEAM-BEAM LIMIT, WHICH FORMULA TO USE?

The beam-beam limit formulae used in the designs of FCCee and CEPC are different! (And you think a basic formula like this should have long been settled?) The formula used for the FCCee design is

$$\xi_y = \frac{r_e N_b B_y^*}{2\pi\gamma \sigma_x^* \sigma_y^* \sqrt{1 + \phi_{piw}^2}}$$

This formula is based on a physical model that treats the beam-beam effect as nonlinear resonances. It predicts a beam-beam limit of ξ_y = 0.16 for FCCee.

The beam-beam limit formula used in the CEPC design is

$$\xi_y = \frac{2845}{2\pi} \sqrt{\frac{U_0}{2\gamma E_0 N_{IP}}} \times F_l$$

where F_l is the beam-beam limit enhancement factor by crab waist scheme and so far it is assumed to be 1.6 for Higgs and 2.6 for Z by the CEPC design [Reference: J. Gao, Nucl. Instrum. Methods A 533, 270 (2004)]. This formula is based on a diffusion model treating beam-beam kicks as random noise. It predicts ξ_y = 0.11 for CEPC. It notably has a dependence on the number of interaction points N_{IP}, and it does not depend on the tunes.

The two formulae have completely different parameter dependences and completely different scalings. Past experience seemed to declare beam-beam limit values closer to the CEPC prediction. On the other hand, latest simulations seem to confirm the FCCee prediction. The two models assume two extreme opposite physical pictures. The nonlinear resonances picture assumes perfect correlation from one beam-beam kick to the next (e.g., perfect correlation is assumed at least for the number of turns in a simulation), while the diffusion picture assumes a complete loss of phase correlation between kicks even in the same turn. Which is correct? One must feel widely unsatisfying when the two most prominent (and costly) colliders of today have used formulae so different as their most basic and the very first design equation!

LONG RANGE BEAM-BEAM EFFECTS

This is no longer a critical issue with a new partial-double-ring design at CEPC.

BEAMSTRAHLUNG

Beamstrahlung is a new issue, but is now well accepted as it should. The need of a flat beam at the collision point and the need of a very large energy aperture are taken into design considerations, affecting the design very seriously.

Slide from Frank Zimmermann:

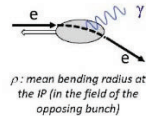
beamstrahlung – potential limit at 175 GeV

synchrotron radiation in the field of opposing bunch at the IPs, 'beamstrahlung', can become lifetime limit for large bunch populations, small horizontal beam size & short bunches

$$\tau_{bs} \propto \frac{\rho^{3/2} \sqrt{\eta}}{\gamma^2 \sigma_x} \exp(A\eta\rho/\gamma^2), \quad \frac{1}{\rho} \approx \frac{Nr_e}{\gamma\sigma_x\sigma_z}$$

η : ring energy acceptance

lifetime expression by V. Telnov, modified version by A. Bogomyagkov et al



for acceptable lifetime, ρ×η must be sufficiently large

- flat beams (large σ_x)
- bunch length
- large momentum acceptance: aiming for ≥1.5% at 175 GeV

-LEP: <1% acceptance, SuperKEKB ~ 1.5%

V. Telnov, A. Bogomyagkov, E. Levichev, D. Shatilov, et al.

Another slide from Frank Zimmermann:

beamstrahlung effect at lower energy

IP photon emission increases equilibrium energy spread & bunch length

$$A \equiv 1.4 \frac{\eta_{IP} \tau_{\delta,SR} r_e^5 N_b^3 \gamma^2}{4T_{rev} \alpha \sigma_x^3}$$

$$\sigma_{\delta,tot}^2 - \sigma_{\delta,SR}^2 = A \left(\frac{\sigma_{\delta,SR}}{\sigma_{\delta,tot} \sigma_{z,SR}} \right)^2$$


$$\sigma_{\delta,tot} = \left[\frac{1}{2} \sigma_{\delta,SR}^2 + \left(\frac{1}{4} \sigma_{\delta,SR}^4 + A \frac{\sigma_{\delta,SR}^2}{\sigma_{z,SR}^2} \right)^{1/2} \right]^{1/2}$$

huge effect: factor 2-5 increase possible! included in the design parameters

K. Yokoya, K. Ohmi, D. Shatilov, F. Zimmermann, et al.

On the other hand, beamstrahlung induced background is not considered too serious for FCCee and CEPC.

Slide from Qinglei Xiu:



Beamstrahlung

Symbol	LEP2	CEPC	ILC 250GeV	ILC 500GeV
Ecm [GeV]	209	240	250	500
N [$\times 10^{10}$]	58	37.1	2	2
σ_x / σ_y [nm]	270000/3500	73700 / 160	729 / 7.7	474 / 5.9
σ_z [μ m]	16000	2260	300	300
β_x / β_y [mm]	1500/50	800 / 1.2	13 / 0.41	11 / 0.48
$\gamma\epsilon_x / \gamma\epsilon_y$ [mm · mrad]	9.81/0.051	1594.5 / 4.79	10 / 0.035	10 / 0.035
$\langle Y \rangle$	2.5e-5	4.7e-4	0.02	0.06

- Characterized by: $\langle Y \rangle = \frac{5}{6} \frac{Nr_e^2 \gamma}{\alpha(\sigma_x + \sigma_y)\sigma_z}$
- The effects of beamstrahlung at CEPC should be much smaller than ILC

2016-10-25

eeFACT2016

16

ROUND BEAMS

Beam-beam effect is expected to become weaker for round beams because the system becomes effectively 1D and the nonlinear dynamical effects become weaker. This is particularly suggested for low energy colliders. For the FCCee and CEPC, however, round beams are ruled out due to beamstrahlung.

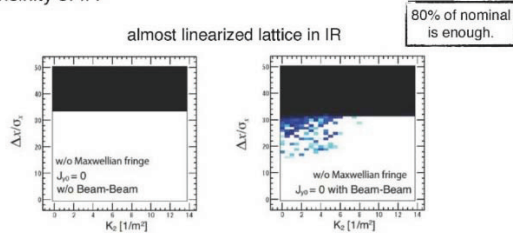
INTERPLAY OF BEAM-BEAM AND LATTICE NONLINEARITIES

This issue was mentioned a few times at the workshop. One example is that the IR nonlinearities (there is no shortage of them!) plus the nonlinearities of the crab waist sextupoles mess up the ingenious and delicate crab waist function. Cancellation technique is needed to further improve the crab waist scheme.

A slide from Yukiyoshi Ohnishi:



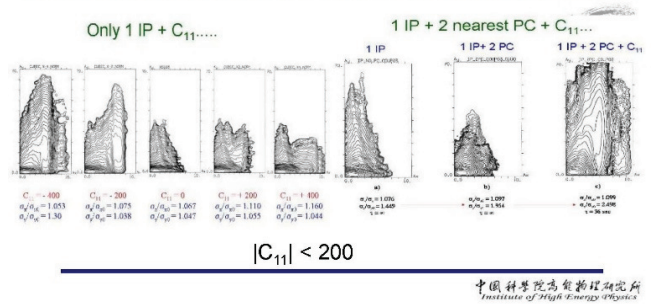
- Cancellation between crab-waist sextupoles does not work because the transfer map is not linear between them.
- The sources of nonlinear terms are fringe field of the final focus quadrupole and kinematic terms from the drift space in the vicinity of IP.



20

Another slide from Qing Qin:

Crosstalk between beam-beam effects and lattice nonlinearities



中国科学院高能物理研究所
Institute of High Energy Physics

SUMMARY

- Important progress is being made. New beam-beam effects are discovered and studied.
- With performance being pushed so hard, more subtleties that were unimportant in the past now arise. New effects keep being discovered.
 - (a) the requirement of crab waist
 - (b) effect of residual nonlinearities after the crab waist cancellation
 - (c) beamstrahlung
 - (d) 3D flip-flop instability
 - (e) coherent x-z oscillation
 - (f) interplay with lattice nonlinearities
 - (g) interplay with collective effects (no discussion at this workshop)
 - (h) etc.

Beam-beam issue is more critical than ever.

- But not all pieces have been settled, including the most basic design formula of the beam-beam limit. As we explore deeper, it is expected that more serious learning is still ahead. It is suggested that there should be at least 10 talks in the beam-beam session in the next 2018 workshop.
- SUPERKEKB and HL-LHC should play important roles in the learning process.

This work was supported by U.S. DOE Contract No. DE-AC02-76SF00515.

SUMMARY OF INJECTOR AND BEAM INJECTION*

J.T. Seeman[†], SLAC National Accelerator Laboratory, CA, USA*Abstract*

This summary covers the Injection and Sources Session of the e+e- Factories Workshop held at Daresbury Laboratory, UK, October 24-27, 2016, which had six presentations. Here we discuss the goals for top-up injection for a collider and their sources and then covers the highlights, discussion topics, and future plans for each presentation. The talks [1-6] will be covered in alphabetical order by author's name.

INJECTION AND SOURCES GOALS

Extracted from the six talks in this session, the required qualifications for injection and sources for present and future e+e- colliders can be broken down into three general areas: parameters, construction, and operation. The desired parameters are full energy injection (up to 175 GeV), varied injected bunch charges (quanta), short fill times from scratch, low detector backgrounds while injecting while taking data, polarization of about 80% for electrons and, if possible, for positrons (under development), well integrated into the collider design, and well instrumented. For construction, the desire is to be inexpensive as possible using existing technology if possible. For operations, the need is for low power costs, reliable running, low maintenance costs with many common-standard units, and bunch number flexibility.

The goals for the injector for an e+e- collider are shown in Table 1 where 50 to 90000 overall bunches are needed and 6 to 1450 mA per beam of stored currents are needed. The injection rates depend on how many bunches are to be injected per booster cycle, the expected beam lifetimes (~10 to 60 min) and the charge per bunch needed to maintain the luminosity near the maximum.

Table 1: Injection Parameters for a Future e+e- Collider

parameter	FCC-ee			CEPC	LEP2
energy/beam [GeV]	45	120	175	120	105
bunches/beam	90000	770	78	50	4
beam current [mA]	1450	30	6.6	16.6	3
luminosity/IP x 10 ³⁴ cm ⁻² s ⁻¹	70	5	1.3	2.0	0.0012
energy loss/turn [GeV]	0.03	1.67	7.55	3.1	3.34
synchrotron power [MW]	100			103	22
RF voltage [GV]	0.08	3.0	10	6.9	3.5

FCC-ee: 2 separate rings
& 2 IPsCEPC: single beam
pipe version

TIANJIAN BIAN (IHEP): DESIGN STUDY OF CEPC BOOSTER

The injector of the proposed CEPC e+e- collider in China has been studied for several years with a converging design. It consists of a linac, positron source, damping ring and, finally, a full energy booster ring in the same tunnel as the collider with a circumference of 63.8 km. The injected bunches go through a septum and then a kicker to be stacked onto (top-up) an existing bunch in the collider. The highest energy of the booster would be 120 GeV for the Higgs energy with an injected emittance of 3.5 nm-rad. A booster optical lattice has been generated which looks acceptable in term of tunability, chromatic corrections, earth's field correction, element error tolerances, and magnet technical features.

The very low magnetic field in the booster at injection energy is a concern with several cures being studied including shielding of the earth's field, reverse bends, special steel, and low energy orbit corrections. A reverse (wiggling) bend scheme is the primary choice at the present (See Figure 1) to boost the magnet field about a factor of 6 (25 gauss to (-129 and +180) gauss).

A computer code has been developed (MOOLA) to optimize the design of a ring lattice. It uses Hamilton canonical coordinates and has fourth order symplectic integration. This code has been used to maximize the properties of the CEPC injector booster lattice and the HEPS light sources lattice.

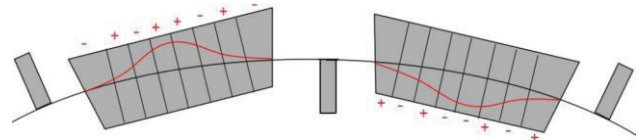


Figure 1: Proposed booster dipole magnet layout to increase the low energy fields in China CEPC.

Further work and discussion:

- 1) Construct a real model of the 25 gauss dipole magnet and test the reproducibility of the low field state.
- 2) Construct a working model of the reverse bend dipole magnet and measure the remnant fields through field reversal.
- 3) Further work on lattice dynamic aperture optimization with MOOLA is ongoing.
- 4) Study if the partial double ring collider design changes the requirements for the CEPC injector.

*Supported by US DOE contract DE-AC02-76SF00515.

[†]seeman@slac.stanford.edu

ZHE DUAN (IHEP): TOP-UP INJECTION SCHEMES FOR HEPS

The High Energy Photon Source (HEPS) is a proposed 6 GeV low emittance light source in Beijing, China, about 90 km from IHEP. The injection energy needs to be 6 GeV and total stored charge of 200 nA in 648 bunches (See Figure 2 and Table 2). The proposed injector scheme contains a linac and a booster with longitudinal on-axis injection into the storage ring. The injected bunches are merged with the stored bunches with longitudinal phase space gymnastics by RF phase manipulations using 166 and 499 MHz RF systems. The time scale is about the synchrotron damping time. A fast RF control feedback loop is needed for these manipulations. Also, a fast injection kicker is needed with about a 1 nsec rise time, 2.5 nsec fall time, and total duration of about 3.5 nsec with a 300 Hz burst-mode repetition rate. A single injection period takes about 200 msec. The longest refill cycle time is 3.5 minutes.

Further work and discussion:

- 1) The effect of IBS on the stored bunches of about 2.8 mm bunch length affecting injection is under study.
- 2) Work on the injection kicker is ongoing.
- 3) The stability of the two frequency RF system under bunch phase merging is under review.
- 4) The effect on injection from different bunch pattern requirement needs to be investigated.

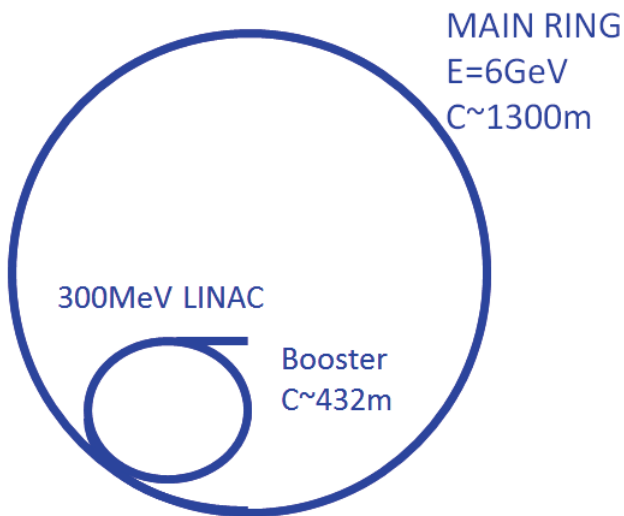


Figure 2: Injector for the future Beijing HEPS light source.

Table 2: Injection Parameters for Beijing HEPS

parameters	648 bunches	60 bunches
charge	1.33 nC	14.4 nC
lifetime (during operation)	30 hours	3 hours
refill time	3.5 min	20 second
number of injection in each refill	4	2
bunch filled in each refill	30 * 4 = 120	30 * 2 = 60
injection time	200 ms * 4	200 ms * 2
total duration of each refill	9 s * 3 = 27 s	9s * 1 = 9 s

TAKUYA NATSUI (KEK): INJECTOR LINAC UPGRADE AND NEW RF GUN FOR SUPERKEKB

The gun and linac for the SuperKEKB collider (7x4 GeV) is being upgraded to provide rapid top-up injection. Several upgrades are needed as the luminosity lifetimes of the SuperKEKB beams are expected to be about 10 to 20 minutes and the stored beam charge is about twice that of KEKB. Also, the emittance of the injected beam needs to be smaller to fit into the reduced SuperKEKB dynamic aperture. The injector must also inject beams into the Photon Factory (2.5 GeV) and Accumulator Ring (6.5 GeV) light sources at KEK. The layout of the injector chain at KEK is shown in Figure 3.

The thermionic gun was used for commissioning of Phase 1. The charge of the electron beam was 1 nC. The charge of positron beam was 1 nC with the new flux concentrator.

The new injector achieved a charge of 1 nC beam generation by using the new photo-cathode RF gun. The laser power stability is acceptable giving a charge stability of about 5%. The beam position stability, however, needs improvement for the RF gun. The emittance was approximately 20 mm-mrad. So overall, the SuperKEKB HER Ring injection tests were successful using the RF gun achieving 10 days of stable injection.

Further work and discussion:

- 1) Work to bring the photo-gun to full specifications is ongoing including laser work.
- 2) More work on the linac emittance preservation is needed.
- 3) Preparation for damping ring commissioning is ongoing.

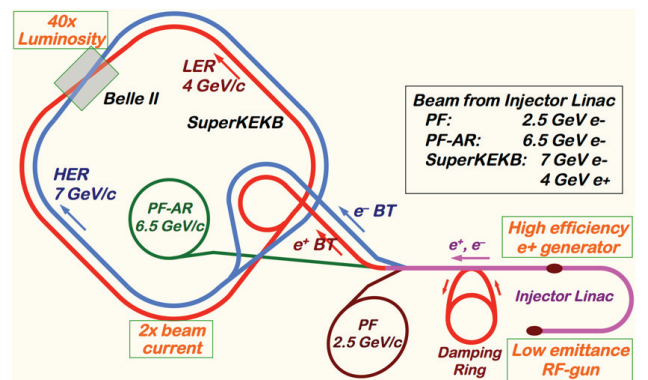


Figure 3: Layout of the injector for SuperKEKB and the KEK light source rings.

SALIM OGUR (CERN): TOWARDS A PRELIMINARY FCC-EE INJECTOR DESIGN

The FCC-ee injector must accommodate from 81 to 91500 bunches to cover four different operational modes (Z, W, H, and tt). The highest energy (175 GeV) but lowest beam current is for tt. The highest number of bunches and highest current is for the Z. The present concept has a 100 Hz 6 GeV linac, a 257 m damping ring at 1.54 GeV for e⁺, and a 100 km booster reaching 175 GeV top energy housed in the same tunnel as the collider. This concept is shown in Figure 4. The linac accelerates two bunches at a time to an energy of 6 GeV and 4×10^{10} particles per bunch. The booster fill time is 4 seconds with 800 bunches with a following ramp to full energy of 6 seconds.

Studies have been started to study the evolution of the electron and positron bunch qualities throughout the injector chain. The beam optics of the linac and of the damping ring have initial lattices which are being studied for dynamic aperture and emittance growth with various component errors. Linac alignment tolerances must be on the order of 100 microns and 0.1 milliradians to keep the injected beam from causing large backgrounds and have good injection efficiencies.

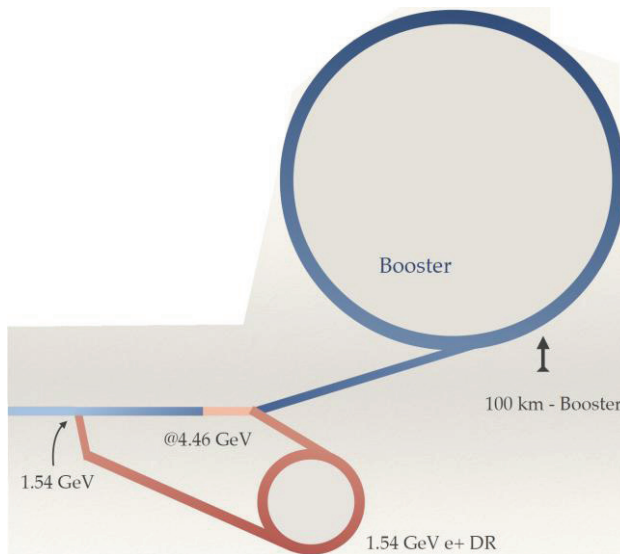


Figure 4: Injector concept for the CERN FCC-ee.

Further work and discussion:

- 1) The whole injection process can be shortened if the linac can accelerate more than 2 electron bunches per pulse (4 bunches is under study).
- 2) The very low magnetic field of the booster at low energy is a concern and further work is planned to investigate the consequences and mitigations.
- 3) Simulated transmission losses have brought up the questions of collimation and the required bunch charges before losses.

- 4) Most of the cost for the injector is in the highest energy booster needed. Are there ways to reduce this?
- 5) The filling time from scratch is about 46 minutes at the Z. A configuration to reduce this time is desired.

JOHN SEEMAN (SLAC): TOP-UP INJECTION SCHEMES

Top-up injection schemes for PEP-II, KEKB and future e⁺e⁻ colliders were discussed. Beams were injected at several Hz in both PEP-II HER and LER to keep the currents constant. In KEKB bunches were injected alternatively every few minutes between electron and positrons. Backgrounds and detector masking are important issues. In Figure 5 is shown the elapsed time after a bunch is injected into PEP-II showing the backgrounds decaying on the order of a synchrotron damping time. In Figure 6 is shown the injection masking of the BaBar detector for about 2000 turns but only centered near part of the turn where the injected bunch is located.

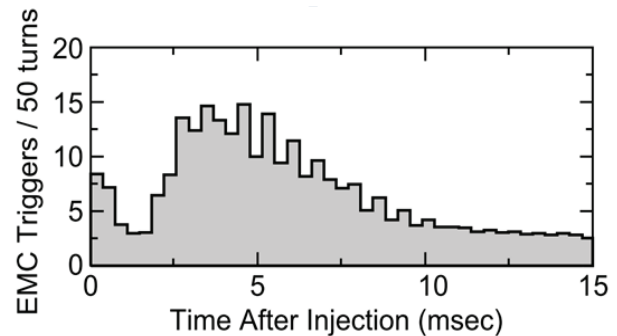


Figure 5: Background in BaBar from a single injected LER bunch during top up injection but it only affects a small part of the ring keeping the data taking efficient.

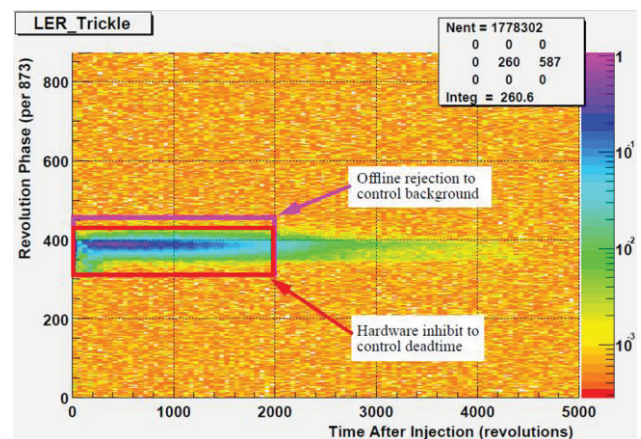


Figure 6: Injection masking for BaBar data taking covering only the injection bunch's segment of the circumference for about 10 milliseconds.

Conclusions from PEP-II and KEKB top-up injection results: Top-up injection will work for a circular e⁺e⁻ factory. Top-up or full charge exchange will work for a

future collider. A full energy injector is needed because of the observed short beam lifetime from beam-beam, Toushek and beam gas effects. The detectors will need to mask out the nearby buckets during damping of the injected bunches during data-taking but not the whole circumference. A single bunch injection controller needs to be worked out in detail for both the accelerator (quanta, feedbacks, jitter) and the detector. Commissioning can be complicated as many issues both on the accelerator and detector arise and both have to work out the problems together: mainly detector backgrounds, beam lifetimes, injection efficiencies, masking, and luminosity versus beam lifetimes.

Further work and discussion:

- 1) Diagnostics are needed to resolve the efficiency of the injected bunches for capture.
- 2) Higher energies could make the power lost in the IR higher per injected particle. Does IR collimation need to be more thorough?
- 3) The detector DAQ needs to be able to make complex masking configurations. How flexible does it need to be?

RONG XIANG (HZDR): ELECTRON AND POSITRON SOURCES

The demands on electron sources for the upcoming new colliders are higher than before in terms of high charge, low emittance and maximum polarization. There are requirements for high current, high brilliance, low emittances, polarization, total charge, as well as stability and reliability. There are several available and future type of sources: thermionic cathode guns (DC, NC-RF), photocathode guns (DC, NC-RF, SC-RF), and photo-induced field emission cathodes (NC-RF, SC-RF). Several new ideas include plasma wakefield accelerators (PWFA) and laser wakefield accelerators (LWFA). In Figure 7 are shown the performance levels of various working guns in terms of brightness and average current.

DC and NC-RF guns are well established. SC RF guns are getting serious attention now with several laboratories leading the effort (e.g. ELBA). SLAC, LBNL, DESY, and others are looking at PWFA and LWFA sources.

For polarization, there are new studies for polarized electron sources beyond strained InGaP or GaAsP cathodes. Multilayer structures are nearing the testing stage.

Further work and discussion:

- 1) Extending cathode lifetimes of total coulombs emitted is an issue, especially for an Electron Ion Collider.
- 2) Investigate the near term results of multilayer photo-polarization sources.
- 3) Work on higher gun fields and cathode voltages.
- 4) Make better models for particle tracking from guns including all 3D effects.
- 5) Work on polarized positron sources has started but more work is needed to make their case viable.

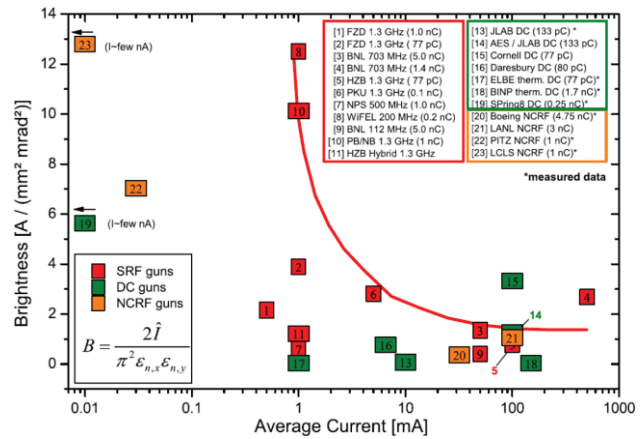


Figure 7: Plot of the trade-off of high brightness and high average currents in existing electron gun sources.

CONCLUSION

The injection session of the e+e- Factory Workshop was well attended, many questions were asked, and discussions were of a very technical nature.

ACKNOWLEDGMENT

The author would like to thank the speakers of the eeFACT2016 Injectors and Sources Session for their clear and interesting presentations.

REFERENCES

- [1] Tianjian Bian, “Design Study of the CEPC Injector”, presented at the e+e- Factory Workshop, October 24-27, 2016, paper TUT2H3.
- [2] Zhe Duan, “Top-Up Injection Schemes for HEPS”, presented at the e+e- Factory Workshop, Daresbury Laboratory, October 24-27, 2016, paper TUT2H4.
- [3] T. Natsui, “Injector Linac Upgrade and New RF Gun for SuperKEKB”, presented at the e+e- Factory Workshop, October 24-27, 2016, paper TUT2H2.
- [4] T. Ogur, “Towards a Preliminary FCC-ee Injector Design”, presented at the e+e- Factory Workshop, Daresbury Laboratory, October 24-27, 2016, paper TUT2H5.
- [5] J. Seeman, “Top-Up Injection Schemes”, presented at the e+e- Factory Workshop, October 24-27, 2016, paper TUT2H1.
- [6] Rong Xiang, “Electron and Positron Sources”, presented at the e+e- Factory Workshop, Daresbury Laboratory, October 24-27, 2016, paper TUT2H6.

SUMMARY OF IMPEDANCE ISSUES AND BEAM INSTABILITIES*

F. Zimmermann[†], CERN, Geneva, Switzerland

Abstract

This paper summarizes the session on impedance issues and beam instabilities at the ICFA workshop on future circular electron-positron factories “eeFACT2016” [1] held at the Cockcroft Institute, Daresbury, from 24 to 27 October 2016. This session also covered active beam stabilization by feedback systems. Beam-beam effects and coherent beam-beam instabilities were addressed separately and, therefore, are not included here.

OVERVIEW

The eeFACT2016 [1] session on impedance issues and beam instabilities featured the following ten presentations:

1. Low SEY Engineered Surface for Electron Cloud Eradication [2], by Reza Valizadeh, STFC;
2. Collective Effects Issues for FCC-ee [3], by Mauro Migliorati, University of Rome La Sapienza;
3. Impedance Measurement Techniques and Lessons from Light Sources [4], by Victor Smalyuk, Brookhaven National Laboratory;
4. Coherent Wave Excitation in a High Current Storage Ring [5], by Alexander Novokhatski, SLAC National Accelerator Laboratory;
5. Electron Cloud and Fast-Ion Instability plus Mitigation Methods for Future Factories [6], by Kazuhito Ohmi, KEK;
6. Electron Cloud at SuperKEKB [7], by Hitoshi Fukuma, KEK;
7. Electron Cloud and Collective Effects in the Interaction Region [8], by Eleonora Belli, CERN and La Sapienza;
8. An Overview of Active Coupled-Bunch Instability Control [9], by Dmitry Teytelman, Dimtel, Inc.;
9. Feedback Experience at DAFNE [10], by Alessandro Drago, INFN/LNF;
10. Instability Issues in CEPC [11], by Na Wang, Institute of High Energy Physics, Chinese Academy of Sciences.

The topics and presentations can be classified according to three grand themes: (1) classical wake fields and instabilities, (2) electron cloud, and (3) ion instability. The focus was on forecasts for the proposed future large circular colliders, CEPC [12] and FCC-ee [13, 14], recent experience during

the commissioning of SuperKEKB [15], and lessons from DAFNE [16] and PEP-II [17].

Concerning classical wake fields and instabilities, in the transverse plane the resistive-wall driven coupled-bunch instability is of greatest concern [3, 11]. Assuming a fractional betatron tune above an integer, for FCC-ee the expected growth time of the fastest growing mode is about 7 turns, but there are many modes with a growth rate of order 10 turns. Fortunately, advanced transverse feedbacks could control instabilities with a damping time of about 1–2 turns. Such feedbacks can be realized either by using multiple BPMs (“folding the ring”) [9], by doubling or quadrupling the feedback system [10], by multiple feedforward systems, or by a combination thereof.

Longitudinally, the potential single-bunch microwave instability driven by the broadband impedance appears to be the most dangerous effect [3, 11]. In addition to the resistive wall, the broadband impedance contains noticeable contributions from the RF cavities, photon stops, etc.

Indeed, many elements are contributing to the total impedance, both transversely and longitudinally. First models of total wake fields are available for FCC-ee and CEPC [3, 11]. Experience from the light sources suggests, however, that reality often differs from expectation [4].

When operating with high beam current and/or with short bunches higher-order mode (HOM) heating and HOM driven instabilities need to be controlled [5]. HOM heating destroyed numerous beam-pipe components at PEP-II and at many other storage rings. A particular topic of ongoing research is HOM excitation around the interaction point [8], where — depending on the various beam-pipe dimensions — a cavity-like object may be formed.

Nowadays powerful codes are available for solving Maxwell's equations inside the beam pipe. Such codes can compute the combined effects of synchrotron radiation, space charge, and wake fields [5].

The electron cloud is a potential threat to positron beams, especially for the Z-pole operation of FCC-ee [6, 8], where even the photoelectrons created by a single bunch passage yield an average electron density above the single-bunch instability threshold. Electron cloud is still an issue for SuperKEKB despite numerous countermeasures incorporated in the design [7], and even after installing additional permanent magnets in the short uncoated aluminium bellows chambers. One reason is that the TiN coating applied for most of the vacuum chambers has proven insufficient to reduce the secondary emission yield to the required low level. A potential, highly efficient cure for future and present machines is the laser surface treatment LASE developed in the UK [2], which can dramatically reduce the secondary emission yield.

* This work was supported in part by the European Commission under the FP7 Capacities project EuCARD-2, grant agreement 312453.

[†] frank.zimmermann@cern.ch

Ion-driven multi-bunch instabilities are being experienced by the SuperKEKB electron beam [7]. First predictions of ion instabilities are available for the FCC-ee [6].

RESISTIVE-WALL INSTABILITY

Due to the large circumferences, one of the most important transverse instabilities for FCC-ee and CEPC is the coupled-bunch instability driven by the resistive wall of the beam pipe. The transverse resistive-wall impedance scales linearly with the circumference, and also with the inverse cubic power of the beam-pipe radius. A small beam pipe is preferred, however, so as to limit the electrical power consumption of the arc magnets. Figure 1 shows the fast rise time for FCC-ee when running on the Z pole, and its dependence on the fractional tune. The right picture reveals that not only a few, but many of the multi-bunch modes exhibit significant growth rates.

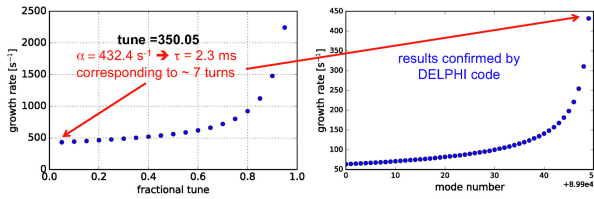


Figure 1: Growth rate of fastest rising mode in FCC-ee, at the Z pole, as a function of fractional tune (left) and growth rate versus coupled-bunch mode number for a betatron tune just above the integer (right) [3] (M. Migliorati). Only the effect of the resistive wall is considered.

ACTIVE INSTABILITY CONTROL

The coupled-bunch instabilities driven by resistive wall, electron-cloud and residual-gas ions can be controlled by active damper systems. Expressed in number of turns the fastest rise times seem short, e.g. less than ten turns, even if in terms of actual time the instabilities are not faster than those in existing machines. Advanced configurations, shown in Fig. 2, can achieve the desired damping times, e.g. multiple BPMs (folding the ring) [9], multiple feedback systems [10], or feedforward systems, based on fast data transfer across the ring [10].

LONGITUDINAL SHORT-RANGE WAKE

The longitudinal short range wake field drives the microwave instability. It has been computed for CEPC and FCC-ee taking into account various contributions. Impedance ingredients for CEPC are illustrated in Fig. 3. The wake fields expected for CEPC and FCC-ee are of similar order of magnitude; see Fig. 4.

MICROWAVE INSTABILITY

The microwave instability is a threat in the longitudinal plane. The longitudinal resistive wall impedance alone already has a large effect on the beam dynamics.

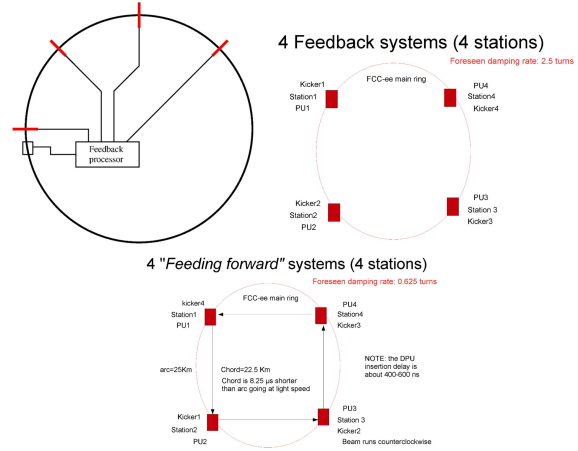


Figure 2: Various damper systems controlling fast coupled-bunch instabilities with a damping time of either a few turns or even less than a turn: (top left) feedback based on multiple BPMs [9] (D. Teytelman), (top right) multiple feedback systems [10] (A. Drago), and (bottom) multiple feed-forward systems [10] (A. Drago).

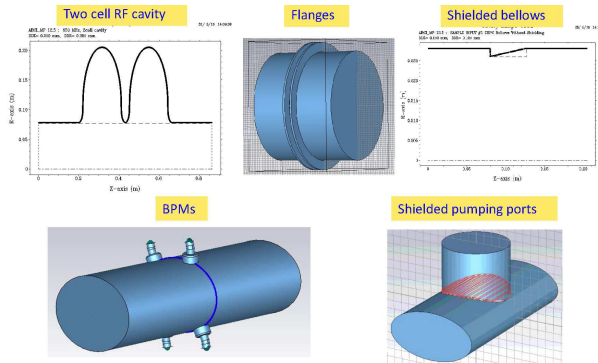


Figure 3: Beam-pipe elements included on the geometric impedance model for CEPC [11] (N. Wang).

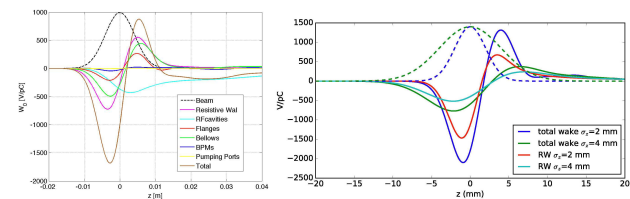


Figure 4: Short-range wake field for CEPC [11] (left) and FCC-ee [3] (right). The CEPC wake field considers contributions from resistive wall, 384 RF cavities, 10,000 flanges, 2300 BPMs, 10,000 bellows, and 10,000 pumping ports [11] (N. Wang). The FCC-ee wake field comprises effects of resistive wall, 10,000 optimized photon stops, 400-MHz RF cavities, and 4,000 double tapers for quadrupoles and BPMs [3] (M. Migliorati).

Figure 5 shows bunch lengthening and energy spread as a function of bunch population for the FCC-ee. The sudden increase in energy spread is the hallmark of the microwave instability. The threshold from a Vlasov-Fokker-Planck solver [18] is slightly above the threshold obtained from the criterion of Ref. [19].

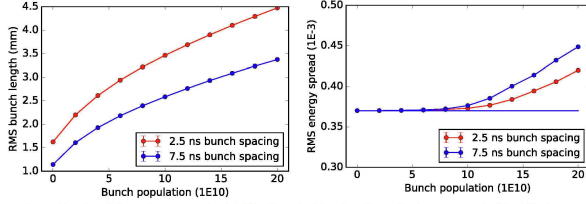


Figure 5: Bunch length (left) and energy spread (right) for two running modes of FCC-ee on the Z pole, as computed by a Vlasov-Fokker-Planck solver [3] (M. Migliorati).

For CEPC Higgs running the Boussard-Keil-Schnell threshold prediction is slightly below the design current, while for operation on the Z pole it is almost 3 times below the design [11]. The potential difficulty is further supported by numerical solutions of the Haissinski equation, which no longer seem to converge at bunch currents close to the Boussard-Keil-Schnell threshold, which is taken as an indication of microwave instability; see Fig. 6.

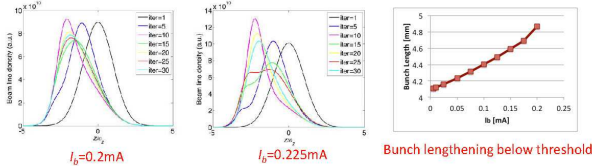


Figure 6: Numerical solution of Haissinski equation for different iterations below (left) and above the microwave threshold (right) [11] (N. Wang).

The onset of the microwave instability appears as an increase in the energy spread. The corresponding change of bunch length often is not easily visible and superimposed on the inductive bunch lengthening. The instability might have complicated character with several thresholds corresponding to different modes of instability. These features are illustrated in Fig. 7.

IMPEDANCE MEASUREMENTS

Impedances can be measured in a variety of ways, as is indicated in Table 1.

A comparison of calculated and measured impedances for various storage-ring light sources is presented in Fig. 8. This comparison suggests that the longitudinal impedance often is smaller than expected, while the measured transverse impedance frequently is larger than computed.

ISBN 978-3-95450-187-8

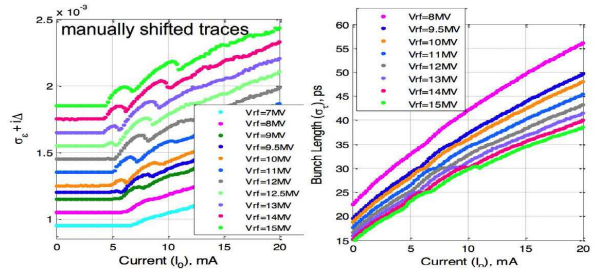


Figure 7: Energy spread and bunch length at NSLS-II, obtained from a Vlasov-Fokker-Planck solver (SPACE code), versus bunch current revealing multiple thresholds of microwave instability [4, 20] (V. Smalyuk).

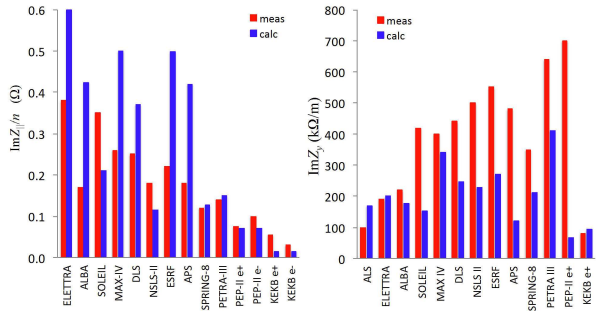


Figure 8: Longitudinal (left) and transverse impedance (right) measured at various light sources compared with the calculated values [4] (V. Smalyuk).

HIGHER-ORDER MODES

Many storage rings operating at high beam current and/or with short bunches have suffered from heating of beam-line components due to higher-order mode (HOM) excitation.

A simple estimate of the loss factor for an obstacle of transverse size Δr in a pipe of radius $r = a$ is [5]

$$k \sim \frac{Z_0 c}{2\pi^{3/2} \sigma_z} \frac{\Delta r}{a}, \quad (1)$$

with σ_x denoting the rms bunch length and Z_0 the vacuum impedance. or a bunch length of 1 mm, radius 10 mm, and obstacle size 1 mm, the loss factor is about 0.1 V/pC.

The higher-order mode power itself can be estimated as [5]

$$P_{HO} \approx \tau_b k I_b^2, \quad (2)$$

where τ_b denotes the bunch spacing, and I_b the total beam current. At a bunch spacing of 2.5 ns, and a current of 2 A the above small loss factor would already result in an HOM power of 1 kW [5].

Example images of the resulting damage at PEP-II are shown in Fig. 9.

If the vertex-detector chamber at the interaction point has a larger size than the incoming and outgoing beam pipes a cavity-like geometry is formed, in which trapped higher-order modes can exist, potentially leading to unwanted, and possibly dangerous heating. Figure 10 presents a calculation of the real part of the impedance for this beam-pipe region,

Table 1: Impedance measurement techniques at light sources [4] (V. Smalyuk).

impedance	measurable effects	instrumentation
longitudinal broadband impedance	bunch lengthening, synchronous phase shift, dispersive orbit distortion, energy spread increase	streak camera, dissector tube, beam-position monitors, RF system diagnostics, pin-hole X-ray camera, synchrotron light monitor
transverse broadband impedance	coherent betatron tune shift, chromatic head-tail damping, orbit distortion (bump method)	beam-position monitors, pinger
transverse narrowband impedance	mode growth / damping of transverse coupled-bunch instabilities	bunch-by-bunch feedback system

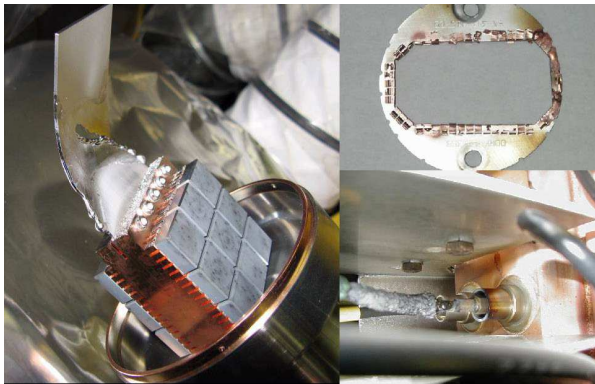


Figure 9: Images of PEP-II spoiler, RF shield and beam-position monitor damaged by higher-order mode heating [5] (A. Novokhatski).

revealing a large number of TM modes in the critical frequency range between 5.74 GHz (cutoff for 20 mm radius) and 9.57 GHz (cutoff for 12 mm radius).

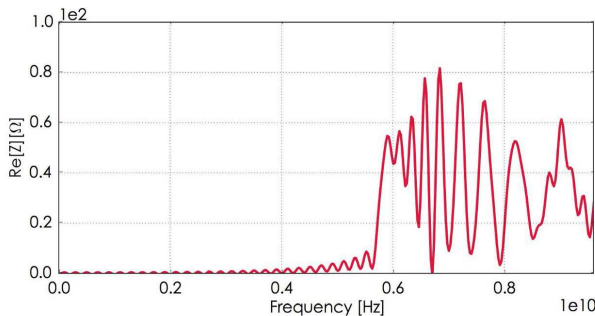


Figure 10: Real part of the longitudinal impedance for the FCC-ee interaction-region chamber as a function of frequency [8] (E. Belli).

ELECTRON-CLOUD EFFECTS

Serious electron cloud effects have been seen in the commissioning phase 1 of SuperKEKB despite a variety of countermeasures incorporated in the design (ante-chambers,

TiN coating, grooved chambers, clearing electrodes). As in KEKB a vertical blow up is observed above a certain threshold of bunch current normalized to bunch spacing.

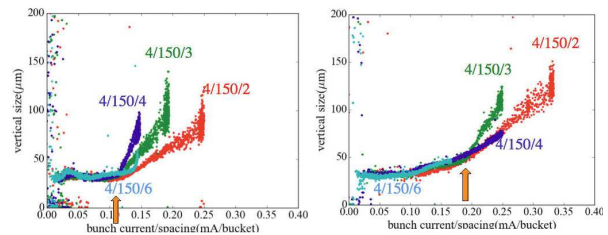


Figure 11: Vertical beam size as a function of bunch current over spacing before (left) and after the installation of permanent magnets around the uncoated bellows chambers (right) [7] (H. Fukuma).

During the phase 1 of SuperKEKB beam commissioning, the installation of permanent magnets (such as to produce a longitudinal “solenoid-like” magnetic field) in the 5% of the ring without TiN coating increased the threshold current of the vertical beam-size blow up by about a factor of two, as is shown in Fig. 11.

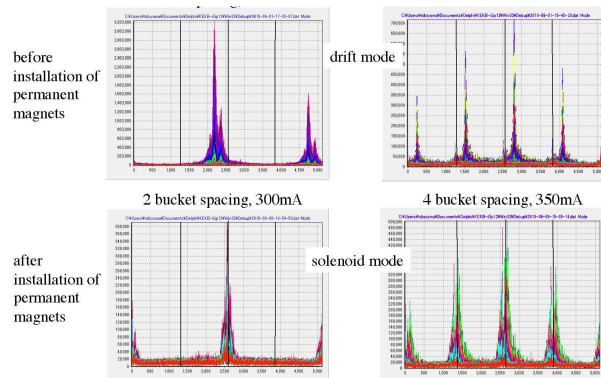


Figure 12: Vertical sideband spectra before (top) and after the installation of permanent magnets in the uncoated bellows chambers (bottom), with two (left) and four bucket bunch spacing (right) [7] (H. Fukuma).

Also the vertical sideband spectrum changed after the installation of the permanent magnets, hinting at a different dynamics of the residual electron cloud (Fig. 12). Significant electron cloud remains in the TiN coated aluminium beam pipe with ante-chamber, which is held responsible for the observed beam-size blow up, based on observations and coincidences like those in Fig. 13.

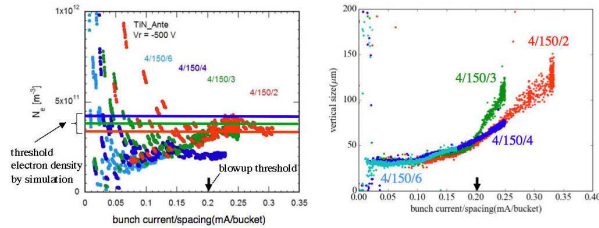


Figure 13: Electron density measured in a TiN coated chamber (left) and vertical beam size (right) as a function of bunch current per bunch spacing, recorded after the installation of permanent magnets in the uncoated bellows chambers [7] (H. Fukuma).

The numbers in Fig. 14 indicate that electron-cloud effects can be a severe issue for the future large circular colliders, especially for the Z-pole running with 2.5-ns bunch spacing at FCC-ee, where the photoelectrons created during the passage of a single bunch may exceed the threshold value for the electron-driven single-bunch instability (value in red).

		CEPC	TLEP-Z	TLEP-W	TLEP-H	TLEP-t
Circumf	C (km)	54	100	100	100	100
Energy	E (GeV)	120	45.5	80	120	175
No. bunches	N_b	49	90300	5162	770	78
Bunch pop	N_p (10^{11})	3.8	0.33	0.6	0.8	1.7
Beam l-density	λ ($10^{10}m^{-1}$)	0.74	3.0	0.3	0.06	0.0013
Beam size (av.)	σ_x/σ_y (μm)	583/32	95/10	164/10	247/11	360/16
Bunch length	$\sigma_{z,tot}$ (mm)	2.6	5.0	3.0	2.4	2.5
Synch. tune	ν_s	0.18	0.015	0.037	0.056	0.075
γ prod. rate	N_{γ} ($/m/e^-$)	0.28	0.059	0.10	0.16	0.23
e prod. rate	$n_{e,prod}$ ($10^{10}m^{-1}$)	1.1	0.020	0.062	0.12	0.39
Electron freq.	$\omega_e/2\pi$ (GHz)	137	127	171	174	171
Electron osci.	$\omega_e\sigma_{z,tot}/c$	7.5	13	11	8.7	9.0
Thr. density	$\rho_{e,th}$ ($10^{10}m^{-3}$)	104	0.78	3.4	7.7	15
Tune shift	$\Delta\nu$ at $\rho_{e,th}$	0.034	0.0025	0.0061	0.0092	0.012

Figure 14: Parameters related to electron-cloud instability [6] (K. Ohmi).

Laser Ablation Surface Engineering (LASE) on a metal surface is a viable solution for reducing the maximum secondary emission yield δ_{max} to values well below 1.0 [2]. Even the initial (unconditioned) $\delta_{max} = 0.93$ for LASE-treated stainless steel is low enough to suppress the electron-cloud build up in machines like the SPS, HL-LHC, or FCC, etc. LASE reduces the secondary emission yield through a combination of two geometrical effects, which can be varied by modifying relevant LASE parameters. Surface resistance measurements indicate that the LASE-produced so-called “shallow groove type with superimposed nano-sphere” is the preferred solution.

ISBN 978-3-95450-187-8

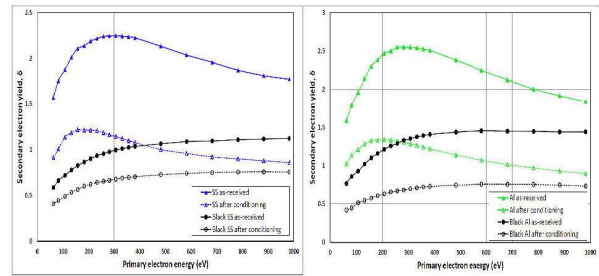


Figure 15: Measured secondary emission yield with and without LASE treatment before and after conditioning: stainless steel (left) and copper (right) [2] (R. Valizadeh).

Another possible mitigation of electron-cloud build up is adding gaps in the bunch train. The resulting reduction of electron-cloud heat load is illustrated in Fig. 16.

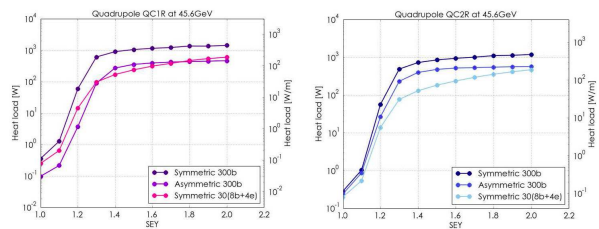


Figure 16: Simulated electron-cloud heat load in the final quadrupoles of FCC-ee, under various conditions, showing the beneficial effect of adding gaps in the bunch train (E. Belli).

ION INSTABILITY

Trapped or transient ions generated by residual gas ionization can drive electron beams unstable. In order to avoid performance degradation due to such instabilities the vacuum pressure should be below 10^{-8} Pa [6], and, in addition, for FCC-ee a bunch-by-bunch feedback with a damping time of about 10 turns will be required. Ion instabilities have already been observed at SuperKEKB during its commissioning phase 1. The present modelling of ion instability appears quite insufficient: for example, the mode spectrum observed at SuperKEKB would be consistent with expectations for a rigidly moving ion cloud much larger than the electron beam, i.e. $\sigma_{i,y} \approx 40 \times \sigma_{y,e}$. A related outstanding question is how ions are (partially) cleared in the abort gap with a duration of a few microseconds. Despite the remaining puzzles, K. Ohmi concluded that the ion instability does not seem to be serious (for present and future colliders) if a good vacuum pressure is realized [6].

REFERENCES

- [1] Joint ICFA/EuCARD-2 Workshop on future circular electron-positron factories “eeFACT2016”, Cockcroft Institute, Daresbury, 24–27 October 2016; <https://eventbooking.stfc.ac.uk/news-events/eeFACT2016-349>

- [2] R. Valizadeh, “Low SEY Engineered Surface for Electron Cloud Eradication,” presented at eeFACT216, Cockcroft Institute, Daresbury, 23-27 October 2016 [1].
- [3] M. Migliorati et al., “Collective Effects Issues for FCC-ee,” Proc. eeFACT216, Cockcroft Institute, Daresbury, 23-27 October 2016 [1].
- [4] V. Smalyuk, “Impedance Measurement Techniques and Lessons from Light Sources,” Proc. eeFACT216, Cockcroft Institute, Daresbury, 23-27 October 2016 [1].
- [5] A. Novokhatski, “Coherent Wave Excitation in a High Current Storage Ring,” Proc. eeFACT216, Cockcroft Institute, Daresbury, 23-27 October 2016 [1].
- [6] K. Ohmi, “Electron Cloud and Fast-ion Instability plus Mitigation Methods for Future Factories,” Proc. eeFACT216, Cockcroft Institute, Daresbury, 23-27 October 2016 [1].
- [7] H. Fukuma, “Electron Cloud at SuperKEKB,” Proc. eeFACT216, Cockcroft Institute, Daresbury, 23-27 October 2016 [1].
- [8] E. Belli, “Electron Cloud and Collective Effects in the Interaction Region,” Proc. eeFACT216, Cockcroft Institute, Daresbury, 23-27 October 2016 [1].
- [9] D. Teytelman, “An Overview of Active Coupled-bunch Instability Control,” Proc. eeFACT216, Cockcroft Institute, Daresbury, 23-27 October 2016 [1].
- [10] A. Drago, “Feedback Experience at DAFNE,” Proc. eeFACT216, Cockcroft Institute, Daresbury, 23-27 October 2016 [1].
- [11] N. Wang, “Instability issues in CEPC,” Proc. eeFACT216, Cockcroft Institute, Daresbury, 23-27 October 2016 [1].
- [12] A. Apyan et al., “CEPC-SPPC Preliminary Conceptual Design Report,” IHEP-CEPC-DR-2015-01, IHEP-AC-2015-01 (2015).
- [13] M. Benedikt, F. Zimmermann, “Towards Future Circular Colliders,” Journal Korean Physical Society 69 (6), 893–902 (2016).
- [14] FCC web site <http://cern.ch/fcc>.
- [15] SuperKEKB web site <http://www.superkekb.kek.jp>
- [16] DAFNE web site <http://www.lnf.infn.it/acceleratori>
- [17] J. Seeman, “Last Year of PEP-II B-Factory Operation,” Proc. 11th European Particle Accelerator Conference, Genoa, Italy, 23–27 June 2008 (2008).
- [18] R. Warnock and J. Ellison, “A General Method for Propagation of the Phase Space Distribution, with Application to the Sawtooth Instability,” presented at 2nd ICFA Advanced Accelerator Workshop on the Physics of High Brightness Beams, University of California, Los Angeles, 9–12 November 1999, SLAC-PUB-8404 (2000).
- [19] K.L.F. Bane, Y. Cai, G. Stupakov, “Comparison of Simulation Codes for Microwave Instability in Bunched Beams,” Proc. IPAC 2010 Kyoto, 23–28 May 2010 (2010) p. 2096.
- [20] G. Bassi, A. Blednykh, and V. Smaluk, “Self-consistent simulations and analysis of the coupled-bunch instability for arbitrary multibunch configurations,” Phys. Rev. Accel. Beams 19, 024401 (2016).

SUMMARY OF MACHINE TUNING SESSION*

M. E. Biagini[†], INFN, Laboratori Nazionali di Frascati, Frascati (RM), Italy*Abstract*

This paper summarizes the work presented at the Machine Tuning session on the low emittance tuning for low emittance lattices and luminosity tuning at colliders.

SESSION TALKS

Optics correction is a key tool to achieve desired performances in an accelerator. It is very important to have a good lattice model so to be able to operate on the real machine in a reliable way. Unavoidable magnet errors, such as displacements, tilts or field errors, will affect the closed orbit, H-Y betatron coupling, H-V dispersion, H-V emittance. Their correction is crucial for reaching the design performances. Beam polarization is also heavily affected by errors, as shown in [1]. For the new generation of e^+e^- accelerators, where low emittance beams are needed to achieve the design luminosity, this is a very important topic to be addressed and solved.

Five talks have been presented on Optics correction (for LHC and SuperKEKB), Errors correction (for FCC-ee) and Luminosity tuning (for KEKB):

1. A. Langner (CERN), “Optics correction at large accelerators”,
2. Y. Ohnishi (KEK), “Optics correction and low emittance tuning at the Phase 1 commissioning of SuperKEKB”,
3. Y. Funakoshi (KEK), “Luminosity tuning at KEKB”,
4. S. Sinyatkin (BINP), “FCC lattice with errors and misalignment”,
5. S. Aumon (CERN), “Coupling and dispersion correction in FCC-ee”.

ERRORS SIMULATION

Errors simulations are needed in order to provide a model of what can be the *real* accelerator. The impact of different errors, such as magnet misalignments, magnet field errors, magnet tilts, BPM gain and position errors, have to be modelled to be able to perform corrections and prepare the online tools needed when running. Also, tolerances to these errors should be computed, in order to set up what are the requirements for the accelerator alignment and magnets quality. Most of the errors are impacting betatron coupling and vertical dispersion, which are particularly important to minimize since modern accelerators, both colliders and synchrotron light sources, aim to very low emittances in both planes.

For the FCC-ee project a study of the errors and misalignments at 175 GeV [2] showed that in the Arcs quadrupoles need to be aligned at 100 μ . Final Focus (FF) quadrupoles were studied separately, due to the high gradients

and β -functions behaviour in the Interaction Region (IR). For these elements there is a strong vertical dispersion excitation due to errors. A tolerance of 25 μ to quadrupole misalignments has been found. This seems a very low value that must be checked with the alignment experts. The use of MADX code turned out not to be ideal for this study since is time consuming and in presence of errors it was difficult to find the closed orbit for a displacement of 100 μ in Arc quadrupoles. However, after closed orbit, betatron coupling and vertical dispersion correction the average ratio between the vertical and horizontal emittances was reduced from an initial 15% to a final 1.4%, as shown in Fig.1 below.

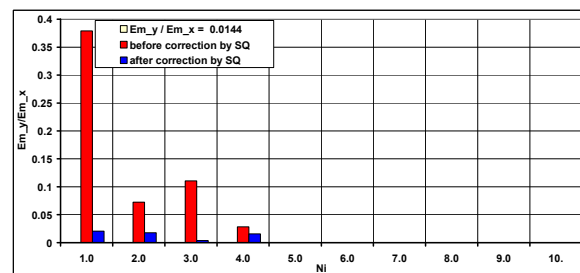


Figure 1: Emittance ratio as a function of optics correction iterations (in red before, in blue after correction).

Another study of betatron coupling and vertical dispersion correction for the FCC-ee 175 GeV [3] was presented. The energy losses in the Arcs at 175 GeV are so large (the so called saw-tooth effect) that a tapering of dipoles, quadrupoles and sextupoles fields is needed. However, this is an expensive requirement, so a study was performed to see if closed orbit correction was still possible by tapering dipoles only, so called “sector-wise” method. The lattice studied was a racetrack type with a “LEP-like IR” with sector-wise tapering. This scheme has shown to have some issues. A quadrupole misplacement tolerance of 20 μ in quadrupoles (here the FF quadrupoles are included in the simulation) has been found after a combination of dispersion free steering and Interaction Point (IP) betatron coupling correction. Fig. 2 shows the dependence of vertical emittance from quadrupole misalignments for this lattice. Future work will be needed to implement the real lattice and full magnets tapering.

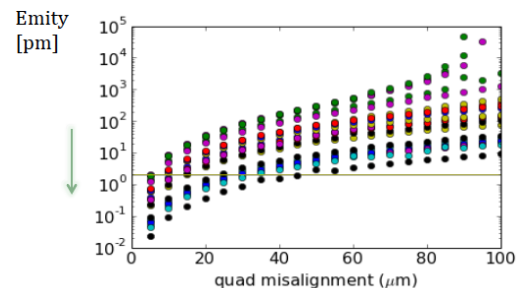


Figure 2: Vertical emittance vs quads misalignments.

* Work partly supported by European Commission, GA 312453

[†] email address

marica.biagini@lnf.infn.it

ERRORS CORRECTION

Errors correction on a running accelerator makes use of different tools and techniques in order to achieve desired performances. The knowledge of the *real* machine and a good model to reproduce the measurements are the key points for successful running.

LHC

An example of how this was implemented at the LHC [4] was shown. The errors correction procedure was continuously improved during the running years. A new turn-by-turn phase advance measurement procedure for the derivation of the β -functions was used, which analyse the data not only at 3 adjacent BPMs, as usually done [5], but considers N number of BPMs in order to improve accuracy and precision. This technique was also used at ALBA and ESRF light sources [6]. Also, a segment-by-segment technique, based on local correction performed via comparison of measured phase advances and optics simula-

tions, was implemented. The resulting β -beating was corrected to about 5%. A waist shift of the IP β -function was observed in 2015 and corrected including gradient modulation measurements in the local correction procedure. The results of errors correction and optics improvements during the running of the LHC are shown in Figs. 3 and 4 below. This shows how continuous work on optics and model understanding is very important to improve the collider performances.

	Beam 1		Beam 2		Year	Energy (TeV)	β^* (cm)
	x	y	x	y			
peak	9 ± 1	9 ± 1	7.0 ± 0.6	6.7 ± 1.7	2012	4.0	60
$\frac{\Delta\beta}{\beta}$ (%)	9.6 ± 1.6	5.0 ± 1.0	11.2 ± 1.1	6.8 ± 1.2	2015	6.5	40
	7.8 ± 0.7	4.5 ± 0.7	5.0 ± 0.4	4.2 ± 0.3	2016	6.5	40
rms	2.6	2.3	2.4	2.2	2012	4.0	60
$\frac{\Delta\beta}{\beta}$ (%)	3.2	1.7	4.0	2.0	2015	6.5	40
	1.6	1.4	1.6	1.5	2016	6.5	40

Figure 3: β -beating correction results over the years.

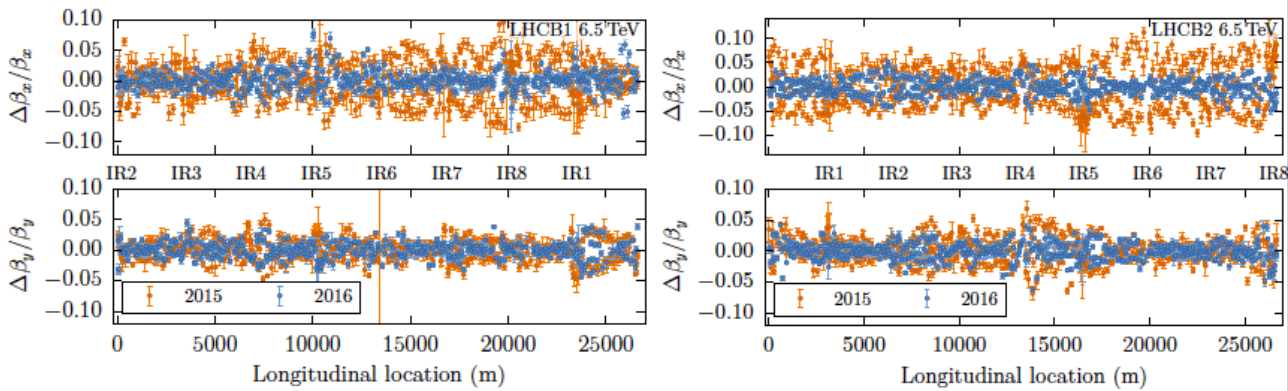


Figure 4: β -beating correction results for LHC Beam 1 (left) and Beam 2 (right).

SuperKEKB

The Phase-1 SuperKEKB accelerator was commissioned in the first 6 months of 2016. In this configuration the two beam did not collide, and beam pipe scrubbing and optics tuning was the main goal. Techniques and tools were the same developed for KEKB B-Factor.

After careful closed orbit and betatron coupling correction, a residual deviation was measured at the location of the Lambertson septum, used for the beam abort system. Leaking field from the septum was exciting residual X-Y coupling. Having spotted the problem, the installation of permanent skew quadrupoles at the septum location has allowed for a satisfactory coupling correction, see Fig. 5.

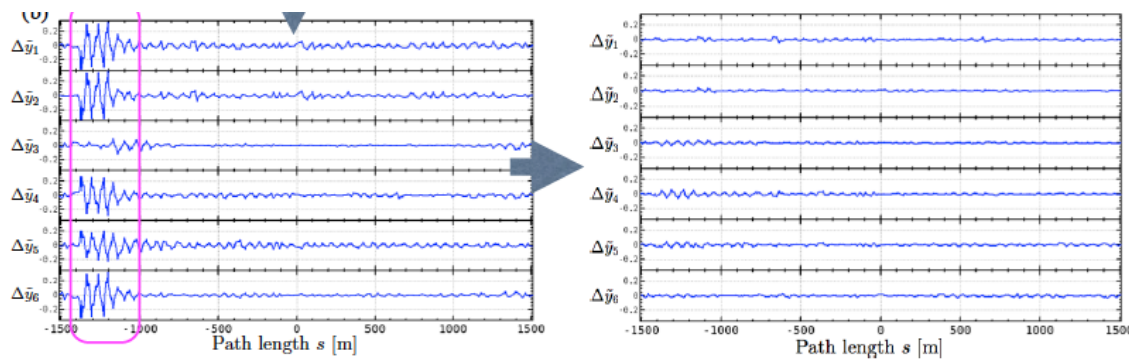


Figure 5: Example of X-Y coupling correction after installation of skew quadrupoles near the Lambertson septum.

Optics correction has worked very well and a vertical emittance of 8 pm has been achieved in the LER after beam-based alignment, optics correction, installation of additional skew quadrupole coils at the focusing sextupoles, and of permanent skew quadrupoles at the Lambertson septum. The evolution of the emittance and dispersion tuning is shown in Fig. 6 below.

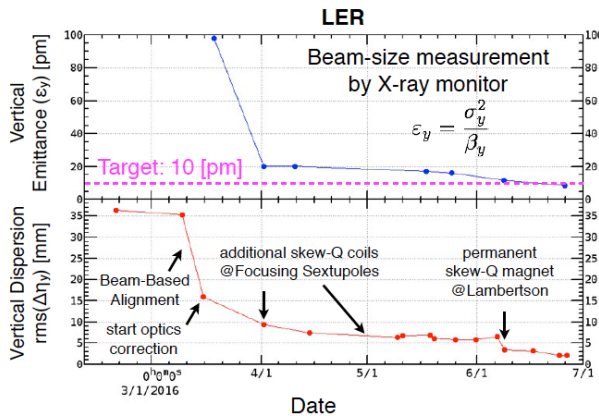


Figure 6: Vertical emittance and dispersion correction in LER.

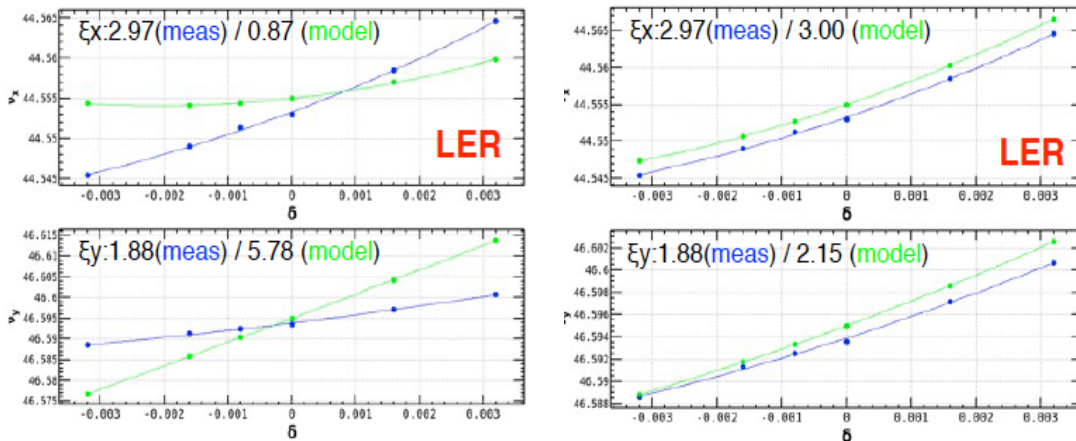


Figure 7: Chromaticity measurements compared to model before (left) and after (right) chromatic phase-advance correction in SuperKEKB LER.

The HER emittance measurement was affected by the performances of the synchrotron X-ray monitor and is far from the model value estimated from the β -function measurements, in spite of the goodness of orbit, dispersion and coupling correction. This problem is still to be addressed.

A large discrepancy was found when comparing chromaticity measurements with model for the LER (see Fig. 7, left plot), while for the HER the values were in good agreement. The problem was found to be due to the not well corrected off-momentum optics, a problem already observed and corrected in KEKB. The source of this off-momentum optics distortion is assumed to be a deviation in the sextupoles field. A few percent correction of the sextupoles settings, computed through an off-momentum phase-advance response matrix technique, was able to correct the discrepancy quite well (see Fig. 7, right plot). Understanding the off-momentum optics is very important and needed for the optimization of the dynamic aperture.

LUMINOSITY TUNING

Luminosity tuning at KEKB was described [6]. During the 20 years of operation the luminosity was increased by performing many and continuous parameter scans. These were routinely done by the operation team, even during physics run. In most of cases, these scans were not efficient, but sometimes an improvement in the luminosity was obtained, so it was very important to continue this luminosity tune-up. The introduction of a downhill simplex method speeded up the parameter search, however the achievable luminosity was not increased with this method. An enormous amount of effort was devoted to daily tuning to increase the beam-beam parameters, reaching the record values of $\xi_x = 0.09$ in HER and $\xi_y = 0.129$ in LER.

A number of tuning knobs were developed during the KEKB operation. Most of the luminosity tuning used the luminosity monitors and the beam size monitor (SR interferometer) as observables. The reliability of those monitors was important.

One of the reasons of high luminosity at KEKB was the short bunch length, which brought a lower β_y , thanks to the lattice flexibility that allowed for a lower momentum compaction. It was also found in operation that a horizontal tune closer to half-integer gave a higher luminosity, just like other factory colliders.

The continuous injection scheme (top-up injection) made the luminosity tuning easier since there were more stable beam conditions.

It was found that the chromaticity of X-Y coupling parameters (R-parameters) at the IP could degrade the luminosity, if the residual values, which depend on machine

errors, are large. To control the chromaticity, skew sextupole magnets, 10 pairs for HER and 4 pairs for LER, were installed during the winter shutdown in 2009. It turned out that the skew sextupoles are very effective to raise the luminosity. The knobs to control the R-chromaticity were introduced for beam operation on May 2009, and the gain in luminosity by these magnets was about 15~17%.

The continuous beam injection was needed in order to increase the integrated luminosity and keep peak luminosity stable, since the beam lifetimes were short. The gain in integrated luminosity was 30%.

A lot of effort was put in commissioning the crab cavities installed in order to compensate for the horizontal crossing angle at the IP (± 11 mrad), which caused synchro-betatron resonances and decreased the tune space for luminosity optimization. It was expected that the beam-beam parameters and the luminosity would be doubled with the crab cavities. Actually the achieved luminosity gain with crab was about 30~40% including the effect of the skew-sextupoles. The beam-beam parameters were also increased but not as much as expected by simulations. The discrepancy between the simulation and the experiment has not been understood yet. A plot of the luminosity tuning with and without crab cavities is shown in Fig. 8.

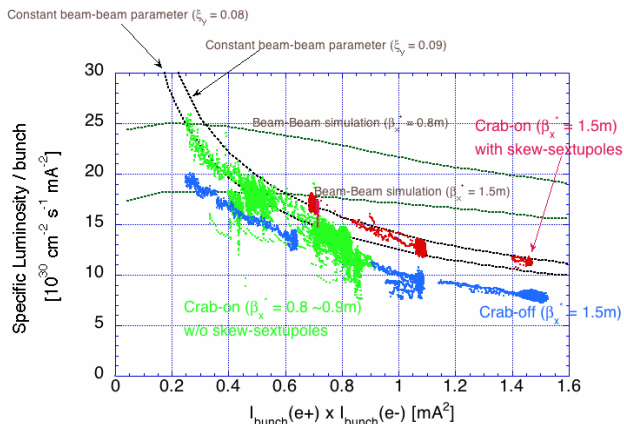


Figure 8: Tuning of luminosity with and without crab cavities.

CONCLUSION

The unavoidable errors in an accelerator (magnet misalignments, field errors, BPMs, ...) must absolutely be corrected in order to achieve design performances such as low emittances and luminosity. Errors affect mostly verti-

cal emittance which is zero in a “perfect” lattice and must be included in the Dynamic Aperture calculation. A number of different tools have been built, at LHC, KEKB and in modern synchrotron light sources, for optics correction on and off-momentum: it is very important the exchange of knowledge between the two communities.

The machine model, built by simulations, must be accurate in order to be able to reproduce the measurements and to perform needed corrections and tuning. Continuous work on optics and model understanding is very important to improve the performances. Turn-by-turn measurements are needed for optimum correction of closed orbit, coupling, vertical dispersion and β -beating.

Understanding the off-momentum optics is also very important and needed for the optimization of the dynamic aperture.

The impact of the high gradient FF quadrupoles has to be taken into account, both for the alignment tolerances, which may result in a particularly low value, and for their influence on the beam emittance growth.

Last but not least is the luminosity tuning is essential to reach and keep the design performances in colliders. The more the available knobs, the easier will be the tune-up.

REFERENCES

- [1] E. Gianfelice-Wendt, presented at eeFACT2016, Daresbury, UK, October 2016, paper MOT4H6.
- [2] S. Sinyatkin, presented at eeFACT2016, Daresbury, UK, October 2016, paper MOT3BH2.
- [3] S. Aumon, presented at eeFACT2016, Daresbury, UK, October 2016, paper TUT3BH4.
- [4] A. Langner, unpublished.
- [5] P. Castro *et al.*, “Betatron Function Measurement at LEP Using the BOM 1000 Turns Facility”, in *Proc. PAC93*, Washington, DC, USA, May 1993, p. 2103.
- [6] A. Langner *et al.*, “Optics Measurement using the N-BPM Method for the ALBA Synchrotron”, in *Proc. IPAC’15*, Richmond, VA, USA, May 2015, paper MOPJE057, pp. 430-433.
- [7] Y. Ohnishi, presented at eeFACT2016, Daresbury, UK, October 2016, paper TUT3BH2.
- [8] Y. Funakoshi, presented at eeFACT2016, Daresbury, UK, October 2016, paper TUT3BH3.

SUMMARY OF BEAM INSTRUMENTATION AND BEAM DIAGNOSTICS SESSION

H. Fukuma[#], High Energy Accelerator Research Organization (KEK), Tsukuba, Japan

Abstract

This report is a summary of the beam instrumentation and beam diagnostics session of the eeFACT2016 workshop.

LIST OF PRESENTATIONS

Talks presented in the beam Instrumentation and beam diagnostics session are:

- Beam Instrumentation Needs for a Future e+e- Collider Based on PEP-II Observations, J. Seeman, SLAC,
- Beam Position Measurements at Synchrotron Light Sources, V. Smalyuk, BNL,
- Beam Instrumentation in SuperKEKB, H. Fukuma, KEK,
- Measurement of Beam Polarization and Beam Energy in One Device, N. Muchnoi, BINP.

SUMMARY OF THE PRESENTATIONS

Beam Instrumentation Needs for a Future e+e- Collider Based on PEP-II Observations

J. Seeman presented needs for various beam measurement requirements and techniques for a future e+e- collider using PEP-II observations.

Future e+e- colliders will operate with many bunches, short bunch lengths, small emittances, high currents, and small beta functions at an interaction point (IP). The stability of the colliding beams with these characteristics will depend on detailed, high precision, and continuous measurements. Since beam parameters of a future e+e- collider are not far from B-factories, observations at PEP-II are useful as a starting point of the discussions.

Various measurement techniques for beam position, beam size, bunch length and beam lifetime were used at PEP-II. IP luminous region parameters such as beam sizes and beta functions were measured using data from PEP-II and BaBar together. Beam instabilities were analyzed and suppressed by the sophisticated bunch-by-bunch feedback system.

HOM generated by the beam with high current and short bunch length causes following serious effects:

- Heating of the vacuum elements
 - Temperature and vacuum rise
 - Chamber deformations and vacuum leaks
 - Decreasing the pumping speed
 - Out gassing

- Multipacting, sparking and breakdowns
 - Vacuum leaks
 - Melting thin shielded fingers
 - Longitudinal instabilities
 - High backgrounds (high radiation level in the detector)
 - Electromagnetic waves outside vacuum chamber
 - Interaction with sensitive electronics
- Many HOM related events such as damage of a cavity tuner and a SiC tile in IR and an overheated vacuum valve occurred at PEP-II. A lot of measurements, for example, an estimation of HOM power from RF power measurements, temperature monitoring and modeling and moderate/fast real-time vacuum pressure monitoring were necessary for identifying damaged parts.

The talk was summarized as:

- Many complicated measurements are needed in a high-power, high-current collider,
- Measure and record versus time as many parameters as possible to diagnose issues,
- Find new innovative measurement techniques,
- Many measurements relate to potential hardware damage to the accelerator,
- Many measurements need to automated and computer monitored to make the accelerator operation safe.

Beam Position Measurements at Synchrotron Light Sources

V. Smalyuk presented beam position measurements at synchrotron light sources mainly based on beam position monitors (BPMs) at NSLS-II.

Modern light sources demand following severe performances for the BPM system:

- Beam stability of 5-10% of the beam size,
- Active interlock system which damps the beam to protect the storage ring and the frontend components from damage by synchrotron radiation if its orbit exceeds the safety limits (e.g. 0.5 mm and 0.25 mrad at insertion devices),
- Fast data transfer and processing for fast orbit feedback systems,
- Flexibility of the system for machine commissioning, lattice optimization and beam studies.

Recent BPM signal processing is mainly based on digital signal processing. A list of BPM signal processing electronics in major light sources shows two third use the Libera digital processor of Instrumentation Technologies, while one third use homemade processors. NSLS-II BPM module is a homemade module whose architecture of analog frontend is based on under-sampling of the signal

#hitoshi.fukuma@kek.jp

ISBN 978-3-95450-187-8

at the 500MHz. An ADC clock is locked to the revolution frequency. Sampling rate of ADC is 310 samplings per turn. Signal processing is “single-bin” DFT calculation at the turn by turn (TbT) rate. BPM resolution reaches about 0.5 μm . Fast orbit feedback is successfully implemented to stabilize orbit oscillation of less than 100Hz. Post mortem data are used to find beam dump sources from, for example, cavity trip, equipment protection system, personnel protection system, power supplies, active interlock and power dips.

Various measurements are possible owing to the TbT digital signal processing. In order to measure the lattice parameters (e.g. betatron tunes, chromaticity, betatron functions and corrector orbit response) so as not to affect the effective beam size enlargement, a small controlled sinusoid disturbance is given to the beam using an actuator such as a strip line and a corrector magnet, and then this frequency component in a data stream (bunch-by-bunch position, turn-by-turn position, fast orbit data) is detected using a digital detector. Data are accumulated over a certain measurement period which determines bandwidth and thus measurement noise.

AC LOCO (Linear Optics from Closed Orbits) is an effective technique of lattice correction. Sine wave excites the beam via fast correctors. Simultaneous excitation of many correctors with different frequencies is possible. Recorded is the fast acquisition (10kHz) data. Synchronous detection is applied to get the beam oscillation amplitude. Standard LOCO technique is applied for fitting the measured orbit response matrix to the model by changing quadrupole strengths, BPM gains and rolls and corrector gains and rolls.

Standard BPM signal processing at NSLS-II looks at the entire turn. Applying a time gate to BPM ADC signals results in resolution improvement by factor of 3 to 4. Unique NSLS-II BPM resolves groups of bunches within a turn by the gated turn-by-turn measurement. TbT data for each train kicked with different amplitude are obtained by a single pulse of a kicker. The single-shot method eliminates possible errors of amplitude dependent tune shift measurements caused by machine drift or jitter.

The reason why the homemade processor instead of commercial processors was adopted at NSLS-II was asked in the discussion session. The answer was that the points choosing the homemade processor were a flexibility to modify the firmware and a cost.

Beam Instrumentation in SuperKEKB

H. Fukuma presented an introduction of instrumentation of SuperKEKB and its performance at phase 1 operation which has just finished in this June.

New narrowband BPM detectors with a detection frequency of 509 MHz have been developed and used together with KEKB detectors. Gain calibration and beam based alignment of BPMs was successfully done using the narrowband system in phase 1 operation.

About 270 gated turn by turn detectors (GTBTs) are to be installed at selected BPMs to measure the optics during collision. A non-colliding pilot bunch is kicked by

the bunch-by-bunch feedback system and then the GTBT measures turn by turn position of the pilot bunch using a fast gate to select the signal of the pilot bunch. In phase 1 operation without beam collision, 117 GTBTs were installed and used for injection tuning, measurement of orbit oscillation and measurement of damping of coherent oscillation.

A special wideband detector is to be installed at four BPMs closest to the IP for orbit feedback to maintain stable collision. A prototype model was tested in phase 1 operation.

A bunch-by-bunch feedback system is upgraded using low noise frontend electronics and new 12 bits iGp digital filters which were developed under US-Japan collaboration (KEK-SLAC). The longitudinal feedback system prepared in LER consists of four DAFNE type kickers, with 2-input and 2-output ports in order to get larger capture range. Observed transverse and longitudinal instabilities in phase 1 operation were successfully damped by the feedback system. The measured damping time of the transverse feedback system was about 0.5ms in both rings.

Three kinds of photon monitors, an x-ray beam size monitor (XRM), a visible synchrotron radiation monitor (SRM) and a large angle beamstrahlung monitor (LABM) are installed in SuperKEKB. The XRM uses coded aperture imaging to measure the vertical beam size. Light from an object is modulated by a mask. The resulting image is calculated through mask response including diffraction and spectral width by Kirchhoff integral over mask for various beam sizes to make a template assuming a Gaussian profile. The beam size is determined by a template fit to the measured image. The vertical size measurement by the XRM in LER in phase 1 operation showed good fill-to-fill repeatability and good agreement between different masks.

The LABM detects beamstrahlung radiation which is the radiation of particles of one beam due to the bending force by the electromagnetic field of the other beam. Beamstrahlung polarization at specific azimuthal points provides information about the beam-beam geometry. The LABM in SuperKEKB is being built mainly in US, mostly at Wayne State University.

In the discussion session a possibility to obtain the non-Gaussian beam profile by arrangement of the measurement system such as masks and filters was pointed out.

Measurement of Beam Polarization and Beam Energy in One Device

N. Muchnoi presented a possibility to measure beam polarization and beam energy in one device. Inverse Compton scattering (ICS) of laser radiation is a currently available reliable method for beam polarization measurement and energy determination. The future high energy lepton colliders require polarized beams and polarimetry, especially for application of resonant depolarization technique for precise beam energy calibration at circular machines.

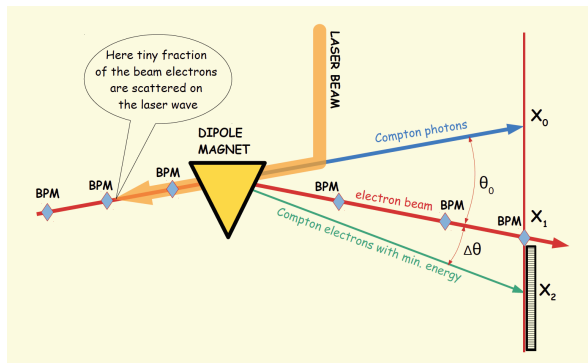


Figure 1: Conceptual layout of the measurement of beam polarization and beam energy.

The proposed method is to measure a 2-dimensional electron distribution of ICS instead of measuring a photon distribution. Compton polarimeters usually deal with scattered photons. At higher electron energies, since the divergence of γ -ray beam is small and high energy synchrotron radiation photons appear, it is reasonable to look at the scattered electrons. One good point is the dimension of the angular distribution of scattered electrons does not depend on the beam energy.

Figure 1 shows a layout of the measurement. Analysis of 2-dimensional distribution of ICS electrons allows to measure beam polarization degree and direction as well as the field integral (Bdl) exactly along a beam trajectory in a conventional magnetic spectrometer. A bending angle of Compton electrons with a minimum energy is proportional to the beam energy. The x-y distribution of scattered electrons is the convolution of the ICS cross section and a transverse distribution of electrons in the beam. The polarization and beam energy are obtained by fitting of the angular distribution of the recoil electrons of ICS.

The proposed approach has no limitations in beam energy. It only requires a small value of vertical emittance of the electron beam.

One comment in the discussion session encouraged a proof-of-principle experiment. Another comment recommended finding an available space to install the detector in the ring.

COMMENTS

Followings are my personal comments.

- Demands for new kind of innovative instrumentations in the rings (FCC and CEPC) did not appear in the workshop as far as I listened. And it was not clear for me what instrumentations are sufficient for the rings. Specifications for the instrumentation will become clear as the design of the machines proceeds.
- Information from existing or past colliders is important to discuss the FCC and CEPC

instrumentation. I hope experience at SuperKEKB gives useful information for their design.

- We need to pay attention to the instrumentation in storage ring light sources because its progress is impressive.

ACKNOWLEDGMENTS

I would like to thank all the speakers of the session for giving us interesting and useful information. I would like to also thank the organizers of the workshop for inviting me to the workshop. I learned much in this workshop.

SRF WORKING GROUP SUMMARY *

R. A. Rimmer[†], Jefferson Lab, Newport News, VA, USA.

Abstract

This working group focussed on the status and challenges of superconducting Radio Frequency (SRF) cavities and systems for present and future high luminosity lepton colliders, the so-called “factories”. Submissions covered the state of the art of SRF cavity designs, HOM damping, high power couplers, operational experiences and the needs of future colliders. Active work on similar SRF systems for the electron complex of a future electron ion collider (EIC) was presented. Much of this technology is also useful for next generation high brightness light sources and other applications.

OVERVIEW

The session contained nine talks covering:

- SRF cavities
- High level parameter optimization
- LLRF controls
- Power couplers
- HOM damping
- New materials and processes

The talks were all of a high standard and packed with useful information but all speakers managed to stay on schedule.

SRF CAVITIES

The success of existing high current SRF cavity designs at CESR and KEK-B, figures 1, 2, which continue to operate reliably after many years of service, prove that the technology is mature and can be relied upon for future applications. However the increasing demands for higher voltage, higher currents, better HOM damping, higher efficiency, lower cost and more compact installations is driving the development of new and more specialized designs. These designs expand upon this experience but are increasingly specialized and optimized for different operating scenarios [1]. Table 1 shows the main parameters of the operating scenarios of FCC-ee.

Looking forward to the highest energy future circular colliders such as FCC and CEPC it is clear that:

- One solution doesn't fit all needs.
- Operating at the Z and W (high current, lower energy) needs 1 or 2 cell cavities, probably 400 MHz).
- Operating at the Higgs or Top energy (lower current, higher energy), could probably benefit from multi-cell cavities, higher frequency.

*Authored by Jefferson Science Associates, LLC under U.S. DOE Contract No. DE-AC05-06OR23177.

[†] rarimmer@jlab.org

NEW DESIGNS

New design concepts were shown that are under consideration for the JLab EIC collider rings and cooler ERL [2] and the FCC-ee rings, figures 3-5. In these designs the cavity shape should be optimized to avoid harmful HOMs being resonant with harmonics of the RF frequency, to minimize the HOM power. The number of cells is determined by the maximum power per coupler and the HOM damping requirements. The higher-current machines favour one or two-cell low frequency cavities, while the higher energy lower current machines may use more cells per cavity and higher frequency. Total RF power is capped and therefore the higher energy machines must run at lower current due to synchrotron radiation.

Table 1: Main Parameters of the FCC Operating Modes

	V_tot	n_bunch	I_beam	σ	E_turnloss
FCC-hh	0.032		500		
Z	0.4 / 0.2	30180 / 91500	1450	0.9/1.6	0.03
W	0.8	5260	152	2	0.33
H	3	780	30	2	1.67
t	10	81	6.6	2.1	7.55



Figure 1: CESR-B type 500 MHz cavity cryomodule produced by Industry.

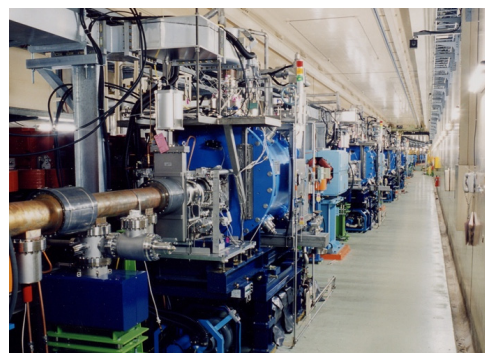


Figure 2: KEK-B type 508 MHz cavity cryostat produced by Industry.

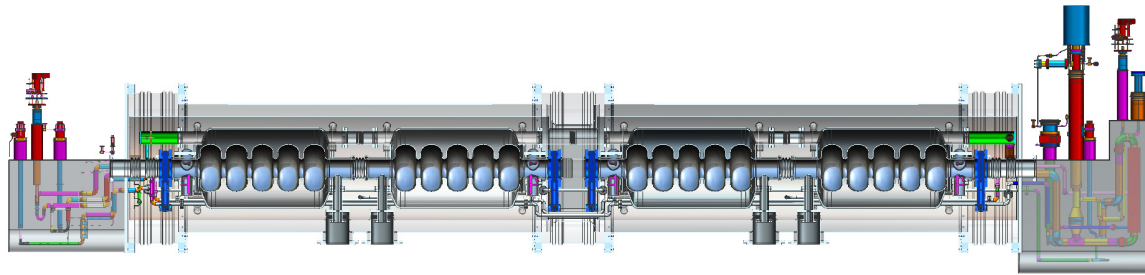


Figure 3: JLab modular cryostat concept. Supply and return end cans and bridging sections are standardised and join together cryounits that can be optimized to hold a variety of cavity types (5-cell ERL cavities illustrated).

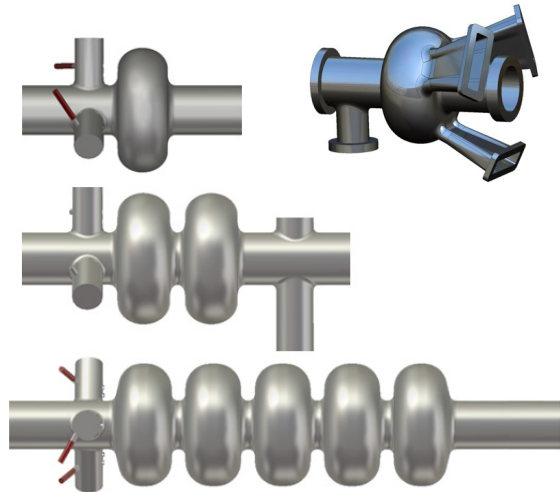


Figure 4: JLab EIC 952.6 MHz concept cavities in single cell, two-cell and five-cell variants, plus single-cell cavity with on-cell damping waveguides.

Modular Cryostat

For the JLab EIC a number of different cavity varieties will be needed including the ion storage ring single-cell cavities (and possibly electron ring cavities) figure 6, crab cavities, figure 7, five-cell cavities for the cooler ERL and single cell cavities for the cooler injector. To avoid having multiple different cryomodule designs it is planned to use a modular concept that can easily accommodate different cavity types with minimal changes. Such a concept could also be useful for other machines. Figure 3 shows the concept.

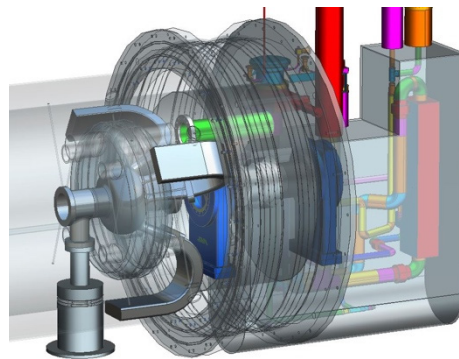


Figure 6: JLab modular cryostat concept with 952.6 MHz "on-cell-damped" cavity. Note the folded waveguides bringing HOM power out to room temperature loads.

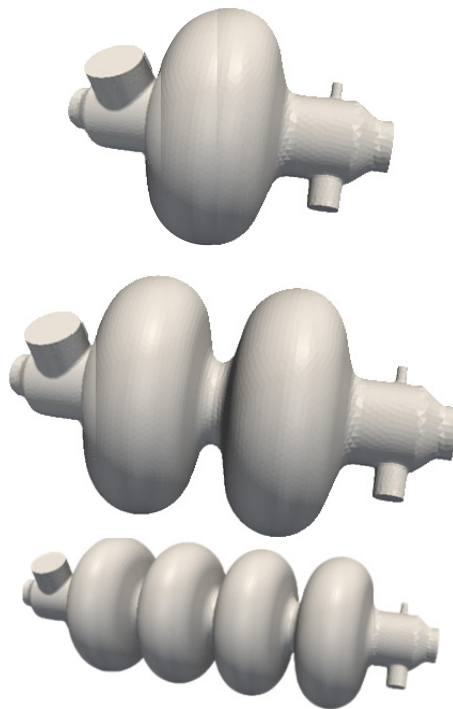


Figure 5: CERN FCC concept cavities in 400 MHz 1-cell, 400 MHz 2-cell and 800 MHz 4-cell varieties.

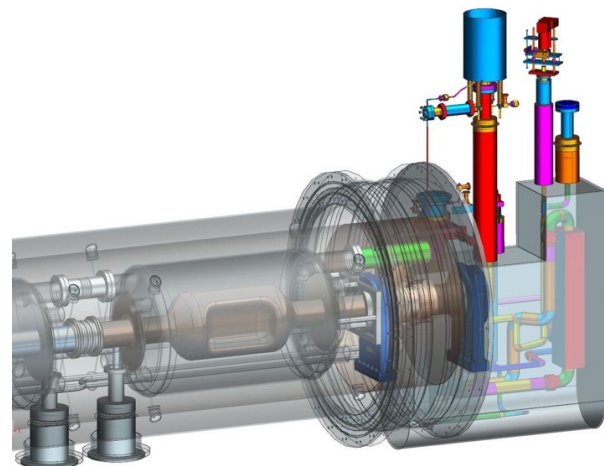


Figure 7: JLab modular cryostat concept with 400 MHz "RF Dipole" crab cavity (HOM dampers not shown).

TECHNOLOGY OPTIMIZATION

The technology choice for each operating scenario is a complex optimization involving many factors as illustrated in figure 8, including as input the beam physics requirements, cost models, expected component performance, efficiencies and experience [3]. Constraints can then be applied including total available wall-plug power or tunnel length, performance limitations such as cavity gradient or coupler power etc. Doing this in a systematic way can quickly eliminate unfavourable technology choices and highlight possible configurations that have either a local optimum or a broader range of applicability. The model can also be quickly updated if any constraint is relaxed as a result of technology development and can highlight which constraints are most limiting and therefore worthy of R&D investment. Applying this methodology to the four FCC-ee scenarios quickly confirms the preference for low frequency and low number of cells per coupler at the Z and W, and the advantage of multi-cells and higher frequencies at the Higgs and Top. The FCC-hh is quite relaxed in comparison and may use the same technology as the Z but with less power required.

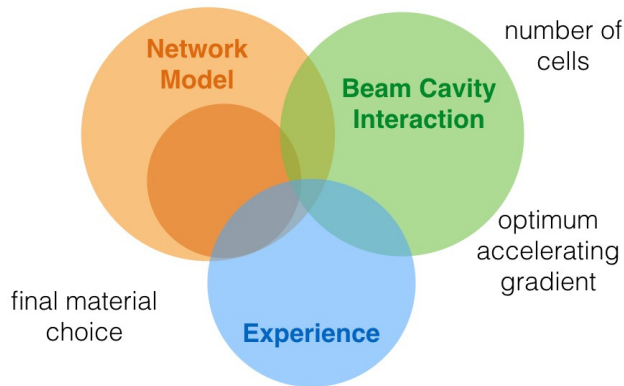


Figure 8: Interplay of factors in determining optimum technology choice.

ENERGY CONSUMPTION

Energy consumption of future large accelerators (FCC, CLIC, ILC, ESS) is in the range relevant for society and public discussion [1]. Figure 9 shows the expected energy consumption for FCC and the expected efficiencies at each stage of conversion. Clearly the biggest loss is in the DC to RF generation stage, where even the best existing high power klystrons have only about 70% efficiency. However recent exciting developments in non-traditional klystron design offer the prospect of raising this above 80 or even 90%. High power magnetrons may also approach these efficiencies and work is under way to test their suitability for SRF accelerator applications.

Cryogenics are another major source of power consumption, however again major steps forward in SRF cavity efficiency have been recently demonstrated with quality factors twice or more higher than the assumed best case for bulk Nb [4]. Figure 10 shows a set of cavity results for the LCLS-II prototype cryomodule in which final N₂ doping was applied directly after H₂ degassing.

Other developments such as Nb₃Sn coated cavities or other new materials may eclipse even these impressive achievements. CEPC is counting on similarly high Q's at both 1.3 GHz and 650 MHz. Table 2 gives the high level operating parameters [4].

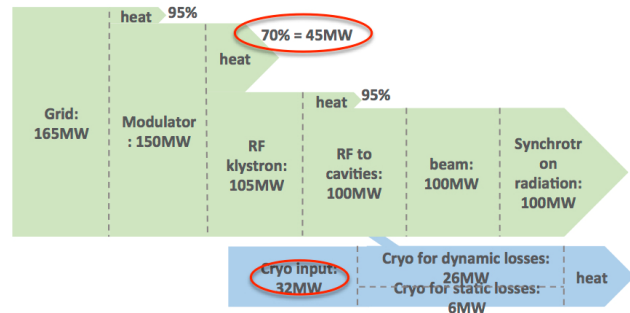


Figure 9: Energy consumption model for FCC-ee.

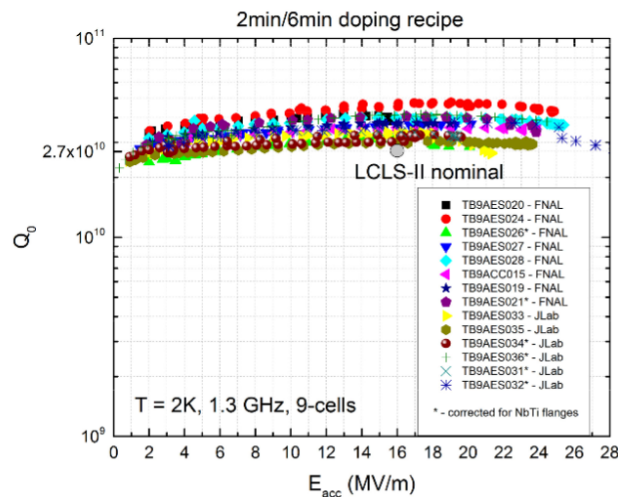


Figure 10: Cavity results after nitrogen doping for high Q_o, adopted by LCLS-II.

Table 2: CEPC Cavity Requirements

Cavity	Qualification	Normal Operation	Max. Operation
650 MHz 2-cell Cavity	VT 4E10 @ 22 MV/m HT 2E10 @ 20 MV/m	2E10 @ 16.5 MV/m	2E10 @ 20 MV/m
1.3 GHz 9-cell Cavity	VT 3E10 @ 25 MV/m	2E10 @ 20 MV/m	2E10 @ 23 MV/m

VT=Vertical Test, HT= Horizontal Test

BEAM STABILITY

Coupled Bunch Instabilities (CBI)

High current storage rings with many bunches are susceptible to collective instabilities driven by the ring impedance, and in particular the narrow band resonances from the RF cavities. Preliminary estimates of the thresholds for the four FCC-ee cases and CEPC were presented. As expected the lowest energy, highest current case has

the lowest threshold, figures 11, 12. However preliminary studies suggest that strongly HOM damped 1-cell cavities such as the JLab on-cell damped design can meet this requirement, figure 13, 14. For the higher energy, lower current cases two- or multi-cell cavities may be acceptable, but strong HOM damping will still be needed and the HOM power will be significant. A very preliminary look at CEPC requirements suggests that a HOM-damped 650 MHz 5-cell scaled from the JLab ERL cavity might be acceptable, figure 15 [2].

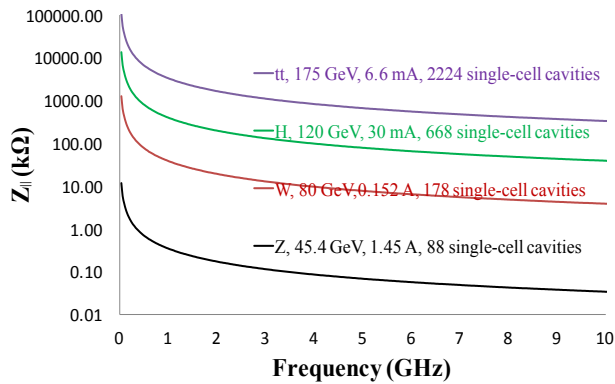


Figure 11: Estimated FCC longitudinal CBI thresholds. Note that the worst case is the lowest energy, highest current Z configuration.

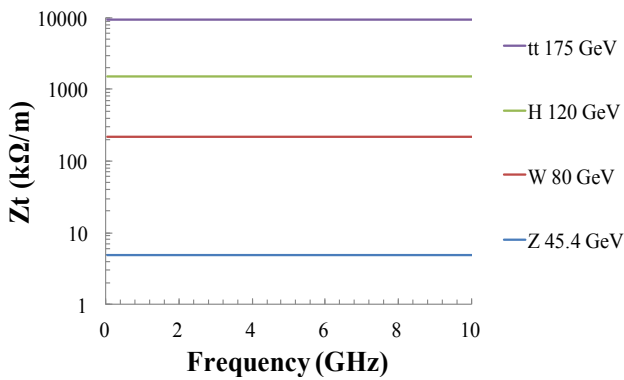


Figure 12: Estimated FCC transverse CBI thresholds.

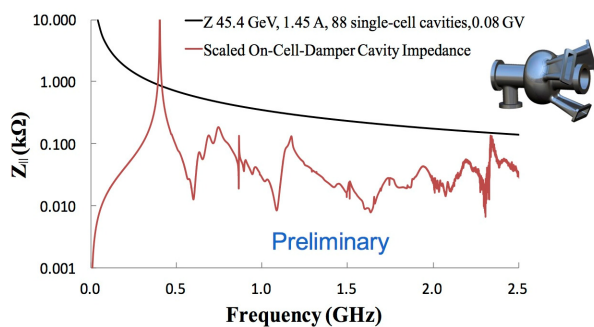


Figure 13: Estimated FCC-Z longitudinal threshold and impedance of the JLab heavily damped 1-cell cavity.

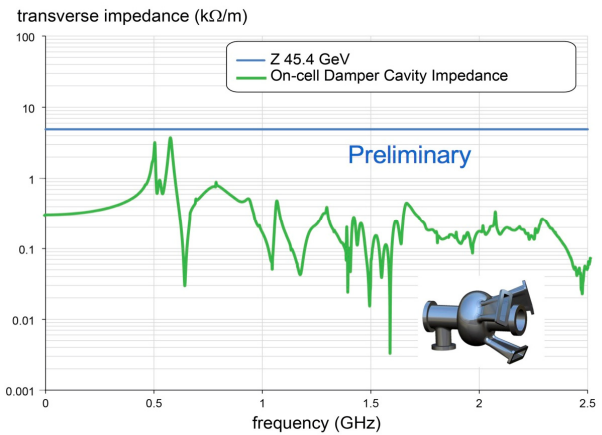


Figure 14: Estimated FCC-Z transverse CBI threshold and cavity impedance.

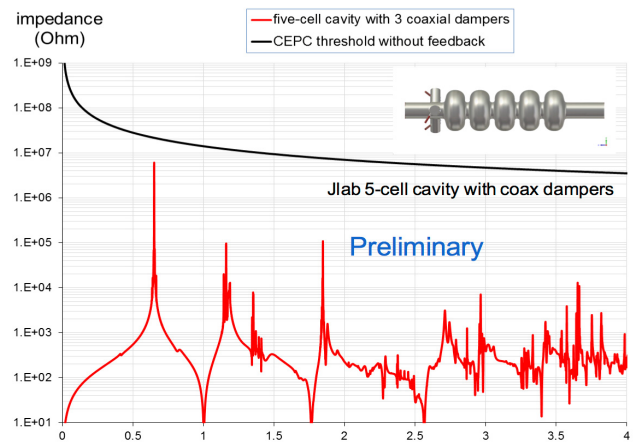


Figure 15: Estimated CEPC longitudinal threshold and impedance of a scaled 650 MHz 5-cell cavity.

With such high beam currents detuning of the fundamental mode will cross multiple revolution frequencies so sophisticated feedback systems such as those used in the B-factories will be needed. This may also have implications for klystron bandwidth and RF power overhead needed.

Robinson Stability and Transient Effects

Such heavily beam loaded RF systems rely on direct feedback to remain Robinson stable, but as the power approaches the klystron limit the stability margin decreases and the systems are less robust against disturbances. Since the rings must run with gaps for abort kickers and ion or perhaps e-cloud clearing, there will be significant amplitude and phase transients in the cavities. The B-factories mitigated this by using the shortest possible gaps (or multiple mini-gaps) and by trying to maintain even fill patterns. RF systems were programmed to learn and adapt to the transients to avoid saturating the klystrons. Transients were matched between the colliding rings to keep the collision point within the acceptable range of the detectors. Figure 14 shows the gap transient in the super KEK-B high-energy ring (HER) [5]. The response is complicated by the mixture of NCRF and SRF cavities. The ringing

during the gap results from the three-coupled-cavity ARES NCRF system. By shaping the current fill in the gap region and offsetting the gaps in the two rings it is possible to match the transients in the two rings to less than one degree of phase, figure 15 [5].

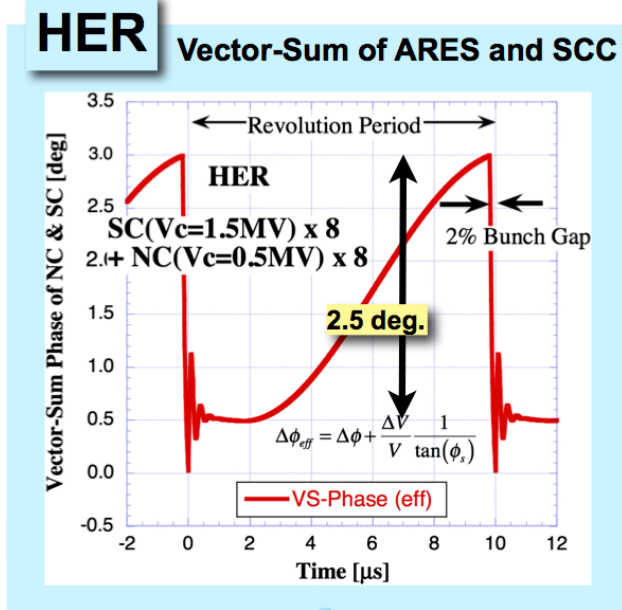


Figure 16: Phase transient in Super KEK-B HER due to beam gap. The ringing directly after the gap is from the ARES 3-cavity system.

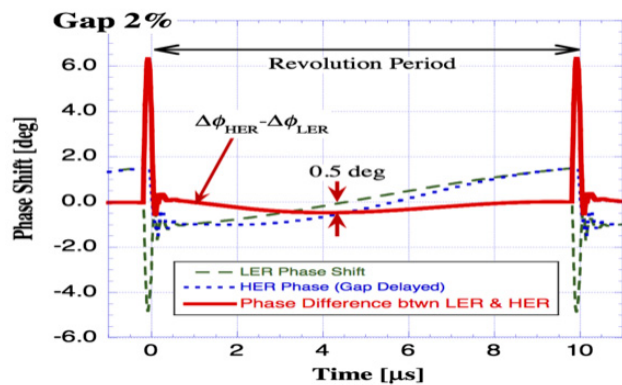


Figure 17: Residual Phase error between the HER and LER after shaping and offsetting the gaps in the two rings.

The new KEK digital LLRF system, figures 15, 16, has been fully commissioned, and features dedicated $m=-1, -2$ and -3 mode dampers to accommodate the large detuning needed in Super KEK-B, figure 17 [5].

The Newly developed digital LLRF control systems were applied to 9 stations in the HER, and successfully operated in phase I commissioning, in which the Super KEK-B rings were scrubbed before installation of the detector.

The $m=-1$ mode damper was tested in the HER, and the coupled bunch instability due to detuned cavities was suppressed successfully. The $m=-2$ and -3 mode damper systems will be implemented in Phase 2.

The CEPC single ring and partial-double rings also have a challenge with beam transients, because they cannot operate with a uniform or near uniform filling pattern. Because of the pretzel scheme intense bunch trains are needed with large gaps in between. Novel cavity detuning schemes such as detuning some cavities by one revolution frequency may be able to compensate the transient along the train providing the phase can recover during the gap. A higher fraction or complete double ring, although more costly, would mitigate this effect and allow higher luminosity.

All these effects will need careful study in the proposed future machines.

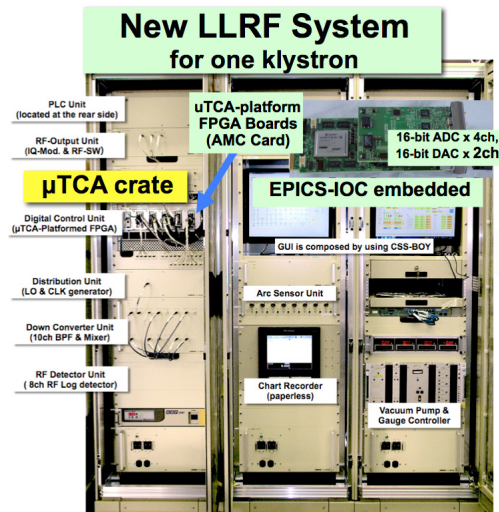


Figure 18: New KEK digital LLRF system.

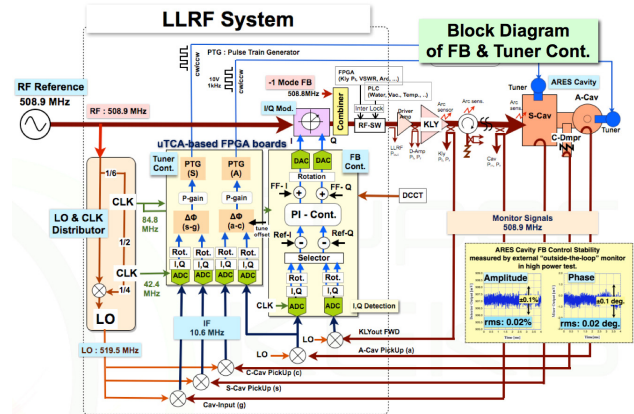


Figure 19: New KEK digital LLRF system schematic.

The $\mu=-2, -3$ mode Damper for SuperKEKB

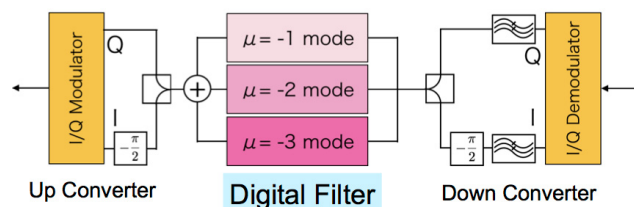


Figure 20: New mode $-1, -2, -3$ filters for super KEK-B.

POWER COUPLERS

The fundamental power coupler (FPC) is one of the most critical parts of any SCRF system [6]. They have high geometric complexity and need many different materials, joining technics, coating technics etc. In the end the cost is comparable to that of a cavity and power coupler failure can lead to serious contamination of the very delicate SC cavity surface. Recovery is time consuming and expensive and may severely impact machine operations. In light of this the couplers must be handled and assembled as cleanly as the cavity and should be qualified and conditioned separately before installation on the cavity.

Power couplers typically are either waveguide type or coaxial and may have planar or cylindrical ceramic windows, figure 21. Increasingly double-window configurations are being used on SRF cavities for additional security. CW power of 500-600 kW has been successfully transmitted into operating accelerators through a single coupler, although MW-class windows have been designed and tested.

Figure 22 shows the result of an arcing event in a high power coaxial coupler. Multiple interlocks monitoring vacuum, light, electronic activity, reflected power etc. should be installed to prevent such failures.

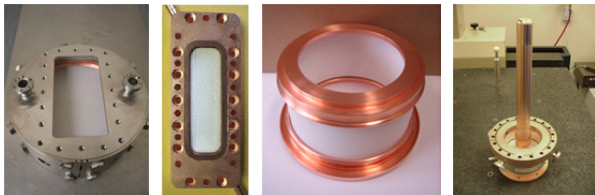


Figure 21: Examples of planar and cylindrical waveguide and coaxial windows.



Figure 22: Example of coaxial power window failure due to arcing.

HOM DAMPERS AND ABSORBERS

Just as critical as the fundamental power coupler, and not far behind in terms of cost and complexity, are the HOM couplers and absorbers. These must damp the dangerous HOMs to Q values that will ensure beam stability and extract or absorb the HOM power safely. They typically must operate close to the cavity and must therefore avoid particulate contamination or outgassing and must

reject the evanescent fundamental mode fields. Again these fall into two main types, coaxial antennas and waveguide types. Beam line absorbers that can absorb HOM power propagating away from the cavity above cut-off are a special case of circular waveguide damper. They have excellent power handling capability and are broadband but they must be spaced sufficiently far from the cavity to allow the fundamental mode to decay.

A number of highly HOM-damped cavities have been developed in the past for high-current storage rings, ERLs and future colliders [7]. The best HOM damping solution depends on beam requirements and practical constraints, and the HOM damping scheme should be developed as part of the cavity system optimization.

Important questions when selecting the HOM damper type include:

- Use single cell storage ring cavities or multi-cell ERL-type cavities?
- Do same order modes (SOMs) present a problem?
- Is damping through the FPC sufficient?
- How to deal with HOM power propagating through the beam pipes (short bunch length – high frequency part of the spectrum)?
- Which RF absorbing material to use?

Examples of existing or proposed HOM damper and absorber designs are shown in figures 23 - 26.

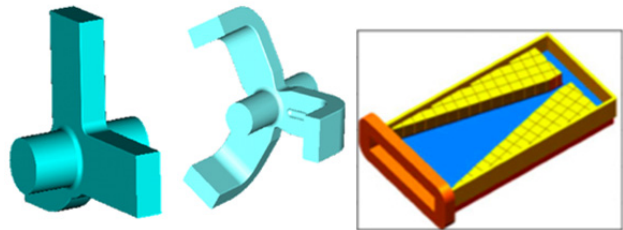


Figure 23: JLab original CEBAF and FEL waveguide HOM dampers and high power load.

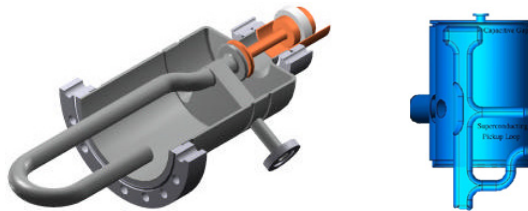


Figure 24: Original and later, modified hook type coaxial HOM couples.

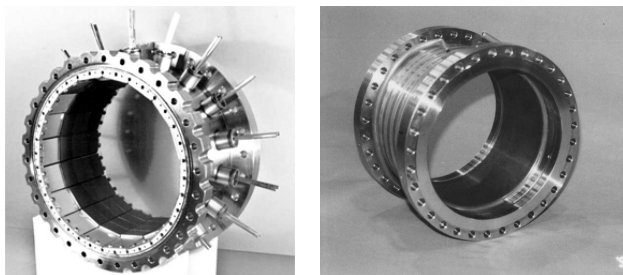


Figure 25: CESR and KEK-B type warm high power beam line HOM absorbers.

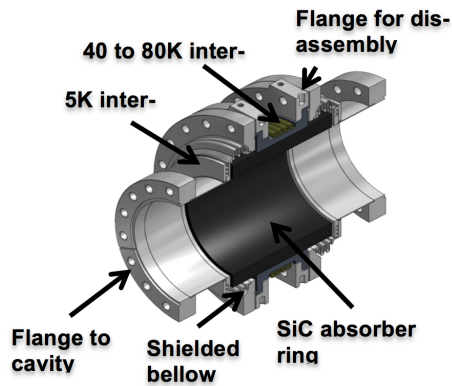


Figure 26: Cornell type cold beam line HOM absorber.

ALTERNATIVE MATERIALS

Recently interest has returned to niobium-tin (Nb_3Sn) as a promising material for higher efficiency and possibly also higher gradients. Recent work at Cornell [7] has shown that the previous Q-slope seen in earlier studies is not a fundamental property of Nb_3Sn , but a result of the forming process. New and exciting results, figure 27, show improved consistency and greatly reduced Q slope up to 16-17 MV/m. Ongoing work at Cornell and also Fermilab and JLab aims to exploit and extend this performance. Figure 28 shows the temperature dependent losses for Nb_3Sn compared to N_2 doped Nb cavities. If these residual resistances can be achieved in real cavities clearly 4K operation is not only viable but preferable.

Advantages of Nb_3Sn include:

- SRF operation at ~4K instead of 2K
- Greatly simplified cryo-system
- Greatly reduced cryo AC power

CERN's general strategy for SRF development is as follows [8]:

- Maintain Nb on Cu technology & infrastructure used for operational machines such as LHC.
- Establish state of the art infrastructure and performance of bulk Nb elliptical and crab cavities using existing recipes.
- R&D: Explore full potential of Nb on Cu, new materials, etc.

At CERN research is also underway into alternative materials, including A15 compounds (Nb_3Sn or V_3Si), on copper. This would add the advantage of a high conductivity substrate to the low losses of the SRF material. To avoid the very high temperature reaction of the “Wuppertal” process CERN is experimenting with sputtering from A15 material targets directly onto copper. Process parameters include:

- 5×10^{-4} mbar < p < 5×10^{-2} mbar
- Sputtering gas: Kr or Ar
- 150 mm alloy targets of Nb_3Sn or V_3Si
- Magnetron sputtering
- Flat samples + *in situ* substrate heating

Two approaches are being pursued, coating followed by annealing to obtain the A15 phase, and high temperature coating to obtain the A15 phase directly. Figure 30 shows the CERN experimental set up for sample studies.

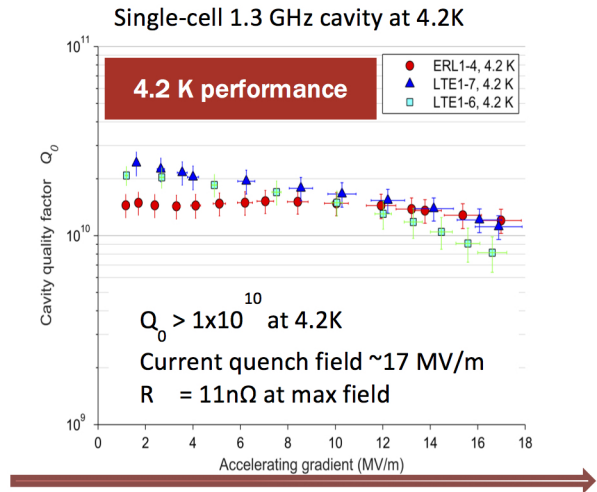


Figure 27: State of the Art and Repeatability of Nb_3Sn in cavity tests at Cornell.

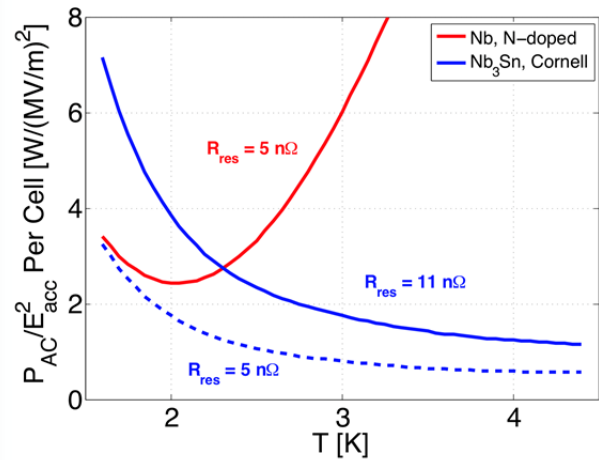


Figure 28: Temperature dependence of cavity losses for Nb_3Sn and N_2 doped Nb (Cornell).

As a first priority coating of spare LHC cavities is proceeding. Figure 29 shows an LHC cavity being prepared for coating. Process parameters are as follows:

- Intended $Q_0 \geq 2 \times 10^9$ @ 5 MV/m
- Cavity as UHV chamber
- Cavity = anode, grounded
- Nb cylindrical cathodes tubes
- Movable electromagnet inside, liquid cooled.
- DC-magnetron sputtering, 6.4 kW, 6.10^{-4} mbar Kr
- 1h 20' coating in 7 steps at low temp. (150°C)
- Layer thickness about 2 mm
- Production cycle = 1.5 month/cavity

Improved Nb on copper coating procedures are also being developed at JLab and CERN using energetic condensation methods such as biased ECR and HIPIMS [9],

figure 31. These methods supply additional energy to the incoming ions to enable high quality fully dense films to be grown without heating the substrate to excessive temperatures. Sample films have been tested in the CERN quadrupole resonator (QPR) and show greatly reduced Q-slope compared to traditional sputtered films, figure 30.



Figure 29: LHC spare cavity assembly for Nb coating.

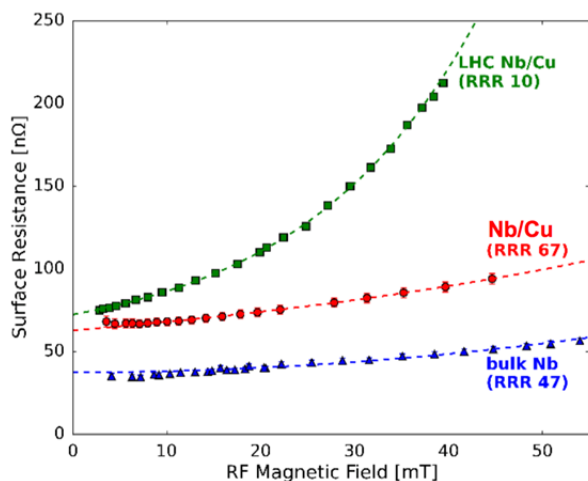


Figure 30: Surface resistance as a function of field for JLAB ECR films, showing greatly reduced non-linear losses (Q-slope). CERN HIPIMS films show very similar characteristics.

CERN is pursuing several FCC-ee prototypes cavities that will be fabricated by advanced spinning technology pioneered by INFN, Frascati. These include “H-machine” 800MHz 1- and 2-cell seamless cavities, and Z-machine” 400MHz 1 cell (+ 2-cells option). These will be fabricated as per the LHC cavities, but seamless. The copper cavities will then be coated with the best available thin film SRF technique.

ISBN 978-3-95450-187-8

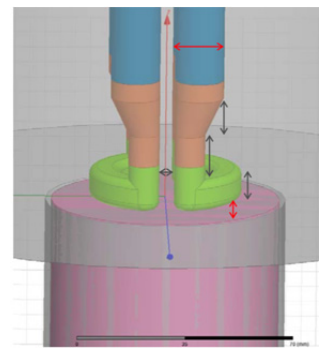


Figure 31: CERN HIPIMS cavity coating system and QPR sample test cavity concept.

CONCLUSIONS

- Good progress in all areas
- Much evidence of productive collaboration
- Valuable lessons and experience still coming from operating machines and new projects
- Much R&D still to be done on:
 - Cavity optimization
 - HOM dampers and loads
 - Power couplers
 - RF controls and gap transients
 - Prototypes and Proof-of-Principle tests

Many thanks to all the participants in this session.

REFERENCES

- [1] O. Brunner, “FCC RF System Parameters for Z, W, H and tt”, eeFACT2016, Daresbury, UK, October 2016, paper WET2H2.
- [2] R. Rimmer *et al.*, “State-of-the-Art SRF Cavities for CW Applications”, eeFACT2016, Daresbury, UK, October 2016, paper WET2H1.
- [3] N. Schwerg *et al.*, “Interrelationships and Limits”, eeFACT2016, Daresbury, UK, October 2016, paper WET2H3.
- [4] Peng Sha and Jiyuan Zhai “New Cavity Techniques and Future Prospects”, eeFACT2016, Daresbury, UK, October 2016, paper WET2H4.
- [5] T. Kobayashi and K. Akai, “LLRF Controls Including Gap Transients at KEKB and Plans for SuperKEKB”, eeFACT2016, Daresbury, UK, October 2016, paper WET2H7.
- [6] Wolf-Dietrich Möller, “High RF Power Couplers for New High Luminosity Colliders”, eeFACT2016, Daresbury, UK, October 2016, paper WET2H5.
- [7] Matthias Liepe, “Higher Order Modes in CW SRF Cavities and Very High Efficiency Nb₃Sn SRF Cavities for Future Circular Colliders”, eeFACT2016, Daresbury, UK, October 2016, paper WET2H6.
- [8] W. Venturini Delsolaro *et al.*, “SRF material R&D for FCC”, eeFACT2016, Daresbury, UK, October 2016, paper WET2H8.
- [9] A. Sublet *et al.*, “Superconducting Radio Frequency Cavities Coating Techniques”, eeFACT2016, Daresbury, UK, October 2016, paper WET2H9.

SUMMARY: JOINT SESSION OF OTHER TECHNOLOGIES AND ENERGY EFFICIENCY

W. Chou, IHEP, Beijing, China

Abstract

This paper summarizes the presentations and discussions at the joint session of “Other Technologies” and “Energy Efficiency.” It also highlights several key issues for R&D in these fields.

INTRODUCTION

For future high energy high luminosity e+e- colliders such as FCC-ee and CEPC, power consumption is a critical issue. The synchrotron radiation power for the two machines is 100 MW each in their present design. Due to limited efficiency to deliver energy to the beam, the wall plug power would be substantially higher than 100 MW. For example, Figure 1 shows the relative power consumption of each system in the CEPC design [1].

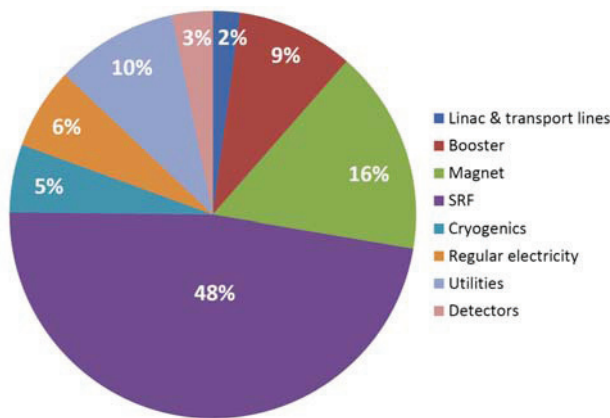


Figure 1: Relative power consumption of each system in the CEPC.

The total power is about 500 MW, which is almost an order of magnitude higher than the power consumption at Fermilab during Tevetron running (58 MW), and three times as high as that at CERN during the 2012 LHC running (183 MW). Assuming 4,000 hours for annual collider operation (i.e., 1.5 Snowmass unit), the electricity alone would cost RMB 1 billion (about USD 150 million). Apparently this is a key R&D item and one has to find a more efficient way to deliver power to the beam.

From Figure 1, it can be seen that the two biggest power consuming systems are SRF (48%) and magnet (16%). This session has two presentations on improving SRF system efficiency (high efficiency klystrons by David Constable and Ken Watanabe, respectively). And one presentation on improving magnet efficiency (Frank Zimmermann).

This session also has two presentations on beam dump, one by Armen Apyan on traditional beam dump, another by Alex Chao on a novel beam dump concept based on beam-plasma interaction. The latter has the potential to

recycle the dumped beam energy so the overall energy efficiency of the collider would be improved.

This session also has a presentation by Oleg Malyshev discussing NEG coating and its recent progress.

HIGH EFFICIENCY KLYSTRON

The wall power is delivered to the beam through a number of steps: modulators, klystrons, waveguides, SRF power coupler, cavity, etc. Among them, the klystron efficiency is the key because it is relatively low (40-50%) compared to other components. Therefore, in order to reduce the collider power consumption, one needs to focus on improving the klystron efficiency.

Constable presented the work of the HEIKA collaboration [2]. Its goal is to increase the efficiency of the FCC-ee HEKCW tube to 90%. The klystron uses multiple beams (16) and employs non-traditional bunching mechanism: one called core oscillation method (COM), another called bunching-alignment-collection (BAC) method. Figure 2 is an illustration of COM. As a proof-of-principle test, a SLAC 5045 S-band klystron has been retrofitted using the BAC scheme and is scheduled for testing in 2016. The efficiency is expected to increase from current 45% to 62.5%.

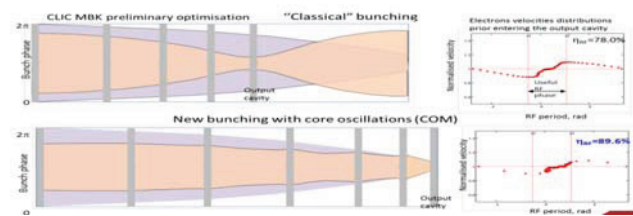
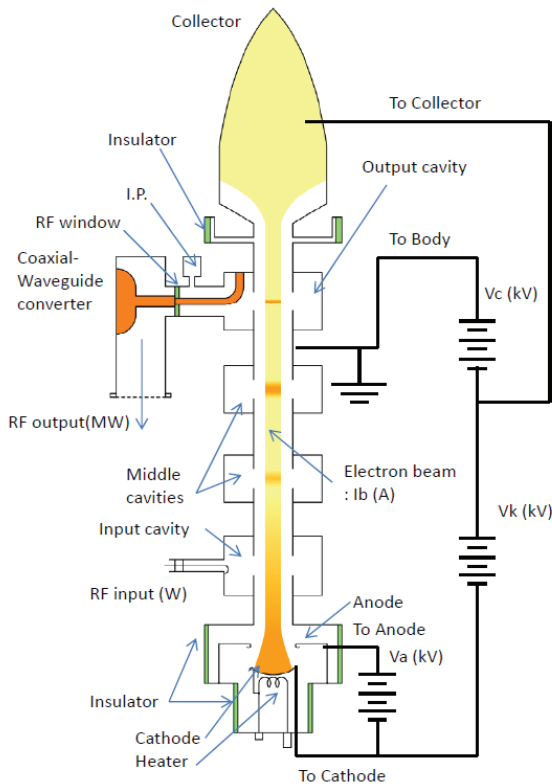


Figure 2: Comparison of the traditional bunching (top) and core oscillation method (COM, bottom). The simulation shows the latter has an efficiency of 89.6% (bottom right).

Watanabe reported the work at KEK in collaboration with Toshiba [3]. It uses a different method called collector potential depression (CPD), which was developed for gyrotron. An insulator is inserted between the body and the collector so a high voltage of Vc (30 kV) can be applied to the body for energy recovery. (Figure 3) A Toshiba E37703 tube was tested and the efficiency was increased from 42% (without CPD) to 62% (with CPD).



* Solenoid magnets set at outside of the cavities to focus the electron beam.

Figure 3: Illustration of a CPD klystron.

NEW MAGNET DRESIGN

Zimmermann presented a new twin-aperture design for FCC-ee dipoles and quadrupoles [4]. (Figures 4 and 5) In addition to their compact size, one big advantage is power saving. If two single aperture quads are used, the total power of the FCC-ee quadrupoles would be 43 MW. But for twin-aperture quads, it is reduced to 21.5 MW, a reduction of 50%.

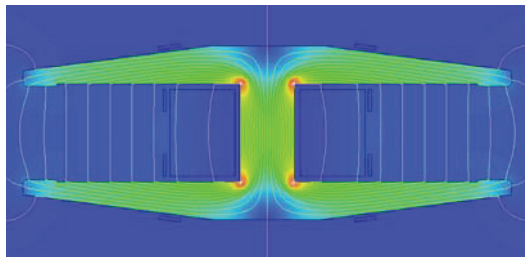


Figure 4: FCC-ee twin-aperture dipole.

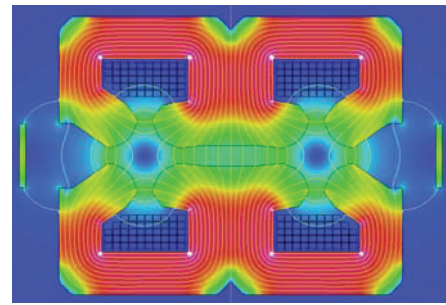


Figure 5: FCC-ee twin-aperture quadrupole.

BEAM DUMP

Apyan presented a design for the FCC-ee extraction line consisting of an abort kicker, a septum, a dilution kicker and an absorber [5]. (Figure 6) It is similar to the LEP beam dump but needs to absorb 0.4 MJ/beam. The absorber is made of aluminium and graphite.

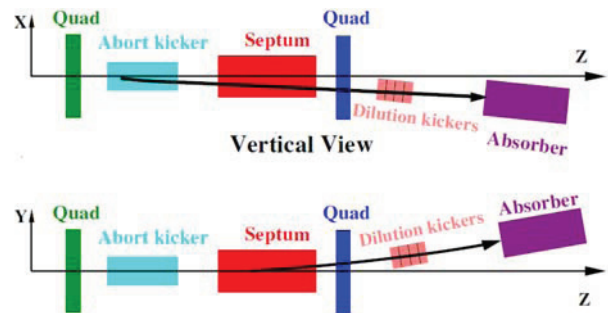


Figure 6: FCC-ee beam extraction line.

Chao reported the formation of a study group of “Green ILC Beam Dump,” including members from KEK, University of California at Irvine, ELI-NP, SLAC and LAPP/IN2P3 [6]. It is funded by JSPS. It uses plasma wakefield deceleration for beam dump replacing solid or liquid absorbers. (Figure 7) The simulation shows that when a beam is dumped into a plasma, it loses 15% of energy after 3 meters. In principle, the dumped energy can be recovered and turned into electricity.

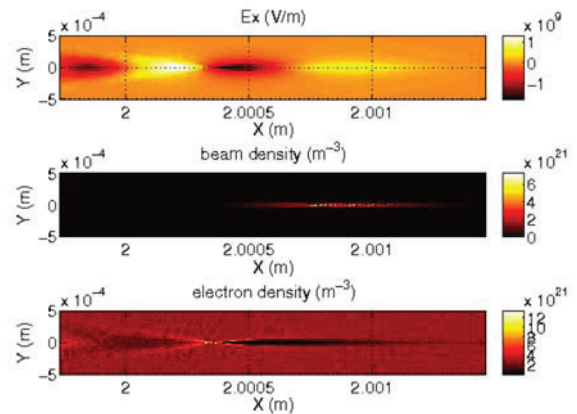


Figure 7: Plasma-beam deceleration simulation.

NEG COATING

Malyshev discussed the recent progress of the NEG coating technology. Unlike NEG strips, which act as a vacuum pump, NEG coating acts as a barrier that prevents gas particles (H_2 , CH_4 , CO , CO_2 , etc.) from being desorbed from the pipe surface. (Figure 8) The activation temperature is relatively low ($190\text{ }^\circ\text{C}$). It has been successfully applied in ESRF (France), ELETTRA (Italy), Diamond (UK), Soleil (France) and LHC straight sections. It is also the choice for the CEPC vacuum chamber eliminating the need of an antechamber (as in the LEP).

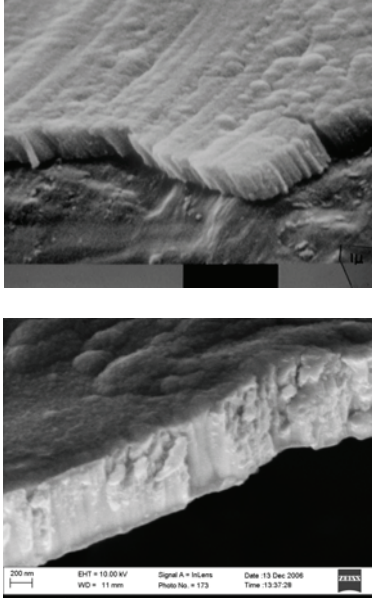


Figure 8: SEM image of NEG coating: top – columnar, bottom – dense.

REFERENCES

- [1] “CEPC-SPPC Preliminary Conceptual Design Report,” Volume II – Accelerator, March 2015, IHEP-CEPC-DR-2015-01, IHEP-AC-2015-01, <http://cepc.ihep.ac.cn/preCDR/volume.html>
- [2] D. Constable, “High Efficiency Klystron Development for Particle Accelerators”, presented at eeFACT2106 Workshop, UK, 2016.
- [3] K. Watanabe, “High efficiency klystron”, presented at eeFACT2106 Workshop, UK, 2016.
- [4] A. Milanese and F. Zimmermann, “New magnet design for FCC-ee”, presented at eeFACT2106 Workshop, UK, 2016.
- [5] A. Apyan, “Extraction line and beam dump for the future electron positron circular collider”, presented at eeFACT2106 Workshop, UK, 2016.
- [6] T. Saeki, A. Chao *et al.*, “Study on the international linear collider beam dump by plasma-wakefield deceleration”, presented at eeFACT2106 Workshop, UK, 2016.

List of Authors

Bold papercodes indicate primary authors

— A —			
Akai, K.	WET2H7	Gurran, L.	WET3AH1
Apyan, A.	WET3AH3	Guzilov, I.A.	WET3AH2
Aßmann, R.W.	THS1H1	— H —	
Aull, S.	WET2H3, WET2H8	Härer, B.	TUT3BH4
Aumon, S.	TUT3BH4	Hannah, A.N.	WET3AH1
— B —		Hayano, H.	WET3BH3
Baikov, A.Yu.	WET3AH2	He, J.	TUT3AH2
Barnyakov, A.M.	TUT2H5	Henry, J.	WET2H1
Belli, E.	TUT3AH1, TUT3AH7	Hill, V.C.R.	WET3AH2
Berkaev, D.E.	MOT3AH3	Holzer, B.J.	TUT3BH4
Biagini, M.E.	THS2H2	— I —	
Bian, T.J.	TUT2H3	Iida, N.	TUT2H5
Blondel, A.P.	MOT4H1, THS1H1, THS1H3	Ilyina, K.	WET2H8, WET2H9
Bogomyagkov, A.V.	MOT3AH4, MOT3BH1	— J —	
Brunner, O.	WET2H2, WET2H3	Jensen, A.	WET3AH2
Burt, G.	WET3AH1, WET3AH2	Jiao, Y.	TUT2H4
Butterworth, A.C.	WET2H3	Juda, P.	WET2H9
— C —		— K —	
Cai, Y.	TUT2H3	Kiselev, V.A.	MOT3AH4
Calatroni, S.	WET2H9	Kobayashi, T.	WET2H7
Castorina, G.	TUT3AH1	Koiso, H.	TUT3BH2
Chao, A.	WET3BH3, THS1H5	Koop, I.	MOT3AH3, MOT4H5
Chen, J.	TUT2H4	Koratzinos, M.	TUT1AH3, TUT2H3
Chou, W.	THS2H6, TUT3AH2	Kowalczyk, R.D.	WET3AH2
Constable, D.A.	WET3AH2	— L —	
Cropper, M.D.	TUT3AH0	Levichev, A.E.	TUT2H5
Cui, X.	TUT2H3	Levichev, E.B.	MOT3AH4, MOT3BH1
— D —		Liepe, M.	WET2H6
Doblhammer, A.	TUT3BH4	Lingwood, C.	WET3AH2
Drago, A.	TUT3AH9	Lou, X.C.	TUT1AH2
Duan, Z.	MOT4H2, TUT2H4	— M —	
— E —		Malyshev, O.B.	TUT3AH0, WET3AH1
Einfeld, D.	MOT4H4	Mane, S.R.	MOT4H7
— F —		Marchesin, R.	WET3AH2
Farinella, D.M.	WET3BH3	Marhauser, F.	WET2H1
Fujimoto, J.	WET3BH3	Marinov, K.B.	WET3AH1
Fukuma, H.	TUT3AH5, TUT3AH6, WET1H3, THS2H3	Marrelli, C.	WET3AH2
Funakoshi, Y.	MOT4H2, TUT3BH2, TUT3BH3, THS1H4	Migliorati, M.	TUT3AH7, TUT3AH1
Furukawa, K.	TUT2H5	Milstein, A.I.	MOT3AH4
— G —		Miyahara, F.	TUT2H5
Gao, J.	MOT3BH3, TUT1AH2, TUT2H3, TUT3AH2	Möller, W.-D.	WET2H5
Geng, H.	MOT3BH3	Morita, A.	TUT3BH2
Gianfelice-Wendt, E.	MOT4H6	Muchnoi, N.Yu.	WET1H4
Gong, D.J.	TUT3AH2	— N —	
Goudket, P.	WET3AH1	Natsui, T.	TUT2H2
		Nikiforov, D.A.	TUT2H5
		Novokhatski, A.	TUT3AH4

— O —

Ogur, S. **TUT2H5**
 Ohmi, K. **TUT1BH2, TUT3AH2, TUT3AH5,**
TUT3AH6
 Ohnishi, Y. **TUT1AH1, TUT3BH2**
 Oide, K. **MOOTH1, TUT2H5, TUT3BH2,**
TUT3BH4, WET3AH3, THS1H2
 Otboev, A.V. **MOT4H5**

— P —

Palmer, R.B. **TUT1AH4**
 Papaphilippou, Y. **TUT2H5**
 Parker, B. **TUT1AH4**
 Peng, Y.M. **TUT2H4**
 Perevedentsev, E. **MOT3AH3**
 Perret-Gallix, D. **WET3BH3**
 Persichelli, S. **TUT3AH1**

— Q —

Qin, Q. **MOOTH3, MOT3BH3, TUT3AH2**

— R —

Ratoff, P.N. **THS2H5**
 Richard, T. **WET2H9**
 Rimmer, R.A. **WET2H1, THS2H4**
 Rogovsky, Yu. A. **MOT3AH3**
 Rosaz, G.J. **WET2H8, WET2H9**
 Rumolo, G. **TUT3AH7**

— S —

Saeki, T. **WET3BH3**
 Satoh, D. **TUT2H2**
 Schwerg, N. **WET2H3**
 Seeman, J.T. **TUT2H1, WET1H1, THS1H6**
 Sha, B. **TUT1AH2, TUT2H3**
 Sha, P. **WET2H4**
 Shatilov, D.N. **MOT3AH4, TUT1BH1**
 Shatunov, P.Yu. **MOT3AH3**
 Shatunov, Y.M. **MOT3AH3, MOT4H5**
 Shwartz, D.B. **MOT3AH3**
 Sian, B.S. **TUT3AH0**
 Sinyatkin, S.V. **MOT3AH4, MOT3BH2**
 Smaluk, V.V. **TUT3AH3, WET1H2**
 Spataro, B. **TUT3AH1**
 Su, F. **MOT3BH3, TUT2H3**
 Sublet, A. **WET2H9**
 Suetsugu, Y. **TUT3AH6**
 Sugimoto, H. **TUT3BH2**
 Sun, Y.S. **TUT3AH2**
 Syrathev, I. **WET3AH2**

— T —

Tajima, T. **WET3BH3**
 Teichert, J. **TUT2H6**
 Teytelman, D. **TUT3AH8**
 Therasse, M. **WET2H3**
 Tobiyama, M. **TUT3AH5, TUT3AH6**
 Turlington, L. **WET2H1**

— V —

Valizadeh, R. **TUT3AH0, WET3AH1**
 Venturini Delsolaro, W. **WET2H8, WET2H9**

— W —

Wang, D. **MOT3BH3, TUT1AH2, TUT2H3,**
TUT3AH2
 Wang, H. **WET2H1**
 Wang, N. **TUT3AH2**
 Wang, Q.Y. **TUT2H4**
 Wang, S. **WET2H1**
 Wang, S. **TUT3AH0**
 Wang, Y. **MOT3BH3, TUT1AH2, TUT2H3,**
TUT3AH2
 Watanabe, K. **WET3BH1**
 Wilde, S. **WET3AH1**

— X —

Xia, G.X. **TUT3AH0**
 Xiang, R. **TUT2H6**
 Xiao, M. **TUT2H3**
 Xiu, Q.L. **TUT1AH2**
 Xu, G. **TUT2H4, TUT3AH2**

— Y —

Yokoya, K. **WET3BH3**
 Yoshida, M. **TUT2H2**

— Z —

Zeng, M. **WET3BH3**
 Zhai, J.Y. **WET2H4**
 Zhang, C. **TUT2H3**
 Zhang, P. **TUT2H4**
 Zhang, R. **TUT2H2**
 Zhang, X. **WET3BH3**
 Zhang, Y. **MOT3BH3, TUT3AH2**
 Zheng, H.J. **TUT3AH2**
 Zhou, D. **TUT3AH2**
 Zhou, X. **TUT2H2**
 Zhu, H. **TUT1AH2**
 Zimmermann, F. **MOT3AH2, TUT2H5, WET3AH3,**
THS1H1, THS2H1
 Zobov, M. **TUT3AH1**

Institutes List

ANSL

Yerevan, Armenia

- Apyan, A.

BINP SB RAS

Novosibirsk, Russia

- Barnyakov, A.M.
- Berkaev, D.E.
- Bogomyagkov, A.V.
- Kiselev, V.A.
- Koop, I.
- Levichev, A.E.
- Levichev, E.B.
- Milstein, A.I.
- Muchnoi, N.Yu.
- Nikiforov, D.A.
- Otboev, A.V.
- Perevedentsev, E.
- Rogovsky, Yu. A.
- Shatilov, D.N.
- Shatunov, P.Yu.
- Shatunov, Y.M.
- Shwartz, D.B.
- Sinyatkin, S.V.

BNL

Upton, Long Island, New York, USA

- Palmer, R.B.
- Parker, B.
- Smaluk, V.V.

CERN

Geneva, Switzerland

- Aßmann, R.W.
- Aull, S.
- Aumon, S.
- Belli, E.
- Brunner, O.
- Butterworth, A.C.
- Calatroni, S.
- Doblhammer, A.
- Härer, B.
- Holzer, B.J.
- Ilyina, K.
- Juda, P.
- Ogur, S.
- Papaphilippou, Y.
- Richard, T.
- Rosaz, G.J.
- Rumolo, G.
- Schwerg, N.
- Sublet, A.
- Syrathev, I.
- Therasse, M.
- Venturini Delsolaro, W.
- Zimmermann, F.

Cockcroft Institute, Lancaster University

Lancaster, United Kingdom

- Burt, G.
- Gurran, L.
- Hill, V.C.R.
- Lingwood, C.

Cockcroft Institute

Warrington, Cheshire, United Kingdom

- Burt, G.

Convergent Computing

Shoreham, New York, USA

- Mane, S.R.

Cornell University (CLASSE), Cornell Laboratory for Accelerator-Based Sciences and Education

Ithaca, New York, USA

- Liepe, M.

DESY

Hamburg, Germany

- Möller, W.-D.

Dimtel

San Jose, USA

- Teytelman, D.

DPNC

Genève, Switzerland

- Blondel, A.P.
- Koratzinos, M.

ESRF

Grenoble, France

- Einfeld, D.

ESS

Lund, Sweden

- Marrelli, C.

Fermilab

Batavia, Illinois, USA

- Chou, W.
- Gianfelice-Wendt, E.

HZDR

Dresden, Germany

- Teichert, J.
- Xiang, R.

IFIN-HH

Bucharest - Magurele, Romania

- Zeng, M.

IHEP

Beijing, People's Republic of China

- Bian, T.J.
- Chen, J.
- Chou, W.
- Cui, X.
- Duan, Z.
- Gao, J.
- Geng, H.
- Gong, D.J.
- He, J.
- Jiao, Y.
- Lou, X.C.
- Peng, Y.M.
- Qin, Q.
- Sha, B.
- Sun, Y.S.
- Wang, D.
- Wang, N.
- Wang, Q.Y.
- Wang, Y.
- Xiao, M.
- Xiu, Q.L.
- Xu, G.
- Zhai, J.Y.
- Zhang, C.
- Zhang, P.
- Zhang, Y.
- Zheng, H.J.
- Zhu, H.

IN2P3

Paris, France

- Perret-Gallix, D.

INFN-Roma1

Rome, Italy

- Migliorati, M.

INFN-Roma

Roma, Italy

- Belli, E.

INFN/LNF

Frascati (Roma), Italy

- Biagini, M.E.
- Castorina, G.
- Drago, A.
- Spataro, B.
- Zobov, M.

Institute of High Energy Physics (IHEP), Chinese Academy of Sciences

Beijing, People's Republic of China

- Sha, P.

Institute of High Energy Physics (IHEP)

People's Republic of China

- Su, F.

JLab

Newport News, Virginia, USA

- Henry, J.
- Marhauser, F.
- Rimmer, R.A.
- Turlington, L.
- Wang, H.
- Wang, S.

JSC Vacuum Devices Basic Technologies

Moscow, Russia

- Guzilov, I.A.

KEK

Ibaraki, Japan

- Akai, K.
- Fujimoto, J.
- Fukuma, H.
- Funakoshi, Y.
- Furukawa, K.
- Hayano, H.
- Iida, N.
- Kobayashi, T.
- Koiso, H.
- Miyahara, F.
- Morita, A.
- Natsui, T.
- Ohmi, K.
- Ohnishi, Y.
- Oide, K.
- Saeki, T.
- Satoh, D.
- Suetsugu, Y.
- Sugimoto, H.
- Tobiyama, M.
- Watanabe, K.
- Yokoya, K.
- Yoshida, M.
- Zhang, R.
- Zhou, D.
- Zhou, X.

KIT

Karlsruhe, Germany

- Härer, B.

L-3

Williamsport, Pennsylvania, USA

- Kowalczyk, R.D.

Lancaster University

Lancaster, United Kingdom

- Burt, G.
- Constable, D.A.
- Gurran, L.
- Ratoff, P.N.

LBNL

Berkeley, California, USA

- Persichelli, S.

Loughborough University

Loughborough, Leicestershire, United Kingdom

- Cropper, M.D.
- Wilde, S.

MFUA

Moscow, Russia

- Baikov, A.Yu.

NSU

Novosibirsk, Russia

- Perevedentsev, E.
- Rogovsky, Yu. A.
- Shatunov, Y.M.

SLAC

Menlo Park, California, USA

- Cai, Y.
- Chao, A.
- Jensen, A.
- Novokhatski, A.
- Seeman, J.T.

- Goudket, P.
- Gurran, L.
- Hannah, A.N.
- Malyshev, O.B.
- Marinov, K.B.
- Sian, B.S.
- Valizadeh, R.
- Wang, S.
- Wilde, S.

TED

Velizy, France

- Marchesin, R.

UCI

Irvine, California, USA

- Farinella, D.M.
- Tajima, T.
- Zhang, X.

UMAN

Manchester, United Kingdom

- Sian, B.S.
- Xia, G.X.

University of Rome "La Sapienza"

Rome, Italy

- Belli, E.

University of Rome La Sapienza

Rome, Italy

- Migliorati, M.

STFC/DL/ASTeC

Daresbury, Warrington, Cheshire, United Kingdom